Deliverable No. 2.4

Public Summary Report of WP2

Grant Agreement no.:	945253
Project Title:	**Advanced PTS Analysis for LTO**
Contractual Submission Date:	30/09/2022
Actual Submission Date:	31/03/2023
Responsible partner:	P1: UJV Rez, a. s. (UJV)

Grant agreement no.	945253
Project full title	Advanced PTS Analysis for LTO

Deliverable number	**D2.4**
Deliverable title	**Public Summary Report of WP2**
Type[1]	R
Dissemination level[2]	PU
Work package number	WP2
Work package leader	P1 - UJV
Author(s)	Pavel Kral and Tomas Nikl and Martin Kratochvil (UJV), Richard Trewin (Fra-G), Markku Puustinen and Giteshkumar Patel (LUT), Ivor Clifford and Gregory Perret (PSI), Andrej Prošek (JSI), Stefan Wenzel and Jürgen Hartung and Inés Mateos Canals (GRS), Piotr Mazgaj (WUT), Lukasz Sokolowski (KIWA), Maksym Vyshemirskyi (SSTC), Vladislav Filonov and Yuliia Filonova and Yaroslav Dubyk (IPP), Jerome Roy (IRSN), Takeshi Takeda and Jinya Katsuyama (JAEA)
Keywords	Pressurized thermal shock, best estimate plus uncertainty, long term operation, reactor pressure vessel, loss-of-coolant accident, emergency core cooling system, system code, mixing code, computational fluid dynamics, human interactions.

---

[1] **Type**: Use one of the following codes (in consistence with the Description of the Action):
    R: Document, report (excluding the periodic and final reports)
    DEM: Demonstrator, pilot, prototype, plan designs
    DEC: Websites, patents filing, press & media actions, videos, etc.
    OTHER: Software, technical diagram, etc.

[2] **Dissemination level**: Use one of the following codes (in consistence with the Description of the Action)
    PU: Public, fully open, e.g. web
    CO: Confidential, restricted under conditions set out in the Model Grant Agreement
    CI: Classified, information as referred to in Commission Decision 2001/844/EC

Table of Contents

List of Figures

13

List of Abbreviations

abs	absolute
ACC	accumulator
AMB	ambient
APAL	Advanced PTS Analysis for LTO
ATHLET	Analysis of THermal-hydraulics of LEaks and Transients
BC	Boundary Condition
BEPU	best estimate plus uncertainty
BREAK	TRACE component
BZN	Bay Zoltán Alkalmazott Kutatási Közhasznú Nonprofit Korlátolt Felelősségű Társaság
C1	UPTF test series
CALC	calculated
CAMP	Code Applications and Maintenance Program
CCFL	countercurrent flow limitation
CCO	cross connection object
CDF	cumulative density function
CFD	computational fluid dynamics
CL	cold leg
CVCS	chemical and volume control system
DC	downcomer of reactor pressure vessel
DCC	direct-contact condensation
DFM	deterministic fracture mechanical
ECC	emergency core cooling
ECCS	emergency core cooling system
EOP	emergency operating procedures
EXP	experimental
FEBA	Flooding Experiments with Blocked Arrays
FILL	TRACE component
FOM	figure of merit
GRS	Association for Reactor Safety (German: Gesellschaft für Reaktorsicherheit)
HCO	heat conduction object
HL	hot leg
HP	high pressure
HPI	high Pressure injection
HPSI	high-pressure safety injection
HTC	heat transfer coefficient
ICAS	International Comparative Assessment Study
ID	identifier
JSI	Jožef Stefan Institute
KIWA	Kiwa Inspecta Technology AB
KWU	Kraftwerk Union AG
LOCA	loss-of-coolant accident
LOOP	loss of offsite power
LP	low pressure
LPI	low pressure injection
LPSI	low-pressure safety injection
LTO	long-term operation
LUT	Lappeenranta-Lahti University of Technology (LUT University)
MCP	main coolant pump
MIX	mixing

MR	management review
MR	modelling region
MSLB	main steam line break
MW	megawatt
N/A	not applicable
N2	nitrogen
NPP	nuclear power plant
OpenFOAM	Open-source Field Operation And Manipulation
PFM	probabilistic fracture mechanical
PI	panel interfaces
PIRT	phenomena identification and ranking table
PRZ	pressuriser
PSI	Paul Scherrer Institut
PTS	pressurized thermal shock
PWR	pressurized-water reactor
RANS	Reynolds-Averaged Navier Stokes
RELAP	Reactor Excursion and Leak Analysis Program
RHR	residual heat removal
RPV	reactor pressure vessel
SB	small break
SBLOCA	small-break loss-of-coolant accident
SI	international system of units
SIS	safety-injection system
SJP	single-junction pipe
SNAP	Symbolic Nuclear Analysis Package
SSC	systems, structures, and components
SSTC	State Enterprise "State Scientific and Technical Center for Nuclear and Radiation Safety"
TDV	time-dependent volume
TE	turbine equipment
TF	time frame
TFO	thermo-fluid objects
TH	thermal-hydraulic
TM	team member
TRACE	TRAC/RELAP Advanced Computational Engine
TRAM	Transient and Accident Management
UH	upper head
UJV	Ústav jaderného výzkumu Řež (in English: Nuclear Research Institute, Rez)
UPTF	Upper Plenum Test Facility
UQ	uncertainty quantification
USNRC	U.S. Nuclear Regulatory Commission
VESSEL	TRACE component
WUT	Warsaw University of Technology

List of Symbols

A_{CL}	flow area of cold leg, m^2
A_{cold}	flow area of cold-water layer, m^2
A_{hot}	flow area of hot-water layer, m^2
A^*	ratio of cold-water to cold-leg flow areas, -
B	characteristic width of velocity profile of jet, m
B_0	width of the jet at the origin, m
B_ρ	characteristic width of density profile of jet, m
C_{CCFL}	constant in CCFL correlation, -
C_{loss}	constant in pressure-loss correlation, -
D_{CL}	diameter of cold leg, m
D_{inj}	diameter of injection pipe, m
Fr_{cold}	Froude number of cold-water layer, -
Fr_{ent}	Froude number in entrainment model, -
Fr_{hot}	Froude number of hot -water layer, -
Fr_{inj}	Froude number of injected water, -
g	gravitational constant, m/s^2
I_1 to I_6	distribution integrals, -
L_{cold}	height of cold-water layer, m
L_{hot}	height of hot-water layer, m
P	density difference between plume centerline and ambient, kg/m^3
r	coordinate perpendicular to the jet axis, m
s	coordinate along the jet axis, m
T_a	ambient temperature, °C
T_0	temperature of the jet at the origin, °C
u_c	centerline velocity of jet, m/s
u_{ent}	velocity of entrained liquid, m/s
u_{inj}	velocity of injected water, m/s
u_0	uniform velocity of jet at the origin, m/s
$\dot{V}_{cold}$	volumetric flow rate of cold-water layer, m^3/s
$\dot{V}_{hot}$	volumetric flow rate of hot-water layer, m^3/s
$\dot{V}_{inj}$	volumetric flow rate of injected water, m^3/s
$\dot{V}_{hot,max}$	maximum volumetric flow rate of hot (entrained) water, m^3/s
$\dot{V}^*$	ratio of hot-water to injected volumetric flows, -
$\dot{V}^*{}_{max}$	maximum value of $\dot{V}^*$, -
W	width of interface between hot-water and cold-water layers, m
z	vertical coordinate, m

<u>Greek symbols</u>

α_{jet}	entrainment coefficient for a pure jet, -
α_{plume}	entrainment coefficient for a pure plume, -
Δp_{loss}	pressure loss due to interfacial friction, Pa
ξ	pressure-loss coefficient, -
λ	ratio of characteristic widths for density deficiency and velocity, -
ρ	density, kg/m^3
ρ^*	ratio of densities for hot water to injected water, -
ρ_a	ambient density, kg/m^3
ρ_c	density at centerline of jet, kg/m^3
ρ_{cold}	density of cold-water layer, kg/m^3
ρ_{hot}	density of hot-water layer, kg/m^3
ρ_{inj}	density of injected water, kg/m^3

ρ_l characteristic density of ambient water, kg/m^3
ρ_0 density of the jet at the origin, kg/m^3

<u>Other symbols</u>
{ }   indicates functional arguments

Subscripts

c   coolant conditions
g   vapour phase/gas
l   liquid phase
sat   saturation conditions
w   wall

1   Introduction

APAL (Advanced PTS Analysis for LTO) is a project funded by the EU within HORIZON 2020 programme. One of the most limiting safety assessments for the long-term operation (LTO) of nuclear power plants (NPPs) is the reactor pressure vessel (RPV) integrity assessment for pressurized thermal shock (PTS). The main objectives of APAL project are establishment of state-of-the-art of LTO improvements having an impact on PTS analysis, development of advanced deterministic and probabilistic PTS assessment methods including thermal hydraulic (TH) uncertainty analyses, the quantification of safety margins for LTO improvements and the development of best-practice guidance. The APAL project consists of 7 work packages (WP):

- WP1 - LTO improvements relevant for PTS event
- **WP2 - Improvement of TH analysis**
- WP3 - Deterministic margin assessment
- WP4 - Probabilistic margin assessment
- WP5 - Definition of best-practice for advanced PTS analysis
- WP6 - Training, Communication, Dissemination and Exploitation
- WP7 - Scientific coordination and project management

This report describes the work and results of WP2 "Improvement of TH analysis". The main objective of the WP2 was the identification and evaluation of uncertainties of thermal-hydraulic (TH) analysis in the frame of PTS assessment. Besides the model uncertainties connected with computer code models and plant uncertainties covering initial and boundary conditions and parameters of nuclear power plant (NPP) systems, the work was also focused on uncertainties connected with human factors. A better assessment of the uncertainties in the thermal hydraulic data was helpful for quantifying their contributions to the overall reactor pressure vessel (RPV) integrity margins and it will provide more insights on the whole PTS analysis. In addition, the effect of selected LTO improvements relevant for PTS analysis (WP1) was analysed at the TH level in WP2. The WP2 consisted of 3 tasks:

In Task 2.1 *Quantification of impact of LTO improvements and human factor on TH analysis boundary conditions*, TH analysis for the base case (SBLOCA with 50 cm^2 break in hot leg (HL) and with loss of offsite power) was performed. Subsequently, analyses for selected LTO improvements were performed. Further, the effect of selected human interactions was evaluated with the help of TH simulations. TH data sets representing selected LTO improvements or human factor were delivered to WP3 and WP4 for deterministic fracture mechanical (DFM) and probabilistic fracture mechanical (PFM) analysis.

In Task 2.2 *Evaluation of uncertainties in TH analysis related to computer code models, plant parameters, and human factors*, uncertainties in thermal-hydraulic analyses for PTS were assessed. Three types of uncertainties were investigated: model uncertainties (connected with computer-code models and the correct prediction of relevant phenomena), plant uncertainties covering initial and boundary conditions and parameters of the NPP systems, and uncertainties connected with human interaction. The determination of the most relevant and important phenomena and parameters for the TH loading during PTS were compiled in a phenomena identification and ranking table (PIRT). Specified and quantified TH input uncertainties related to each computer code model used, plant parameters, and human factors are summarized in this report.

In the Task 2.3 *Performance of the TH uncertainty analysis and export of TH data sets* the uncertainty analyses of SBLOCA in 1300 MWe PWR were performed. The input uncertainties and their distributions were based on results of Task 2.2 of APAL. The system thermal-hydraulic and mixing calculations were done with several different computer codes and statistical tools. Defined sets of resulting TH data were prepared – enveloping single set and best-estimate single set of TH data plus a statistical set of TH data (e.g., 59 sets of TH data for one-side tolerance limit according to Wilk's method [1][2]). These TH data sets were transferred to structural and fracture mechanic analyses within WP3 and WP4 of APAL.

1.1   Structure of report

Sections 2 and 3 are common to all Tasks of WP2: Section 2 provides a short description of the reactor design specifications which is used as a basis for the simulation models in Task 2.1. Used computer codes and simulation models are presented in Section 3.

Sections 4 to 8 describes work in Task 2.1 *Quantification of impact of LTO improvements and human factor on TH analysis boundary conditions*: Results of the base case are provided in Section 4. Effect of LTO improvements and human factor is analysed in Section 5 and Section 6, respectively. Section 7 presents results of supplementary long-term analyses. Comparison and evaluation of impact of LTO improvements and human factor is done in Section 8.

Sections 9 to 11 describe work in Task 2.2 *Evaluation of uncertainties in TH analysis related to computer code models, plant parameters, and human factors*: Section 9 documents development of PIRT. The theory of Wilk's method and other UE methods are described in Section 10. Section 11 documents quantification of the uncertainties in the parameters for the boundary and initial conditions and plant design, quantification of the uncertainties in the parameters of the computer models, and quantification of the uncertainties in the parameters for the human factors.

Sections 12 to 20 describe performance and evaluation of uncertainty analyses in Task 2.3 *Performance of the TH uncertainty analysis and export of TH data sets*: Section 12 to 19 contain results of UJV with RELAP5, Framatome with KWU-MIX, JSI with RELAP, WUT with RELAP5, KIWA with RELAP5, SSTC with RELAP5, GRS with ATHLET, and PSI with TRACE, respectively. Section 20 presents comparison of results of the uncertainty analyses.

Section 21 concludes the WP2 of the APAL project.

1.2   Acknowledgement

2 Reactor design specifications

2.1 Reactor design

The assumed plant type used in the analysis presented in this report was a German design 1300 MW four-loop PWR. The same reactor design was used earlier in the International Comparative Assessment Study of Pressurized-Thermal-Shock in Reactor Pressure Vessels (ICAS/RPV-PTS) under the Organization for Economic Co-operation and Development (OECD) [3]. The ICAS Project brought together an international group of experts from research, utility and regulatory organizations to perform a comparative evaluation of analysis methodologies employed in the assessment of RPV integrity under PTS loading conditions.

The internal measurements of the fictitious RPV and the cold legs (CLs) to be used in the analysis in the APAL project correspond to those of the Upper Plenum Test Facility (UPTF) in Mannheim, Germany. In order to harmonize the calculation models used in the TH analysis and structural mechanics a CAD model of the RPV was developed by PSI and provided to all participants. The model was based on the geometry of the RPV used in the ICAS project but had a larger wall thickness and modified inlet and outlet nozzles. Figure 1 through Figure 4 present the geometry of the RPV used in the TH and structural analysis in the APAL project.
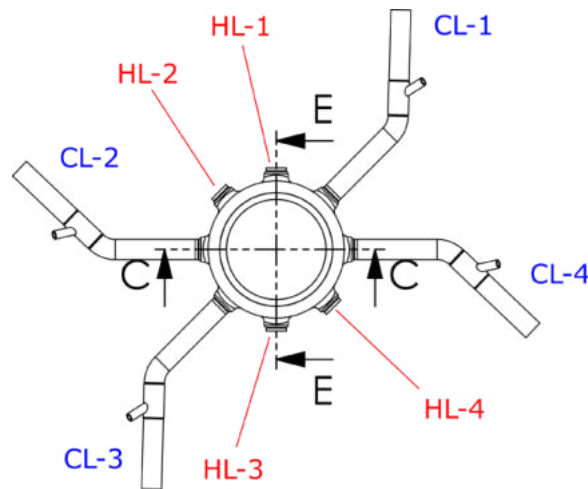
Figure 1: Top View showing the Layout of the Hot and Cold Legs.
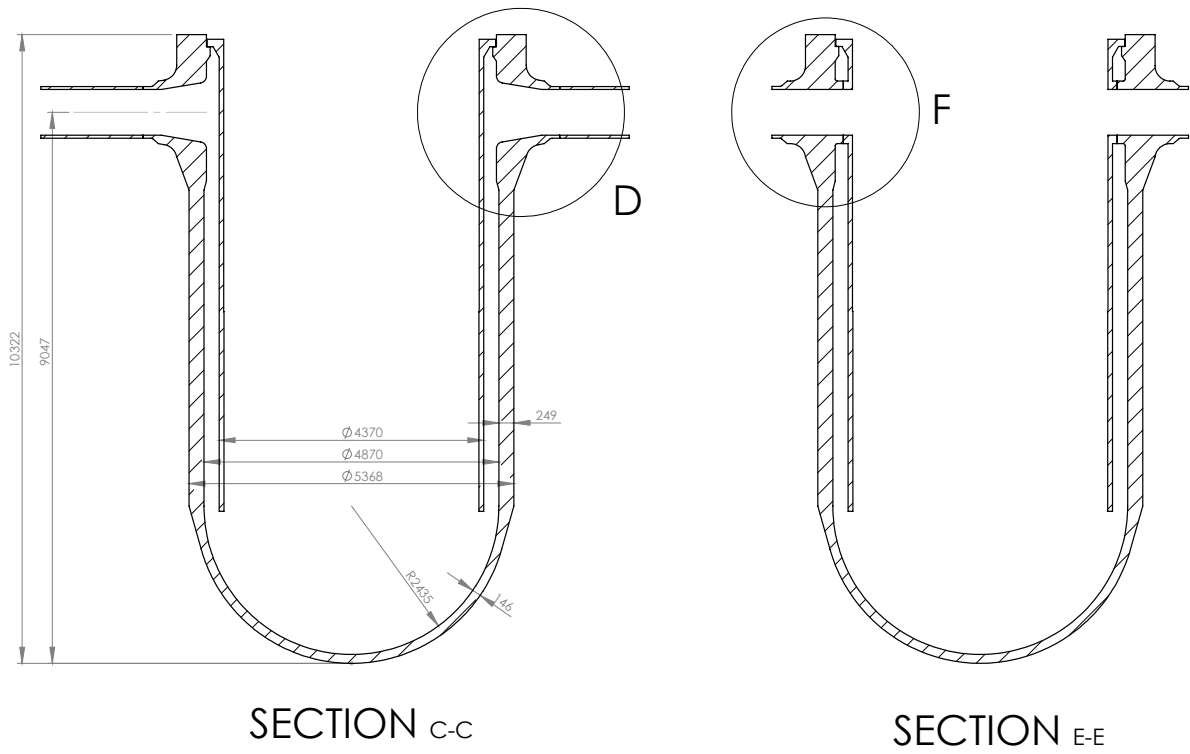
Figure 2: Sections through the RPV and Downcomer (DC).
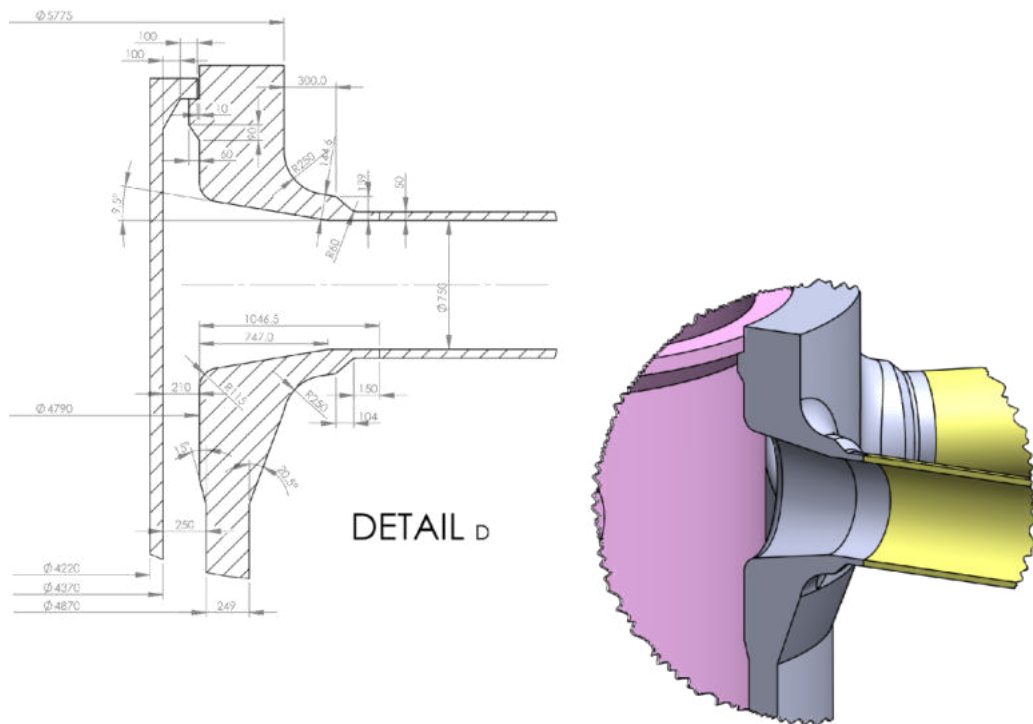
Figure 3: Details of the RPV Inlet Nozzles.
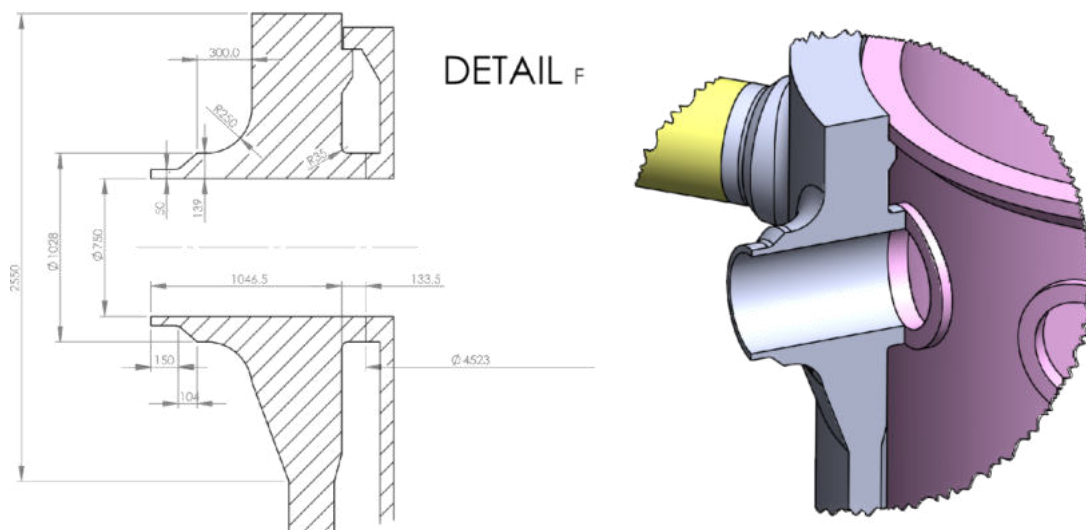
Figure 4: Details of the RPV Outlet Nozzles.

2.2   Simulated case

The assumed transient in the calculations presented in the following chapters is an asymmetric (plume cooling) loading condition due to a HL break of 50 cm^2 and loss of offsite power. The break was in the HL of loop No.1. One of the four high-pressure safety injection (HPSI) trains was assumed to be down for maintenance (Loop 1). A second train was assumed to fail at the start of the transient (Loop 4). Therefore, only two of the four loops (Loop 2 and Loop 3) received emergency core cooling water from the high-pressure safety injection pumps. All four loops received injection from the low-pressure safety injection (LPSI) pumps. Only the four accumulators (ACCs) connected to CLs were active. The four ACCs connected to HLs were deactivated. The transient results approximated the thermal-hydraulic data used in the ICAS project for transient T2 [3].

2.3   Specifications used in simulations

The key reactor design specifications used in the simulations are listed below. The listed values are those used in the base case calculations, and they are taken from the RELAP5 input deck. Values used in the simulations with other codes might differ slightly from the values below.

- **Reactor thermal power**
  3.765e9 W
  Plus pump power from main coolant pumps: 2.005e7 W

- **Primary loop flow rates and temperatures**
  5150 kg/s per loop
  325 °C in HL
  293 °C in CL

- **DC to upper head (UH) bypass flow rate**
  ~200 kg/s

- **Primary and secondary side pressures**
  157.5 bar in HL
  68.2 bar in steam dome

- **Total primary side volume**

462.5 m^3
363 m^3 without pressurizer

- **Pressuriser volume and initial level**
  Water volume above surge line: 35.9 m^3
  Steam volume above surge line: 23.6 m^3 (total volume 59.5 m^3)
  Water level above surge line: 6.78 m

- **ACC volume, pressure and fill level**
  Total height: 11.3078 m
  Volume water: 34 m^3, level: 8.5428 m
  Volume nitrogen blanket: 11 m^3
  Nitrogen pressure: 26 bar

- **Setpoints for HPI, ACCs and LPI**
  Maximum HPI pressure: 110 bar(abs.)
  Maximum LPI pressure: 10 bar(abs.)
  ACC pressure: 26 bar
  LPI water temperature: 15 °C
  HPI water temperature: 15 °C
  ACC water temperature: 20 °C

- **HPI and LPI injection curves (mass flow vs pressure)**
  Maximum LPI flow rate: 165 kg/s per loop
  Maximum HPI flow rate: 65 kg/s per loop

Figure 5 presents the flow rates of the HPI and LPI pumps as a function of pressure. The values of the pump curves used in the input decks of the simulation codes are listed in Table 1.
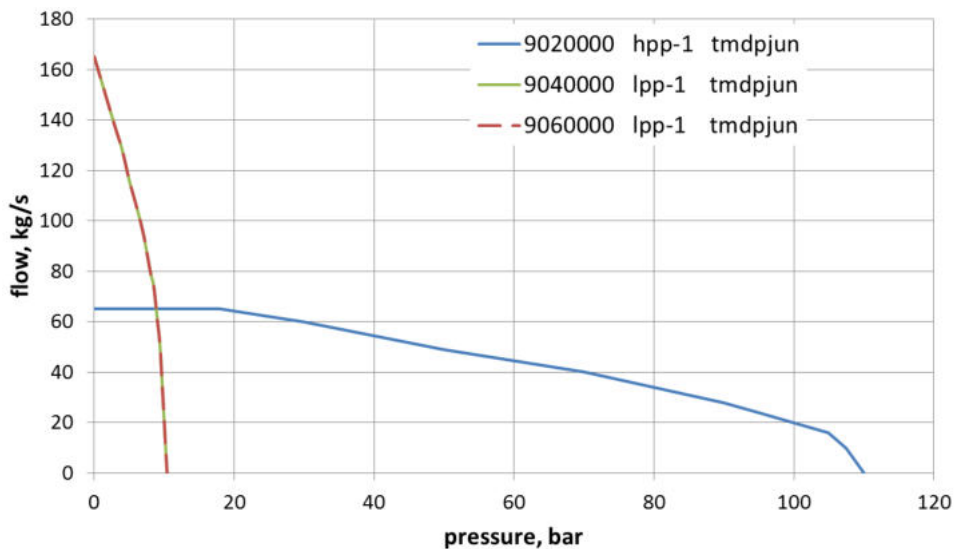
Figure 5: Pressure-flow relationship for HPI and LPI pumps.

Table 1: Pressure-flow relationships for HPI and LPI pumps

High-pressure injection		Low-pressure injection	
pressure, bar	flow, kg/s	pressure, bar	flow, kg/s
0	65	0	165
10	65	1.6	150

30	60		3	137
50	49		4	128
70	40		5	116
90	28		6	106
95	24		7	95
100	20		8	80
105	16		8.5	74
107.5	10		9	61
110	0		9.4	50
			10	20
			10.4	0

3   Used computer codes and models

Thermal hydraulic system codes RELAP5, ATHLET and TRACE, mixing codes KWU-MIX and GRS-MIX, and CFD codes Fluent and OpenFOAM were used in the simulations in Task 2.1. The simulated case was a SBLOCA with break in HL and with loss of offsite power.

3.1 RELAP5

3.1.1 RELAP5 code

The RELAP5/MOD3.3Patch05 computer code was used for system thermal-hydraulic calculation of the ICAS T2 SBLOCA. The RELAP5 code is based on a nonhomogeneous and nonequilibrium model for the two-phase system that is solved by a fast, partially implicit numerical scheme to permit economical calculation of system transients. The code includes many generic component models from which general systems can be simulated. The component models include pumps, valves, pipes, heat releasing or absorbing structures, reactor point kinetics, electric heaters, jet pumps, turbines, separators, ACCs, and control system components. In addition, special process models are included for effects such as form loss, flow at an abrupt area change, branching, choked flow, boron tracking, and non-condensable gas transport. The code models the coupled behaviour of the reactor coolant system and the core for loss-of-coolant accidents and operational transients such as anticipated transient without scram, loss of offsite power, loss of feedwater, and loss of flow.

3.1.2 RELAP5 model of KWU-1300 and ICAS T2 transient

A medium-detailed model of KWU-1300 and ICAS T2 transient (SBLOCA) was prepared in frame of the APAL project. Nodalization of reactor is shown in Figure 6, nodalization of primary loops with SG in Figure 7 and Figure 8. All 4 loops are modelled individually. The reactor DC is modelled by 8 parallel channels (ANNULUS components) connected by cross-flow junctions. The DC nodalization is shown in Figure 6 and further information to DC modelling are given in Figure 9 and Table 2 and Table 3. Modelling of ECCS system (HPIS, LPIS, ACC) is shown in figures with loops nodalization - Figure 7 and Figure 8.

Figure 6: RELAP5 nodalization of RPV.

Figure 7: RELAP5 nodalization of Loop 1.
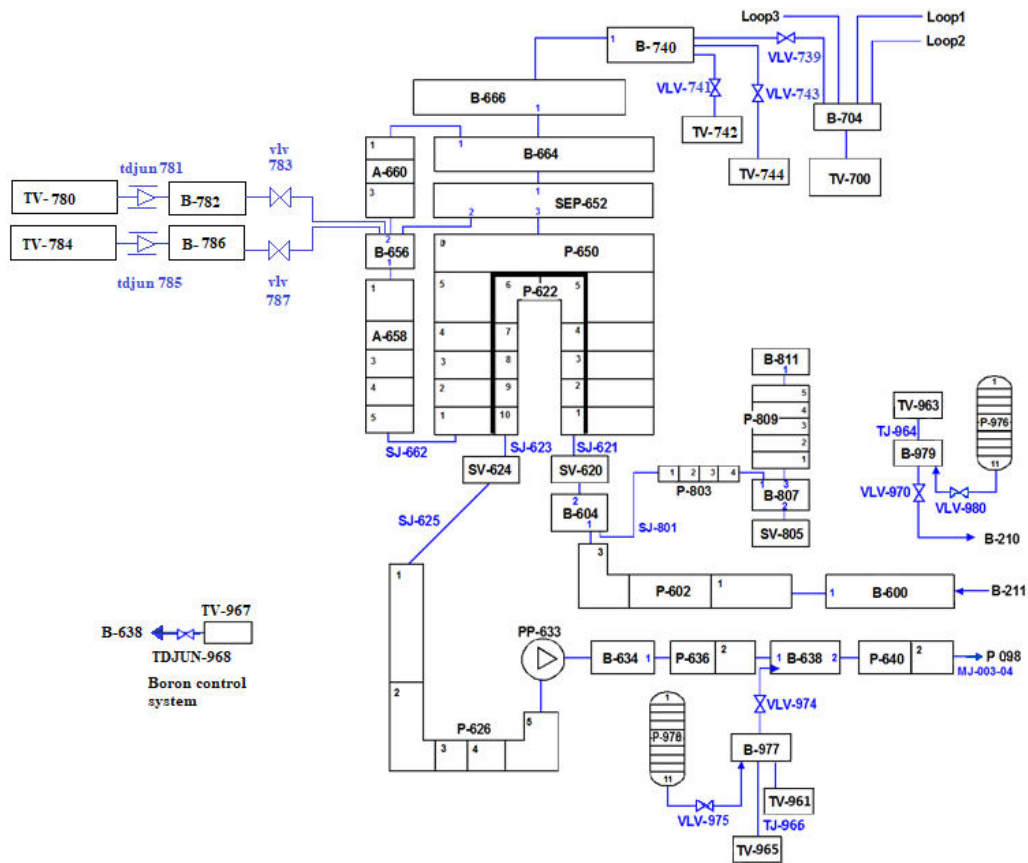
Figure 8: RELAP5 nodalization of Loop 4 with PRZ.
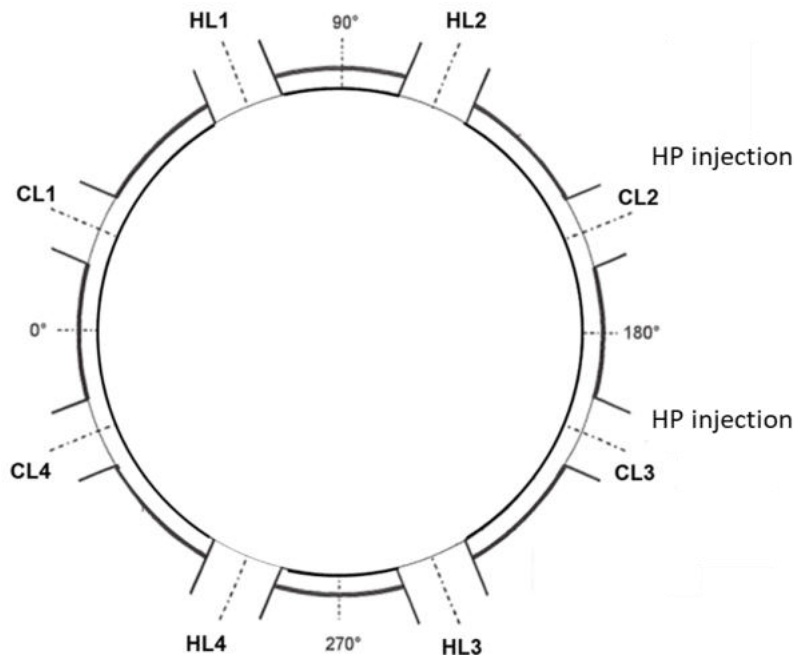
Figure 9: RELAP5 names for the four loops.

Table 2: Orientation of inlet/outlet nozzles

Nozzle	No of DC channel in R5 model	Azimuthal angle

CL1	091	22.5 °
HL1		67.5 °
HL2		112.5 °
CL2	094	157.5 °
CL3	095	202.5 °
HL3		247.5 °
HL4		292.5 °
CL4	098	337.5 °

Table 3: Elevation of (sub)volumes in DC channels (with respect to CL axis)

Volume	Elevation of centre of volume [m]
01	+0.5725
02	0.0
03	-1.13
04	-2.083
05	-2.638
06	-3.3215
07	-3.9745
08	-4.6275
09	-5.2809
10	-5.9335
11	-6.5155

3.2 ATHLET (GRS)

3.2.1 ATHLET code

The thermal-hydraulic computer code ATHLET (Analysis of THermal-hydraulics of LEaks and Transients) is under continued development by the GRS (Gesellschaft für Anlagen- und Reaktorsicherheit) [4] for the analysis of operational conditions, abnormal transients and all kinds of leaks and breaks in nuclear power plants. The aim of the code development is to cover the whole spectrum of design basis and beyond design basis accidents (without core degradation) for PWRs, BWRs, SMRs and future Gen IV reactors with one single code. The main code features are:

- advanced thermal-hydraulic modelling (compressible fluids, mechanical and thermal non-equilibrium of vapour and liquid phase, thermal mixing for hot and CL injection),
- availability of diverse working fluids: light or heavy water, helium, sodium, lead or lead-bismuth eutectic, supercritical carbon dioxide, molten salts as well as user-provided single-phase (non-boiling) working fluids,
- heat generation, heat conduction and heat transfer to single- or two-phase fluid considering structures of different geometry, e.g., rod or pebble bed,
- interfaces to specialized numerical models such as 3D neutron kinetic codes or 3D CFD codes for coupled multiphysics or multiscale simulations,
- control of ATHLET calculation by call-backs to programming language independent user code enabling the coupling of external models,
- plug-in technique for user provided code extensions,
- numerous pre- and post-processing tools,
- continuous and comprehensive code validation.

ATHLET was applied to system TH analysis for PTS assessments especially for thermal mixing phenomena in the CL and DC region but also for best-estimate plus uncertainty investigations in the past.

3.2.2   ATHLET model for KWU-1300 and ICAS T2 transient

The main specifications of the RELAP5 and ATHLET models are presented in Table 4. Small differences exist in the loop flow rate, CL temperature, DC to UH bypass flow rate and SG secondary side pressure. The latter is adjusted in the ATHLET model to set the initial reactor thermal power to the given value of 3750 MW. The 100 K/h secondary cooldown follows in qualitative and quantitative terms the behaviour as used in the RELAP5 model so that there is no significant influence on the transient progression. The loop temperature in the ATHLET model was set to the original initial conditions of the ICAS study [3]. Only minor differences in the results were seen when a test with the CL temperature used in RELAP5 model was run with ATHLET.

Figure 10 through Figure 12 show the basic nodalization of the ATHLET model. The thermal-hydraulic modelling approach is equal to the one used in RELAP5 as described in 3.1.2, where all major components are included. Differences are given in the modelling of the SG U-tubes, where the ATHLET model provides three parallel U-tube groups with different length in order to be able to simulate counter wise flow directions in different U-tubes during a transient. Furthermore, the ECCS injection lines and the ACC are modelled with interconnected thermal-hydraulic pipes to consider possible interference of HP, LP and ACC injection, as depicted in Figure 11. The DC is modelled with 16 azimuthal channels in the PTS relevant region. The model includes a basic control system to ensure stable steady-state operation and to represent the major safety signals such as SCRAM, turbine and pump trip, emergency core cooling system (ECCS) and ACC injection. A summary of volumes for different components of the primary system is given in Table 5 with comparisons against the reference RELAP5 model values.

Table 4. Comparison of main specifications for normal operation between RELAP5 and ATHLET models

Specification	RELAP5	ATHLET
Reactor thermal power	3.765e9 W	3750e9 W
Loop flow rates	5150 kg/s	4670 kg/s
Loop temperatures	325°C HL, 293°C CL	320°C HL, 285°C CL
DC to UH bypass flow rate	200 kg/s	194 kg/s
Primary and sec. side press.	157.5 bar, 68.2 bar	156.5 bar, 60.2 bar
ACC volume, pressure and fill level, temperature	34 m³, 26 bar, 8.5428 m, 20°C	34 m³, 26 bar, 8.5428 m, 20°C
Setpoints for HPI, LPI, temp.	110 bar, 10 bar, 15°C	110 bar, 10 bar, 15°C

Table 5. Comparison of ATHLET and Reference RELAP5 Model Volumes

Region	RELAP5 Volume [m³]	ATHLET Volume [m³]
Total primary side	423.6	424.3
TPS without PRZ	357.5	356.9
RPV + Core	137.9	142.1
PRZ + Surge Line	66.1	67.4
Loop (each)	54.8	53.7
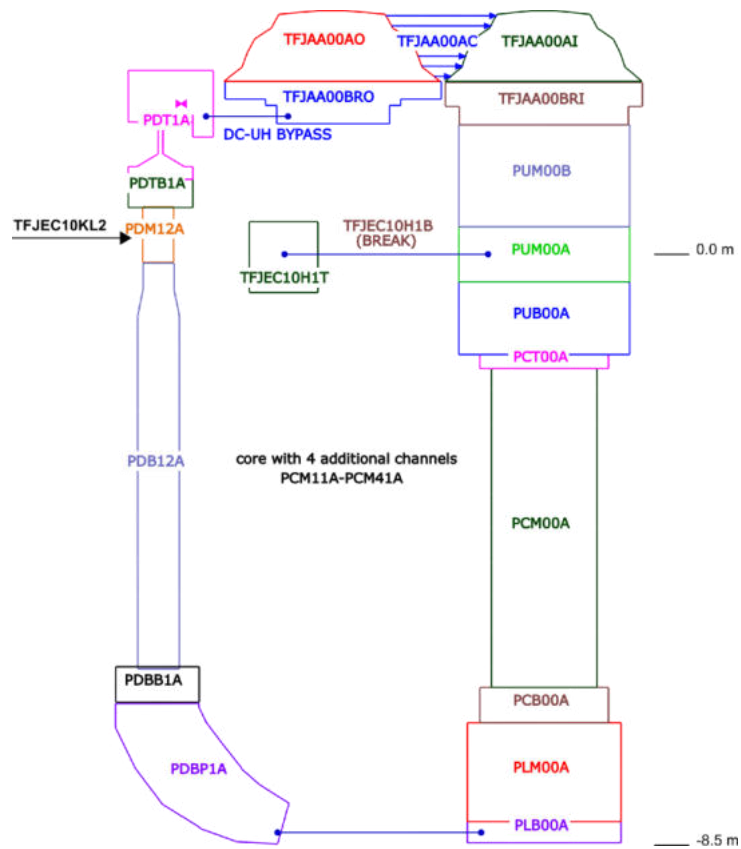
Figure 10: ATHLET nodalization of RPV (reduced).
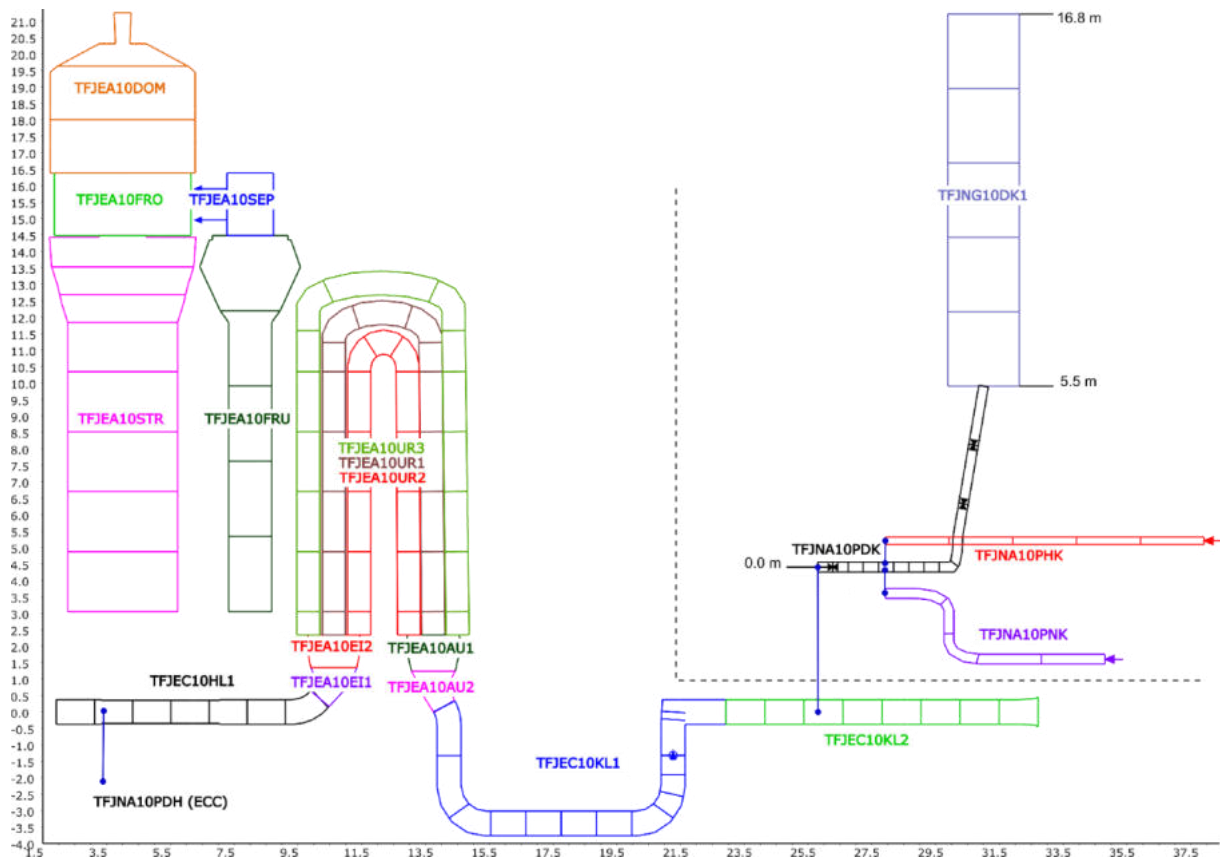
Figure 11: ATHLET Loop 1 nodalization with ECCS (Loop 2 - 4 symmetrically).
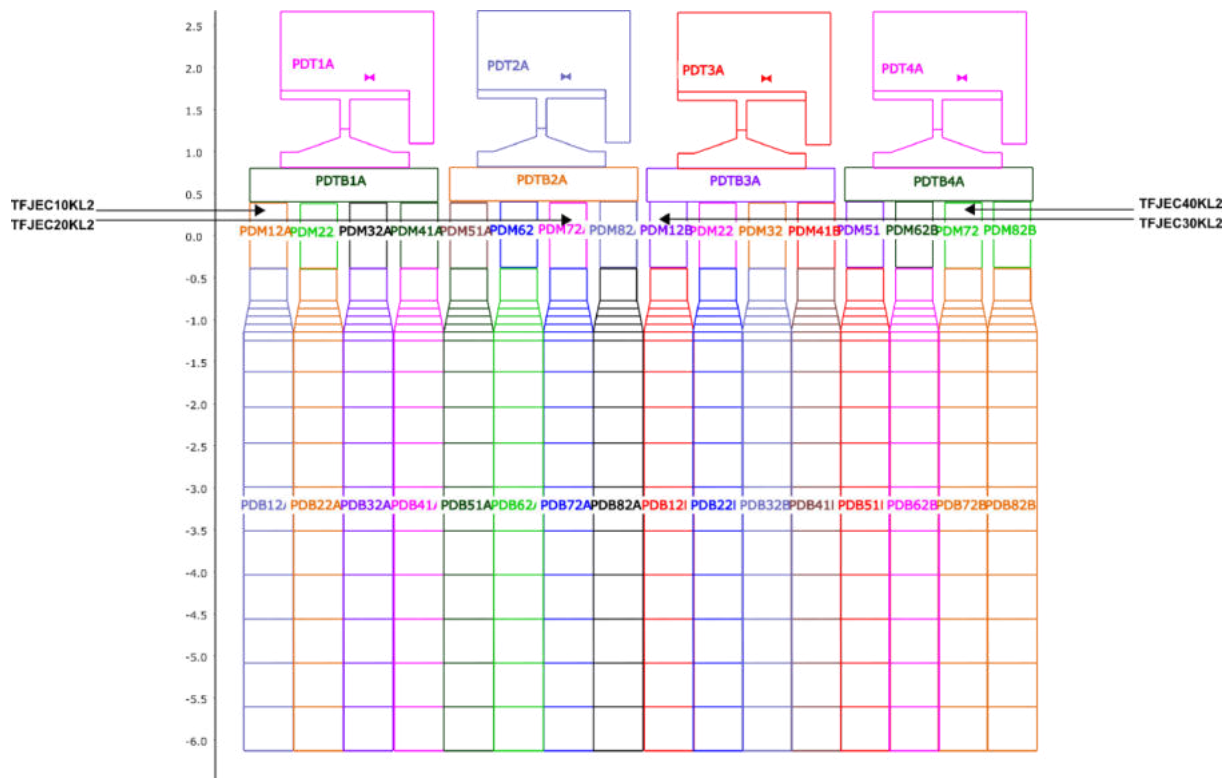
Figure 12: ATHLET DC nodalization.

3.3 TRACE (PSI)

3.3.1 TRACE code

The TRAC/RELAP Advanced Computational Engine (TRACE - formerly called TRAC-M) is the latest in a series of advanced, best-estimate reactor systems codes developed by the U.S. Nuclear Regulatory Commission (USNRC) for analysing transient and steady-state neutronic-thermal-hydraulic behaviour in light water reactors. TRACE has been designed to perform best-estimate analyses of loss-of-coolant accidents (LOCAs), operational transients, and other accident scenarios in pressurized light-water reactors (PWRs) and boiling light-water reactors (BWRs) [5]. It can also model phenomena occurring in experimental facilities designed to simulate transients in reactor systems. Models used include multidimensional two-phase flow, non-equilibrium thermodynamics, generalized heat transfer, reflood, level tracking, and reactor kinetics. Automatic steady-state and dump/restart capabilities are also provided.

The partial differential equations that describe two-phase flow and heat transfer are solved using finite volume numerical methods. The heat-transfer equations are evaluated using a semi-implicit time-differencing technique. The fluid-dynamics equations in the spatial one-dimensional (1D), two-dimensional (2D), and three-dimensional (3D) components use, by default, a multi-step time differencing procedure that allows the material Courant-limit condition to be exceeded. A more straightforward semi-implicit time-differencing method is also available, should the user demand it. The finite-difference equations for hydrodynamic phenomena form a system of coupled, nonlinear equations that are solved by the Newton-Raphson iteration method. The resulting linearized equations are solved by direct matrix inversion. For the 1D network matrix, this is done by a direct full-matrix solver; for the multiple-vessel matrix, this is done by the capacitance matrix method using a direct banded-matrix solver. TRACE takes a component-based approach to modelling a reactor system. Each physical piece of equipment in a flow loop can be represented as some type of component, and each component can be further nodalized into some number of physical volumes (also called cells) over

which the fluid, conduction, and kinetics equations are averaged. The number of reactor components in the problem and the manner in which they are coupled are arbitrary. There is no built-in limit for the number of components or volumes that can be modelled; the size of a problem is theoretically only limited by the available computer memory. Reactor hydraulic components in TRACE include PIPEs, PLENUMs, PRIZERs (pressurizers), CHANs (BWR fuel channels), PUMPs, JETPs (jet pumps), SEPDs (separators), TEEs, TURBs (turbines), HEATRs (feedwater heaters), CONTANs (containment), VALVEs, and VESSELs (with associated internals). HTSTR (heat structure) and REPEAT-HTSTR components modelling fuel elements or heated walls in the reactor system are available to compute 2D conduction and surface-convection heat transfer in Cartesian or cylindrical geometries. POWER components are available as a means for delivering energy to the fluid via the HTSTR or hydraulic component walls. FLPOWER (fluid power) components are capable of delivering energy directly to the fluid (such as might happen in waste transmutation facilities). RADENC (radiation enclosures) components may be used to simulate radiation heat transfer between multiple arbitrary surfaces. FILL and BREAK components are used to apply the desired coolant-flow and pressure boundary conditions, respectively, in the reactor system to perform steady-state and transient calculations. EXTERIOR components are available to facilitate the development of input models designed to exploit TRACE's parallel execution features.

For more than ten years, the TRACE code has been the primary systems analysis code within the STARS code system [6] at PSI. The US NRC codes are available in the framework of the CAMP (Code Applications and Maintenance Program) agreement between PSI and US NRC. The base deck development is normally done by direct translation of the plant drawings into a TRACE input deck using the SNAP (Symbolic Nuclear Analysis Package) user interface [7]. If necessary, an external scripting is used to reduce development time and improve quality. In general, the model development follows US NRC Regulatory Guides 1.157 and 1.203 and the TRACE modelling guidelines [9][10][11].

3.3.2   TRACE model for KWU-1300 and ICAS T2 transient

The TRACE model of the APAL ICAS reference reactor includes all major primary system components, including the primary piping, main coolant pumps (MCPs), steam generator (SG) U-tubes, pressuriser (PRZ) and RPV, as well as the secondary system from the SGs to the turbine inlet valve. All four loops of the reference reactor are explicitly nodalized. Figure 13 shows the basic primary and secondary side nodalization for coolant loop 4, i.e., the loop containing the PRZ. The RPV and reactor core are modelled using separate 3D cylindrical VESSEL components. As shown in Figure 14, the RPV uses 16 azimuthal sectors, 16 axial slices and one radial ring in the DC region; the DC is therefore effectively 2D in the DC region. Because the fuel response during the LOCA transient is not a quantity of interest, the discretisation in the core region is considered of low importance; A single fuel channel with 17 axial nodes is assumed. A point kinetics model for the reactor power is used. The core bypass and DC-to-upper-head (UH) bypass flows are included in RPV component, while the DC-to-HL bypass flows are modelled using separate SINGLE-JUNCTION components. The ACCs are modelled using 1D PIPE components. All other safety injection feeds are modelled using FILL components. The control system includes all the basic signals and controllers needed to ensure stable steady-state operation, as well as the major safety signals such as SCRAM, pump trip, emergency core cooling system (ECCS) and ACC injection. The control system also includes major operator actions such as safety injection pump isolation and secondary side shutdown.

The break is modelled using a VALVE component in TRACE in which choked flow modelling has been enabled. TRACE's offtake modelling is not used at the break, i.e., the break flow is a homogeneous two-phase mixture, and no effort is made to capture the effects of possible liquid/vapour stratification in the vicinity of the break.

A summary of volumes for different components of the primary system is given in Table 6 with comparisons against the reference RELAP5 model values. Overall, the total system volume is within ~1% of the reference values.
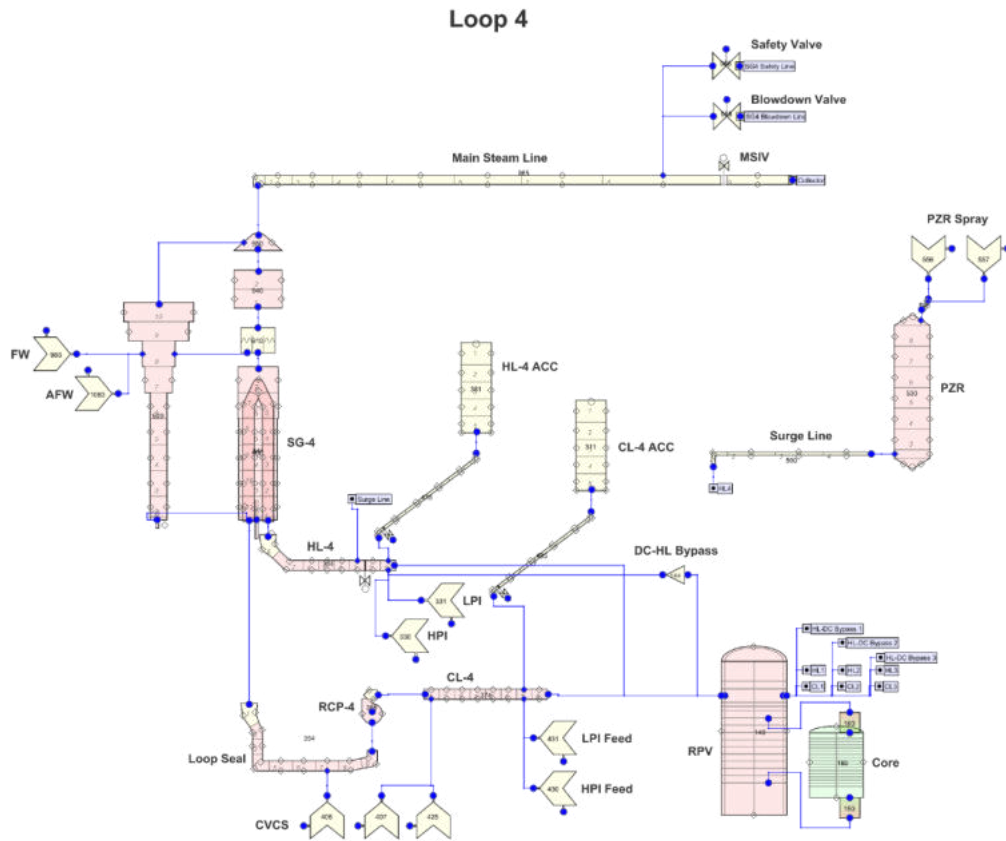
Figure 13: TRACE Nodalization of APAL ICAS Reference Reactor showing Loop 4 Containing the Pressuriser.
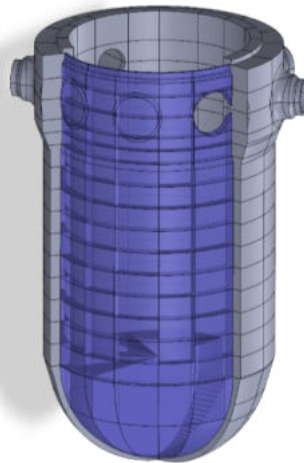
Figure 14: 3D Nodalization of the RPV DC.

Table 6: Comparison of TRACE and Reference RELAP5 Model Volumes

Region	RELAP5 Volume (m³)	TRACE Volume (m³)
Total Primary Side (TPS)	423.6	418.5
TPS excluding PRZ	357.5	351.7
RPV and Core	137.9	138.3
PRZ and Surge Line	66.1	67.5
Volume per loop	54.8	53.2

3.3.2.1   Code version

An in-house version of TRACE based on the NRC version 5 patch 5 has been used for all analyses. This in-house version includes one significant code change, which should be noted. The original code exhibits unphysical pressure response when modelling the filling of vertically oriented components with subcooled water due to an over-estimation of the liquid to vapour interfacial heat transfer. The in-house version reverts to the method used in the original TRACE version 5. This is not a perfect fix but has been shown to improve the pressure response significantly for SBLOCA and similar transients. Sensitivity analyses have shown, however, that the results for this version do not differ significantly from the original TRACE version 5 patch 5.

3.4   KWU-MIX (Fra-G)

3.4.1   KWU-MIX code

At Framatome GmbH, the thermal-hydraulic analyses for PTS consist of two steps. The first step is a system analysis performed with RELAP5, as described in Section 3.1. The second step is a mixing analysis performed with KWU-MIX or with a CFD code. An advantage of the mechanistic-models in KWU-MIX is the speed at which the mixing analyses are performed. Therefore, multiple analyses can be performed in a time span on the order of minutes, which makes it possible to perform sensitivity analyses on parameters such as the break size.

The output of the system analysis contains data that is provided directly to the fracture-mechanics analysis (e.g., ABAQUS in Figure 15). The output of the system analysis also contains input data for the mixing analysis. These data include the pressure and temperature of the bulk fluid (outside of the plumes and stripes that form below the cold-leg nozzles). These data also include the flow rate through the MCPs and the injection flow rates of the ACC and ECC pumps.
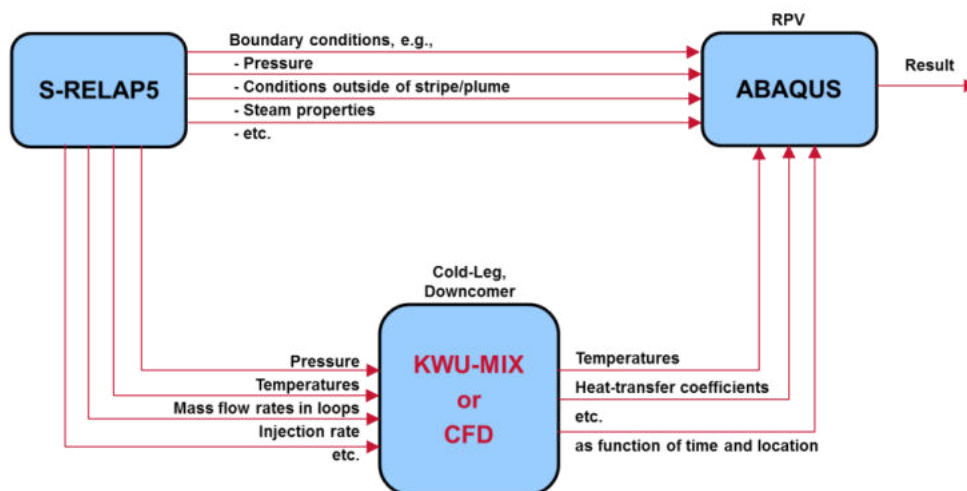
Figure 15: Sequence of analyses for PTS at Framatome GmbH.

For simulating cold-coolant injection from the ECC system into the hot water in the CL, KWU-MIX calculates the entrainment of the hot water into the flow of cold water. The entrainment is due to turbulent mixing between the two streams. When no hot water is present, KWU-MIX calculates the condensation rate of the steam on the cold water.

A schematic of the flows in the loop seal, CL, and DC, along with locations of the various modelling regions (MR) in KWU-MIX, are shown in Figure 16, which is adapted from Iyer et al. [12]. The cold water from the ECC system is injected into the CL at MR1. The cold water flows from the injection location along the bottom of the CL (MR2) to the inlet of the RPV (MR3), and through the DC of the RPV (MR4).
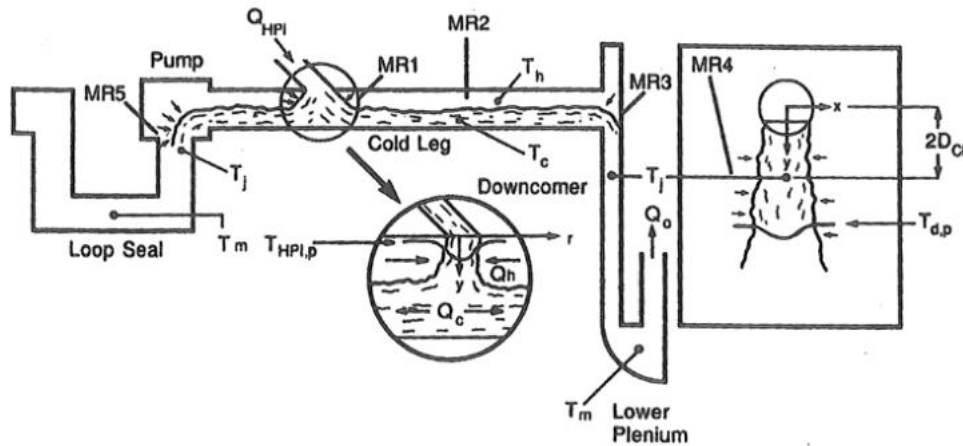
Figure 16: Schematic of KWU-MIX modelling regions in the CL and DC during ECC injection.

During a SBLOCA, if the rate of loss of the primary coolant from the leak is so small that it can be compensated by the injected cold coolant from the ECC system, then the DC remains filled or nearly filled with water. If the water level in the DC is above the water level that the ECC water would attain if it were flowing alone in the CL, then hot water from the DC flows into the CL. At the location where ECC water is injected into the CL (MR1), the jet of ECC water entrains some hot water, and the mixture forms a layer on the bottom of the CL. The cold water flows from the injection location to the RPV as a stratified layer under a layer of hot water flowing in the opposite direction from the DC to the location where it is entrained into the cold-water layer (MR2). At the connection between the cold-leg nozzle and the DC (MR3), the cold water turns downward into the DC of the RPV, and additional mixing occurs. In the DC, the cold water forms a buoyant jet (also referred to as a plume), and hot water from outside of the plume in the DC is entrained with the cold-water plume (MR4). As a result, the temperature of the mixture of ECC water and entrained hot water increases in the direction of flow from the injection location through the CL and in the DC. The phenomenon of the cold ECC water entraining hot surrounding water into its flow is referred to as "liquid-liquid mixing". It is shown schematically on the right-hand side of Figure 17.
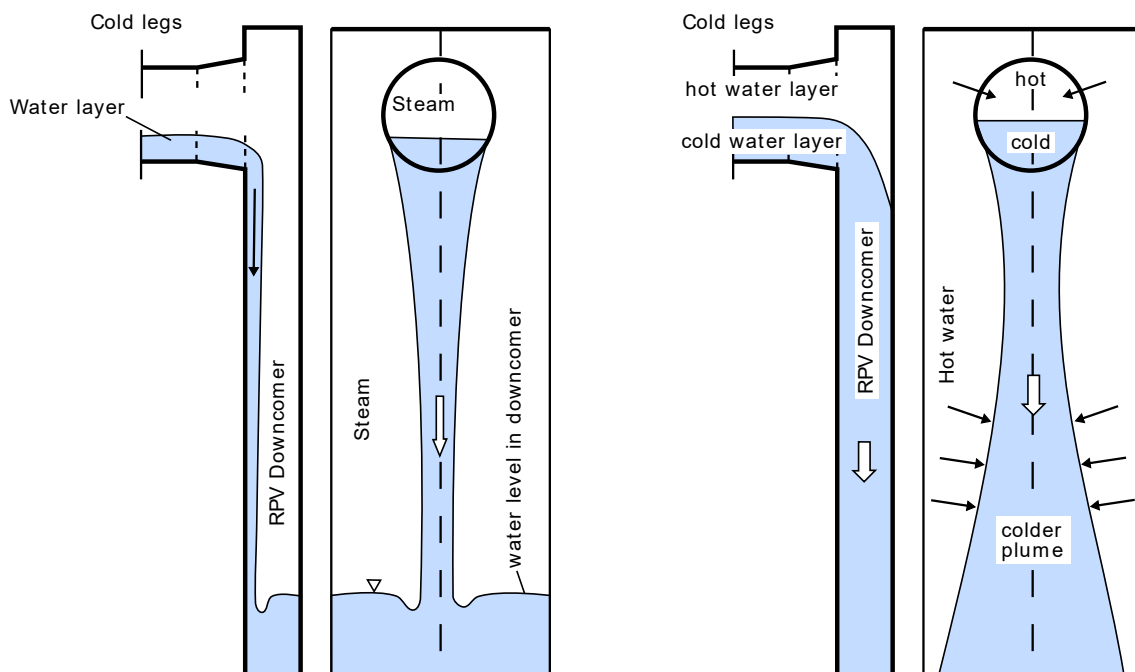
Figure 17: Stripe cooling (left part) and plume cooling (right part) of the RPV inside wall, adapted from [13].

If the rate of loss of the primary coolant from the leak is so large that it cannot be replaced by the injected cold coolant from the ECC system, then the volume of the hot primary-side coolant is reduced until none remains in the CLs and the upper region of the DC. It is shown schematically on the left-hand side of Figure 17. The injected cold water from the ECC system is exposed to steam, which condenses on its surface (MR1), and the mixture of ECC water and condensate flows from the injection location along the bottom of the CL to the cold-leg nozzle (MR2) and into the DC of the RPV. At the connection between the CL and DC (MR3), either the cold water will stay attached to the cold-leg nozzle, or the water will detach from the cold-leg nozzle and flow as a jet of cold water to the core barrel. The geometry and flow conditions determine which of these two scenarios will occur. If the cold water stays attached to the cold-leg nozzle, then it flows as a stripe of falling water on the wall of the RPV in the DC (MR4). The phenomenon of steam condensing on the surface of stripe is referred to as "direct-contact condensation" (DCC) in order to distinguish it from condensation of a solid surface. When the stripe of falling water reaches the top of the water in the DC, it forms a buoyant jet, and liquid-liquid mixing occurs as described above.

3.4.2   KWU-MIX model for KWU-1300 and ICAS T2 transient

The leak size of the LOCA in the ICAS T2 transient is small enough to prevent the liquid level in the DC from sinking below the bottom of the CL. Therefore, phenomena that occur during liquid-liquid mixing are simulated in KWU-MIX. The models for the various phenomena like mixing near the injection location, countercurrent flow of stratified water layers in the CL and mixing in the DC are described next.

3.4.2.1   *Liquid-Liquid Mixing in the Cold Leg*

Entrainment of hot water into the ECC water during a period of loop-flow stagnation is simulated differently for low injection flow rates than for high injection flow rates, as described by Theofanous and Yan [14]. When the flow rate of injected water is low, the hot water is entrained directly on the jet of cold water, as shown on the left-hand side of Figure 18. In this case, stratified flow occurs, which requires that the Froude number be less than approximately four. If the flowrate of injected water is large, the injected water fills the CL at the injection location, as shown on the right-hand side of Figure 18. In this case, entrainment occurs at the location where the flow regime changes to stratified flow.

| (a) low injection flow | (b) high injection flow |
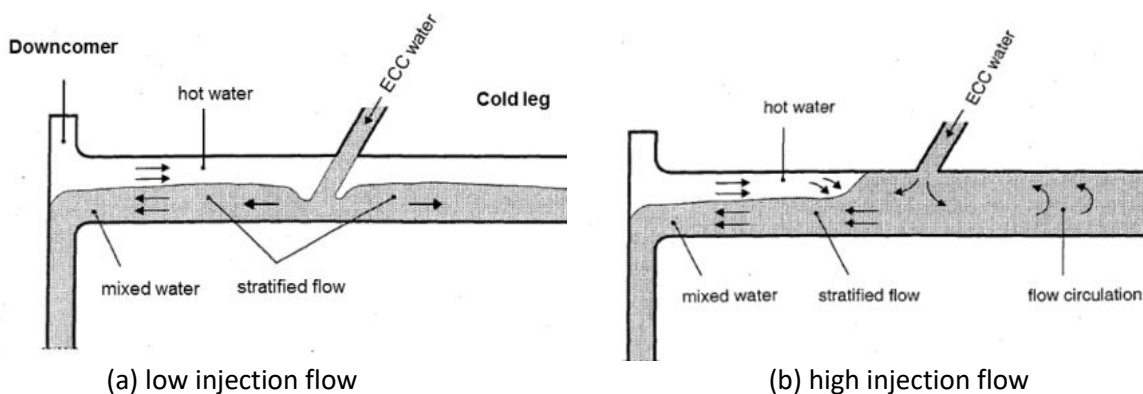
Figure 18: Flow patterns at the injection location in the CL.

The flow rate of entrained hot water into the jet of cold ECC water, $\dot{m}_{ent}$, is defined as a fraction of the injected flow rate, $\dot{m}_{ECC}$. The fraction is defined as $\varepsilon = \frac{\dot{m}_{ent}}{\dot{m}_{ECC}}$.

For low injection flow rates, ε is obtained either from a correlation that depends on the orientation of the connection of the injection pipe, or the boundary-layer model similar to that described by Trewin can be applied [15].

For large injection flow rates, the geometry of the injection pipe is of minor importance, and the entrainment depends on the pressure difference that leads to the flow-regime transition. The mixing,

which takes place at the locus of flow pattern transition from circulation to stratification, is driven by the pressure differential. The maximum flow rate of entrained hot water is limited by the "countercurrent flow limitation" (CCFL), which is a function of the Froude numbers of the two stratified layers of water in the CL near the RPV inlet.

If loop-flow stagnation has not occurred, the flow of water from the MCP causes greater mixing at the injection location than if there is no water from the MCP. If this case, the criterion of Nourbakhsh and Theofanous can be used for determining whether the injected flow completely mixes with the loop flow at the injection location [16]. If the streams do not completely mix, the amount of mixing can be calculated with a model by Kim [17]. Alternatively, KWU-MIX applies the method described above for fluid-fluid mixing at the inlet of the RPV given by Trewin with a modification to account for the MCP flow [15]. An example of the result is shown in Figure 19, which shows the result from KWU-MIX imposed on a photograph of an experiment reported by Fan [18]. The experiment was on a buoyant jet injected vertically downward into a liquid of uniform density with a uniform crossflow from left to right. The upper and lower boundaries of the plume calculated by KWU-MIX are the red curves, and the calculated centerline of the plume is the blue line. The velocity distribution is the green Gaussian curve that is assumed in the integral solution to the Navier-Stokes equations in KWU-MIX. If the plume comes into contact with the pipe wall, then an additional boundary condition is set in the solution to the Navier-Stokes equations.
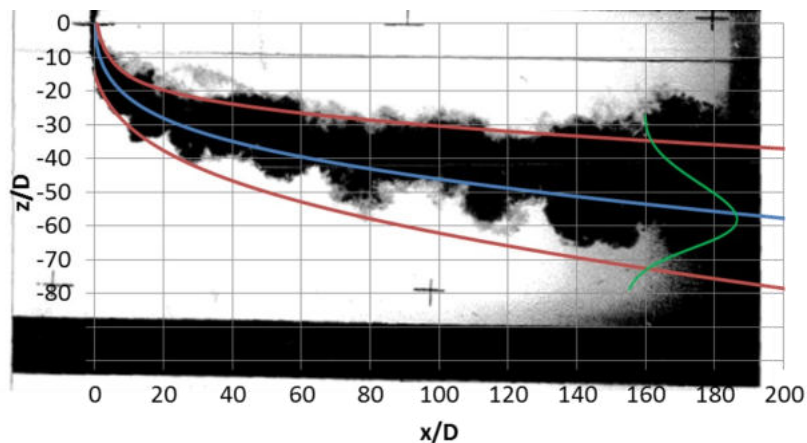
Figure 19: Trajectory of injected cold water into a stream of hot water.

3.4.2.2   Liquid-Liquid Mixing at the Entrance to the Downcomer (MR3)

The model is similar to that described by Michas and Papanicolaou [19], but the model in KWU-MIX includes the friction drag in the momentum equation, and the angle of injection is arbitrary rather than in the horizontal direction. Models of this type are widely used and have been shown to agree with experimental data. (See, e.g., Chen and Rodi [20]).

3.4.2.3   Liquid-Liquid Mixing in the Downcomer (MR4)

For a DC filled with hot water (MR4 in Figure 16), cold water entering the DC from the CL forms a buoyant jet. Figure 20 shows a schematic of a buoyant jet along with the defining parameters for a heavy fluid (cold liquid) injected into a lighter fluid of the same phase (warm liquid). The velocity of the buoyant jet at the origin, u_0, is assumed to be in vertically downward direction. Therefore, the coordinate s aligns with the direction of gravity, which is denoted the z-coordinate. The direction perpendicular to the direction of flow, r, is the horizontal direction.

As long as the ambient density, $\rho_a\{z\}$, is less than the density at the origin, ρ_0, the buoyant jet is said to have positive buoyancy. In this case, the buoyant jet continues to flow downward, as shown in the upper region of the buoyant jet in Figure 20. However, if the ambient density increases with distance from the origin, the centerline density of the buoyant jet becomes equal to the ambient density at a distance sufficiently far from the origin. This location is the point of neutral buoyancy, and the buoyant

jet is a pure jet, by definition. At greater distances from the origin, the buoyant jet is said to have negative buoyancy, and the flow decelerates. Eventually, the velocity becomes zero, and the flow spreads horizontally and then upward to the point of neutral buoyancy, as shown in the lower region of the buoyant jet in Figure 20.

The model as implemented in KWU-MIX assumes that the ambient density is uniform. Therefore, the buoyant jet continues to flow downward, as shown in the upper region of the buoyant jet in Figure 20. At the origin, the inertia is greatest. If the buoyancy force is negligible compared to the inertial force, the buoyant jet is said to be a pure jet. At distances far from the origin, the inertia is dominated by the buoyancy, and the buoyant jet is called a plume.

The trajectory of the cold-water layer leaving the CL and flowing into the DC is calculated in KWU-MIX with a mechanistic model of a buoyant jet. An integral method was used to derive a similarity solution for the distributions of velocity and density in a turbulent jet and plume. The integral model rests on boundary-layer theory, and the equations of motion are derived from the corresponding conservation equations for mass, momentum, and energy. The expression for the turbulence model is derived from the conservation equation for mechanical energy (Fox [21]). It involves a single correlation constant, which is derived from experiments.
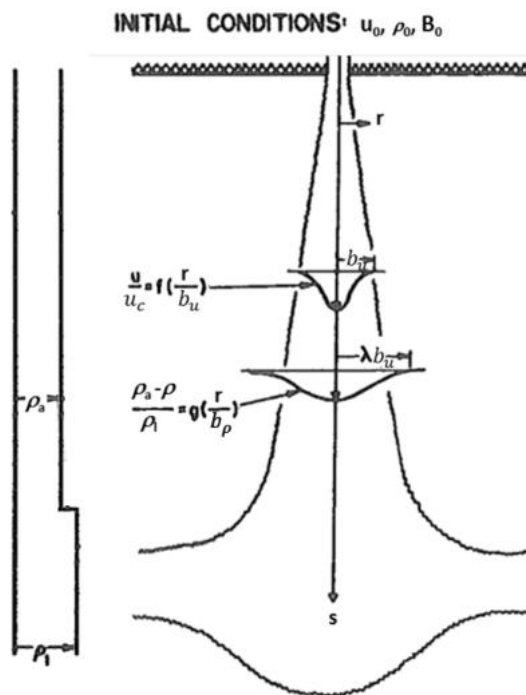
Figure 20: Schematic of a vertical buoyant jet.

Because the KWU-1300 reactor is a four-loop PWR, and because the two loops with high-pressure ECC injection are neighbouring each other, it is conservatively assumed in KWU-MIX that the two plumes merge at some distance below the cold-leg nozzles. Above the elevation where the two plumes intersect, the entrainment rate and width of each plume is simulated as if it were flowing alone. Only the direction of flow is affected by the neighbouring plume. Below the elevation where the two plumes intersect, the plumes are treated as a new, single plume, with its hypothetical origin at a much higher elevation. The result is shown schematically in Figure 21.
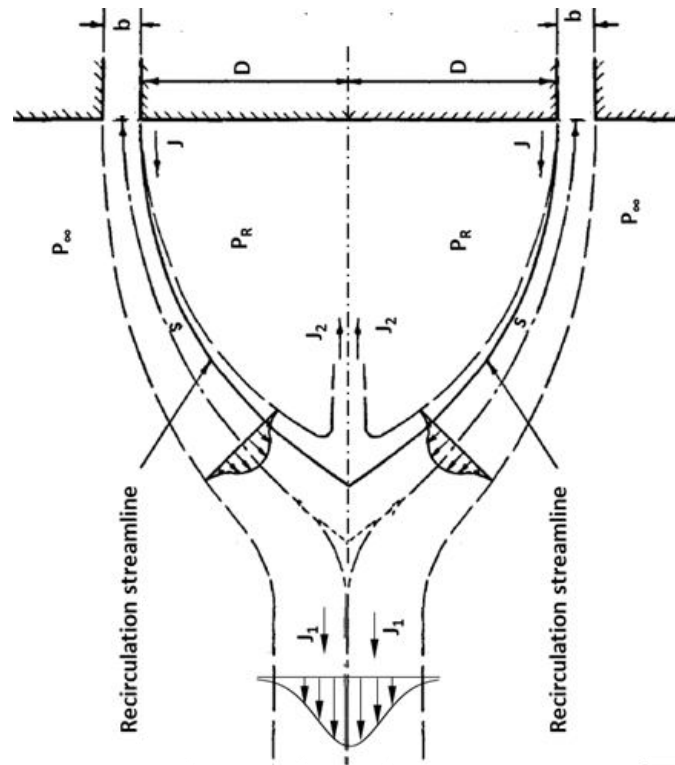
Figure 21: Schematic of the trajectory of two merging plumes in the DC.

The model in KWU-MIX is based on the model by Bourque and Newman [22] of the Coanda effect, where a plume is drawn to a boundary due to the impediment to entrainment caused by the boundary. In Figure 21, the boundary is the vertical axis of symmetry between the two inlets to the RPV, where the two inlets are separated by a distance of 2·D. The impediment to entrainment causes the pressure between the two plumes, indicated by p_R in Figure 21, to be less than the pressure outside of the plumes, indicated by p_∞. The hot water entrained by the plume at elevations above where the plumes merge mixes with the plume, just as for individual plumes. But a flow equal to the entrained flow on the inside of each plume is separated from the plume when the two plumes merge. The separated flow, indicated by J_2, recirculates in the region between the plumes. The streamline separating the entrained flow from the original flow, J, is also shown in Figure 21. The combined plumes have a flow, J_1., equal to 2·J plus the entrained flow from the sides outside of the two plumes. The combined plumes have a peak velocity greater than that of an individual plume. Therefore, the heat-transfer coefficients are greater after merging than before merging.

3.5   GRS-MIX (GRS)

3.5.1   GRS-MIX code

Detailed thermal hydraulic boundary conditions are requested for PTS analysis of a reactor pressure vessel. The UPTF and HDR test facilities provided comprehensive experimental data about the thermal mixing in the CL and DC of the primary circuit of a KWU-Type PWR. Based on these test data Sonnenburg [23] developed correlations taking into account the relevant geometric and thermal-hydraulic parameters. These correlations were combined to a computer model (mixing code) named GRS-MIX. Using the calculated results of a thermal-hydraulic code (e. g. ATHLET) this model allows the prediction of local temperatures and local heat transfer coefficients in the DC. By using these local predictions, a structural-mechanical PTS analysis can make use of experimentally assured boundary conditions. The following phenomena are addressed in the model:

   a)   thermal mixing in the CL,
   b)   thermal mixing in the DC,
   c)   heat transfer between fluid and reactor pressure vessel walls in the DC.

48

For thermal mixing in the CL, a calculation approach was developed based on UPTF-TRAM experimental data from the test C1. This approach uses the analogy between thermal mixing on a water jet and convective heat transfer on a jet. The heat transfer coefficient defined by the calculation approach for thermal mixing on the jet surface turned out to be constant at 400 kW/m^{2}K and therefore independent of the mass flow in the jet, of temperature differences between the jet and the ambient flid and also independent of geometric scaling.

It was recognized in the experiments that the phenomenon of counter-current flow limitation limits thermal mixing in the CL when certain admixing mass flows are reached. A geometry dependency of the correlation constant C for the counter-current flow limitation was also determined for GRS-MIX based on the UPTF-TRAM and HDR data. This geometry dependency takes into account the position of the ECCS line connection in relation to the position of the CL nozzle at the DC.

A calculation approach for thermal mixing in the DC is part of GRS-MIX using the same analogy for convective heat transfer on jets. The heat transfer coefficient defined by this calculation approach for thermal mixing at the plume in the DC was determined to be constant at 7 MW/m^{2}K and also independent of the mass flow in the plume and independent of temperature differences between the plume and the ambient fluid. The heat transfer between the plume and the reactor pressure vessel wall was determined using the UPTF-TRAM experimental data. A heat transfer correlation according to Dittus and Boelter is implemented with a correction factor of 1.65 and the usage of the correlation by Chen and Chen for determining the velocity used in the Reynolds number calculation. Details of the model description are to be found in [23].

3.5.2 GRS-MIX model for KWU-1300 and ICAS T2 transient

The model approach for simulating the KWU-1300 reactor and ICAS T2 transient using the GRS-MIX code is equivalent to the general description given in chapter 3.4.2. The GRS-MIX algorithm is able to distinguish between four different scenarios to calculate PTS relevant parameters from the given transient conditions, namely

- water level above the CL,
- water level between upper edge of CL and ECC injection nozzle,
- water level between ECC injection nozzle and lower edge of CL,
- water level below lower edge of CL.

For ICAS T2 the liquid level in DC does not fall below the bottom of the CL and liquid-liquid mixing and the formation of a cold plume in the DC is simulated by GRS-MIX.

For the given model of the KWU-1300 reactor configuration the GRS-MIX relevant geometric data used is presented in Table 7. The course of pressure, ECCS temperature and mass flow, hot (ambient) water temperature in the CL, ambient temperature in DC and the water level in the DC during the transient are given by external system code results (e. g. ATHLET, RELAP5).

In contrast to the KWU-MIX code, GRS-MIX is not capable of taking into account the merging of two neighbouring plumes. Rather, the falling plumes are modelled individually only interacting by a change of ambient temperature if they are close enough to influence water temperature at their respective hot water probe positions.

Table 7. Geometric data used for GRS-MIX simulations of ICAS T2 benchmark

Geometric Parameter	Unit	Value
Diameter of ECCS injection line	m	0.300
Diameter of CL	m	0.750
Connection height of ECCS line relative to CL bottom	m	0.225
Connection angle between ECCS and CL	deg	60.00
Distance of ECCS injection point to CL nozzle	m	5.751
Gap width in DC	m	0.250
Length of cone in CL nozzle	m	0.660
Expansion angle of the cone relative to the cone axis	deg	6.394
Radius at the overflow from CL to DC	m	0.109

3.5.3   ECC-MIX injection model

The thermal mixing in the CL can significantly influence the coolant temperature at the inlet of the DC and thus further influence the mixing processes on the way to the core inlet. In the context of thermal-hydraulic PTS investigations with TH system codes (e.g., ATHLET) these processes could be represented by complex nodalization schemes that divides the CL into multiple horizontal layers. Since such a nodalization is elaborated, thus prone to errors and unsuitable for reactor simulations and brings certain pitfalls in terms of validation and reproducibility, a model based on GRS-MIX was developed and implemented in the ATHLET code, which calculates the mixture mass flow and its temperature using a standard nodalization and directs it directly into the DC [23][24][25]. The model is available in the current ATHLET version 3.2 and part of the INJECTION submodule . In addition to the data generally available in the ATHLET network, the model requires further information to be specified by the user. This includes the place where the 'hot' ('ambient') water temperature and density is probed in a reference control volume (e.g. PC-DCA-M CV9 in Figure 22) as well as the destination for the redirected mixture mass flow (e.g. PV-DCA-B CV2 in Figure 22). The model calculates the mixture mass flow and its temperature based on the mixing ratio ε.
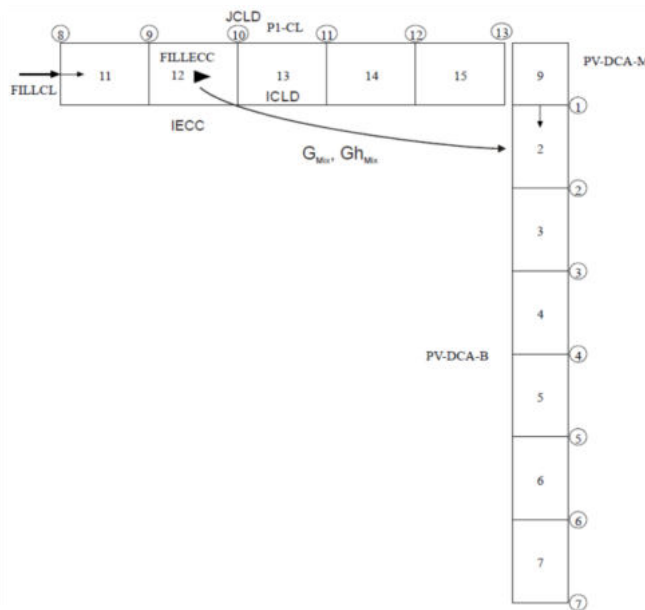
Figure 22: Nodalization example for usage of the ECCMIX model in ATHLET [24].

When calculating the mixture mass flow and its enthalpy, a distinction is made between two cases:

   a)   counterflow limitation not effective and

b)   counterflow limitation effective.

In case a) the mixture mass flow with its determined enthalpy is redirected as calculated into the user defined DC control volume based on the mixing ratio. In case b) the mixture mass flow is calculated using a smaller mixing ratio as a result of the counter-current flow limitation. If there is a global flow of hot water from the DC towards the pump in the CL, this hot water is added to the mixture, which increases its enthalpy. For this purpose, the part of the water mass flow in the cold branch downstream of the ECCS injection point is used that exceeds the model-intern calculated admixture mass flow. Global flow in the direction of the DC is not explicitly taken into account by the model.

For cases in which the boron tracking model and / or the model for dissolved gas is used, the boron or gas content of the mixture mass flow directed into the annulus must be determined. The calculation is carried out analogously to the determination of the enthalpy flow.

Details of the model implementation in ATHLET can be taken from the ATHLET Model and Methods guide [4] .

3.6   Fluent/OpenFOAM (UJV, LUT)

3.6.1   Fluent code

In the last decade, there has been a significant expansion of 3D CFD codes in the field of stationary and non-stationary flow calculations. Among others, nuclear energy has seen a higher use of these CFD codes, mainly because traditional one-dimensional codes cannot predict satisfactorily some of the phenomena in the reactor – such as the mixing of coolant or cold plume behaviour in the reactor DC.

Fluent is a commercial 3D CFD code that solves Navier-Stokes equations using the control volume approach. Compared to its open-source counterparts, Fluent is more widely used and optimized, so that computations are generally faster compared to for example OpenFOAM, meaning the additional license fees are usually justified by much lower computational costs.

As engineering flows are mostly of turbulent nature when dealing with CFD simulations, most of the time turbulent flows need to be solved. In engineering applications integral quantities need to be calculated, to obtain such quantities, solving turbulent flows with a turbulence model is not only sufficient, but recommend too, as in this way it is possible to obtain reliable solutions in a more efficient and cost-effective way. An averaging operation can be applied to the Navier-Stokes equations to obtain the mean equations of fluid flows called Reynolds Averaged Navier-Stokes (RANS) equations. These are very similar to the original equations but contain some additional terms in the momentum equations called Reynolds stress terms that are unknown and need to be modelled. The numerical simulation is then driven by a turbulence model which is arbitrarily selected to find out the effect of turbulence fluctuation on the mean fluid flow.

3.6.2   Fluent model for KWU-1300 and ICAS T2 transient

Computational mesh was created in software Fluent Meshing 19 (see Figure 23). Initial CAD model, from which the CFD mesh was created, consists of 4 CLs with small section of ECC injection pipe and DC, computational domain ends at the core inlet as the modelling of the core would be far too computationally expensive.
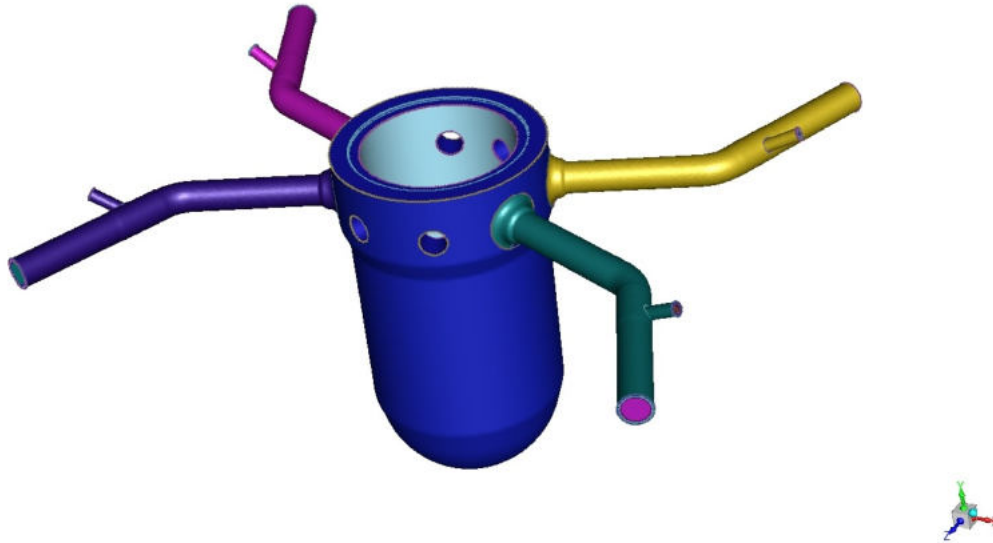
Figure 23: CAD model for the CFD calculation.

Model includes the 6 mm thick cladding on the inner walls of the CLs and DC, cladding is modelled with 3 cells across its thickness, which is a generally agreed number to capture heat transfer phenomena in such thin layers. Because of high velocity gradients in the boundary layer, dense prism layer was created at each wall of the domain – height of the first cell is 0.5 mm, growth rate (height of the next layer divided by the current one) 1.35 and total number of layers is 12. These settings should ensure that for the varying boundary conditions the value of y+ does not exceed 100, which is necessary for the turbulence models used later in the calculation. Table 8 lists the cell count in different regions of the model. Figure 24 and Figure 25 depict computational mesh in the CL, DC and bottom part of the domain.

Table 8: Cell counts in the Fluent model

Region	Cell Count
Base Metal	294 712
Cladding	611 315
Fluid	2 453 149
Total	3 359 176
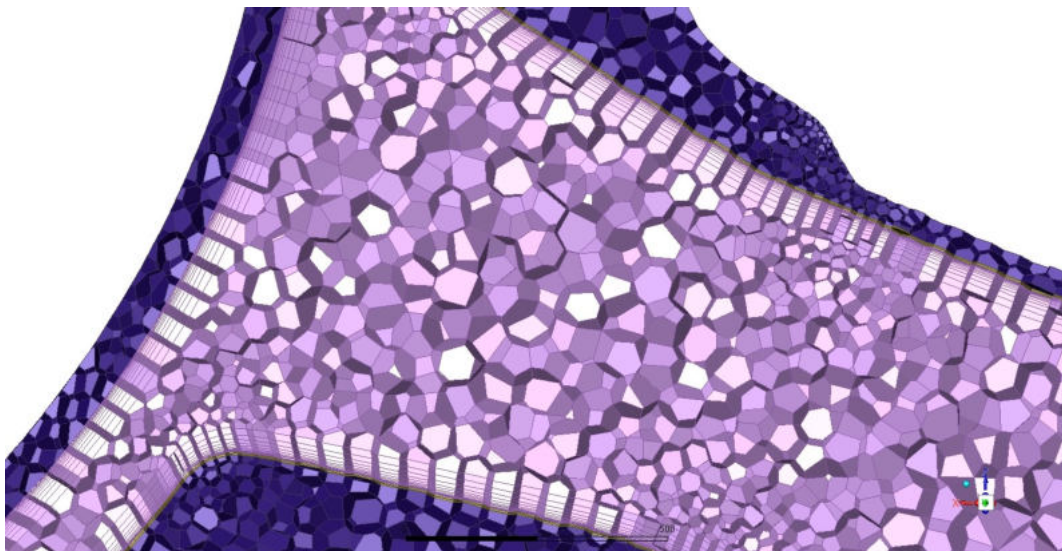
Figure 24: CFD mesh in the transition from CL to DC.

Figure 25: CFD mesh in the bottom part of the domain.

3.6.3   OpenFOAM code

In the field of nuclear safety analysis, CFD has become an increasingly popular tool for thermo-hydraulic investigations. There are many commercial and open-source CFD codes available. In recent years, the OpenFOAM code has been gaining popularity worldwide. OpenFOAM is a free and open-source CFD toolbox that was first released by OpenCFD Ltd. in 2004. OpenFOAM stands for Open-source Field Operation And Manipulation. OpenFOAM is written in the C++ programming language and has an extensive range of features to solve anything from complex fluid flows involving chemical reactions, turbulence, heat-mass transfer, acoustics, solid mechanics, and electromagnetics [26].

Compared to the commercial solvers, the benefits of open-source CFD codes are their transparency, infinite customizability, and the lack of license fees, which brings the cost structure of massively parallel computation down to a feasible level. Compared to other open-source CFD codes, the benefits of OpenFOAM are a large, active, and growing user base, parallelization, and an object-oriented code structure that makes it fast and easy to implement new models and solvers in the top-level code.

Like other software e.g., ANSYS, there are some methods available to create a mesh in OpenFOAM. OpenFOAM has its native meshing utilities for creating a mesh e.g., blockMesh, snappyHexMesh, cfMesh, foamyHexMesh, extrudeMesh. The 'blockMesh' utility is a structured hexahedral mesh generator that is well suited to simple geometries that can be described by a few blocks. However, it is challenging to apply for complex geometries with a large number of blocks due to book-keeping requirements. For complex geometries, the mesh generation utility called snappyHexMesh can be used. It generates 3D meshes containing hexahedra and split-hexahedra from a triangulated surface geometry in Stereolithography (STL) format.

It is also possible to create a mesh using third-party software, such as ANSYS, Gambit, PointWise, ICEM, and then use the in-built OpenFOAM mesh conversion utilities to convert it to the OpenFOAM format. Also, there is a number of OpenFOAM mesh manipulation utilities for checking and modifying the mesh including rotations, transform, etc.

3.6.4   OpenFOAM model for KWU-1300 and ICAS T2 transient

LUT University aimed to simulate the UPTF-TRAM Test C1 Run 21a2 case with the OpenFOAM. The grid was generated using Ansys Meshing and converted to OpenFOAM format (Figure 26). Base metal and cladding are excluded from the simulation because the two-phase OpenFOAM solver is not yet able to simulate them. Thus, only the fluid region is considered. Several probes were placed to record flow fields (Figure 27).
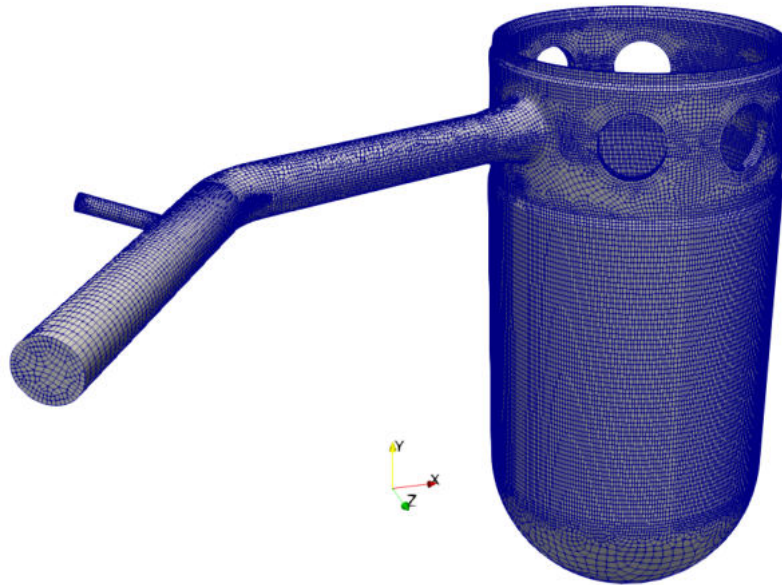
Figure 26: CFD mesh for OpenFOAM of the UPTF facility.
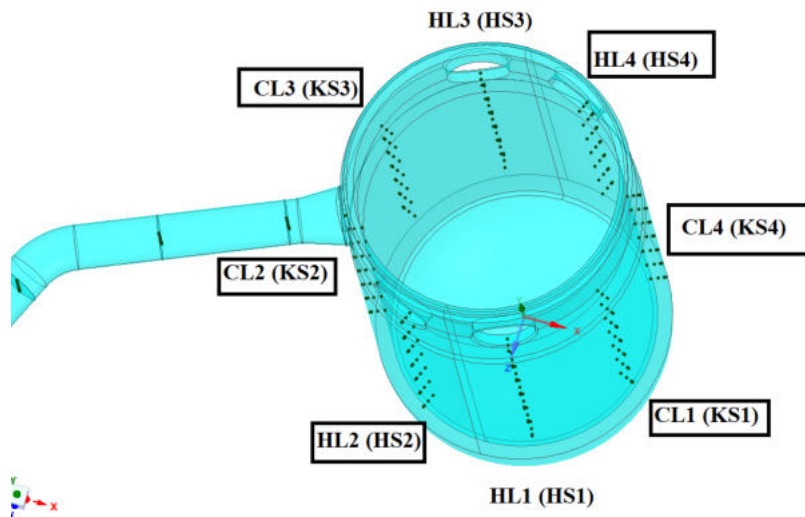
Figure 27: Probe locations for OpenFOAM simulations.

The compressible two-phase solver called 'reactingTwoPhaseEulerFoam' is used in which the flow system can be simulated with the Eulerian-Eulerian two-fluid approach. This solves the conservation of mass, momentum, and energy for both phases. Figure 28 shows the initialization of the volume fractions in the domain. The test vessel pressure was held constant at approximately 17 bar having Nitrogen above the water level. The temperature of stagnant water and Nitrogen was initialized at 461 K. The simulation was performed with the adaptive time stepping and max CFL (Courant-Friedrichs-Lewy condition) less than 1. Due to poor convergence, time-stepping goes smaller than 10e-06 s. In this simulation, the mass transfer at the interface is neglected to lessen the complexity. However, this two-phase solver (Eulerian-Eulerian) of OpenFOAM is well suitable for bubbly flows with heat and mass transferability. The UPTF case is more like stratified flow which is quite challenging to model with bubbly flows solvers due to the lack of suitable momentum transfer sub-models in OpenFOAM. Furthermore, in the OpenFOAM simulation, a huge reverse/backflow was noted at the outlet which leads to a large mass imbalance in the domain which could be the main reason for divergence.
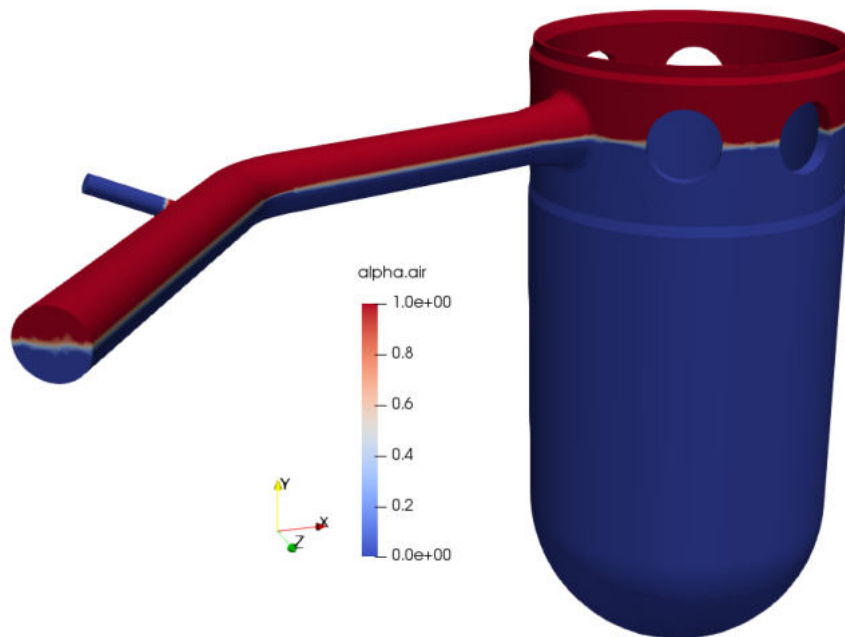
Figure 28: Volume fraction initialization in the domain.

After having issues with two-phase solver, a stratified flow solver could be next option. Thus, the Volume-Of-Fluid (VOF) method-based solver is being tested. This solver can treat two compressible and non-isothermal immiscible fluids using a phase-fraction-based interface capturing approach.

The momentum and other fluid properties are of the "mixture" and a single momentum equation is solved. Either with mixture or two-phase transport modelling may be selected. In the mixture approaches a single laminar, RAS or LES model can be selected to model the momentum stress.

Also, a single-phase flow solver can be used for UPTF-TRAM Test simulation in which only the liquid phase will be simulated. Thus, the Nitrogen will be omitted by removing the gas phase space from the RPV CFD domain (Figure 29 (a)). Furthermore, the CFD domain will be simplified by removing lower-DC part (Figure 29 (b)). This simplification might help in nonphysical rapid pressure fluctuation at the outlet. However, the effect of this simplification is not known yet. This simplified domain will be used with two-phase solver both with 'reactingTwoPhaseEulerFoam' and 'VOF' method.
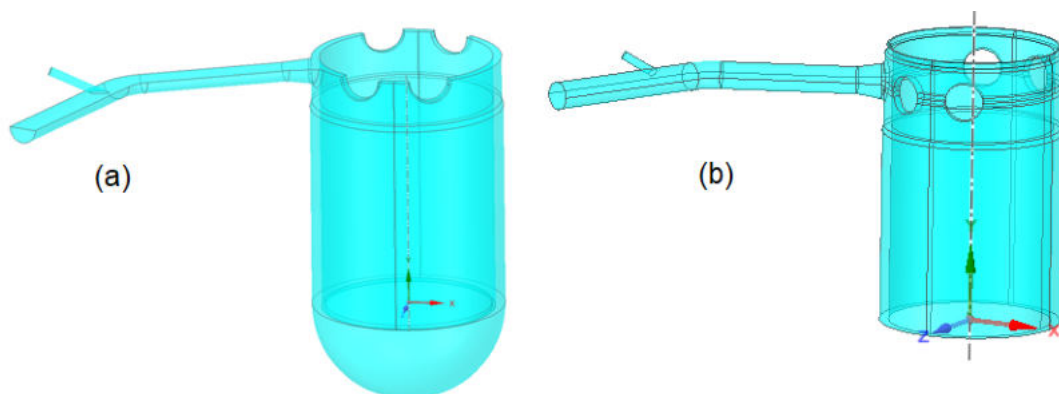
Figure 29: Simplified CFD domain of the UPTF-TRAM Test C1 Run 21a2 case.

Due to the above-mentioned problems encountered with the OpenFOAM modelling of the UPTF-TRAM Test C1 Run 21a2 case no calculation results are available to be included in this report.

4   Description and results of Task 2.1 base case calculations

4.1   RELAP5 results

4.1.1   Base case SBLOCA by UJV

A SBLOCA (50 cm²) with break in the core outlet region of KWU-1300 and with loss of offsite power was simulated with RELAP5/MOD3.3 Patch5 code version in UJV Rez. The scenario was prepared according to the ICAS T2 transient [3].

The initial parameters of the base case calculation "kwu76" are shown in the Table 13. The sequence of main events is summarised in Table 9. Time-dependent graphs showing the evolutions of the major system parameters are given in Figure 30 through Figure 41. Figure 42 shows a SNAP visualization of the RELAP5 results at time of 2405 s into the transient.

Table 9: Sequence of Events for the Reference SBLOCA in RELAP5 Simulations

Cause	Event	Time (s)
Primary pressure < 132 bars	Reactor trip Turbine trip Emergency signal Signal sec.-side cooldown (100K/hr auto.) MCPs trip	44
Analysis assumption	Loss of offsite power	44
Emergency signal + 12 s	Signal ECC system to start DG	56
Primary pressure < 110 bars	Emergency cooling signal for HPI pumps	79
HPI pumps running	HP injection	85
Primary pressure < 26 bars	ACC injection	2780
Primary pressure < 10 bars	Emergency coolant signal for LPI pumps	4550
LPI pumps running	LP injection	4555
ECCS injection stronger than break flow	PRZ level recovery	4700
End of calculation		4900

Occurrence of break 50 cm² in HL region leads to quick drop of primary pressure and PRZ level. After the pressure drops below 132 bar, the reactor and turbine are tripped, and the emergency core cooling system is actuated. Also, the loss of offsite power is assumed at time of reactor trip, leading among other to MCPs coast-down and transfer from forced to natural circulation.

After reaching saturation pressure in the primary system the pressure drop is counteracted by steam (void) production in primary system and slowed down as can be seen in Figure 30. The automated activation of the secondary side cooldown decreases the secondary side pressure with a 100 K/h cooldown trend which leads the pressure progression in the primary circuit until the late phase of the transient where the LPI is initiated.

The HPIS injection is actuated after pressure drop under 110 bars. In the analyses injection of 2 trains of HPIS into CL2 and CL3 is assumed and modelled. At time 2780 s after the transient initiation the ACC injection is initiated (primary pressure < 26 bars) and start to fill up the primary circuit. With the start of the LPI pumps at ~4550 s the coolant loss is stably compensated, and primary pressure stabilized slightly under 10 bar. The pressurizer level is restored after 4700 s (Figure 34 (b)).

(a)   (b)
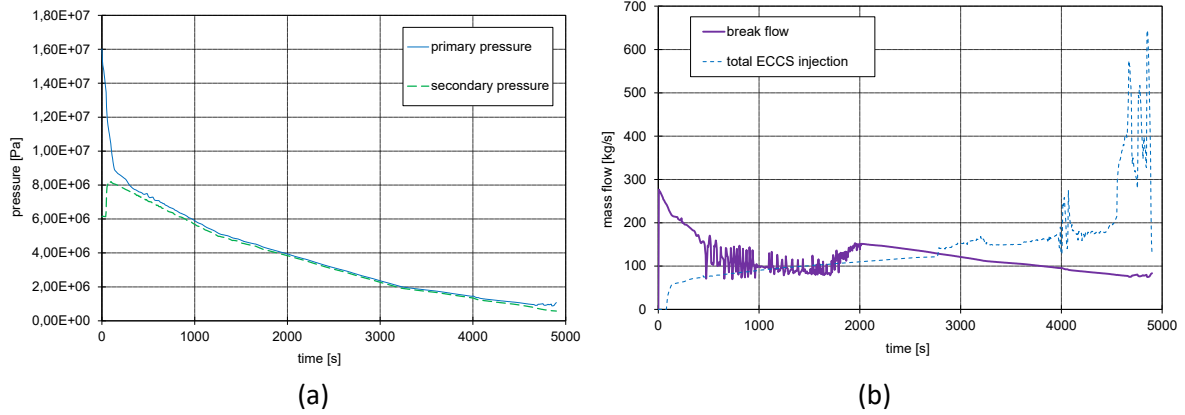
Figure 30: (a) System Pressures and (b) Break and ECCS Flow Rate.

(a)   (b)

Figure 31: (a) HPIS Injection and (b) LPIS Injection.

(a)   (b)
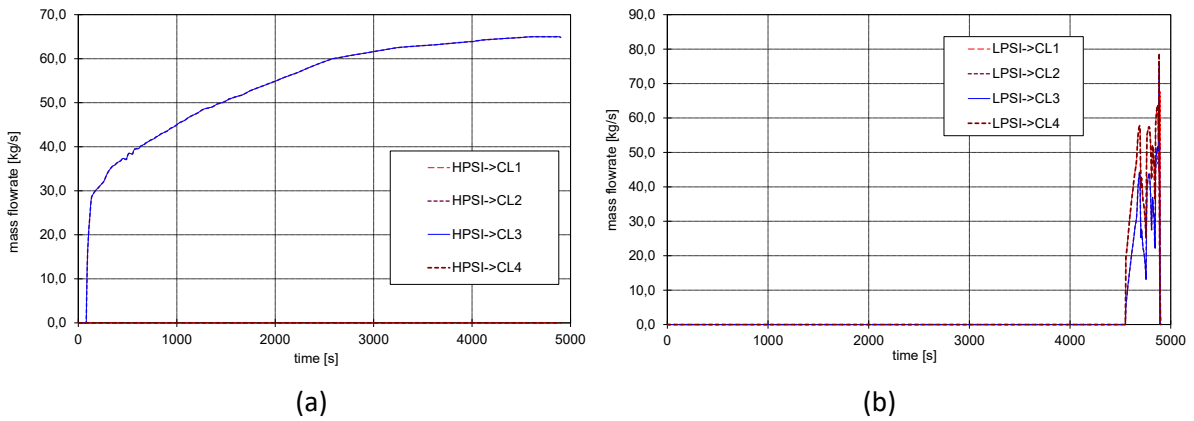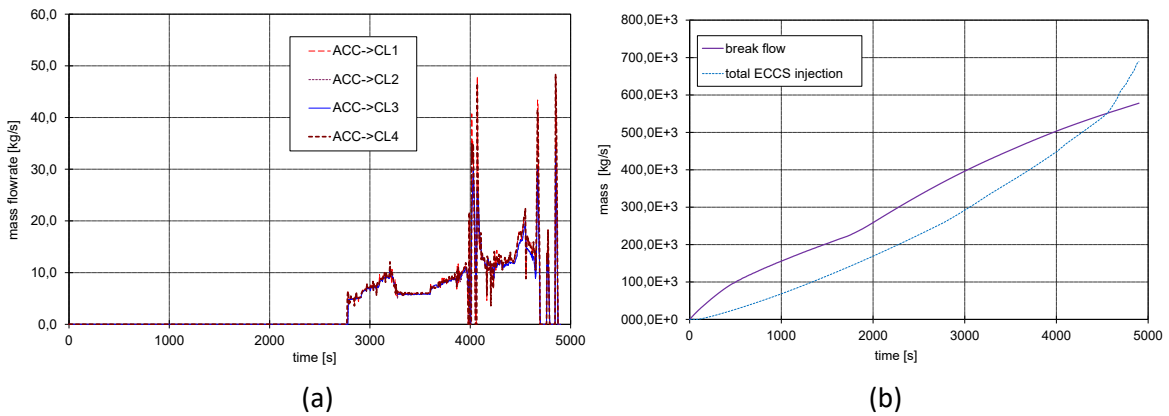
Figure 32: (a) ACC Injection and (b) Integrated Break and ECCS Flow.

(a)   (b)
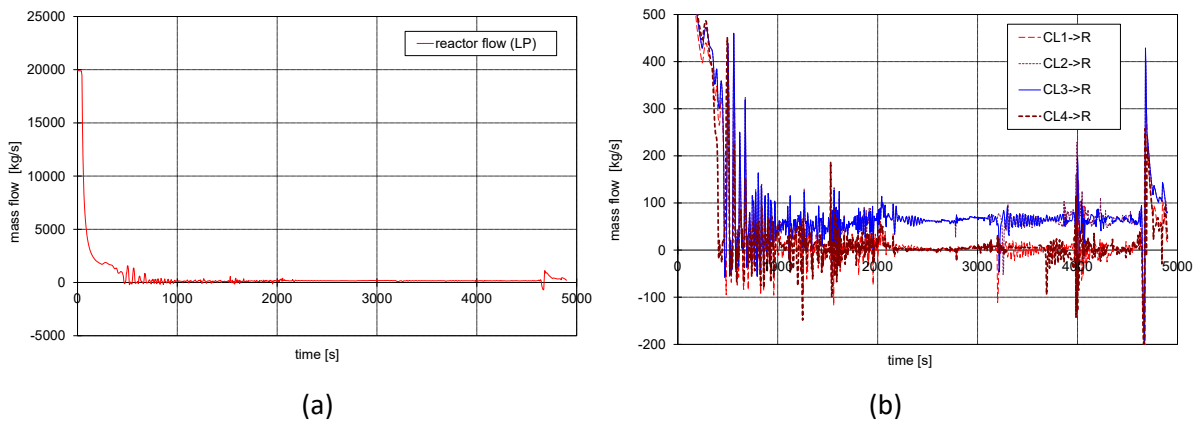
Figure 33: (a) Reactor LP Flow and (b) Reactor Inlet Flows (detail).

(a)   (b)
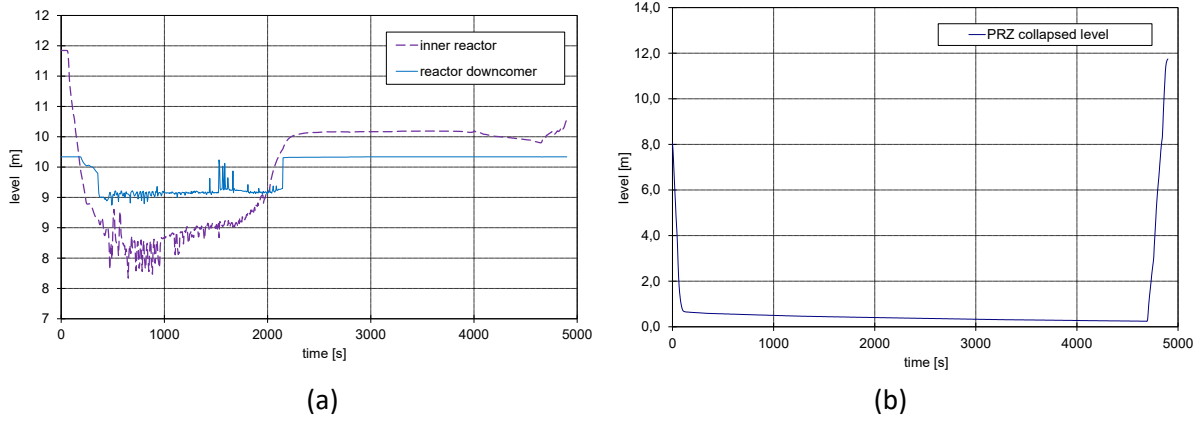
Figure 34: (a) Collapsed Liquid Levels in Reactor and (b) Pressurizer.

(a)   (b)
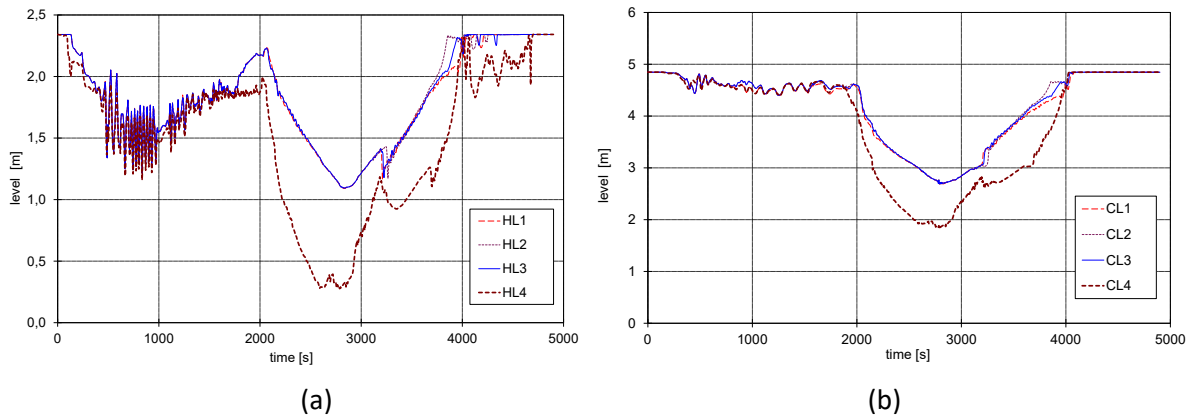
Figure 35: (a) Collapsed Liquid Levels in HLs and (b) in CLs by SG.

(a)   (b)
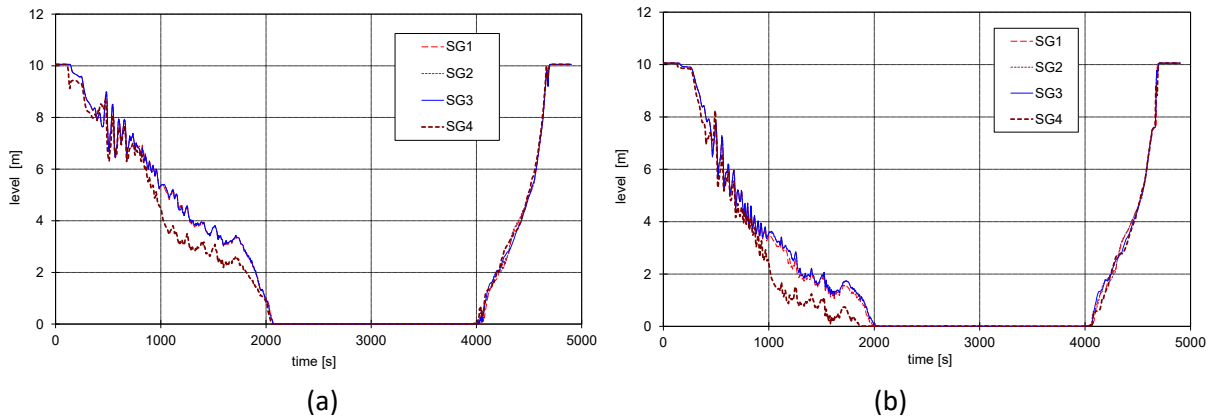
Figure 36: (a) Collapsed Liquid Levels in SG tubing Upward and (b) in SG tubing Downward Part

(a)   (b)
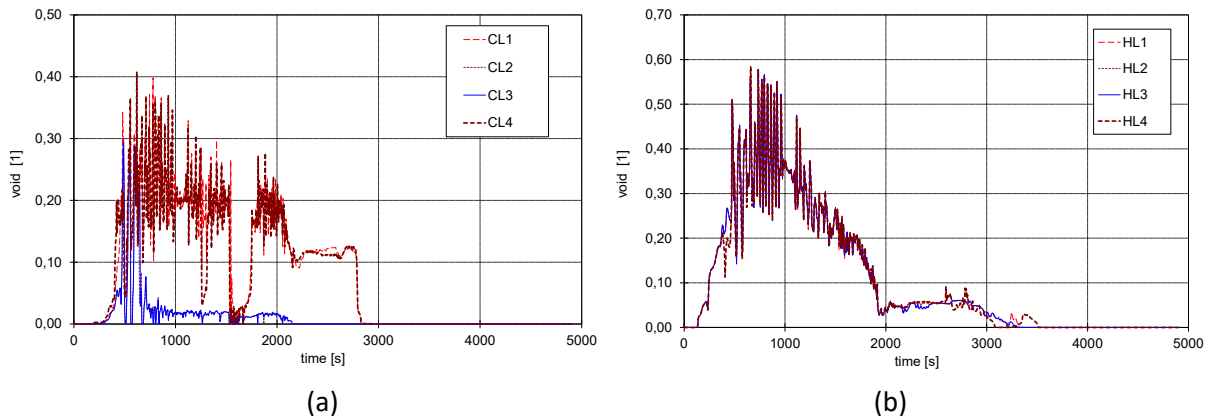
Figure 37: (a) Void Fraction in Reactor Inlet Nozzles and (b) in Reactor Outlet Nozzles.

58

(a)   (b)
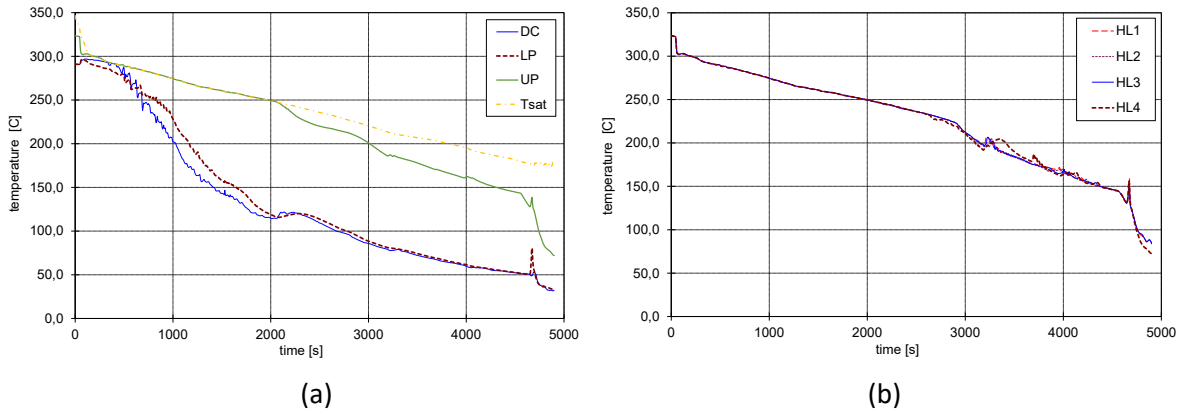
Figure 38: (a) Coolant Temperatures in Reactor and (b) Coolant Temperatures in HLs.

(a)   (b)
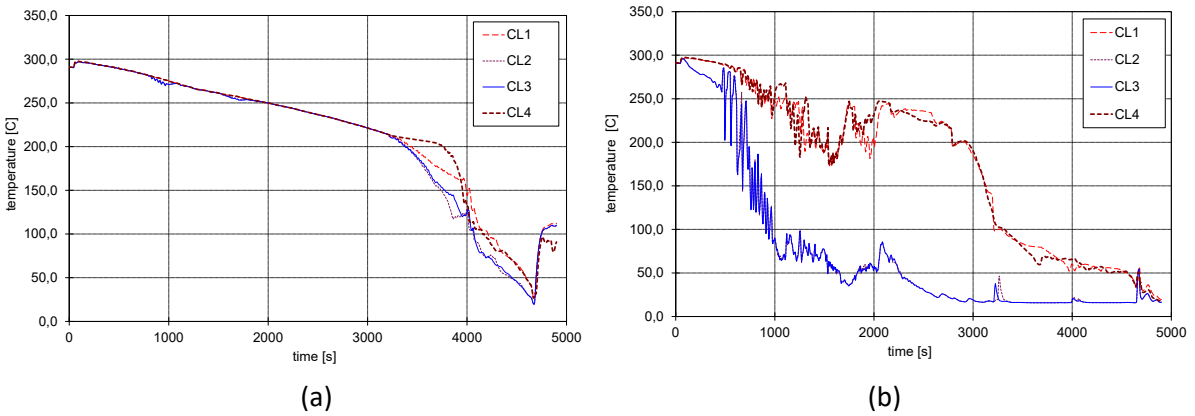
Figure 39: (a) Coolant Temperatures in CLs Loop Seal and (b) Reactor Inlet Nozzles.

(a)   (b)
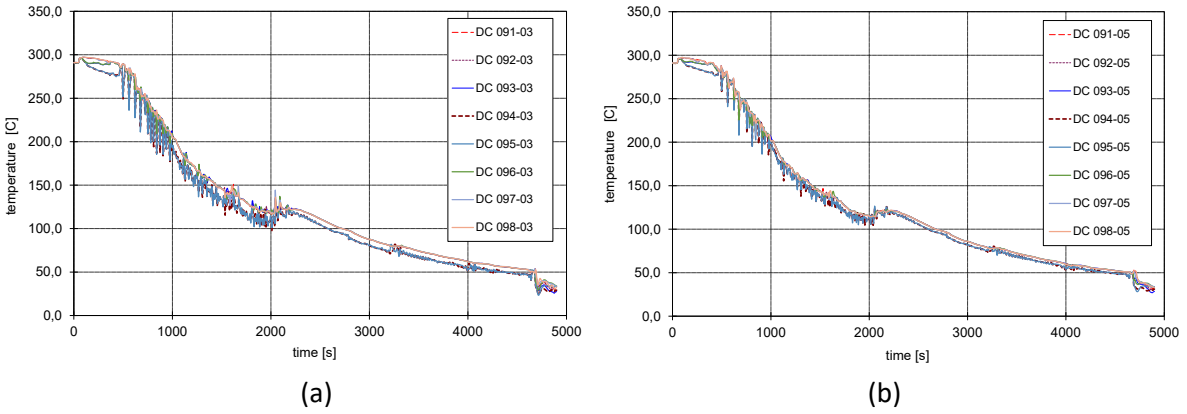
Figure 40: (a) Circumferential Coolant Temperatures in DC Control Volumes in Layer 3 at Elevation 1.13 m and (b) in Layer 5 at Elevation 2.638 m.

(a)   (b)
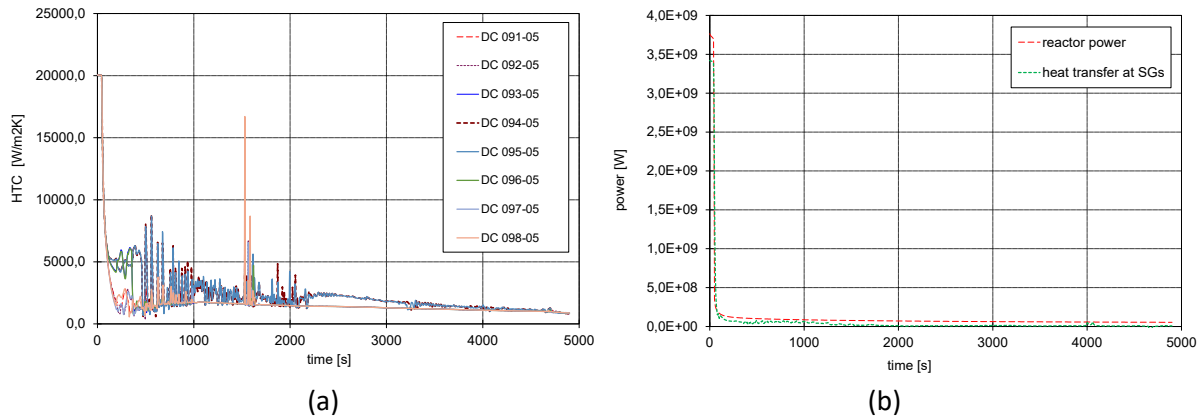
Figure 41: (a) HTC at RPV Inner Surface around DC at 2.638 m and (b) Reactor and SGs Power.

59
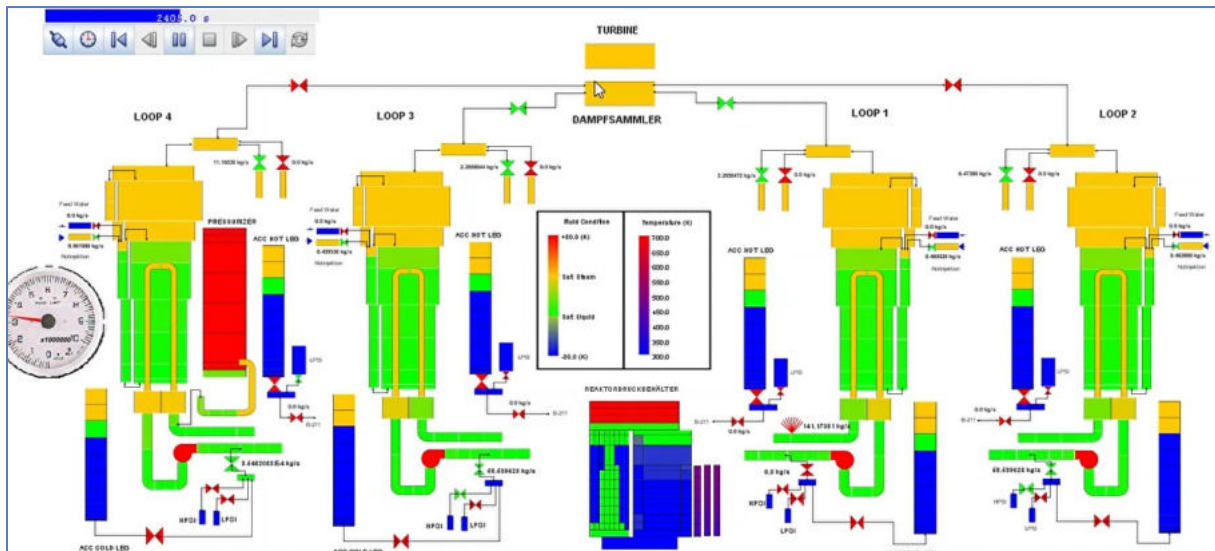
Figure 42: SNAP visualization of the RELAP5 results at time 2405 s.

4.1.2   Base case SBLOCA by JAEA

JAEA has conducted as an in-kind contribution to the APAL project calculations of the base case for the reference SBLOCA employing RELAP5/MOD3.3 code (Patch 2 - version 3.3ef). Some modifications were made to the input data that was provided by UJV, to better match the defined boundary conditions.

Table 10 summarizes the sequence of events in the base case. The corresponding variables of the individual parameters for the evaluation are the same as those used in other RELAP5 code simulations. The evaluation time is up to 5000 s after the break. Time-dependent graphs are given in Figure 43 through Figure 55.

Table 10: Sequence of Events for the Base Case SBLOCA by RELAP5/MOD3.3

Cause	Event	Time (s)
Primary pressure < 132 bar	Reactor trip, turbine trip, emergency signal, signal second.-side cooldown (100 K/h auto.), MCPs trip	45
Emergency signal + 12 s	Signal ECCS system to start	57
Primary pressure < 110 bar	Emergency cooling signal for HPI pumps	59
HPI signal + 20 s	HPI pumps running	79
HPI pump running + 3 s	HP injection	82
Primary pressure < 26 bar	ACC injection	2786
Primary pressure < 10 bar	Emergency coolant signal for LPI pumps	4502
LPI signal + 25 s	LPI pumps running	4527
LPI pumps running + 3 s	LP injection	4530
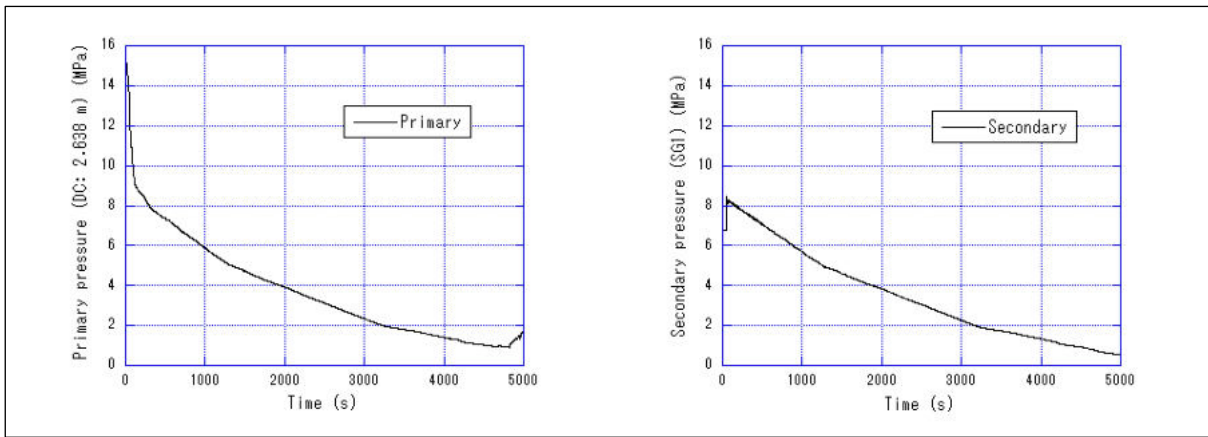
(a)   (b)

Figure 43: (a) Primary pressure (DC: 2.638 m under CL nozzles) and (b) secondary pressure.
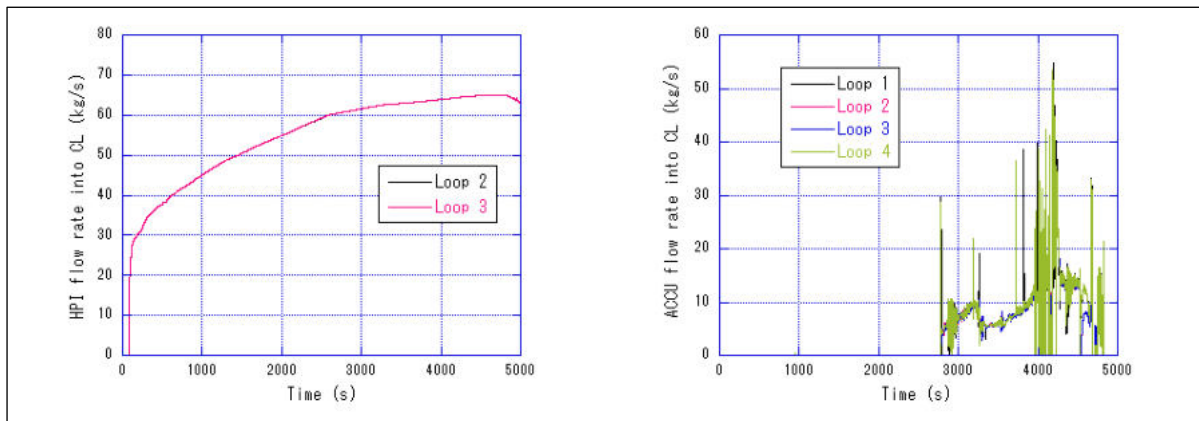
(a)   (b)

Figure 44: (a) HPI flow rates into CLs and (b) ACCU flow rates into CLs.
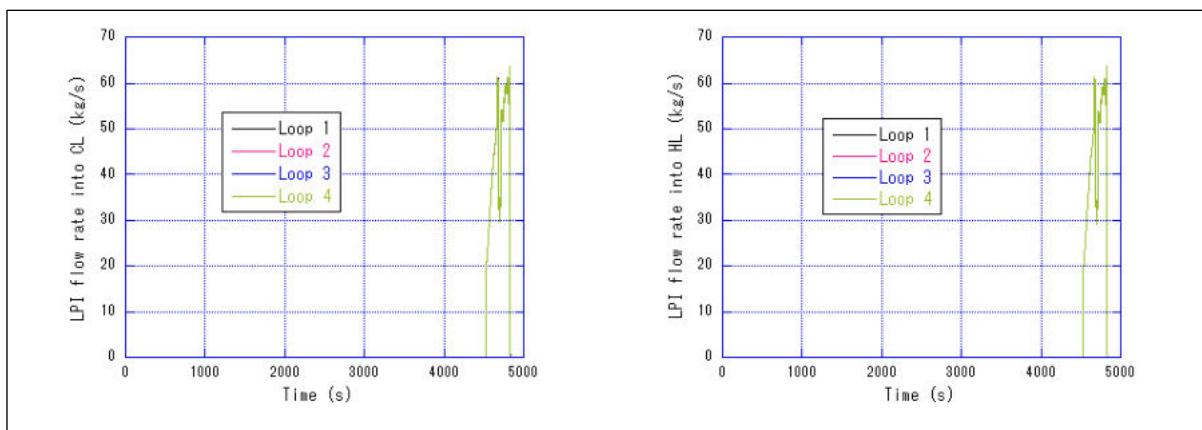
(a)   (b)

Figure 45: LPI flow rates into (a) CLs and (b) HLs.
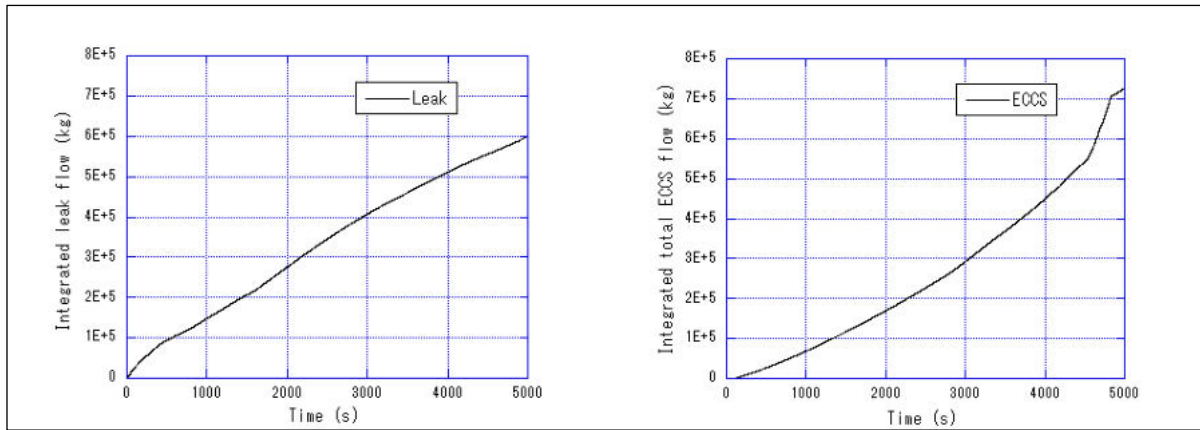
(a)   (b)

Figure 46: Integrated (a) leak flow and (b) total ECCS flow.
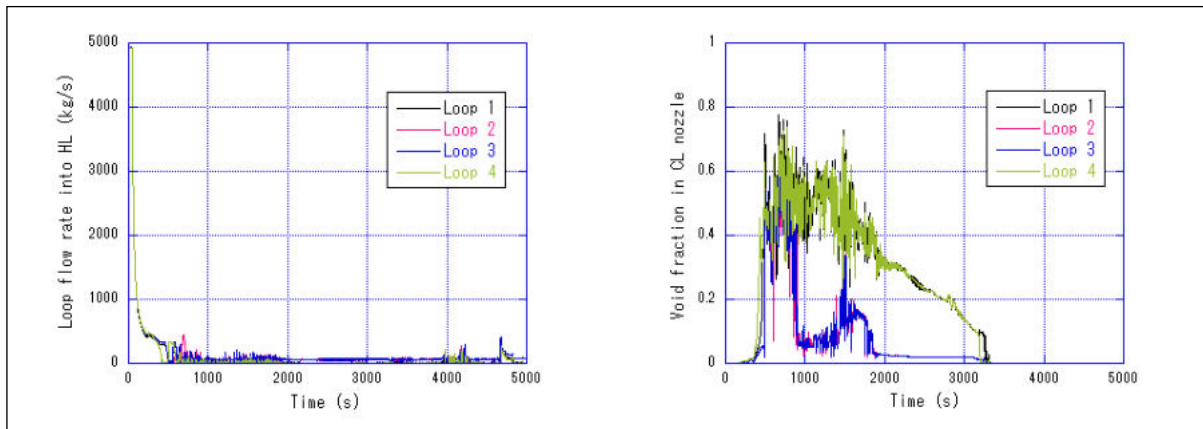
(a)   (b)

Figure 47: (a) Loop flow rates in HLs and (b) void fractions in CL nozzles.
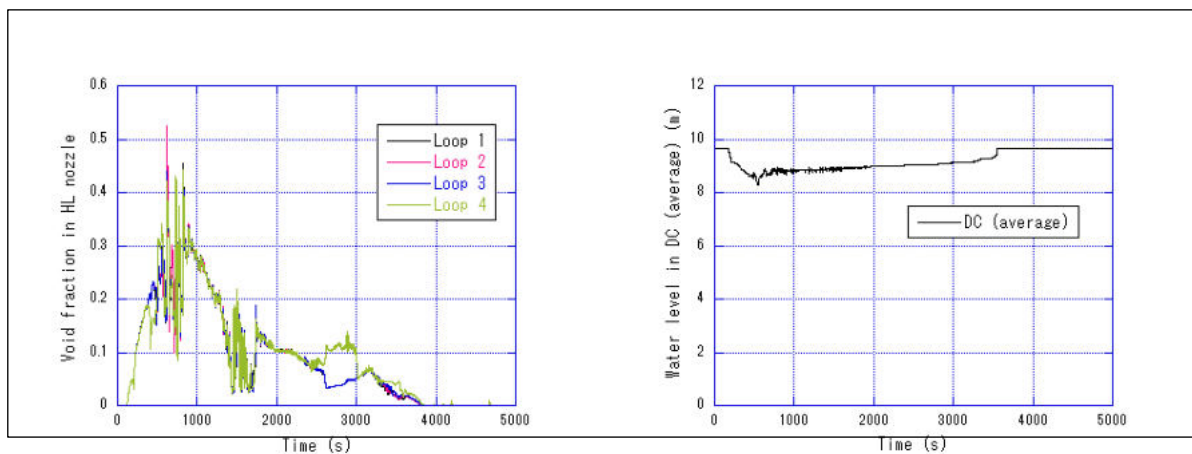
(a)   (b)

Figure 48: (a) Void fractions in HL nozzles and (b) water level in DC (average).
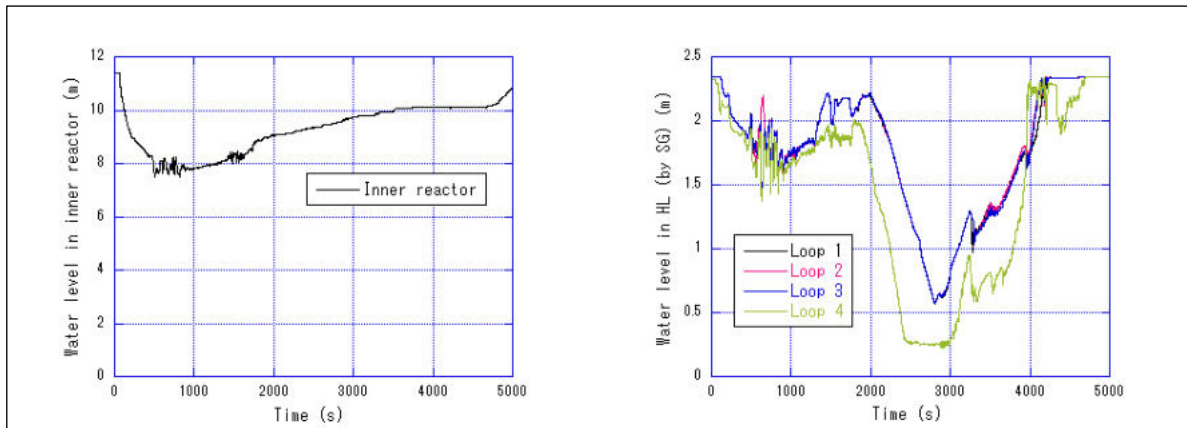
(a)　　　　　　　　　　　　　　　　　　　　　(b)

Figure 49: Water level in (a) inner reactor and (b) HLs (by SGs).
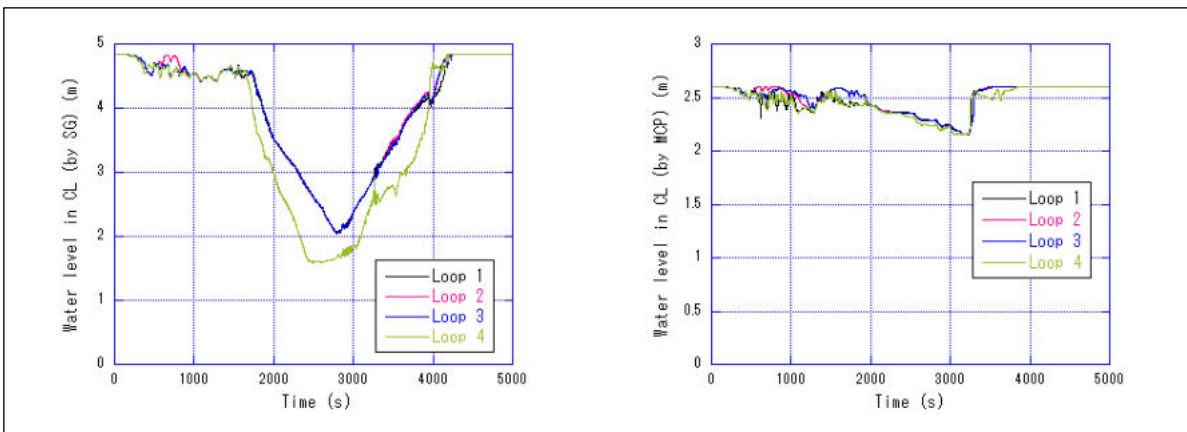
(a)　　　　　　　　　　　　　　　　　　　　　(b)

Figure 50: Water levels in CLs by (a) SGs and (b) MCPs.
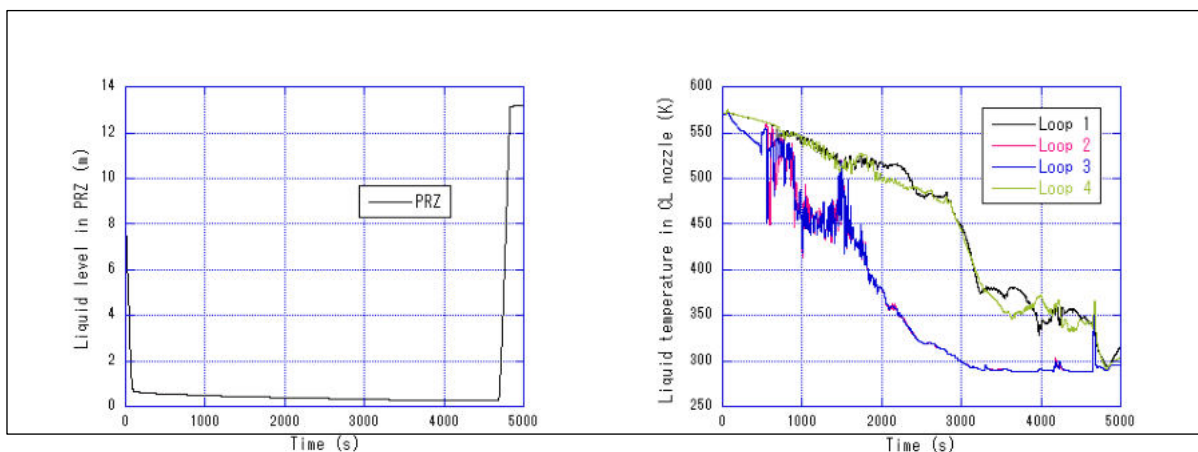
(a)　　　　　　　　　　　　　　　　　　　　　(b)

Figure 51: (a) Liquid level in PRZ and (b) liquid temperatures in CL nozzles.

(a)   (b)
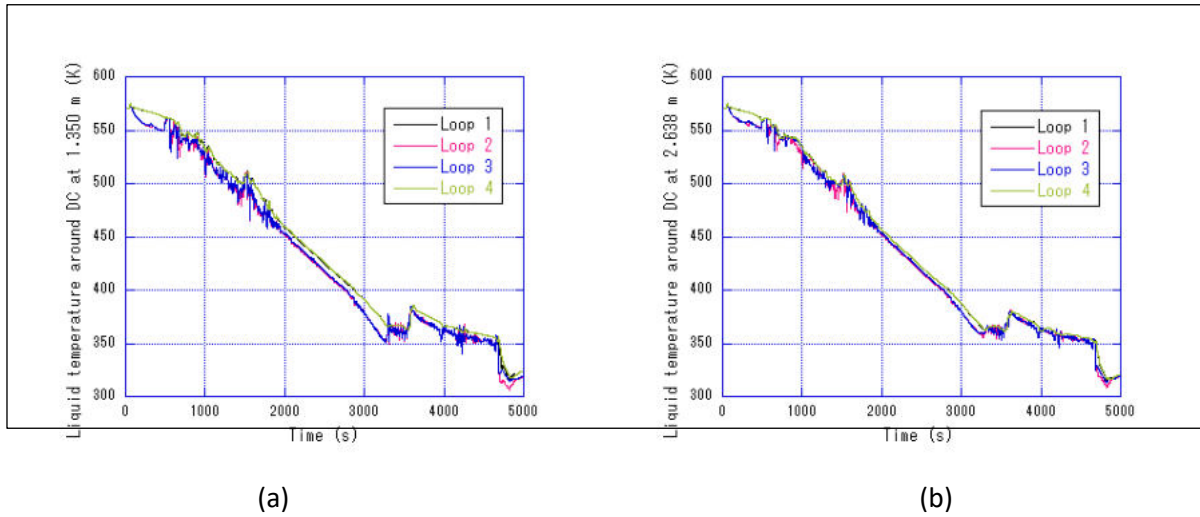
Figure 52: Liquid temperatures around DC at (a) 1.350 m and (b) 2.628 m.

(a)   (b)
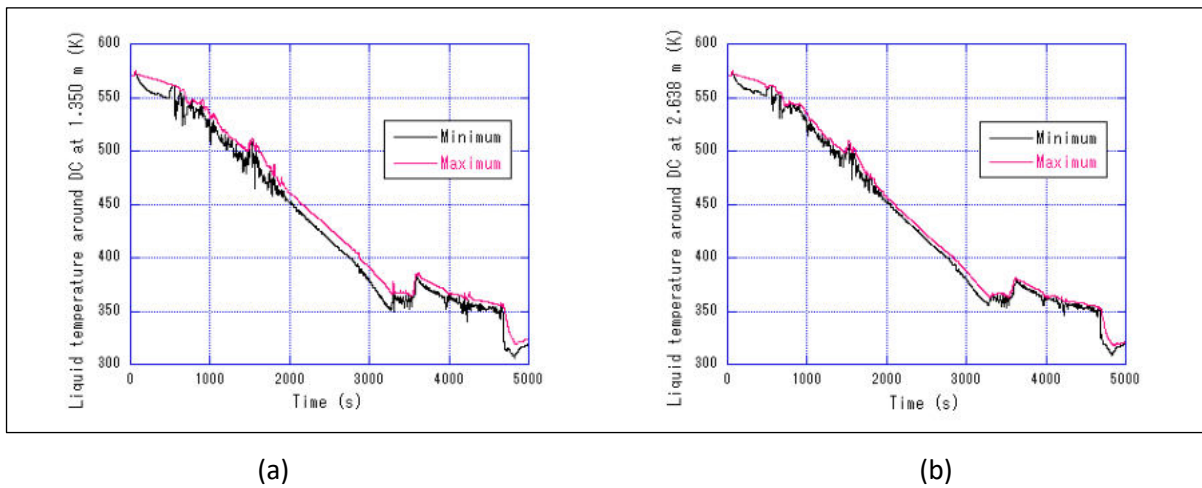
Figure 53: Minimum and maximum liquid temperatures around DC at (a) 1.350 m and (b) 2.638 m.

(a)   (b)
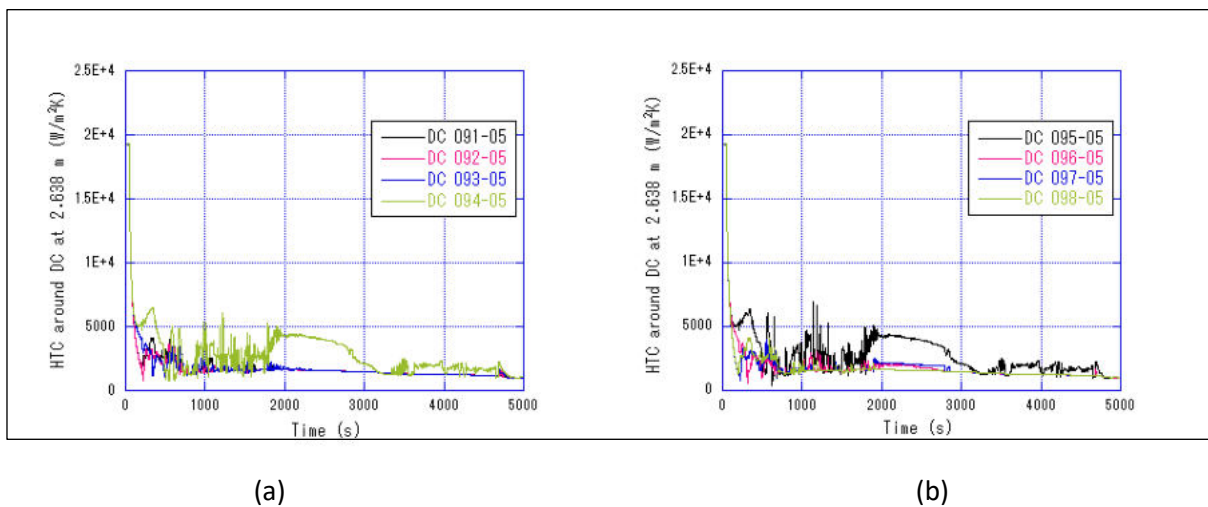
Figure 54: HTCs around DC at 2.638 m in (a) DC 091-05 through DC 094-05 and (b) DC 095-05 through DC 098-05.
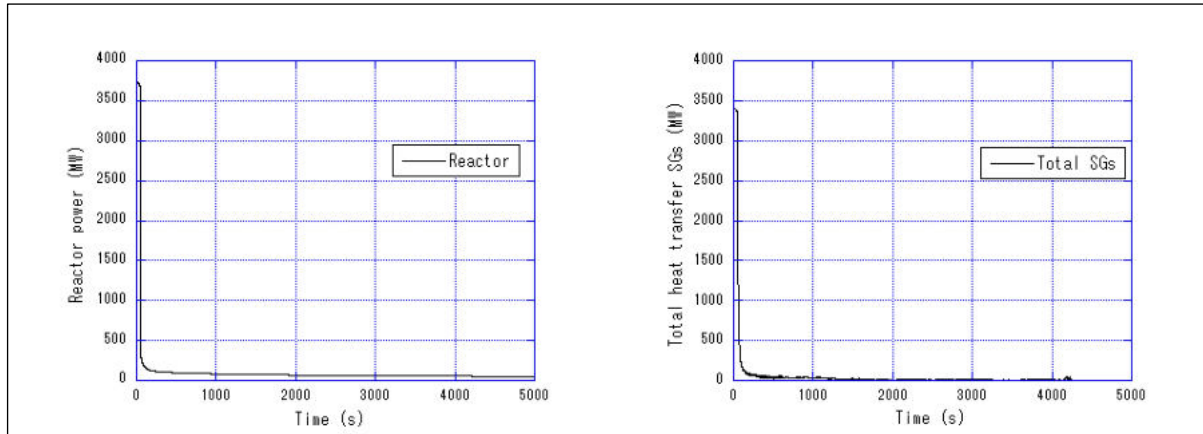
(a)   (b)

Figure 55: (a) Reactor power and (b) heat transfer in all SGs.

4.2 ATHLET results

4.2.1 Base case SBLOCA by GRS

A simulation of a SBLOCA (50 cm²) with break in the core outlet region and with loss of offsite power was simulated with AC2 2021 alpha (ATHLET 3.3 alpha). The sequence of events is summarised in Table 11. Time-dependent graphs showing the evolutions of the major system parameters are given in Figure 56 through Figure 63.

Table 11: Sequence of Events for the Reference SBLOCA in ATHLET Simulations

Cause	Event	Time (s)
Primary pressure < 132 bars	Reactor trip Turbine trip Emergency signal Signal sec.-side cooldown (100K/hr auto.) MCPs trip	30
Emergency signal + 12 s	Signal ECC system to start	42
Primary pressure < 110 bars	Emergency cooling signal for HPI pumps	56
HPI signal + 20 s	HPI pumps running	76
HPI pumps running + 3 s	HP injection	79
Primary pressure < 26 bars	ACC injection	2707
Primary pressure < 10 bars	Emergency coolant signal for LPI pumps	4469
LPI Signal + 25 s	LPI pumps running	4494
LPI pumps running + 3 s	LP injection	4497

After the break initiation, the primary pressure drops quickly below 132 bar, what trips the reactor and turbine and actuates the emergency core cooling system. When the saturation pressure of the primary system is reached the pressure drop is counteracted by void production as can be seen in Figure 56 (a) and Figure 58 (a). The automated activation of the secondary side cooldown decreases the secondary side pressure with a 100 K/h cooldown rate which leads the pressure progression in the primary circuit until the late phase of the transient where the LPI starts and stabilizes the pressure to ~10 bar after ~4700 s. 2700 s after the transient initiation the ACCs inject and start to fill up the primary circuit. When the liquid level in the primary circuit reaches the break position the leak mass flow quickly rises

and stabilizes at ~200 kg/s (see Figure 57 (a)). With the start of the LPI pumps at ~4500 s the coolant loss is fully compensated.

(a)   (b)
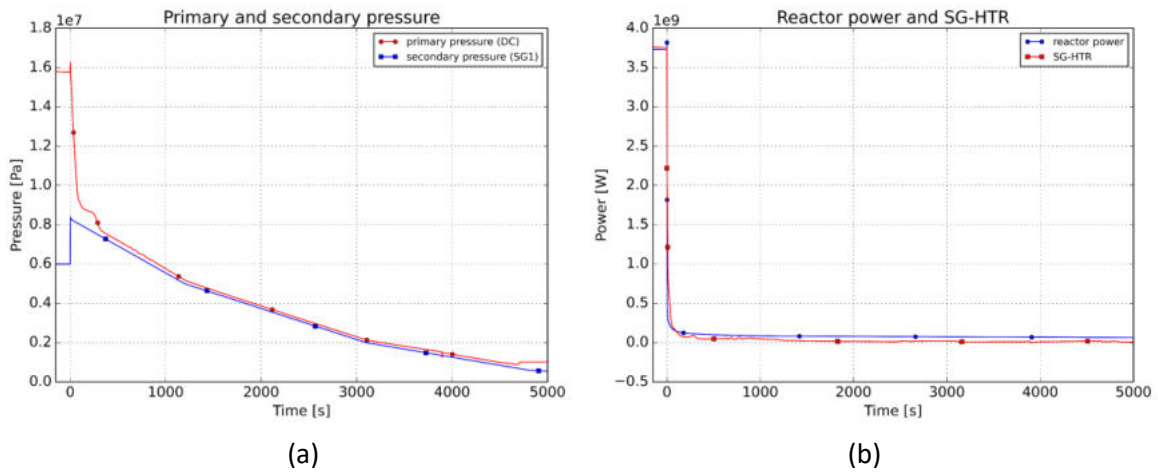
Figure 56: (a) System Pressures and (b) Reactor Power and Heat Removal by all SGs.

(a)   (b)
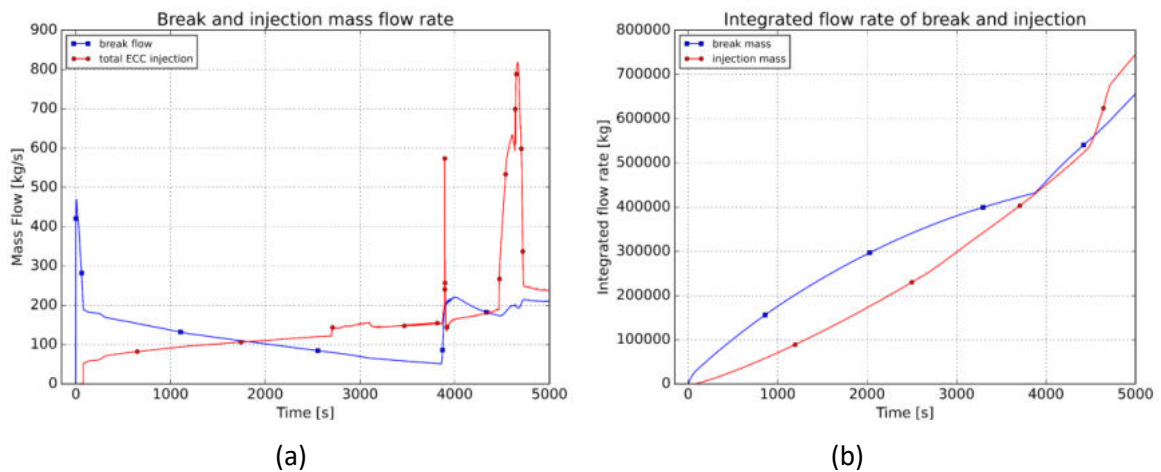
Figure 57: (a) Break Flow Rate and (b) Integrated Coolant Loss and Injection.

(a)   (b)
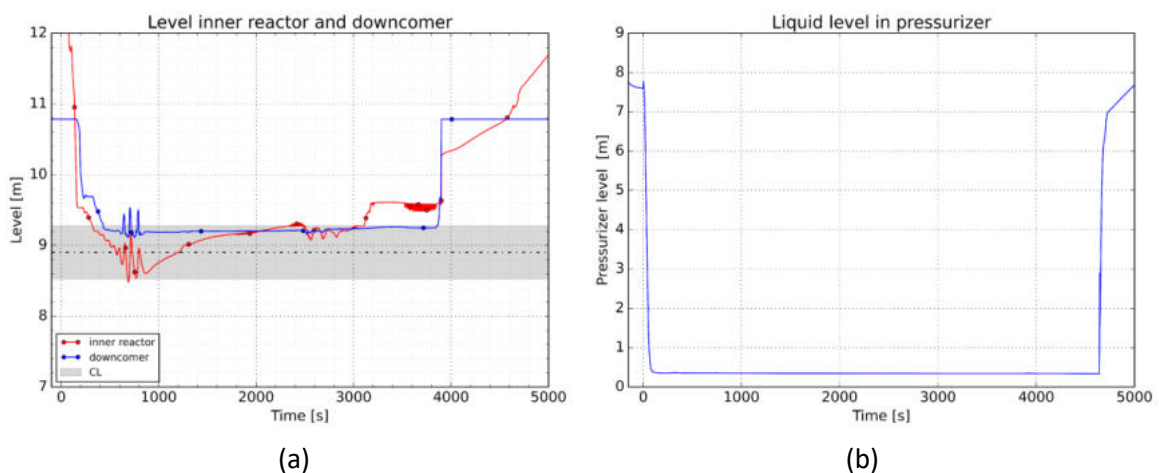
Figure 58: (a) DC Liquid Level and (b) PRZ Liquid Level.

66

(a)   (b)
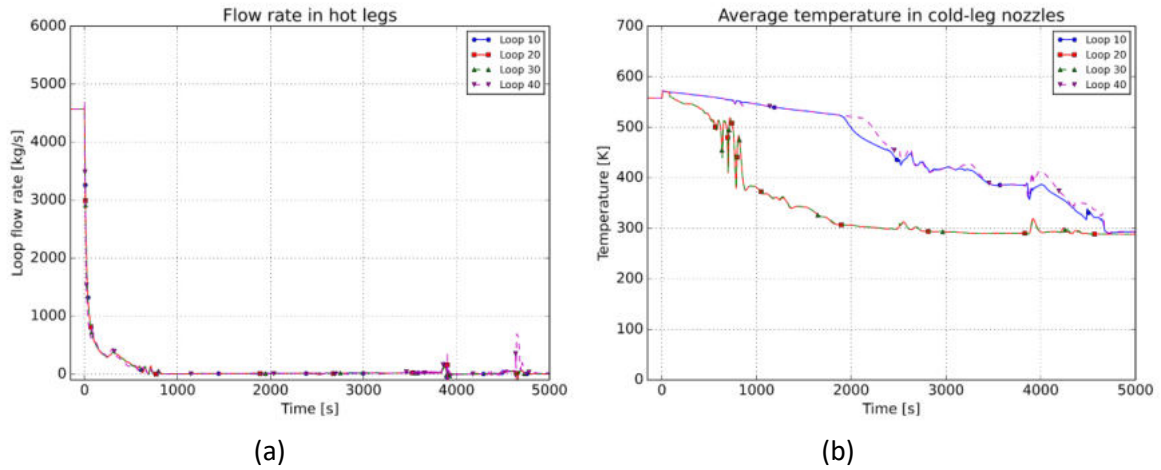
Figure 59: (a) HL Flow Rates and (b) Temperatures in the RPV Inlet Nozzles.

(a)   (b)
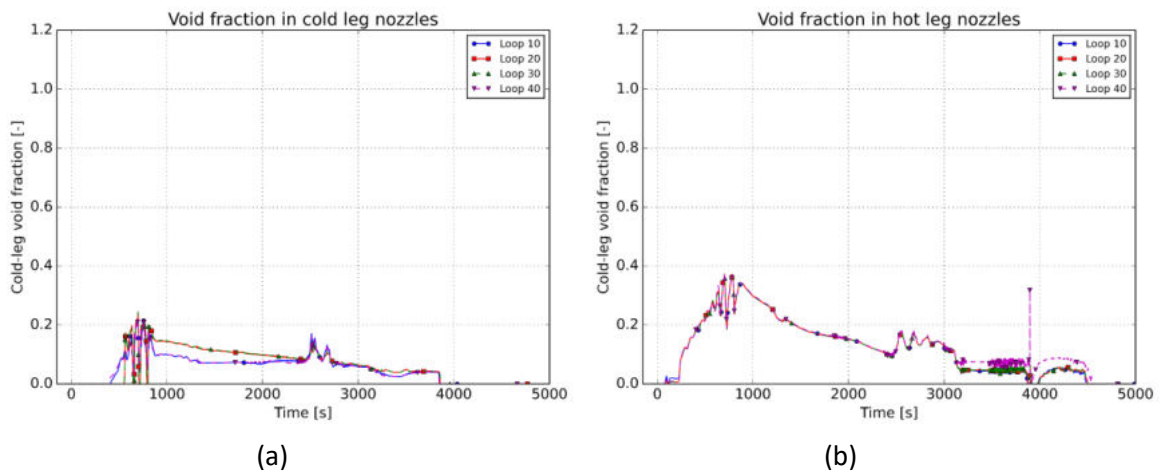
Figure 60: Void Fraction at the (a) RPV Inlet Nozzles and (b) RPV outlet Nozzles.

(a)

(b)

(c)

(d)

(e)

(f)
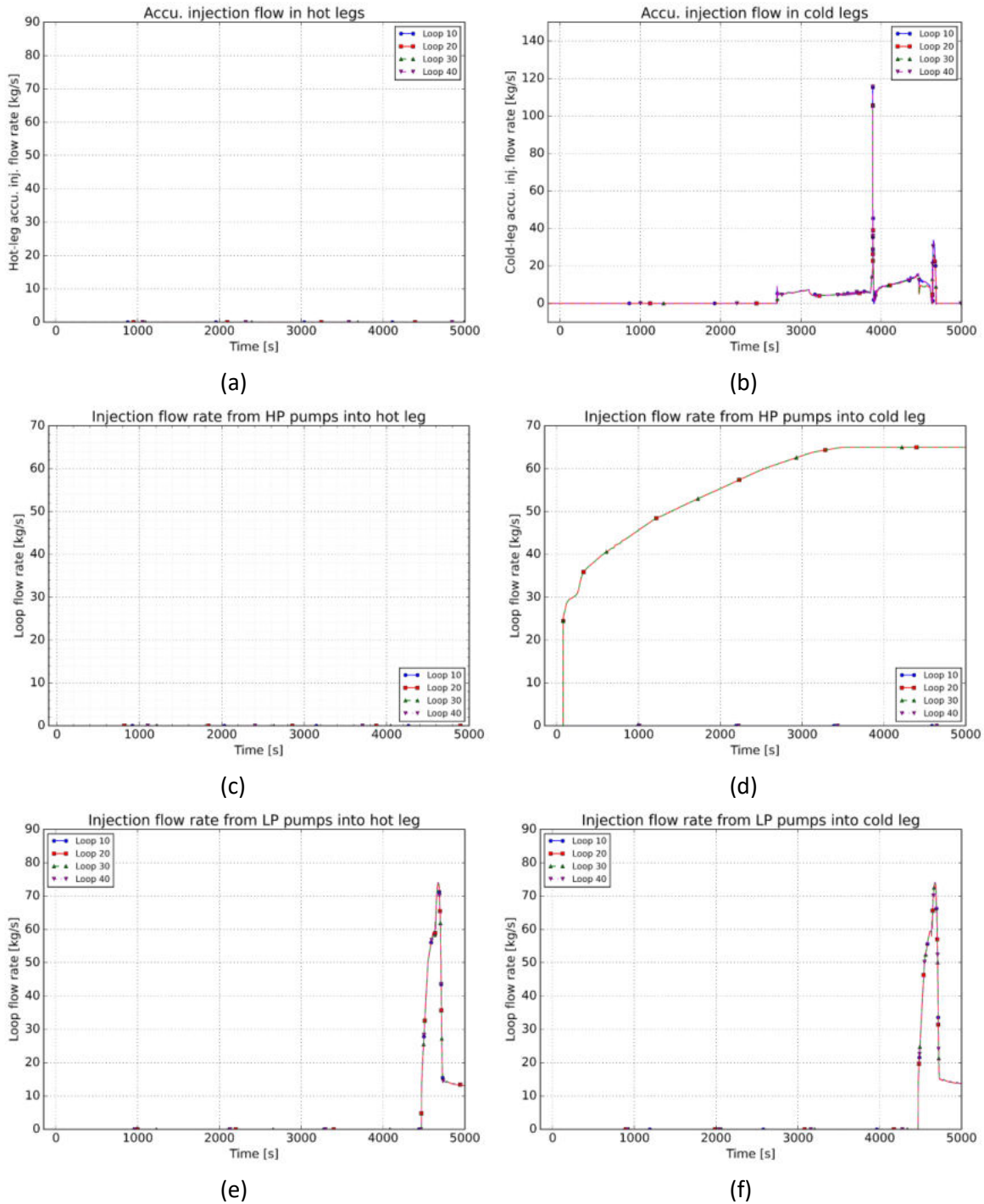
Figure 61: (a) HL and (b) CL ACC Flow Rates, (c) HL and (d) CL HPI Flow Rates, and (e) HL and (f) CL LPI Flow Rates.

(a)   (b)
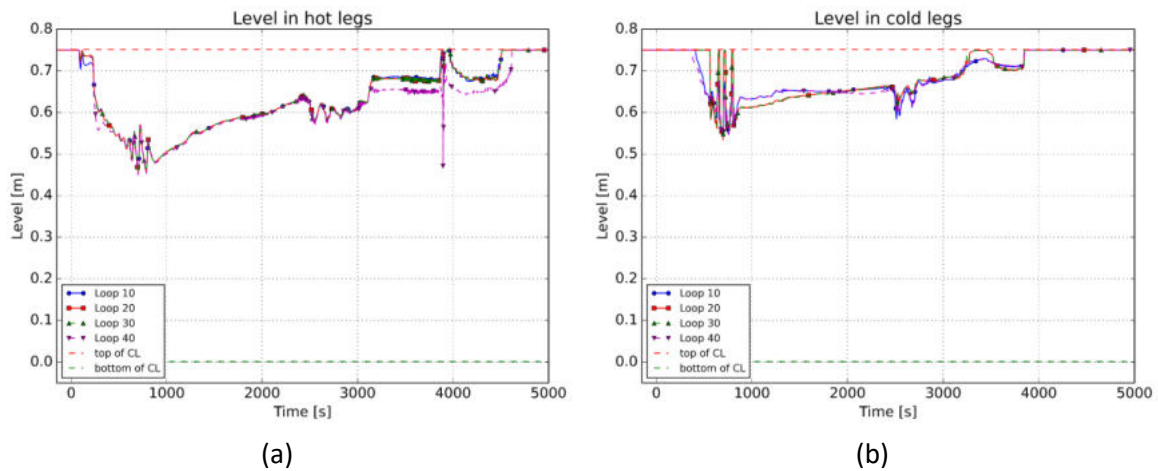
Figure 62: Collapsed Liquid levels in the (a) HLs and (b) CLs.
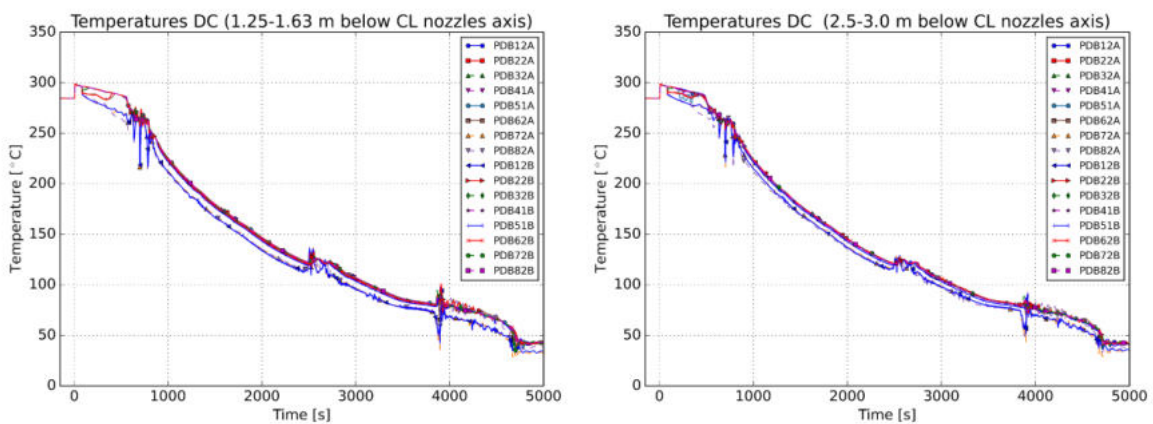
Figure 63: Circumferential Coolant Temperatures in DC Control Volumes Covering 1.350 m (left) and 2.638 m (right) below the RPV Inlets.

4.2.2   Influence of Injection Model and Mixing Code (ATHLET, ECCMIX, GRSMIX)

The base case was simulated applying the ATHLET integrated injection model ECC-MIX (see chapter 3.5.3) and the temperatures and heat transfer coefficients in the DC at the postulated weld positions 1.350 m and 2.638 m below the CL symmetry axis were additionally calculated using the mixing code GRS-MIX (see chapter 3.5.1). Results in comparison to the transient simulation without applying a mixing model (case "ATHLET" only) are depicted below for the key quantities of interest in Figure 64 to Figure 71. It can be seen that the application of the ECC-MIX model influences the amount of void that builds up in the main coolant pipes (Figure 66) and the DC (Figure 64; right). This is mainly due to the way the injection model is implemented in ATHLET and redirects parts of the injected mass flow (the mixture mass flow) from the ECCS injection point directly into the DC as described in chapter 3.5.3, [4][24]. A consequence is an influence on the fluid enthalpy and the void at the break position that goes to zero ~500 s earlier applying ECC-MIX (see Figure 66; left) and thus leads to an earlier increase in coolant loss mass flow (see Figure 65; left). Figure 67 and Figure 69 show that using ECC-MIX leads to lower temperatures at the postulated weld positions 1.35 m and 2.638 m below the CL symmetry axis of up to -20 K. By calculating local temperatures with GRS-MIX based on the results of the "ATHLET" base case an immediate decrease can be observed for both investigated positions (see Figure 70) with a maximum deviation of -35 K at the 1.35 m position. At the position 2.638 m below the CL the temperature deviation between the results of ECC-MIX and GRS-MIX is small. Figure 71 shows that GRS-MIX predicts a higher HTC than the "ATHLET" only and ECC-MIX case. The use of the integrated injection model ECC-MIX and mixing code GRS-MIX thus seems to have a clear influence on

69

the predicted temperatures and HTCs in the DC when compared to the results obtained with only ATHLET.
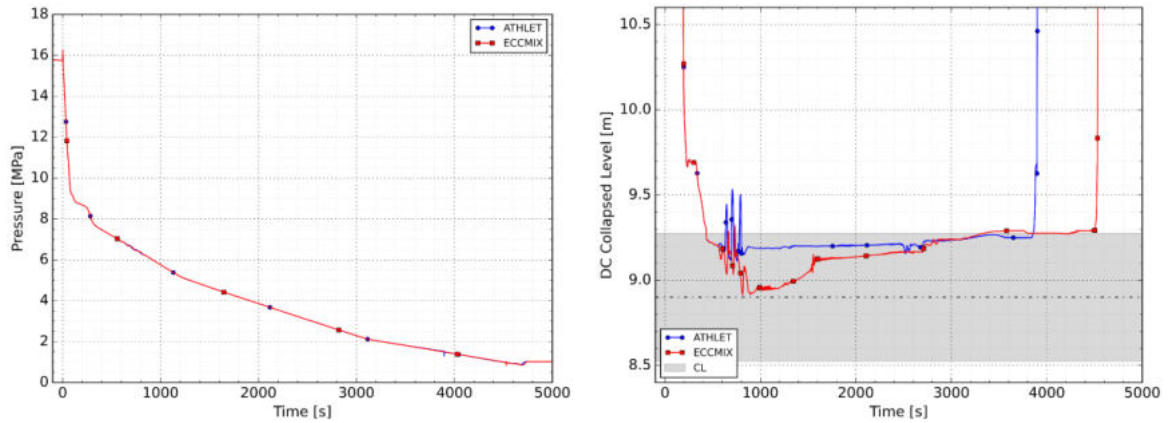
Figure 64: Comparisons of (left) Pressure in the DC at 2.638 m below the CL Axis and (right) DC Level for TH Results ("ATHLET") only and used Mixing Model (ECCMIX).
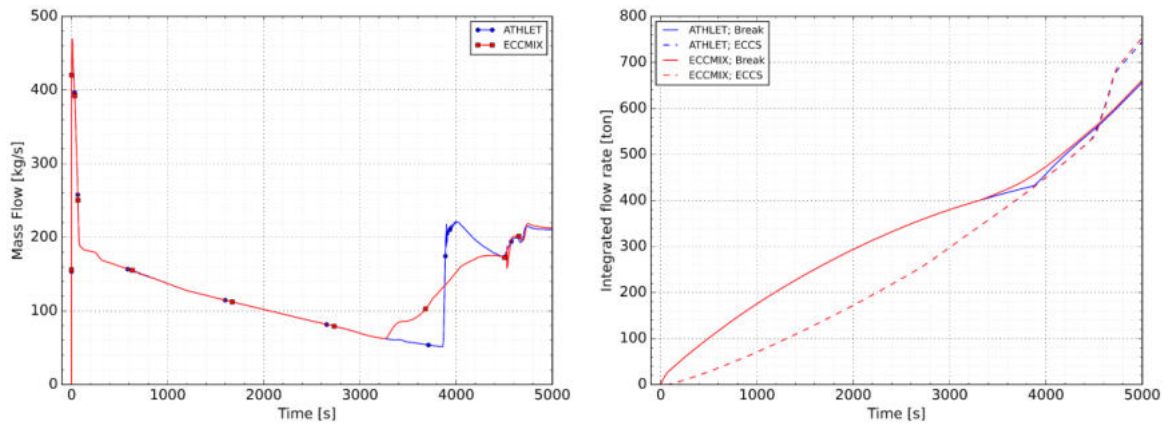
Figure 65: Comparisons of (left) Break Flow and (right) Time-integrated Coolant Loss and ECCS Injection for TH Results ("ATHLET") only and used Mixing Model (ECCMIX).
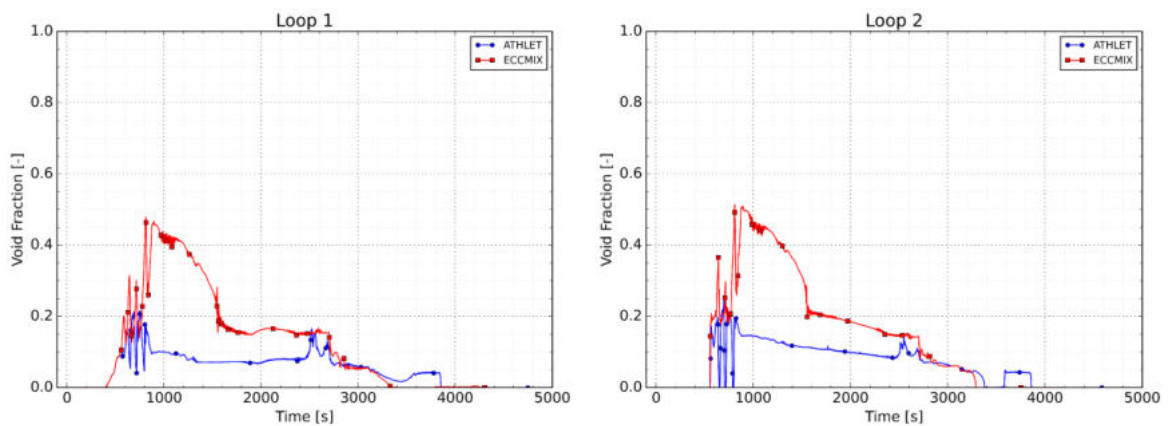
Figure 66: Comparisons of Void Fraction at the RPV Inlets of Loops 1 and 2 for TH Results ("ATHLET") only and used Mixing Model (ECCMIX).
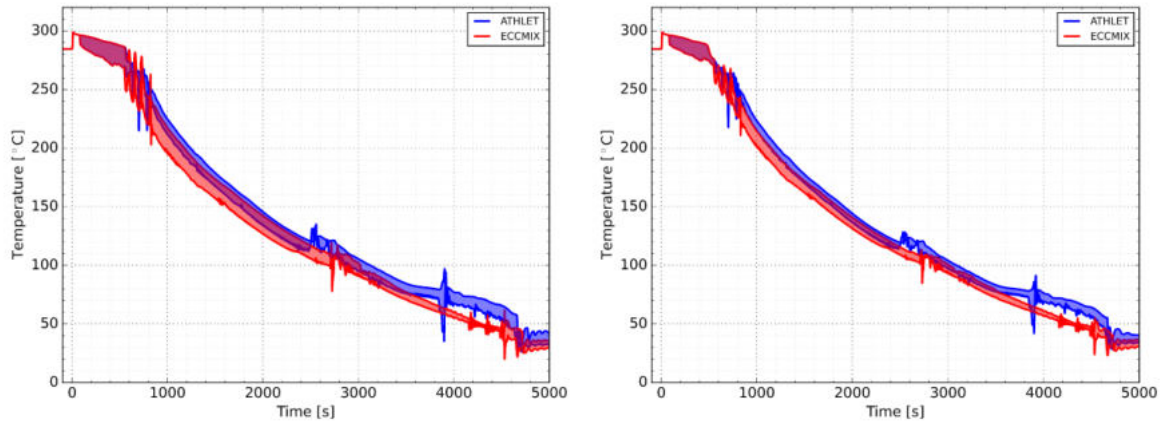
Figure 67: Comparisons of DC Coolant Temperature Range (Minimum to Maximum) at (left) 1.35 m and (right) 2.638 m below the CL Axis for TH Results ("ATHLET") only and used Mixing Model (ECCMIX).
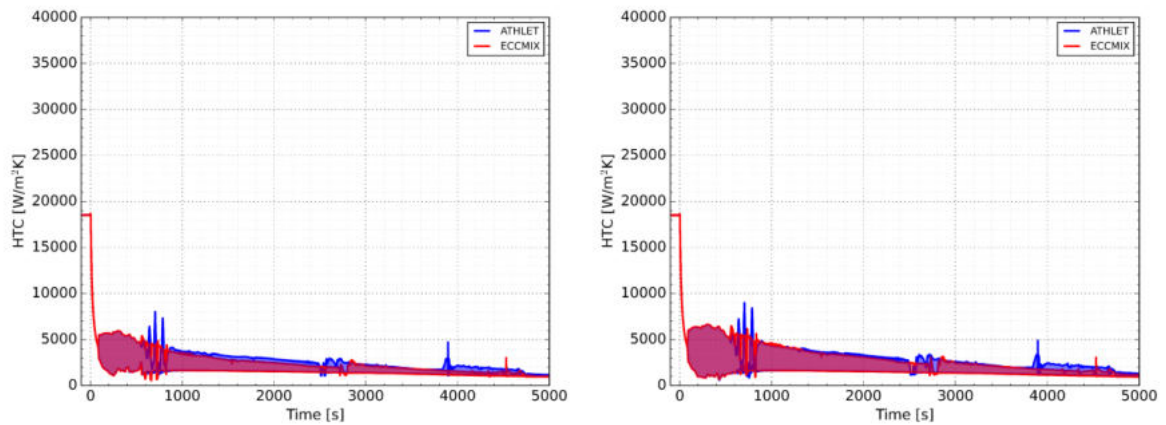
Figure 68: Comparisons of DC HTC Range (Minimum to Maximum) at (left) 1.35 m and (right) 2.638 m below the CL Axis for TH Results only and used Mixing Model (ECCMIX).
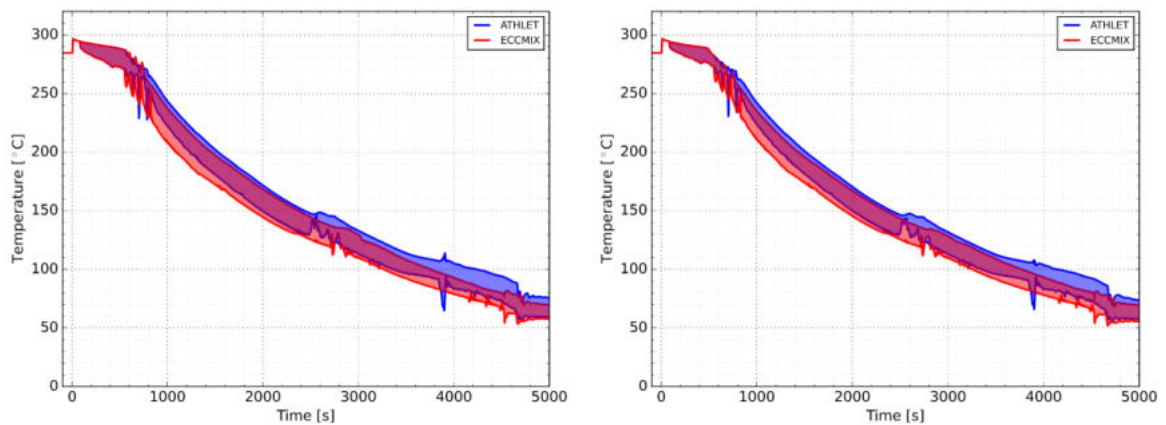
Figure 69: Comparisons of RPV Inner Surface Temperature Range (Minimum to Maximum) at (left) 1.35 m and (right) 2.638 m below the CL Axis for TH Results only and used Mixing Model (ECCMIX).
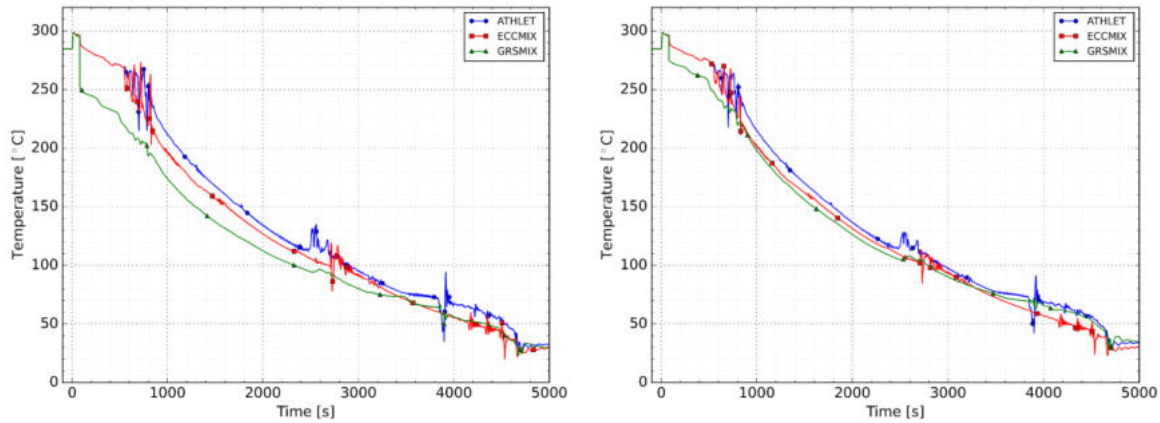
Figure 70: Comparisons of DC Coolant Temperature at (left) 1.35 m and (right) 2.638 m below the CL Axis for TH Results ("ATHLET") only and used Mixing Model and Code (ECCMIX, GRSMIX).
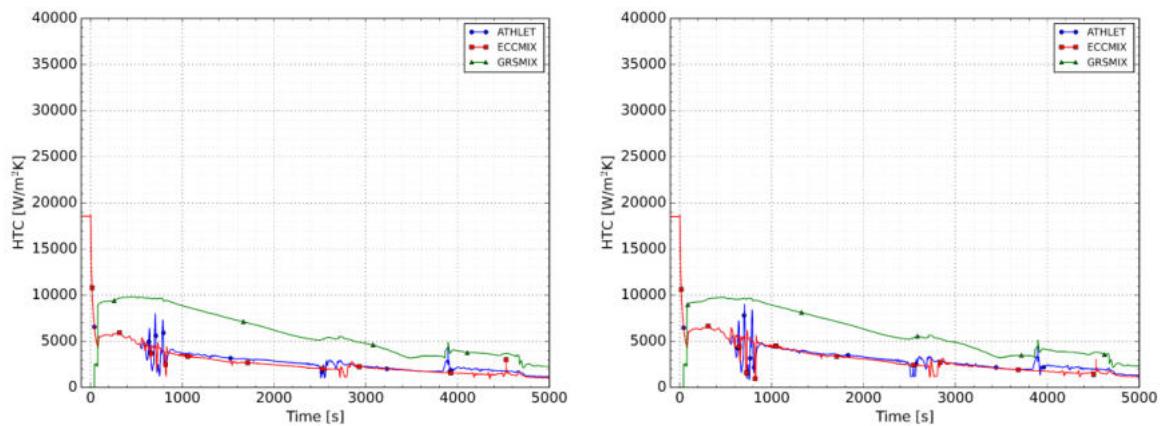
Figure 71: Comparisons of DC HTC at (left) 1.35 m and (right) 2.638 m below the CL Axis for TH Results ("ATHLET") only and used Mixing Model and Code (ECCMIX, GRSMIX).

4.3   TRACE results

4.3.1   Base case SBLOCA by PSI

The reference SBLOCA is a 50 cm^2 break in Hot Leg 1. The sequence of events is listed in Table 12.

Table 12: Sequence of Events for the Reference SBLOCA in TRACE simulations

Cause	Event	Time (s)
Primary pressure < 132 bars	Reactor trip Turbine trip Emergency signal Signal sec.-side cooldown (100K/hr auto.) MCPs trip	42
Emergency signal + 12 s	Signal ECC system to start	54
Primary pressure < 110 bars	Emergency cooling signal for HPI pumps	74
HPI signal + 20 s	HPI pumps running	94
HPI pumps running + 3 s	HP injection	97
Primary pressure < 26 bars	ACC injection	2494
Primary pressure < 10 bars	Emergency coolant signal for LPI pumps	4364
LPI Signal + 25 s	LPI pumps running	4389

LPI pumps running + 3 s	LP injection	4392

Time-dependent graphs showing the evolutions of the major system parameters are given in Figure 72 through Figure 79. After the initiating event, the primary pressure drops relatively quickly to the saturation pressure of the primary system, leading to reactor trip and activation of the ECC system and high-pressure safety injection (HPSI). This initial depressurization causes significant void formation in the primary system, which is seen as a drop in the system liquid levels in Figure 72c. Due to the automated activation of secondary side cooldown, the secondary pressure decreases according to the specified 100 K/h cooldown rate for the remainder of the transient. The primary pressure generally follows the secondary pressure for the duration of the transient. At ~2200 s, the primary pressure drops relatively quickly below the secondary pressure. This is believed to be due to the refilling of the upper plenum and hot legs, leading to an increase in break flow rate. After ~2500 s the ACCs inject, causing the liquid levels in primary system to quickly recover. After the low-pressure injection (LPI) starts, the total safety injection flow rate is sufficient to fully compensate the coolant loss from the break, and the primary pressure stabilizes around the pump head of the LPI pumps.

4.3.2 Downcomer Coolant Temperature and HTC

Since parts of the DC are uncovered during the transient, the effective coolant temperature and heat transfer coefficient (HTC) must be calculated taking multi-phase effects into account. In TRACE, the heat transfer is the sum of three components, the heat transfer to the liquid phase ($q''_{w,l}$), to the vapour/gas phase ($q''_{w,g}$), and the direct boiling ($q''_{w,sat}$).

$$q''_{w,l} = h_{w,l}(T_w - T_l)$$

$$q''_{w,g} = h_{w,g}(T_w - T_g)$$

$$q''_{w,sat} = h_{w,sat}(T_w - T_{sat})$$

where h is the heat transfer coefficient and the subscripts w, l, g and sat refer to the wall, liquid phase, vapour phase/gas and saturation conditions, respectively. The total heat flux can be written as the sum of these three components.

$$q''_{w,c} = h_{w,c}(T_w - T_c) \tag{1}$$

where the subscript c refers to the effective coolant conditions and

$$h_{w,c} = h_{w,l} + h_{w,g} + h_{w,sat} \tag{2}$$

$$T_c = \frac{h_{w,l}T_l + h_{w,g}T_g + h_{w,sat}T_{sat}}{h_{w,c}} \tag{3}$$

Figure 80 and Figure 81 show the predicted effective coolant temperature T_c and heat transfer coefficient $h_{w,c}$ at several axial locations below the lip of each RPV inlet. The axial locations, which correspond to positions of interest for downstream thermomechanical analysis, are shown in Figure 83. In the upper elevations of the DC, we see somewhat lower coolant temperatures in the loops with injection (loops 2 and 3), especially in the first ~900 s of the transient. Here the cooling effect of the safety injection is more clearly seen. Lower down in the RPV, however, the temperature and HTC are relatively homogeneous. The underlying explanation for this behaviour, the coolant mixing and upward propagation of a thermal stratification layer, is visible in Figure 82.

Figure 82 shows unwrapped colour plots of the subcooling and HTC distributions in the DC region below the RPV inlets at selected time points. We can see that, early in the transient, TRACE predicts a stratification layer forming in the DC. This stratification layer moves upwards relatively quickly and, consistent with the observations for Figure 80, the temperature distribution becomes more uniform below this level. Studies in Task 2.2 of APAL have shown that TRACE tends to over-estimate the mixing

in the DC. Thus, in reality, we would expect the temperatures below the loops without HPI (loops 1 and 4) to be closer to the 100 K/h cooldown curve (Figure 80).

The subcooling in the DC is significant, highlighting that the 100 K/h cooldown rate is exceeded and confirming that this transient is PTS relevant.

(a)   (b)
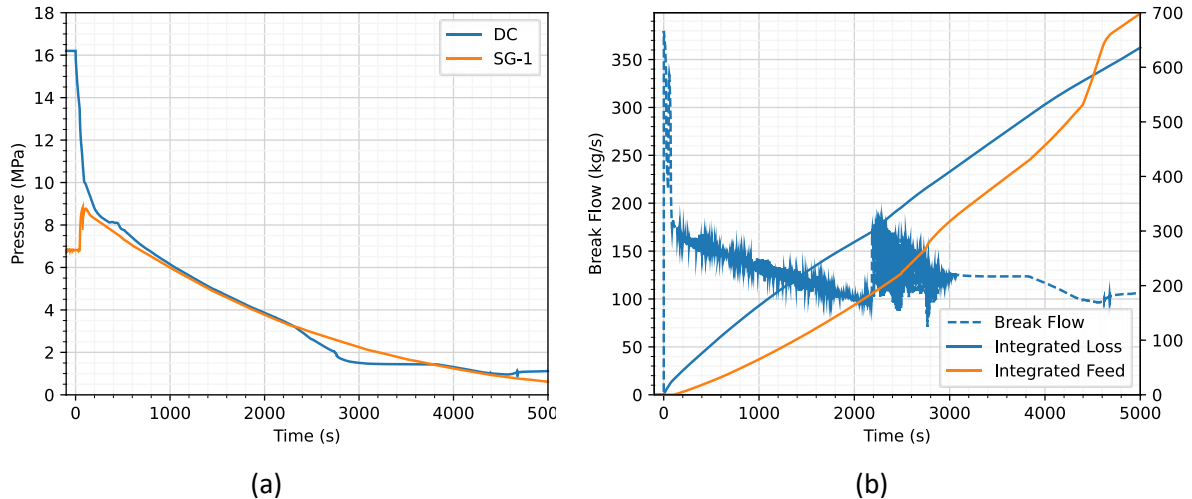
Figure 72: (a) System Pressures and (b) Break Flow Rate and Integrated Coolant Loss and Injection.
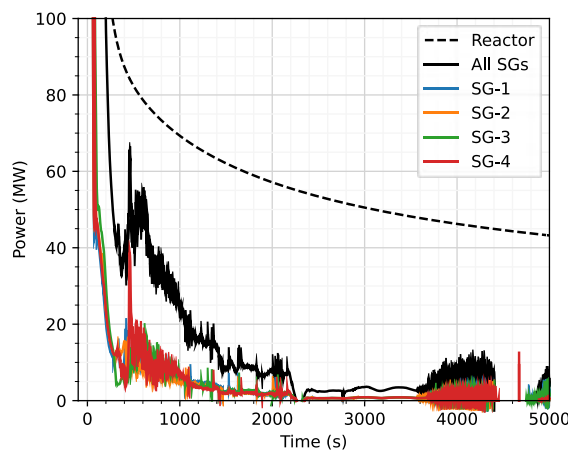
Figure 73: Reactor Power and Heat Removal by all SGs.

(a)   (b)
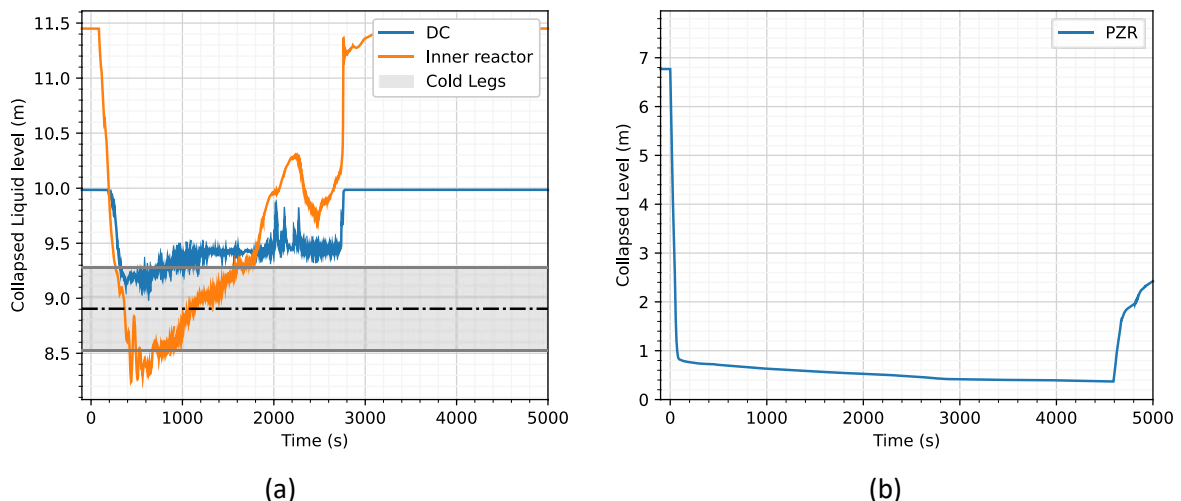
Figure 74: (a) DC Liquid Level and (b) PRZ Liquid Level.

(a)   (b)
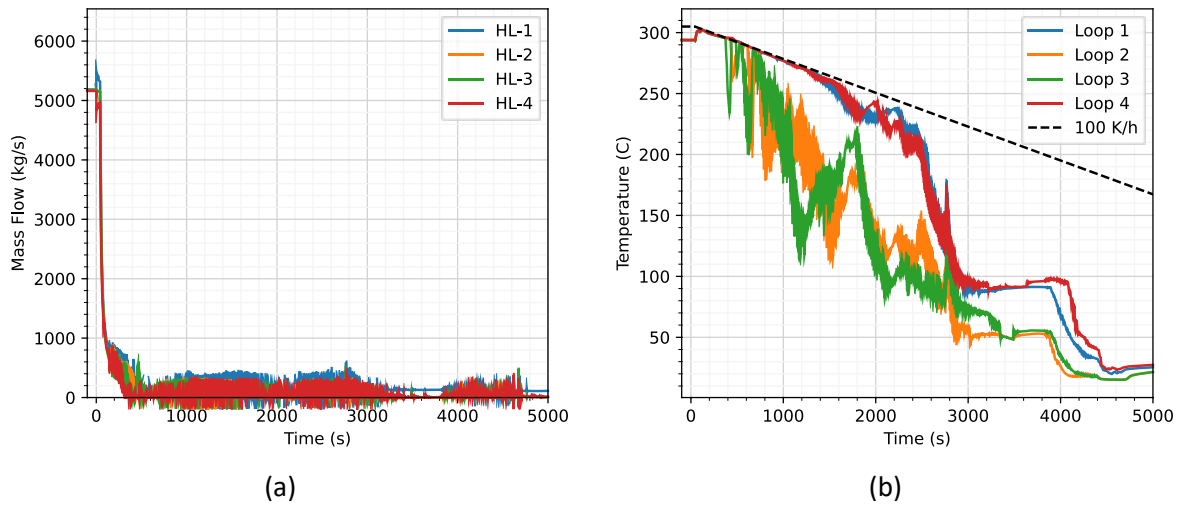
Figure 75: (a) HL Flow Rates and (b) Temperatures in the RPV Inlet Nozzles.

(a)   (b)
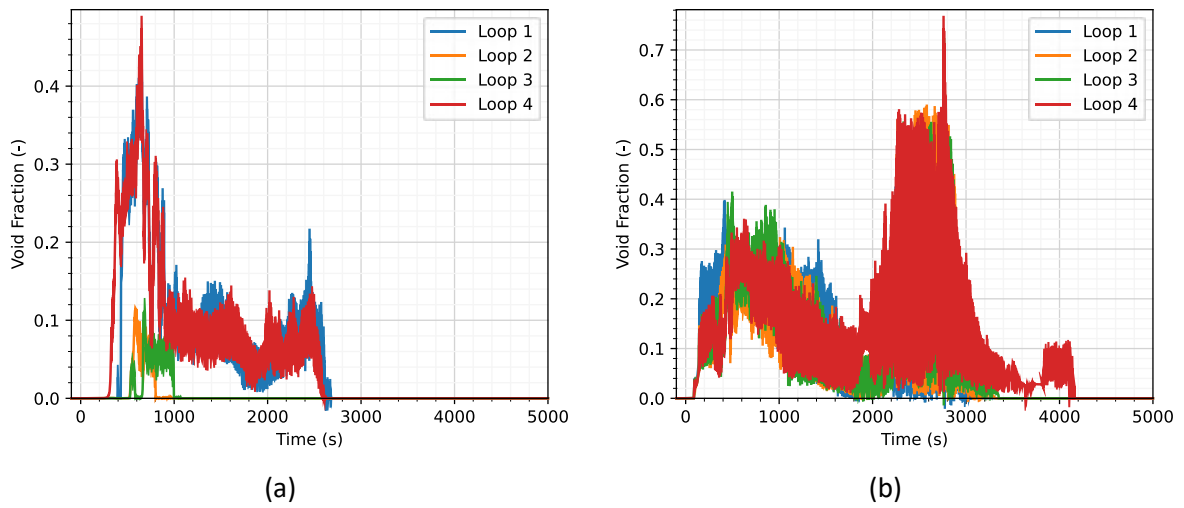
Figure 76: Void Fraction at the (a) RPV Inlet Nozzles and (b) RPV outlet Nozzles.
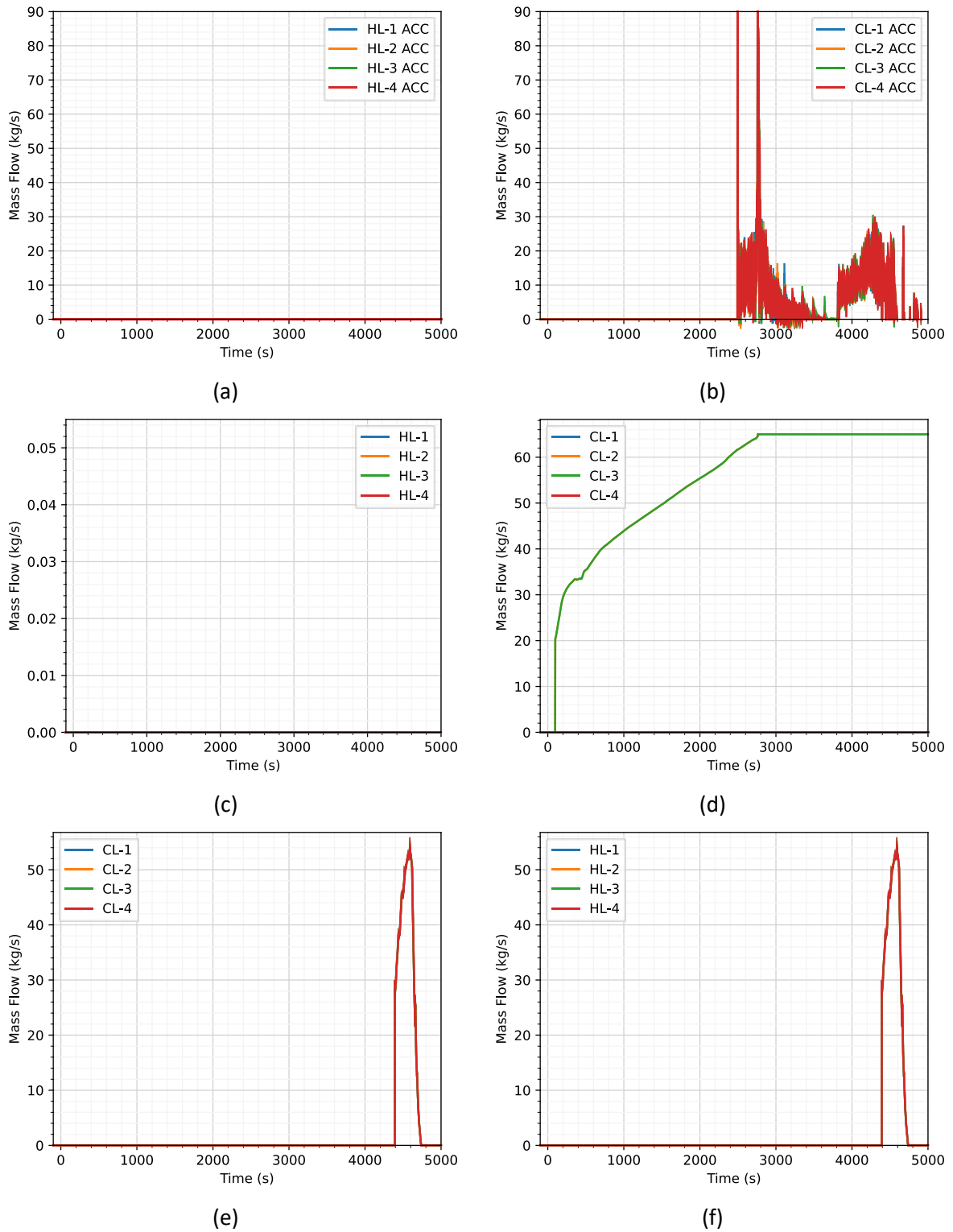
Figure 77: (a) HL and (b) CL ACC Flow Rates, (c) HL and (d) CL HPI Flow Rates, and (e) HL and (f) CL LPI Flow Rates.

(a)

(b)

(c)

(d)
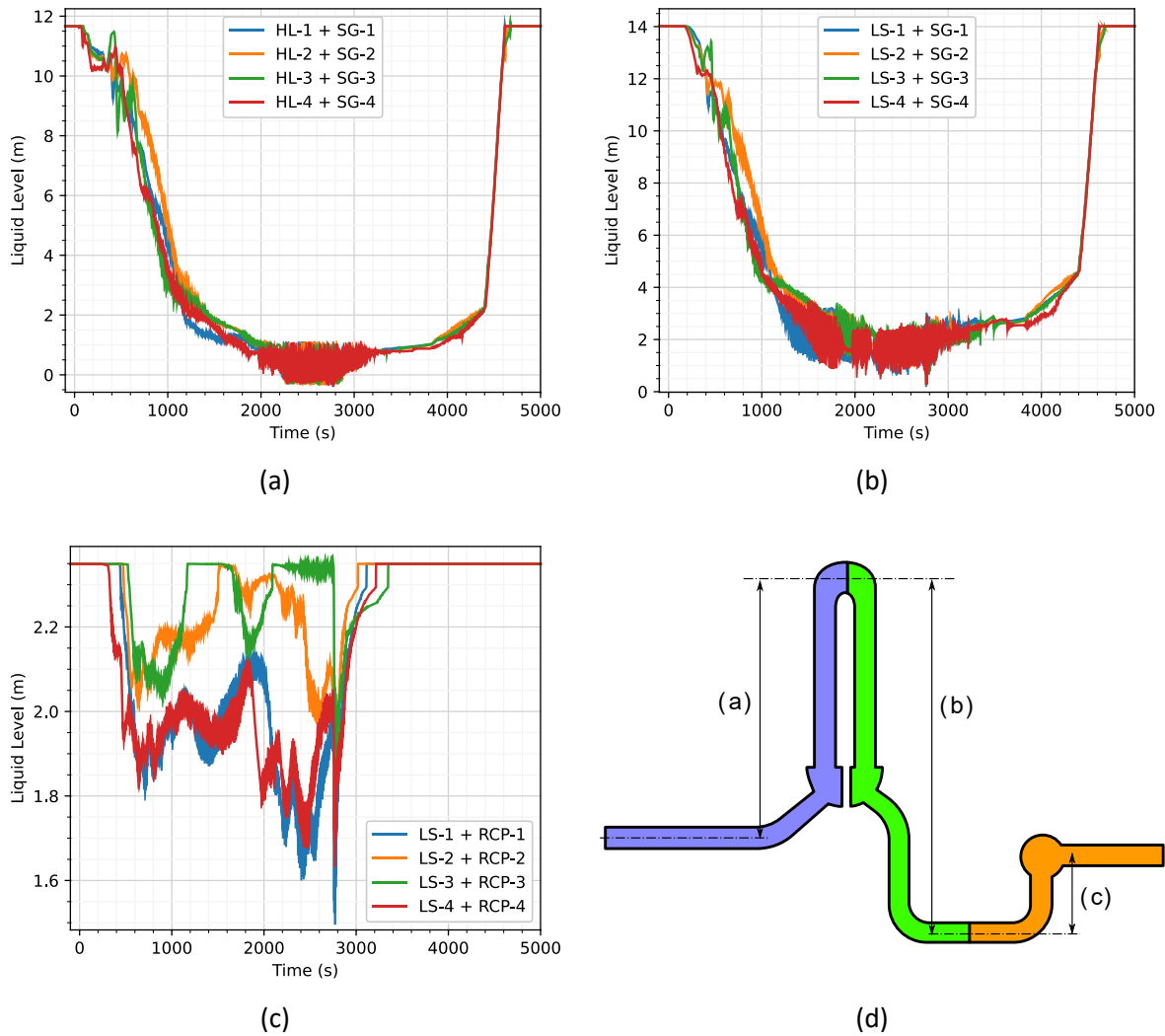
Figure 78: Collapsed Liquid levels in (a) the HL and HL Side of the SG, (b) the SG and Loop Seals and (c) the Loop Seals and RCPs as Illustrated in (d).

(a)

(b)
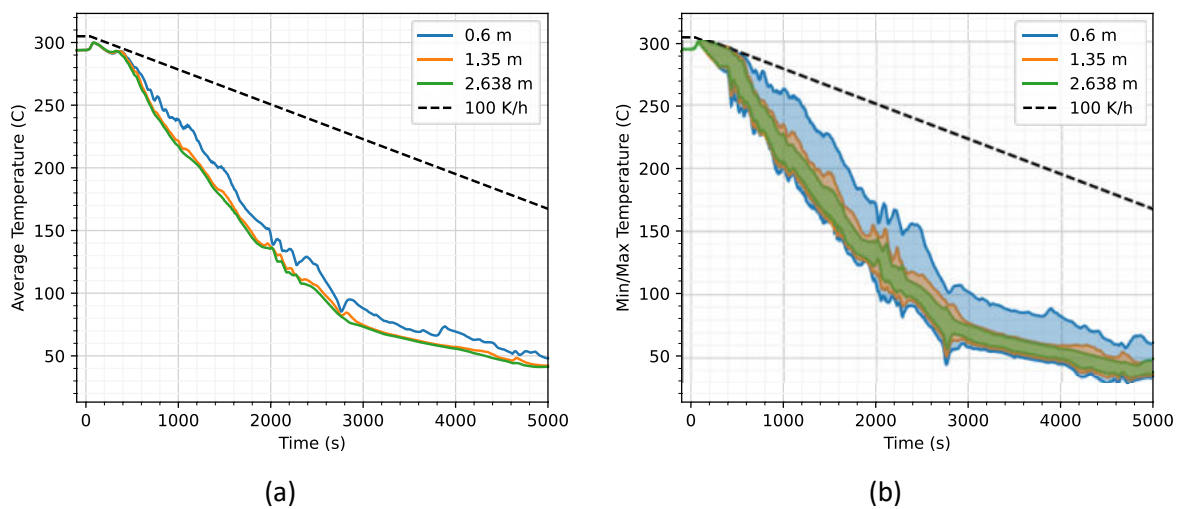
Figure 79:(a) Azimuthally-averaged and (b) Minimum and Maximum Coolant Temperatures in the DC at Fixed locations Below the RPV Inlets.
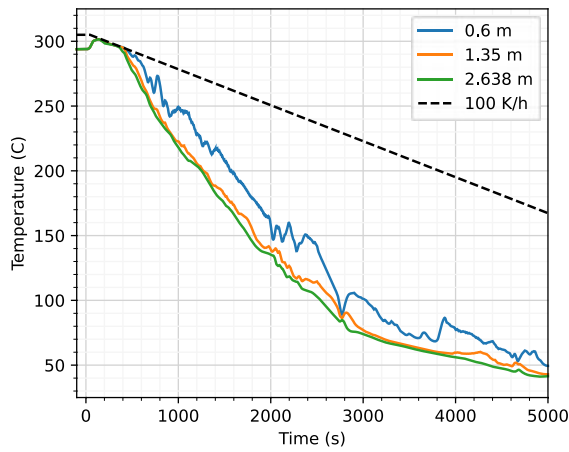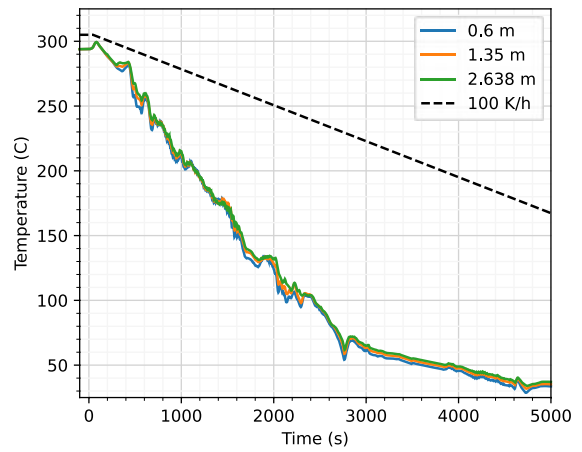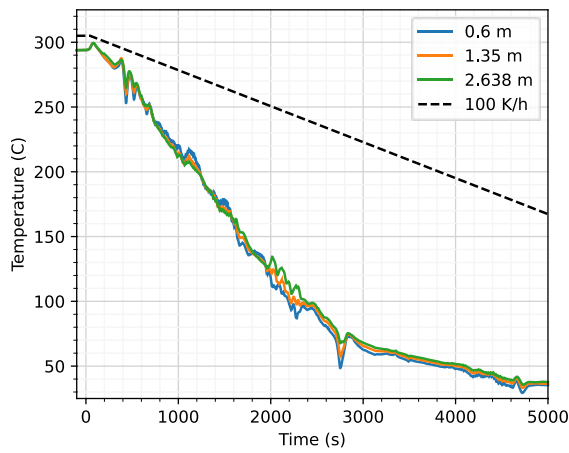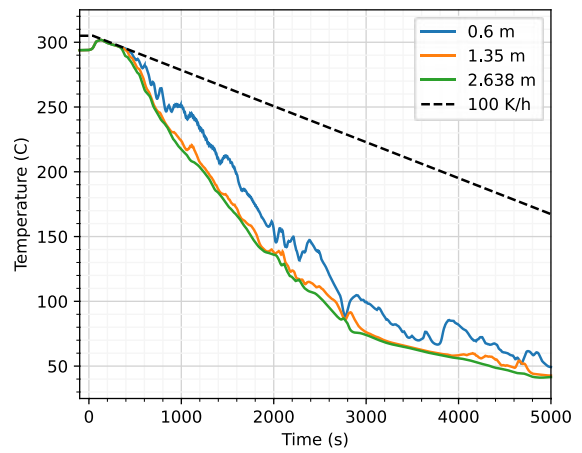
Figure 80: Coolant Temperatures at Fixed Axial Locations below the RPV Inlets.
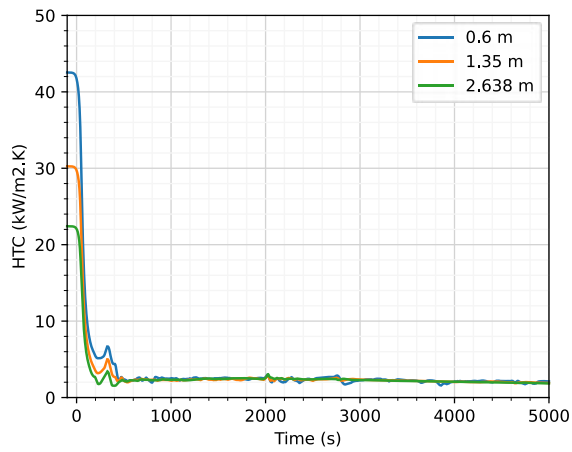
Loop 1
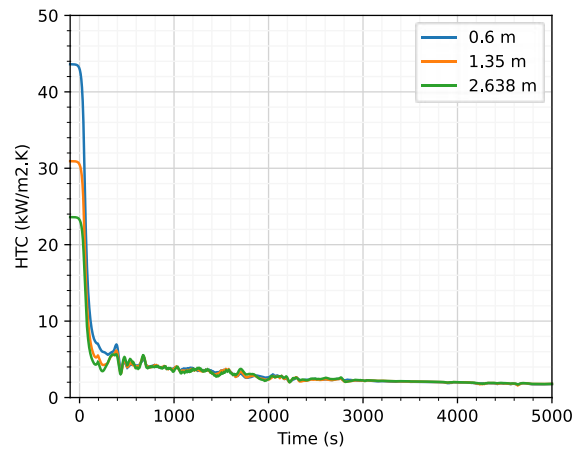
Loop 2
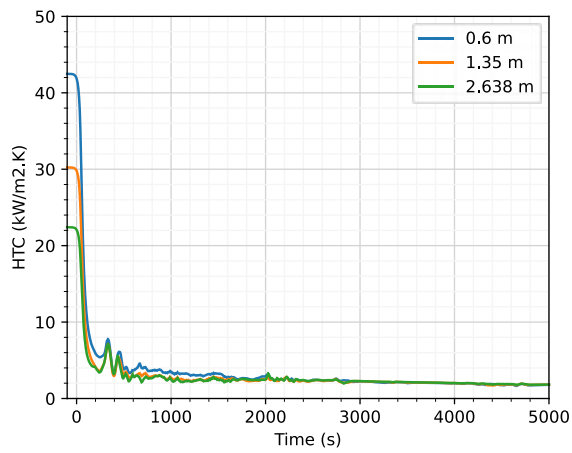
Loop 3
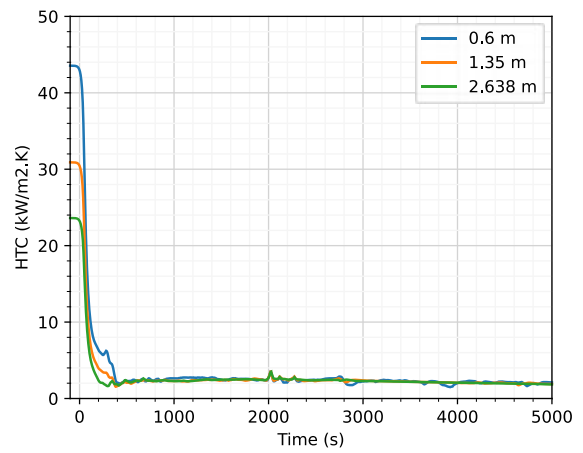
Loop 4

Figure 81: Heat Transfer Coefficient at Fixed Locations below the RPV Inlets.
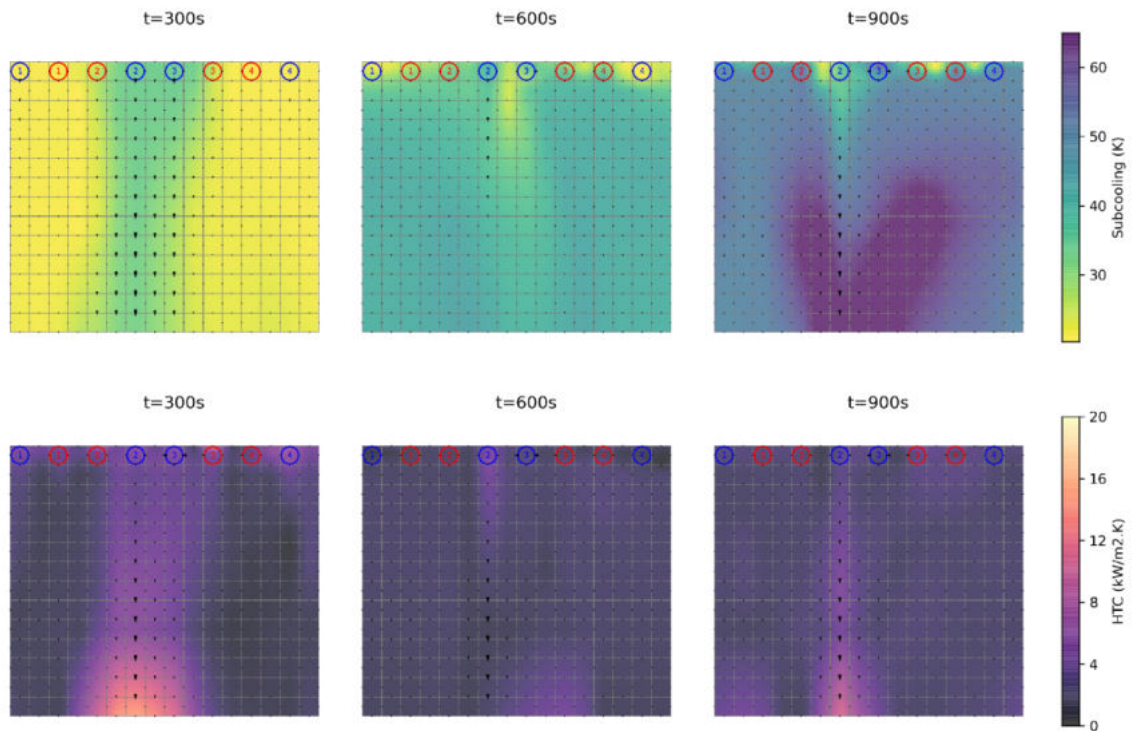
Figure 82: Unwrapped Colour Plot[3] of the (top) Coolant Subcooling $T_{sat} - T_c$ and (bottom) Heat Transfer Coefficient at Different Time Points during the Transient. The plots are overlaid with vectors showing the mass flux distribution.
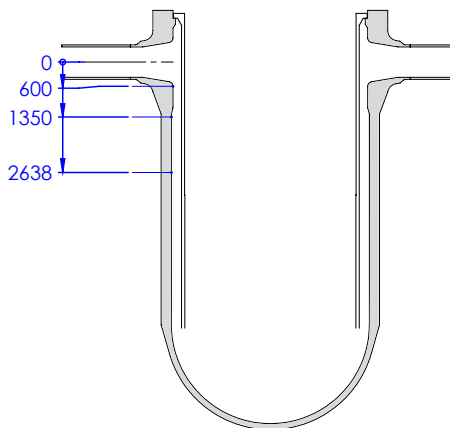
Figure 83: Axial Locations for the Sampling of Coolant Temperature and HTC.

4.4   Comparison of RELAP5, TRACE and ATHLET base case results

This section presents selected comparisons of RELAP5, ATHLET and TRACE simulation results for the reference case. The data for these comparisons were provided by UJV, GRS and PSI respectively.

4.4.1   Results for Nominal Operation

The major system parameters for nominal operation are summarised in Table 13, in which they have been compared against the reference values for the KWU-1300 and ICAS T2 transient.

---

[3] Colour plots are generated using a conservative grid mapping algorithm, which maps the integrated coarse node average values from TRACE onto a bivariate spline surface and thereafter extracts point values on a refined grid by taking the derivative of the spline. The resulting surface conserves the node average values while ensuring a continuous function between nodes.

Table 13: Summary of Results for Nominal Operation

Parameter	Reference Value	RELAP	ATHLET	TRACE
Total Power (MW)	3765	3765	3750	3765
Total Primary Flow (kg/s)	20600	20141	18666	20878
Loop Flows (kg/s)	5150	5036 / 5042 / 5037 / 5026	4667 / 4665 / 4667 / 4667	5229 / 5226 / 5213 / 5210
Core Bypass Flow (%)	-	0.74	2.87	3.41
DC Upper Head Bypass Flow (%)	0.97	0.99	1.05	1.14
DC to HL Bypass Flow (%)	-	not modelled	1.01	0.89
Total Bypass Flow (%)	-	1.73	4.93	5.44
Primary Pressure in HL (bar)	157.5	157.5	157.9	157.5
SG Pressures (bar)	68.2	61.60 / 61.54 / 61.60 / 61.60	60.10 / 60.15 / 60.02 / 60.02	68.2 / 68.3 / 68.3 / 68.2
SG level in DC (m)		11.87 / 11.86 / 11.87 / 11.87	12.81 / 12.75 / 12.72 / 12.72	not reported
SG recirculation ratio (-)		2.99 / 2.98 / 2.98 / 2.99	3.50	not reported
PRZ Level (m)	6.78	6.76	6.53	6.77
CL Temperature (C)	293	291.0	284.5 / 284.6 / 284.5 / 284.5	293.9 / 294 / 293.9 / 293.9
HL Temperature (C)	325	324.0	320.2 / 320.6 / 320.5 / 320.6	325.3 / 325.3 / 325.3 / 325.3

4.4.2   Base Case SB-LOCA

Comparison plots for selected system parameters are provided in Figure 84 through Figure 90.
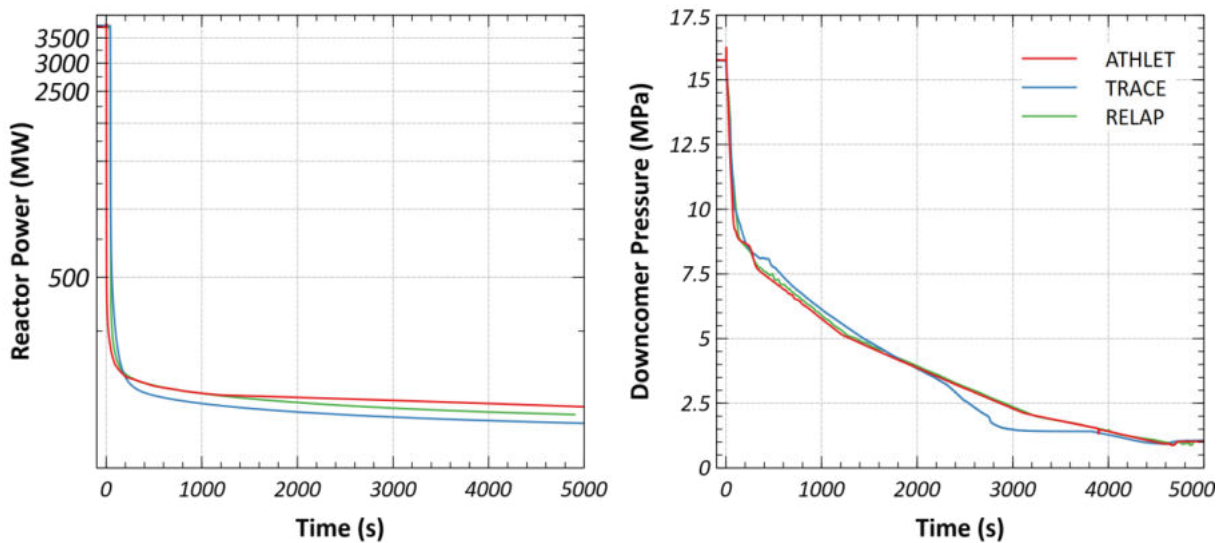
Figure 84: Comparison between RELAP5, ATHLET and TRACE results for the reference case showing the (left) reactor power and (right) DC pressure.
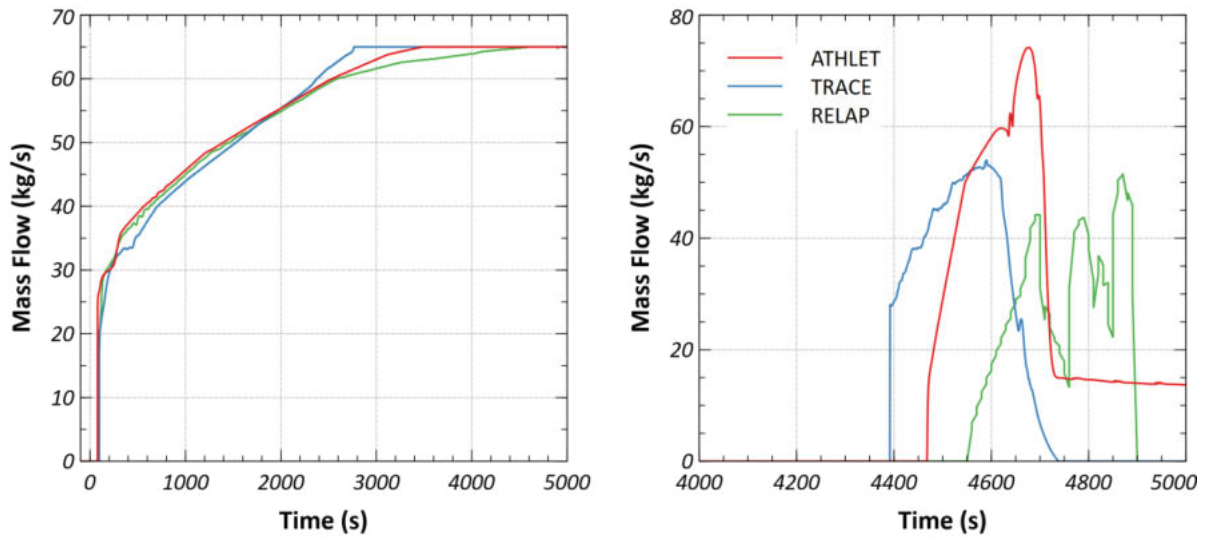
Figure 85: Comparison between RELAP5, ATHLET and TRACE results for the reference case showing the (left) HPI injection and (right) LPI injection in CL-2.
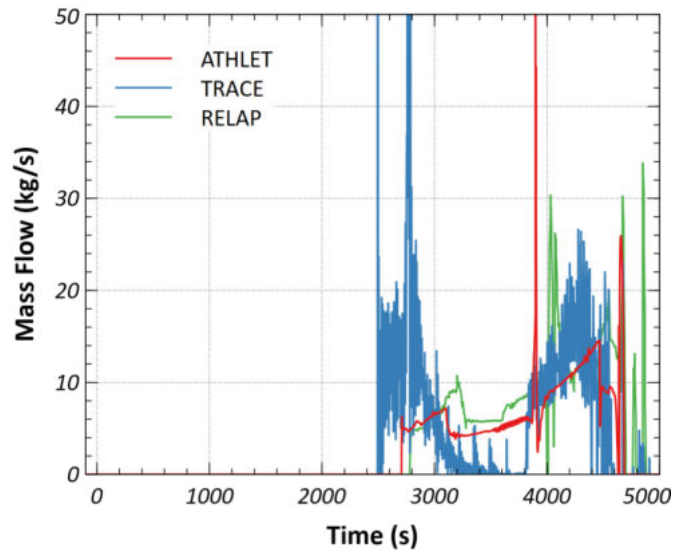
Figure 86: Comparison between RELAP5, ATHLET and TRACE results for the reference case showing the ACC injection in CL-2.
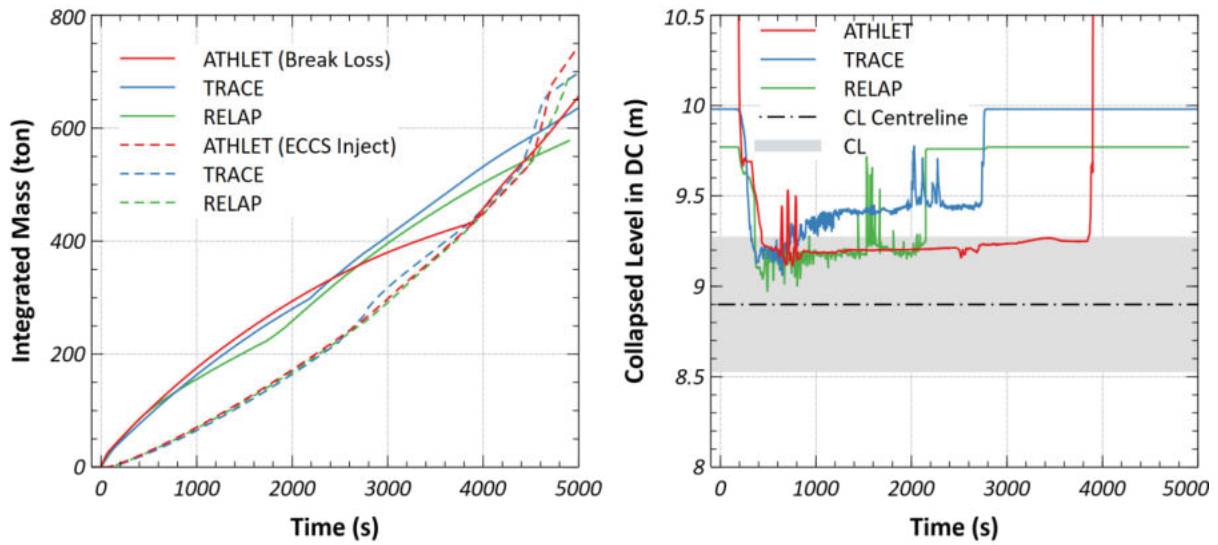
Figure 87: Comparison between RELAP5, ATHLET and TRACE results for the reference case showing the (left) integrated break loss and ECCS injection and (right) collapsed liquid level in the DC.
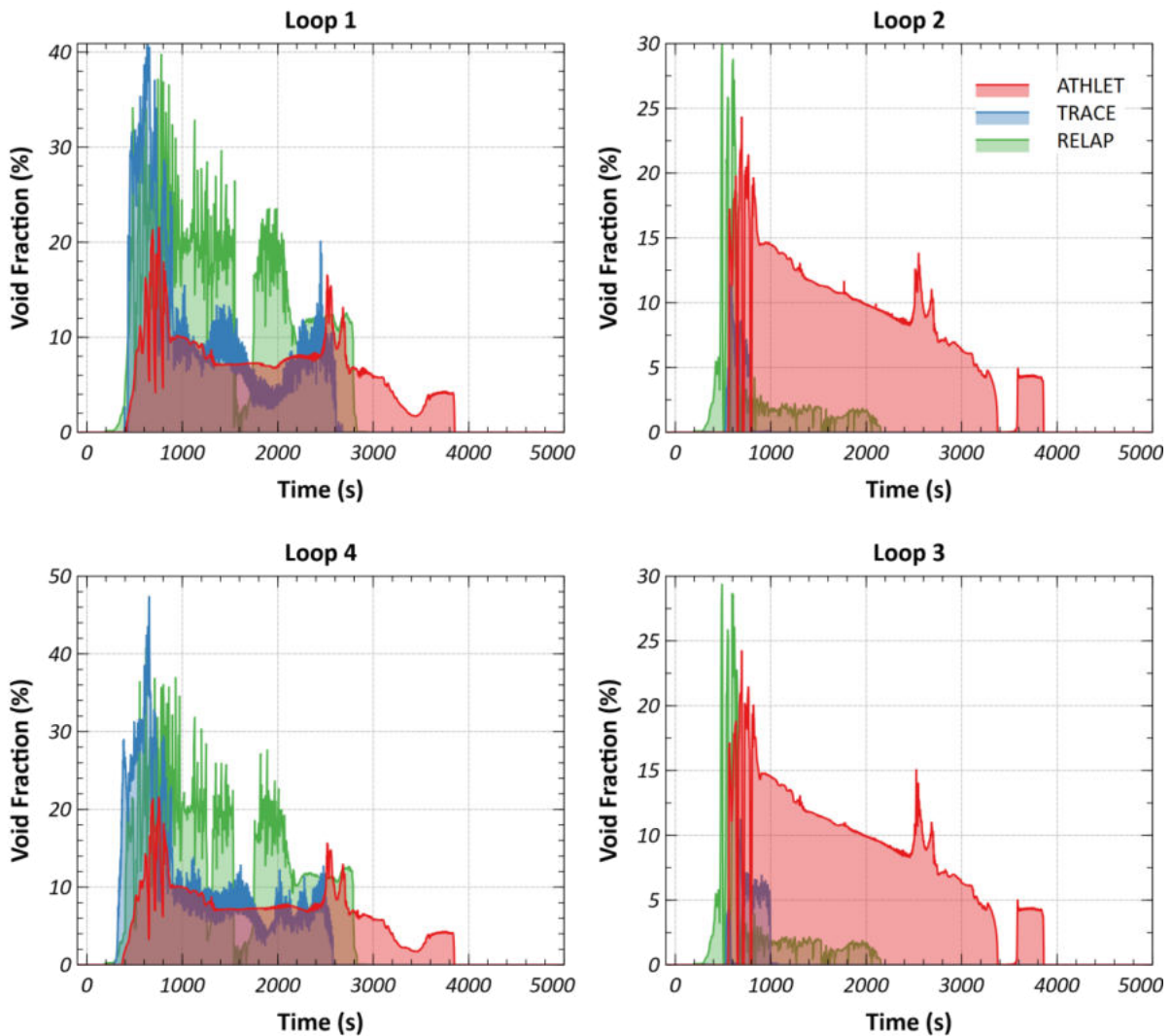
Figure 88: Comparison between RELAP5, ATHLET and TRACE results for the reference case showing the void fraction in the RPV inlet nozzles.
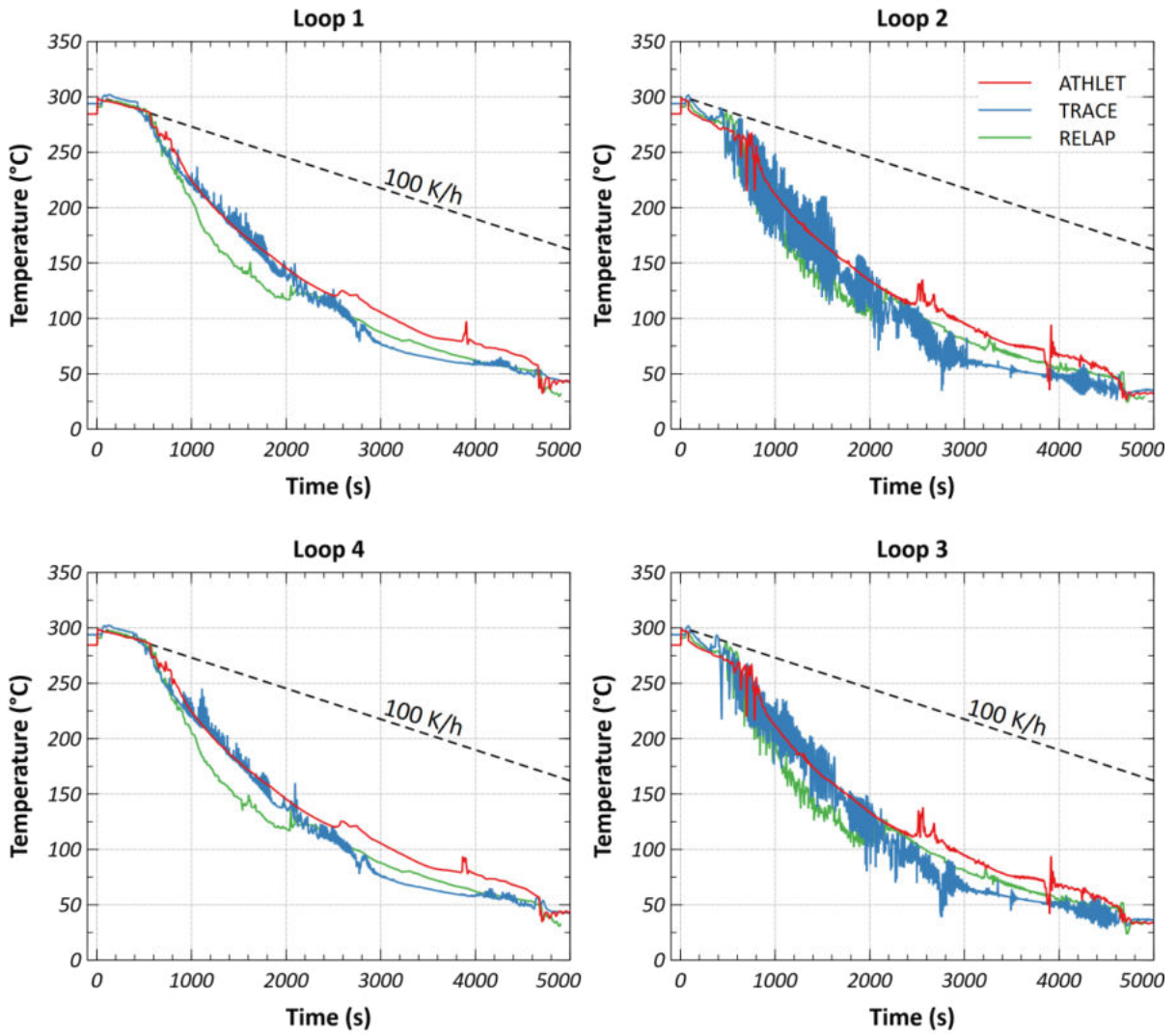
Figure 89: Comparison between RELAP5, ATHLET and TRACE results for the reference case showing the coolant temperatures in the DC 1.35 m below the CL centreline.
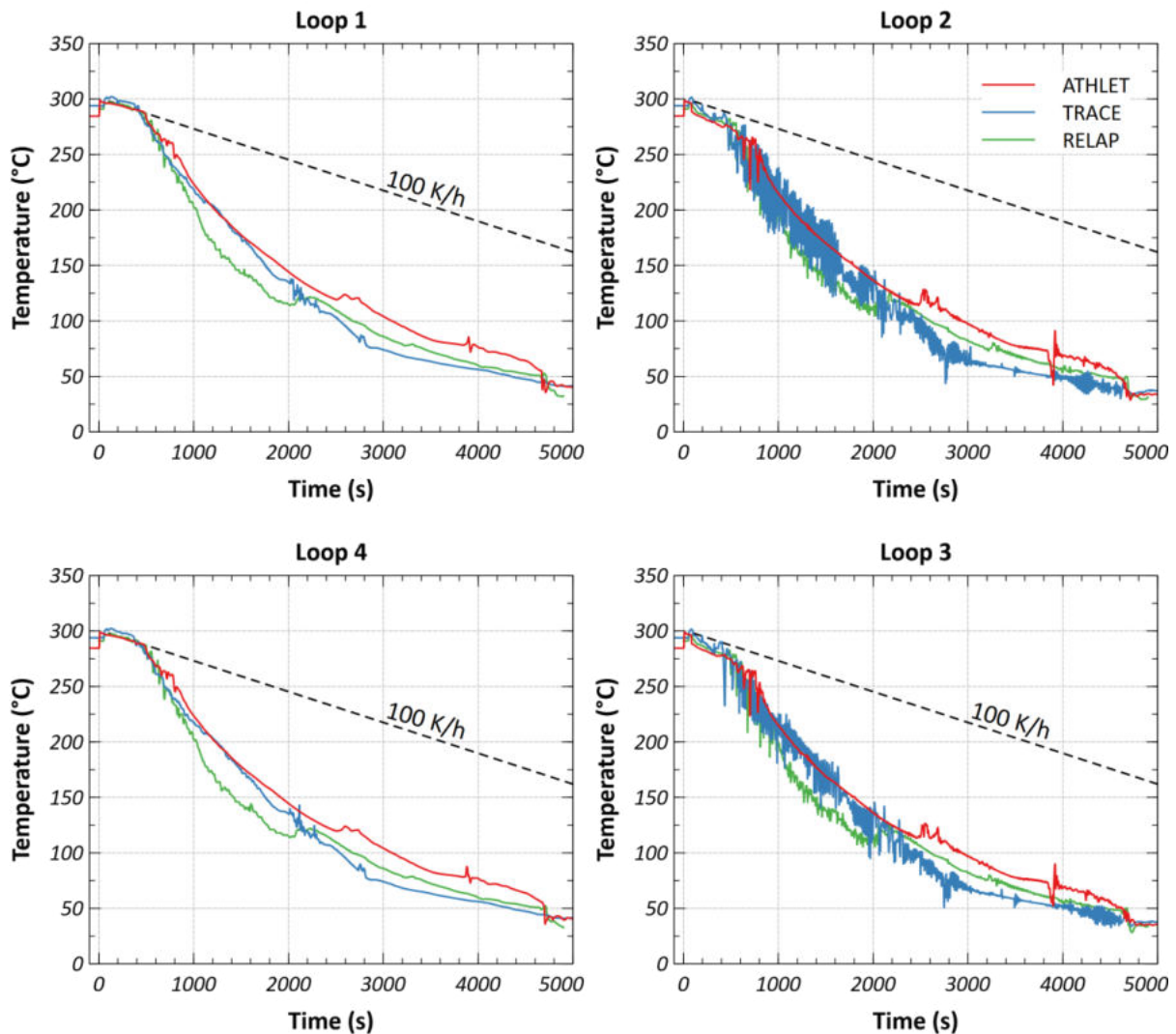
Figure 90: Comparison between RELAP5, ATHLET and TRACE results for the reference case showing the coolant temperatures in the DC 2.638 m below the CL centreline.

Between the codes there are differences in the used choked flow models and thus in the flow rates from the leak during critical discharge conditions (comp. Figure 57). Due to these differences in the leak flow, the primary pressure curves slightly diverge from each other. TRACE in particular shows a relatively large increase in leak flow rate around ~2200 s, due to the refilling of the upper plenum and hot legs, which causes a relatively sharp decrease in primary pressure around the same time. This results in an earlier start-up and initially higher flow rate of the ACC injection in the TRACE simulation compared to the RELAP5 and ATHLET. As a result of these differences in the flow rate and timing of ECC injection, the coolant inventories and distributions are slightly different in all three simulations (see the DC level in Figure 87). Temperature in the DC experiences a small stepwise increase both in the RELAP5 simulation (at about 2000 s) and in the ATHLET simulation (at about 2500 s) and stays at an elevated value compared to the TRACE result until the start-up of the LPI pumps. A possible explanation for this stepwise increase of temperature in the DC could be condensation in CL2 and CL3 where HPI takes place. This condensation leads to a short-term reverse of flow which leads to large turbulences also in the DC and thus to temperature increase in the DC. While the TRACE results do show signs of disturbances in the coolant temperatures around the same time, this coincides with the relatively sharp decrease in TRACE's primary pressure after ~2200 s discussed above, which likely suppresses this effect.

4.5   KWU-MIX results

Results from the system analysis performed with RELAP5, as described in Section 4.1, were used as input to the fluid-mixing analysis performed with KWU-MIX. The simulation with KWU-MIX of the base case, i.e., a SBLOCA (50 cm²) with the break in the core outlet region of a KWU-1300 PWR and with loss of offsite power, produced data for the temperatures and heat-transfer coefficients as a function of time and location.

4.5.1   Cold-leg nozzle

The end of the CL is the right-hand end of MR2 in KWU-MIX, as shown in Figure 16. At this location, the models have finished calculating the amount of hot water that is entrained into the cold ECC water, and temperature of the resulting mixture. Figure 91 shows the temperature of the hot water as a function of time, and it is indicated by the grey curve labelled "hot layer in cold-leg nozzle". At the start of the transient, this temperature is the same as the temperature from RELAP5, which is the curved labelled "DC" as shown in Figure 38. As soon as the ECC injection begins and the flow of water in the loop through the MCP is small enough to prevent complete mixing in the CL, KWU-MIX calculates a separate temperature for the hot water based on an energy balance for all the mixing regions. Therefore, starting at approximately 350 s, the hot-water temperature is slightly different from the RELAP5 result.

Also shown in Figure 91 is the temperature of the cold water that results from the mixing of ECC water and entrained hot water. This temperature is indicated by the blue curve labelled "cold layer in cold-leg nozzle. This temperature is calculated by KWU-MIX starting at 350 s also, as soon as incomplete mixing occurs. Recall that the temperature of the ECC water is 15 °C, which is also shown in Figure 91, but it is an input to KWU-MIX rather than a result. The temperature of the cold-water layer is closer to the temperature of the ECC water than to the temperature of the hot water. This indicates that the mass flow rate of entrained hot water is less than the flow rate of ECC water.
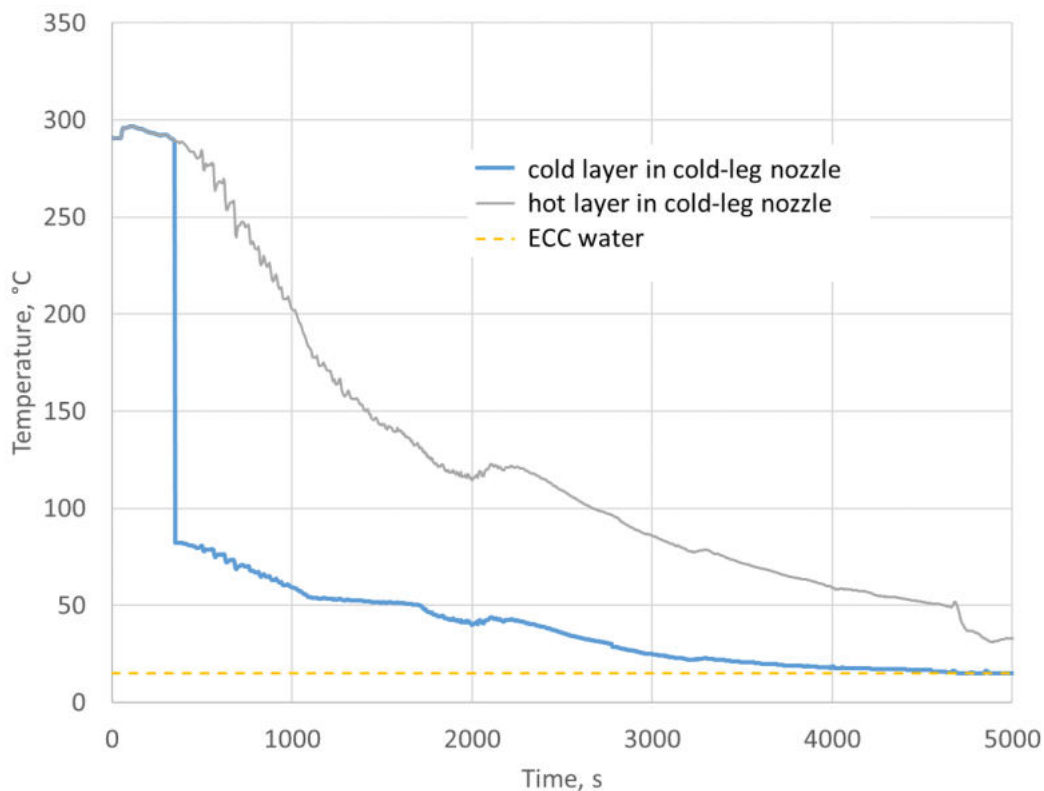
Figure 91: Temperatures of the cold-water and hot-water layers at the end of the nozzle of Cold Leg 2 and 3 calculated by KWU-MIX.

The height of the cold-water layer above the cold-leg axis at the end of the cold-leg nozzle is shown in Figure 92 as a function of time. Initially, when the ECC flow rate is small, the height of the cold-water lay is approximately 0.2 m above the bottom of the CL. With increasing ECC flow, as shown in Figure 31, the height of the cold-water layer increases correspondingly.
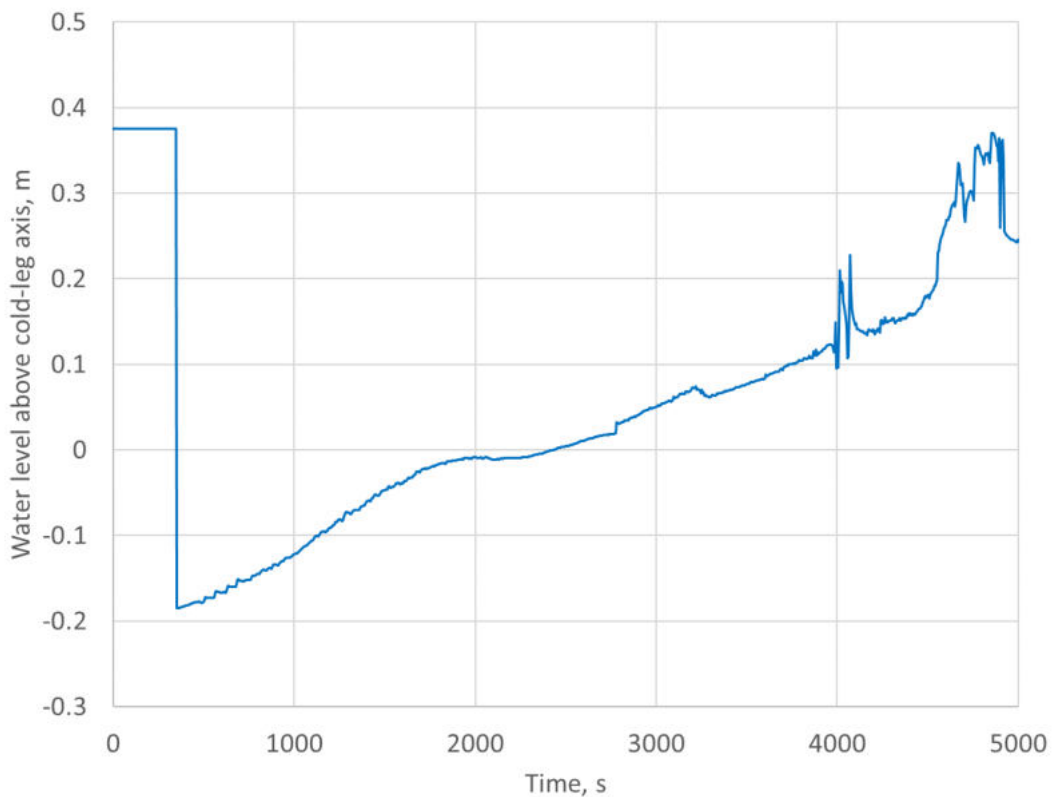
Figure 92: Height of cold-water layer above the axis of Cold Leg 2 and 3 at the inlet of the cold-leg nozzle calculated by KWU-MIX.

The height of the cold-water layer shown in Figure 92 determines the width of the plume at its origin in the DC of the RPV, just below the bottom of the cold-leg nozzle.

4.5.2   Inner surface of RPV wall

The transition from the end of the cold-leg nozzle to the top of the plume the RPV is referred to as MR3 in Figure 16, but it is not modelled in KWU-MIX. Instead, KWU-MIX uses the conditions at the end of MR2 as the inlet boundary conditions for MR4. Consequently, the height of the cold-water layer in the cold-leg nozzle, labelled H_c in Figure 92, determines the width of the plume at its origin in the DC.

Figure 93 shows the widths of the plumes at various distances below the cold-leg axis in the DC. The origin of the plume is 0.45 m below the cold-leg axis, which is at the bottom of the diffusor. This is the light blue curve labelled 0.45 m in Figure 93. As soon as a plume is formed at approximately 350 s, its width is approximately 0.65 m, which is less than the diameter of the end of the diffusor. The width of the plume at its origin increases with time, corresponding to the increase in the cold-water flow rate. The width reaches a maximum when the cold-water layer in the CL reaches the axis. The maximum width of the plume is less than 0.9 m, however, because the cold water accelerates, and its width narrows as it sinks in the diffusor.
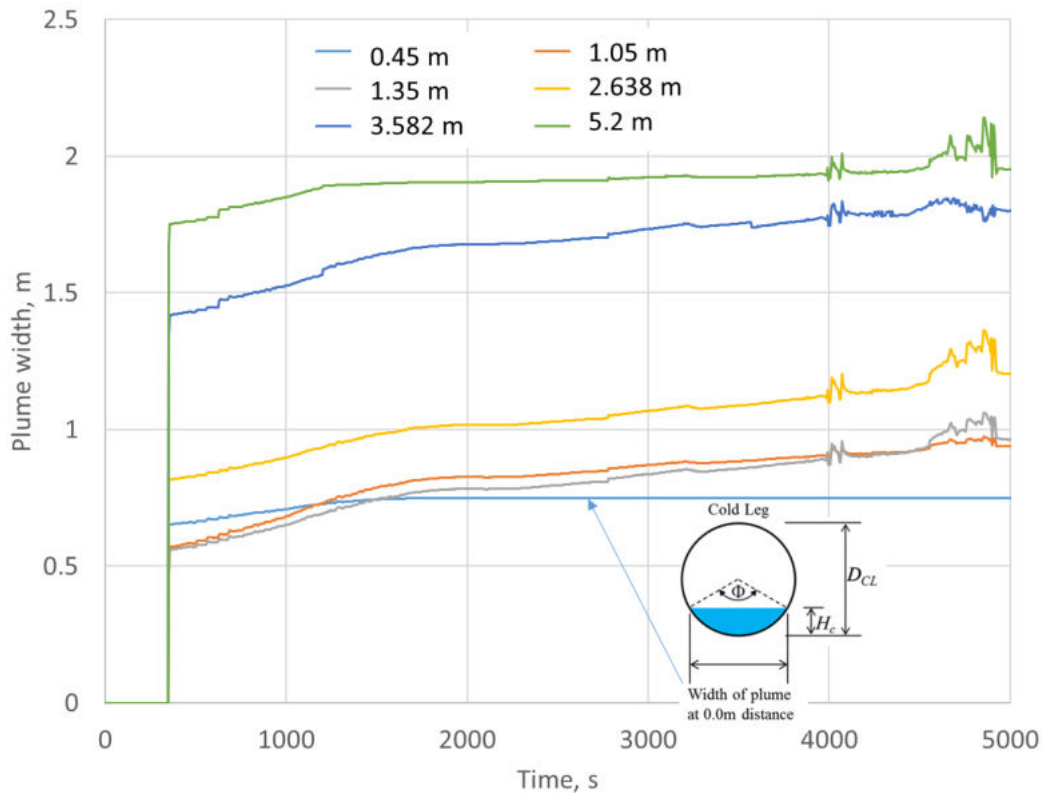
Figure 93: KWU-MIX widths of the plume at various distances below the axis of the Cold Leg 2 & 3

in the DC.

At a distance of 1.05 m below the cold-leg axis, the width of the plume is smaller than at its origin early in the transient. This is due to the strong buoyancy force that accelerates the flow in the plume, which causes the plume to become narrower. Later in the transient, this phenomenon still exists, but its magnitude decreases with time as the temperature differences decrease and the buoyance also decreases. The plume width at 1.35 m below the cold-leg axis is similar to the width at 1.05 m

The two neighbouring plumes at lower elevations (greater distances below the cold-leg axis) are merged for the entire transient. The width of the merged plume is given for the distances of 2.638 m, 3.582 m and 5.2 m below the cold-leg axis in Figure 93.

The temperatures at the centers of the plumes are shown in Figure 94 for various distances below the cold-leg axis. The light-blue curve labelled 0.45 m in the legend is the centerline temperature at the origin of the plume, which is at the bottom of the cold-leg nozzle. This temperature is the same as the blue curve labelled "cold layer in cold-leg nozzle" shown in Figure 91. The curves for greater distances from the origin are progressively warmer. The dark-blue curve labelled "ambient" is the temperature outside of the plume. This temperature is the same as the grey curve labelled "hot layer in cold-leg nozzle" shown in Figure 91.
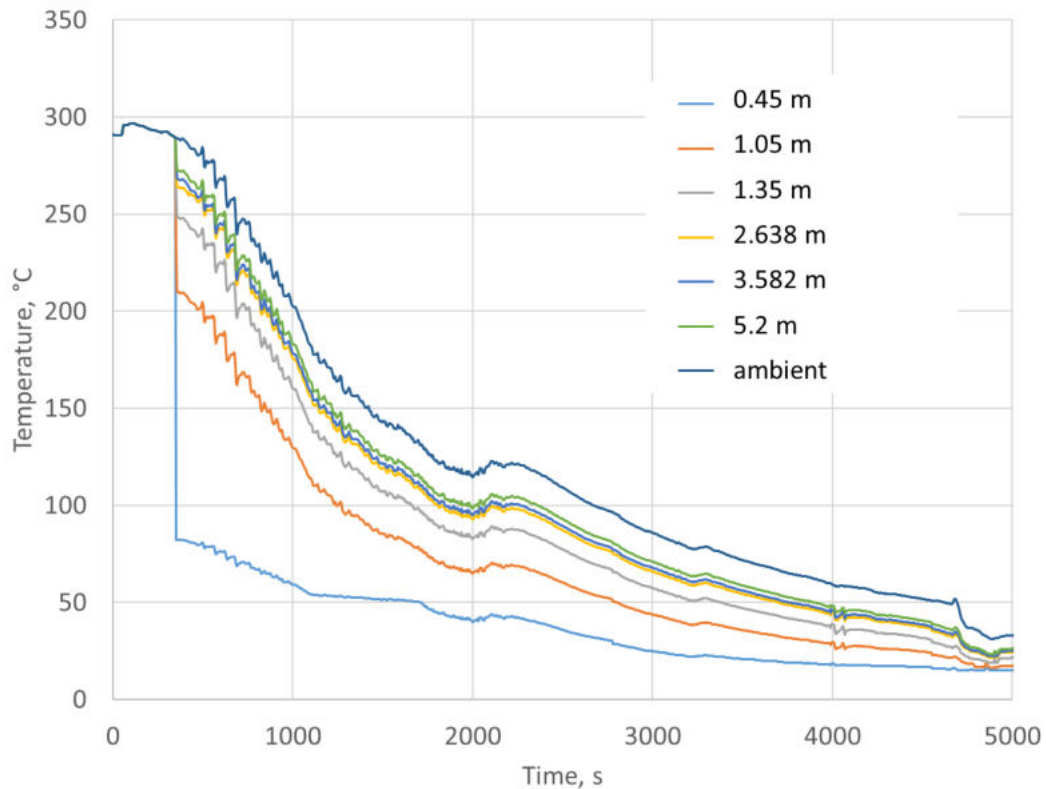
Figure 94: KWU-MIX temperatures at the middle of the plume at various distances below the axis of Cold Leg 2 & 3 in the DC.

Each curve in Figure 94 shows the temperature at one location, and the coordinates are at the elevation shown in the legend and at the circumferential location on the RPV wall where the plume is coldest. But the temperature throughout the plumes has a Gaussian distribution along the circumference of the RPV wall. An example is shown in Figure 95, which shows the temperature as a function of the circumferential location for various elevations at a time equal to 1000 s.

The temperature profile at the origin of the plume is the blue curve labelled "0.45 m" in the legend of Figure 95. The axis of the cold-leg nozzle in Loop 2 is at a circumferential location of 6.69 m, and the axis of the nozzle in Loop 3 is at 8.61 m. The coldest temperature for the plumes at a distance of 0.45 m below the axis of Cold Leg 2 as taken from Figure 94 at 1000 s is 59.2 °C. This is the minimum temperature for the blue curve at the circumferential location of 6.69 m. The plume below Cold Leg 3 has the same temperature, and so the curve has a value of is 59.2 °C at a circumferential location of 8.61 m also. Between the two circumferential locations, the temperature increases to the ambient temperature as taken from Figure 94 at 1000 s. This temperature is 202.5 C.

The small temperature depressions at circumferential locations of 0.96 m and 14.34 m are below the cold-leg nozzles of Loop 1 and Loop 4. The depressions are a result of a small flow of cold water from the CVCS system.
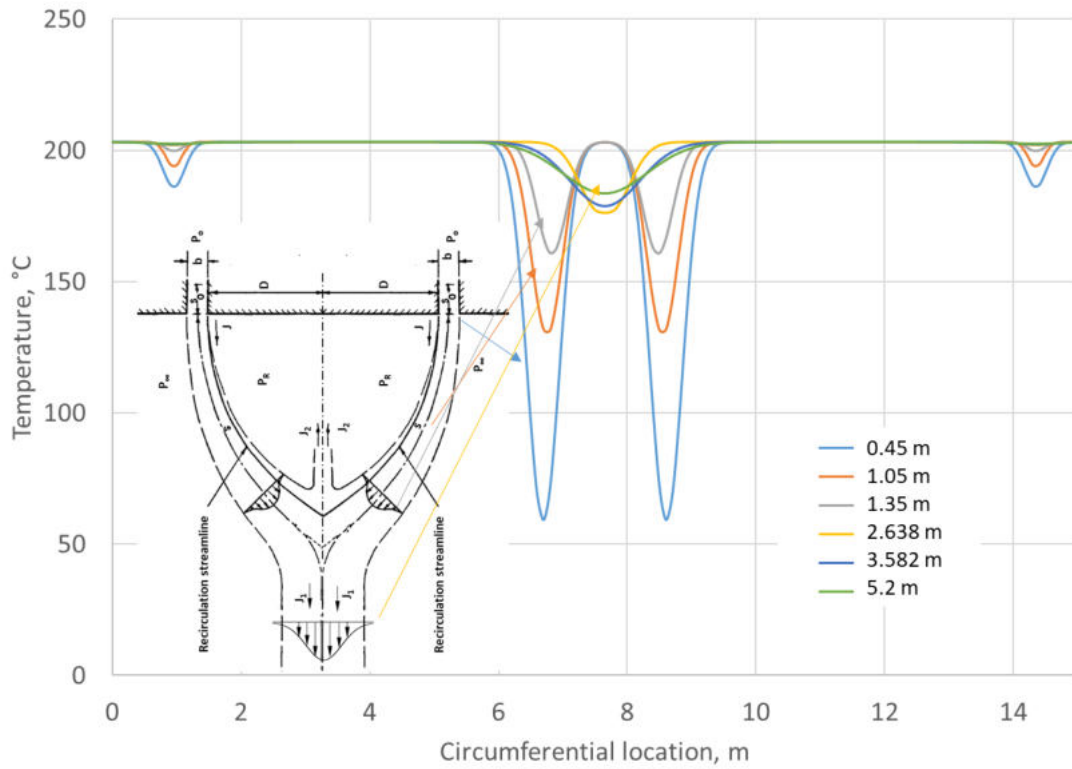
Figure 95: KWU-MIX temperatures at the middle of the plume at various distances below the axis of the cold-leg in the DC at 1000 s.

The HTCs in the DC also have Gaussian distributions, and the widths are equal to those for the temperature shown in Figure 93 divided by a factor of 1.1045, which was taken from Chen [20]. The maximum values for the HTCs in the plumes as a function of time are shown in Figure 96 for various distances below the cold-leg axis. The light-blue curve labelled 1.05 m in the legend is the centerline HTC near the top of the plume. The curves for greater distances from the origin are progressively greater because the buoyancy force continues to accelerate the flow more than the inertia of the entrainment tends to decelerate the flow.
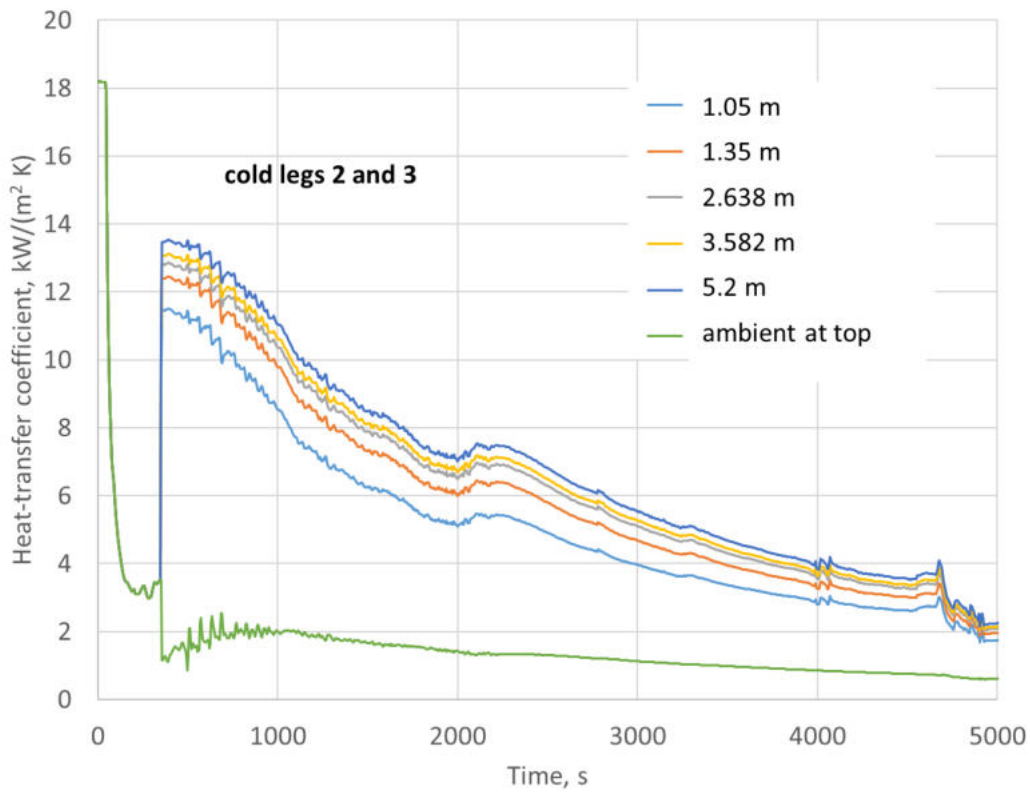
Figure 96: KWU-MIX heat-transfer coefficients at the middle of the plume at various distances below the axis of Cold Leg 2 & 3 in the DC.

Also shown in Figure 97 is the HTC outside of the plumes near the cold-leg nozzle. The HTC outside of the plume increases with distance from the cold-leg nozzle, as shown in Figure 98. The increase in the HTC is due to a larger recirculation flow outside of the plume with increasing distance from the cold-leg nozzle. Near the cold-leg nozzle, the recirculation flow outside of the plume is only as large as the entrainment flow rate at that location. Farther from the cold-leg nozzle, the recirculation flow is equal to the entrainment flow integrated over the higher distances. Near the bottom of the DC, the recirculation flow is equal to the entire flow of entrained water, and so the HTC is largest at this location.
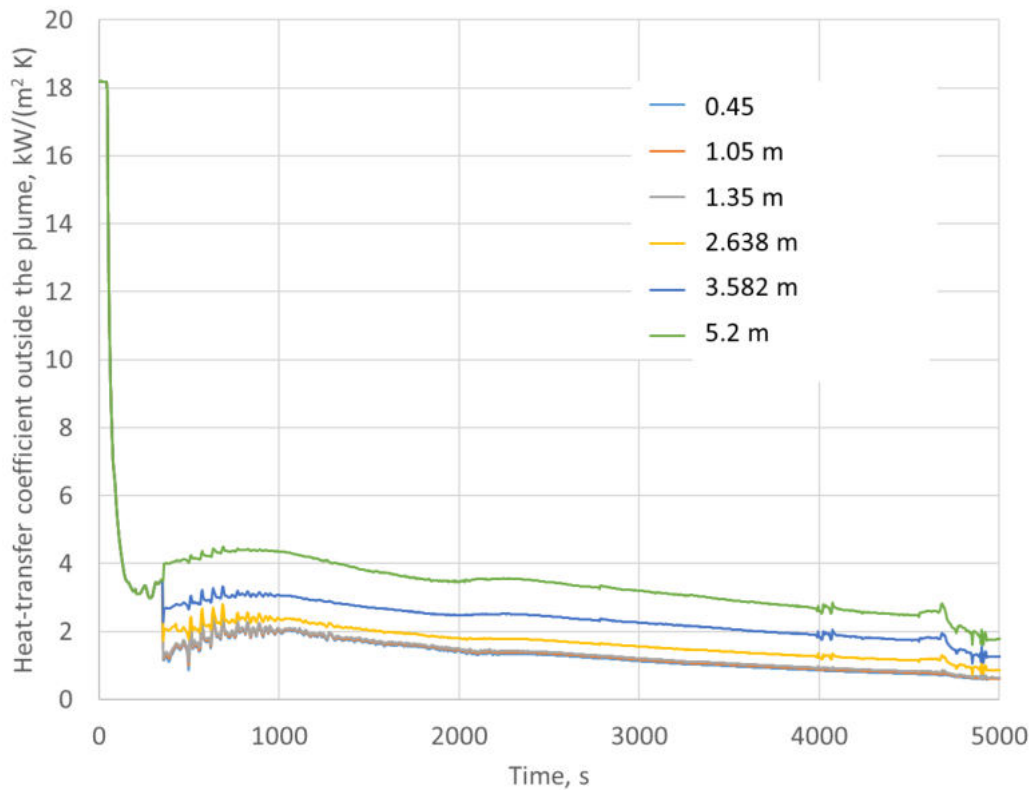
Figure 97: KWU-MIX heat-transfer coefficients outside of the plume at various distances below the cold-leg axis in the DC.

Each curve in Figure 97 shows the HTC at one location, and the location's coordinates are at the elevation shown in the legend and at the circumferential location on the RPV wall where the plume is coldest. But the HTC throughout the plumes has a Gaussian distribution along the circumference of the RPV wall, just as the temperature does. An example is shown in Figure 98, which shows the HTC as a function of the circumferential location for various elevations at a time equal to 1000 s.

The HTC profile near the origin of the plume is the blue curve labelled "1.05 m" in the legend of Figure 98. Recall that the axis of the cold-leg nozzle in Loop 2 is at a circumferential location of 6.69 m, and that the axis of the nozzle in Loop 3 is at 8.61 m. The largest HTC for the plumes at a distance of 1.05 m below the axis of Cold Leg 2 as taken from Figure 97 at 1000 s is 8.535kW/(m^2 K). This is the maximum HTC for the blue curve at the circumferential location of 6.69 m in Figure 98. The plume below Cold Leg 3 has the same HTC, and so the curve has the sane value at a circumferential location of 8.61 m. Between the two circumferential locations, the HTC decreases to the ambient value as taken from Figure 97 at 1000 s. This HTC is 2.067 kW/(m^2 K).

The smaller HTC peaks at circumferential locations of 0.96 m and 14.34 m are below the cold-leg nozzles of Loop 1 and Loop 4. The depressions are a result of a small flow of cold water from the CVCS system.

92
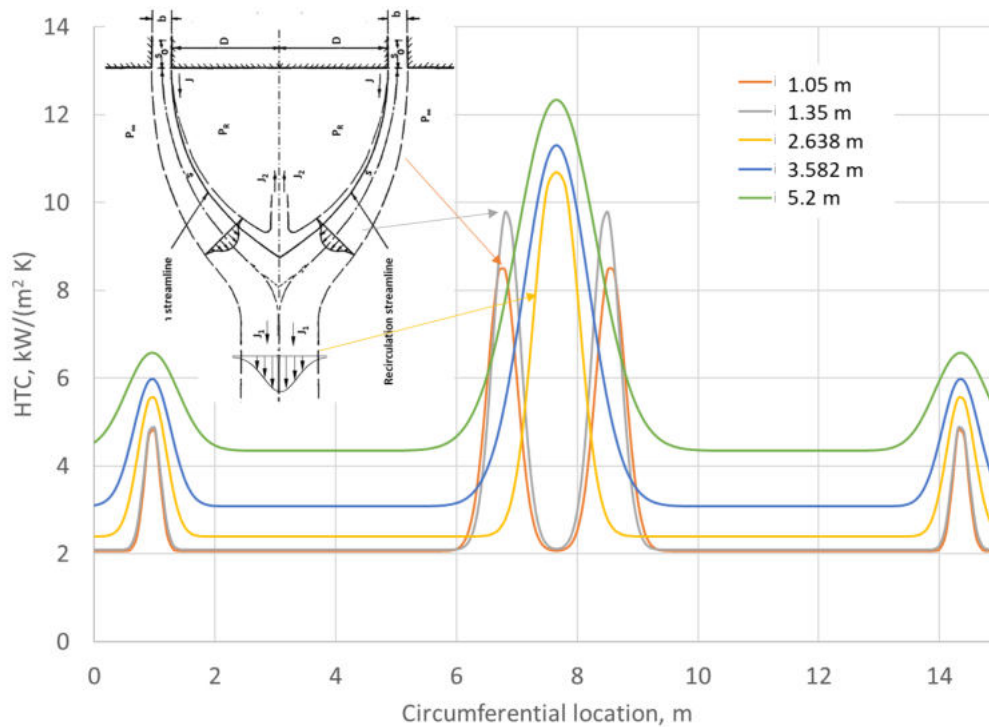
Figure 98: KWU-MIX temperatures heat-transfer coefficients at the middle of the plume at various distances below the axis of the cold-leg in the DC.

Figure 98 shows HTC profiles for five additional distances below the cold-leg axes. At a distance of 1.035 m, the circumferential location of the largest HTC below Cold Leg 2 is slightly closer to the circumferential location of the largest HTC value below Cold Leg 3. This is due to the merging phenomenon described in Section 3.4.2 and shown in in Figure 21. The distance between the circumferential locations of the largest HTCs below Cold Leg 2 and 3 decreases from 1.05 m to 1.35 m below the cold-leg axis. At a distance of 2.638 m below the cold-leg axis, the two plumes have merged, and only a single Gaussian distribution is shown. The HTC distributions at greater distances are similar, with the width increasing and the largest HTC increasing with distance from the cold-leg axis.

4.6   FLUENT results

Results from the system analysis performed with RELAP5, as described in Section 4.1, were used as input to the CFD mixing calculation performed with the Fluent computer code. Fluent calculations are very slow and therefore only preliminary temperature and velocity fields from the base case simulations can be described in this chapter. More complete results of the base case and LTO case of heating HPIS tanks will be provided later and possibly included in the forthcoming reports under WP3 and WP4.

The four images in Figure 99 show the velocity and temperature fields in the Cold leg 2 at 385s after the break. At this time there is relatively small mass flow through the leg itself, so the cold ECC water also flows back towards the CL pump, as can be seen from the images showing the side view of the CL.
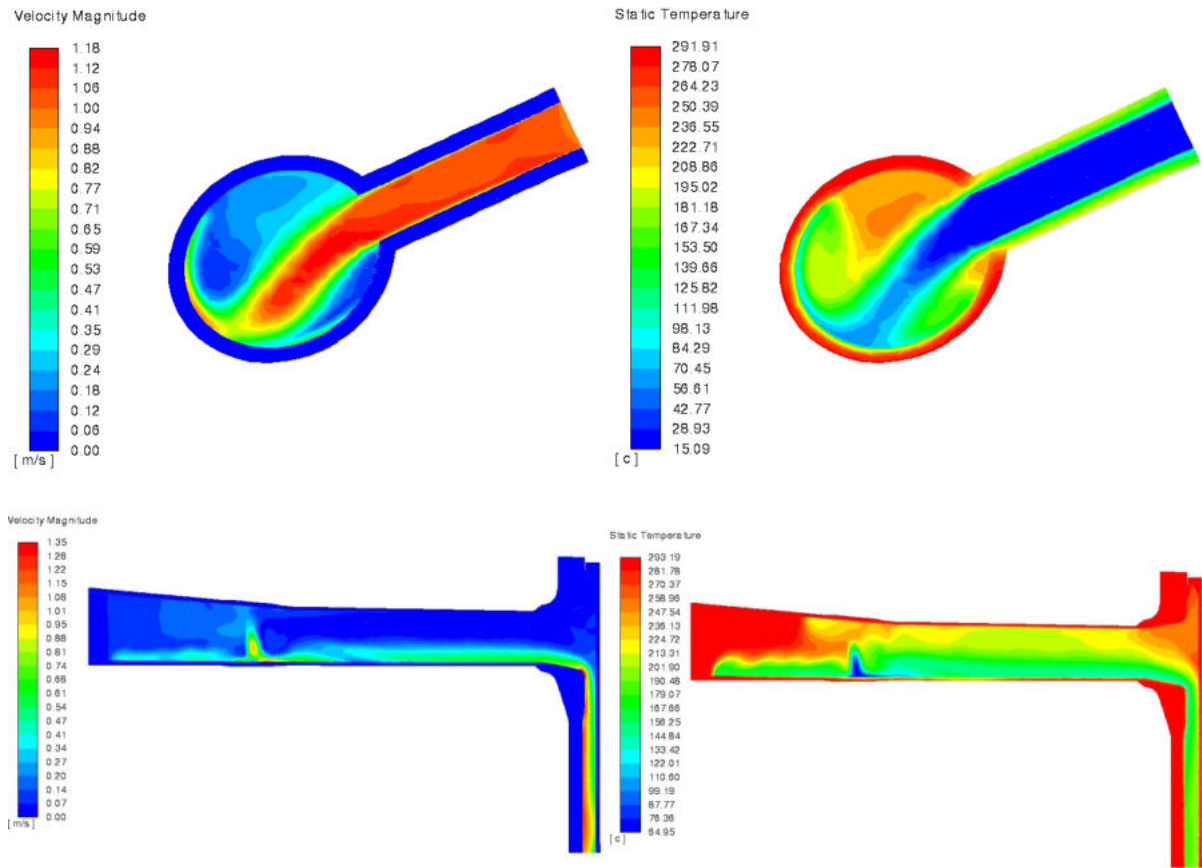
Figure 99: Velocity and temperature fields in Cold leg 2 at 385s after the break.

Shape of the cold water plume in the DC below the Cold leg 2 can be better observed from Figure 100. In the left image is cold plume at time 385 *s*, same as in Figure 99 above. At this time, the plume is still developing. After 100 s (in the right image) it can be seen that the developed plume oscillates.
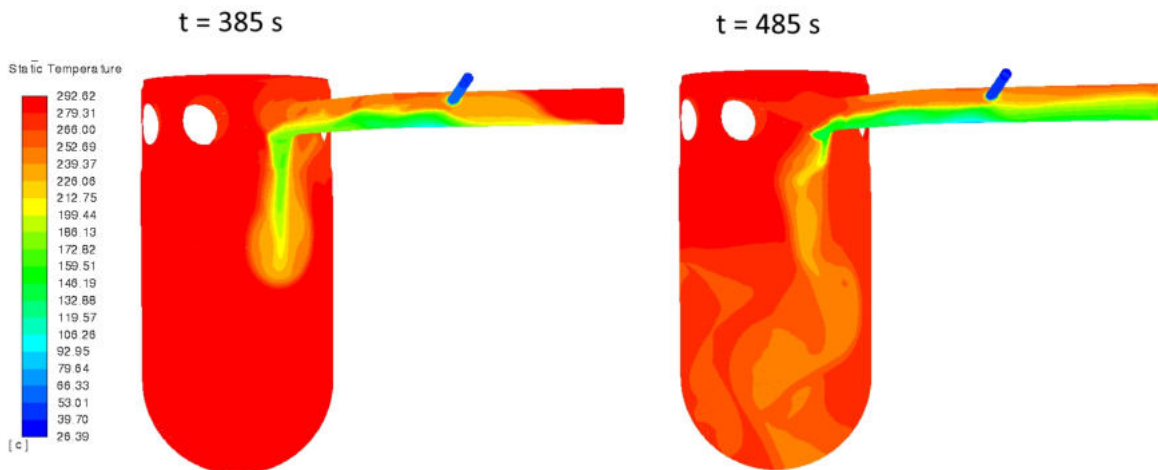
Figure 100: Cold water plume in DC below Cold leg 2.

5   Simulation results for LTO improvements

Information on the already applied or further potential LTO improvements with an impact on the plant resistance against PTS and RPV brittle fracture (that would result with high probability in core melt and severe accident) have been collected in Task 1.5 of the APAL project [8]. Most of the modifications are related to the parameters of the ECC system since actuation of the ECCS has a major impact on PTS. Some LTO improvements concentrate on aging management of RPVs and other systems, structures, and components (SSC). In some plants, modifications of EOPs have also been implemented to reduce the risk of PTS.

From the LTO improvements identified and presented in the Task 1.5 report, those having an impact on the pressure, temperature, and HTC histories in the DC region of the RPV in a postulated SBLOCA were selected to be used in the TH analysis in Task 2.1. As Task 2.1 also deals with the influence of human actions in PTS events, relevant operator actions were selected for analysis as well. Table 14 presents the cases chosen to be calculated in Task 2.1. The table also shows which computer codes were used in each simulated case. Table 15 shows the specifications used in each simulated case.

Table 14: LTO improvements and human actions simulated in Task 2.1

LTO improvement / Human action	System Code / Partner	MIX Code / Partner
1. Heating of water in the HPIS tanks	RELAP5/UJV RELAP5/WUT TRACE/PSI	Fluent/UJV[4]
2. Heating of water in the ACCs	RELAP5/WUT TRACE/PSI ATHLET/GRS	ECC-MIX/GRS KWU-MIX/Fra-G
3. Heating of water in the LPIS tanks	RELAP5/WUT TRACE/PSI ATHLET/GRS	ECC-MIX/GRS KWU-MIX/Fra-G
4. Decreasing the HPSI head	RELAP5/SSTC TRACE/PSI ATHLET/GRS	ECC-MIX/GRS
5. Decreasing the HPSI capacity	RELAP5/KIWA RELAP5/SSTC TRACE/PSI	
6. Reduction of HPIS flow (operator action)	RELAP5/WUT	KWU-MIX/Fra-G
7. Decreasing of ACC pressure	RELAP5/JSI RELAP5/WUT TRACE/PSI	
8. Change of cooldown rate (operator action)	RELAP5/WUT	KWU-MIX/Fra-G
9. Isolation of ACCs (operator action)	RELAP5/Fra-G	KWU-MIX/Fra-G

Table 15: Specifications used in simulations of LTO improvements and human actions

LTO improvement / Human action	Simulated change
1. Heating of water in the HPIS tanks	Heated from 15 °C to 45 °C (UJV and WUT one step; PSI: steps of 10 °C)
2. Heating of water in the ACCs	Heated from 20 °C to 50 °C (WUT: one step; PSI and GRS: steps of 10 °C)

---

[4] Note: Fluent results of this LTO improvement are not included in this report since the calculations were still in progress at the time of publication.

3. Heating of water in the LPIS tanks	Heated from 15 °C to 45 °C (WUT: one step; PSI and GRS: steps of 10 °C)
4. Decreasing the HPSI head	Decreased down to 75% (in 5% decrements)
5. Decreasing the HPSI capacity	Decreased down to 75% (in 5% decrements)
6. Reduction of HPIS flow (operator action)	Reduced at 1800 s to one pump
7. Decreasing of ACC pressure	Decreased from 26 bar to 20 bar (JSI and PSI: in 2 bar steps)
8. Change of cooldown rate (operator action)	Changed from 100 K/h to 200 K/h
9. Isolation of ACCs (operator action)	Isolated at 500 s

Simulations for each were run with different codes and selected quantities of interest were compared against the base case to determine whether they are advantageous from a PTS perspective. The results are presented in the sections that follow.

5.1 Heating of water in HPIS tanks

5.1.1 RELAP5 results by UJV

The heat-up of the water in the HPIS tanks is simulated by increasing the injection temperature from the reference value 15°C to the LTO value 45 °C. Comparative plots for key quantities of interest are provided in Figure 101 through Figure 105. The calculations show that the increased injection temperature results in a higher temperature of the water in the reactor DC during the entire transient after initiation of HPSI. Also, other system parameters like DC level or break flow are slightly affected by the studied LTO improvement.

(a)   (b)
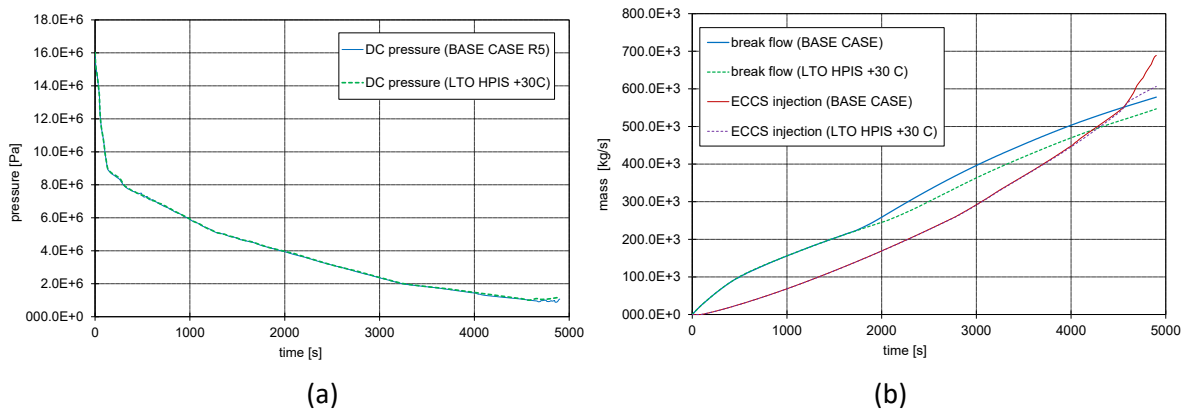
Figure 101: Comparison of (a) Primary Pressures and (b) Break and ECCS Flow Integral.

(a)   (b)
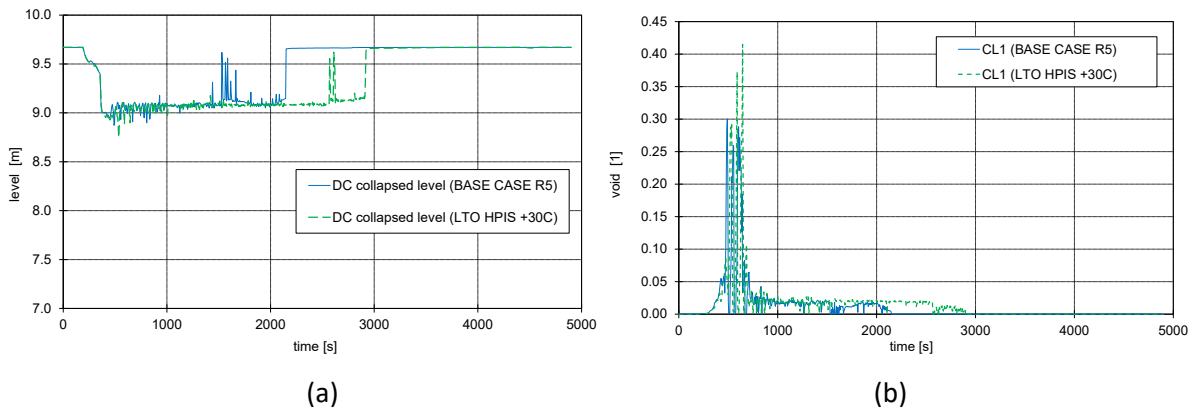
Figure 102: Comparison of (a) Reactor DC Levels and (b) Void Fraction at Reactor Inlet from CL2.

96

(a)   (b)
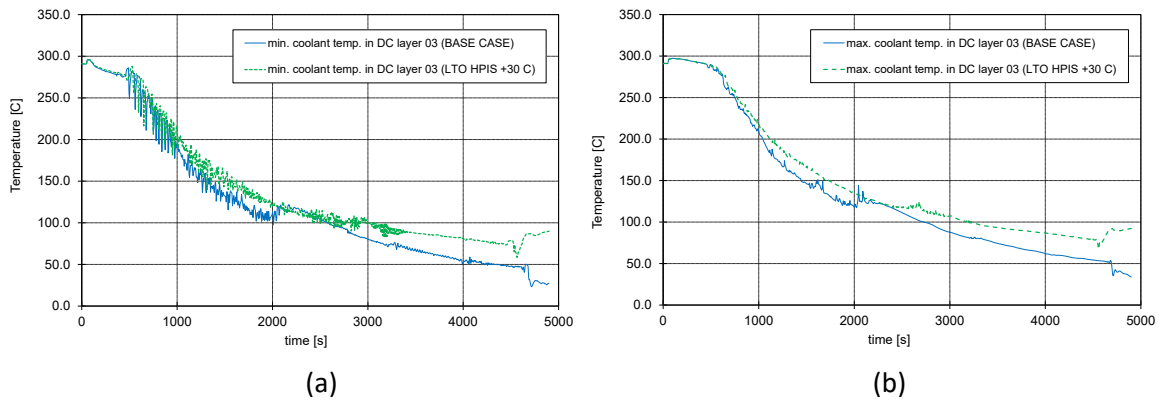
Figure 103: Comparison of (a) Minimum Coolant Temperatures in DC Control Volumes in Layer 3 at Elevation 1.13 m and (b) Maximum Coolant Temperatures in DC Control Volumes in Layer 3.

(a)   (b)
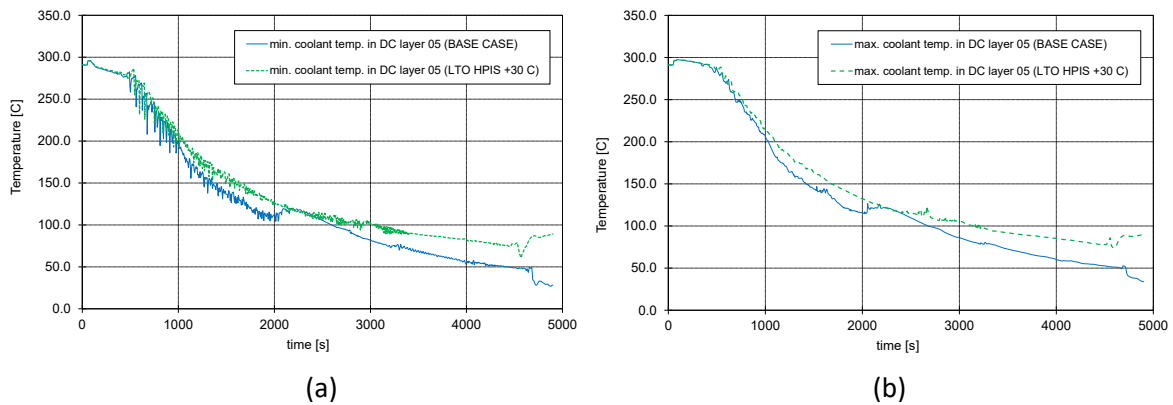
Figure 104: Comparison of (a) Minimum Coolant Temperatures in DC Control Volumes in Layer 5 at Elevation 2.638 m and (b) Maximum Coolant Temperatures in DC Control Volumes in Layer 5.
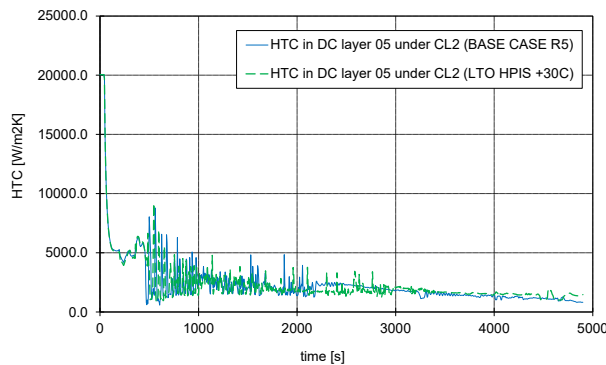
Figure 105: Comparison of HTC at RPV Inner Surface under CL2 at elevation 2.638 m.

5.1.2   RELAP5 results by WUT

The heating of the water in the HPI tanks is simulated by increasing the injection temperature from the reference value of 15°C to 45 °C. Comparative plots for key quantities of interest are provided in Figure 106 through Figure 111. The calculations show that the increased injection temperature results in a higher temperature of the water in the DC during the entire transient. The proposed LTO improvement affects the break flow and liquid levels until the initiation of the ACCs (around 2790 s). The LTO improvement could potentially be beneficial from a PTS perspective.
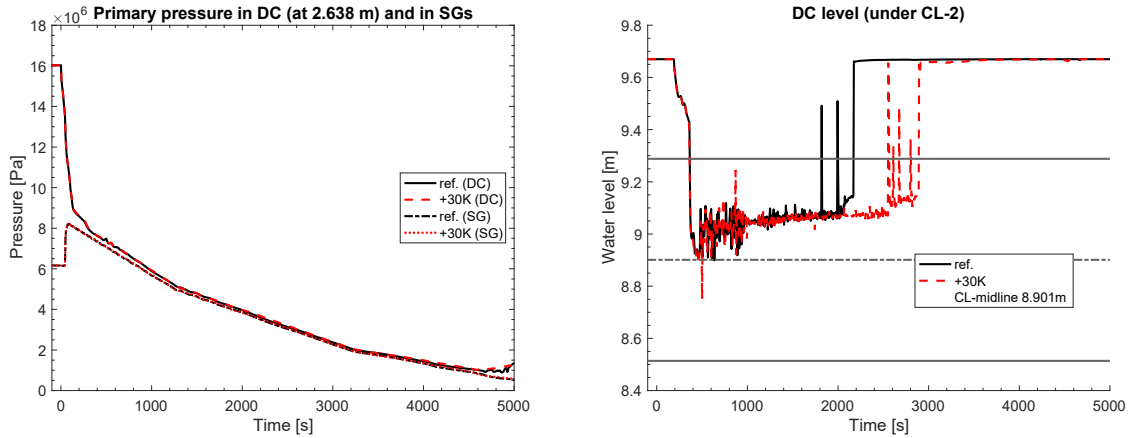
Figure 106: Comparisons of (left) pressure in the DC at 2.638 m below the CL-2 axis and (right) DC level for different HPI injection temperatures.
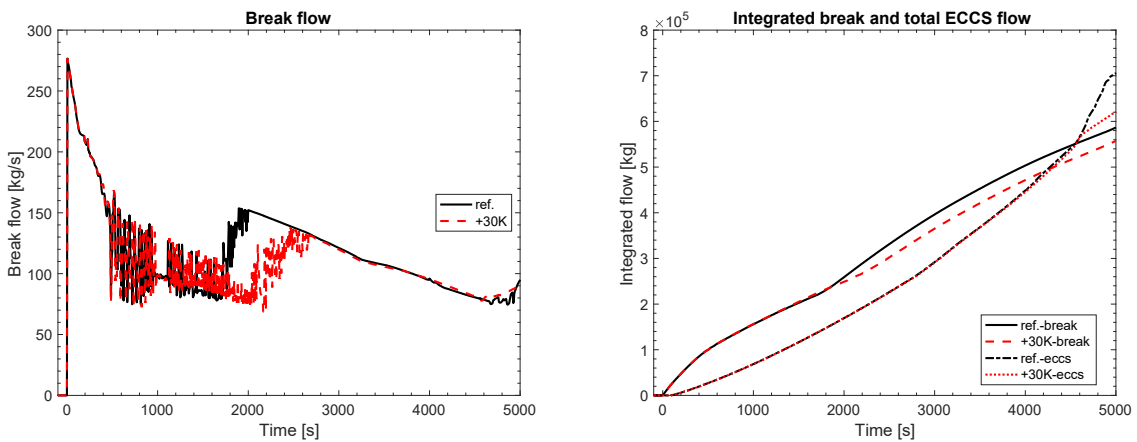
Figure 107: Comparisons of (left) Break flow and (right) time-integrated coolant loss and ECCS injection for different HPI injection temperatures.
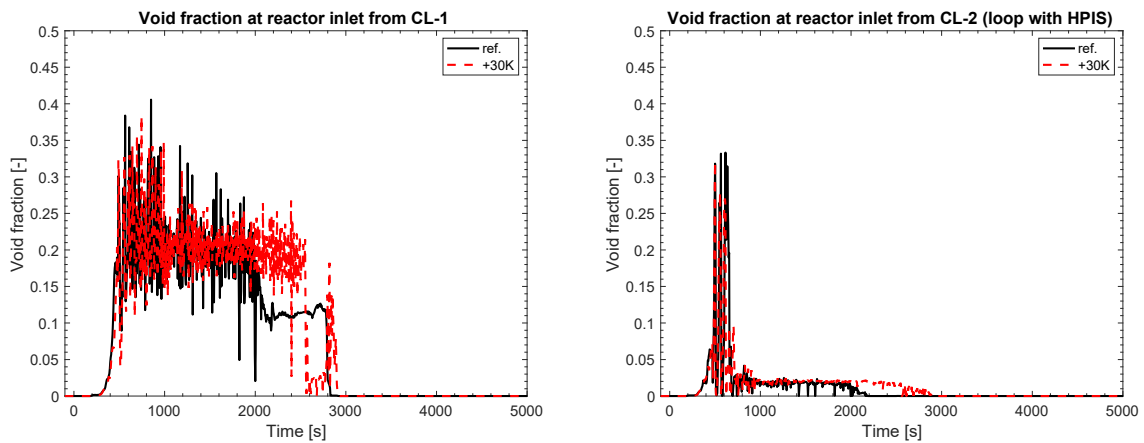
Figure 108: Comparisons of void fraction at the RPV Inlets of Loops 1 and 2 for different HPI injection temperatures.
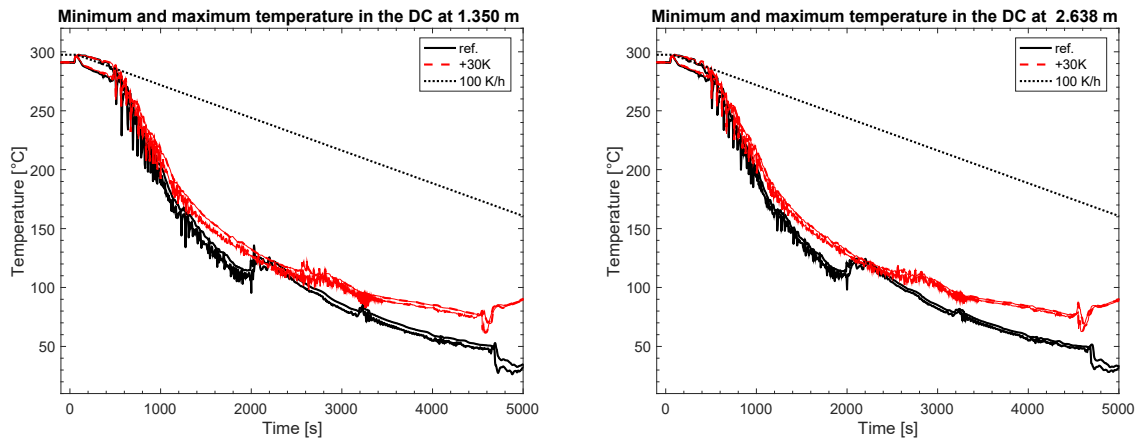
Figure 109: Comparisons of DC coolant temperature range (minimum to maximum) at (left) 1.35 m and (right) 2.638 m below the CL axis for different HPI injection temperatures.
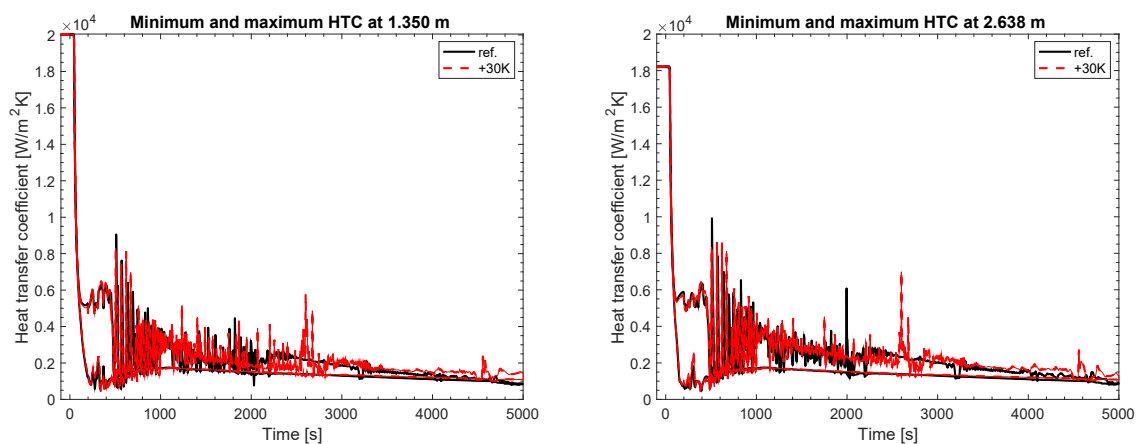
Figure 110: Comparisons of DC HTC range (minimum to maximum) at (left) 1.35 m and (right) 2.638 m below the CL axis for different HPI injection temperatures.
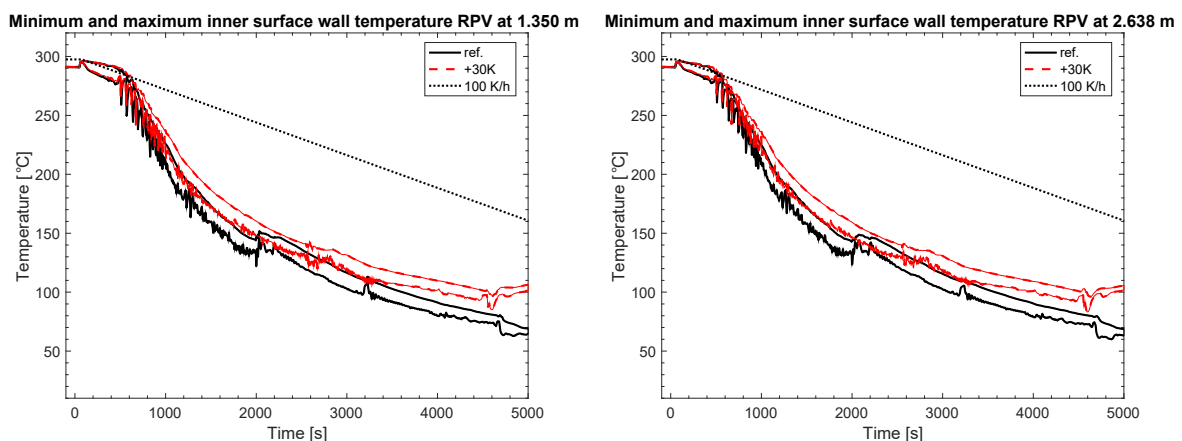
Figure 111: Comparisons of RPV inner surface temperature range (minimum to maximum) at (left) 1.35 m and (right) 2.638 m below the CL axis for different HPI injection temperatures.

5.1.3   TRACE results by PSI

Heating of the water in the HPI tanks is simulated by changing the injection temperature in 10 K increments from the reference value of 15°C to 45 °C. Comparative plots for key quantities of interest are provided in Figure 112 through Figure 117. The increased injection temperature results in a clear reduction in the cooling rate in the DC throughout the entire transient. This proposed LTO

99

improvement affects the break flow, system pressure and liquid levels only after the ACC injection, where the impact of the cold ACC injection on system pressures is somewhat compensated for by the warmer HPI. The LTO improvement could potentially be beneficial from a PTS perspective.
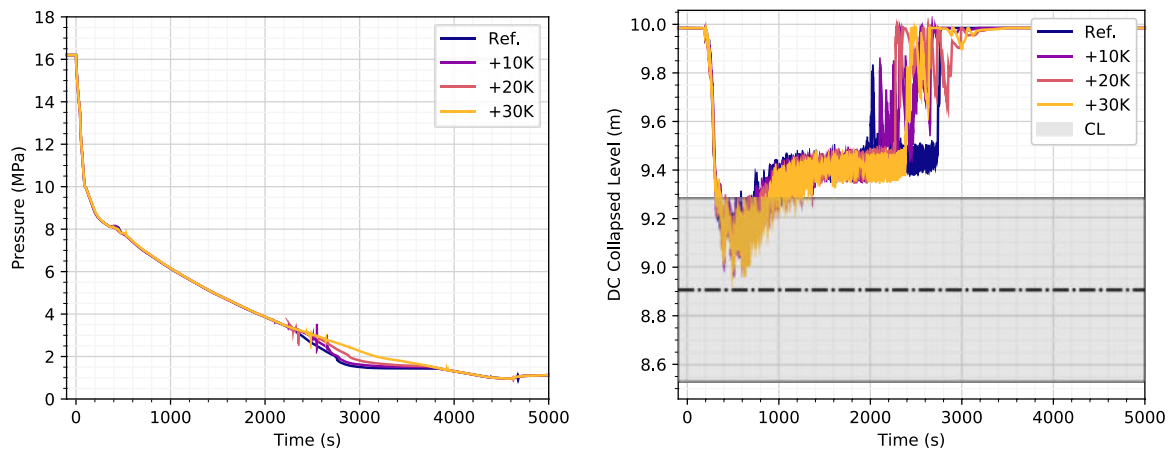
Figure 112: Comparisons of (left) Pressure in the DC at 2.638 m below the CL Axis and (right) DC Level for different HPI Injection Temperatures.
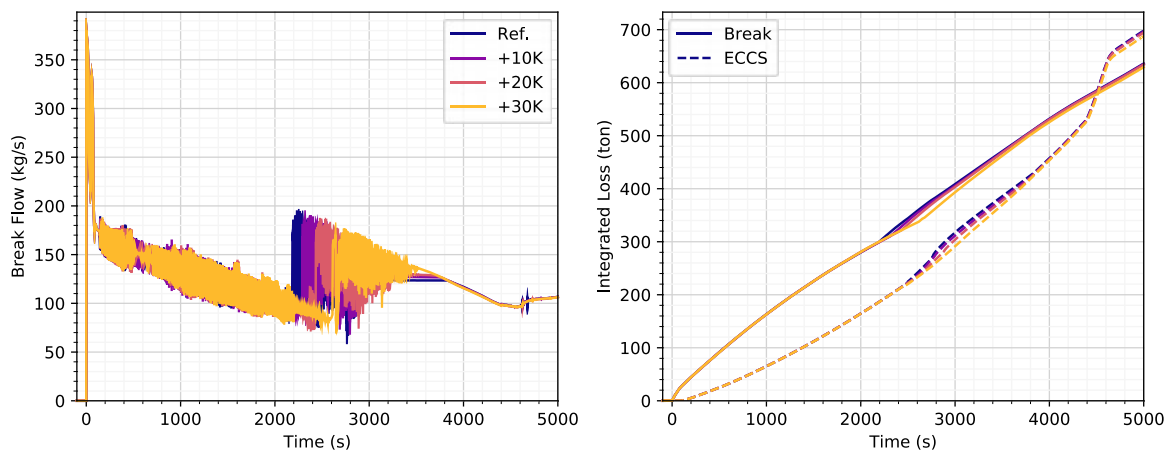
Figure 113: Comparisons of (left) Break Flow and (right) Time-integrated Coolant Loss and ECCS Injection for different HPI Injection Temperatures.
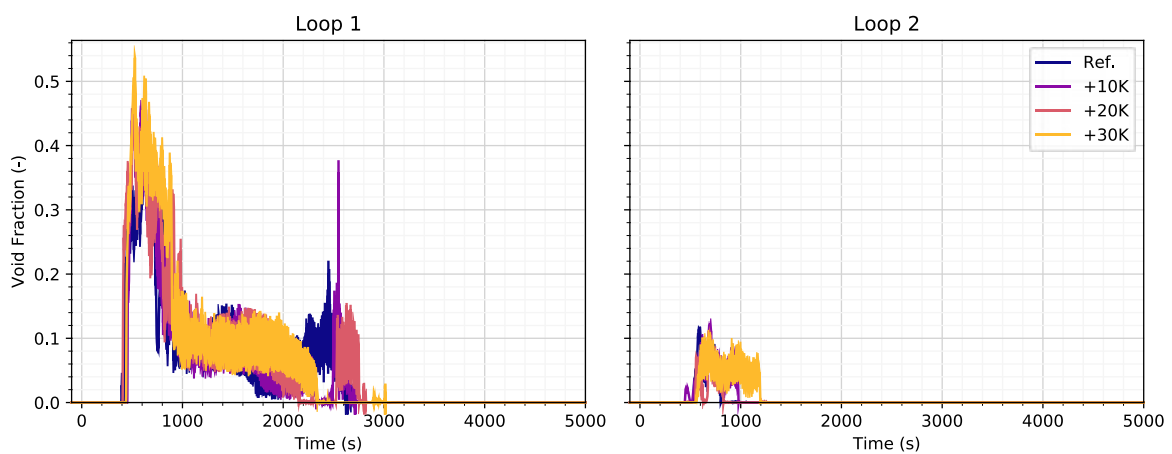
Figure 114: Comparisons of Void Fraction at the RPV Inlets of Loops 1 and 2 for different HPI Injection Temperatures.

100
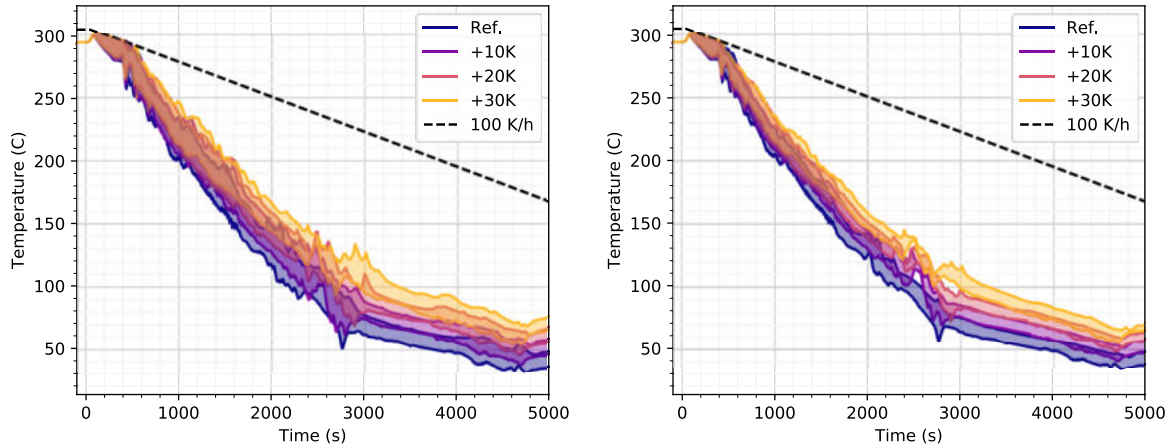
Figure 115: Comparisons of DC Coolant Temperature Range (Minimum to Maximum) at (left) 1.35 m and (right) 2.638 m below the CL Axis for different HPI Injection Temperatures.
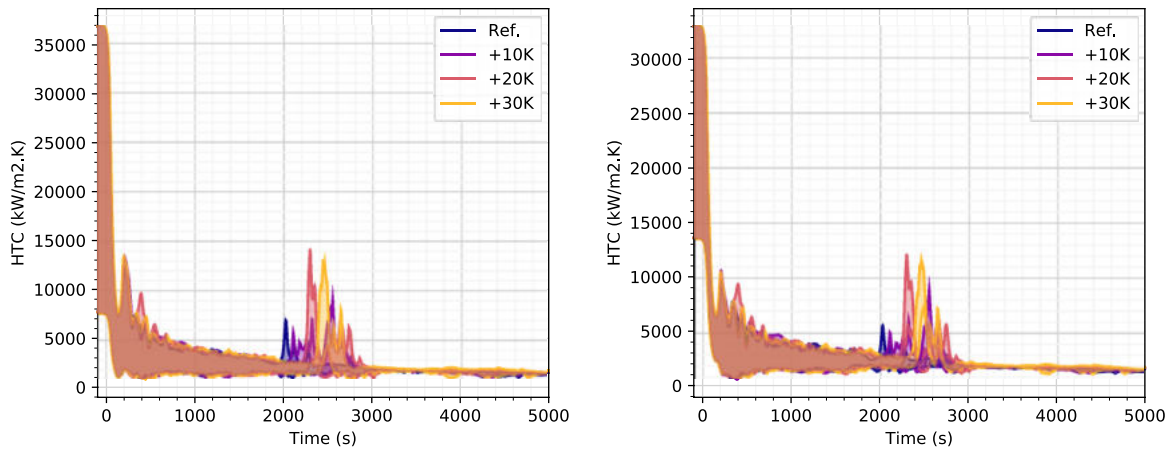
Figure 116: Comparisons of DC HTC Range (Minimum to Maximum) at (left) 1.35 m and (right) 2.638 m below the CL Axis for different HPI Injection Temperatures.
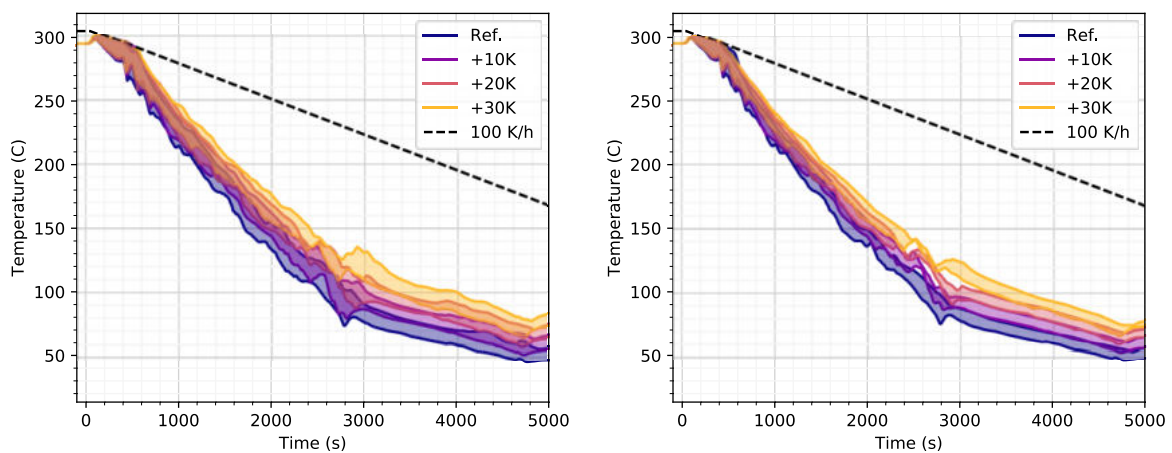
Figure 117: Comparisons of RPV Inner Surface Temperature Range (Minimum to Maximum) at (left) 1.35 m and (right) 2.638 m below the CL Axis for different HPI Injection Temperatures.

5.2   Heating of water in accumulators

5.2.1   RELAP5 results by WUT

The heating of the water in the ACCs is simulated by increasing the water injection temperature from the reference value of 20 °C to 50°C. Comparative plots for key quantities of interest are provided in Figure 118 through Figure 123. The calculations show that only after the initiation of the ACC (around 2790 s) the differences in the result (around 2790 s) can be observed. The LTO improvement results in the slightly higher temperature in the DC after the beginning of the flow from ACCs. The LTO improvement provides no significant benefit from a PTS perspective.
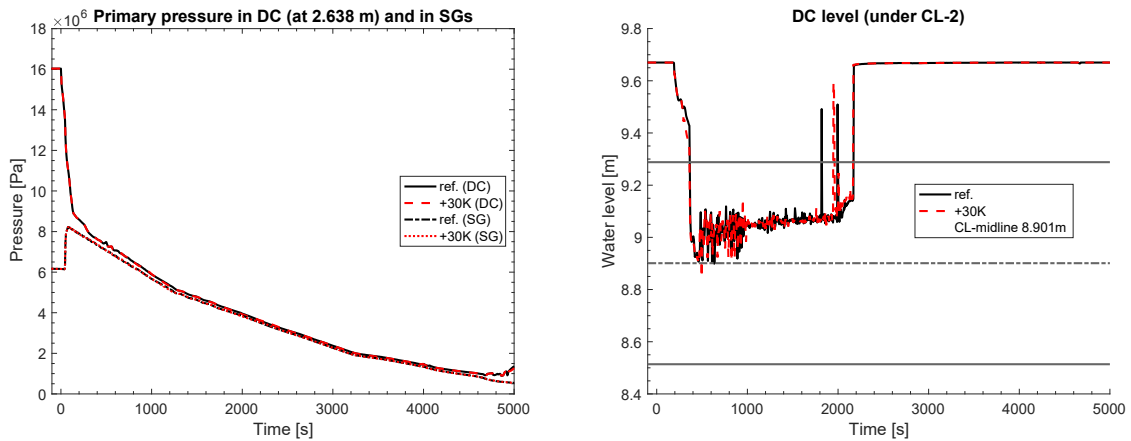
Figure 118: Comparisons of (left) pressure in the DC at 2.638 m below the CL-2 axis and (right) DC level for different ACC water temperatures.
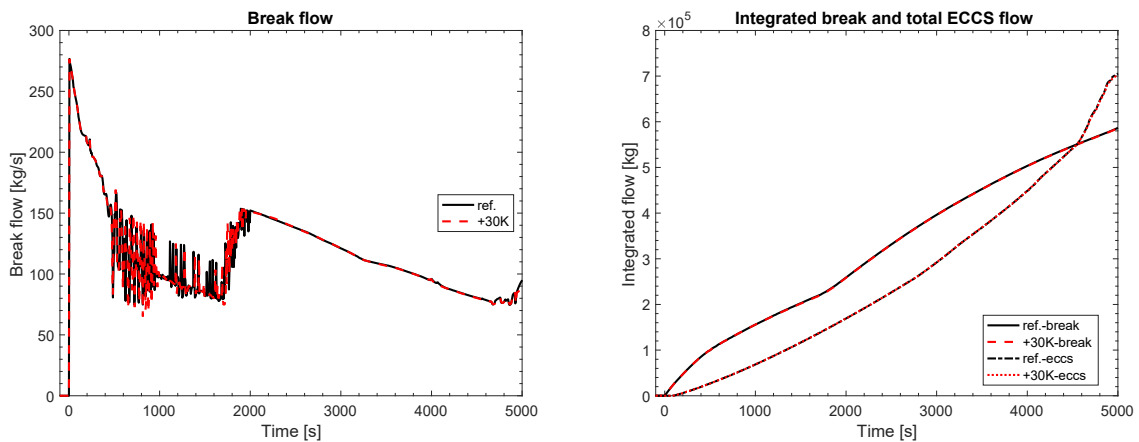
Figure 119: Comparisons of (left) Break flow and (right) time-integrated coolant loss and ECCS injection for different ACC water temperatures.
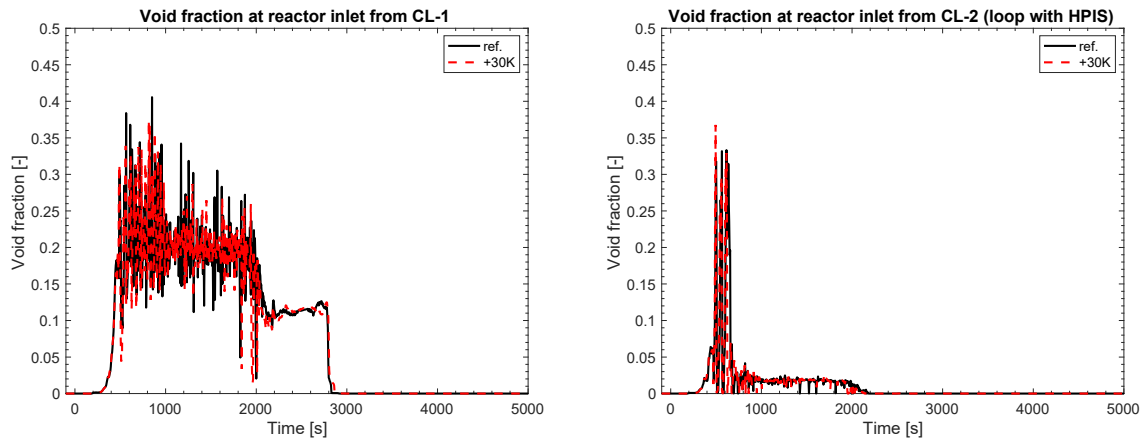
Figure 120: Comparisons of void fraction at the RPV Inlets of Loops 1 and 2 for different ACC water temperatures.
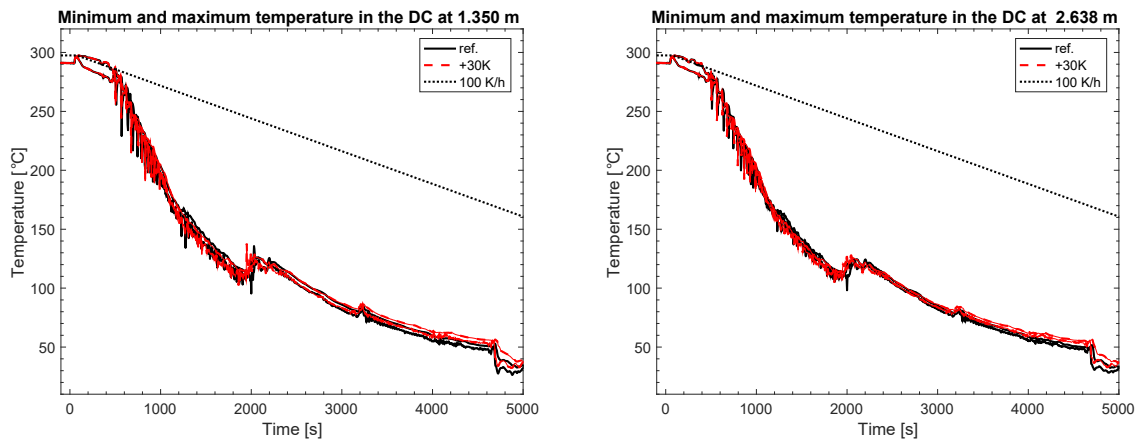
Figure 121: Comparisons of DC coolant temperature range (minimum to maximum) at (left) 1.35 m and (right) 2.638 m below the CL axis for different ACC water temperatures.
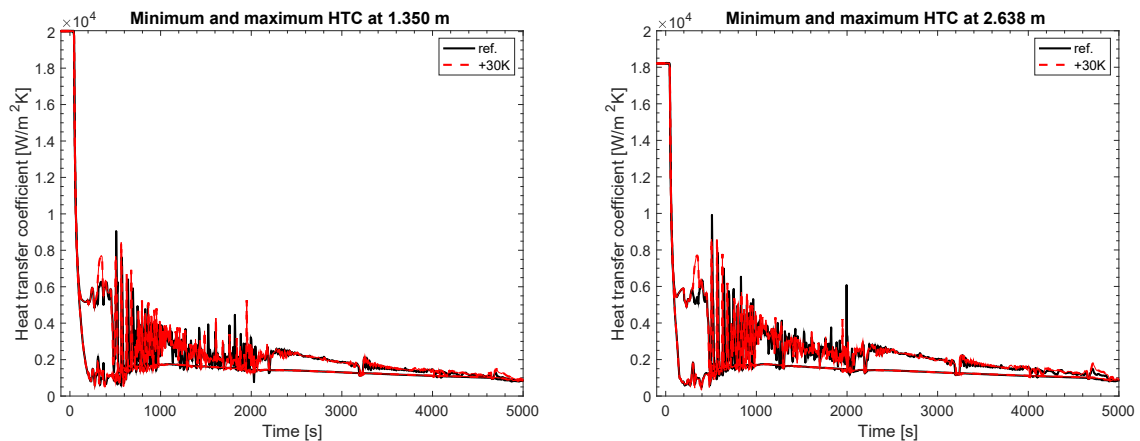
Figure 122: Comparisons of DC HTC Range (Minimum to Maximum) at (left) 1.35 m and (right) 2.638 m below the CL Axis for different ACC water temperatures.
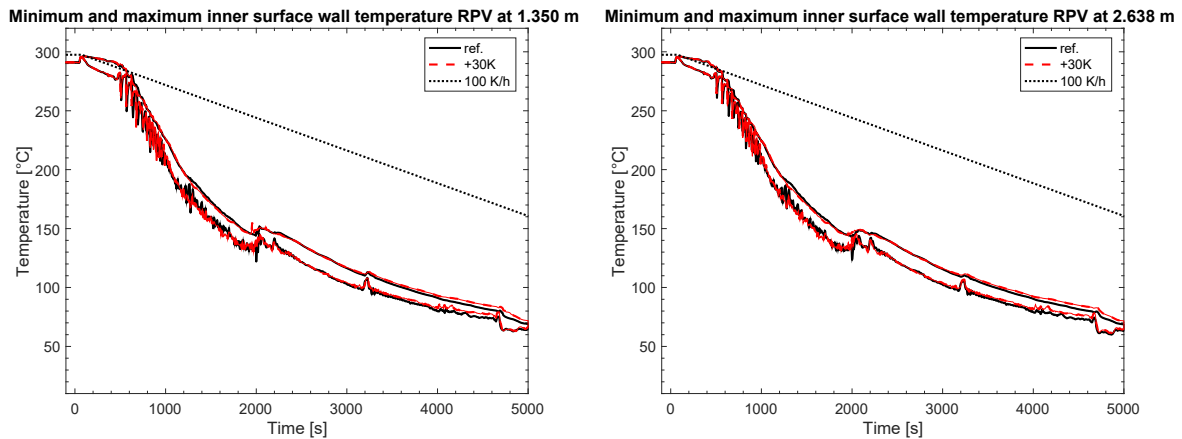
Figure 123: Comparisons of RPV inner surface temperature range (minimum to maximum) at (left) 1.35 m and (right) 2.638 m below the CL axis for different ACC water temperatures.

5.2.2   TRACE results by PSI

The heating of the coolant in the ACCs is simulated by changing the initial temperature within the ACCs in 10 K increments between 20 °C to 50 °C. Comparative plots for key quantities of interest are provided in Figure 124 through Figure 129. While we see a small impact of the warmer ACC coolant during the period of ACC injection (~2500 s), the overall impact of this proposed LTO improvement on both the system behaviour and the DC temperatures is small for this particular transient. Thus, the simulation results suggest that this LTO improvement provides no significant benefit from a PTS perspective in this case.
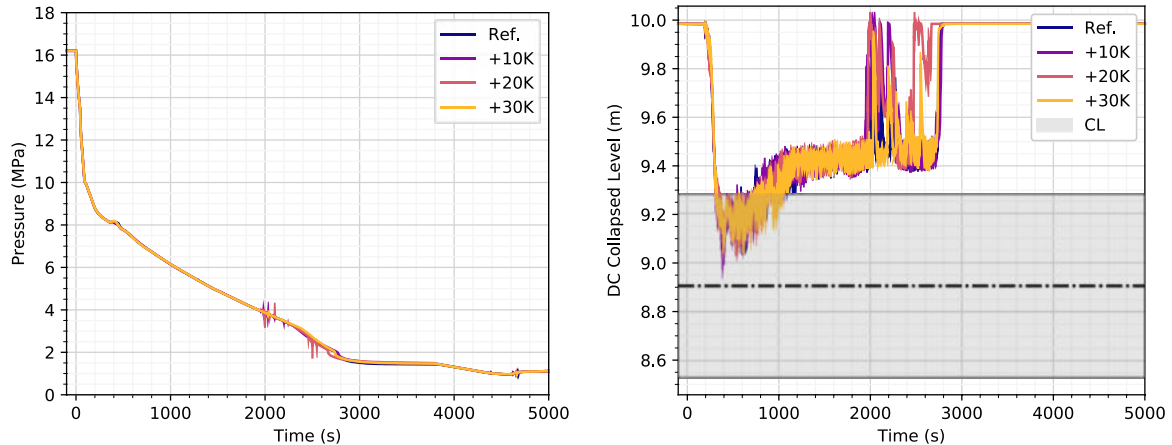
Figure 124: Comparisons of (left) Pressure in the DC at 2.638 m below the CL Axis and (right) DC Level for different ACC Temperatures.

104
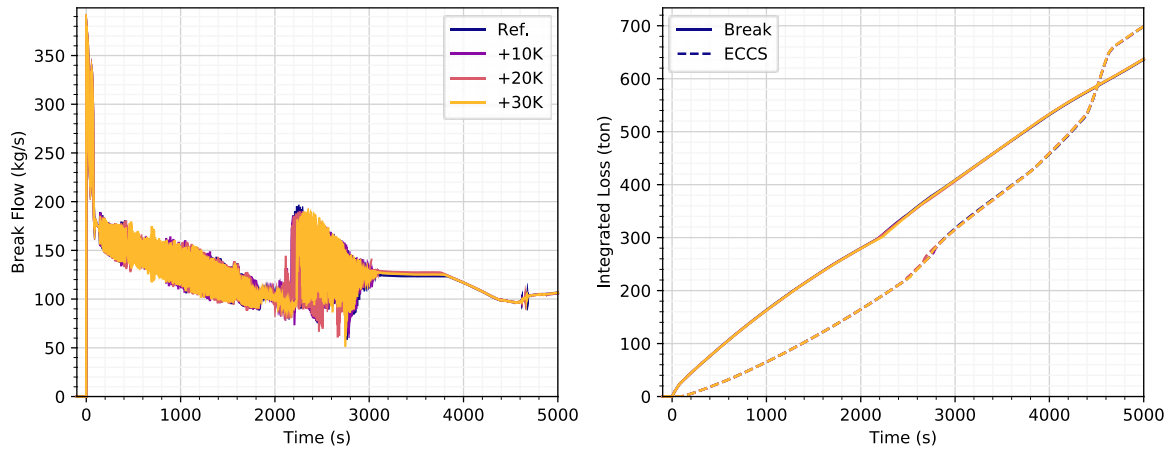
Figure 125: Comparisons of (left) Break Flow and (right) Time-integrated Coolant Loss and ECCS Injection for different ACC Temperatures.
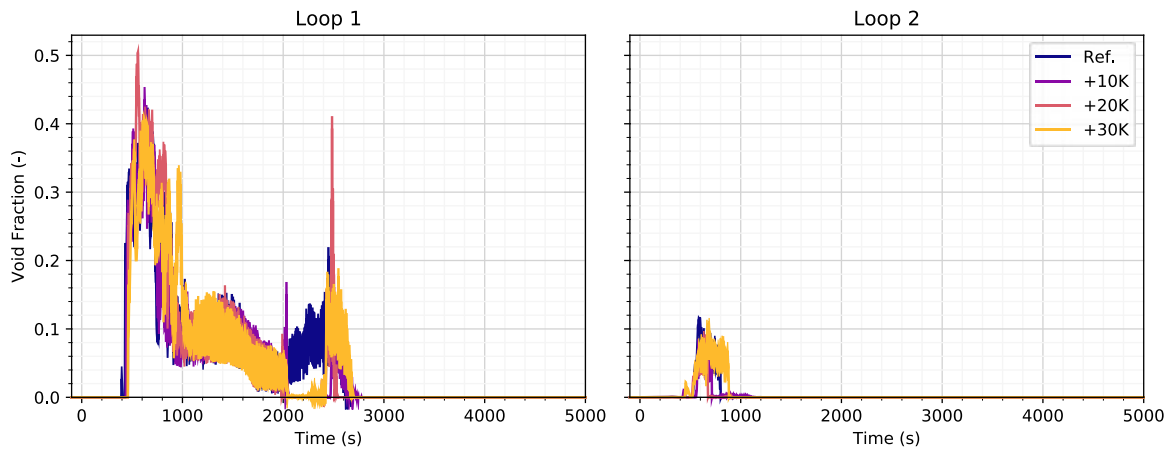
Figure 126: Comparisons of Void Fraction at the RPV Inlets of Loops 1 and 2 for different ACC Temperatures.
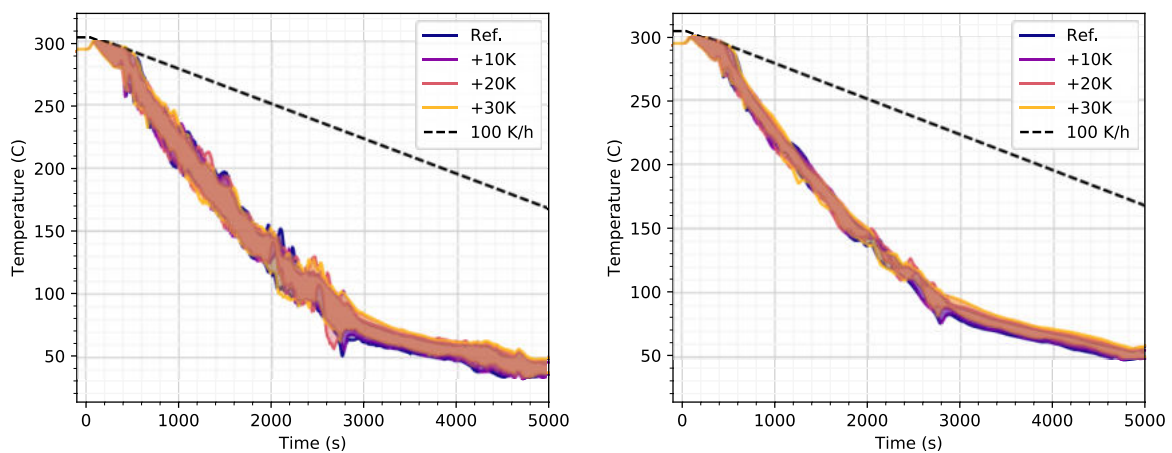
Figure 127: Comparisons of DC Coolant Temperature Range (Minimum to Maximum) at (left) 1.35 m and (right) 2.638 m below the CL Axis for different ACC Temperatures.

105
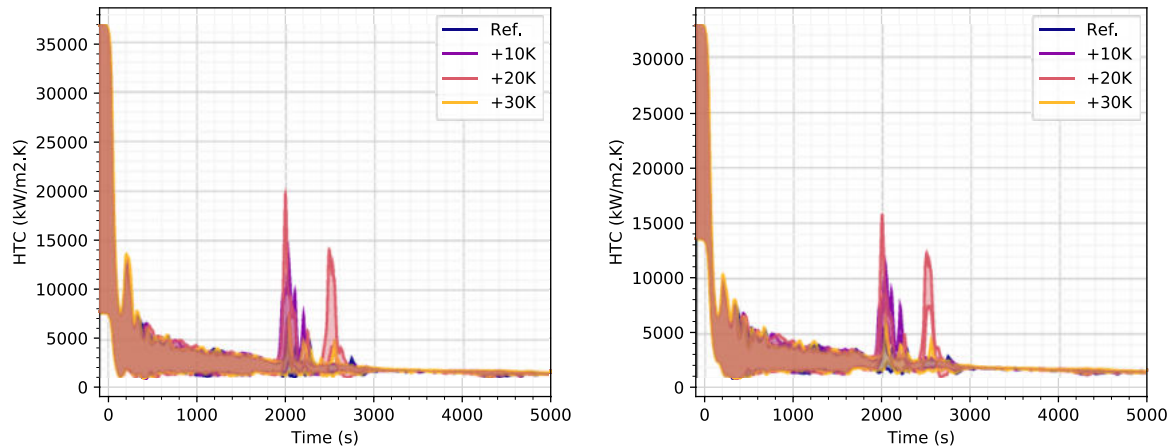
Figure 128: Comparisons of DC HTC Range (Minimum to Maximum) at (left) 1.35 m and (right) 2.638 m below the CL Axis for different ACC Temperatures.
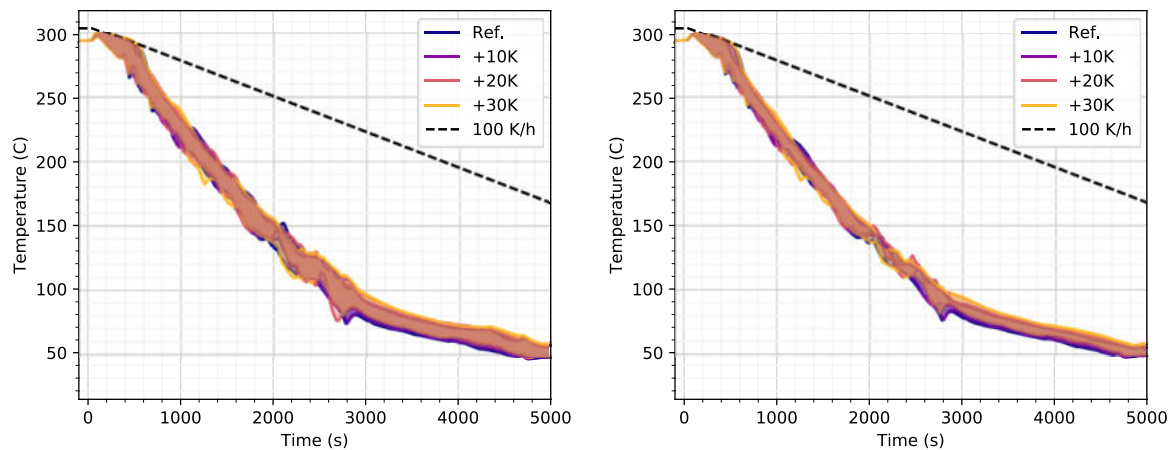
Figure 129: Comparisons of RPV Inner Surface Temperature Range (Minimum to Maximum) at (left) 1.35 m and (right) 2.638 m below the CL Axis for different ACC Temperatures.

5.2.3 ATHLET results by GRS

The heating of the coolant in the ACCs is simulated by changing the initial temperature within the ACCs in 10 K increments between 20 °C to 50 °C based on variation of the fluid specific enthalpy. Comparative plots for key quantities of interest are provided in Figure 130 through Figure 135. Conclusions that can be drawn from the results of the ACC heating as LTO improvement are consistent with what is given in 5.2.1 and 5.2.2: a small effect on the relevant temperatures in the DC (< 10 K) is seen after the ACC injection start up (t > 3000 s), no significant impact is expected for the given configuration.
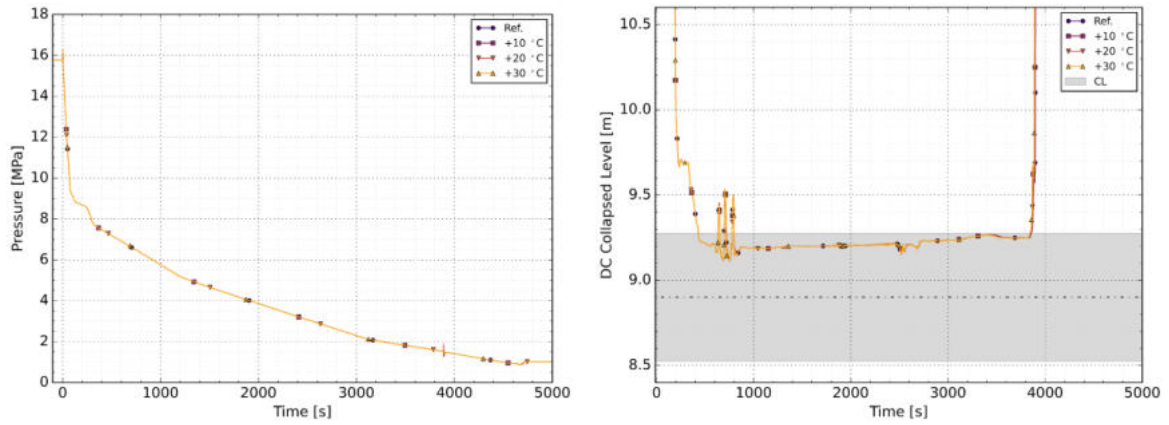
Figure 130: Comparisons of (left) Pressure in the DC at 2.638 m below the CL Axis and (right) DC Level for different ACC Temperatures.
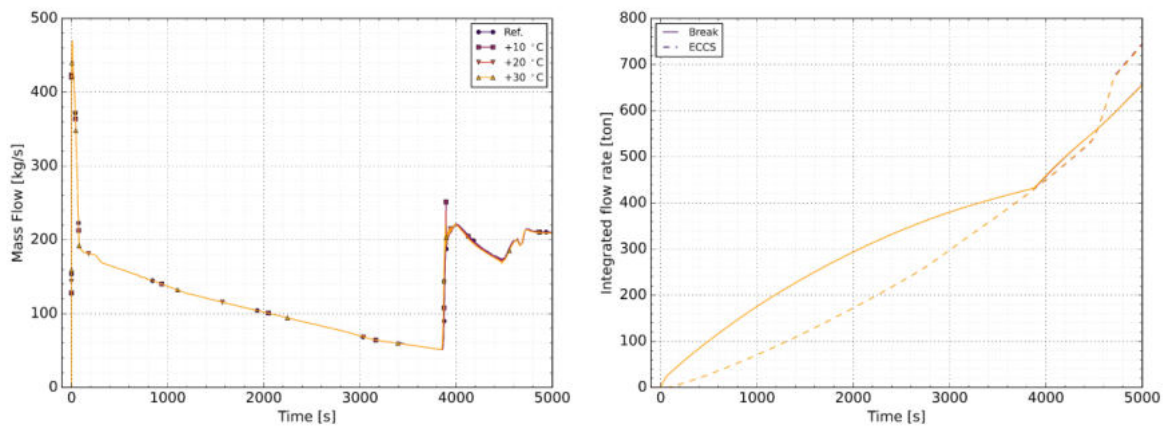
Figure 131: Comparisons of (left) Break Flow and (right) Time-integrated Coolant Loss and ECCS Injection for different ACC Temperatures.
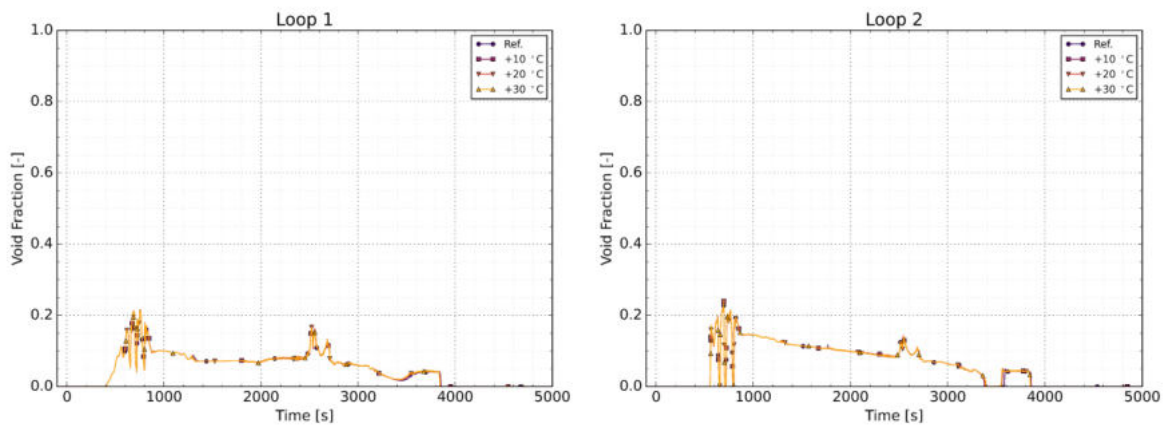
Figure 132: Comparisons of Void Fraction at the RPV Inlets of Loops 1 and 2 for different ACC Temperatures.
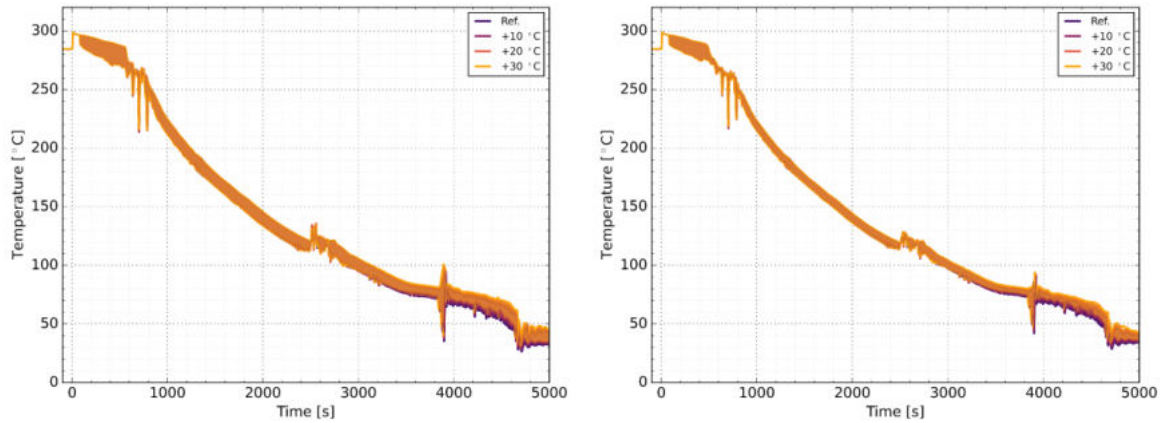
Figure 133: Comparisons of DC Coolant Temperature Range (Minimum to Maximum) at (left) 1.35 m and (right) 2.638 m below the CL Axis for different ACC Temperatures.
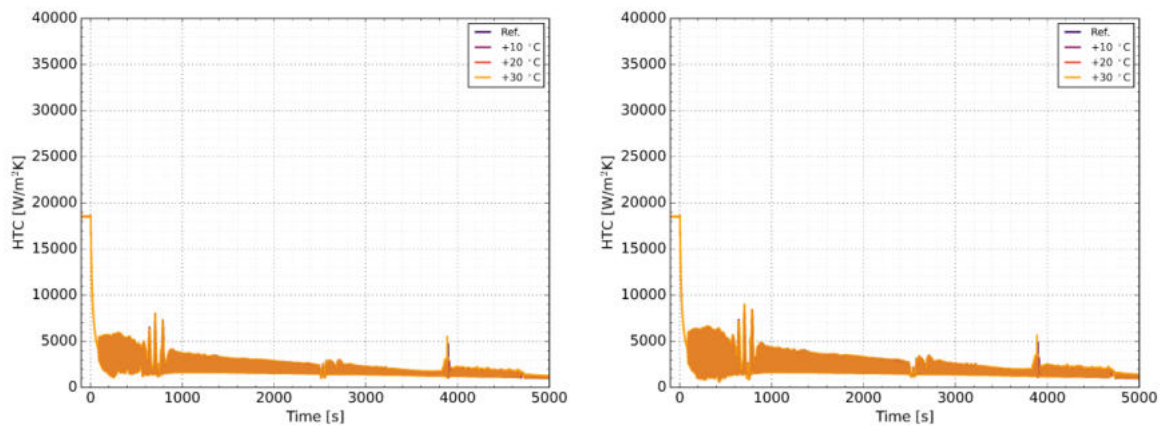
Figure 134: Comparisons of DC HTC Range (Minimum to Maximum) at (left) 1.35 m and (right) 2.638 m below the CL Axis for different ACC Temperatures.
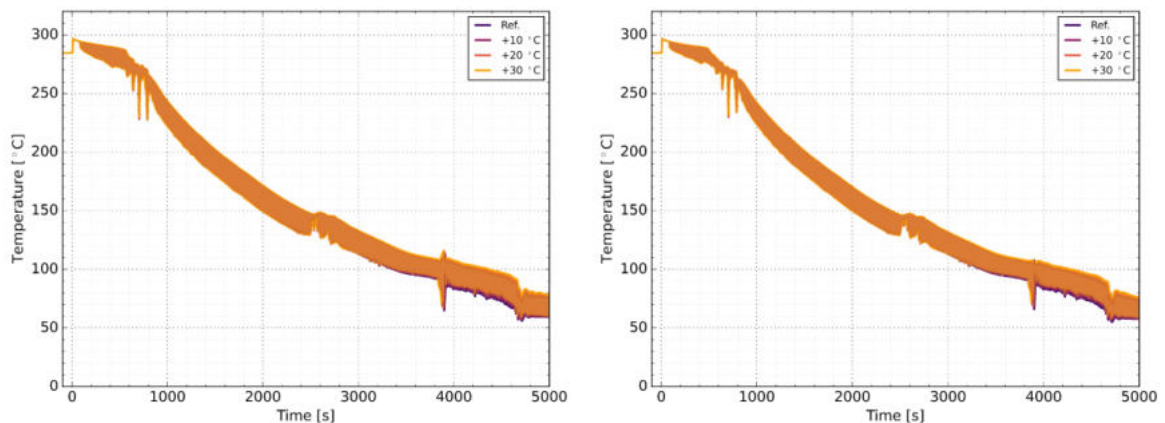
Figure 135: Comparisons of RPV Inner Surface Temperature Range (Minimum to Maximum) at (left) 1.35 m and (right) 2.638 m below the CL Axis for different ACC Temperatures.

5.2.4   ECC-MIX results by GRS

The heating of the coolant in the ACCs is simulated identical to the method described in 5.2.3 by changing the initial temperature within the ACCs in 10 K increments between 20 °C to 50 °C. Comparative plots for key quantities of interest are provided in Figure 136 through Figure 141. By applying the mixing model ECC-MIX a large impact on the results can be seen during the ACC injection

108

phase (> 3000 s) compared to the results with no mixing model used given in 5.2.3. Furthermore, the void fraction in both loop 1 and loop 2 is higher compared to the results given in Figure 132. This is due to the model implementation approach, where parts of the cold injected water from the ECCS are artificially removed from the injection point and redirected directly into the DC as described in chapter 3.5.3. The rise in DC temperature at the postulated weld positions (Figure 139 and Figure 141) after ACC injection (t > 2700 s) is < 15 K for the proposed LTO improvement in the presented simulation results. The overall conclusions that can be drawn from the results of the ACC heating as LTO improvement are consistent with what is given in 5.2.1 and 5.2.2: no significant impact is expected for the given configuration.
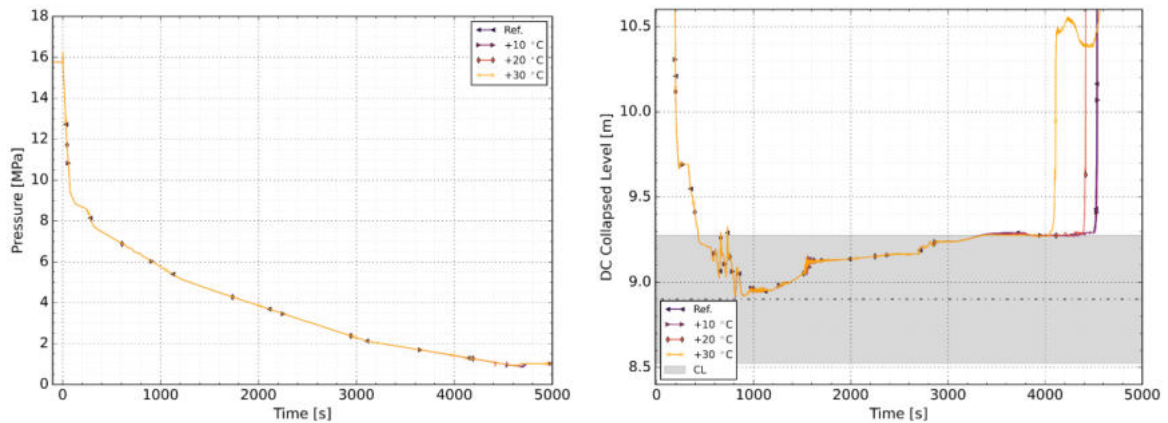
Figure 136: Comparisons of (left) Pressure in the DC at 2.638 m below the CL Axis and (right) DC Level for different ACC Temperatures.
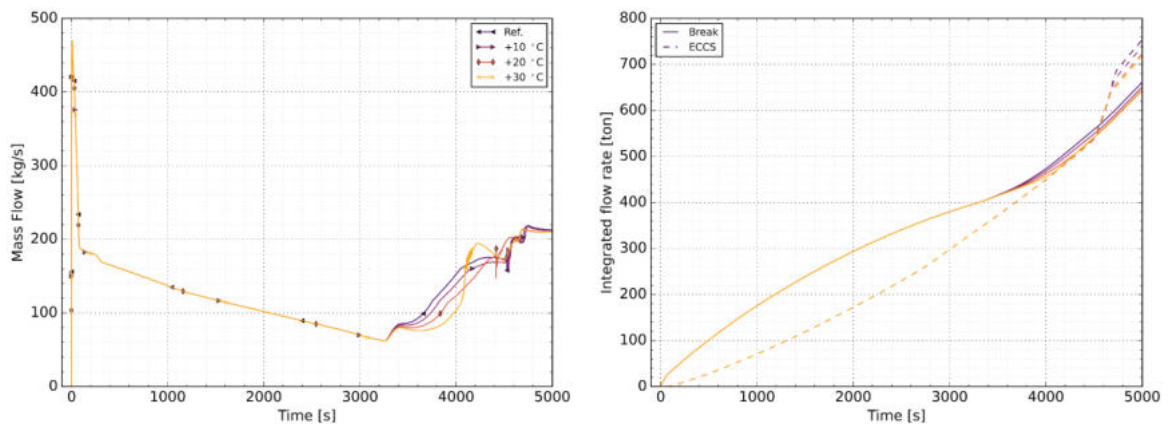
Figure 137: Comparisons of (left) Break Flow and (right) Time-integrated Coolant Loss and ECCS Injection for different ACC Temperatures.
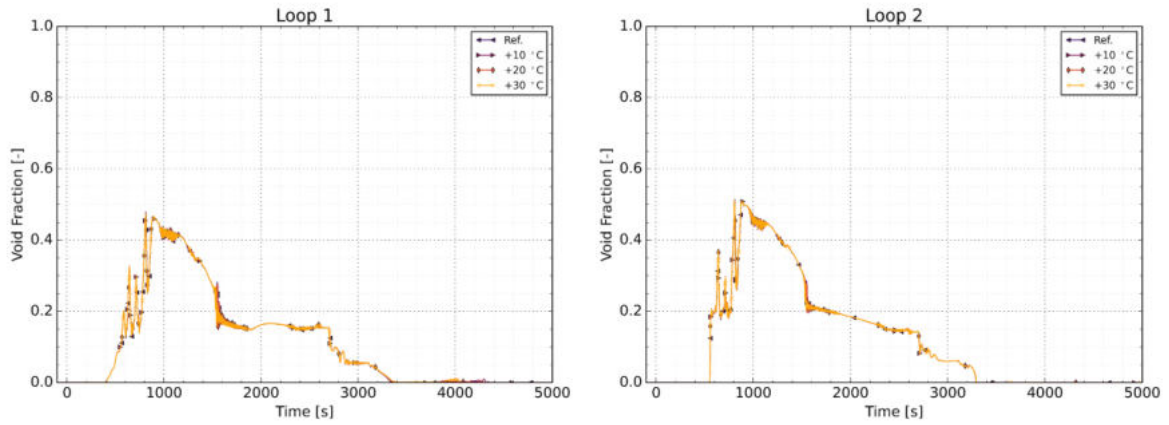
Figure 138: Comparisons of Void Fraction at the RPV Inlets of Loops 1 and 2 for different ACC Temperatures.
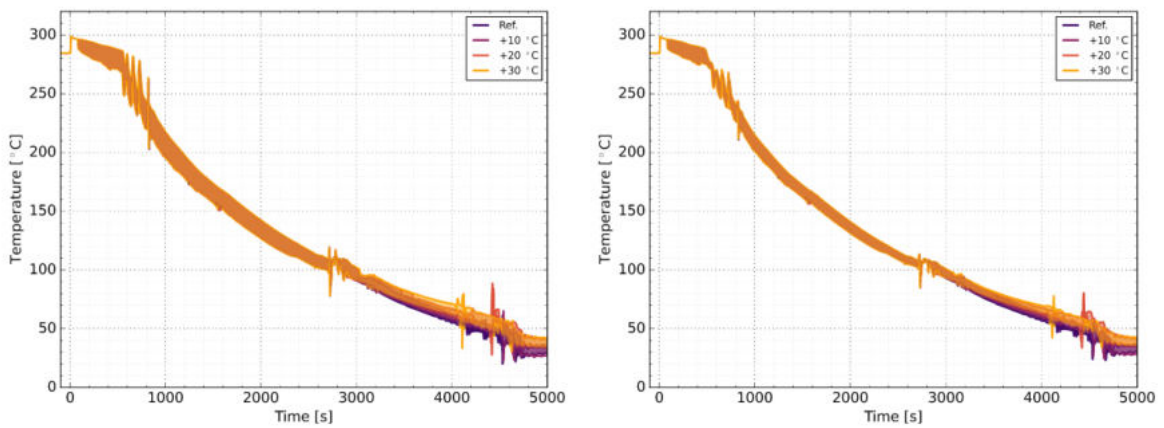
Figure 139: Comparisons of DC Coolant Temperature Range (Minimum to Maximum) at (left) 1.35 m and (right) 2.638 m below the CL Axis for different ACC Temperatures.
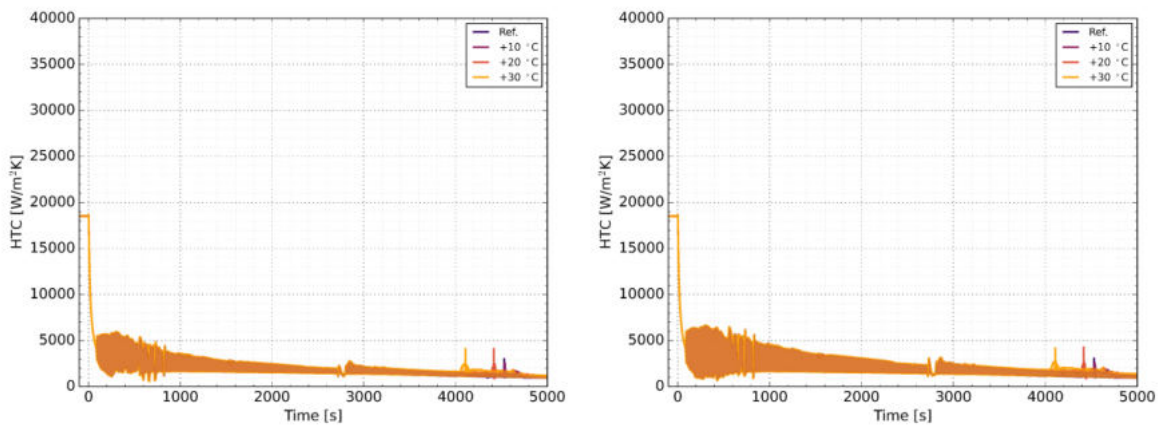
Figure 140: Comparisons of DC HTC Range (Minimum to Maximum) at (left) 1.35 m and (right) 2.638 m below the CL Axis for different ACC Temperatures.
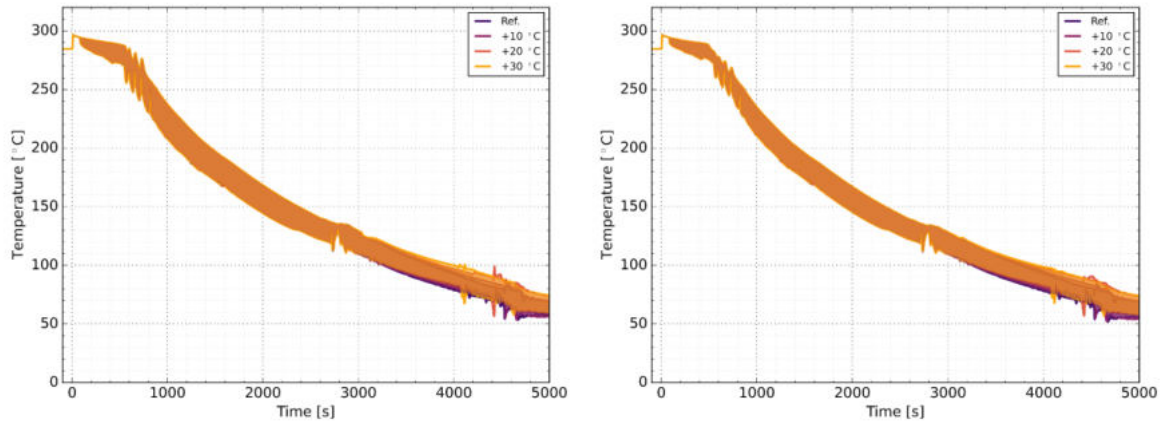
Figure 141: Comparisons of RPV Inner Surface Temperature Range (Minimum to Maximum) at (left) 1.35 m and (right) 2.638 m below the CL Axis for different ACC Temperatures.

5.2.5   Influence of Injection Model and Mixing Code (ATHLET, ECCMIX, GRSMIX)

The following Figure 142 and Figure 143 depict the influence of heating the ACCs to the maximum considered amount of +30 °C in comparison of the three investigated configurations with ATHLET only, applying the ECC-MIX model and calculation DC temperatures and heat transfer coefficients with GRS-MIX. The influence between the used approaches is consistent with the description given in chapter 4.2.2. The influence due to the heating of the ACCs indicated by the dashed lines is very small an obviously only identifiable during the ACC injection at t > 3000 s.
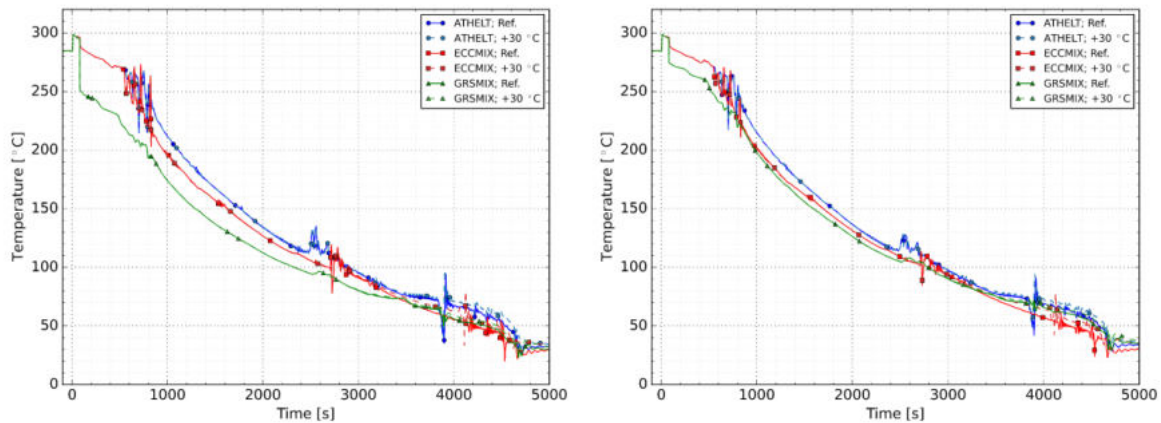
Figure 142: **Comparisons of DC Coolant Temperature at (left) 1.35 m and (right) 2.638 m below the CL Axis for Reference Case and Increasing ACC Temperature by 30 °C for TH Results only, using Injection Model and Mixing Code (ECCMIX, GRSMIX).**
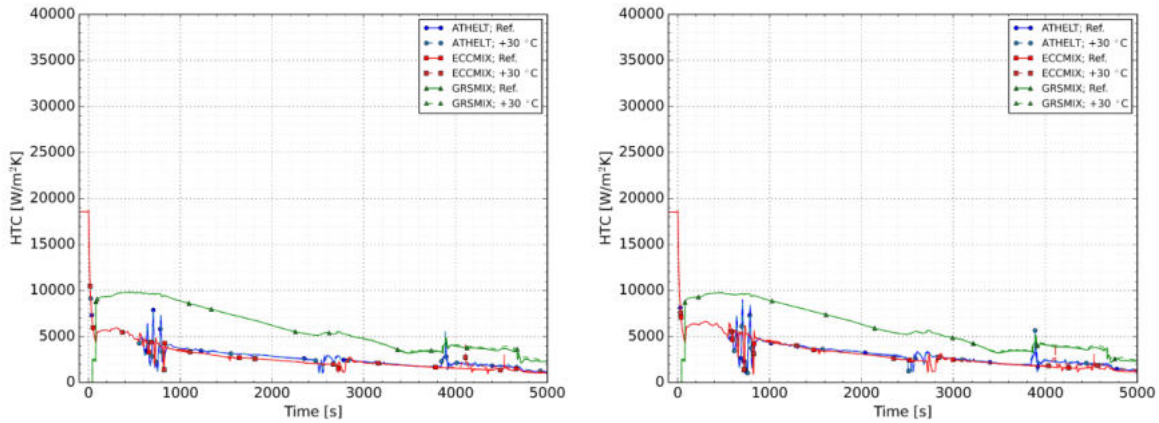
Figure 143: Comparisons of DC HTC at (left) 1.35 m and (right) 2.638 m below the CL Axis for Reference Case and Increasing ACC Temperature by 30 °C for TH Results only, using Injection Model and Mixing Code (ECCMIX, GRSMIX).

5.2.6   KWU-MIX results by Fra-G

Results from the system analysis performed with RELAP5, as described in Section 5.2.1, were used as input to the fluid-mixing analysis performed with KWU-MIX. The simulation with KWU-MIX of the increased ACC temperature from 20°C to 50°C produced data for the temperatures and HTCs as a function of time and location in the cold-leg nozzle and in the plumes in the DC. The flow rate of ECC water input to KWU-MIX from the calculation by RELAP5 is shown in Figure 144 for each of the CLs. The injection of ACC water is seen in the increased flow starting at 2800 s. The low-pressure pumps supply water starting at 4550 s.
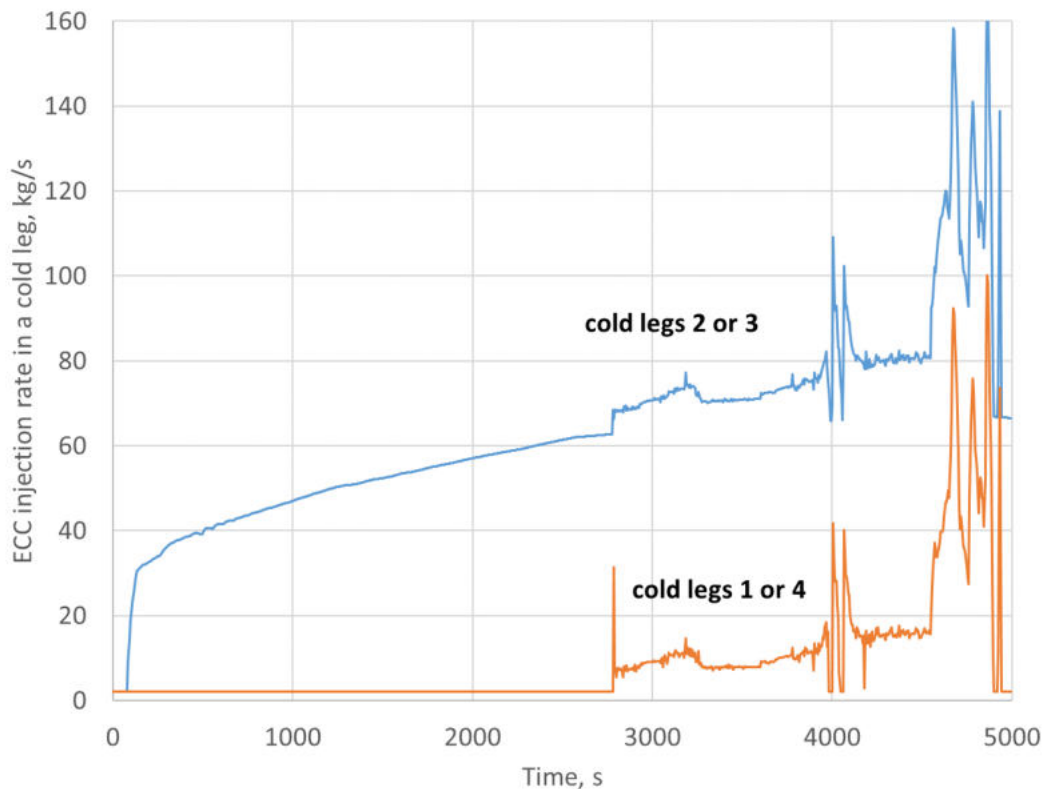
Figure 144: Flow rate of injected ECC water into each of the CLs as calculated by RELAP5.

5.2.6.1   Cold-leg nozzle

The end of the CL is the right-hand end of MR2 in KWU-MIX, as shown in Figure 16. At this location, the models have finished calculating the amount of hot water that is entrained into the cold ECC water, and temperature of the resulting mixture. Figure 145 shows the temperature of the hot water as a function of time, and it is indicated by the grey curve labelled "hot layer in cold-leg nozzle". At the start of the transient, this temperature is the same as the temperature from RELAP5. The flow of water in the loop through the MCP is small enough to prevent complete mixing in the CL starting at 330 s, after which time KWU-MIX calculates a separate temperature for the hot water based on an energy balance for all the mixing regions.

Also shown in Figure 145 is the temperature of the cold water near the cold-leg nozzle that results from the mixing of ECC water and entrained hot water. This temperature is indicated by the blue curve labelled "cold layer in cold-leg nozzle. This temperature is calculated by KWU-MIX starting at 330 s also, as soon as incomplete mixing occurs. Recall that the temperature of the ECC water is 15 °C, which is also shown in Figure 145, but it is an input to KWU-MIX rather than a result. The temperature of the cold-water layer is closer to the temperature of the ECC water than to the temperature of the hot water. This indicates that the mass flow rate of entrained hot water is less than the flow rate of ECC water.
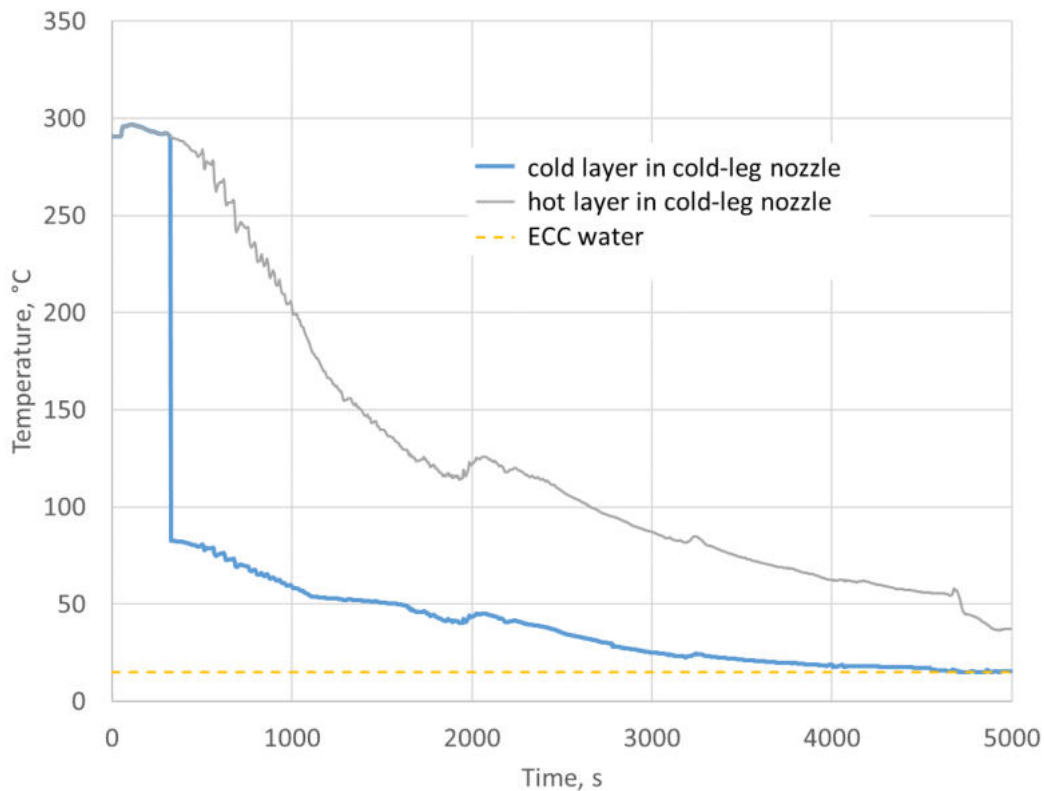
Figure 145: Temperatures of the cold-water and hot-water layers at the end of the nozzle of Cold Leg 2 and 3 calculated by KWU-MIX.

The height of the cold-water layer above the cold-leg axis at the end of the cold-leg nozzle is shown in Figure 146 as a function of time. Initially, when the ECC flow rate is small, the height of the cold-water lay is approximately 0.25 m below the axis of the CL. With increasing ECC flow, as shown in Figure 144, the height of the cold-water layer increases correspondingly.
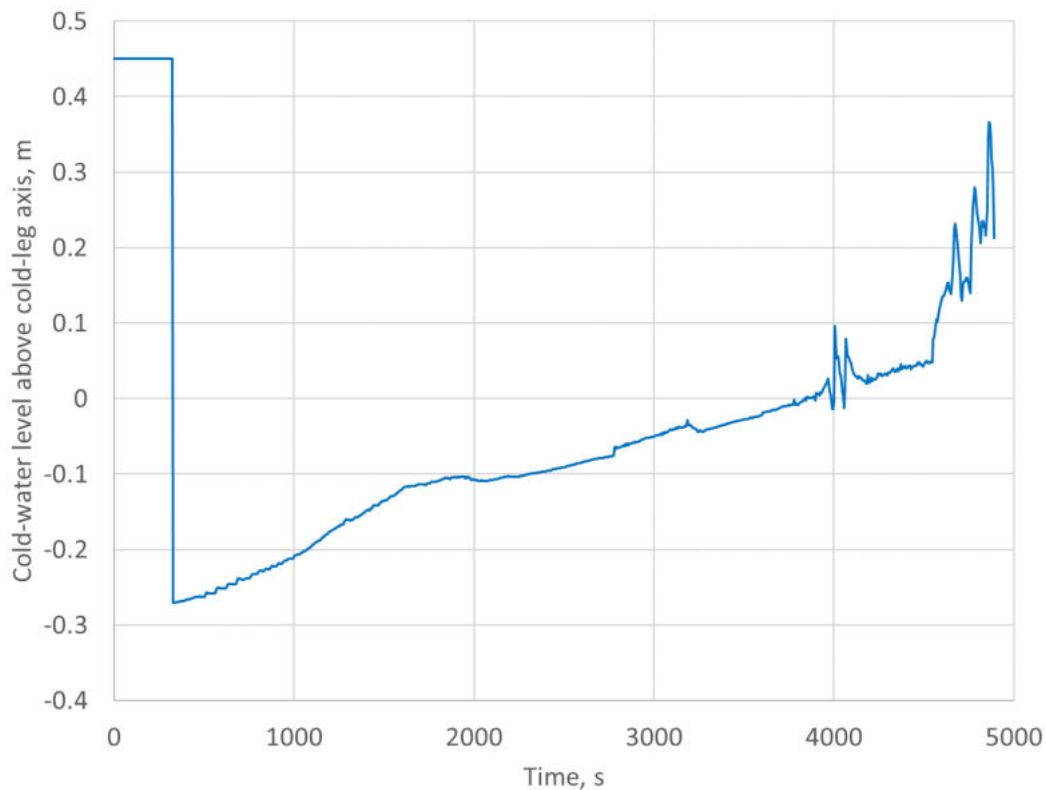
Figure 146: Height of cold-water layer above the axis of Cold Leg 2 and 3 at the inlet of the cold-leg nozzle calculated by KWU-MIX.

The height of the cold-water layer shown in Figure 146 determines the width of the plume at its origin in the DC of the RPV, just below the bottom of the cold-leg nozzle.

A comparison of Figure 145 with Figure 91 shows that heating the water in the ACC has only a reduction in the temperature of the cold-water layer entering the cold-leg nozzle. Because the leak size is small, the warmer water in the ACC is diluted by the injected flow from the HPIS.

5.2.6.2   *Inner surface of RPV wall*

The transition from the end of the cold-leg nozzle to the top of the plume the RPV is referred to as MR3 in Figure 16, but it is not modelled in KWU-MIX. Instead, KWU-MIX uses the conditions at the end of MR2 as the inlet boundary conditions for MR4. Consequently, the height of the cold-water layer in the cold-leg nozzle, labelled H_c in Figure 147, determines the width of the plume at its origin in the DC.

Figure 147 shows the widths of the plumes at various distances below the cold-leg axis in the DC. The origin of the plume is 0.45 m below the cold-leg axis, which is at the bottom of the diffusor. This is the light blue curve labelled 0.45 m in Figure 147. As soon as a plume is formed at approximately 330 s, its width is approximately 0.65 m, which is less than the diameter of the end of the diffusor. The width of the plume at its origin increases with time, corresponding to the increase in the cold-water flow rate. The width reaches a maximum when the cold-water layer in the CL reaches the axis. The maximum width of the plume is not greater than the cold-leg diameter, however, because the cold water accelerates, and its width narrows as it sinks in the diffusor.

114
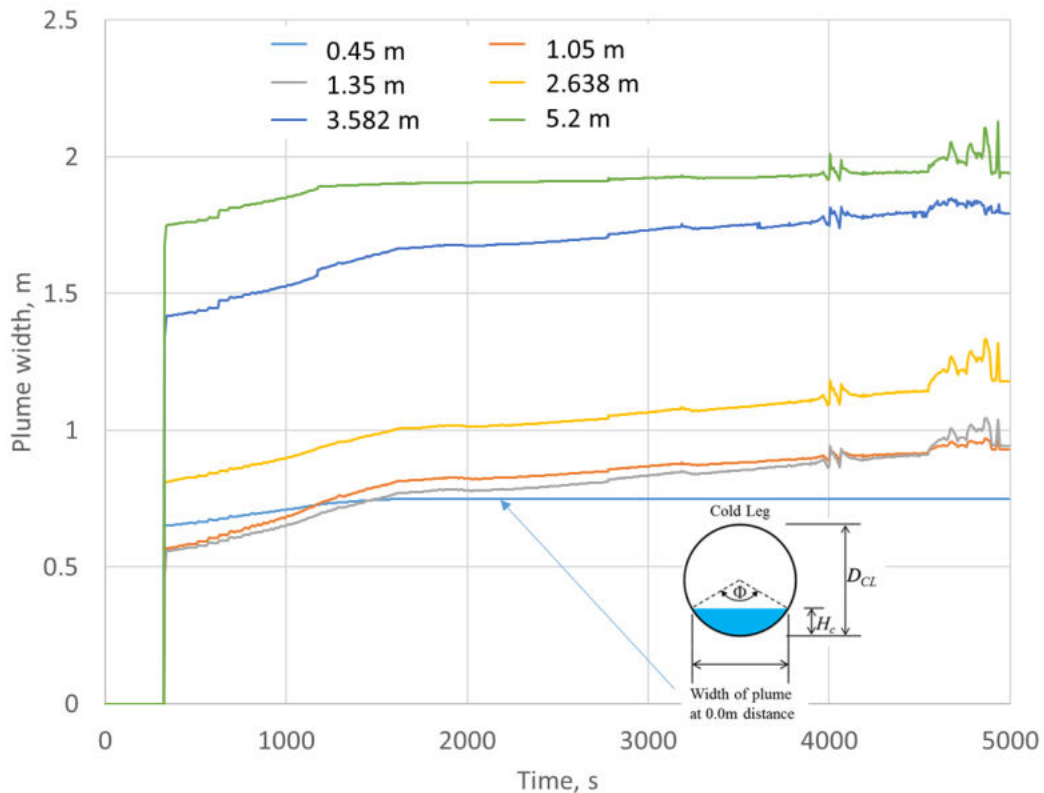
Figure 147: KWU-MIX widths of the plume at various distances below the axis of the Cold Leg 2 & in the DC.

At a distance of 1.05 m below the cold-leg axis, the width of the plume early in the transient is smaller than at its origin. This is due to the strong buoyancy force that accelerates the flow in the plume, which causes the plume to become narrower. Later in the transient, this phenomenon still exists, but its magnitude decreases with time as the temperature differences decrease and the buoyance also decreases. The plume width at 1.35 m below the cold-leg axis is similar to the width at 1.05 m due to this same phenomenon.

The two neighbouring plumes at lower elevations (greater distances below the cold-leg axis) are merged for the entire transient. The width of the merged plume is given for the distances of 2.638 m, 3.582 m and 5.2 m below the cold-leg axis in Figure 147.

The temperatures at the centers of the plumes are shown in Figure 148 for various distances below the cold-leg axis. The light-blue curve labelled 0.45 m in the legend is the centerline temperature at the origin of the plume, which is at the bottom of the cold-leg nozzle. This temperature is the same as the blue curve labelled "cold layer in cold-leg nozzle" shown in Figure 145. The curves for greater distances from the origin are progressively warmer. The dark-blue curve labelled "ambient" is the temperature outside of the plume. This temperature is the same as the grey curve labelled "hot layer in cold-leg nozzle" shown in Figure 145.

115
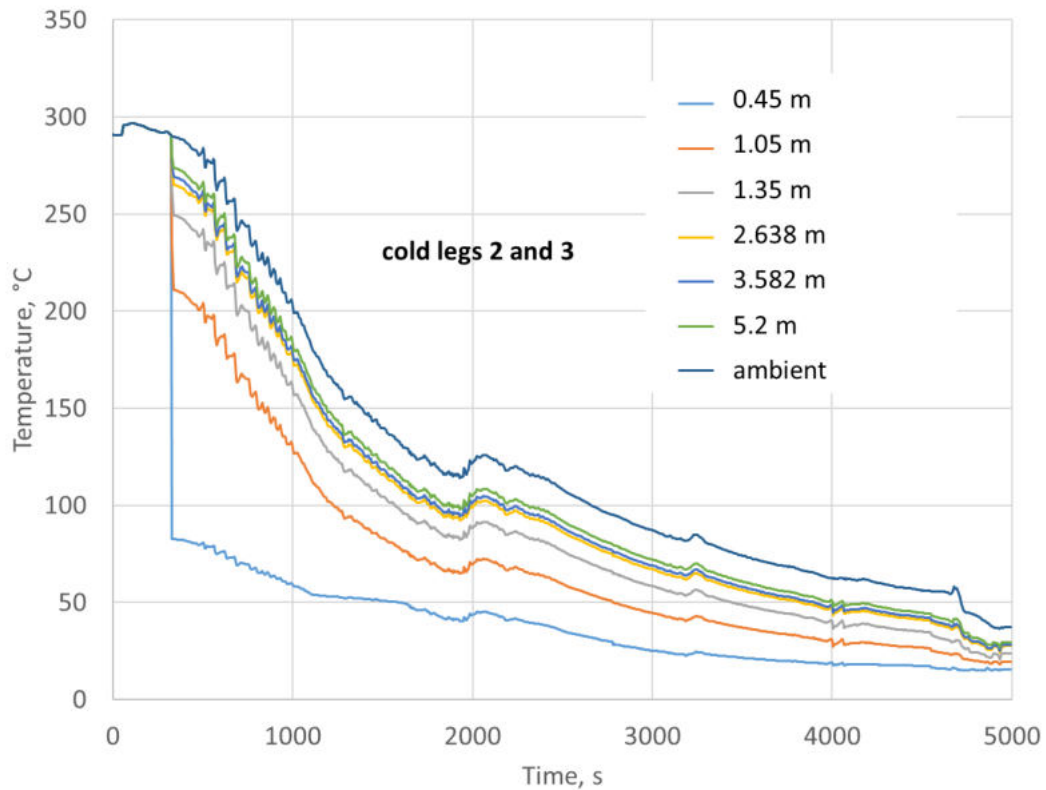
Figure 148: KWU-MIX temperatures at the middle of the plume at various distances below the axis of Cold Leg 2 & 3 in the DC.

Each curve in Figure 148 shows the temperature at one location, and the coordinates are at the elevation shown in the legend and at the circumferential location on the RPV wall where the plume is coldest. But the temperature throughout the plumes has a Gaussian distribution along the circumference of the RPV wall. An example is shown in Figure 149, which shows the temperature as a function of the circumferential location for various elevations at a time equal to 1000 s.

The temperature profile at the origin of the plume is the blue curve labelled "0.45 m" in the legend of Figure 149. The axis of the cold-leg nozzle in Loop 2 is at a circumferential location of 6.69 m, and the axis of the nozzle in Loop 3 is at 8.61 m. The coldest temperature for the plumes at a distance of 0.45 m below the axis of Cold Leg 2 as taken from Figure 148 at 1000 s is 60 °C. This is the minimum temperature for the blue curve at the circumferential location of 6.69 m. The plume below Cold Leg 3 has the same temperature, and so the curve has a value of is 60 °C at a circumferential location of 8.61 m also. Between the two circumferential locations, the temperature increases to the ambient temperature as taken from Figure 148 at 1000 s. This temperature is 205 C.

The small temperature depressions at circumferential locations of 0.96 m and 14.34 m are below the cold-leg nozzles of Loop 1 and Loop 4. The depressions are a result of a small flow of cold water from the CVCS system.
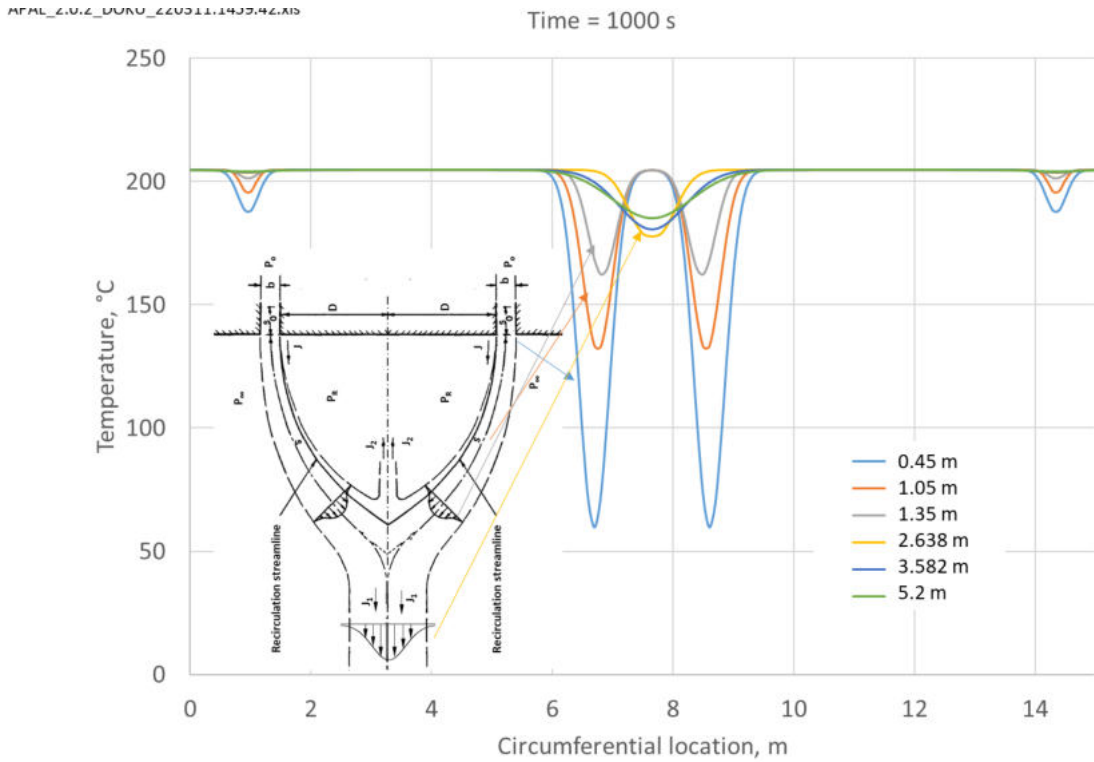
Figure 149: KWU-MIX temperatures at the middle of the plume at various distances below the axis of the cold-leg in the DC at 1000 s.

The HTCs in the DC also have Gaussian distributions, and the widths are equal to those for the temperature shown in Figure 147 divided by a factor of 1.1045, which was taken from Chen [20]. The maximum values for the heat-transfer coefficients in the plumes as a function of time are shown in Figure 150 for various distances below the cold-leg axis. The light-blue curve labelled 1.05 m in the legend is the centerline heat-transfer coefficient near the top of the plume. The curves for greater distances from the origin are progressively greater because the buoyancy force continues to accelerate the flow more than the inertia of the entrainment tends to decelerate the flow.
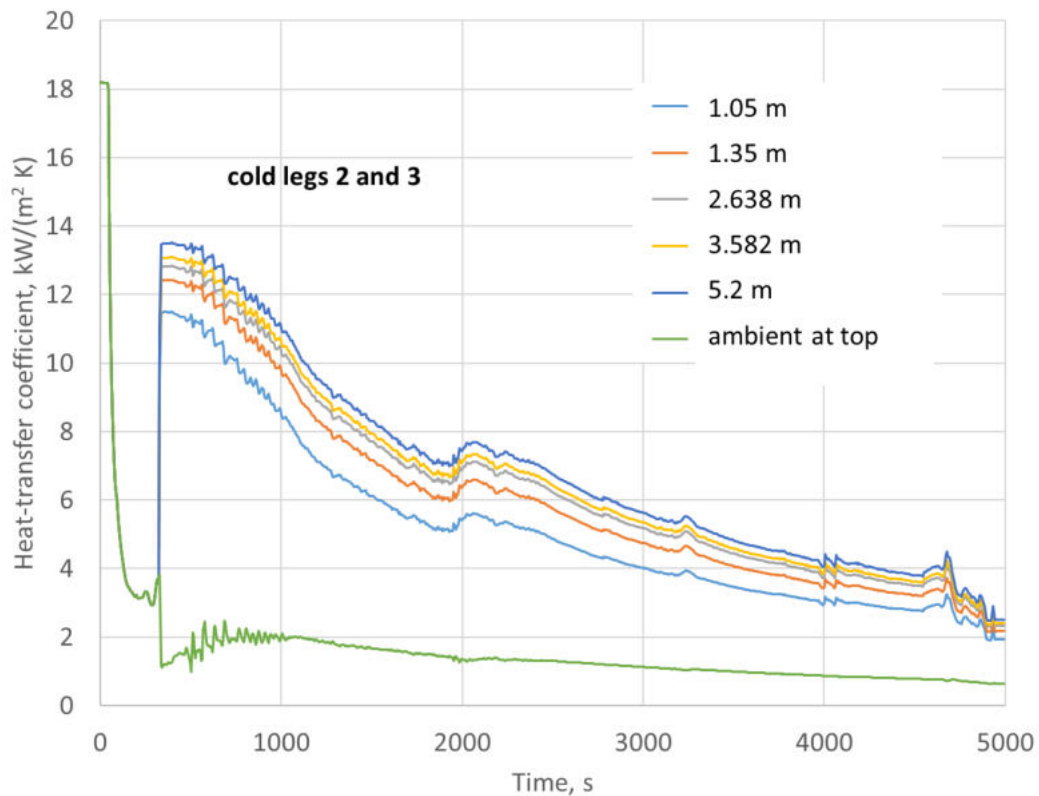
Figure 150: KWU-MIX heat-transfer coefficients at the middle of the plume at various distances below the axis of Cold Leg 2 & 3 in the DC.

Also shown in Figure 150 is the HTC outside of the plumes near the cold-leg nozzle. This is the green curve labelled "ambient at top". The HTC outside of the plume increases with distance from the cold-leg nozzle, as shown in Figure 151. The increase in the HTC is due to a larger recirculation flow outside of the plume with increasing distance from the cold-leg nozzle. Near the cold-leg nozzle, the recirculation flow outside of the plume is only as large as the entrainment flow rate at that location. Farther from the cold-leg nozzle, the recirculation flow is equal to the entrainment flow integrated over the higher distances. Near the bottom of the DC, the recirculation flow is equal to the entire flow of entrained water, and so the HTC is largest at this location.
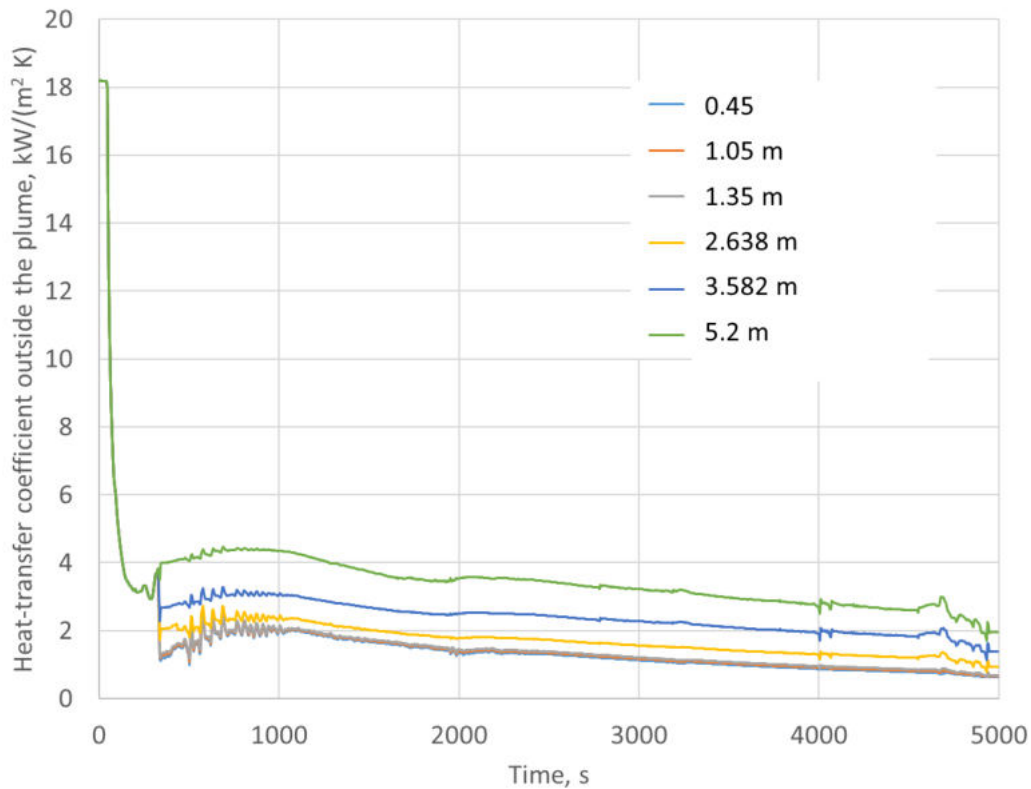
Figure 151: KWU-MIX heat-transfer coefficients outside of the plume at various distances below the cold-leg axis in the DC.

Each curve in Figure 150 shows the HTC at one location, and the location's coordinates are at the elevation shown in the legend and at the circumferential location on the RPV wall where the plume is coldest. But the HTC throughout the plumes has a Gaussian distribution along the circumference of the RPV wall, just as the temperature does. An example is shown in Figure 152, which shows the HTC as a function of the circumferential location for various elevations at a time equal to 1000 s.

The HTC profile near the origin of the plume is the blue curve labelled "1.05 m" in the legend of Figure 152. Recall that the axis of the cold-leg nozzle in Loop 2 is at a circumferential location of 6.69 m, and that the axis of the nozzle in Loop 3 is at 8.61 m. The largest HTC for the plumes at a distance of 1.05 m below the axis of Cold Leg 2 as taken from Figure 150 at 1000 s is 8.5 kW/(m^2 K). This is the maximum HTC for the blue curve at the circumferential location of 6.69 m in Figure 152. The plume below Cold Leg 3 has the same HTC, and so the curve has the sane value at a circumferential location of 8.61 m. Between the two circumferential locations, the HTC decreases to the ambient value as taken from Figure 151 at 1000 s. This HTC is 1.94 kW/(m^2 K).

The smaller HTC peaks at circumferential locations of 0.96 m and 14.34 m are below the cold-leg nozzles of Loop 1 and Loop 4. The depressions are a result of a small flow of cold water from the CVCS system.

119
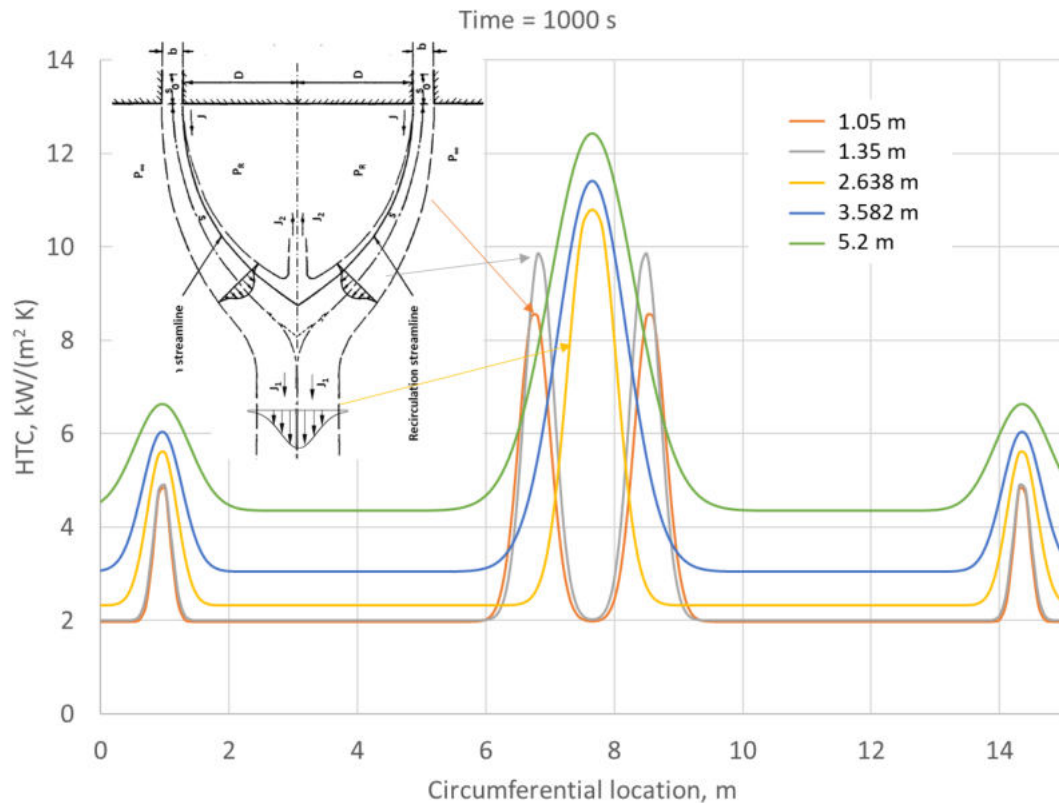
Figure 152: KWU-MIX temperatures heat-transfer coefficients at the middle of the plume at various distances below the axis of the cold-leg in the DC at 1000 s.

Figure 152 shows HTC profiles for four additional distances below the cold-leg axes. At a distance of 1.035 m, the circumferential location of the largest HTC below Cold Leg 2 is slightly closer to the circumferential location of the coldest temperature value below Cold Leg 3. This is due to the merging phenomenon described in Section 3.4.2 and shown in in Figure 21. The distance between the circumferential locations of the largest HTCs below Cold Leg 2 and 3 decreases from 1.05 m to 1.35 m below the cold-leg axis. At a distance of 2.638 m below the cold-leg axis, the two plumes have merged, and only a single Gaussian distribution is shown. The HTC distributions at greater distances are similar, with the width increasing and the largest HTC increasing with distance from the cold-leg axis.

A comparison of the temperatures in Figure 148 with those from the base case shown in Figure 94 leads to the conclusion that heating the water in the ACCs has a small effect on the temperatures in the plumes in the DC. This follows directly from the small effect that the ACC injection has on the temperatures at the inlet to the cold-leg nozzle.

The HTCs in Figure 150 are nearly the same as those for the base case, shown in Figure 96. The HTCs are a function of the velocity, and the velocity in the plume is a result of buoyancy force and inertia. The buoyancy force is a function of the temperature difference between the plume and the ambient, which is nearly the same for the base case and for this case. The inertia is a result of the injection flow rate, which is also nearly the same for the base case and for this case. Consequently, the HTCs are nearly the same for the two cases.

5.3   Heating of water in LPIS tanks

5.3.1   RELAP5 results by WUT

The heating of the water in the LPI tanks is simulated by increasing the injection temperature from the reference value of 15 °C to 45 °C. Comparative plots for key quantities of interest are provided in

Figure 153 through Figure 158. The injection of water from LPI tanks is realized around 4550 s, so it is very late in the transient. The calculations show that there is insignificant impact on the water level and water temperature in the DC till the end of transient (5000 s). The studied LTO improvement provides no benefit from a PTS perspective.
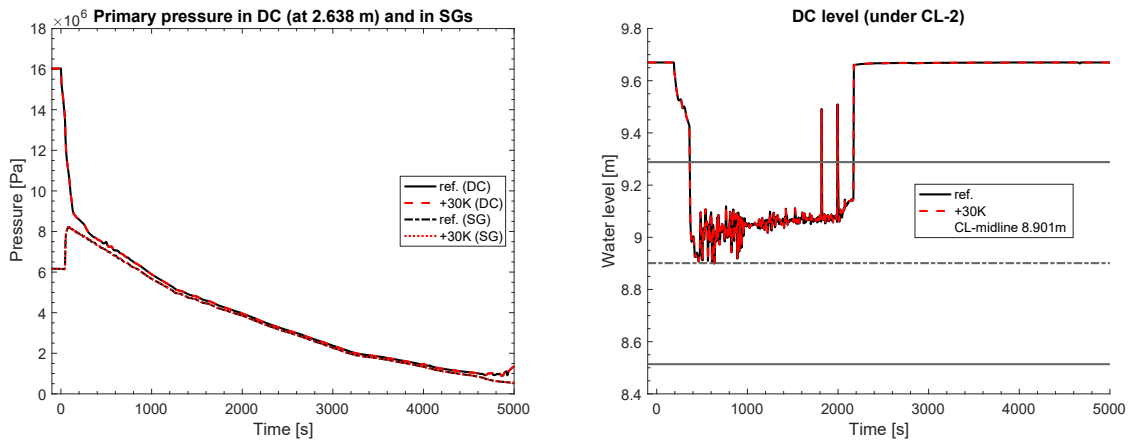
Figure 153: Comparisons of (left) pressure in the DC at 2.638 m below the CL-2 axis and (right) DC water level for different LPI water injection temperatures.
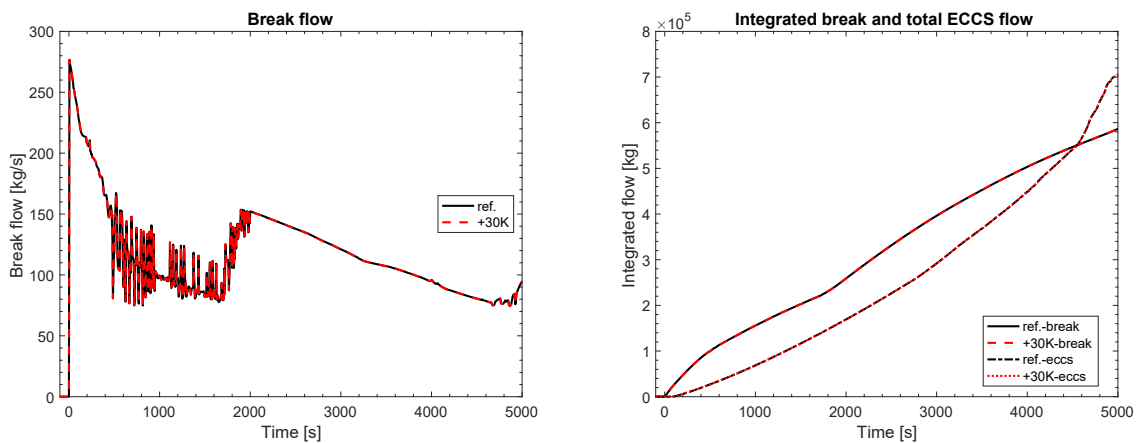
Figure 154: Comparisons of (left) Break flow and (right) time-integrated coolant loss and ECCS injection for different LPI water injection temperatures.
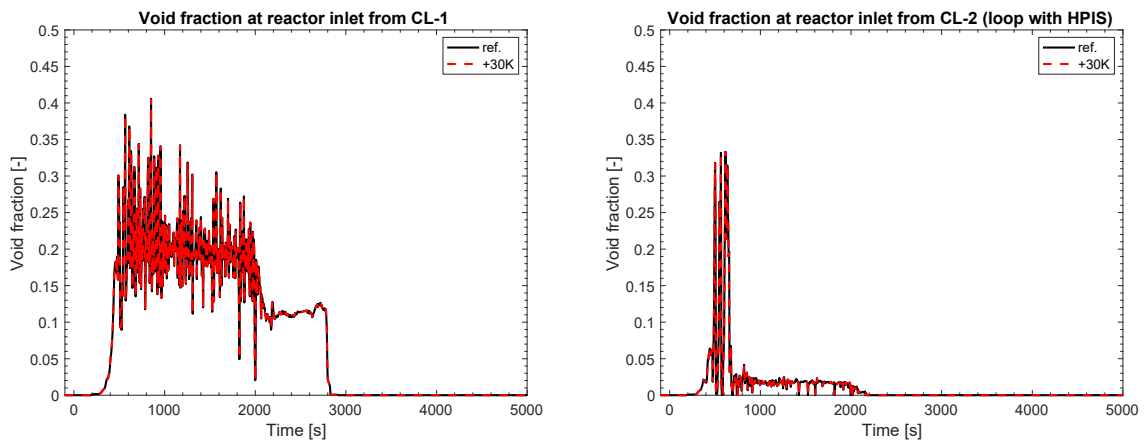
Figure 155: Comparisons of void fraction at the RPV inlets of Loops 1 and 2 for different LPI water injection temperatures.
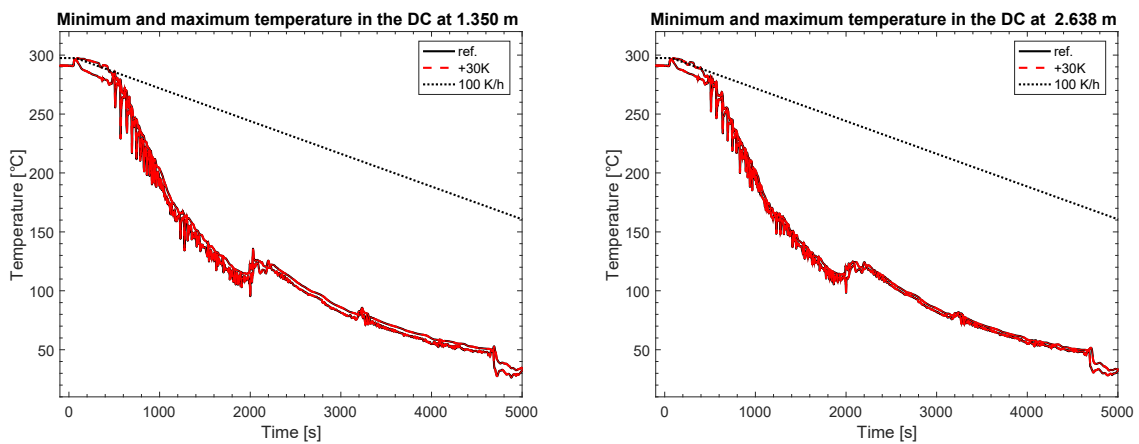
Figure 156: Comparisons of DC coolant temperature range (minimum to maximum) at (left) 1.35 m and (right) 2.638 m below the CL axis for different LPI water injection temperatures.
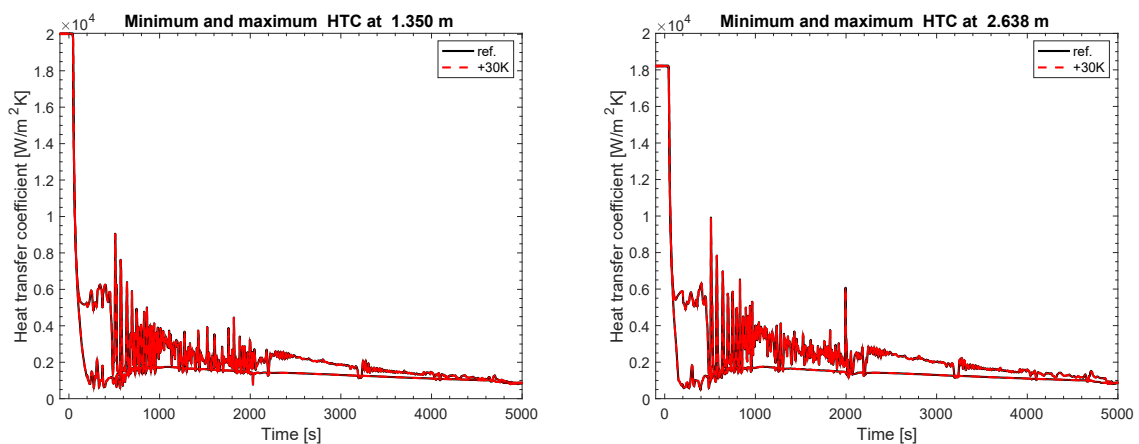
Figure 157: Comparisons of DC HTC range (minimum to maximum) at (left) 1.35 m and (right) 2.638 m below the CL axis for different LPI water injection temperatures.
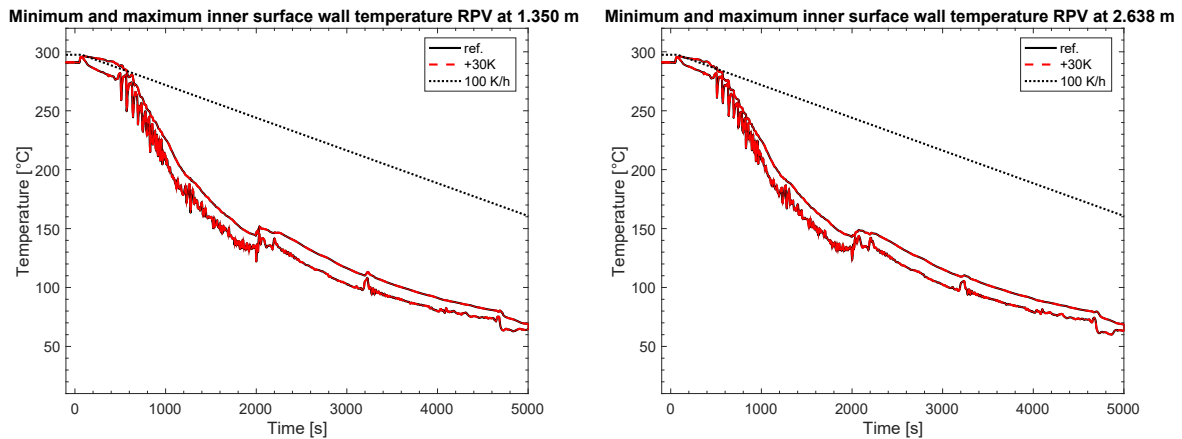
Figure 158: Comparisons of RPV inner surface temperature range (minimum to maximum) at (left) 1.35 m and (right) 2.638 m below the CL axis for different LPI water injection temperatures.

5.3.2   TRACE results by PSI

Heating of the water in the LPI tanks is simulated by changing the injection temperature in 10 K increments from the reference value of 15°C to 45 °C. Comparative plots for key quantities of interest are provided in Figure 159 through Figure 164. Since the LPI is initiated very late in the transient, the increased injection temperature has a relatively minor effect on the system response and DC temperatures until the end of the transient. Thus, for this particular transient, heating of LPI has only a very small benefit from a PTS perspective. For other transients, e.g., intermediate and large-break LOCAs, the benefit is expected to be more apparent.
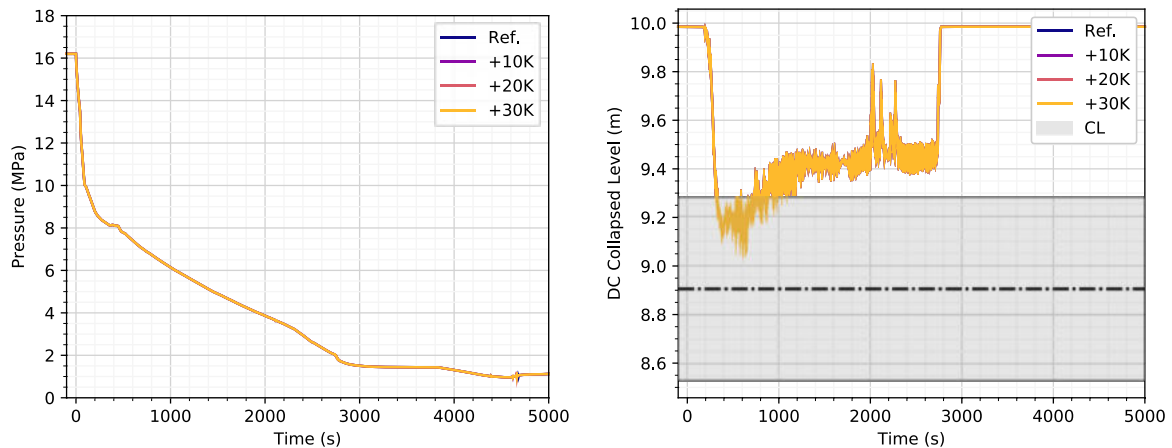
Figure 159: Comparisons of (left) Pressure in the DC at 2.638 m below the CL Axis and (right) DC Level for different LPI Temperatures.

123
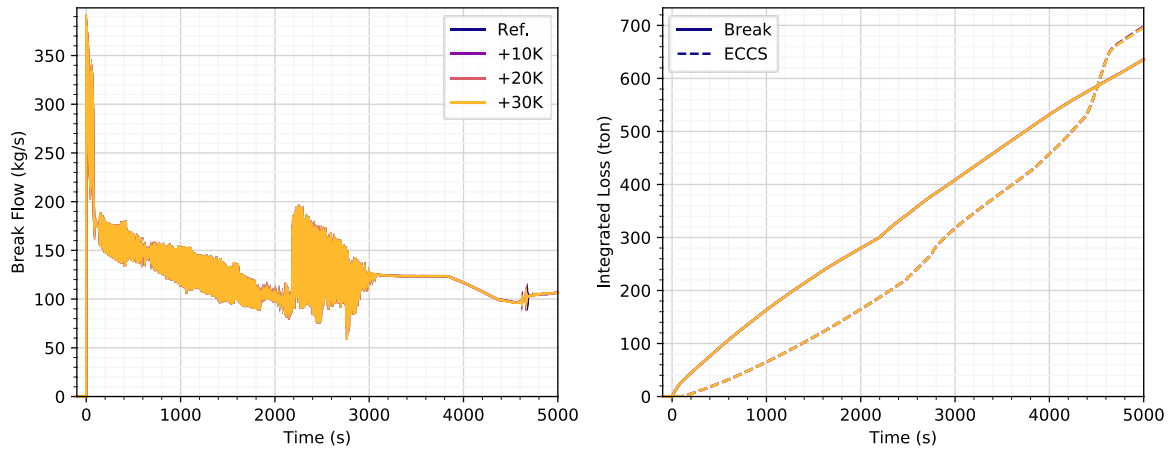
Figure 160: Comparisons of (left) Break Flow and (right) Time-integrated Coolant Loss and ECCS Injection for different LPI Temperatures.
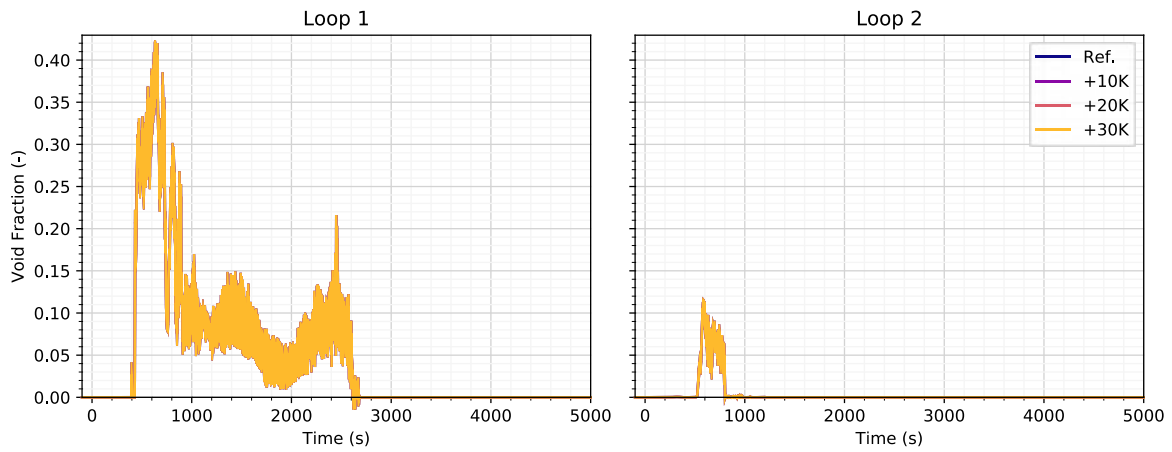
Figure 161: Comparisons of Void Fraction at the RPV Inlets of Loops 1 and 2 for different LPI Temperatures.
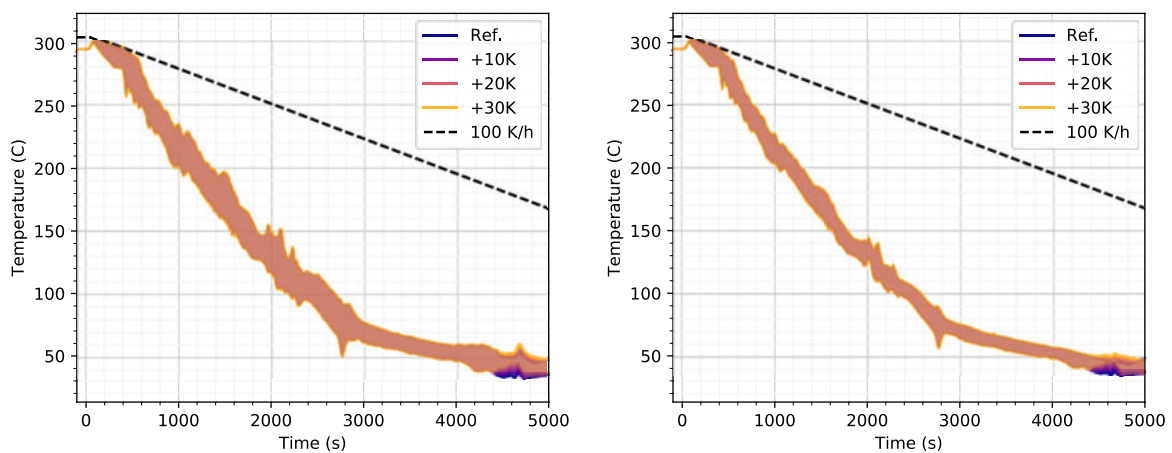
Figure 162: Comparisons of DC Coolant Temperature Range (Minimum to Maximum) at (left) 1.35 m and (right) 2.638 m below the CL Axis for different LPI Temperatures.

124
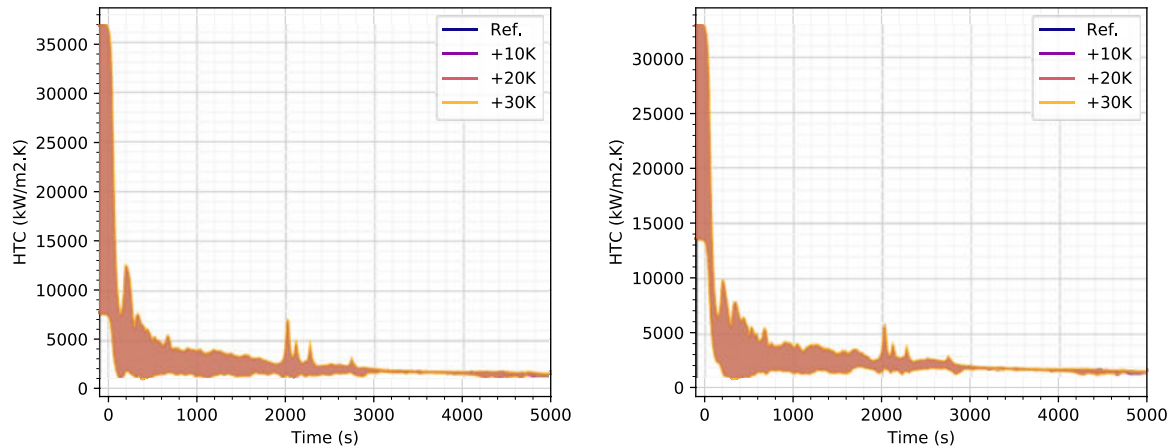
Figure 163: Comparisons of DC HTC Range (Minimum to Maximum) at (left) 1.35 m and (right) 2.638 m below the CL Axis for different LPI Temperatures.
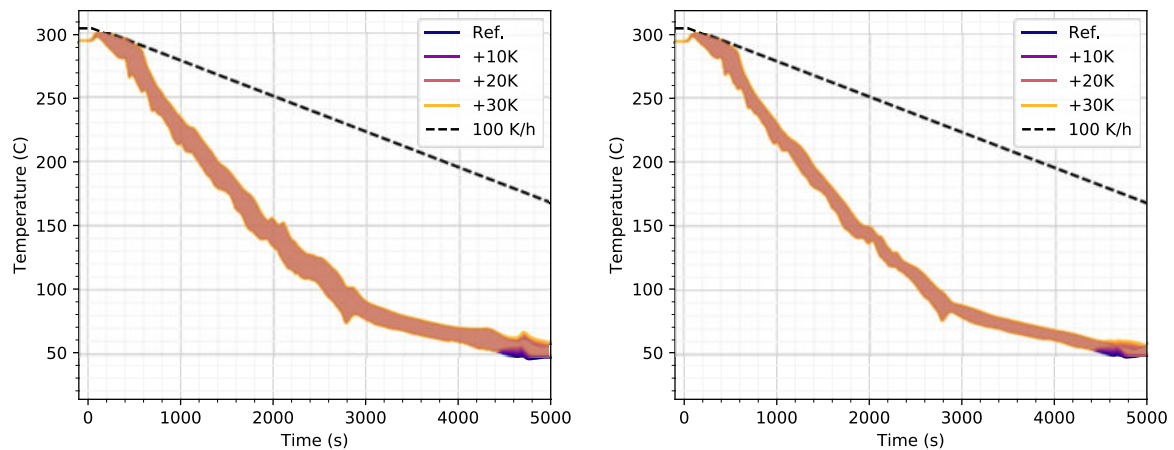
Figure 164: Comparisons of RPV Inner Surface Temperature Range (Minimum to Maximum) at (left) 1.35 m and (right) 2.638 m below the CL Axis for different LPI Temperatures.

5.3.3   ATHLET results by GRS

Heating of the water in the LPI tanks is simulated by changing the injection temperature in 10 K increments from the reference value of 15°C to 45 °C. Comparative plots for key quantities of interest are provided in Figure 165 through Figure 170. The overall conclusions that can be drawn from the results of the LPI tank heating as LTO improvement are consistent with what is given in 5.3.1 and 5.3.2: minor impact is expected for this particular transient.
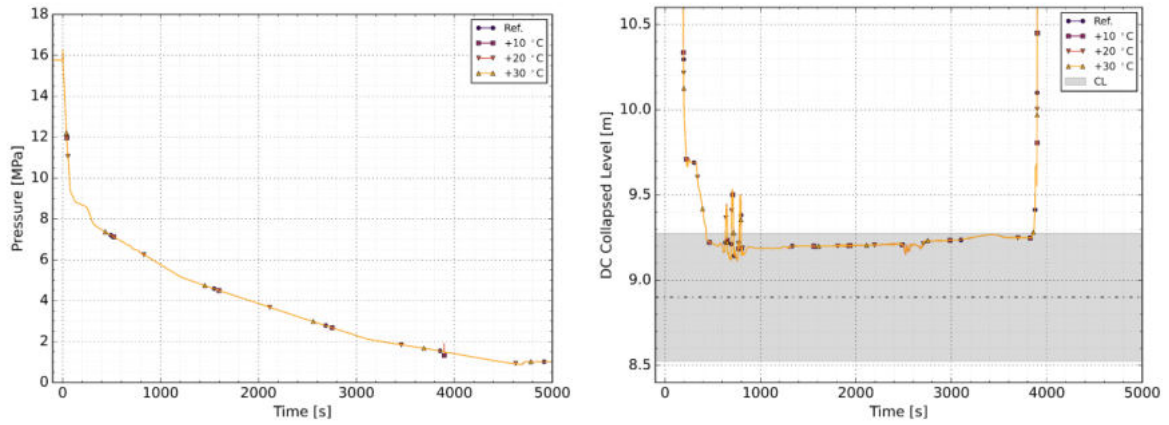
Figure 165: Comparisons of (left) Pressure in the DC at 2.638 m below the CL Axis and (right) DC Level for different LPI Temperatures.
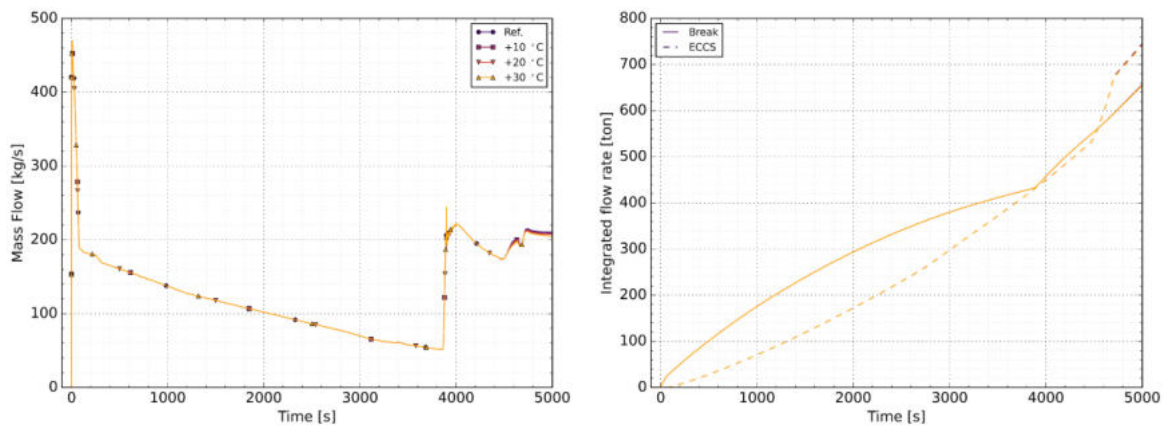
Figure 166: Comparisons of (left) Break Flow and (right) Time-integrated Coolant Loss and ECCS Injection for different LPI Temperatures.
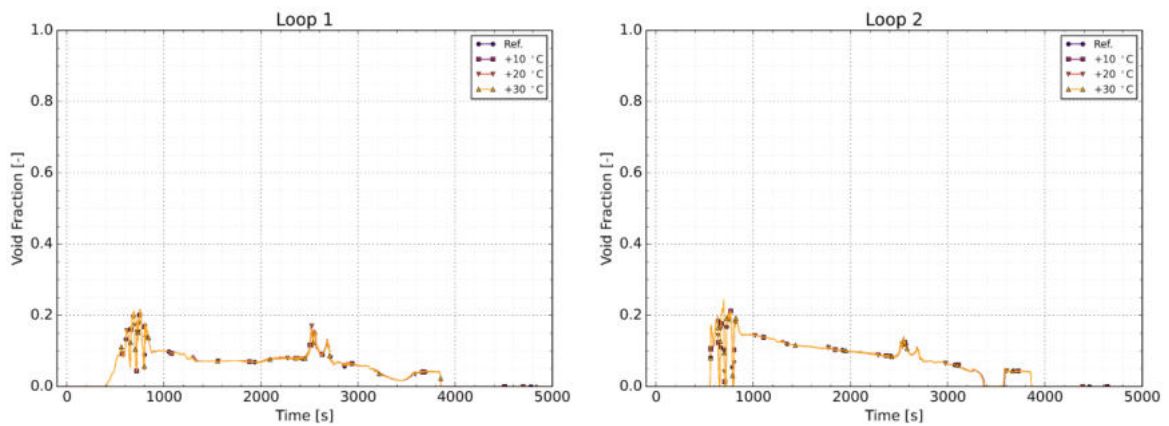
Figure 167: Comparisons of Void Fraction at the RPV Inlets of Loops 1 and 2 for different LPI Temperatures.
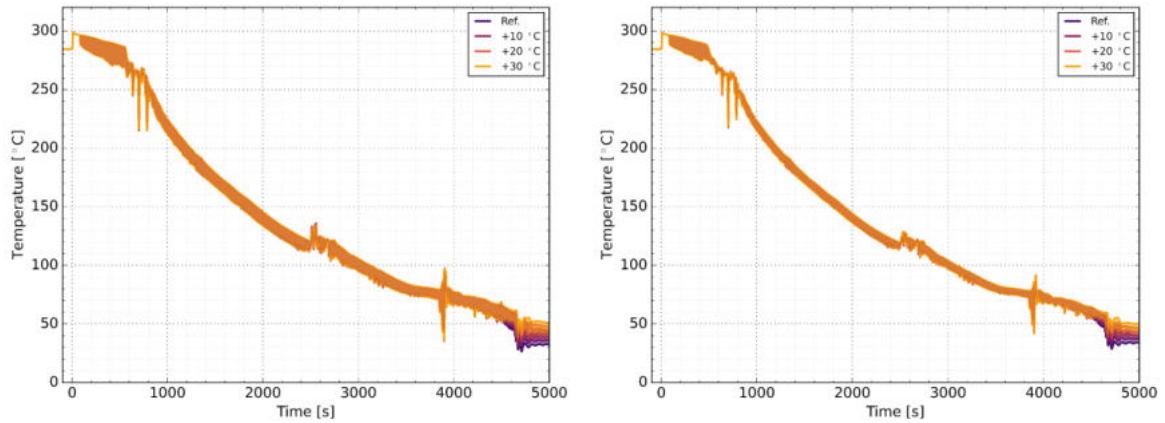
Figure 168: Comparisons of DC Coolant Temperature Range (Minimum to Maximum) at (left) 1.35 m and (right) 2.638 m below the CL Axis for different LPI Temperatures.
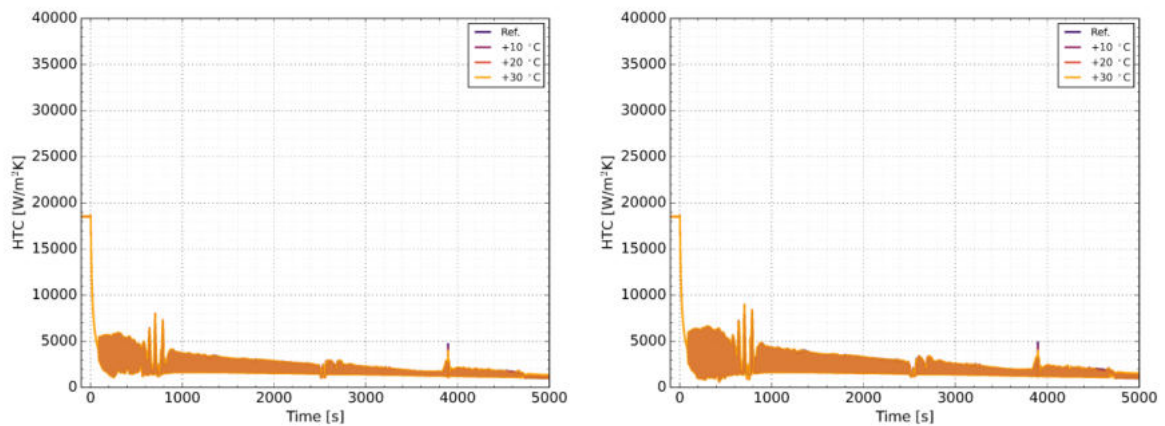
Figure 169: Comparisons of DC HTC Range (Minimum to Maximum) at (left) 1.35 m and (right) 2.638 m below the CL Axis for different LPI Temperatures.
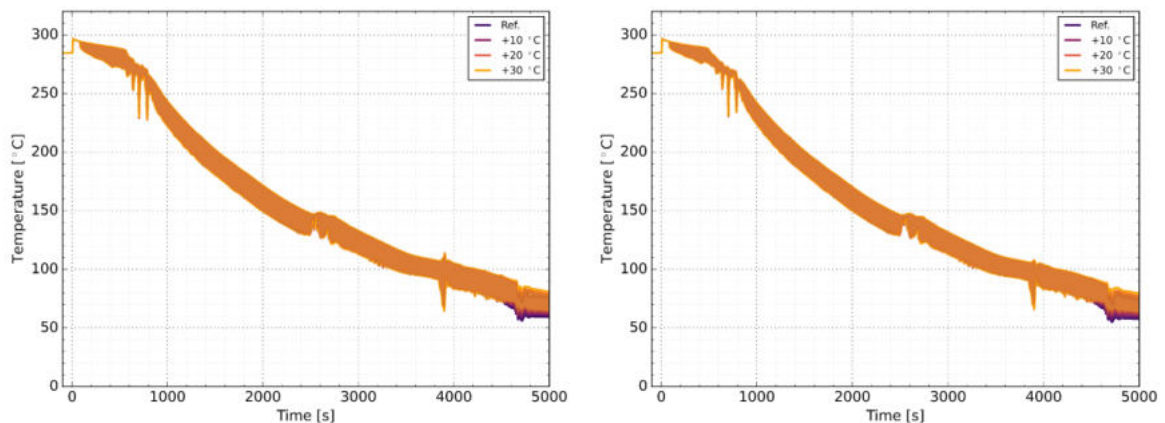
Figure 170: Comparisons of RPV Inner Surface Temperature Range (Minimum to Maximum) at (left) 1.35 m and (right) 2.638 m below the CL Axis for different LPI Temperatures.

5.3.4   ECC-MIX results by GRS

Heating of the water in the LPI tanks is simulated by changing the injection temperature in 10 K increments from the reference value of 15°C to 45 °C. Comparative plots for key quantities of interest are provided in Figure 171 through Figure 176. An influence of the LPI tank heating when applying the ECC-MIX model in ATHLET can only be observed in the last 500 s of the investigated time range of the

127

transient and is in the order of the investigated temperature variation in the LPI tanks at the postulated weld positions in the DC (see Figure 174). The overall conclusions that can be drawn from the results of the LPSI tank heating as LTO improvement are consistent with what is given in 5.3.1 and 5.3.2: no significant impact is expected for this particular transient.
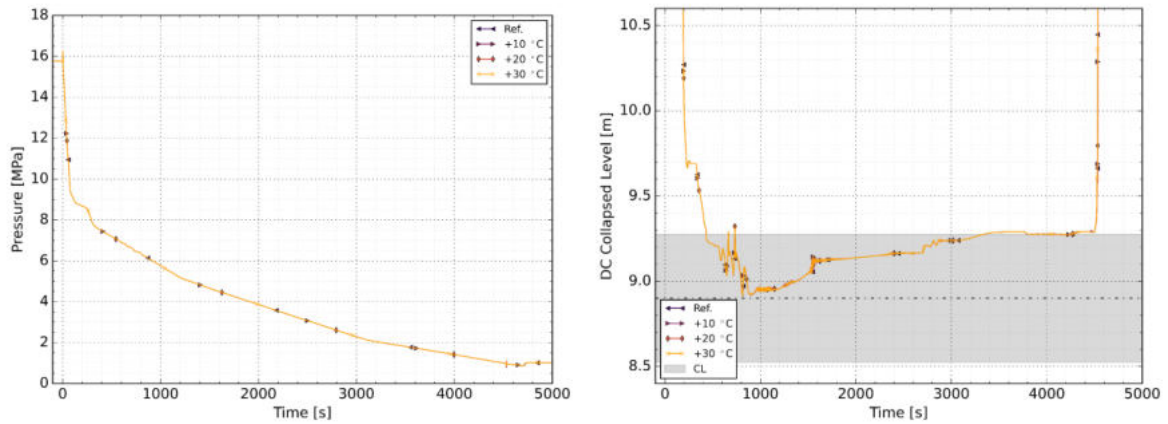
Figure 171: Comparisons of (left) Pressure in the DC at 2.638 m below the CL Axis and (right) DC Level for different LPI Temperatures.
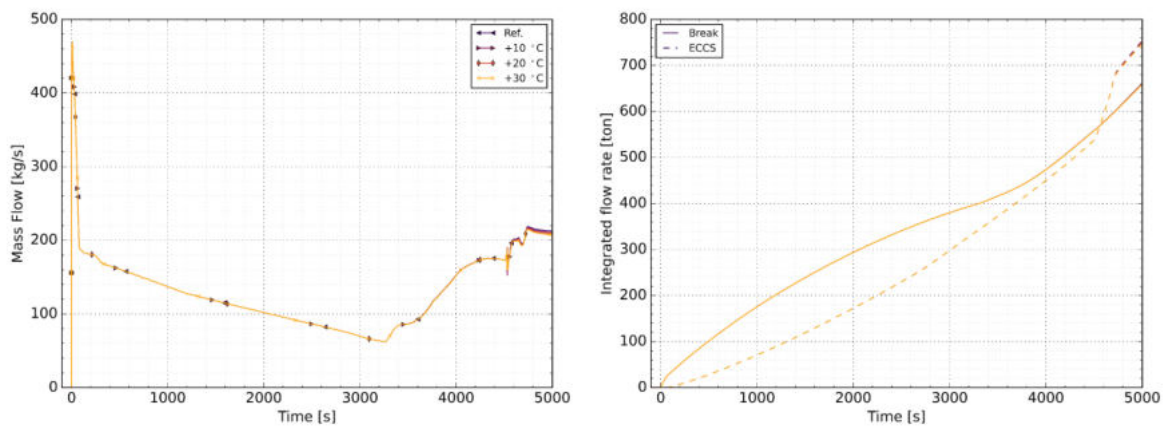
Figure 172: Comparisons of (left) Break Flow and (right) Time-integrated Coolant Loss and ECCS Injection for different LPI Temperatures.
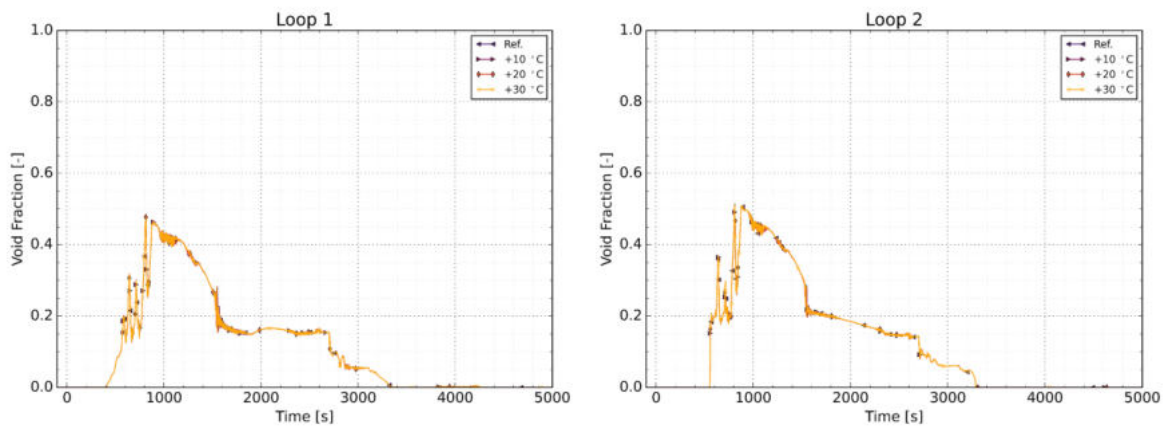
Figure 173: Comparisons of Void Fraction at the RPV Inlets of Loops 1 and 2 for different LPI Temperatures.
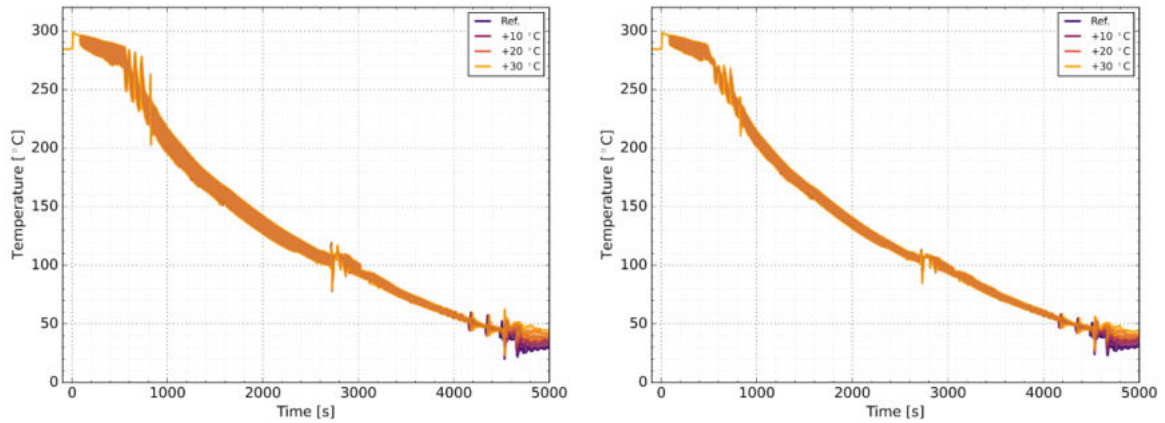
Figure 174: Comparisons of DC Coolant Temperature Range (Minimum to Maximum) at (left) 1.35 m and (right) 2.638 m below the CL Axis for different LPI Temperatures.
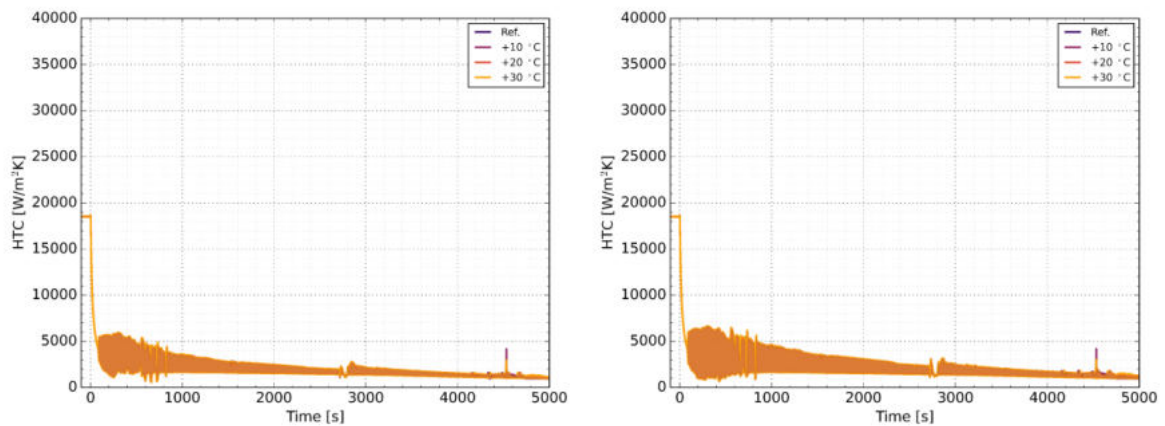
Figure 175: Comparisons of DC HTC Range (Minimum to Maximum) at (left) 1.35 m and (right) 2.638 m below the CL Axis for different LPI Temperatures.
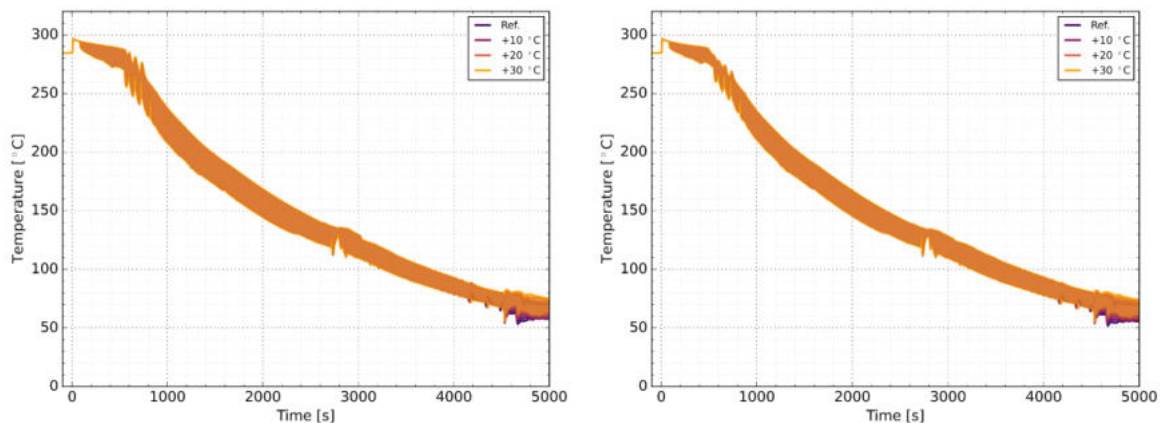
Figure 176: Comparisons of RPV Inner Surface Temperature Range (Minimum to Maximum) at (left) 1.35 m and (right) 2.638 m below the CL Axis for different LPI Temperatures.

5.3.5   Influence of Injection Model and Mixing Code (ATHLET, ECCMIX, GRSMIX)

The following Figure 177 and Figure 178 depict the influence of heating the LPI tank to the maximum considered amount of +30 °C in comparison of the three investigated configurations with ATHLET only, applying the ECC-MIX model and calculation DC temperatures and heat transfer coefficients with GRS-MIX. The influence between the used approaches is consistent with the description given in

129

chapter 4.2.2. The influence due to the heating of the LPSI water indicated by the dashed lines is very small an obviously only identifiable during the LPI injection at t > 4500 s.
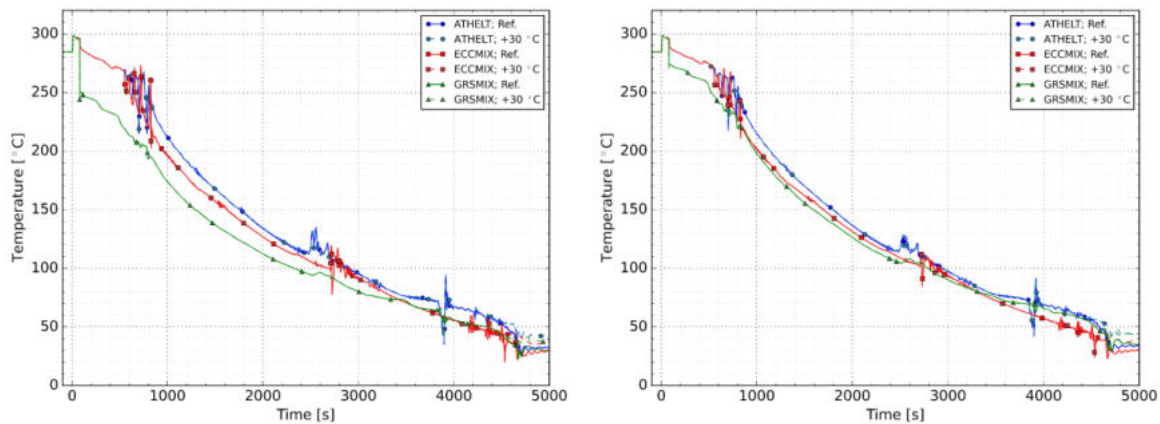
Figure 177: Comparisons of DC Coolant Temperature at (left) 1.35 m and (right) 2.638 m below the CL Axis for Reference Case and Increasing LPSI Temperature by 30 °C for TH Results only, using Injection Model and Mixing Code (ECCMIX, GRSMIX).
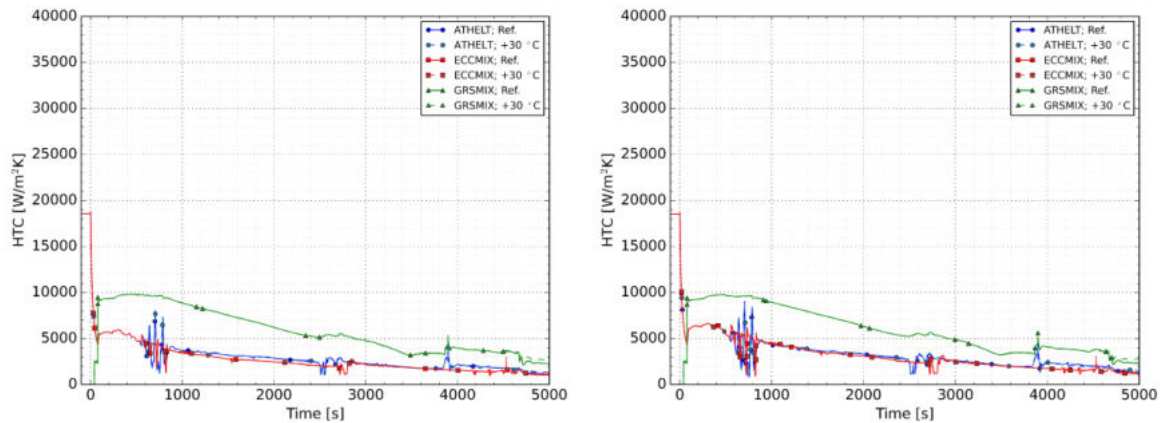
Figure 178: Comparisons of DC HTC at (left) 1.35 m and (right) 2.638 m below the CL Axis for Reference Case and Increasing LPSI Temperature by 30 °C for TH Results only, using Injection Model and Mixing Code (ECCMIX, GRSMIX).

5.3.6   KWU-MIX results by Fra-G

Results from the system analysis performed with RELAP5, as described in Section 5.3.1, were used as input to the fluid-mixing analysis performed with KWU-MIX. The simulation with KWU-MIX of the increased LPIS temperature from 15 °C to 45°C produced data for the temperatures and HTCs as a function of time and location in the cold-leg nozzle and in the plumes in the DC. The flow rate of ECC water input to KWU-MIX from the calculation by RELAP5 is shown in Figure 179 for each of the CLs. The injection of LPIS water is seen in the increased flow starting at 4550 s.
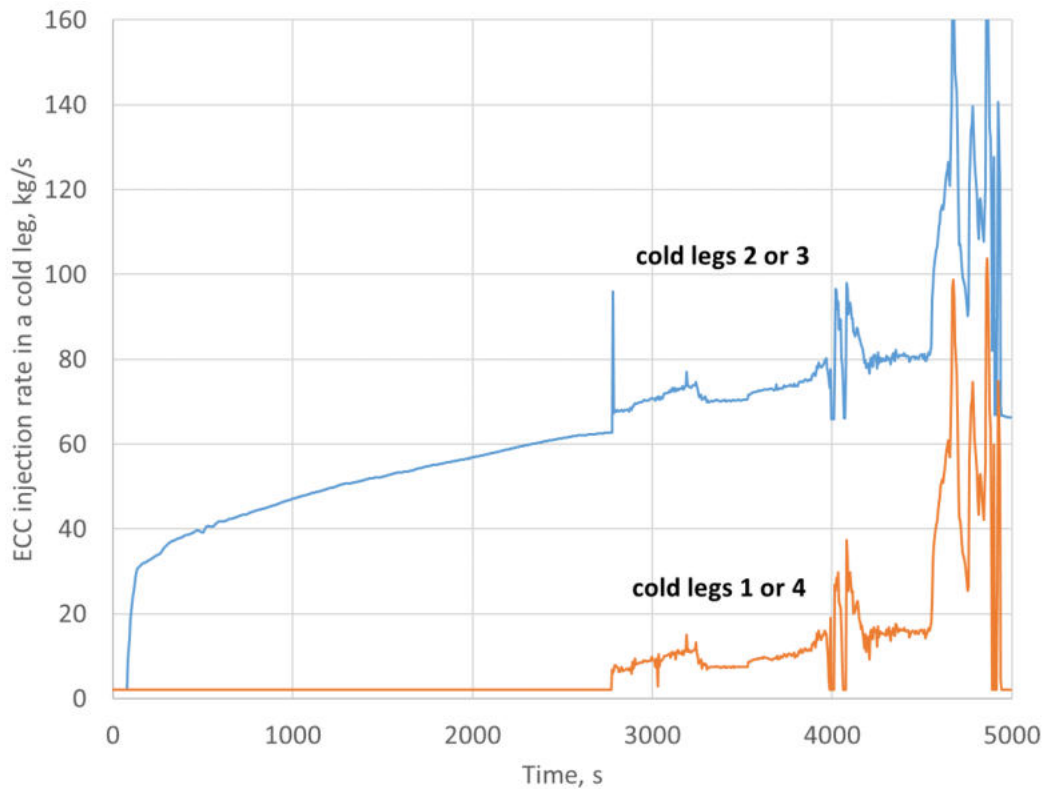
Figure 179: Flow rate of injected ECC water into each of the CLs as calculated by RELAP5.

5.3.6.1   Cold-leg nozzle

The end of the CL is the right-hand end of MR2 in KWU-MIX, as shown in Figure 16. At this location, the models have finished calculating the amount of hot water that is entrained into the cold ECC water, and temperature of the resulting mixture. Figure 180 shows the temperature of the hot water as a function of time, and it is indicated by the grey curve labelled "hot layer in cold-leg nozzle".

Also shown in Figure 180 is the temperature of the cold water near the cold-leg nozzle that results from the mixing of ECC water and entrained hot water. This temperature is indicated by the blue curve labelled "cold layer in cold-leg nozzle. This temperature is calculated by KWU-MIX starting at 330 s also, as soon as incomplete mixing occurs. The effect of the warmer LPIS temperature is seen at times from 4550 s until the maximum injection flow rate at 4700 s, during which the temperature at the end of the CL increases slightly.
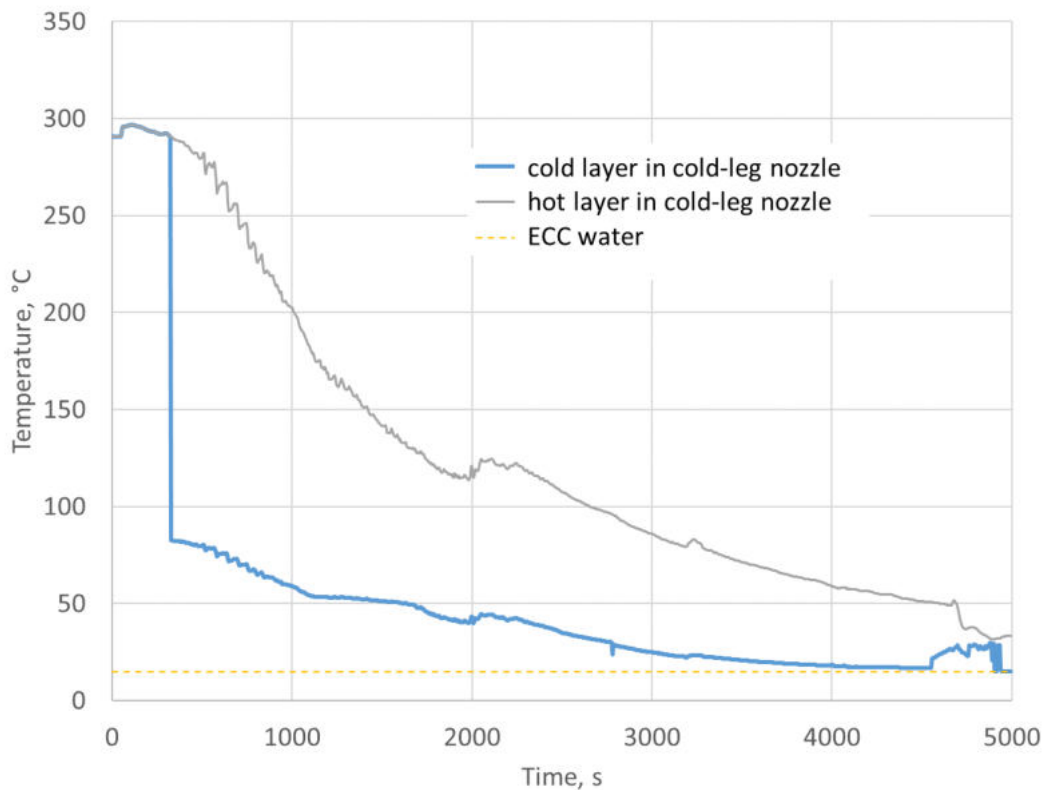
Figure 180: Temperatures of the cold-water and hot-water layers at the end of the nozzle of Cold Leg 2 and 3 calculated by KWU-MIX.

The height of the cold-water layer above the cold-leg axis at the end of the cold-leg nozzle is not significantly different from the curve in Figure 92. Therefore, the width of the plume at its origin as shown in Figure 93 is not significantly different either.

A comparison of Figure 180 with Figure 91 shows that heating the water in the LPSI tanks to 40°C does not significantly change the temperature of the hot water flowing from the DC into the CL during the time span for LPSI from approximately 4550 s until the end of the simulation. However, the increased temperature of the LPSI water increases the temperature in the cold-water layer at the cold-leg nozzle to approximately 30 °C. This has the potential to partially offset the effect of the increased HTC that occurs during LPSI injection from until 4700 s for both the base case and this case.

5.3.6.2   *Inner surface of RPV wall*

The temperatures at the centers of the plumes are shown in Figure 181 for various distances below the cold-leg axis. The light-blue curve labelled 0.45 m in the legend is the centerline temperature at the origin of the plume, which is at the bottom of the cold-leg nozzle. This temperature is the same as the blue curve labelled "cold layer in cold-leg nozzle" shown in Figure 180. The curves for greater distances from the origin are progressively warmer. The dark-blue curve labelled "ambient" is the temperature outside of the plume. This temperature is the same as the grey curve labelled "hot layer in cold-leg nozzle" shown in Figure 180.

132
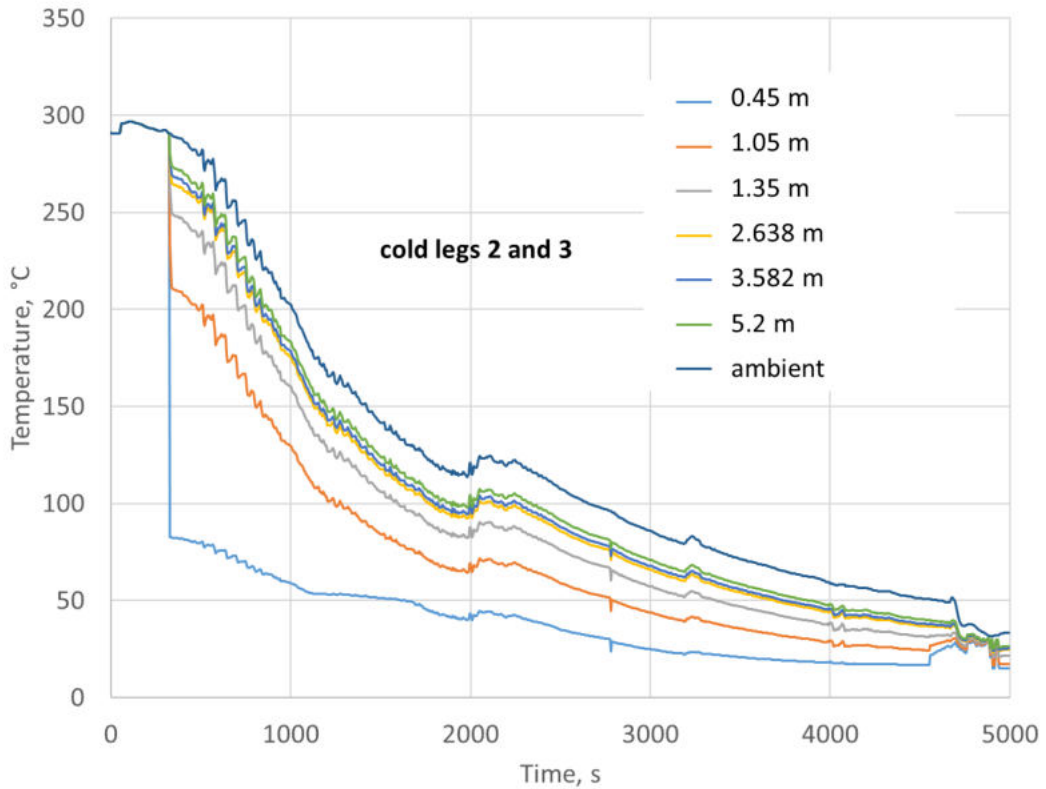
Figure 181: KWU-MIX temperatures at the middle of the plume at various distances below the axis of Cold Leg 2 & 3 in the DC.

The heat-transfer coefficients in the DC also have Gaussian distributions, and the widths are equal to those for the temperature divided by a factor of 1.1045, which was taken from Chen [20]. The maximum values for the heat-transfer coefficients in the plumes as a function of time are shown in Figure 182, and they are approximately the same as those in Figure 96. The HTCs outside of the plumes are nearly the same as those in Figure 97.
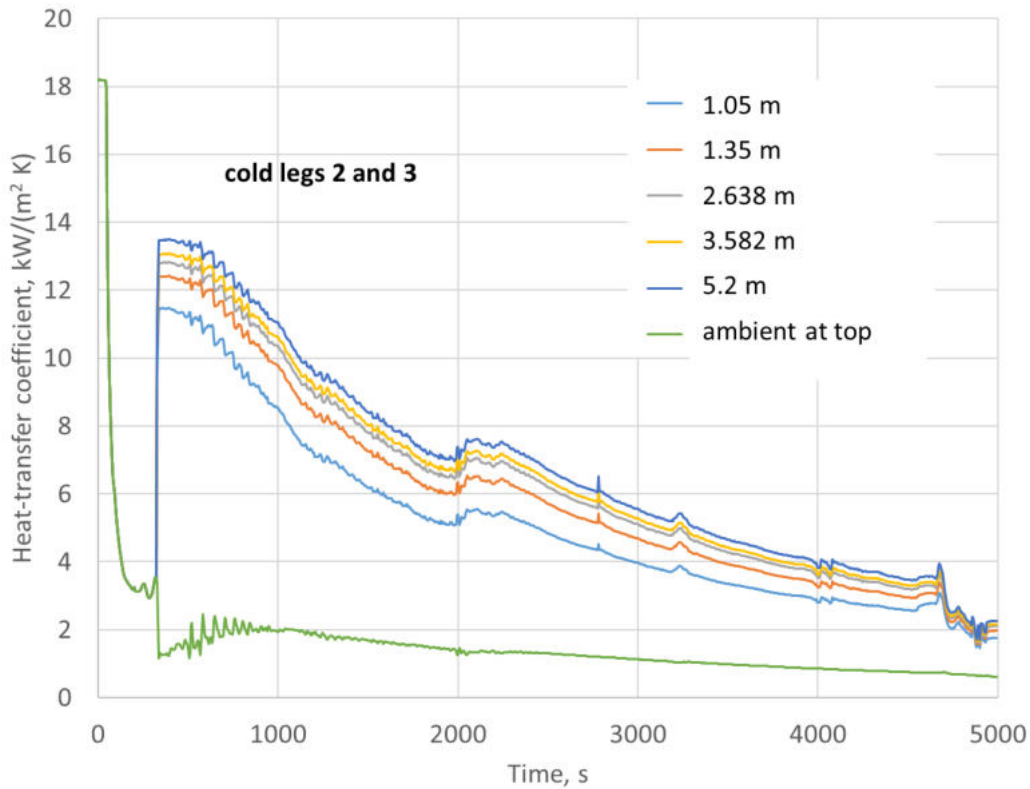
Figure 182: KWU-MIX heat-transfer coefficients at the middle of the plume at various distances below the axis of Cold Leg 2 & 3 in the DC.

The HTCs during the time span from 4550 s until the peak injection flow rate at 4700 s are slightly larger near the bottom of the DC for the base case than for this case, due to the slightly larger velocity for the base case that results from the slightly larger temperature difference between the plume and the ambient.

5.4   Decreasing HPI head

5.4.1   TRACE results by PSI

Decreasing of the HPI pump head is simulated by scaling the pressure component of the HPI pump curve down to 75% of the reference value in 5% decrements, as illustrated in Figure 183.
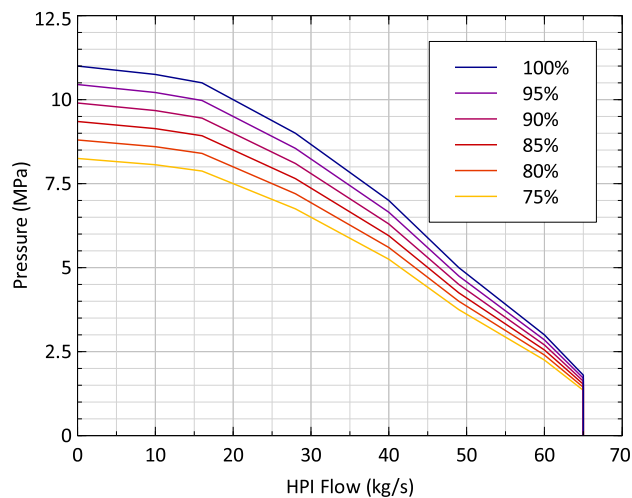
Figure 183: HPI Pump Curves assumed for Assessing of the Impact of Reduced HPI head.

Comparative plots for key quantities of interest are provided in Figure 184 through Figure 189. Reducing the HPI head leads to a later HPI injection. This has a significant effect on several system parameters, in particular the liquid levels. As in the case of reduced HPI capacity (discussed in chapter 6.5), this proposed LTO improvement decreases the rate of cooling in the RPV in the early stages of the transient (up to ~ 2000 s). After the ACCs inject, however, the rate of cooling increases significantly. The cooling rate during ACC injection is increased so much in the period 2000 to 3000 s that one might expect a higher risk of PTS for this proposed LTO improvement. This would need to be confirmed using thermo-mechanical and fracture mechanics simulations.

Separately, for the case of 75% head, there is a significant reduction in the liquid level in the DC and CL levels between 1200 and 2200 s. While not shown in the figures provided, this is accompanied by a decrease in the core liquid level. This proposed LTO improvement therefore potentially increases the risk of core uncovery and fuel failure.
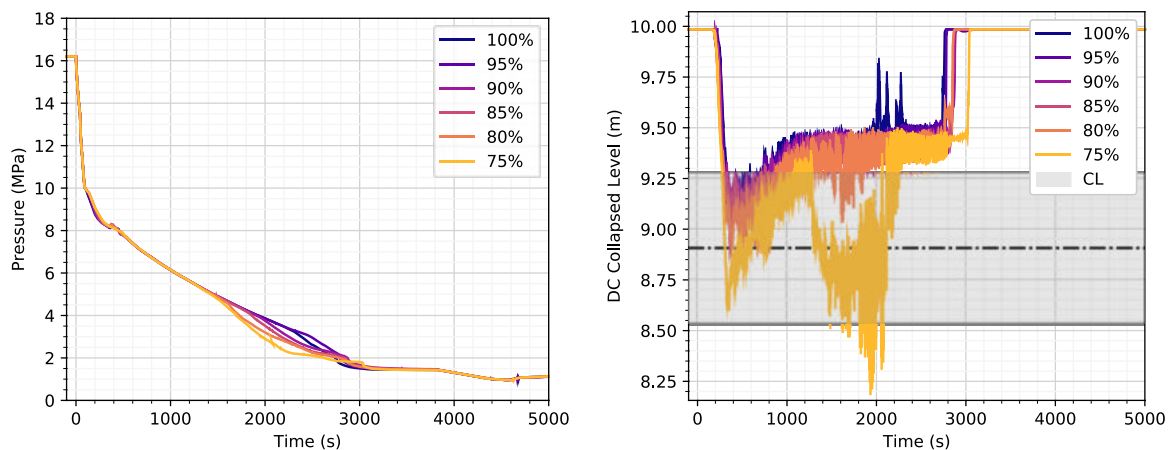
Figure 184: Comparisons of (left) Pressure in the DC at 2.638 m below the CL Axis and (right) DC Level for different HPI Pump Heads.
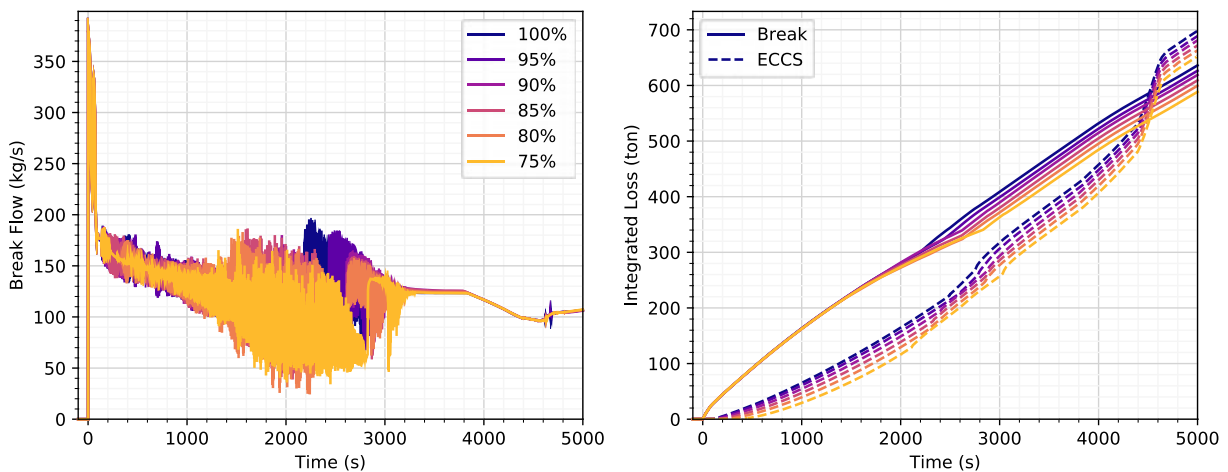
Figure 185: Comparisons of (left) Break Flow and (right) Time-integrated Coolant Loss and ECCS Injection for different HPI Pump Heads.

135
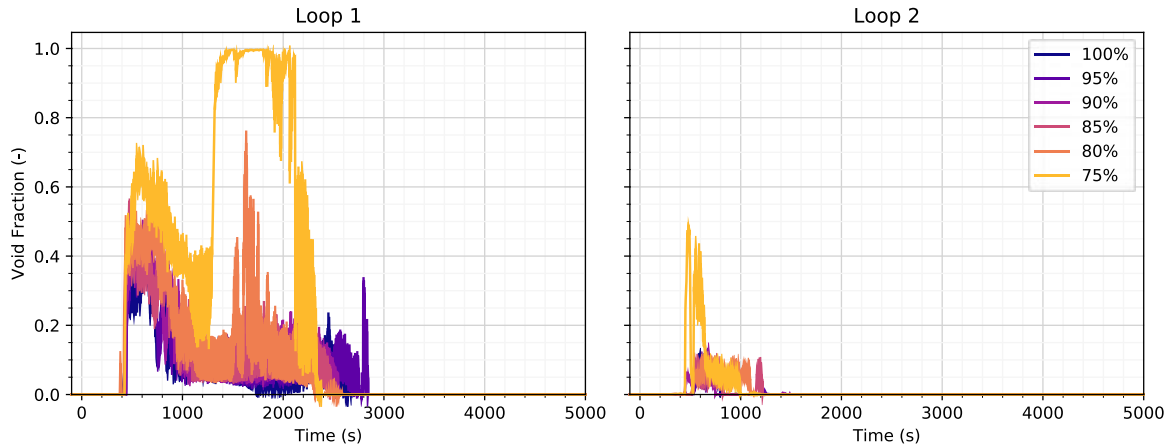
Figure 186: Comparisons of Void Fraction at the RPV Inlets of Loops 1 and 2 for different HPI Pump Heads.
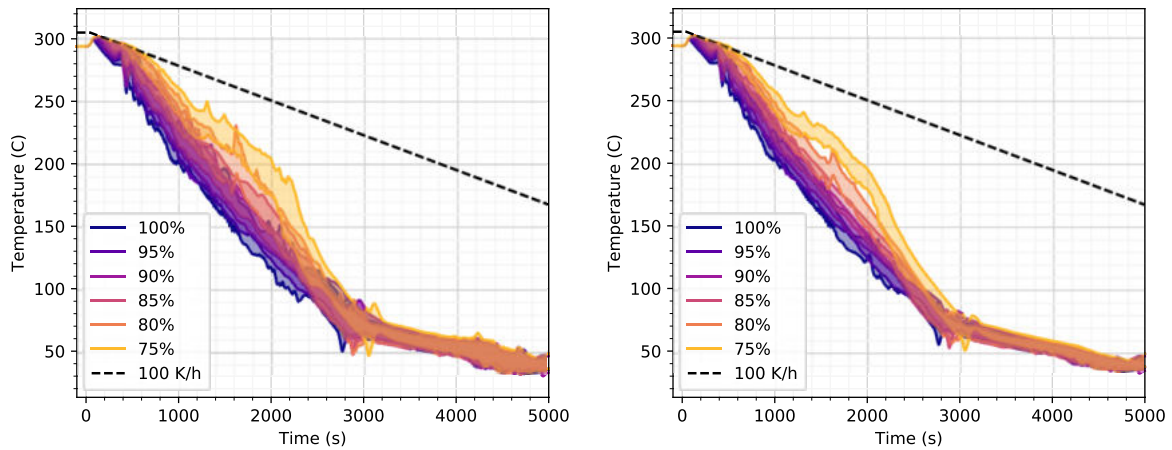
Figure 187: Comparisons of DC Coolant Temperature Range (Minimum to Maximum) at (left) 1.35 m and (right) 2.638 m below the CL Axis for different HPI Pump Heads.
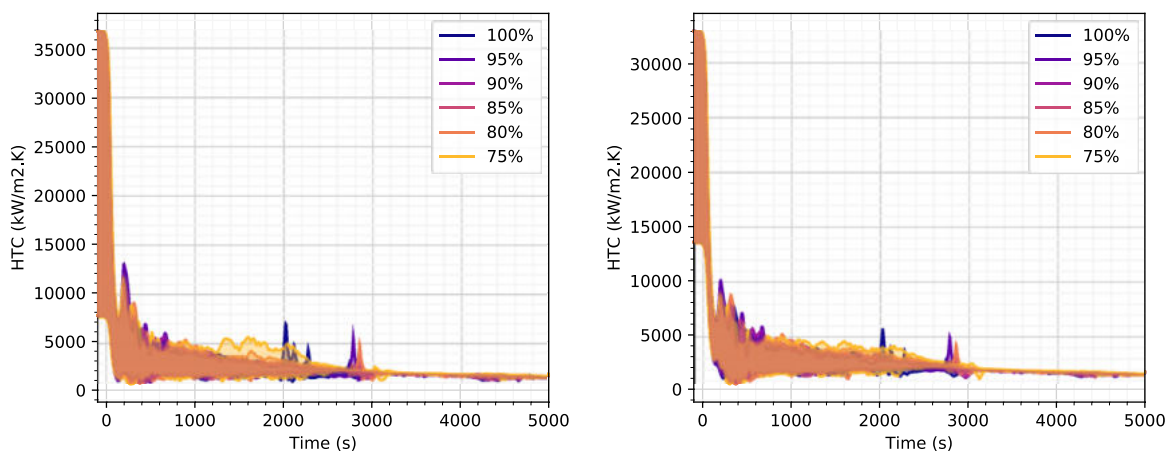
Figure 188: Comparisons of DC HTC Range (Minimum to Maximum) at (left) 1.35 m and (right) 2.638 m below the CL Axis for different HPI Pump Heads.
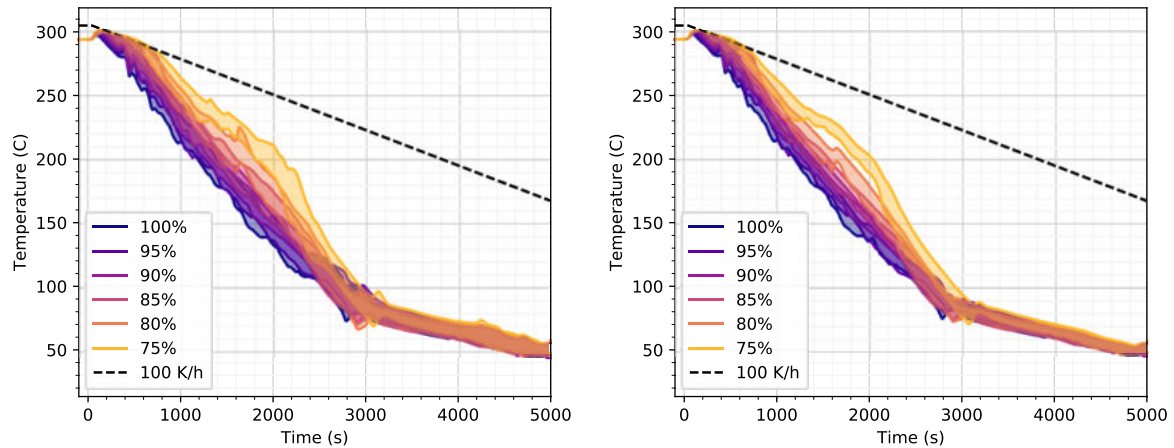
Figure 189: Comparisons of RPV Inner Surface Temperature Range (Minimum to Maximum) at (left) 1.35 m and (right) 2.638 m below the CL Axis for different HPI Pump Heads.

5.4.2   RELAP5 results by SSTC

Comparative analysis was performed with application of Relap5/mod3.3 (version "lf") code. Decreasing of the HPI pump head pressure was simulated by SSTC NRS via scaling of the pressure component of the HPI pump curve down to 75%. Degree of reduction and the decrement (5%) was selected according to the similar approach of PSI and GRS (see chapters 5.4.1, 5.4.3 respectively), as illustrated in Figure 190. The "base" (100%) flow rate characteristic of HPI pumps was taken from the Table 1.
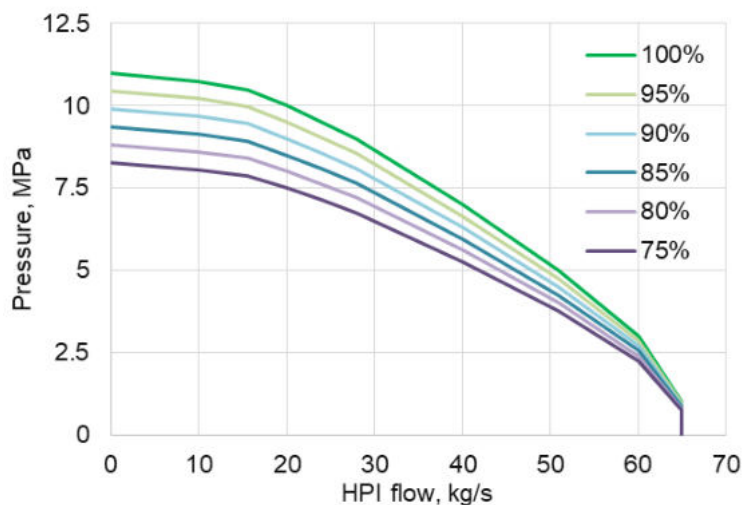
Figure 190: HPI Pump Curves assumed for Assessing of the Impact of Reduced HPI head.

Comparative plots for key parameters are provided in Figure 191 - Figure 196. Reducing the HPI head pressure leads to a later HPI injection (starting time of HPI injection for 100%, 95%, 90%, 85%, 80%, 75% of the design pump head is 85 s, 95 s, 105 s, 120 s, 225 s, 280 s respectively). This aspect affects several parameters, in particular the liquid levels in the primary system and temperatures in the DC. Based on the results of performed analysis it can be noted that decreasing of HPI head pressure reduces the rate of RPV cooldown before restoration of DC level (by 30-40 °C in comparison with "base" case). After the filling of the DC the difference between DC cooling decreases for different HPI flow characteristics. At the end of the transient all DC temperatures generally agree.

Additionally, it should be noted that in the case of HPI head pressure reduction down to 75 - 85% of design value the coolant level in the DC stay decreased for a longer time (2670-3540 s), while in other cases DC level was restored at 2100 - 2200 s.
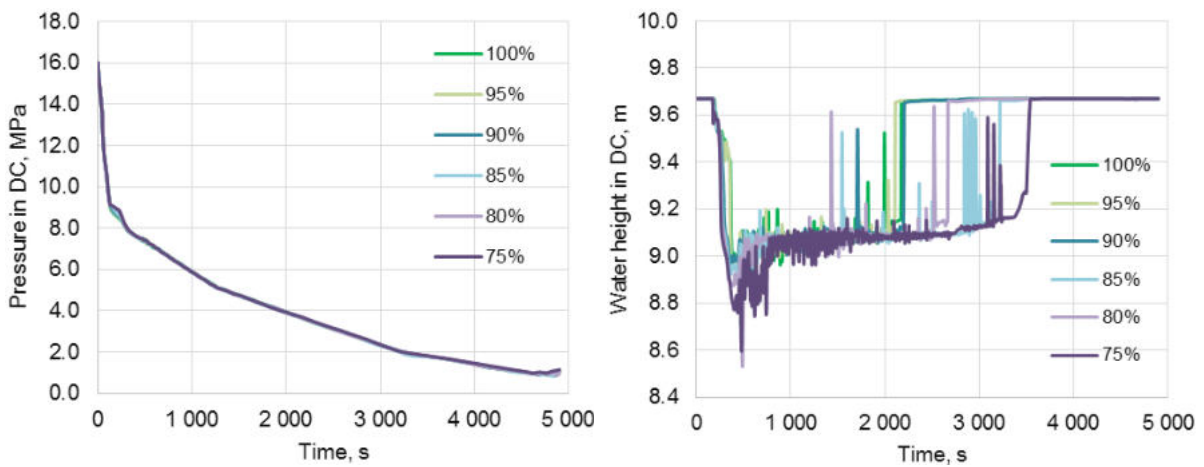
Figure 191: Comparisons of Pressure in the DC at 2.638 m below the CL Axis (left) and DC Level (right) for different HPI Pump Heads.
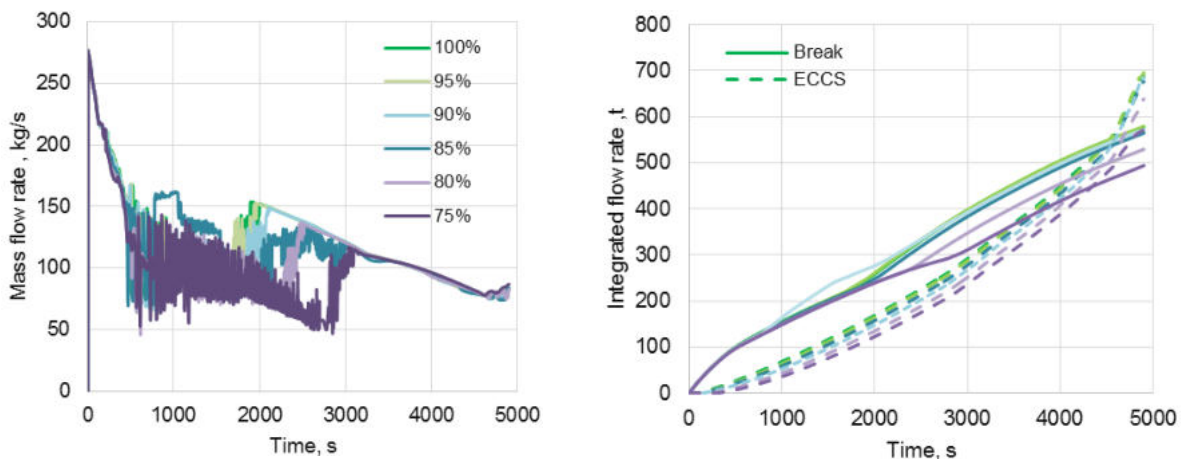
Figure 192: Comparisons of Break Flow (left) and Time-integrated Coolant Loss and ECCS Injection (right) for different HPI Pump Heads.
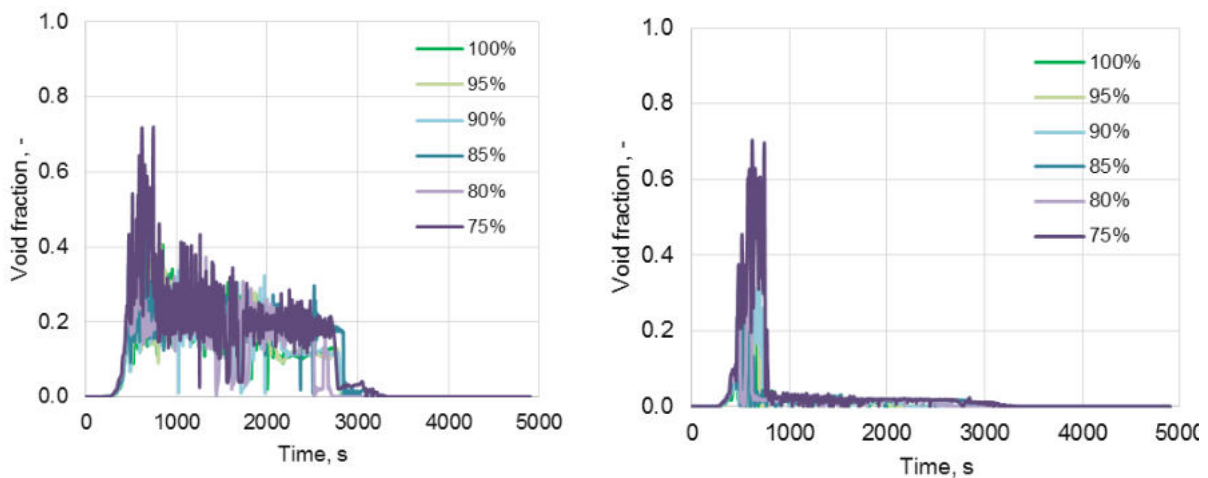
Figure 193: Comparisons of Void Fraction at the RPV Inlets of Loops 1 (left) and 2 (right) for different HPI Pump Heads.

138
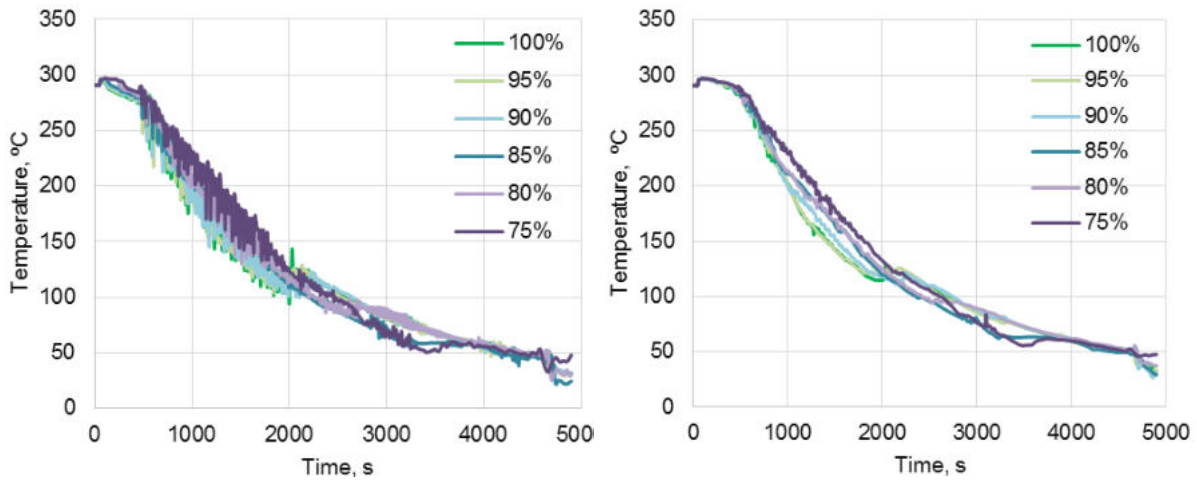
Figure 194: Comparisons of DC Coolant Temperature Range at 1.35 m (left) and 2.638 m (right) below the CL Axis for different HPI Pump Heads.
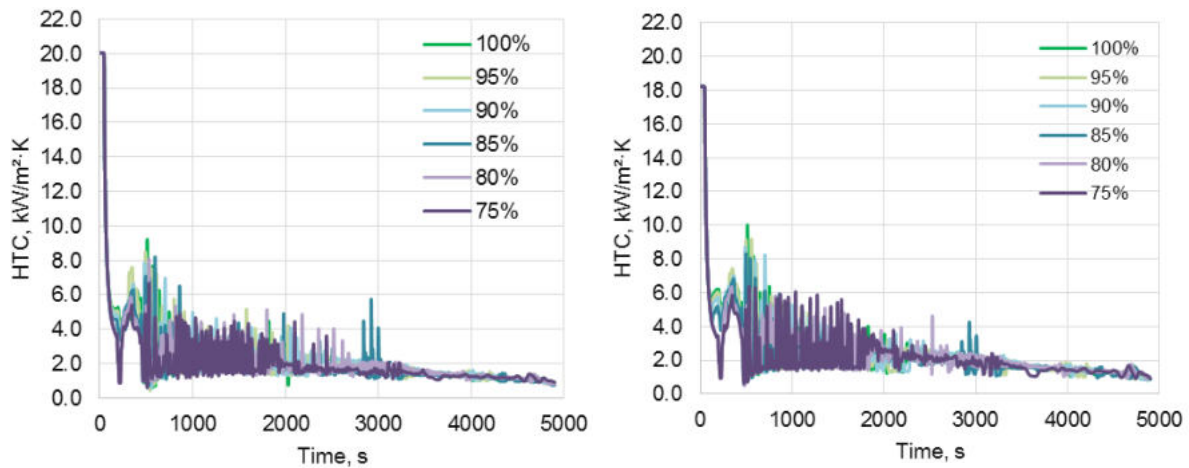
Figure 195: Comparisons of DC HTC Range at 1.35 m (left) and 2.638 m (right) below the CL Axis for different HPI Pump Heads.
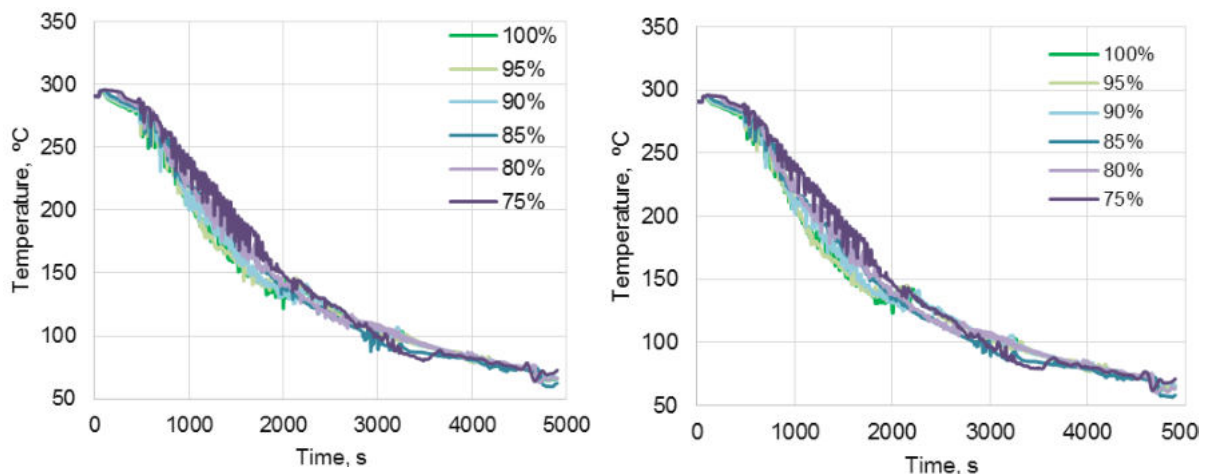
Figure 196: Comparisons of RPV Inner Surface Temperature Range at 1.35 m (left) and 2.638 m (right) below the CL Axis for different HPI Pump Heads.

5.4.3   ATHLET results by GRS

In the ATHLET simulations the decreasing of the HPI pump head is simulated identically to the approach described in 5.4.1 and illustrated in Figure 183 by scaling the pressure component of the

HPI pump curve down to 75% of the reference value in 5% decrements. Comparative plots for key quantities of interest are provided in Figure 197 through Figure 204. Reducing the HPI head can lead to a later HPI injection as depicted in Figure 199 (right). This effects several system parameters and in particular void fraction in the loops as well as the liquid level in the primary circuit. The proposed LTO improvement reduces the cooling conditions in the performed simulations until the ACC start to inject at ~2700 s. However, in the late phase of the transient (between 4200 s and 4800 s) a drop of the fluid temperature in the DC during ACC and LP injection for decreasing HPI pump head can be observed (see Figure 202). This may lead to unfavourable conditions with respect to PTS and is consistent with the TRACE results presented in 5.4.1 in qualitative terms. This phenomenon is related to less coolant loss for lower HPI head conditions, since subcritical discharge conditions at the break are reached later on while injection of cold water is almost the same (see Figure 199 (right) and Figure 200). From Figure 199 (left) it can be seen that the total mass in the primary circuit is higher for lower HPI head configurations in the relevant time frame. This results from the shifted balance between injection and loss of coolant due the time shift in onset of subcritical discharge flow and the refilling of the primary circuit (see Figure 197; right).

The significant drop in liquid level of the primary circuit for 75 % HPI pump head, that was observed in the TRACE simulations (see Figure 184) did not emerge in the TH simulations using ATHLET. Conclusions that can be drawn from the results of the HPI pump head reduction as LTO improvement are consistent with what is given in 5.4.1.
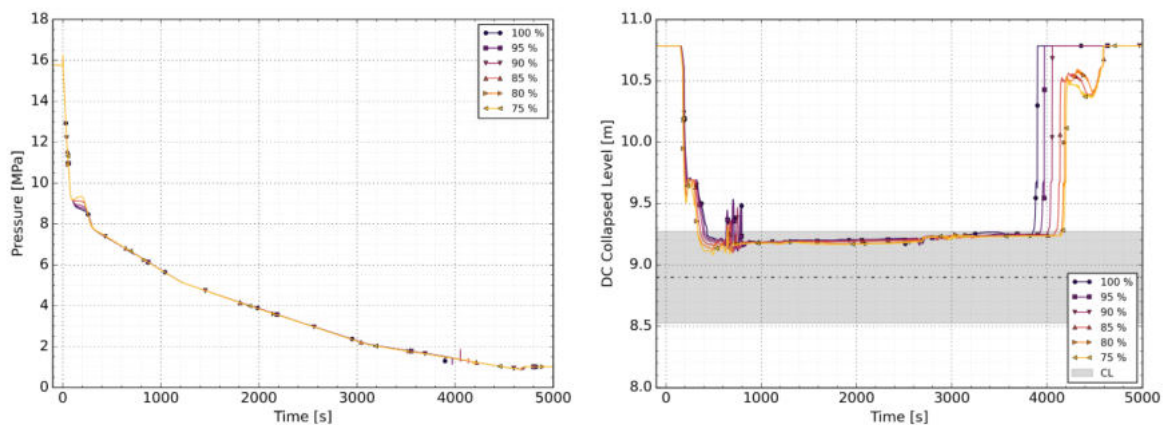
Figure 197: Comparisons of (left) Pressure in the DC at 2.638 m below the CL Axis and (right) DC Level for different HPI Pump Heads.
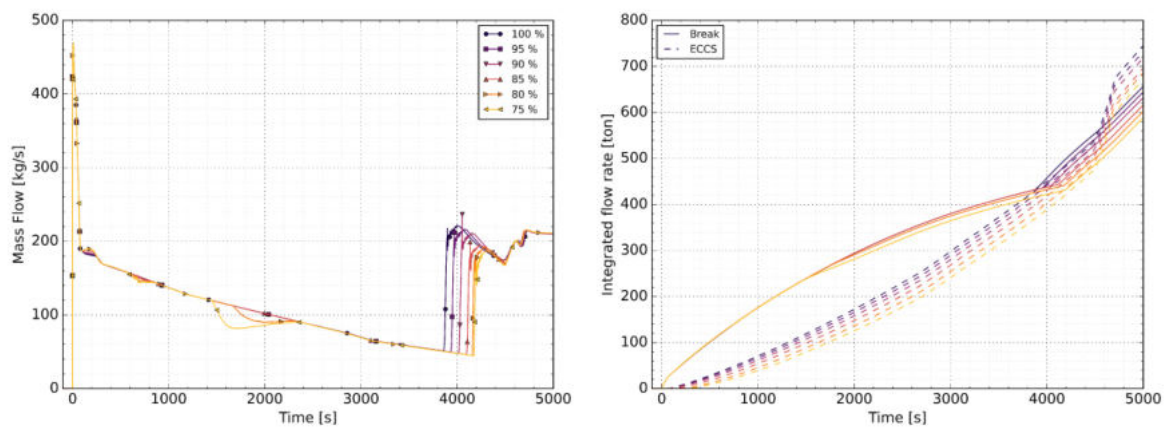
Figure 198: Comparisons of (left) Break Flow and (right) Time-integrated Coolant Loss and ECCS Injection for different HPI Pump Heads.
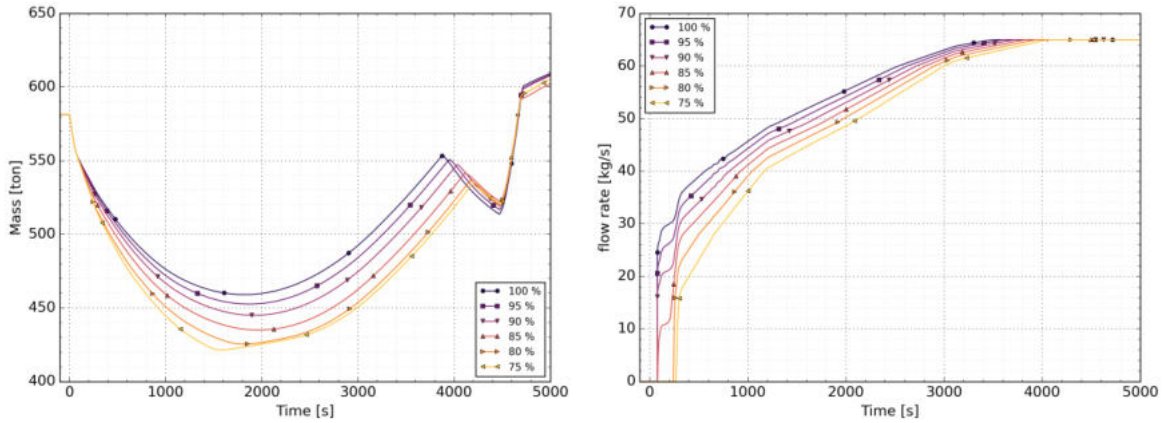
Figure 199: Comparisons of (left) the Total Mass in primary circuit and (right) HPI Flow Rate in loop 2 for different HPI Pump Heads.
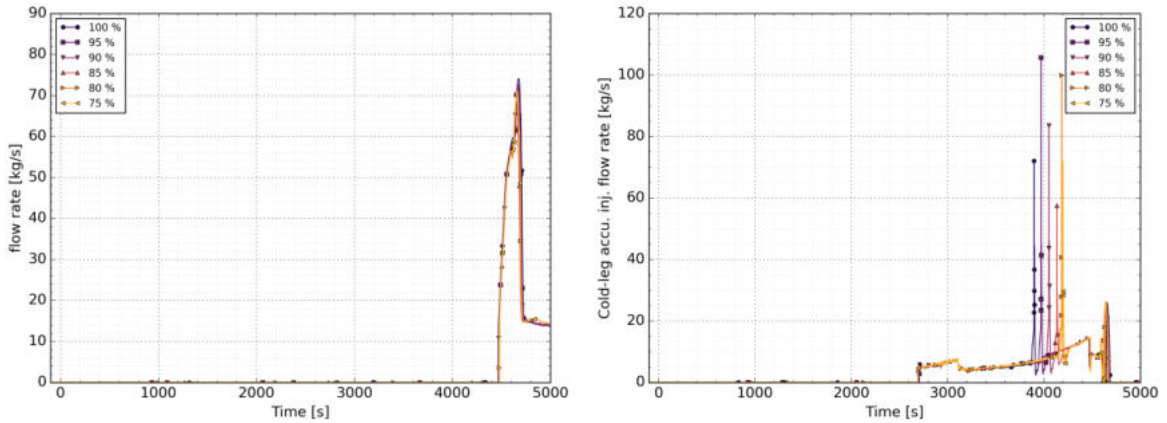
Figure 200: Comparisons of (left) LPI Flow Rate and (right) ACC Injection Rate for different HPI Pump Heads, both exemplarily in loop 2.
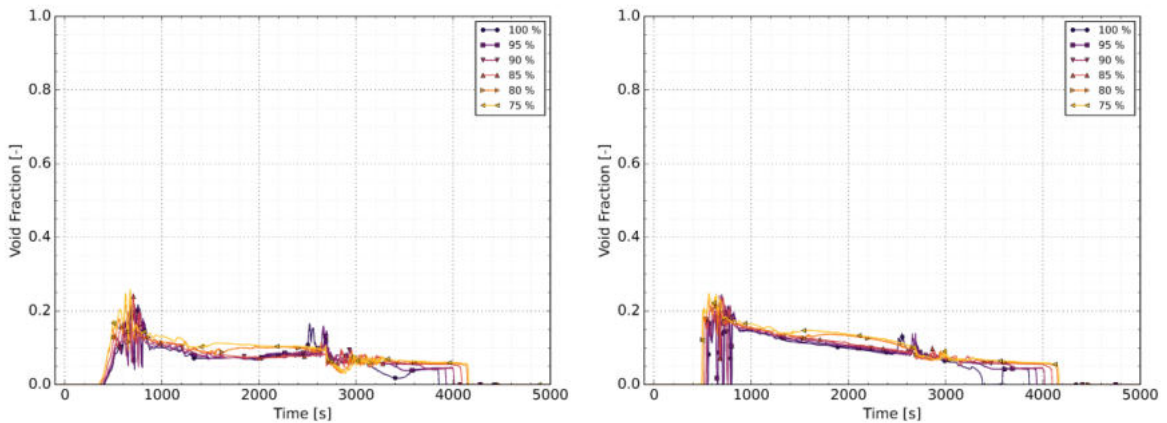
Figure 201: Comparisons of Void Fraction at the RPV Inlets of Loops 1 and 2 for different HPI Pump Heads.
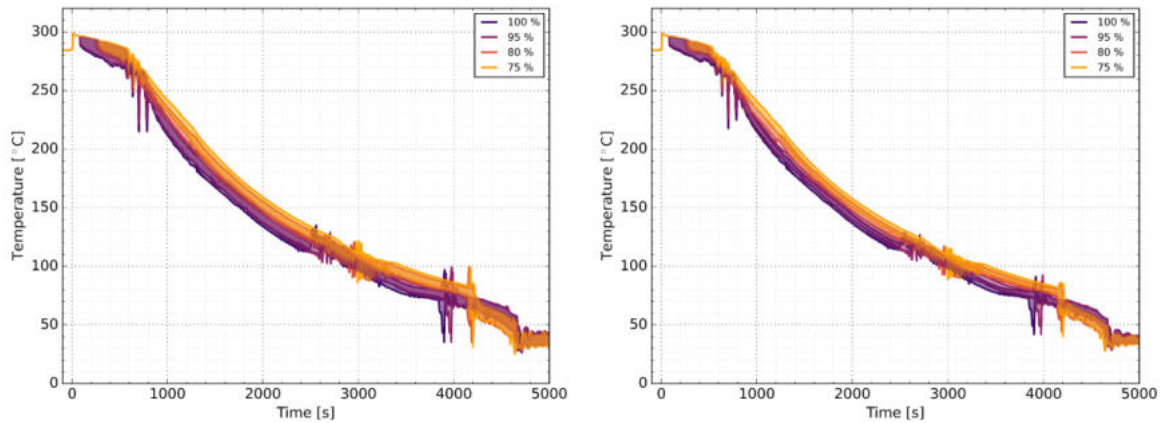
Figure 202: Comparisons of DC Coolant Temperature Range (Minimum to Maximum) at (left) 1.35 m and (right) 2.638 m below the CL Axis for different HPI Pump Heads.
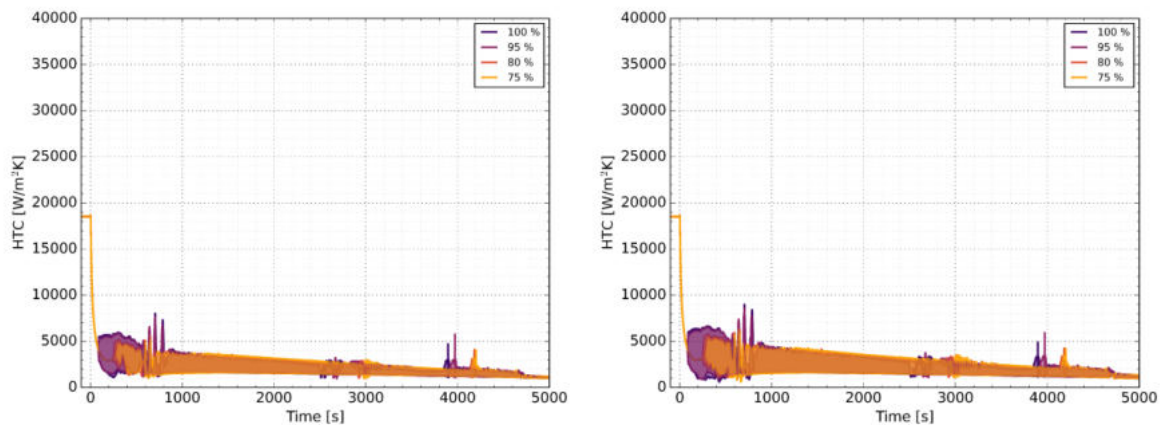
Figure 203: Comparisons of DC HTC Range (Minimum to Maximum) at (left) 1.35 m and (right) 2.638 m below the CL Axis for different HPI Pump Heads.
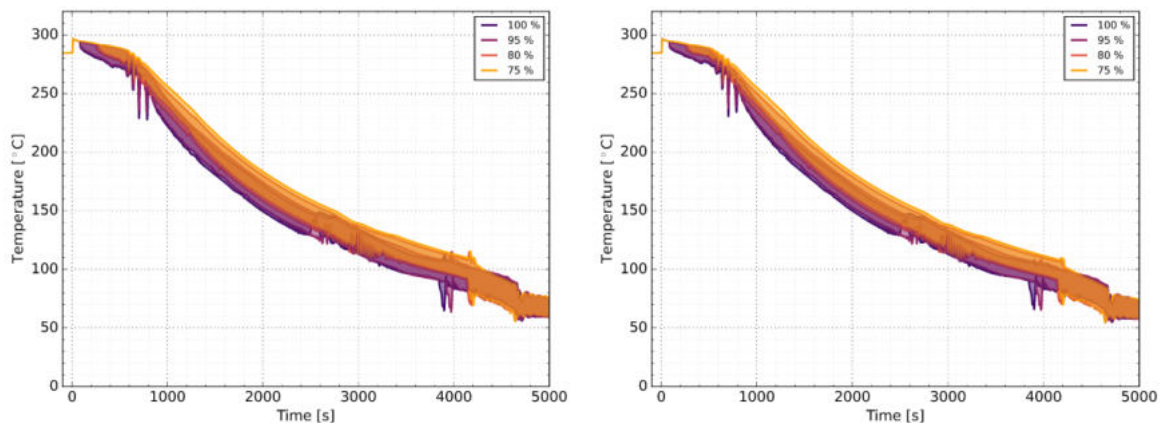
Figure 204: Comparisons of RPV Inner Surface Temperature Range (Minimum to Maximum) at (left) 1.35 m and (right) 2.638 m below the CL Axis for different HPI Pump Heads.

5.4.4   ECC-MIX results by GRS

For the ATHLET simulations with applied ECC-MIX model the decreasing of the HPI pump head is simulated identically to the approach described in 5.4.1 and illustrated in Figure 183 by scaling the pressure component of the HPI pump curve down to 75% of the reference value in 5% decrements. In the comparative plots for key quantities of interest provided in Figure 205 through Figure 210 the

142

qualitative influence of the proposed LTO improvements is comparable the results presented in 5.4.3 using the ATHLET code without mixing model. However, a cliff edge effect can be observed when the HPI pump head is reduced to 95 % of the reference value and below. This results from the time when pure liquid reaches the break position, and the void fraction drops to zero in loop 1 as depicted in Figure 207 (left). For 95 % HPI pump head and lower values the void keeps above zero for at least another 500 s and a void-liquid mixture discharges from the break, which significantly effects the coolant loss mass flow. In consequence, in particular the DC level (Figure 205; right) and break mass flow (Figure 206; left) differs qualitatively when the HPI pump head is reduced. The unfavourable cooling conditions observed in the ATHLET only simulation as described in 5.4.3 were a reduction in the HPI pump head lead to lower temperatures in the DC during ACC and LP injection is not observed when applying the ECC-MIX model as can be seen in Figure 208 through Figure 210. However, overall conclusions that can be drawn from the results of the HPI pump head reduction as LTO improvement are consistent with what is given in 5.4.1.
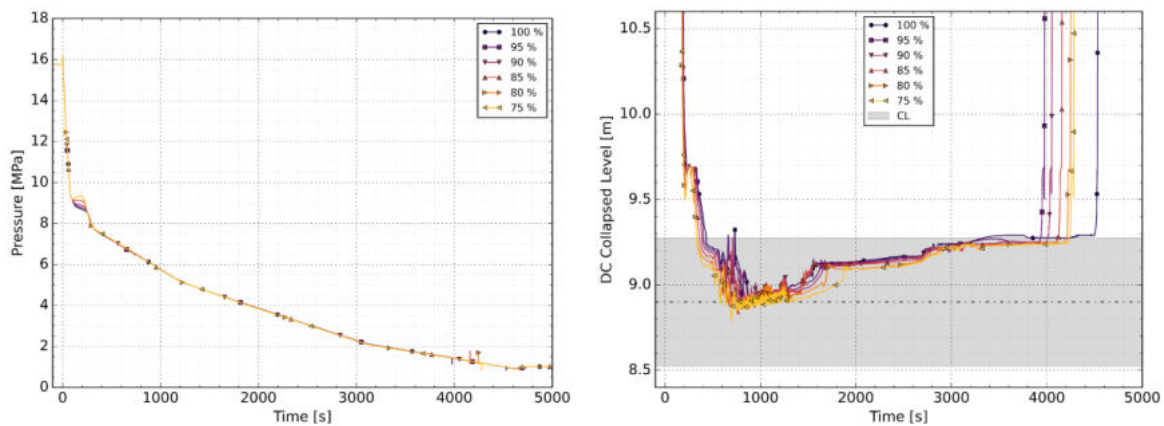
Figure 205: Comparisons of (left) Pressure in the DC at 2.638 m below the CL Axis and (right) DC Level for different HPI Pump Heads.
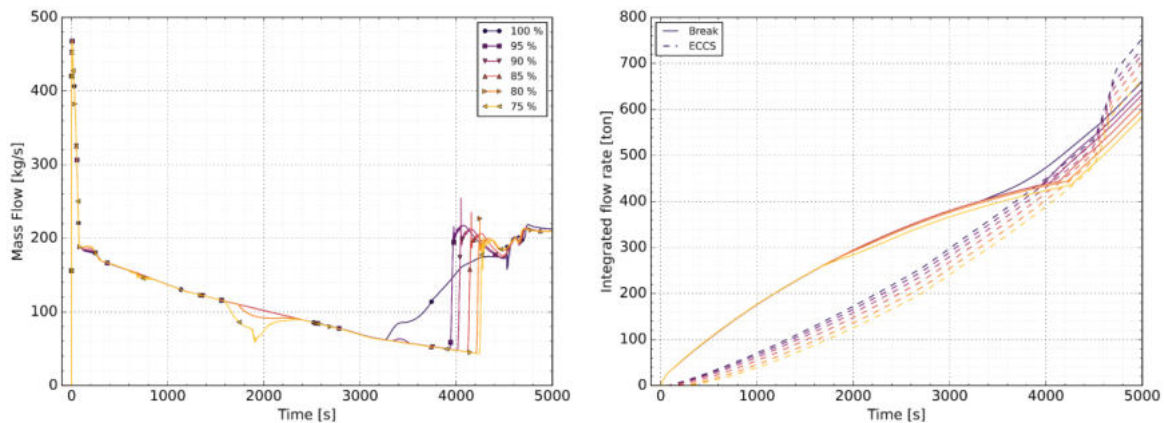
Figure 206: Comparisons of (left) Break Flow and (right) Time-integrated Coolant Loss and ECCS Injection for different HPI Pump Heads.

143
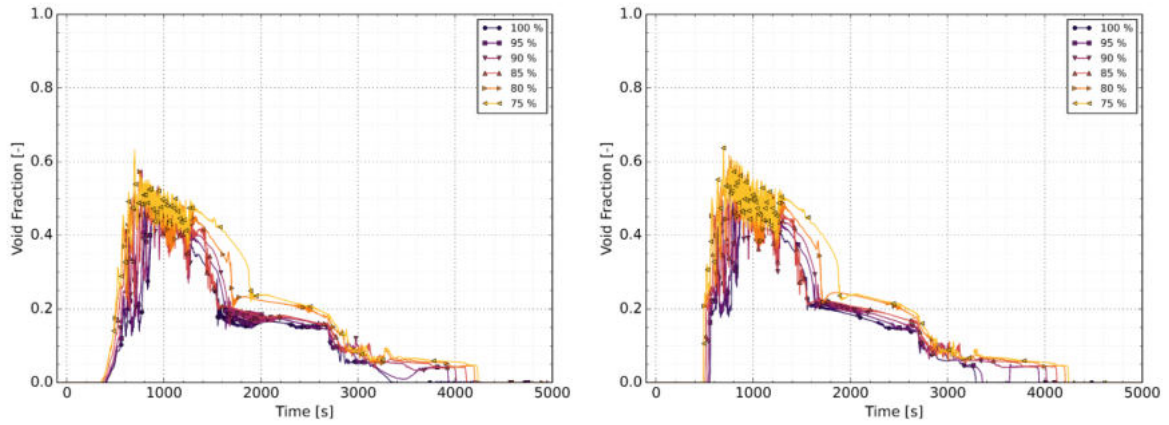
Figure 207: Comparisons of Void Fraction at the RPV Inlets of Loops 1 and 2 for different HPI Pump Heads.
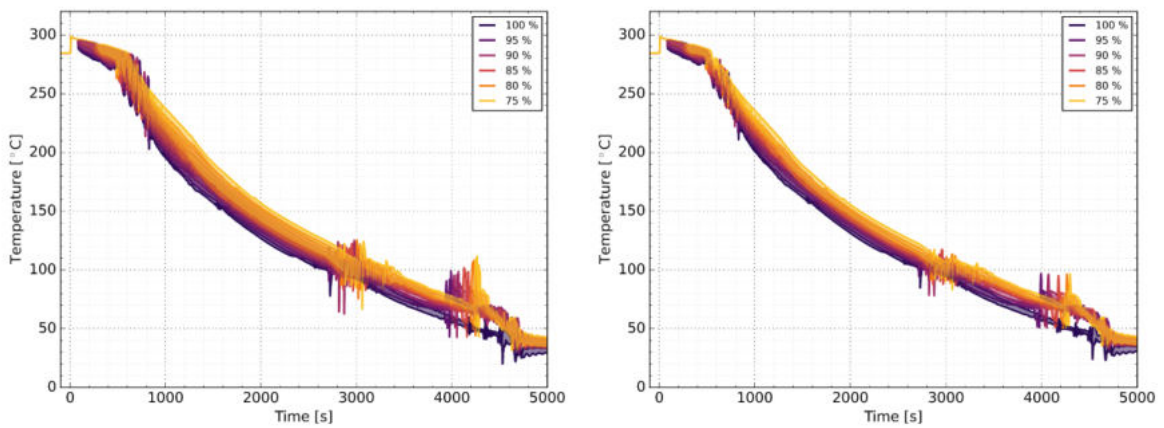
Figure 208: Comparisons of DC Coolant Temperature Range (Minimum to Maximum) at (left) 1.35 m and (right) 2.638 m below the CL Axis for different HPI Pump Heads.
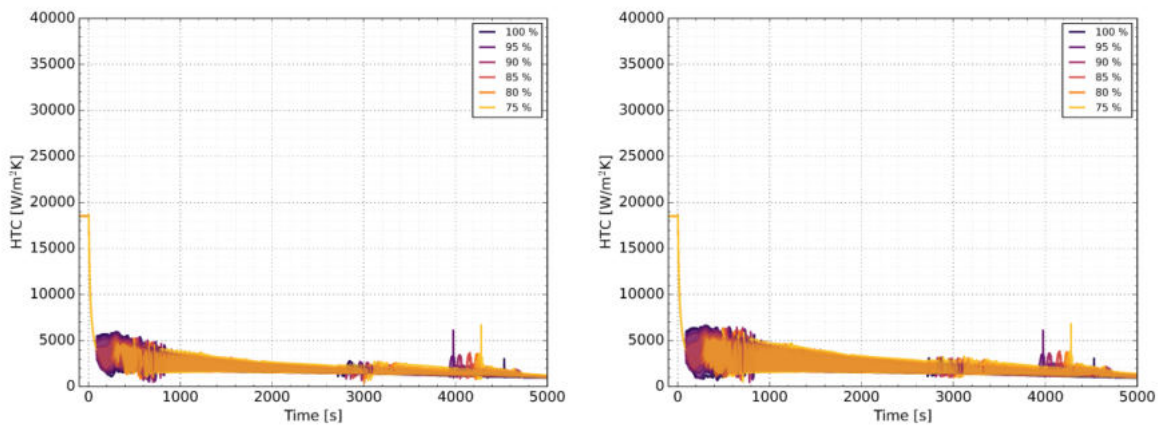
Figure 209: Comparisons of DC HTC Range (Minimum to Maximum) at (left) 1.35 m and (right) 2.638 m below the CL Axis for different HPI Pump Heads.
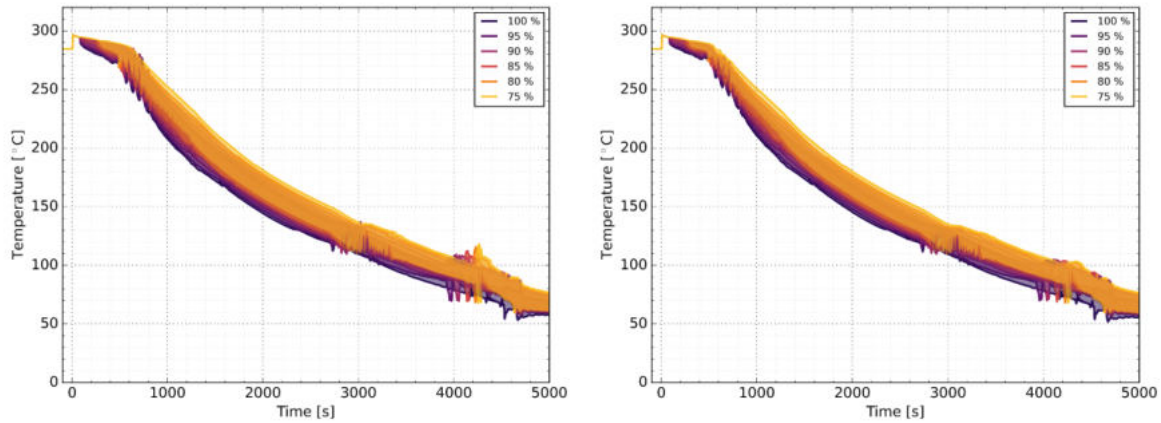
Figure 210: Comparisons of RPV Inner Surface Temperature Range (Minimum to Maximum) at (left) 1.35 m and (right) 2.638 m below the CL Axis for different HPI Pump Heads.

5.4.5   Influence of Injection Model and Mixing Code (ATHLET, ECCMIX, GRSMIX)

The following Figure 211 and Figure 212 depict the influence of the reduction of the HPI pump head to the minimum considered value of 75 % in comparison of the three investigated configurations with ATHLET only, applying the ECC-MIX model and calculation DC temperatures and heat transfer coefficients with GRS-MIX. The influence between the used approaches is consistent with the description given in chapter 4.2.2. The influence due to reduction of the HPI pump head indicated by the dashed lines is clearly distinguishable from the beginning of the transient (after HPI with p < 110 bar) and comparable in quantitative terms for all three used approaches.
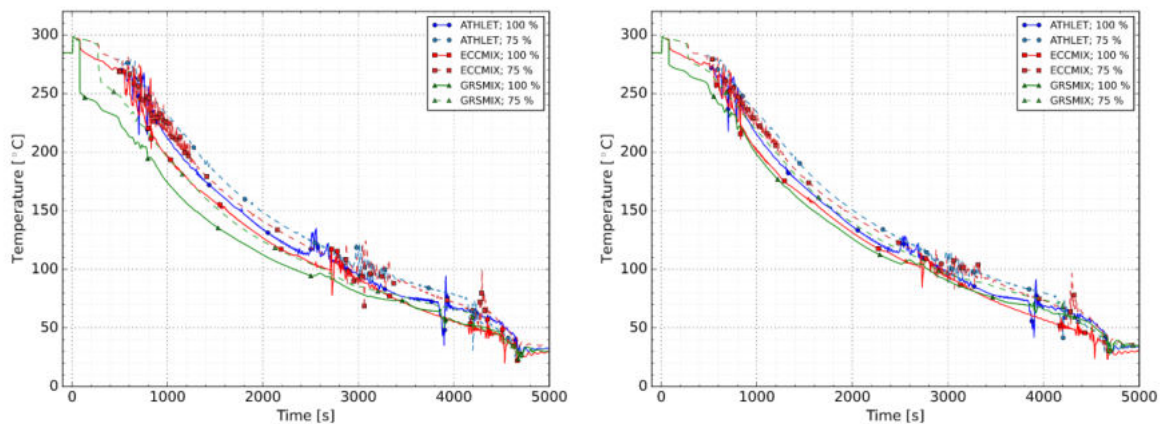
Figure 211: Comparisons of DC Coolant Temperature at (left) 1.35 m and (right) 2.638 m below the CL Axis for Reference Case and HPI Pump Head Decrease to 75 % for TH Results only, using Injection Model and Mixing Code (ECCMIX, GRSMIX).

145
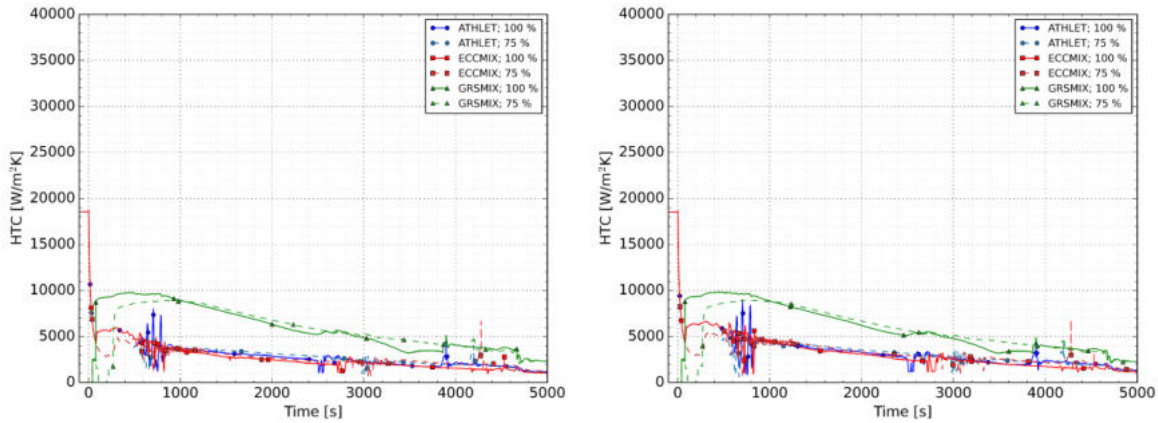
Figure 212: Comparisons of DC HTC at (left) 1.35 m and (right) 2.638 m below the CL Axis for Reference Case and HPI Pump Head Decrease to 75 % for TH Results only, using Injection Model and Mixing Code (ECCMIX, GRSMIX).

5.5 Decreasing HPI capacity

5.5.1 RELAP5 results by KIWA

Decreasing of the HPI capacity is simulated by uniformly scaling the HPI pump flow rates down to 75% of the nominal values in 5% decrements as shown in **Figure 213**.
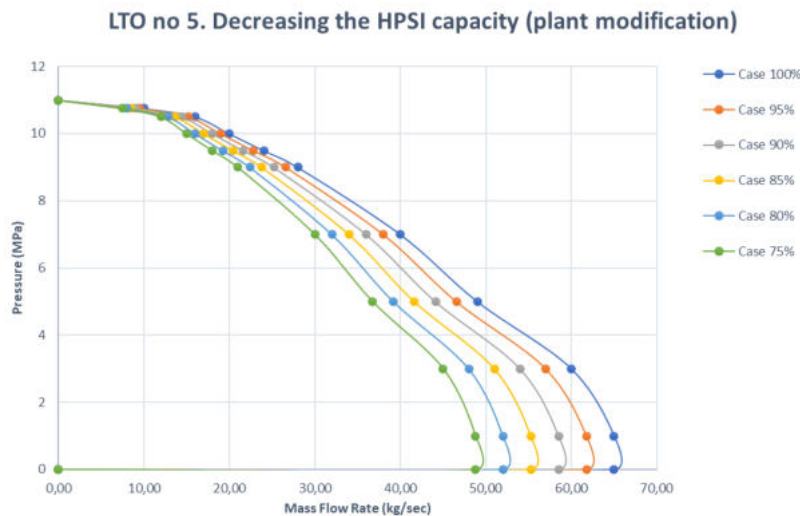
Figure 213: HPI Pump Curves assumed for Assessing of the Impact of Reduced HPI Capacity.

Comparative plots for key quantities of interest are provided in Figure 214 through Figure 218. The input file "input.stst.1300MW_4loop_v5" distributed on 22 September 2021 was used in the calculations. The code that was used for these computations was relap5-m33p5(km)-win32-ifc-opt-b2-snap which was released on October 2016 and compiled by IFC 13.1. This is an older version than versions used in other computations (lf). The main results are that the proposed LTO improvement might have some relevant impact on the major system parameters as coolant and wall temperatures in the DC. In Figure 217 there are presented DC coolant temperatures at 1.13 m and 2.638 m below the CL Axis for different HPI pump capacities. It can be concluded that by decreasing rate of cooling (via HPI pumps) the coolant temperatures can be reduced to some extent as well. Thus, the more the decrease in HPI flows is the more a risk of PTS is reduced. Benefits proposed and presented in this LTO improvement in the early stage of the transient can be mitigated to some extent by the increased temperature gradients in DC that appears after the accumulator injections.

146
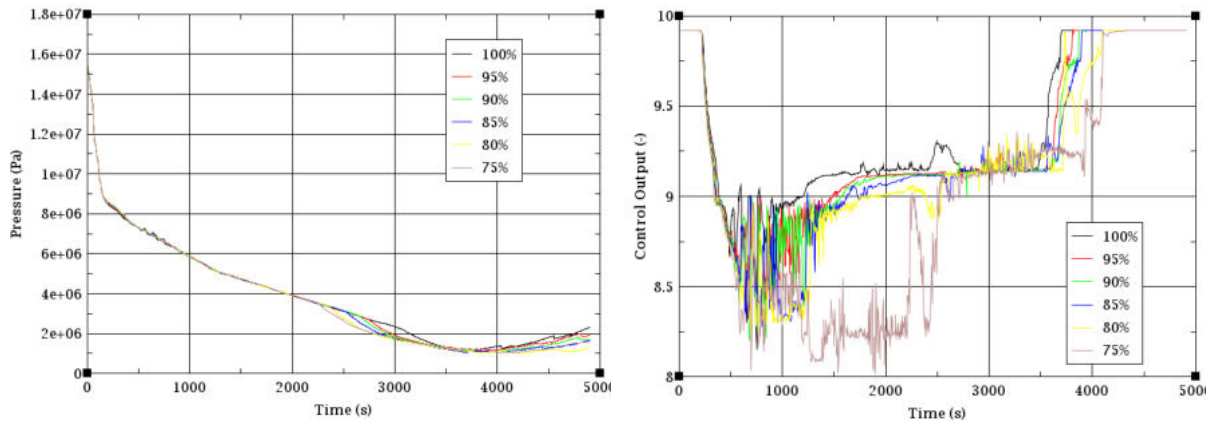
Figure 214: Comparisons of (left) Pressure in the DC at 2.638 m below the CL Axis and (right) DC Level for different HPI Pump Capacities.
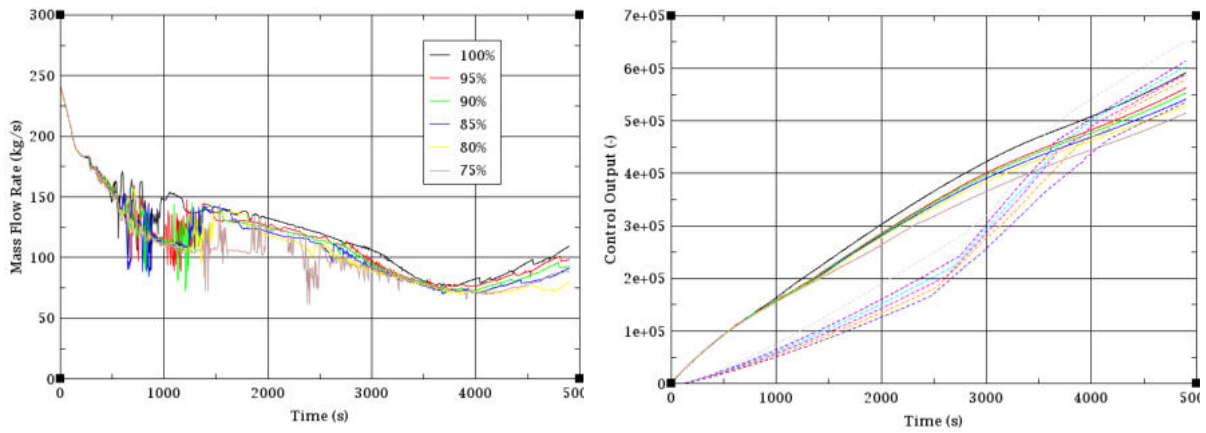
Figure 215: Comparisons of (left) Break Flow and (right) Time-integrated Coolant Loss and ECCS Injection for different HPI Pump Capacities.
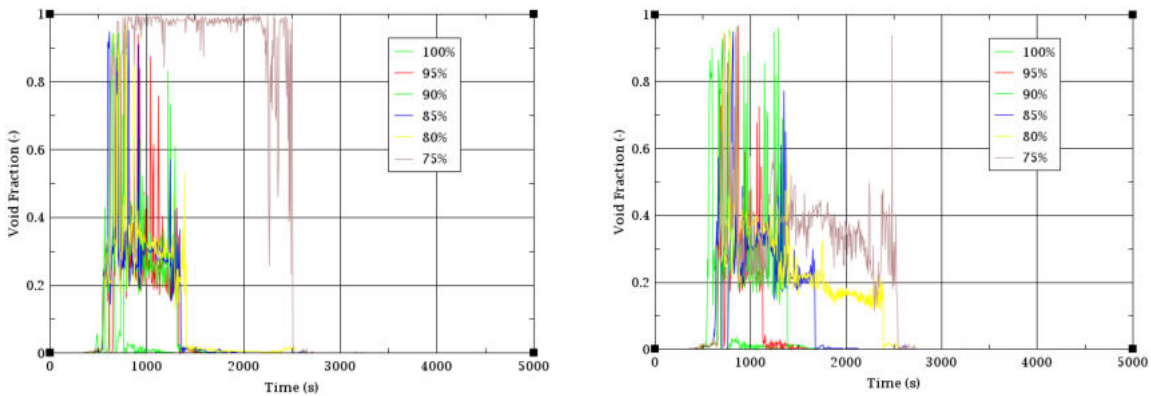
Figure 216: Comparisons of Void Fraction at the RPV Inlets of Loops 1 and 2 for different HPI Pump Capacities.

147
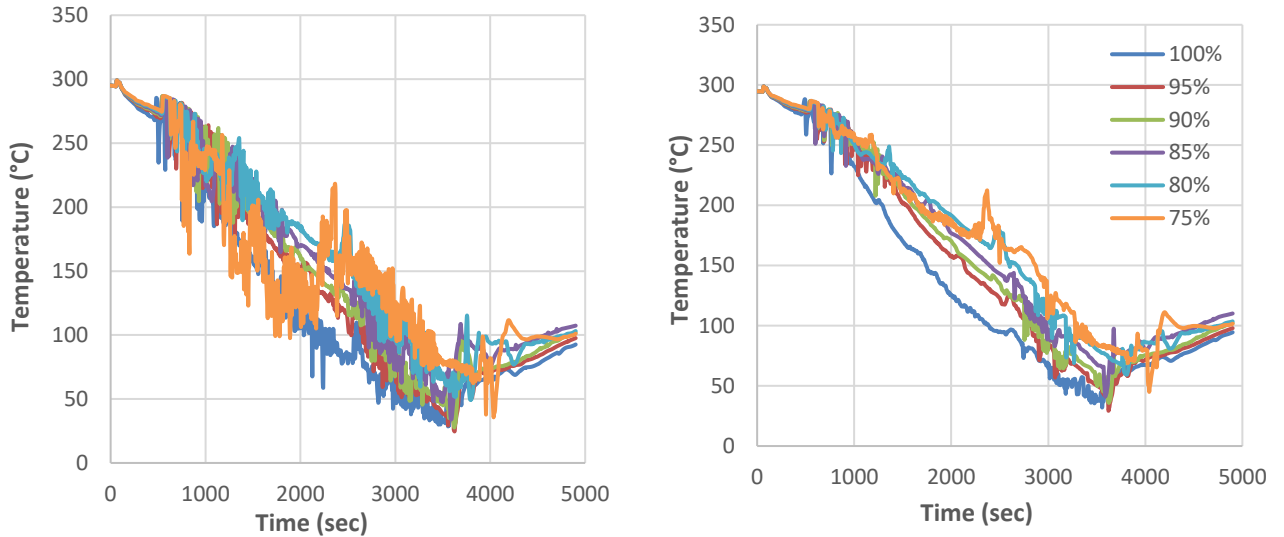
Figure 217: Comparisons of DC Coolant Temperature Range at (left) 1.13 m and (right) 2.638 m below the CL Axis for different HPI Pump Capacities.
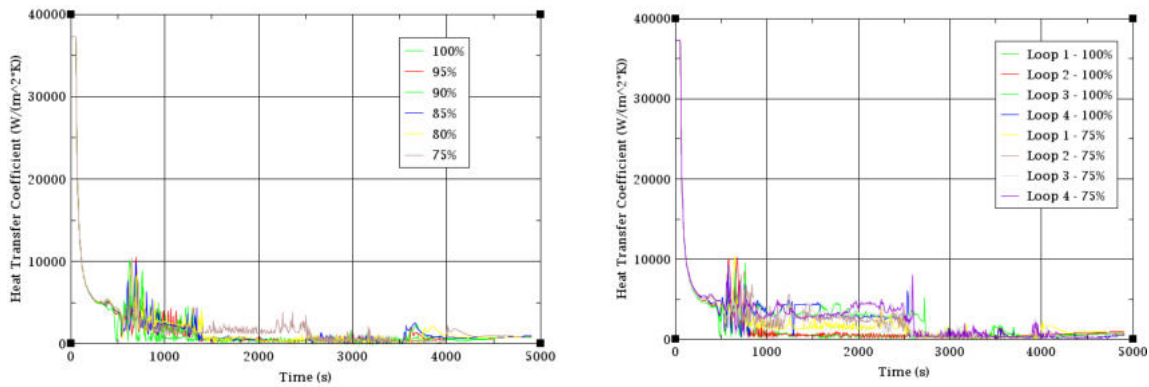
Figure 218: Comparisons of DC HTC Range at (left) 1.13 m for different HPI Pump Capacities and loops 1-4 (right).

5.5.2   TRACE results by PSI

Decreasing of the HPI capacity is simulated by uniformly scaling the HPI pump flow rates down to 75% of the nominal values in 5% decrements as shown in Figure 219.
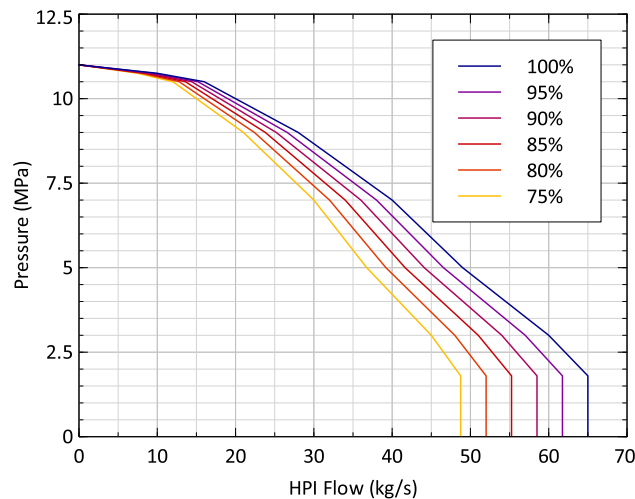
Figure 219: HPI Pump Curves assumed for Assessing of the Impact of Reduced HPI Capacity.

Comparative plots for key quantities of interest are provided in Figure 220 through Figure 225. This proposed LTO improvement does have a noticeable impact on the major system parameters, especially at primary pressures below around 4 MPa, where the difference in pump flow is largest. The coolant and wall temperatures in the DC are also significantly affected by the reduced pump flow. In particular, the rate of cooling in the RPV seems to be lower in the early stages of the transient (up to ~ 2000 s). After the ACCs inject, however, the rate of cooling increases significantly. The cooling rate during ACC injection is increased so much in the period 2000 to 3000 s that one might expect a higher risk of PTS for this proposed LTO improvement. This would, of course, need to be confirmed using thermo-mechanical and fracture mechanics simulations. Ultimately, however, the temperatures in the DC are increased at the end of the transient.
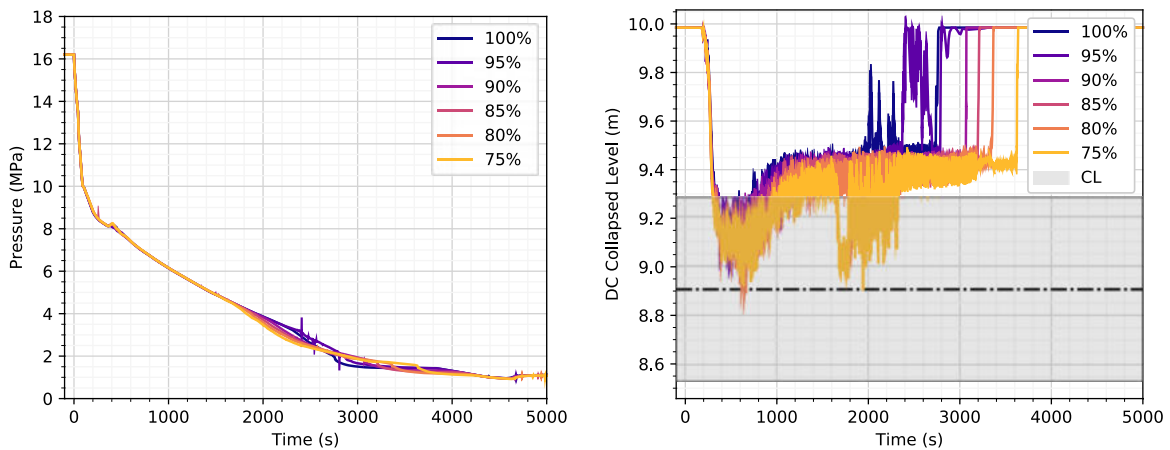
Figure 220: Comparisons of (left) Pressure in the DC at 2.638 m below the CL Axis and (right) DC Level for different HPI Pump Capacities.
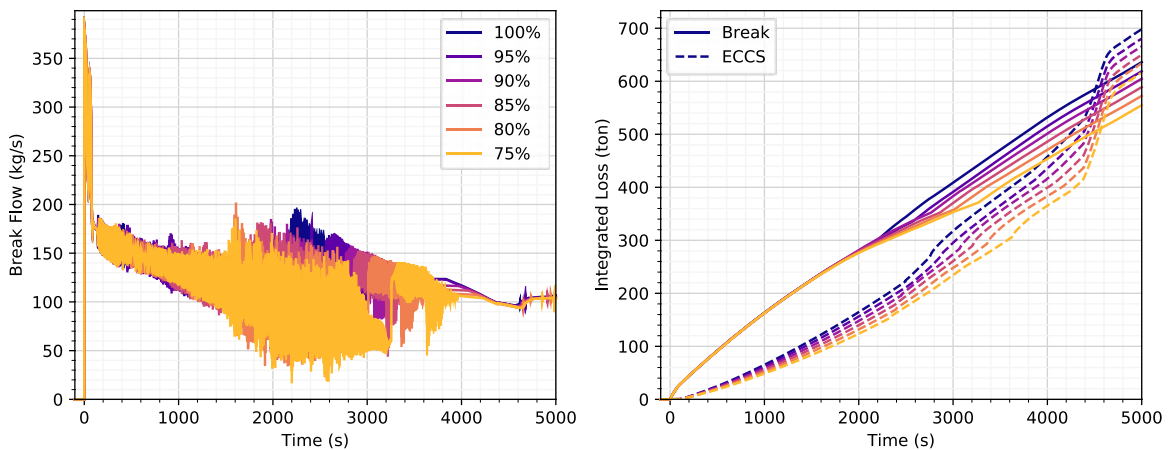
Figure 221: Comparisons of (left) Break Flow and (right) Time-integrated Coolant Loss and ECCS Injection for different HPI Pump Capacities.

149
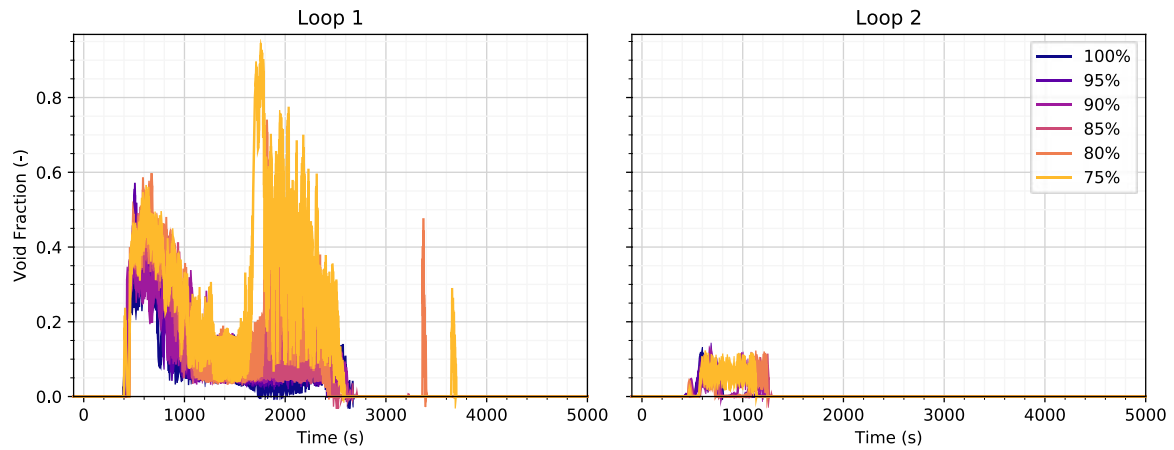
Figure 222: Comparisons of Void Fraction at the RPV Inlets of Loops 1 and 2 for different HPI Pump Capacities.
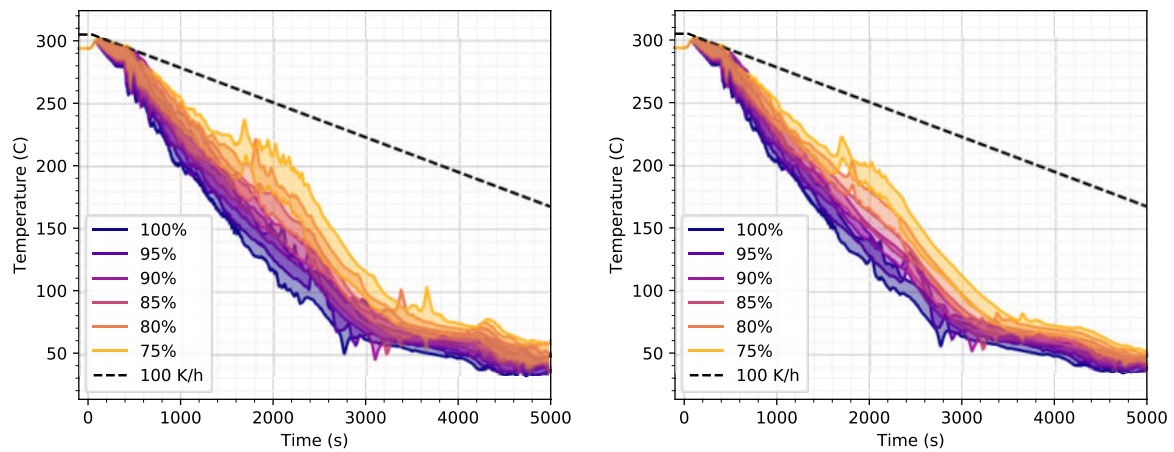
Figure 223: Comparisons of DC Coolant Temperature Range (Minimum to Maximum) at (left) 1.35 m and (right) 2.638 m below the CL Axis for different HPI Pump Capacities.
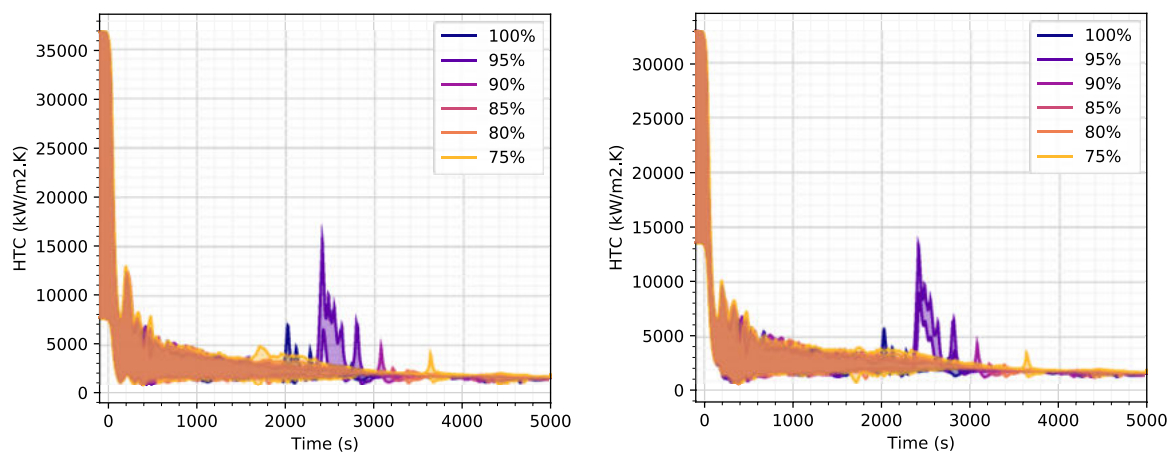
Figure 224: Comparisons of DC HTC Range (Minimum to Maximum) at (left) 1.35 m and (right) 2.638 m below the CL Axis for different HPI Pump Capacities.
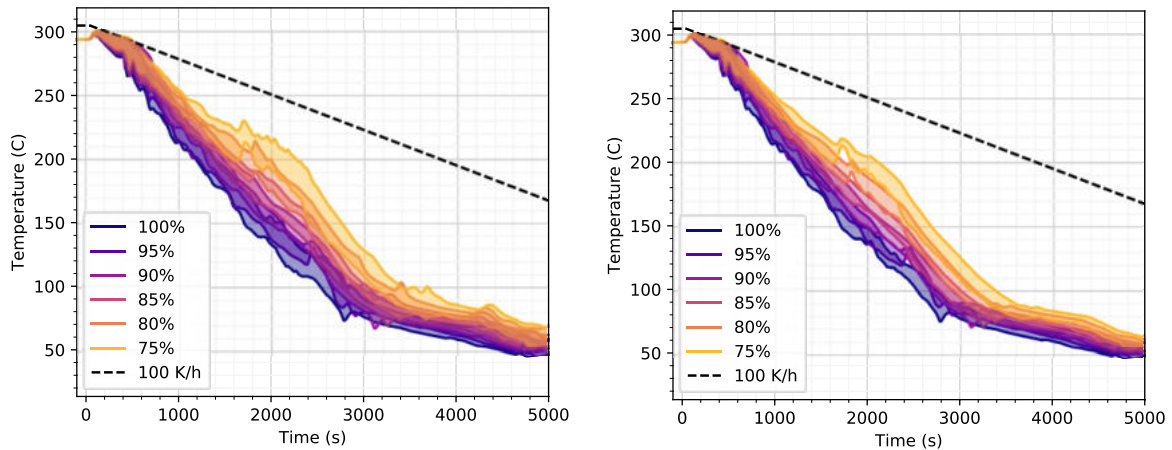
Figure 225: Comparisons of RPV Inner Surface Temperature Range (Minimum to Maximum) at (left) 1.35 m and (right) 2.638 m below the CL Axis for different HPI Pump Capacities.

5.5.3   RELAP5 results by SSTC

Comparative analysis was performed with application of Relap5/mod3.3 (version "lf") code. Decreasing of the HPI pump capacity was simulated by SSTC NRS via scaling of the flow component of the HPI pump curve down to 75%. Degree of reduction and the decrement (5%) was selected according to the similar approach of PSI (see chapter 5.5.2), as illustrated in Figure 226. The "base" (100%) flow rate characteristic of HPI pumps was taken from the Table 1.
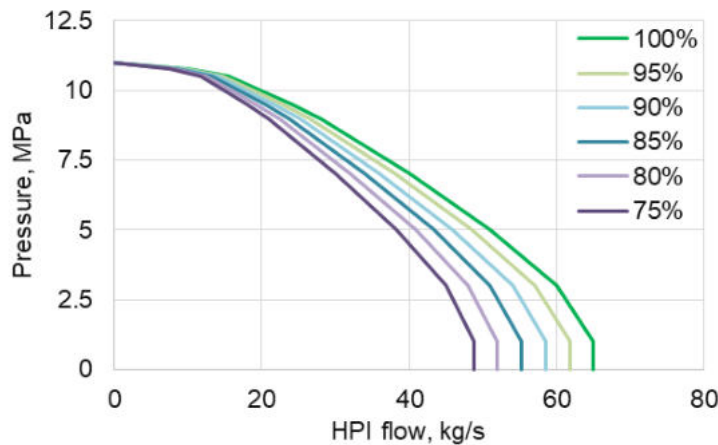
Figure 226: HPI Pump Curves assumed for Assessing of the Impact of Reduced HPI capacity.

Comparative plots for key parameters are provided in Figure 227 - Figure 232. Results of performed analysis show that reducing of the HPI capacity significantly affects primary parameters (in particular DC level and temperature). At the early phase of transients (up to ~2200 s) DC temperature rise follows the rate of HPI capacity reducing. The maximum DC temperature increase (30-50 °C in comparison with "base" case) is observed in the scenario with reduction of HPI capacity from 100% of design curve to 75%. However, after filling primary side with coolant (~2200-3400 s) DC temperatures generally agree. Summarizing, one can conclude that analysed LTO improvement potentially may affect results of RPV strength analysis.
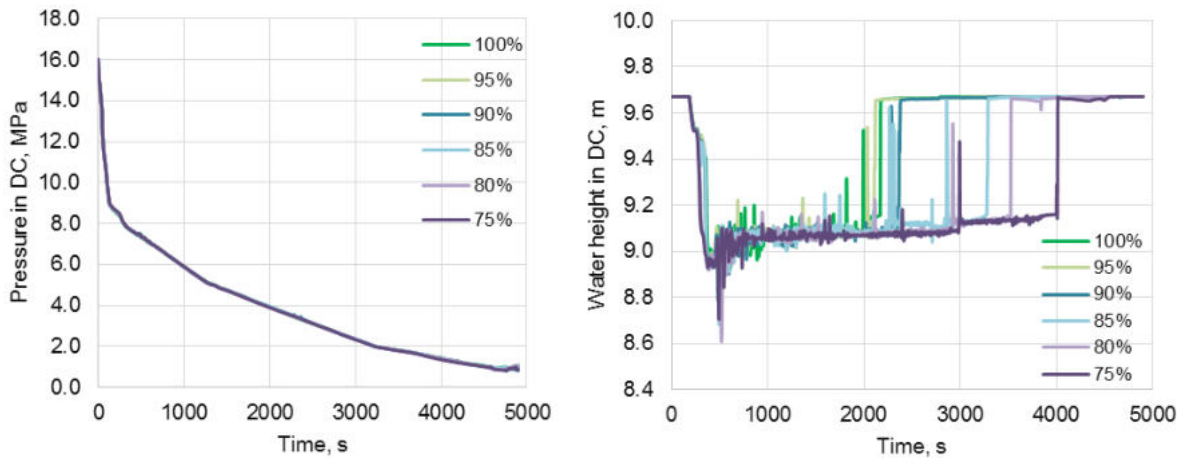
Figure 227: Comparisons of Pressure in the DC at 2.638 m below the CL Axis (left) and DC Level (right) for different HPI Pump Capacities.
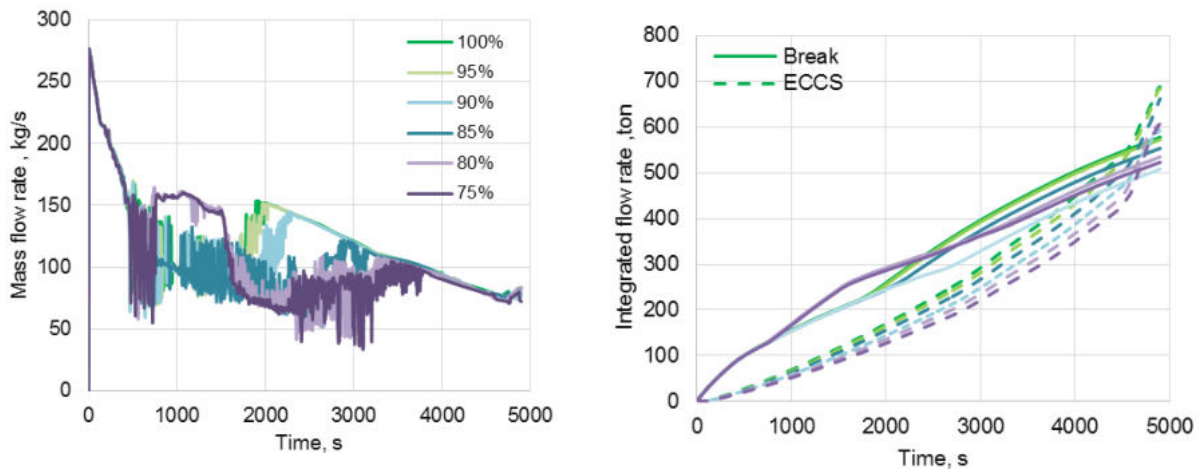
Figure 228: Comparisons of Break Flow (left) and Time-integrated Coolant Loss and ECCS Injection (right) for different HPI Pump Capacities.
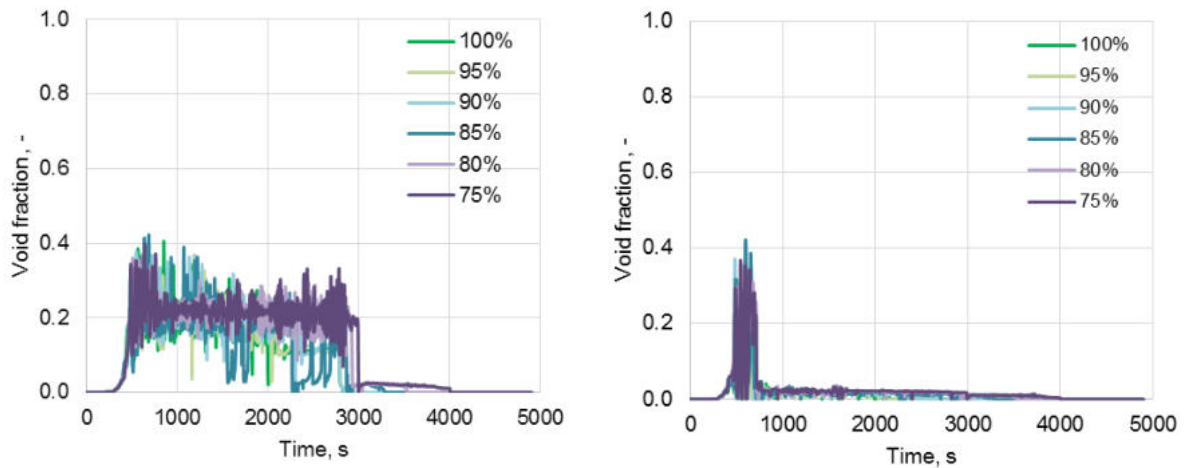
Figure 229: Comparisons of Void Fraction at the RPV Inlets of Loop 1 (left) and Loop 2 (right) for different HPI Pump Capacities.
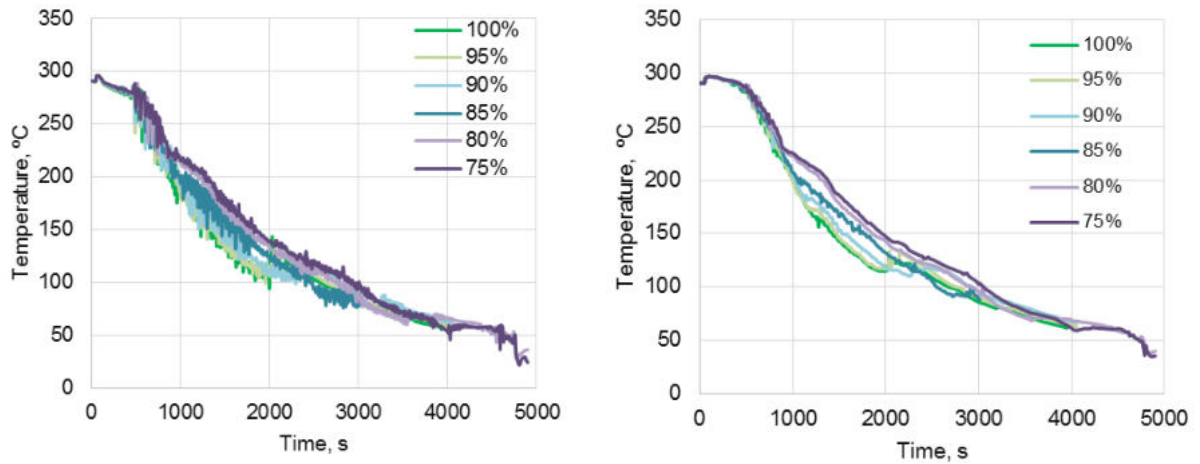
Figure 230: Comparisons of DC Coolant Temperature Range at 1.35 m (left) and 2.638 m (right) below the CL Axis for different HPI Pump Capacities.
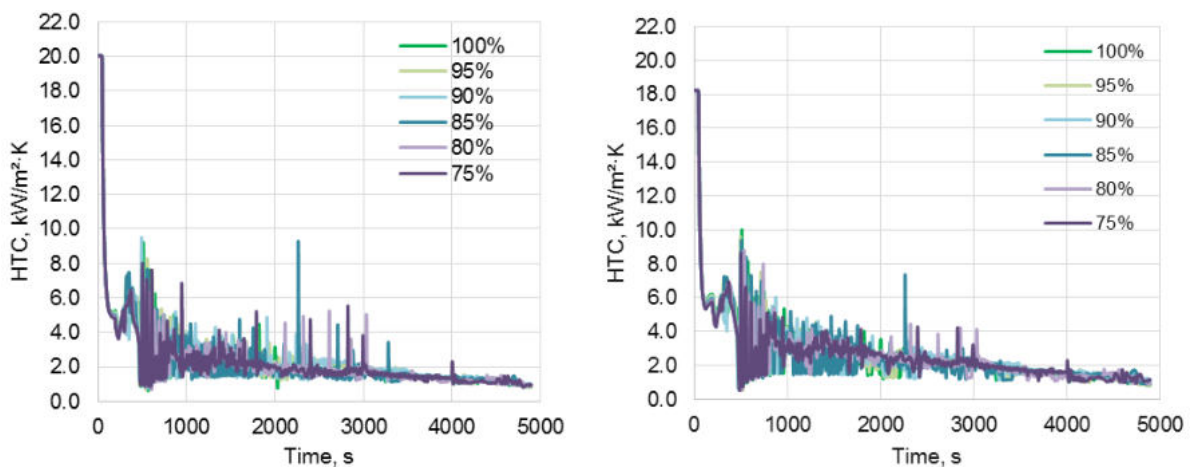
Figure 231: Comparisons of DC HTC Range at 1.35 m (left) and 2.638 m (right) below the CL Axis for different HPI Pump Capacities.
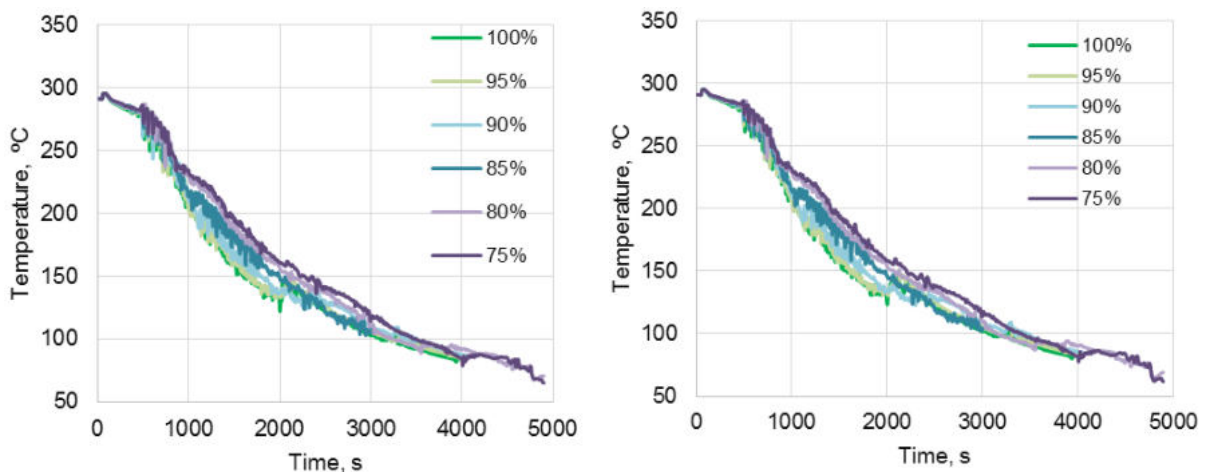
Figure 232: Comparisons of RPV Inner Surface Temperature Range at 1.35 m (left) and 2.638 m (right) below the CL Axis for different HPI Pump Capacities.

5.6   Decreasing of accumulator pressure

5.6.1   RELAP5 results by JSI

For calculations the RELAP5/MOD3.3 Patch 5 (version 3.3km from July 2016) has been used. The proposed LTO improvement of decreasing of ACC pressure is modelled by decreasing the initial pressure opening setpoint in the ACCs from the nominal value of 2.6 MPa to 2 MPa (four cases, 0.2 MPa reductions). The modifications in the ACCs setpoint pressures have been introduced at 2500 s, i.e. before the primary pressure dropped below 2.6 MPa. The reason for this was the "kwu76" base case input model, in which the ECCS isolation valves "randomly" spuriously open for a while before 500 s in Cold leg 1 and 4 (note: in loops 2 and 3 HP injection is assumed) and Hot Legs 2 and 3 (note: assumption that no injection in loops 1 and 4 is available therefore ECCS check valves are set by logic into closed position), providing temporary flow through ECCS isolation valves from a volume before them (see Figure 233). The timings of these "random" openings were influenced by introducing RELAP5 ACC cards with different opening setpoints, and this was sufficient to visibly influence further transient progression. Therefore, it was decided to make a restart from the base case calculation with introducing ACCs opening pressure setpoint modelling change at 2500 s to clearly see just the impact of decreased ACC opening setpoint, which to our opinion models the real situation.
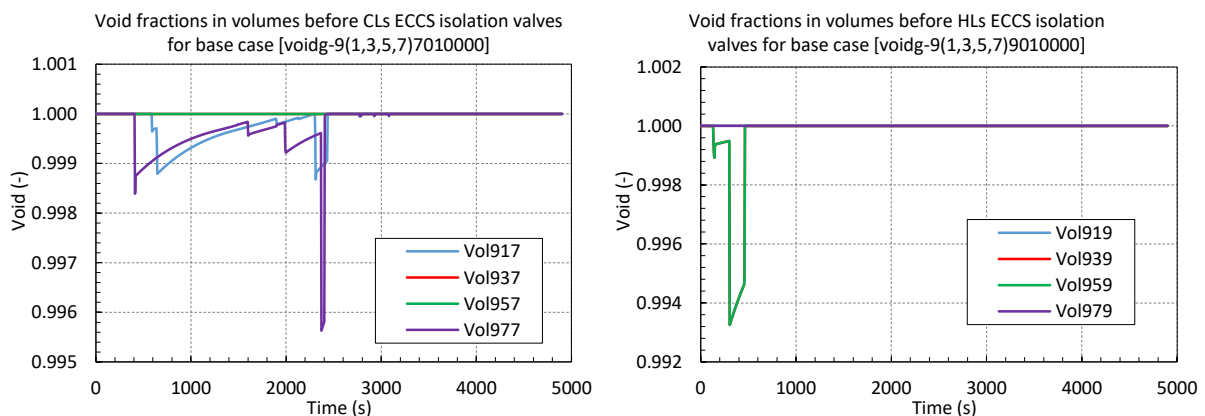
Figure 233: RELAP5 comparisons of void fractions in volumes before (left) CLs ECCS isolation valves and (right) HLs ECCS isolation valves for base case calculation.

In Figures 234 through 239 the impact of ACC pressure opening setpoint decrease can be seen. The slight differences occur after the CL ACCs injection around 2770 s for base case (ACC opening setpoint 2.6 MPa). The primary pressure and water level in DC shown in Figure 234 are only slightly impacted. In Figure 235(right) are also visible some slight differences between integrated ECCS flows due to ACC injection (app. 5 tons difference between the cases, where the ECCS injected mass is highest for 2.6 MPa case due to earlier injection). However, when LP injection started, this difference disappears. Earlier ACC injection causes earlier CL gas void fraction decrease to zero as shown in Figure 236. The influence on minimum and maximum DC temperature (see Figure 237) and heat transfer coefficient (see Figure 238), respectively, is very small. Also, RPV inner surface temperature range (minimum and maximum) shown in Figure 239 only slightly changed.

To conclude, the impact of decreasing ACC opening setpoint is very small, partly due to the fact that both HP and LP injections pump flow rates are higher than ACC flows. Also, the time difference between 2.6 MPa and 2.0 MPa cases injection start is around 400 s, what means around 16 tons of injected mass for all 4 ACCs what is less than 2% of total injected mass (see Figure 235).
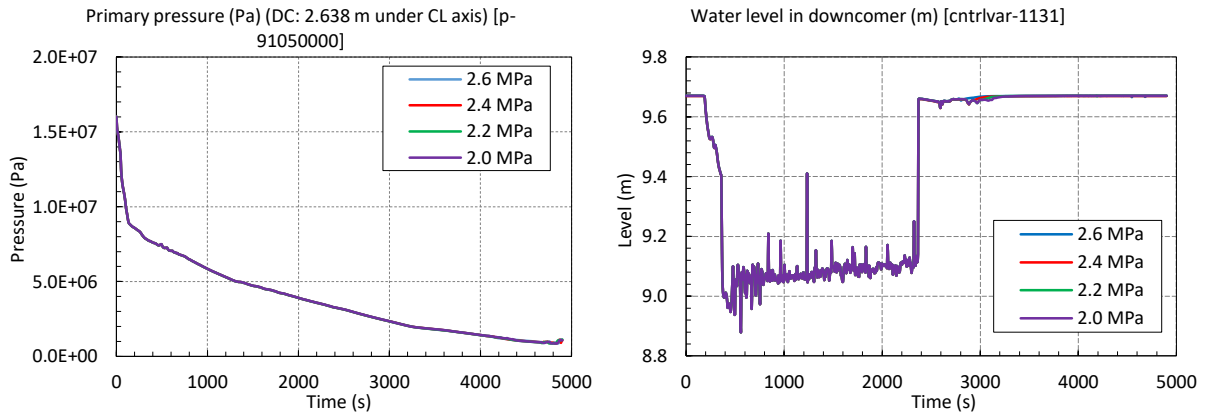
Figure 234: RELAP5 comparisons of Pressure in the DC at 2.638 m below the CL Axis (left) and DC Level for different ACC Pressures (right).
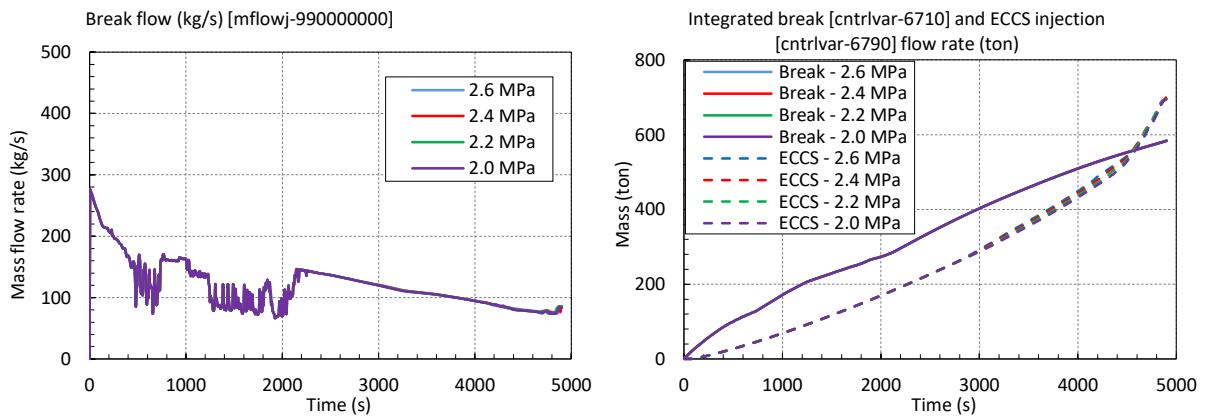
Figure 235: RELAP5 comparisons of Break Flow (left) and Time-integrated Coolant Loss and ECCS Injection for different ACC Pressures (right).
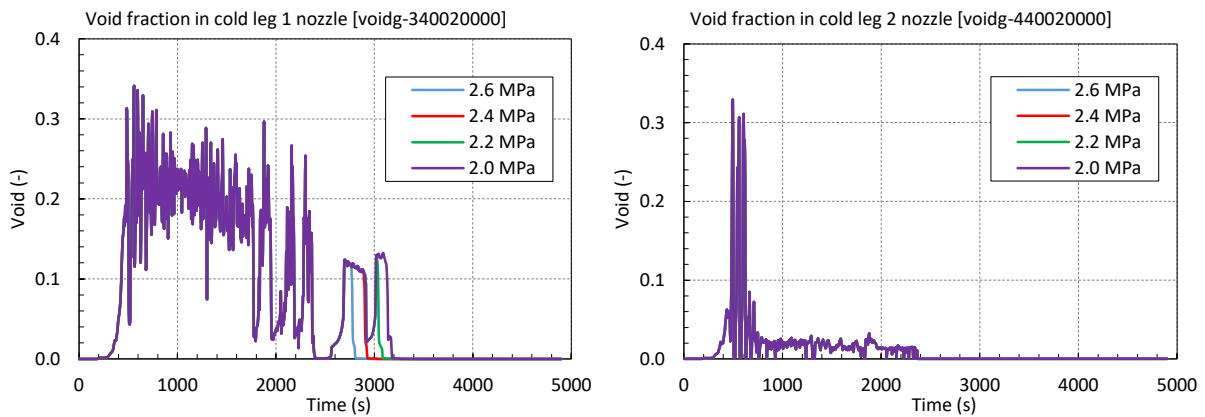
Figure 236: RELAP5 comparisons of Void Fraction at the RPV Inlets of Loops 1 (left) and 2 (right) for different ACC Pressures.

Minimum [cntrlvar-5301] and maximum [cntrlvar-5311]
temperature in the DC at 1.13 m (°C)

Minimum [cntrlvar-5302] and maximum [cntrlvar-5312]
temperature in the DC at 2.638 m (°C)
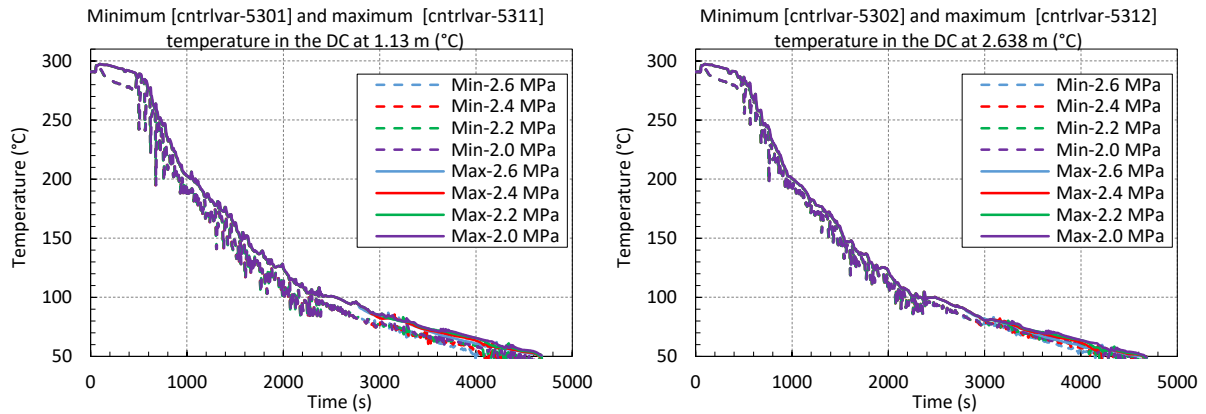
Figure 237: RELAP5 comparisons of DC Coolant Temperature (Minimum and Maximum) at 1.13 m (left) and 2.638 m (right) below the CL Axis for different ACC Pressures.

Min and max HTC around the DC at 1.13 m under CLs axis
(DC 09(1-8)-03) (W/m2-K) [hthtc-240(1-8)00300]

Min and max HTC around the DC at 2.638 m under CLs
axis (DC 09(1-8)-05) (W/m2-K) [hthtc-240(1-8)00500]
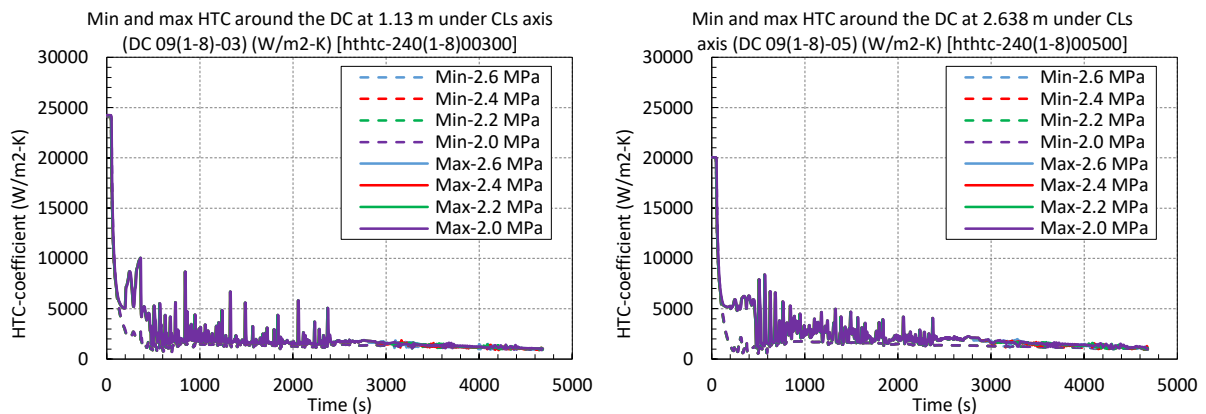
Figure 238: RELAP5 comparisons of DC HTC (Minimum and Maximum) at 1.13 m (left) and 2.638 m (right) below the CL Axis for different ACC Pressures.

Min and max RPV Inner Surface Temperature at 1.13 m
under CLs axis (°C) [httemp-240(1-8)00301]

Min and max RPV Inner Surface Temperature at 2.638 m
under CLs axis (°C) [httemp-240(1-8)00501]
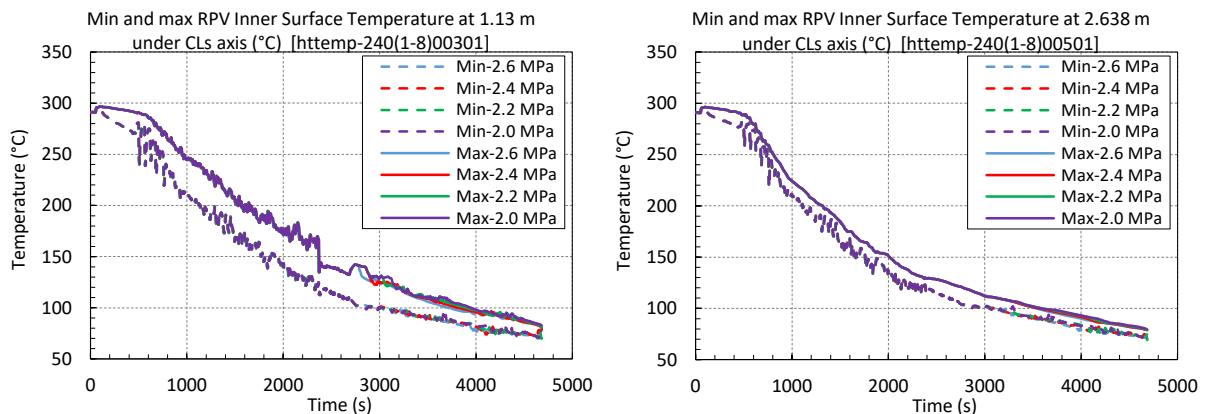
Figure 239: RELAP5 comparisons of RPV Inner Surface Temperature Range (Minimum and Maximum) at 1.13 m (left) and 2.638 m (right) below the CL Axis for different ACC Pressures.

5.6.2   RELAP5 results by WUT

The reduction of the ACC pressure is simulated by decreasing the ACC pressure from the reference value of 26 bar to 20 bar. Comparative plots for key quantities of interest are provided in Figure 240 through Figure 245. The calculations show that the decrease of the ACC pressure slightly increases the water temperature in the DC due to the fact that the ACC injection is postponed from 2790 s to 3160 s and additionally due to the fact that lower amount of water is injected. The studied LTO improvement provides no significant benefit from a PTS perspective.
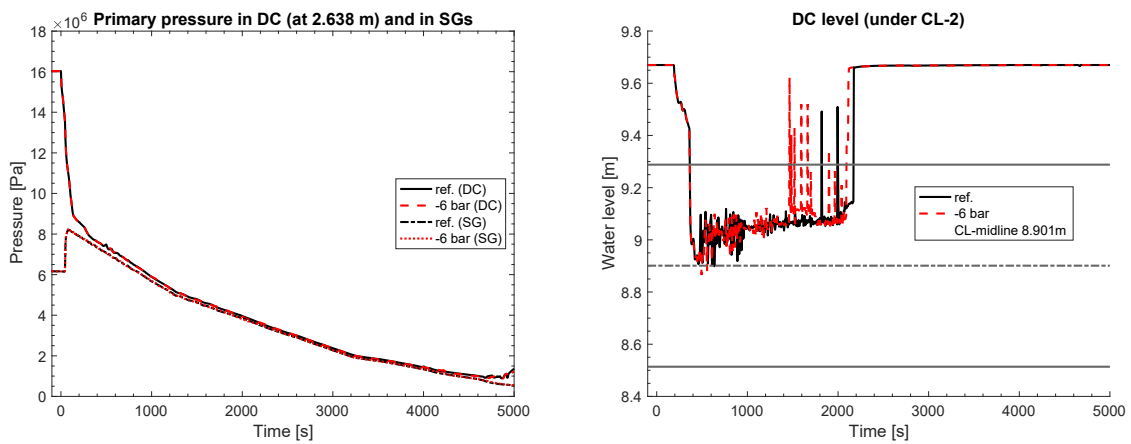
Figure 240: Comparisons of (left) pressure in the DC at 2.638 m below the CL-2 axis and (right) DC level for different ACC pressures.
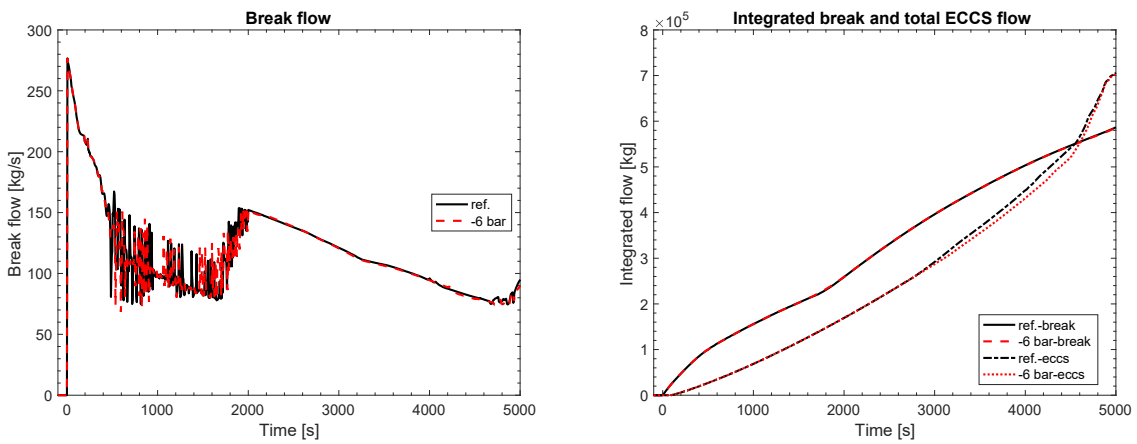
Figure 241: Comparisons of (left) Break flow and (right) time-integrated coolant loss and ECCS injection different ACC pressures.
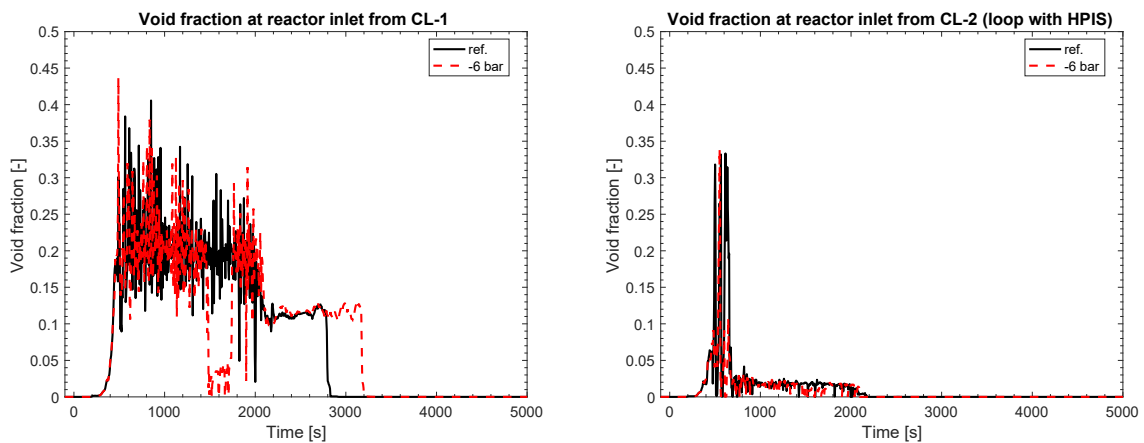
Figure 242: Comparisons of void fraction at the RPV Inlets of Loops 1 (left) and 2 (right) for different ACC pressures.
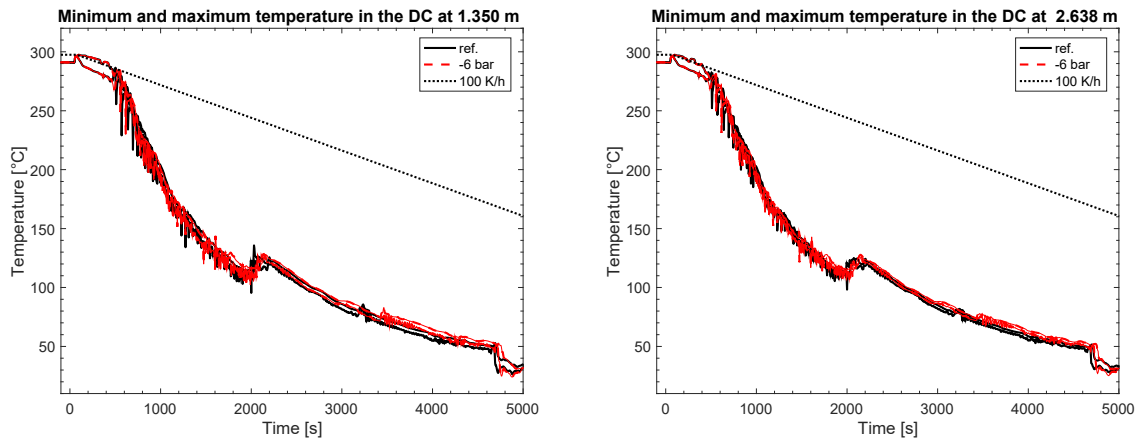
Figure 243: Comparisons of DC coolant temperature range (minimum to maximum) at (left) 1.35 m and (right) 2.638 m below the CL axis for different ACC pressures.
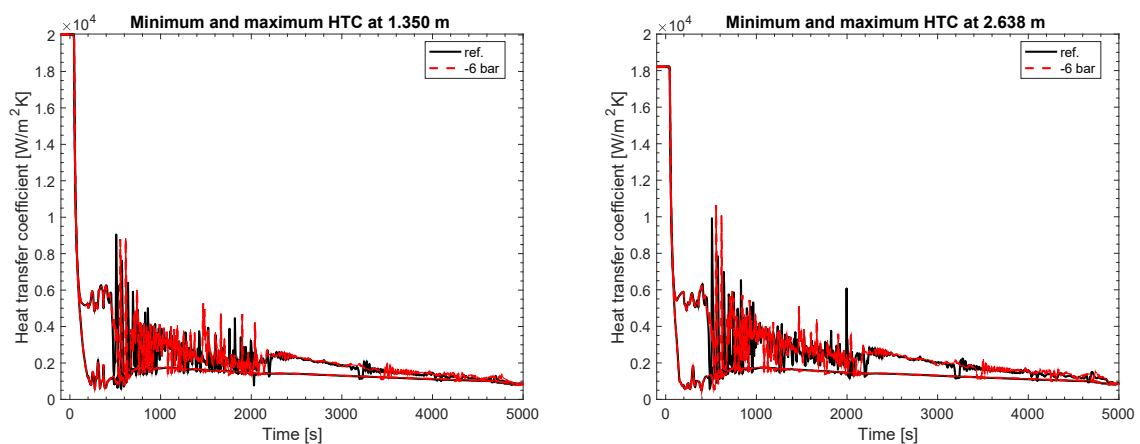
Figure 244: Comparisons of DC HTC range (minimum to maximum) at (left) 1.35 m and (right) 2.638 m below the CL Axis for different ACC pressures.
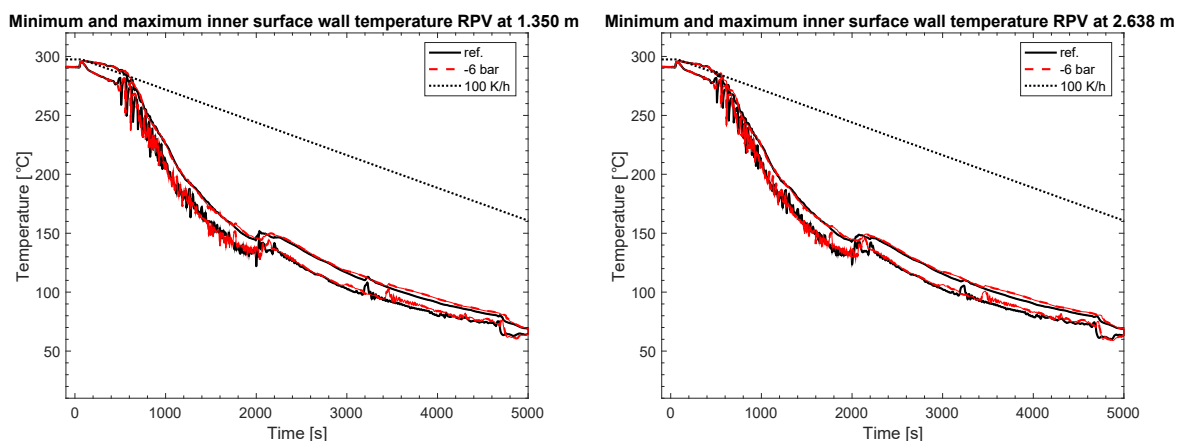
Figure 245: Comparisons of RPV inner surface temperature range (minimum to maximum) at (left) 1.35 m and (right) 2.638 m below the CL axis for different ACC pressures.

5.6.3   TRACE results by PSI

This proposed LTO improvement is modelled by reducing the initial pressure in the ACCs from the nominal value of 2.6 MPa to 2 MPa in decrements of 2 bar. Comparative plots for key quantities of interest are provided in Figure 246 through Figure 251. While the reduced ACC pressure does have some effect on the results between 2000 and 3000 s, the overall impact on PTS is likely small for this particular SB-LOCA scenario.

158
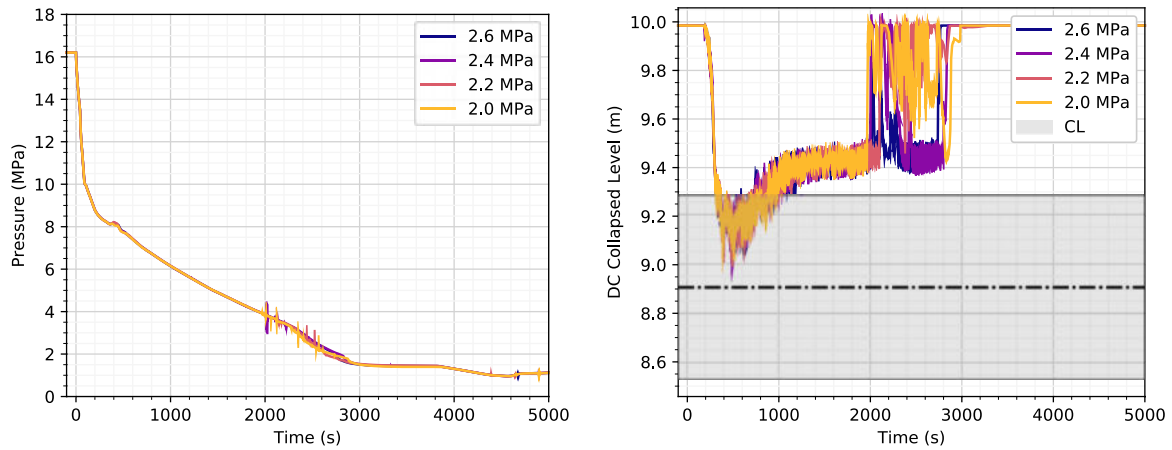
Figure 246: Comparisons of (left) Pressure in the DC at 2.638 m below the CL Axis and (right) DC Level for different ACC Pressures.
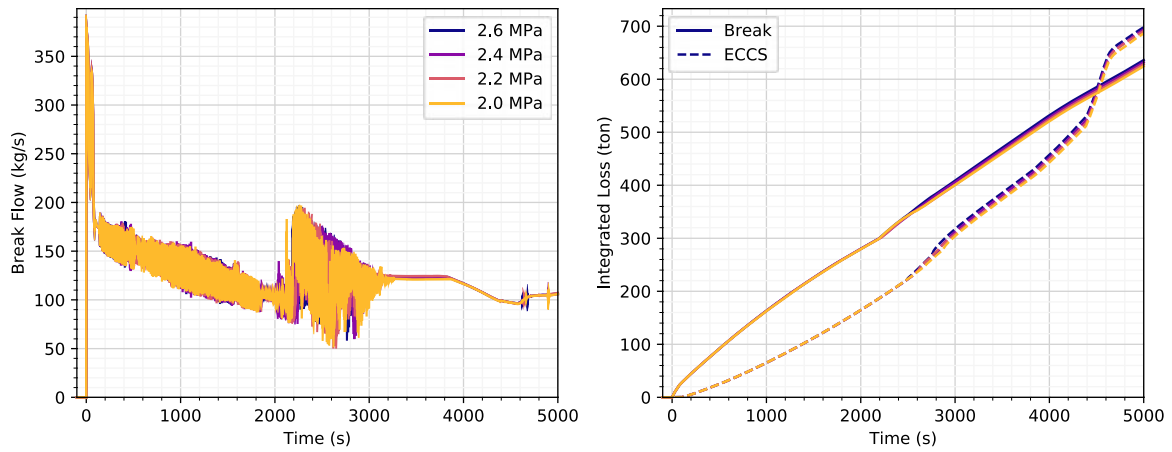
Figure 247: Comparisons of (left) Break Flow and (right) Time-integrated Coolant Loss and ECCS Injection for different ACC Pressures.
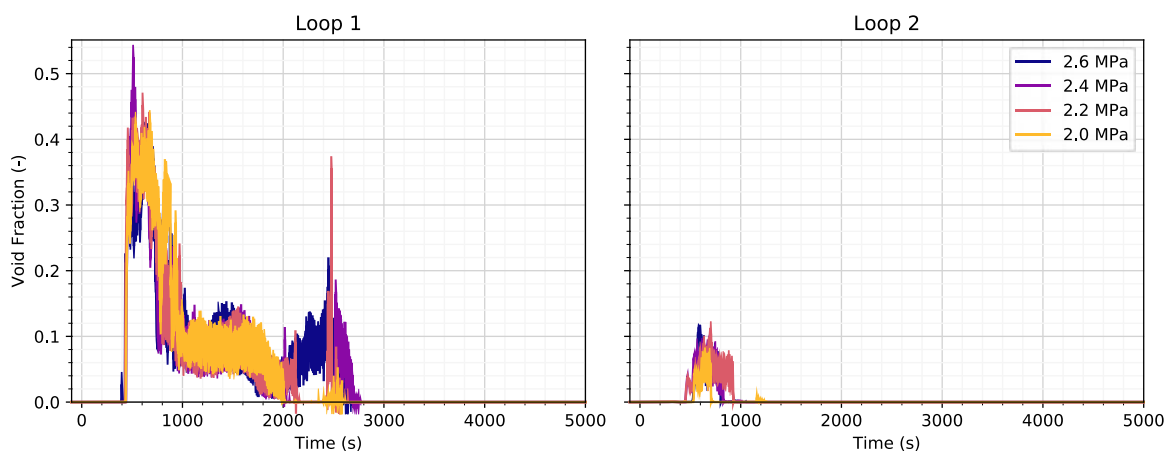
Figure 248: Comparisons of Void Fraction at the RPV Inlets of Loops 1 and 2 for different ACC Pressures.
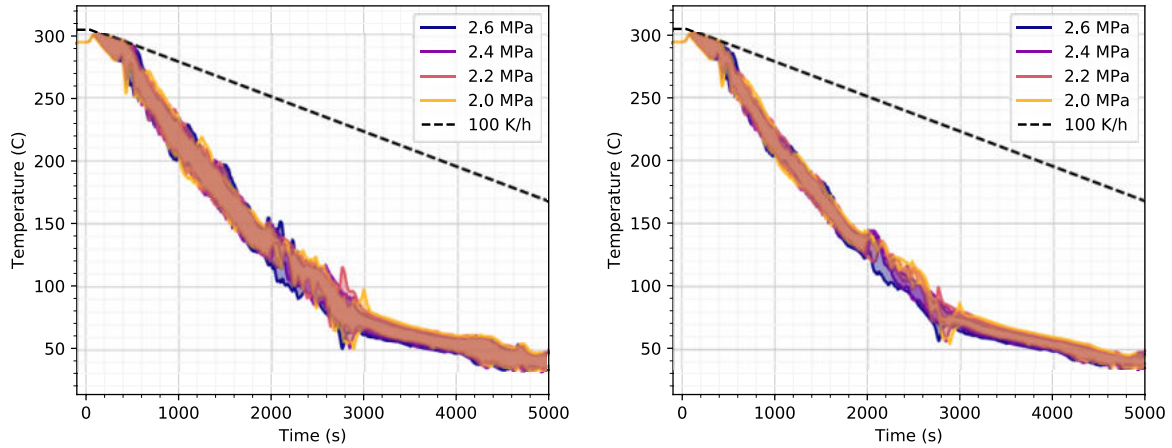
Figure 249: Comparisons of DC Coolant Temperature Range (Minimum to Maximum) at (left) 1.35 m and (right) 2.638 m below the CL Axis for different ACC Pressures.
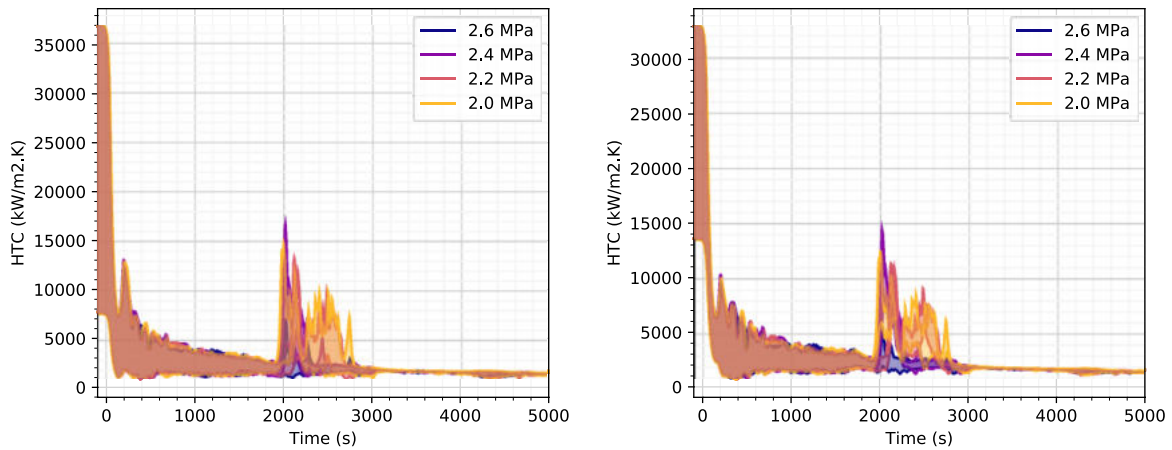
Figure 250: Comparisons of DC HTC Range (Minimum to Maximum) at (left) 1.35 m and (right) 2.638 m below the CL Axis for different ACC Pressures.
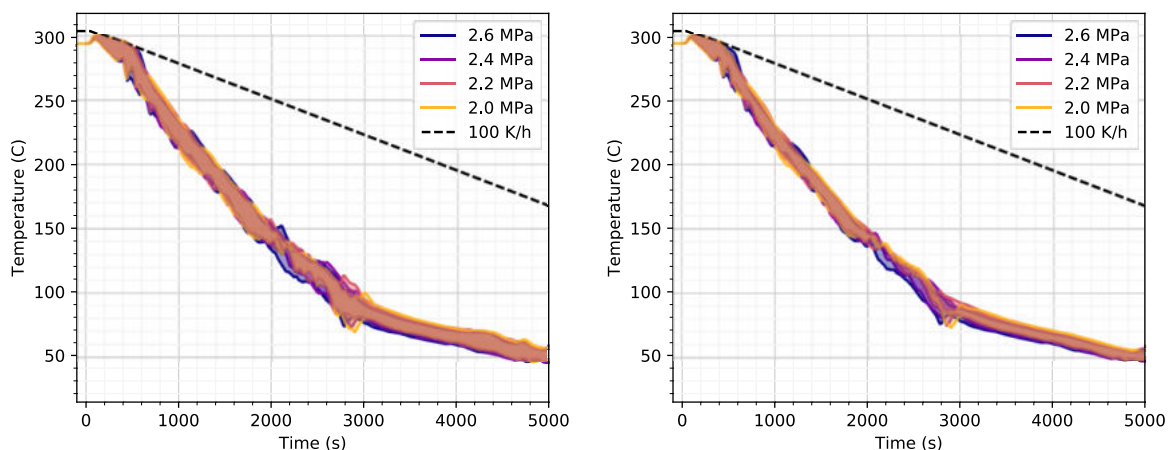
Figure 251: Comparisons of RPV Inner Surface Temperature Range (Minimum to Maximum) at (left) 1.35 m and (right) 2.638 m below the CL Axis for different ACC Pressures.

160

5.7 Summary of LTO improvements

Of the six potential LTO improvements considered in the TRACE simulations by PSI, only the heating of water in HPI tanks showed a clear benefit for the SBLOCA considered. A summary of conclusions for the considered LTO improvements is given in Table 16.

Table 16: Summary of Conclusions for Candidate LTO Improvements based on the TRACE simulations by PSI

LTO Improvement	Conclusion
Heating of water in HPI tanks	Potentially beneficial
Heating of water in ACCs	No clear benefit for SBLOCA
Heating of water in LPI tanks	No clear benefit for SBLOCA
Decreasing the HPI head	Unclear. Potentially detrimental
Decreasing the HPI capacity	Unclear. Potentially detrimental
Decreasing the ACC pressure	No clear benefit for SBLOCA

Of the four potential LTO improvements considered in the RELAP5 simulations by WUT, only the heating of water in HPI tanks show a clear benefit for the considered transient (SBLOCA). A summary of conclusions for the considered LTO improvements is given in Table 17.

Table 17: Summary of Conclusions for Candidate LTO Improvements based on the RELAP5 simulations by WUT

LTO Improvement	Conclusion
Heating of water in HPI tanks	Potentially beneficial
Heating of water in ACCs	Insignificant benefit for SBLOCA
Heating of water in LPI tanks	Insignificant for SBLOCA
Decreasing the ACC pressure	Insignificant benefit for SBLOCA

Heating of water in HPI tanks was simulated with RELAP5 by UJV. The simulation results indicate that the increased injection temperature results in a higher temperature of the water in the reactor DC (Table 18).

Table 18: Conclusion for Candidate LTO Improvement based on the RELAP5 simulations by UJV

LTO Improvement	Conclusion
Heating of water in HPI tanks	Potentially beneficial

Of the two potential LTO improvements considered in the RELAP5 simulations by SSTC the reduced HPI head led to a reduction in RPV cooldown rate before restoration of DC level, which can be considered as a beneficial effect for the SBLOCA transient in question. Decreasing HPI capacity showed increased DC temperature before filling the primary side with coolant and therefore also this can be seen as beneficial from the PTS point of view. Table 19 summarizes the conclusions from the SSTC simulations of LTO improvements.

Table 19: Summary of Conclusions for Candidate LTO Improvements based on the RELAP5 simulations by SSTC

LTO Improvement	Conclusion
Decreasing HPI head	Potentially beneficial in the early phase of the transient
Decreasing HPI capacity	Potentially beneficial in the early phase of the transient

161

KIWA simulated one LTO improvement with RELAP5, namely the decreasing HPI capacity. The results show that the proposed LTO improvement does have some impact on the major system parameters as coolant and wall temperatures in the DC. It can be concluded that by decreasing rate of cooling (via HPI pumps) the coolant temperatures can be reduced to some extent as well. Thus the more the decrease in HPI flows is the more a risk of PTS is reduced. Benefits proposed and presented in this LTO improvement in the early stage of the transient can be mitigated to some extent by the increased temperature gradients in DC that appears after the accumulator injections (Table 20).

Table 20: Conclusion for Candidate LTO Improvement based on the RELAP5 simulations by KIWA

LTO Improvement	Conclusion
Decreasing HPI capacity	Potentially beneficial in the early phase of the transient. These benefits might be however reduced by the accumulator injection in later phase of the transient.

Decreasing ACC pressure was simulated with RELAP5 by JSI. RELAP5 calculations showed that this LTO improvement has very small impact on the results, partly due to the fact that in the selected scenario both HP and LP injections pump flow rates are higher than ACC flows. No clear benefit for SBLOCA could be seen (Table 21).

Table 21: Conclusion for Candidate LTO Improvement based on the RELAP5 simulations by JSI

LTO Improvement	Conclusion
Decreasing ACC pressure	No clear benefit for SBLOCA

Heating of water in ACCs and heating of water in LPIS tanks were the LTO cases simulated with the KWU-MIX code by Fra-G. A comparison of the temperatures in Figure 148 with those from the base case shown in Figure 94 leads to the conclusion that heating the water in the ACCs has a small effect on the temperatures at the cold-leg nozzle and in the plumes in the DC. This follows directly from the small effect that the ACC injection has on the temperatures at the inlet to the cold-leg nozzle, which is due to the small leak size and correspondingly small injection flow rate. The HTCs in Figure 150 are nearly the same as those for the base case, shown in Figure 96. The HTCs are a function of the velocity, and the velocity in the plume is a result of buoyancy force and inertia. The buoyancy force is a function of the temperature difference between the plume and the ambient, which is nearly the same for the base case and for this case. The inertia is a result of the injection flow rate, which is also nearly the same for the base case and for this case. Consequently, the HTCs are nearly the same for the two cases.

A comparison of Figure 180 with Figure 91 shows that heating the water in the LPSI tanks to 40°C increases the temperature of the cold-water layer at the cold-leg nozzle to approximately 30 °C during the time span for LPSI from approximately 4550 s until the end of the simulation. This has the potential to partially offset the effect of the increased HTC that occurs during LPSI injection for both the base case and this case. The downstream temperatures in the plumes in the DC are correspondingly higher after 4550 s.

The HTCs during the time span from 4550 s until the peak injection flow rate at 4700 s are slightly larger near the bottom of the DC for the base case than for this case, due to the slightly larger velocity for the base case that results from the slightly larger temperature difference between the plume and the ambient. A summary of conclusions for the considered LTO improvements is given in Table 22.

Table 22: Summary of Conclusions for Candidate LTO Improvements based on the KWU-MIX simulations by Fra-G

LTO Improvement	Conclusion
Heating of water in ACC	Insignificant for SBLOCA

Heating of water in LPIS tanks	Potentially beneficial

Of the three potential LTO improvements considered in the ATHLET simulations by GRS, none showed a clear benefit regarding PTS for the investigated plant model and break size. This applies for the stand-alone code calculation with ATHLET with and without applying ATHLET's inherent mixing model ECC-MIX as well as for using GRS-MIX in post-TH-simulations on ATHLET simulation results. For the LTO improvement decreasing HPI head a drop of the fluid temperature in the DC during ACC and LP injection was observed which potentially leads to detrimental conditions. However, this behaviour was not equally reproduced when the mixing codes ECC-MIX or GRS-MIX where applied. A final assessment of this LTO improvement based on the accomplished simulations by GRS could not be achieved. A summary of conclusions for the considered LTO improvements is given in Table 23.

Table 23: Summary of Conclusions for Candidate LTO Improvements based on the ATHLET and GRS-MIX simulations by GRS

LTO Improvement	Conclusion
Heating of water in ACC	Insignificant benefit for SBLOCA
Heating of water in LPI tanks	Insignificant benefit for SBLOCA
Decreasing the HPI head	Unclear. Potentially detrimental

The final assessment of the effect of different LTO improvements will be done in WP3 and WP4 of the APAL project.

6   Simulation results of the impact of human factors

6.1   Reduction of HPIS flow by operator

6.1.1   RELAP5 results by WUT

The reduction of HPIS flow by operator is simulated by switching off 1 of 2 HPIS pumps 1800 s after the initiation of the break. Comparative plots for key quantities of interest are provided in Figure 252 through Figure 257. The calculations show that the reduction of HPI injection, meaning less injected cold water to RCS, results in a higher temperature of the water in the DC starting at 1800 s. Additionally, the lower break flow, the lower water level in the DC and the higher void fraction is observed after this operator action. The studied LTO improvement could potentially be beneficial from a PTS perspective.
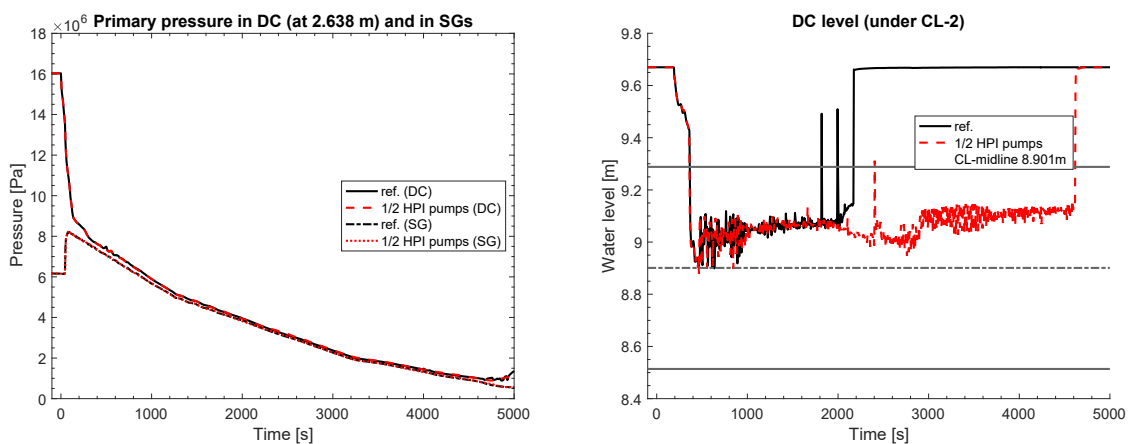
Figure 252: Comparisons of (left) pressure in the DC at 2.638 m below the CL-2 axis and (right) DC water level for the reduction of HPIS flow by operator.

163
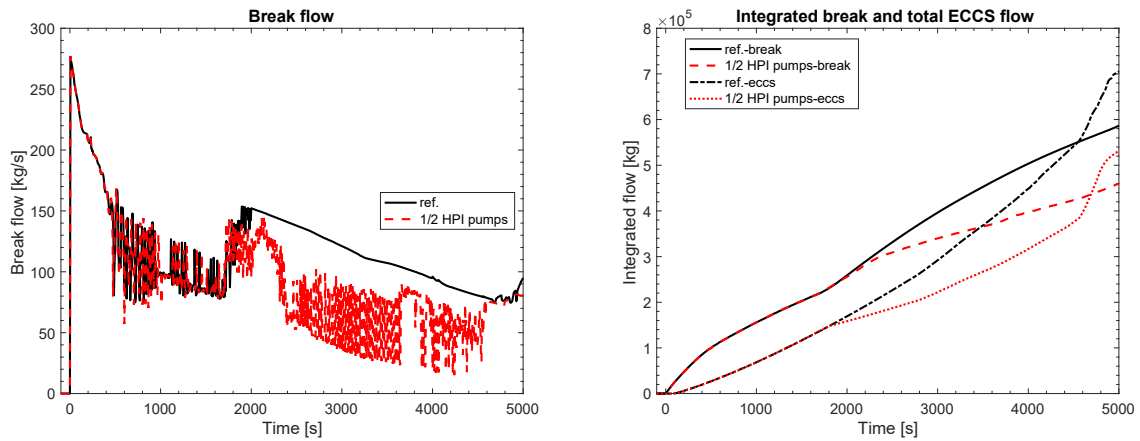
Figure 253: Comparisons of (left) Break flow and (right) time-integrated coolant loss and ECCS injection for the reduction of HPIS flow by operator.
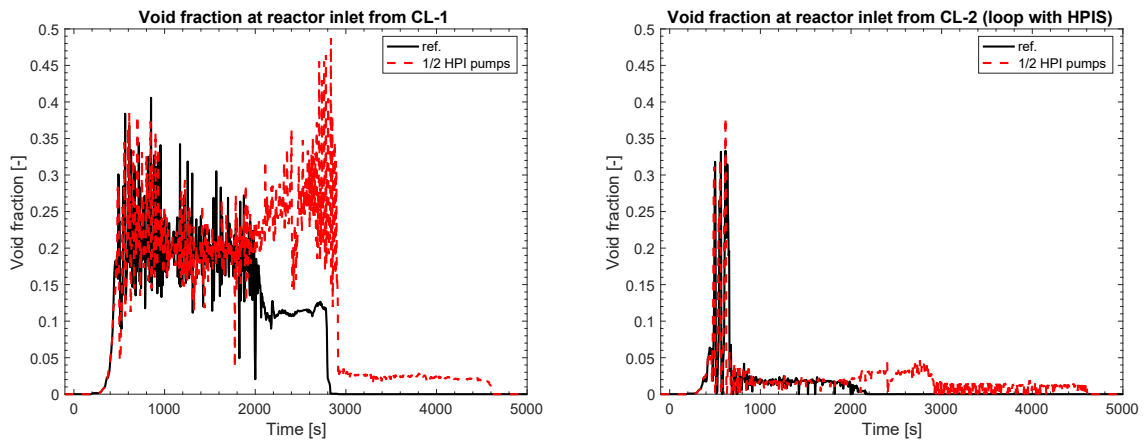
Figure 254: Comparisons of void fraction at the RPV inlets of Loops 1 and 2 for the reduction of HPIS flow by operator.
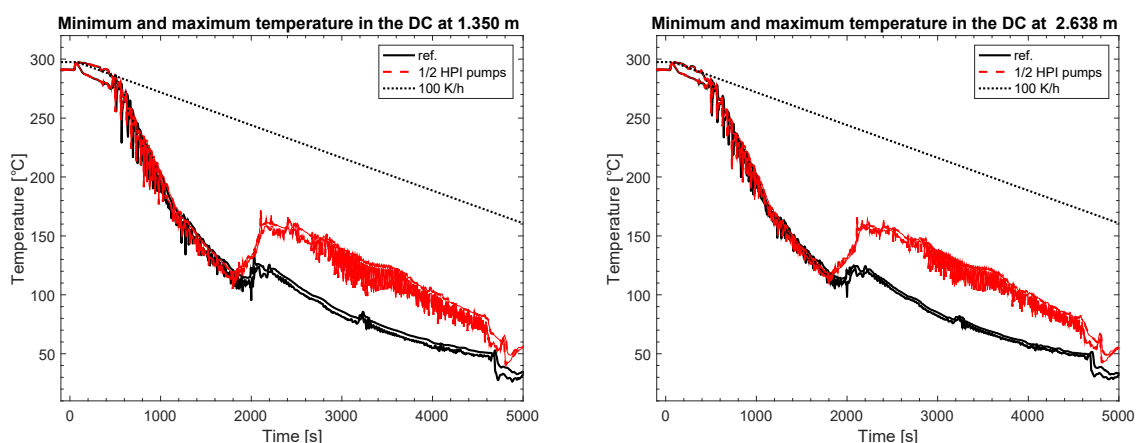
Figure 255: Comparisons of DC coolant temperature range (minimum to maximum) at (left) 1.35 m and (right) 2.638 m below the CL axis for the reduction of HPIS flow by operator.
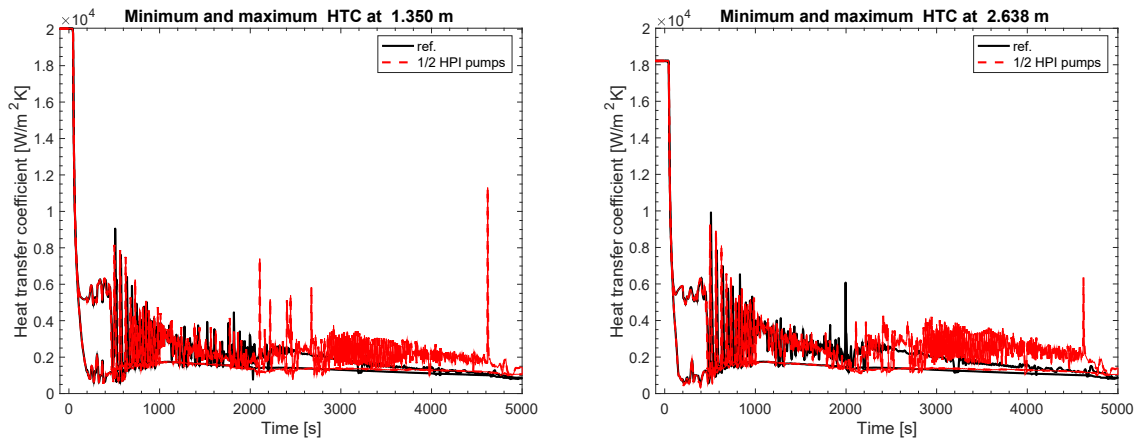
Figure 256: Comparisons of DC HTC range (minimum to maximum) at (left) 1.35 m and (right) 2.638 m below the CL axis for the reduction of HPIS flow by operator.
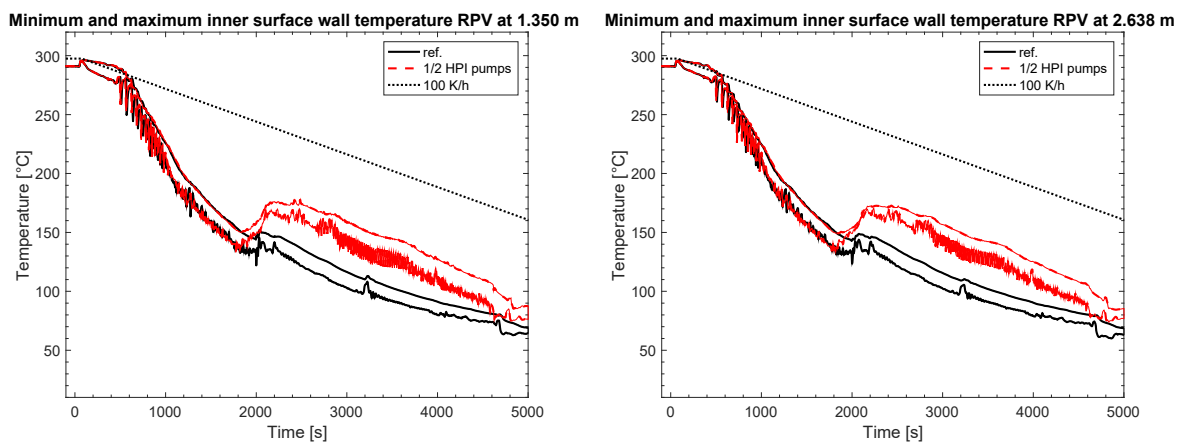
Figure 257: Comparisons of RPV inner surface temperature range (minimum to maximum) at (left) 1.35 m and (right) 2.638 m below the CL axis for the reduction of HPIS flow by operator.

6.1.2   KWU-MIX results by Fra-G

Results from the system analysis performed with RELAP5, as described in Section 6.1.1, were used as input to the fluid-mixing analysis performed with KWU-MIX. The simulation with KWU-MIX of the deactivation of one of the two active HPIS pumps at 1800 s after the initiation of the break produced data for the temperatures and heat-transfer coefficients as a function of time and location in the cold-leg nozzle and in the plumes in the DC. The flow rate of ECC water as calculated by RELAP5 is shown in Figure 258 for the two CLs with HPIS injection.
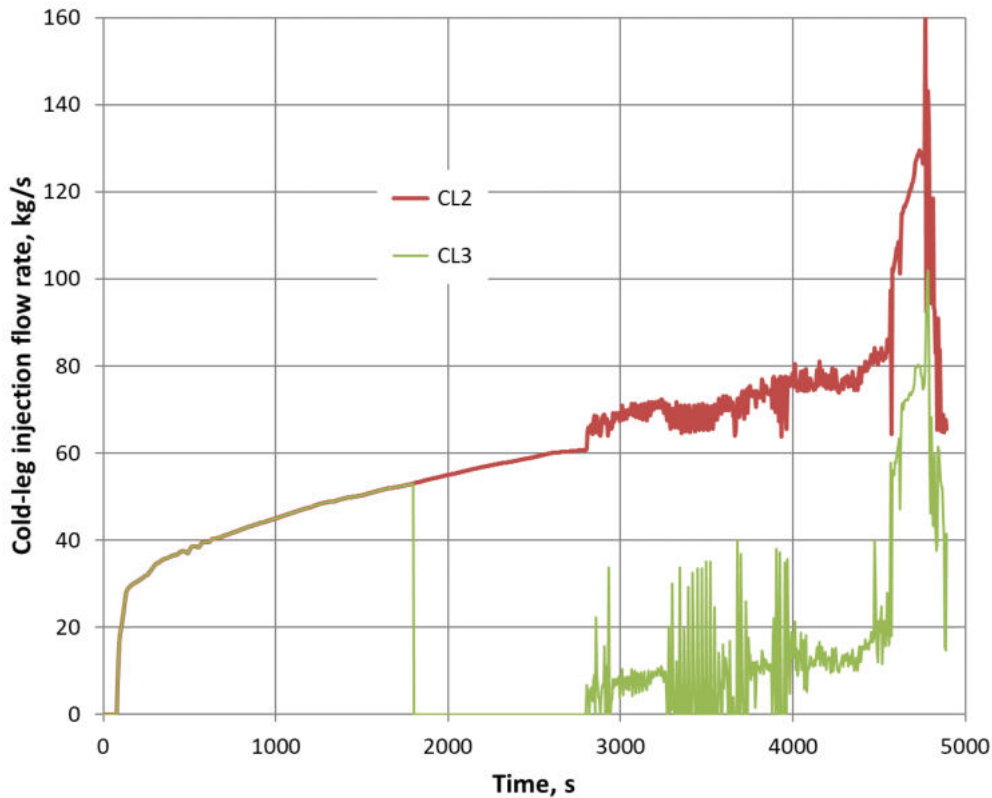
Figure 258: Flow rate of injected ECC water into each of the CLs as calculated by RELAP5.

6.1.2.1   Cold-leg nozzle

The end of the CL is the right-hand end of MR2 in KWU-MIX, as shown in Figure 16. At this location, the models have finished calculating the amount of hot water that is entrained into the cold ECC water, and temperature of the resulting mixture. Figure 259 shows the temperature of the hot water as a function of time, and it is indicated by the grey curve labelled "hot layer in cold-leg nozzle". At the start of the transient, this temperature is the same as the temperature from RELAP5. The flow of water in the loop through the MCP is small enough to prevent complete mixing in the CL starting at 330 s, after which time KWU-MIX calculates a separate temperature for the hot water based on an energy balance for all the mixing regions. The effect of the deactivation of the HPSI in CL3 at 1800 s is seen by the increased water temperature in the DC. This is the water that forms the hot-water layer, whose temperature is seen in Figure 259.

Also shown in Figure 259 is the temperature of the cold water near the cold-leg nozzle in CL2 that results from the mixing of ECC water and entrained hot water. This temperature is indicated by the blue curve labelled "cold layer in cold-leg nozzle. This temperature is calculated by KWU-MIX starting at 330 s also, as soon as incomplete mixing occurs. Recall that the temperature of the ECC water is 15 °C, which is also shown in Figure 259, but it is an input to KWU-MIX rather than a result. The temperature of the cold-water layer is closer to the temperature of the ECC water than to the temperature of the hot water. This indicates that the mass flow rate of entrained hot water is less than the flow rate of ECC water. The increase in water temperature in the cold-water layer at 1800 s is also a consequence of the deactivation of the HPSI in CL3.

166
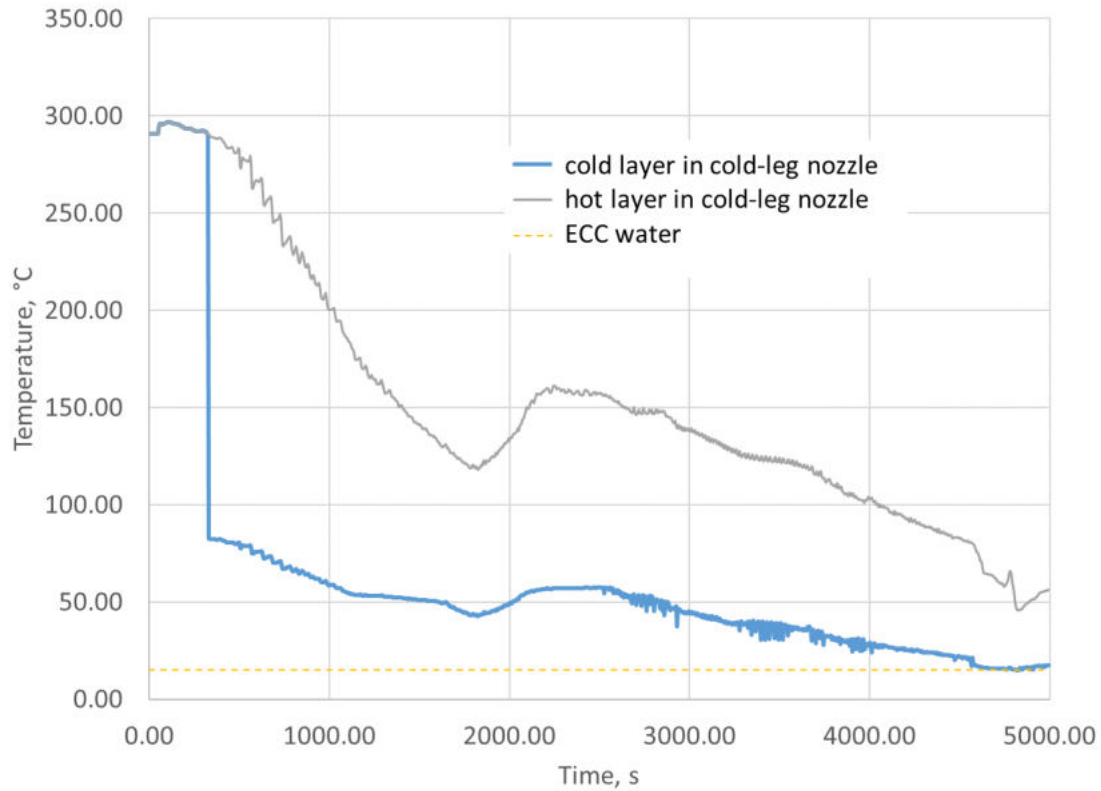
Figure 259: Temperatures of the cold-water and hot-water layers at the end of the nozzle of Cold Leg 2 calculated by KWU-MIX.

The height of the cold-water layer above the cold-leg axis at the end of the cold-leg nozzle is shown in Figure 260 as a function of time. Initially, when the ECC flow rate is small, the height of the cold-water lay is approximately 0.28 m below the axis of the CL. With increasing ECC flow, as shown in Figure 260, the height of the cold-water layer increases correspondingly. A decrease occurs at 1800 s when the HPSI in CL3 is deactivated.

167
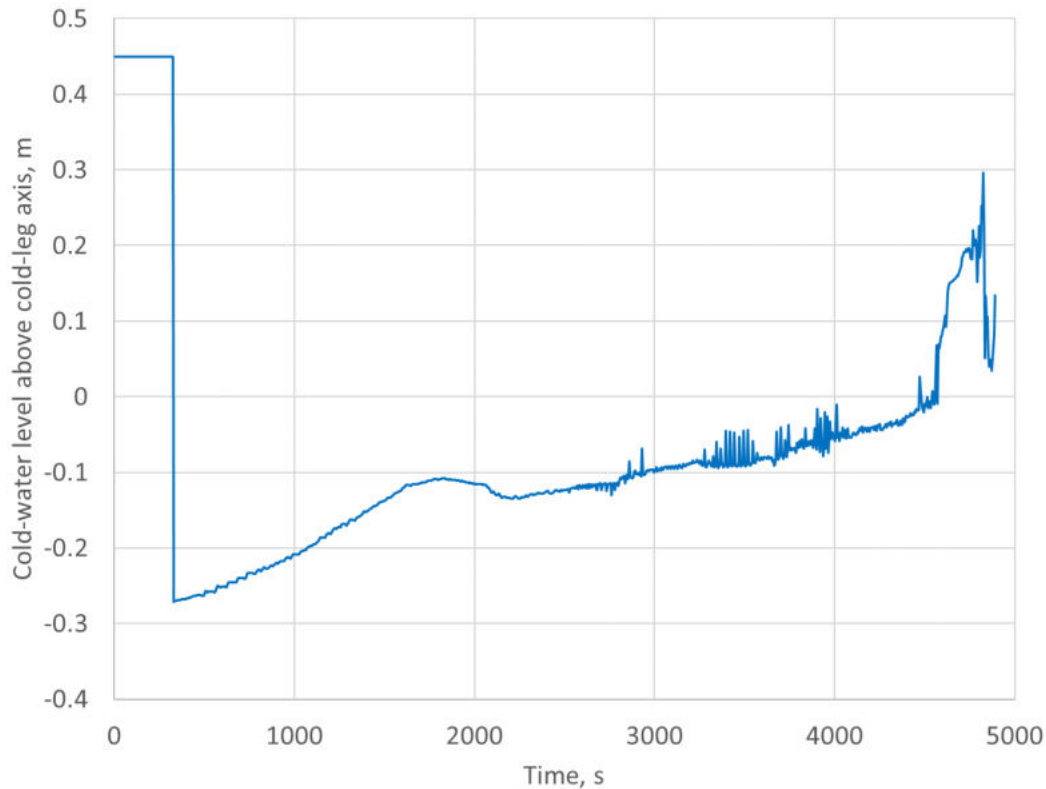
Figure 260: Height of cold-water layer above the axis of Cold Leg 2 at the inlet of the cold-leg nozzle calculated by KWU-MIX.

The height of the cold-water layer shown in Figure 260 determines the width of the plume at its origin in the DC of the RPV, just below the bottom of the cold-leg nozzle.

6.1.2.2   Inner surface of RPV wall

The transition from the end of the cold-leg nozzle to the top of the plume the RPV is referred to as MR3 in Figure 16, but it is not modelled in KWU-MIX. Instead, KWU-MIX uses the conditions at the end of MR2 as the inlet boundary conditions for MR4. Consequently, the height of the cold-water layer in the cold-leg nozzle, labelled H_c in Figure 261, determines the width of the plume at its origin in the DC.

Figure 261 shows the widths of the plumes at various distances below the cold-leg axis in the DC. The origin of the plume is 0.45 m below the cold-leg axis, which is at the bottom of the diffusor. This is the light blue curve labelled 0.45 m in Figure 261. As soon as a plume is formed at approximately 330 s, its width is approximately 0.675 m, which is less than the diameter of the end of the diffusor. The width of the plume at its origin increases with time, corresponding to the increase in the cold-water flow rate. The width reaches a maximum when the cold-water layer in the CL reaches the axis. The maximum width of the plume is not greater than the cold-leg diameter, however, because the cold water accelerates, and its width narrows as it sinks in the diffusor.

168

APAL_2.0.2_DOKU_220323.1638.56.xlsx
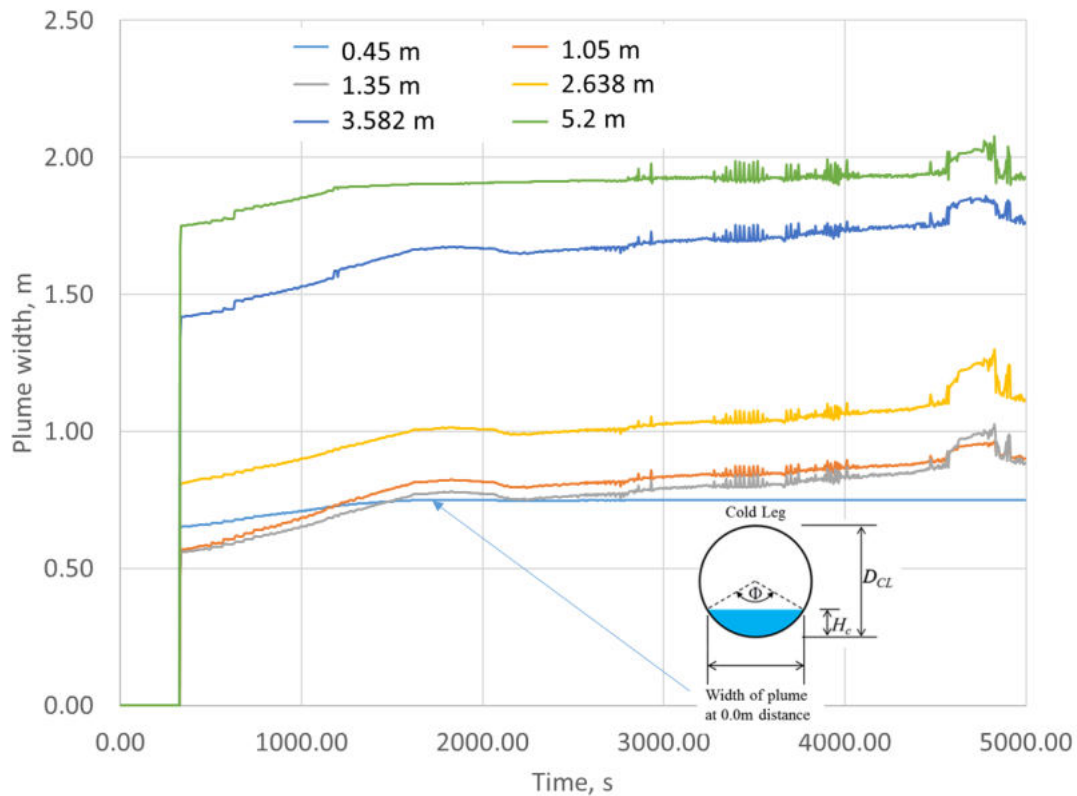
Figure 261: KWU-MIX widths of the plume at various distances below the axis of the Cold Leg 2 in the DC.

At a distance of 1.05 m below the cold-leg axis, the width of the plume early in the transient is smaller than at its origin. This is due to the strong buoyancy force that accelerates the flow in the plume, which causes the plume to become narrower. Later in the transient, this phenomenon still exists, but its magnitude decreases with time as the temperature differences decrease and the buoyance also decreases. The plume width at 1.35 m below the cold-leg axis is slightly less than at 1.05 m due to this same phenomenon.

The two neighbouring plumes at lower elevations (greater distances below the cold-leg axis) are merged until 1800 s. After the HPSI stops injecting, there is only one plume in the DC.

The temperatures at the centers of the plumes are shown in Figure 262 for various distances below the cold-leg axis. The light-blue curve labelled 0.45 m in the legend is the centerline temperature at the origin of the plume, which is at the bottom of the cold-leg nozzle. This temperature is the same as the blue curve labelled "cold layer in cold-leg nozzle" shown in Figure 260. The curves for greater distances from the origin are progressively warmer. The dark-blue curve labelled "ambient" in Figure 262 is the temperature outside of the plume. This temperature is the same as the grey curve labelled "hot layer in cold-leg nozzle" shown in Figure 260.

APAL_2.0.2_DOKU_220323.1638.56.xlsx
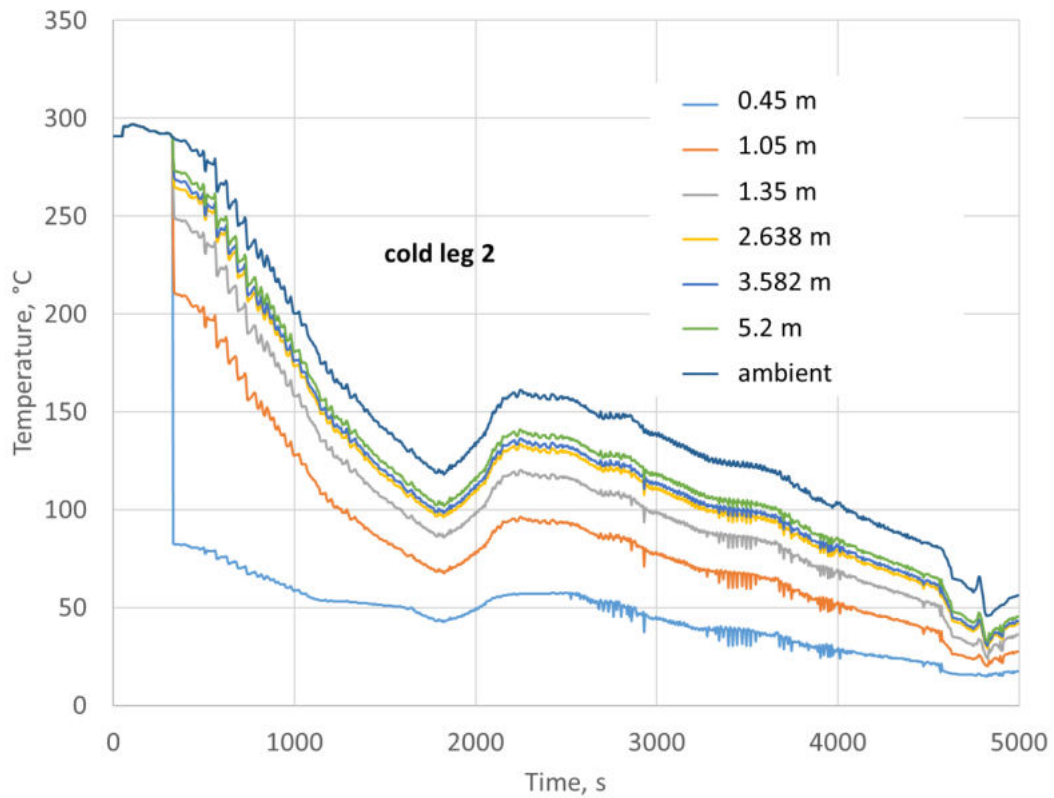
Figure 262: KWU-MIX temperatures at the middle of the plume at various distances below the axis of Cold Leg 2 in the DC.

The HTCs in the DC also have Gaussian distributions, and the widths are equal to those for the temperature shown in Figure 261 divided by a factor of 1.1045, which was taken from Chen [20]. The maximum values for the HTCs in the plumes as a function of time are shown in Figure 263 for various distances below the cold-leg axis. The light-blue curve labelled 1.05 m in the legend is the centerline HTC near the top of the plume. The curves for greater distances from the origin are progressively greater, because the buoyancy force continues to accelerate the flow more than the inertia of the entrainment tends to decelerate the flow.

170
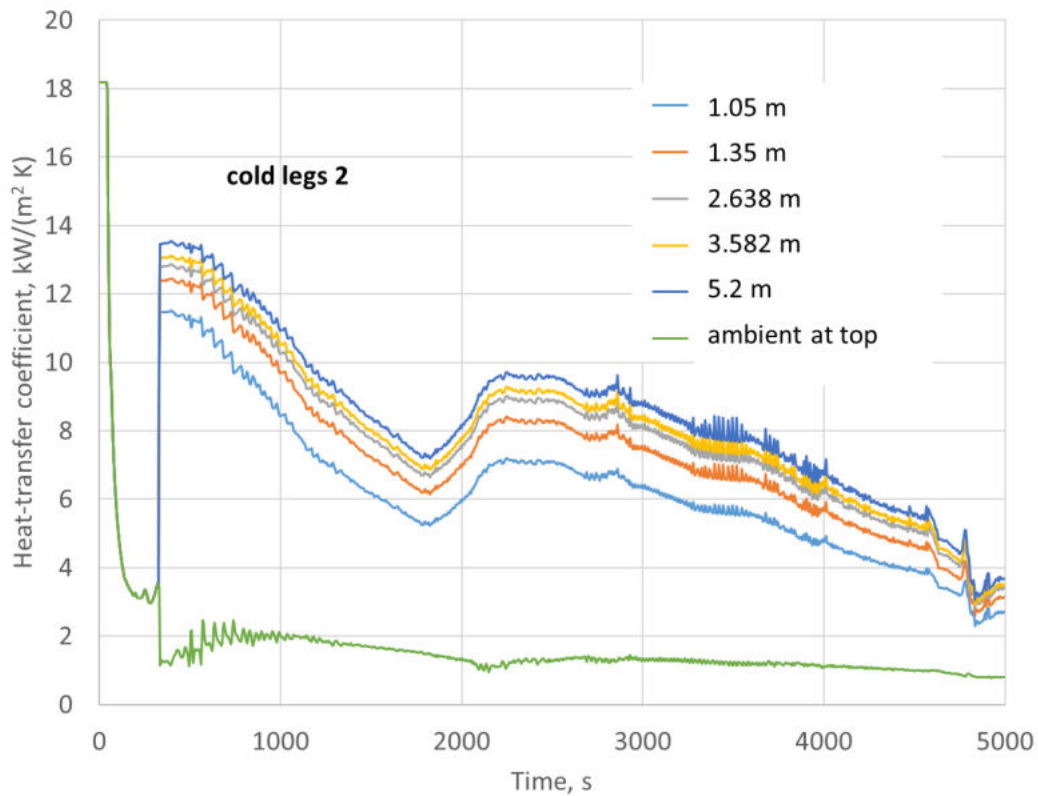
Figure 263: KWU-MIX heat-transfer coefficients at the middle of the plume at various distances below the axis of Cold Leg 2 & 3 in the DC.

Also shown in Figure 263 is the heat-transfer coefficient outside of the plumes near the cold-leg nozzle. This is the green curve labelled "ambient at top". The heat-transfer coefficient outside of the plume increases with distance from the cold-leg nozzle, as shown in Figure 264. The increase in the heat-transfer coefficient is due to a larger recirculation flow outside of the plume with increasing distance from the cold-leg nozzle. Near the cold-leg nozzle, the recirculation flow outside of the plume is only as large as the entrainment flow rate at that location. Farther from the cold-leg nozzle, the recirculation flow is equal to the entrainment flow integrated over the higher distances. Near the bottom of the DC, the recirculation flow is equal to the entire flow of entrained water, and so the heat-transfer coefficient is largest at this location.
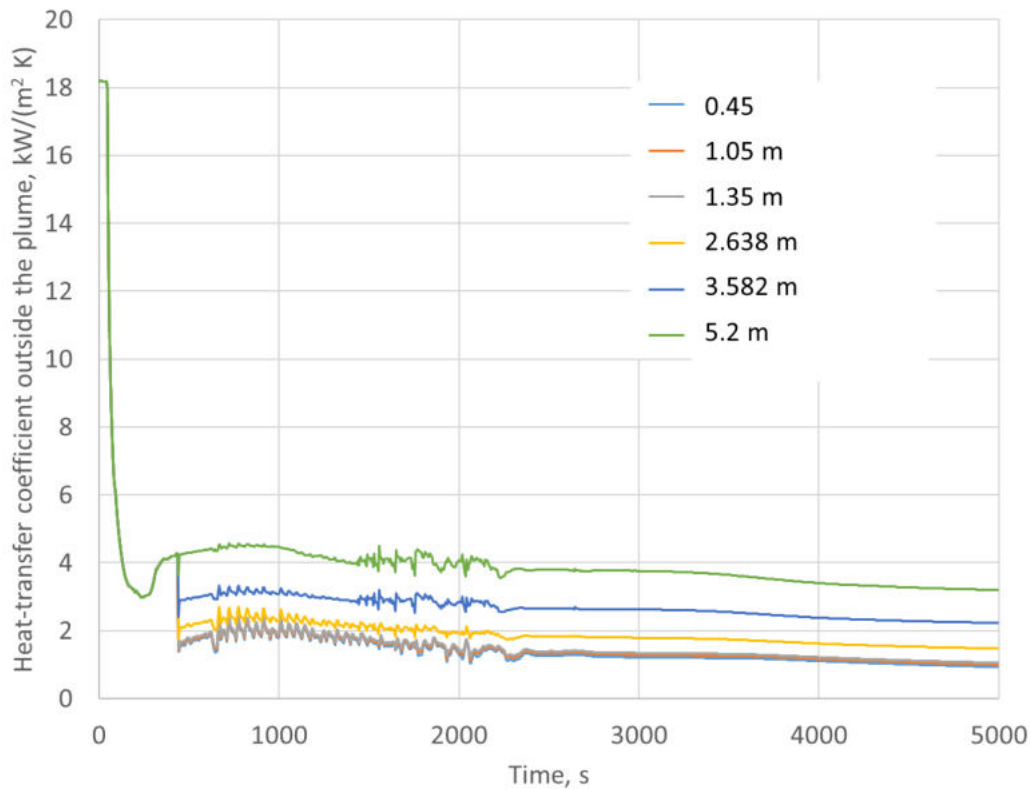
Figure 264: KWU-MIX heat-transfer coefficients outside of the plume at various distances below the cold-leg axis in the DC.

6.2 Increasing secondary-side cooldown rate by operator

6.2.1 RELAP5 results by WUT

The increase of the secondary side cooldown rate by operator is simulated by increase the cooldown of the secondary side from 100 K/h to 200 K/h. Comparative plots for key quantities of interest are provided in Figure 265 through Figure 270. The calculations show that the increase of the secondary side cooldown rate results in a faster depressurization of the primary and the secondary side. Due to the faster depressurization, the reduced time-integrated break flow and the increased time-integrated ECCS injection flow is observed up to around 4500 s. The proposed LTO improvement results in the increase of the water temperature in the DC after 2000 s. The studied LTO improvement could potentially be beneficial from a perspective of higher water temperature in DC, but at the same time, it could be detrimental from a perspective of the faster pressure drop in DC. The overall benefit of this LTO improvement needs to be verified by the structural analysis.
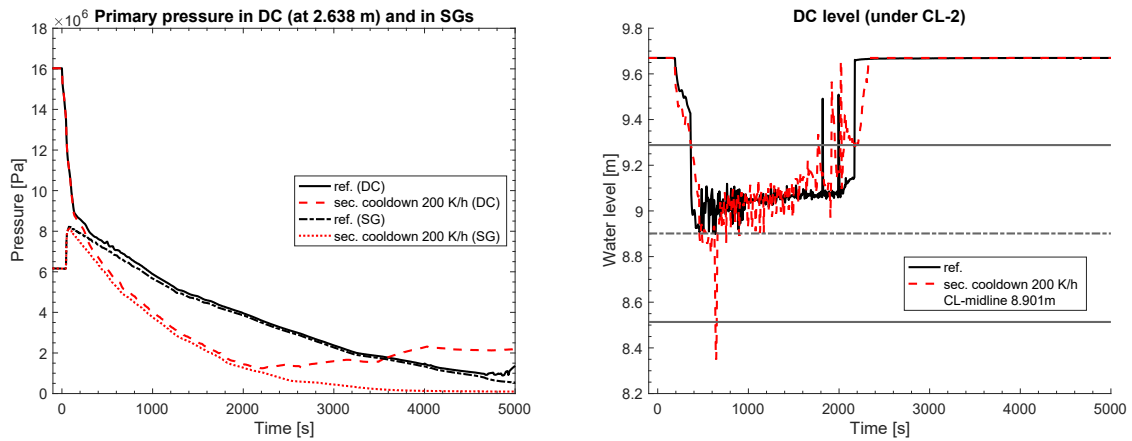
Figure 265: Comparisons of (left) pressure in the DC at 2.638 m below the CL-2 axis and (right) DC level for the increasing secondary side cooldown rate by operator.
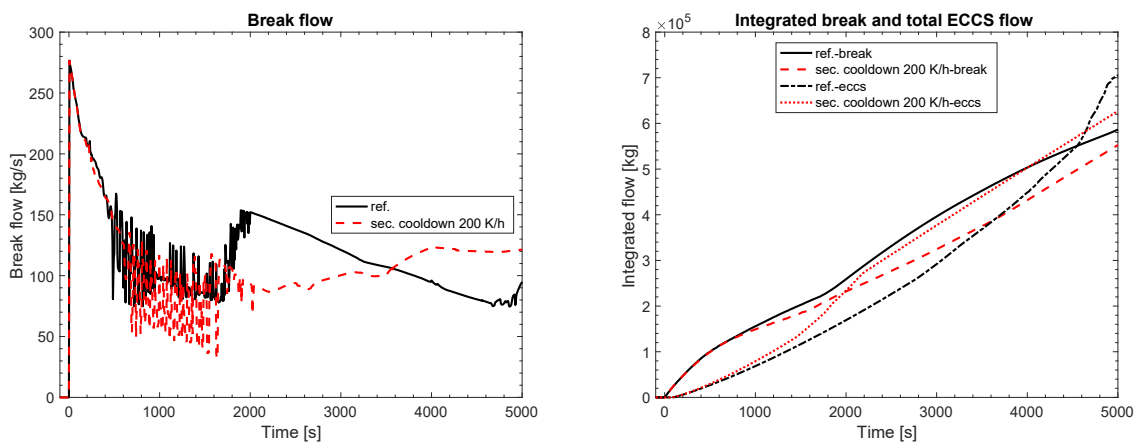
Figure 266: Comparisons of (left) Break flow and (right) time-integrated coolant loss and ECCS injection for the increasing secondary side cooldown rate by operator.
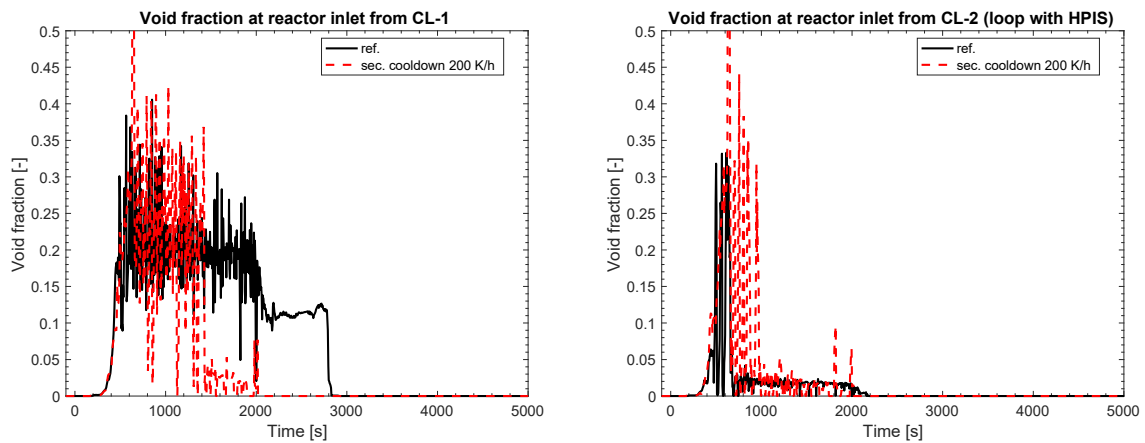
Figure 267: Comparisons of void fraction at the RPV inlets of Loops 1 and 2 for the increasing secondary side cooldown rate by operator.
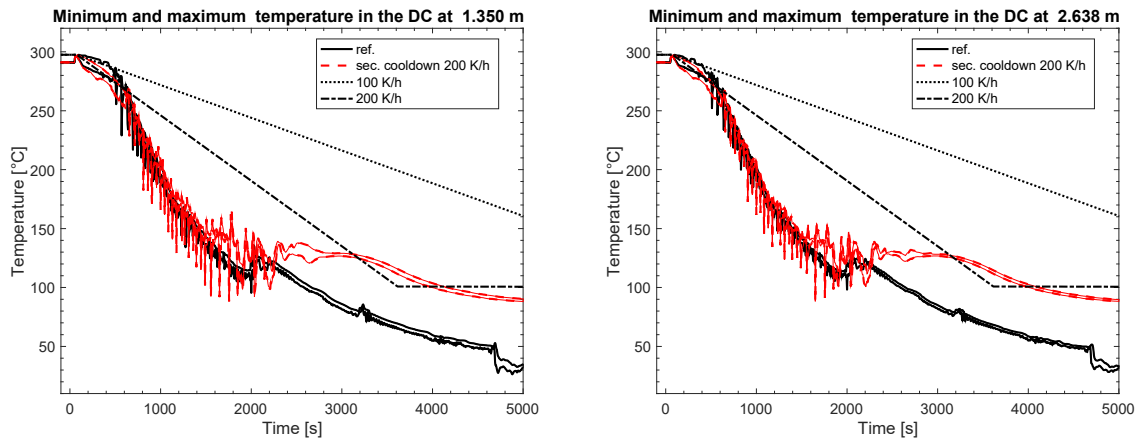
Figure 268: Comparisons of DC coolant temperature range (minimum to maximum) at (left) 1.35 m and (right) 2.638 m below the CL axis for the increasing secondary side cooldown rate by operator. The 200 K/h curve becomes flat at 3540 s – the pressure at SGs reaches 1 bar and for that pressure, the saturation temperature is around 100 °C.
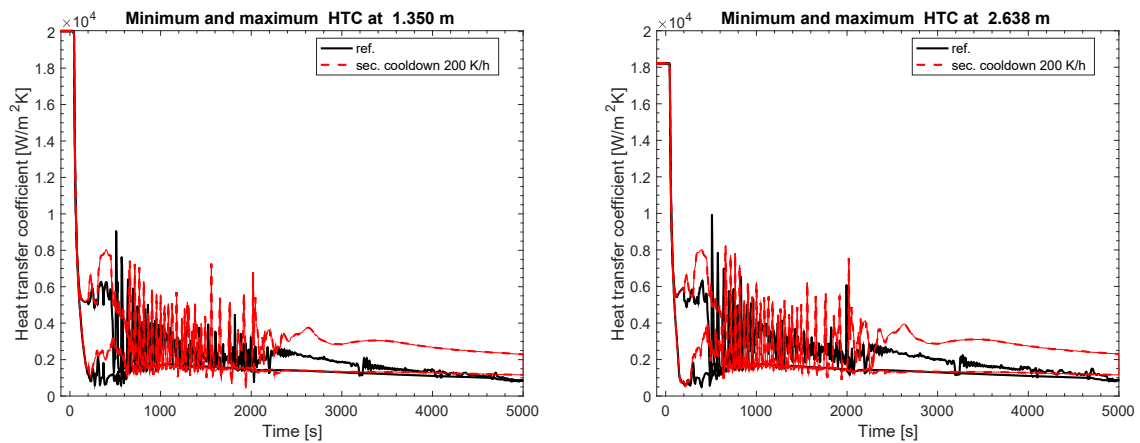
Figure 269: Comparisons of DC HTC range (minimum to maximum) at (left) 1.35 m and (right) 2.638 m below the CL axis for the increasing secondary side cooldown rate by operator.
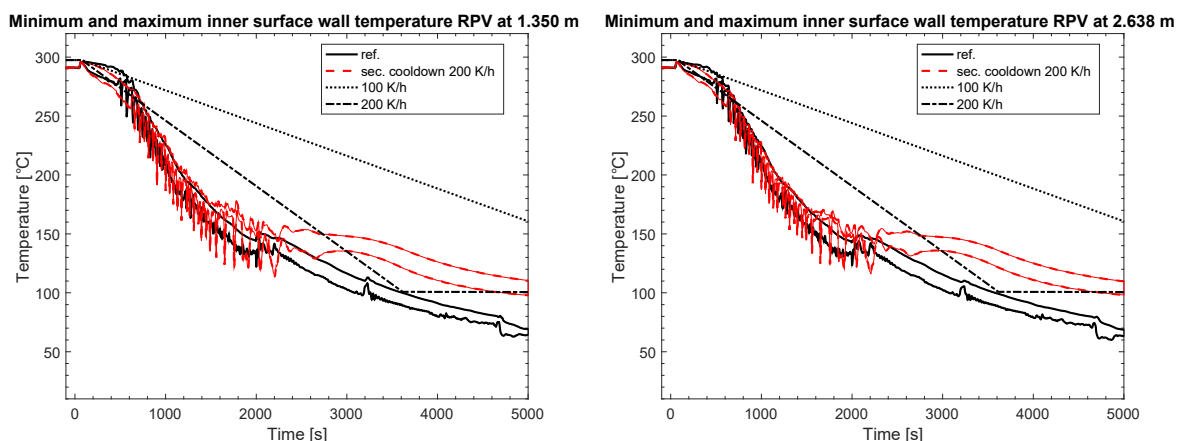
Figure 270: Comparisons of RPV inner surface temperature range (minimum to maximum) at (left) 1.35 m and (right) 2.638 m below the CL axis for the increasing secondary side cooldown rate by operator. The 200 K/h curve becomes flat at 3540 s – the pressure at SGs reaches 1 bar and for that pressure, the saturation temperature is around 100 °C.

6.2.2   KWU-MIX results by Fra-G

Results from the system analysis performed with RELAP5, as described in Section 6.2.1, were used as input to the fluid-mixing analysis performed with KWU-MIX. The simulation with KWU-MIX of the increased secondary-side cooldown rate by operator produced data for the temperatures and heat-transfer coefficients as a function of time and location in the cold-leg nozzle and in the plumes in the DC. The flow rate of ECC water as calculated by RELAP5 is shown in Figure 271 for each of the CLs. The injection of ACC water is seen in the increased flow from 1440 s until 2215 s. The pressure, as shown in the left-hand plot of Figure 265, never sinks below 10 bar, and so the low-pressure injection does not occur. The two available high-pressure pumps supply water continuously after 85 s.
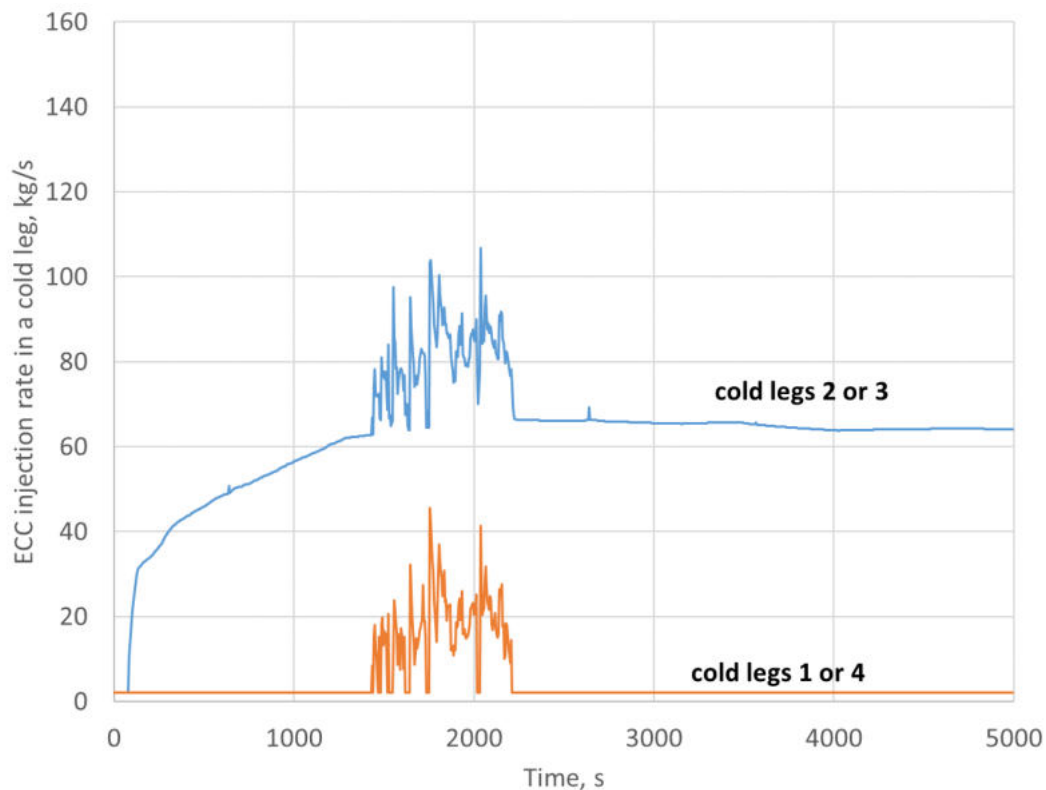
Figure 271: Flow rate of injected ECC water into each of the CLs as calculated by RELAP5.

6.2.2.1   Cold-leg nozzle

The end of the CL is the right-hand end of MR2 in KWU-MIX, as shown in Figure 16. At this location, the models have finished calculating the amount of hot water that is entrained into the cold ECC water, and temperature of the resulting mixture. Figure 272 shows the temperature of the hot water as a function of time, and it is indicated by the grey curve labelled "hot layer in cold-leg nozzle". At the start of the transient, this temperature is the same as the temperature from RELAP5. The flow of water in the loop through the MCP is small enough to prevent complete mixing in the CL starting at 435 s, after which time KWU-MIX calculates a separate temperature for the hot water based on an energy balance for all the mixing regions.

Also shown in Figure 272 is the temperature of the cold water near the cold-leg nozzle that results from the mixing of ECC water and entrained hot water. This temperature is indicated by the blue curve labelled "cold layer in cold-leg nozzle. This temperature is calculated by KWU-MIX starting at 435 s also, as soon as incomplete mixing occurs. Recall that the temperature of the ECC water is 15 °C, which is also shown in Figure 272, but it is an input to KWU-MIX rather than a result. The temperature of the cold-water layer is closer to the temperature of the ECC water than to the temperature of the hot water. This indicates that the mass flow rate of entrained hot water is less than the flow rate of ECC water.

175
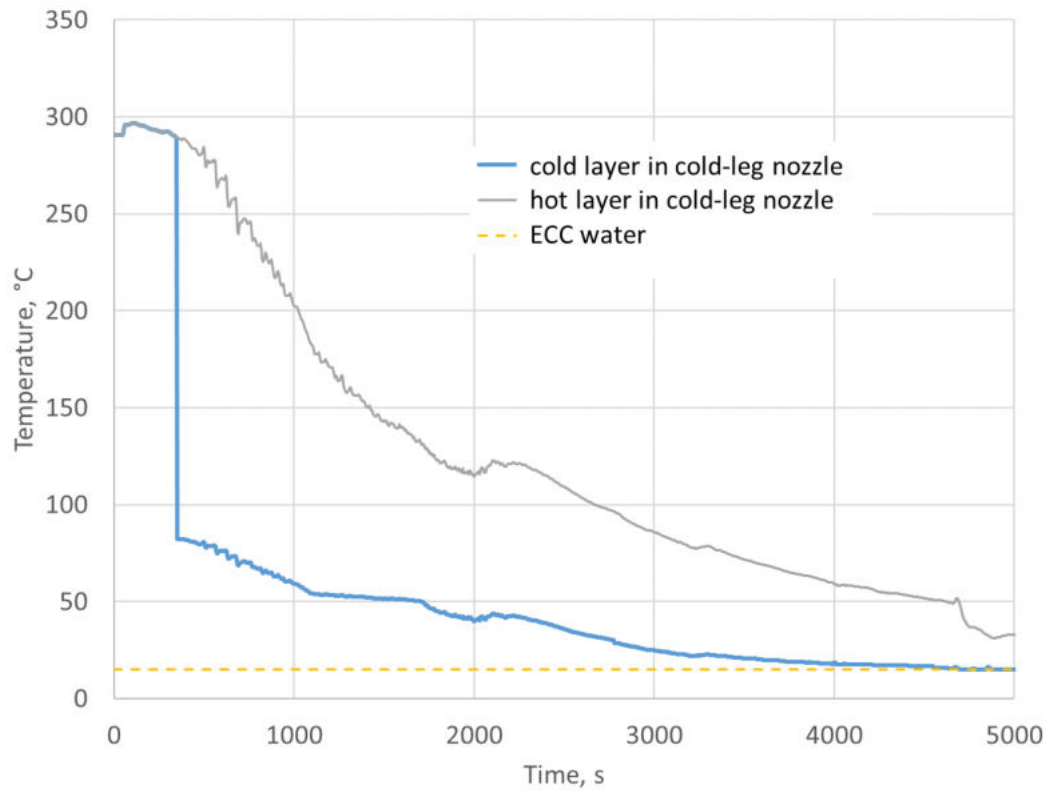
Figure 272: Temperatures of the cold-water and hot-water layers at the end of the nozzle of Cold Leg 2 and 3 calculated by KWU-MIX.

The height of the cold-water layer above the cold-leg axis at the end of the cold-leg nozzle is shown in Figure 273 as a function of time. Initially, when the ECC flow rate is small, the height of the cold-water lay is approximately 0.25 m below the axis of the CL. With increasing ECC flow, as shown in Figure 271, the height of the cold-water layer increases correspondingly.
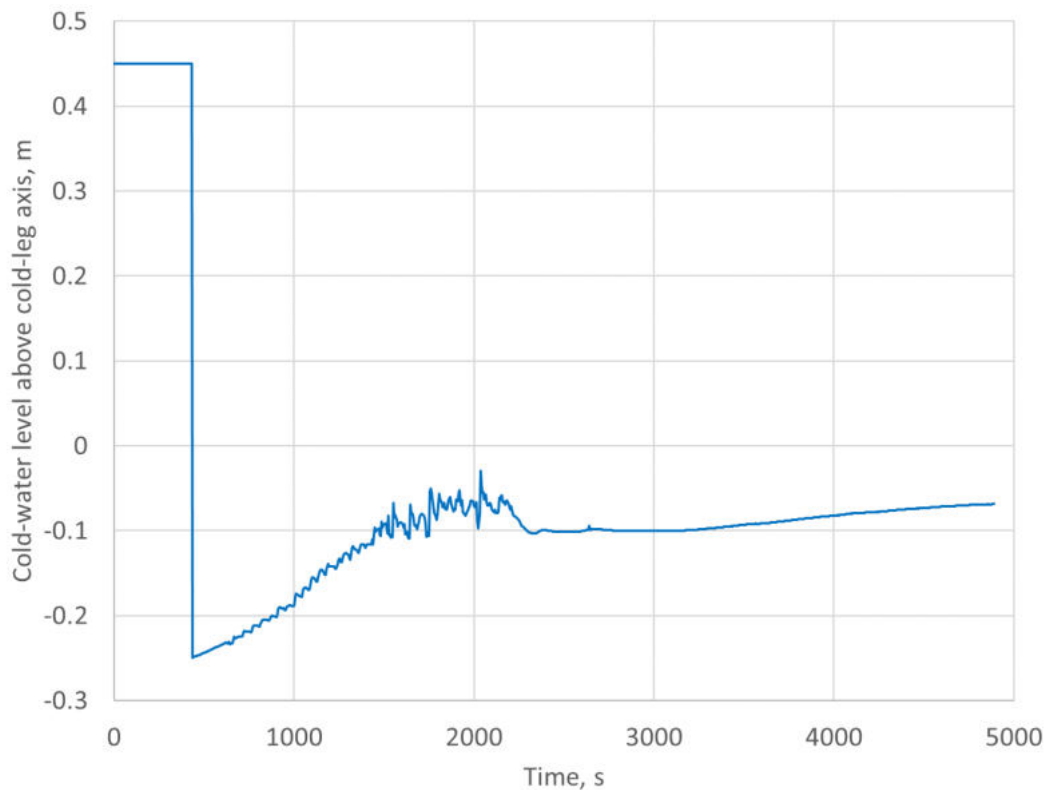
Figure 273: Height of cold-water layer above the axis of Cold Leg 2 and 3 at the inlet of the cold-leg nozzle calculated by KWU-MIX.

The height of the cold-water layer shown in Figure 273 determines the width of the plume at its origin in the DC of the RPV, just below the bottom of the cold-leg nozzle.

6.2.2.2 Inner surface of RPV wall

The transition from the end of the cold-leg nozzle to the top of the plume the RPV is referred to as MR3 in Figure 16, but it is not modelled in KWU-MIX. Instead, KWU-MIX uses the conditions at the end of MR2 as the inlet boundary conditions for MR4. Consequently, the height of the cold-water layer in the cold-leg nozzle, labelled H_c in Figure 274, determines the width of the plume at its origin in the DC.

Figure 274 shows the widths of the plumes at various distances below the cold-leg axis in the DC. The origin of the plume is 0.45 m below the cold-leg axis, which is at the bottom of the diffusor. This is the light blue curve labelled 0.45 m in Figure 274. As soon as a plume is formed at approximately 435 s, its width is approximately 0.675 m, which is less than the diameter of the end of the diffusor. The width of the plume at its origin increases with time, corresponding to the increase in the cold-water flow rate. The width reaches a maximum when the cold-water layer in the CL reaches the axis. The maximum width of the plume is not greater than the cold-leg diameter, however, because the cold water accelerates, and its width narrows as it sinks in the diffusor.

177

APAL_2.0.2_DOKU_220311.0848.15.xlsx
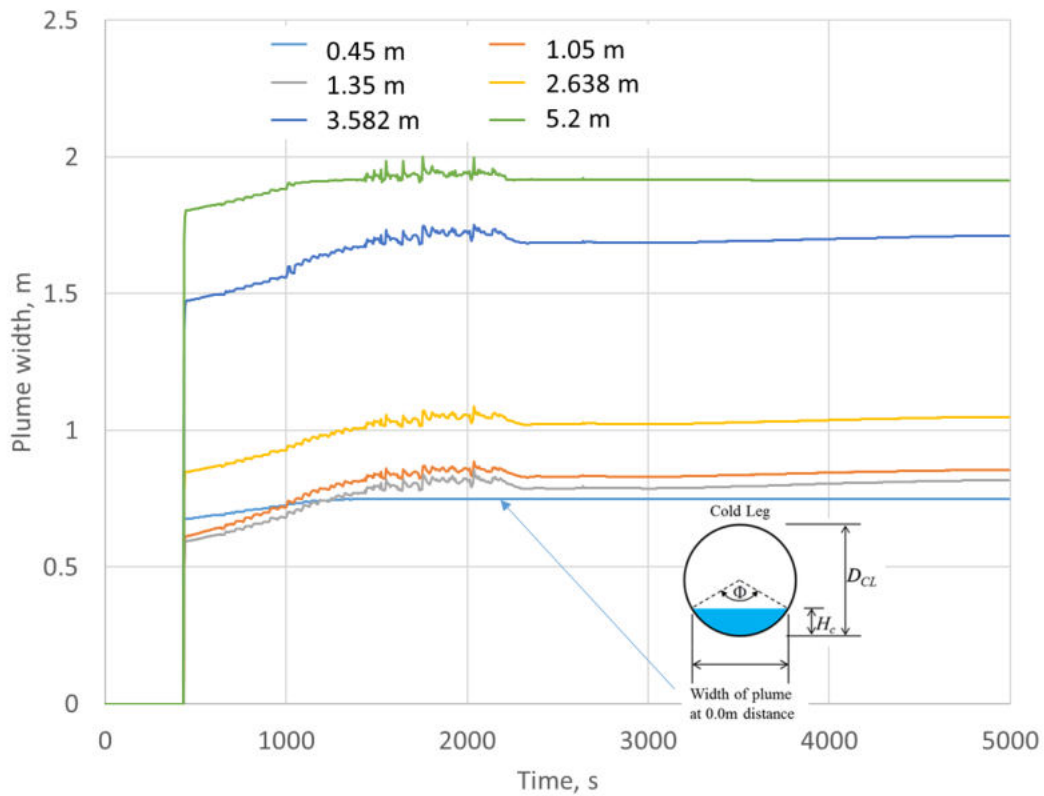
Figure 274: KWU-MIX widths of the plume at various distances below the axis of the Cold Leg 2 & 3 in the DC.

At a distance of 1.05 m below the cold-leg axis, the width of the plume early in the transient is smaller than at its origin. This is due to the strong buoyancy force that accelerates the flow in the plume, which causes the plume to become narrower. Later in the transient, this phenomenon still exists, but its magnitude decreases with time as the temperature differences decrease and the buoyance also decreases. The plume width at 1.35 m below the cold-leg axis is slightly less than at 1.05 m due to this same phenomenon.

The two neighbouring plumes at lower elevations (greater distances below the cold-leg axis) are merged for the entire transient. The width of the merged plume is given for the distances of 2.638 m, 3.582 m and 5.2 m below the cold-leg axis in Figure 274.

The temperatures at the centers of the plumes are shown in Figure 275 for various distances below the cold-leg axis. The light-blue curve labelled 0.45 m in the legend is the centerline temperature at the origin of the plume, which is at the bottom of the cold-leg nozzle. This temperature is the same as the blue curve labelled "cold layer in cold-leg nozzle" shown in Figure 272. The curves for greater distances from the origin are progressively warmer. The dark-blue curve labelled "ambient" is the temperature outside of the plume. This temperature is the same as the grey curve labelled "hot layer in cold-leg nozzle" shown in Figure 272.
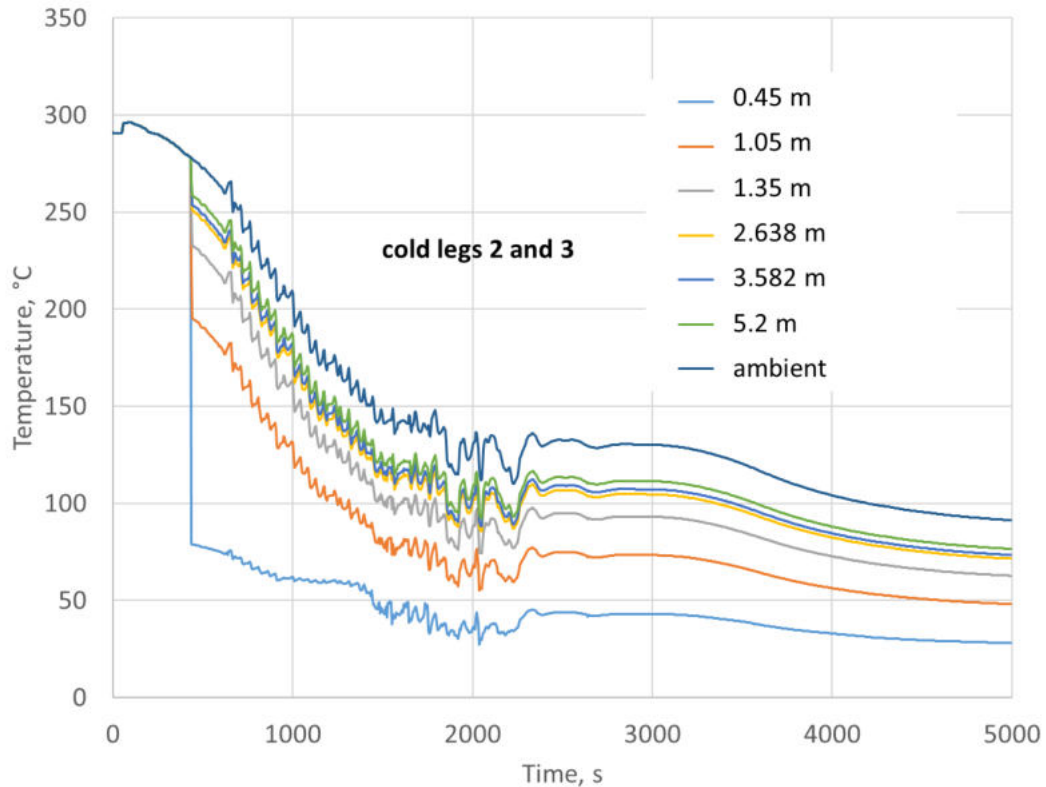
Figure 275: KWU-MIX temperatures at the middle of the plume at various distances below the axis of Cold Leg 2 & 3 in the DC.

Each curve in Figure 275 shows the temperature at one location, and the coordinates are at the elevation shown in the legend and at the circumferential location on the RPV wall where the plume is coldest. But the temperature throughout the plumes has a Gaussian distribution along the circumference of the RPV wall. An example is shown in Figure 276, which shows the temperature as a function of the circumferential location for various elevations at a time equal to 1000 s.

The temperature profile at the origin of the plume is the blue curve labelled "0.45 m" in the legend of Figure 276. The axis of the cold-leg nozzle in Loop 2 is at a circumferential location of 6.69 m, and the axis of the nozzle in Loop 3 is at 8.61 m. The coldest temperature for the plumes at a distance of 0.45 m below the axis of CL 2 as taken from Figure 275 at 1000 s is 62 °C. This is the minimum temperature for the blue curve at the circumferential location of 6.69 m. The plume below Cold Leg 3 has the same temperature, and so the curve has a value of is 62 °C at a circumferential location of 8.61 m also. Between the two circumferential locations, the temperature increases to the ambient temperature as taken from Figure 275 at 1000 s. This temperature is 209 C.

The small temperature depressions at circumferential locations of 0.96 m and 14.34 m are below the cold-leg nozzles of Loop 1 and Loop 4. The depressions are a result of a small flow of cold water from the CVCS system.
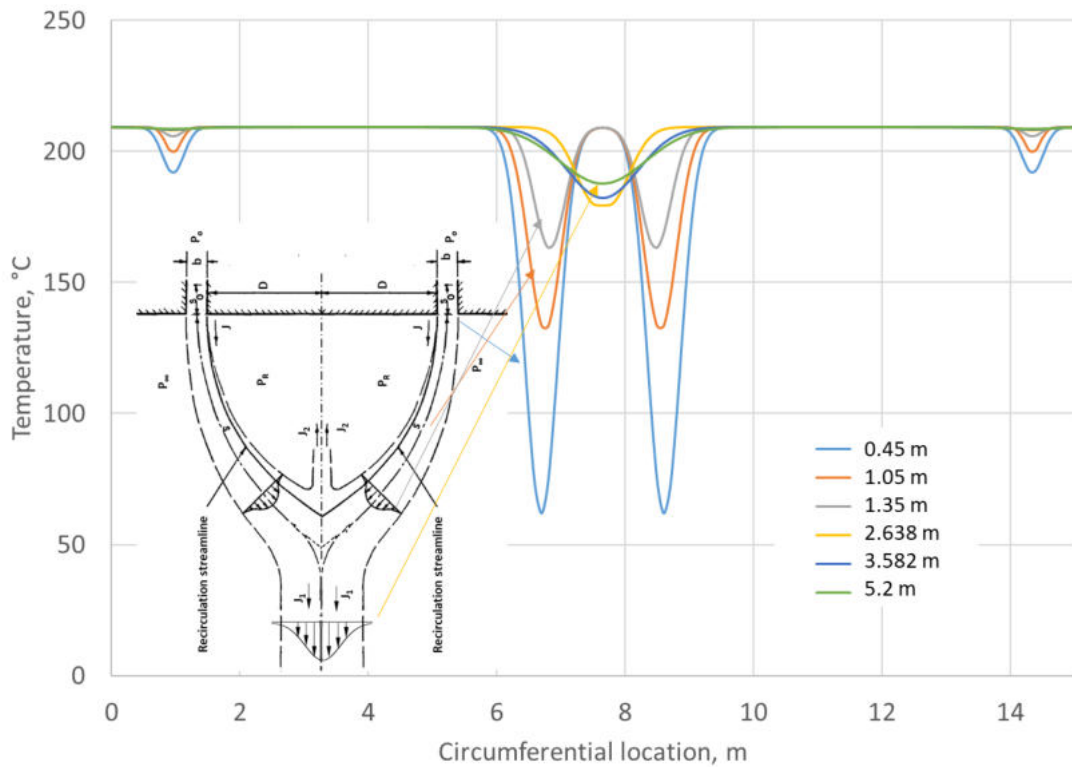
Figure 276: KWU-MIX temperatures at the middle of the plume at various distances below the axis of the cold-leg in the DC at 1000 s.

The heat-transfer coefficients in the DC also have Gaussian distributions, and the widths are equal to those for the temperature shown in Figure 274 divided by a factor of 1.1045, which was taken from Chen [20]. The maximum values for the heat-transfer coefficients in the plumes as a function of time are shown in Figure 277 for various distances below the cold-leg axis. The light-blue curve labelled 1.05 m in the legend is the centerline heat-transfer coefficient near the top of the plume. The curves for greater distances from the origin are progressively greater, because the buoyancy force continues to accelerate the flow more than the inertia of the entrainment tends to decelerate the flow.
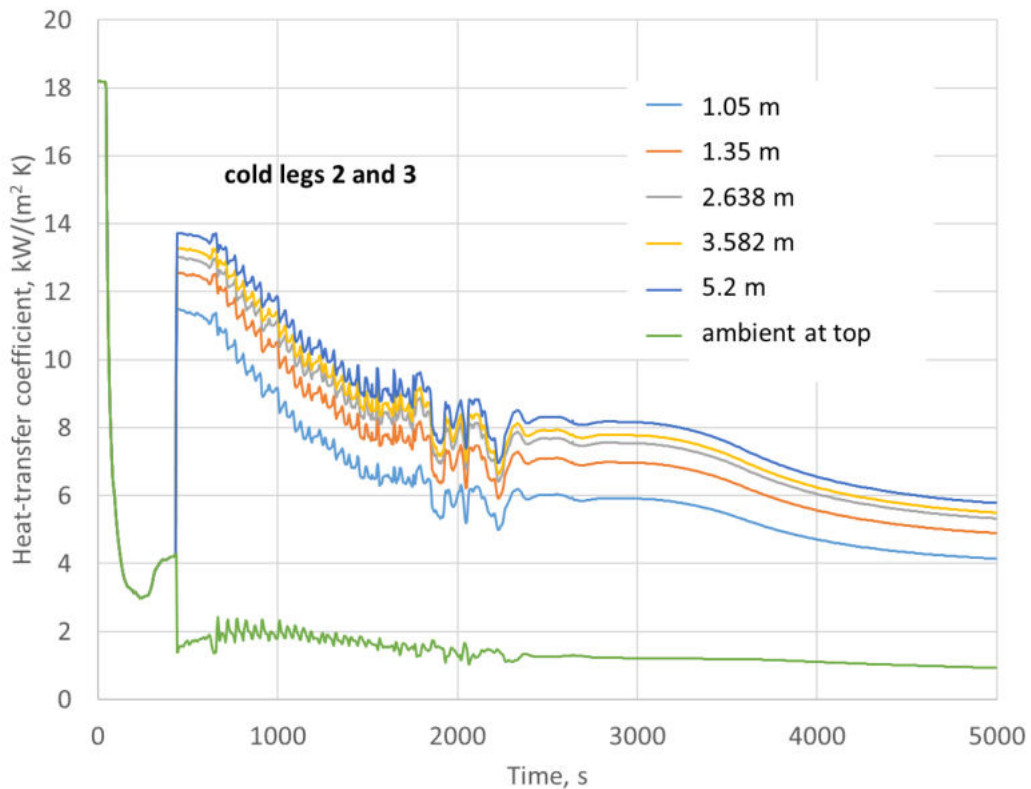
Figure 277: KWU-MIX heat-transfer coefficients at the middle of the plume at various distances below the axis of Cold Leg 2 & 3 in the DC.

Also shown in Figure 277 is the heat-transfer coefficient outside of the plumes near the cold-leg nozzle. This is the green curve labelled "ambient at top". The heat-transfer coefficient outside of the plume increases with distance from the cold-leg nozzle, as shown in Figure 278. The increase in the heat-transfer coefficient is due to a larger recirculation flow outside of the plume with increasing distance from the cold-leg nozzle. Near the cold-leg nozzle, the recirculation flow outside of the plume is only as large as the entrainment flow rate at that location. Farther from the cold-leg nozzle, the recirculation flow is equal to the entrainment flow integrated over the higher distances. Near the bottom of the DC, the recirculation flow is equal to the entire flow of entrained water, and so the heat-transfer coefficient is largest at this location.

181
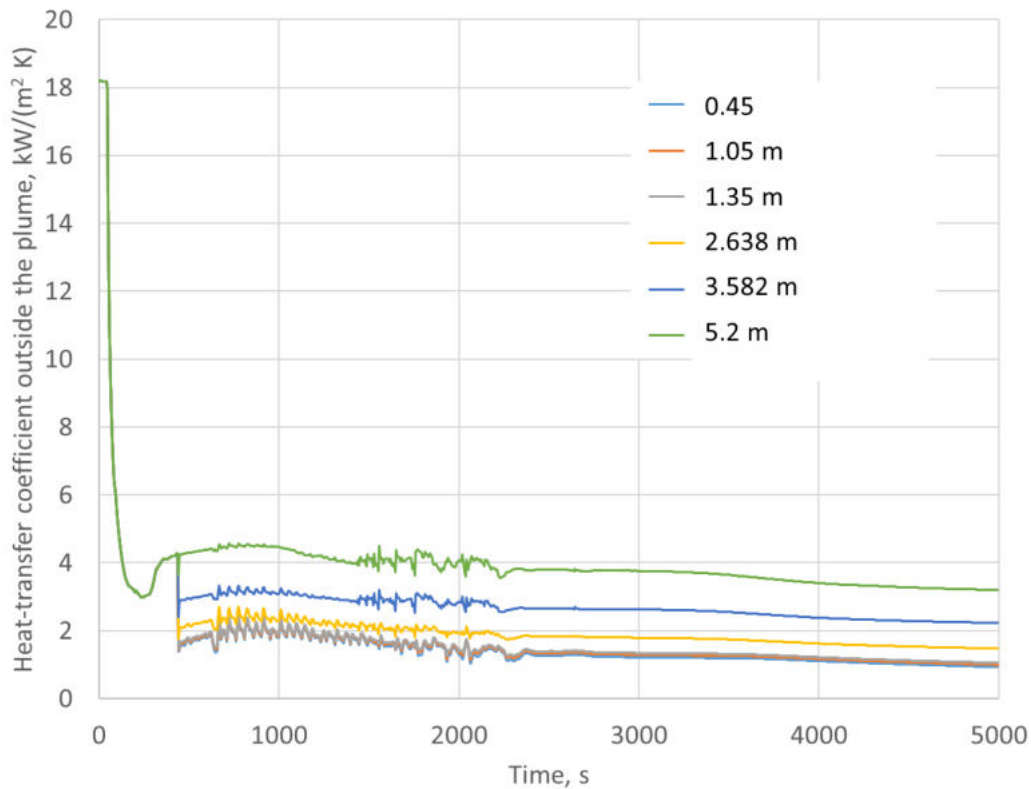
Figure 278: KWU-MIX heat-transfer coefficients outside of the plume at various distances below the cold-leg axis in the DC.

Each curve in Figure 277 shows the heat-transfer coefficient at one location, and the location's coordinates are at the elevation shown in the legend and at the circumferential location on the RPV wall where the plume is coldest. But the heat-transfer coefficient throughout the plumes has a Gaussian distribution along the circumference of the RPV wall, just as the temperature does. An example is shown in Figure 279, which shows the heat-transfer coefficient as a function of the circumferential location for various elevations at a time equal to 1000 s.

The heat-transfer coefficient profile near the origin of the plume is the blue curve labelled "1.05 m" in the legend of Figure 279. Recall that the axis of the cold-leg nozzle in Loop 2 is at a circumferential location of 6.69 m, and that the axis of the nozzle in Loop 3 is at 8.61 m. The largest heat-transfer coefficient for the plumes at a distance of 1.05 m below the axis of Cold Leg 2 at 1000 s as taken from Figure 277 is 9.1 kW/(m^2 K). This is the maximum heat-transfer coefficient for the blue curve at the circumferential location of 6.69 m in Figure 279. The plume below Cold Leg 3 has the same heat-transfer coefficient, and so the curve has the sane value at a circumferential location of 8.61 m. Between the two circumferential locations, the heat-transfer coefficient decreases to the ambient value as taken from Figure 279 at 1000 s. This heat-transfer coefficient is 1.83 kW/(m^{2}K).

The smaller heat-transfer coefficient peaks at circumferential locations of 0.96 m and 14.34 m are below the cold-leg nozzles of Loop 1 and Loop 4. The depressions are a result of a small flow of cold water from the CVCS system.
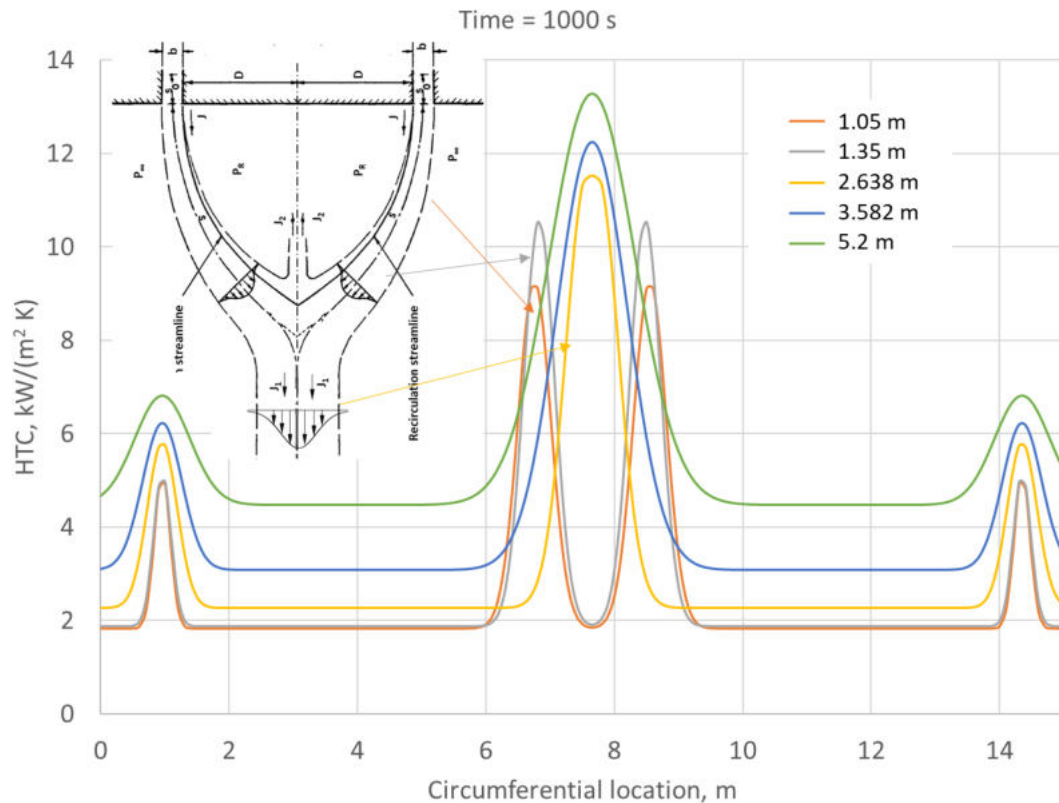
Figure 279: KWU-MIX heat-transfer coefficients at the middle of the plume at various distances below the axis of the cold-leg in the DC at 1000 s.

Figure 279 shows heat-transfer-coefficient temperature profiles for four additional distances below the cold-leg axes. At a distance of 1.035 m, the circumferential location of the largest heat-transfer coefficient temperatures below Cold Leg 2 is slightly closer to the circumferential location of the coldest temperatures value below Cold Leg 3. This is due to the merging phenomenon described in Section 3.4.2 and shown in in Figure 21. The distance between the circumferential locations of the largest heat-transfer coefficients below Cold Leg 2 and 3 decreases from 1.05 m to 1.35 m below the cold-leg axis. At a distance of 2.638 m below the cold-leg axis, the two plumes have merged, and only a single Gaussian distribution is shown. The heat-transfer coefficient distributions at greater distances are similar, with the width increasing and the largest heat-transfer coefficient increasing with distance from the cold-leg axis.

6.3   Isolation of accumulators by operator

6.3.1   RELAP5 results by Fra-G

Results from the system analysis performed with RELAP5, as described in Section 4.1, were repeated with the addition of a time for ACC isolation at 500 s. Because the pressure for this break size does not decrease to 26 bar until after 500 s, the ACCs were isolated before they could inject. The result is a pressure transient as shown in Figure 280 (a). When compared with primary-side pressure shown in Figure 30 (a), the results are nearly identical.

(a)   (b)
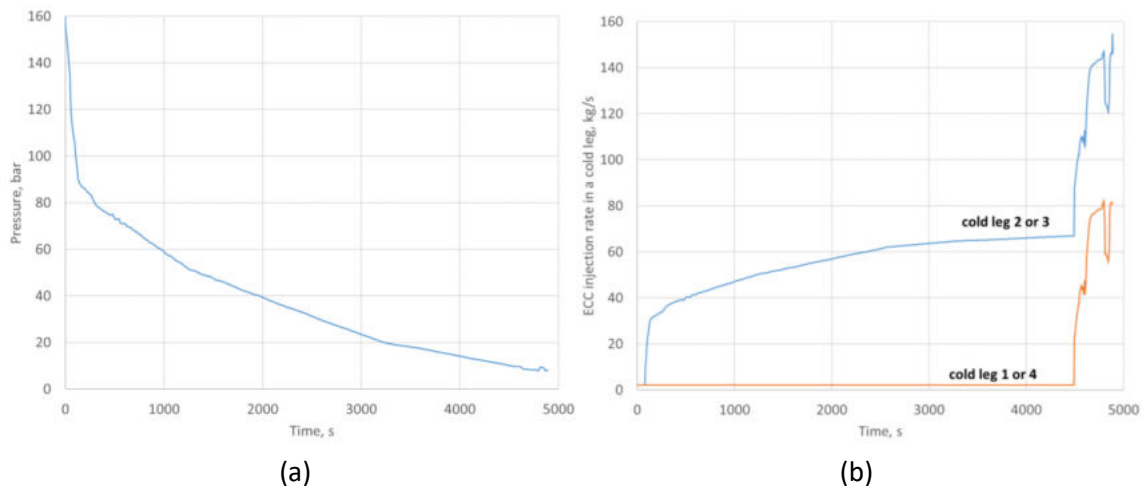
Figure 280: (a) Primary-Side Pressure and (b) ECCS Flow Rate per Loop.

In Figure 280 (b) is the injection flow rate per loop. There is no increase in the flow rate due to the ACC at 1800 s, which is different from the curve in Figure 30 (b).

The water level in the DC is not significantly different than the level in Figure 34 (a). The temperature of the water in the DC is also similar to the blue curve labelled "DC" in Figure 38 (a). The most significant differences appear in the results in unmixed regions in the CL and DC, which can be obtained from a mixing-analysis program, such as KWU-MIX. This is discussed next.

6.3.2   KWU-MIX results by Fra-G

Results from the system analysis performed with RELAP5, as described in Section 6.3.1, were used as input to a mixing analysis, such as described in Section 4.5. Only the system-analysis input from RELAP5 were different than in Section 4.5, and none of the user-supplied input data to KWU-MIX were changed, so the primary differences are the results of the lack of ACC injection starting at approximately 2800 s.

6.3.2.1   Cold-leg nozzle

The temperatures from KWU-MIX for the cold-water layer and hot-water layer at the end of the CL near the cold-leg nozzle are shown as the blue curve labelled "cold layer in cold-leg nozzle" in Figure 281. At this location, the models have finished calculating the amount of hot water that is entrained into the cold ECC water, and temperature of the resulting mixture at the end of the CL. The cold-water temperature for the base case with ACC injection as seen in Figure 91 has a small decrease in temperature from 2800 s until 3200 s, and this is missing in Figure 281. The temperatures prior to that are the same in the two figures.

Figure 281 also shows the temperature of the hot water as a function of time, and it is indicated by the grey curve labelled "hot layer in cold-leg nozzle". This temperature is the same as the temperature from RELAP5, which is the curved labelled "DC" as shown in Figure 38 (a).

184

APAL_2.0.2_DOKU_220206.1717.02.xlsx
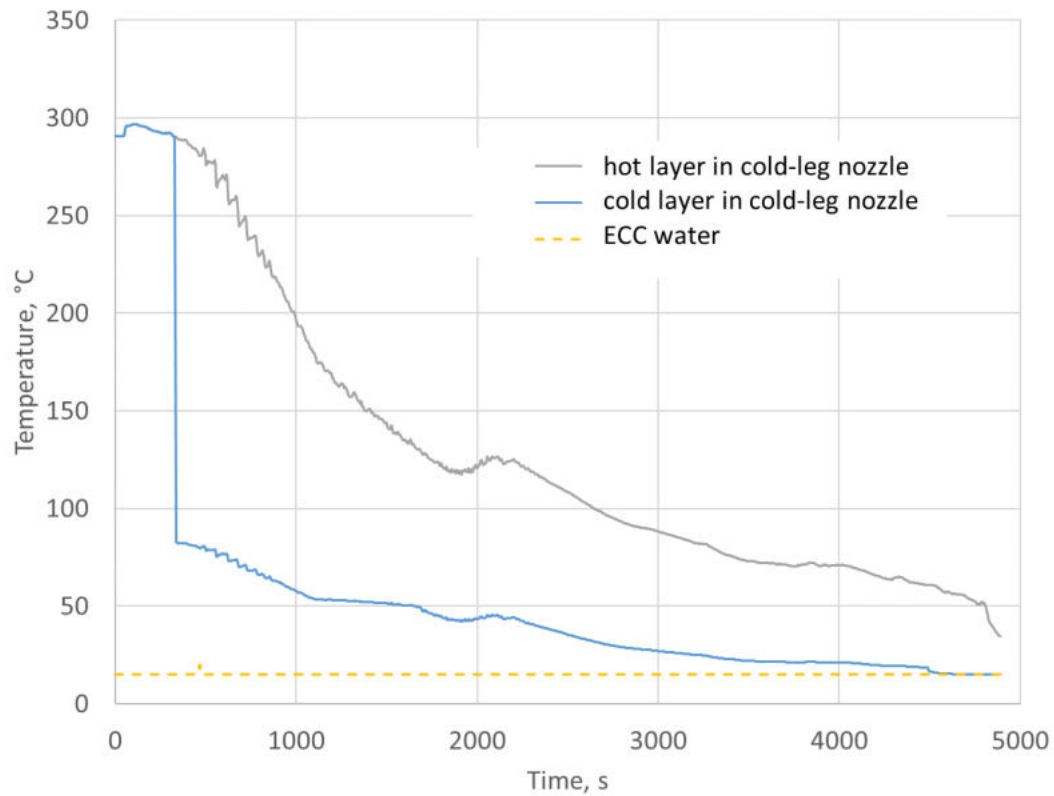
Figure 281: Temperatures of the cold-water and hot-water layers at the end of the nozzle of Cold Leg 2 and 3 calculated by KWU-MIX.

The height of the cold-water layer above the cold-leg axis at the end of the cold-leg nozzle is shown in Figure 282 as a function of time. These curves are similar to those in Figure 92 prior to ACC injection. From 2800 s until 3200 s, Figure 92 shows a slight increase in the height of the cold-water layer, but this is missing in Figure 282, due to the absence of ACC injection.
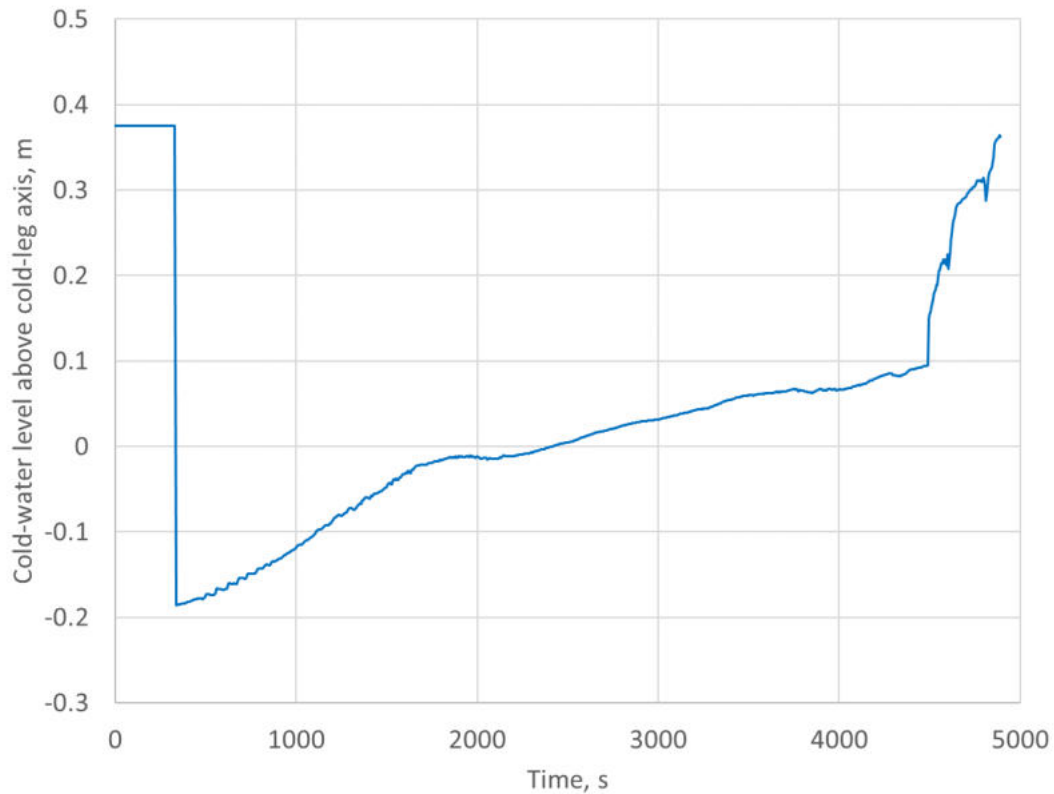
Figure 282: Height of cold-water layer above the axis of Cold Leg 2 and 3 at the inlet of the nozzle, calculated by KWU-MIX.

The height of the cold-water layer shown in Figure 282 determines the width of the plume at its origin in the DC of the RPV, just below the bottom of the cold-leg nozzle.

6.3.2.2 Inner surface of RPV wall

Figure 283 shows the widths of the plumes at various distances below the cold-leg axis in the DC. The origin of the plume is 0.45 m below the cold-leg axis, which is at the bottom of the diffusor. This is the light blue curve labelled 0.45 m in Figure 283. As soon as a plume is formed at approximately 350 s, its width is approximately 0.65 m, which is less than the diameter of the end of the diffusor. The width of the plume at its origin increases with time, corresponding to the increase in the cold-water flow rate. The width reaches a maximum when the cold-water layer in the CL reaches the axis. The maximum width is equal to the diameter of the CL. The width of the plume does not expand, because the cold water accelerates, and its width narrows as it sinks in the diffusor.
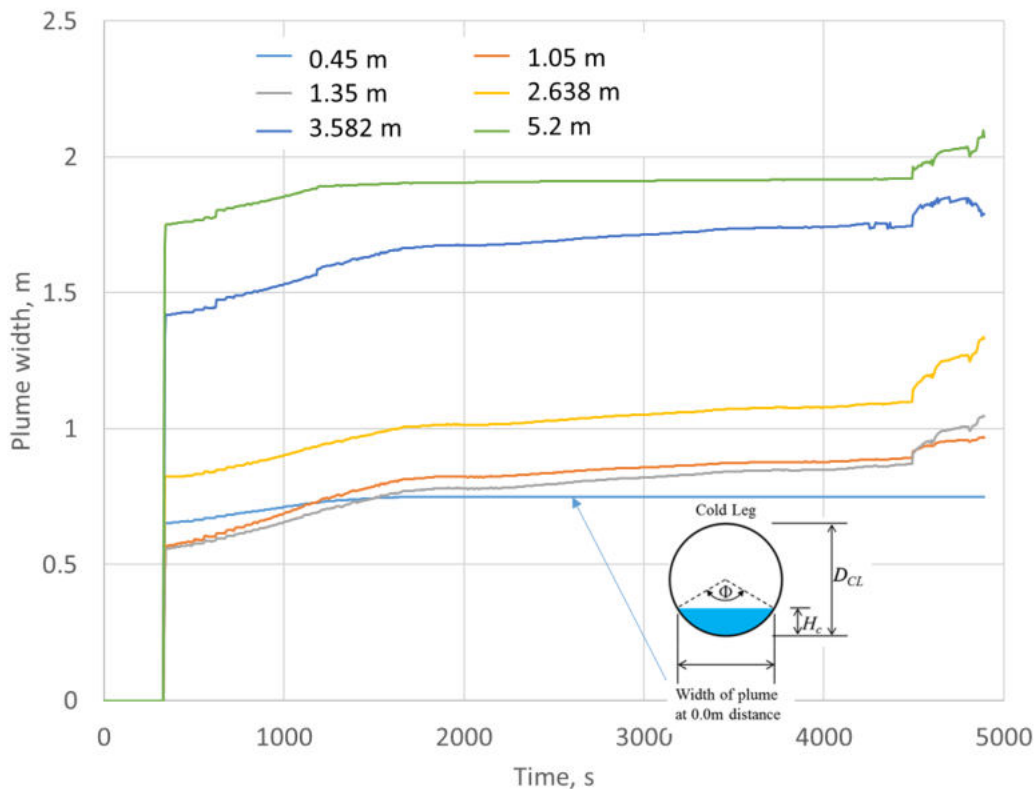
Figure 283: KWU-MIX widths of the plume at various distances below the axis of the Cold Leg 2 & 3in the DC.

At a distance of 1.05 m below the cold-leg axis, the width of the plume is smaller than at its origin early in the transient. This is due to the strong buoyancy force that accelerates the flow in the plume, which causes the plume to become narrower. Later in the transient, this phenomenon still exists, but its magnitude decreases with time as the temperature differences decrease and so the buoyance also decreases.

These curves are similar to those in Figure 93 prior to ACC injection. From 2800 s until 3200 s, Figure 93 shows a slight increase in the width of the plume, but this is missing in Figure 283, due to the absence of ACC injection.

The two neighbouring plumes at lower elevations (greater distances below the cold-leg axis) are merged for the entire transient. The width of the merged plume is given for the distances of 2.638 m, 3.582 m and 5.2 m below the cold-leg axis in Figure 283. These curves are also similar to those in Figure 93, except for the absence of the small increase from 2800 s until 3200 s in Figure 283.

The temperatures at the centers of the plumes as a function of time are shown in Figure 284 for five distances below the cold-leg axis. The light-blue curve labelled 0.45 m in the legend is the centerline temperature at the origin of the plume, which is at the bottom of the cold-leg nozzle. This temperature is the same as the blue curve labelled "cold layer in cold-leg nozzle" shown in Figure 281. The curves for greater distances from the origin are progressively warmer. The dark-blue curve labelled "ambient" is the temperature outside of the plume. This temperature is the same as the grey curve labelled "hot layer in cold-leg nozzle" shown in Figure 281. Compared to the corresponding figure for the base case, Figure 94, the curves in Figure 284 are similar except for the absence of a small decrease in temperature from 2800 s until 3200 s due to the absence of ACC injection.

187
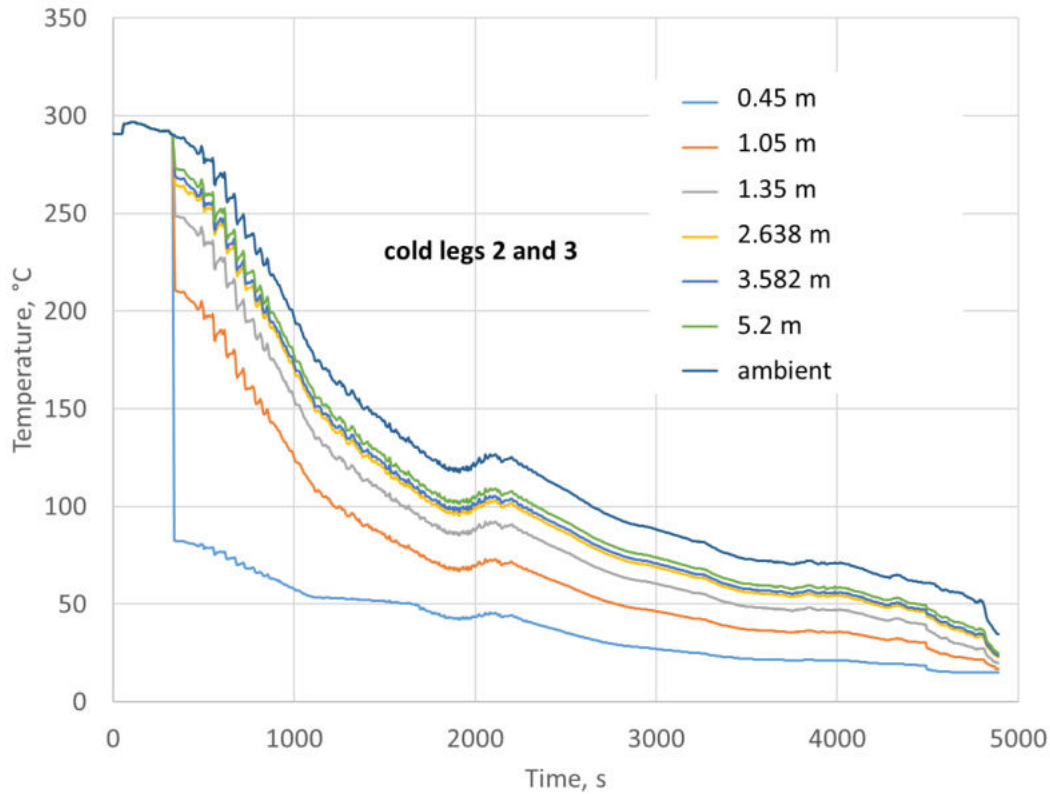
Figure 284: KWU-MIX temperatures at the middle of the plume at various distances below the axis of Cold Leg 2 and 3 in the DC.

Gaussian distributions of the temperatures along the circumference of the RPV wall are also similar with ACC injection and without.

The maximum values for the heat-transfer coefficients in the plumes as a function of time are shown in Figure 285 for various distances below the cold-leg axis. The light-blue curve labelled 1.05 m in the legend is the centerline temperature near the top of the plume. The curves for greater distances from the origin are progressively greater because the buoyancy force continues to accelerate the flow more than the inertia of the entrainment tends to decelerate the flow.

APAL_2.0.2_DOKU_220206.1717.02.xlsx
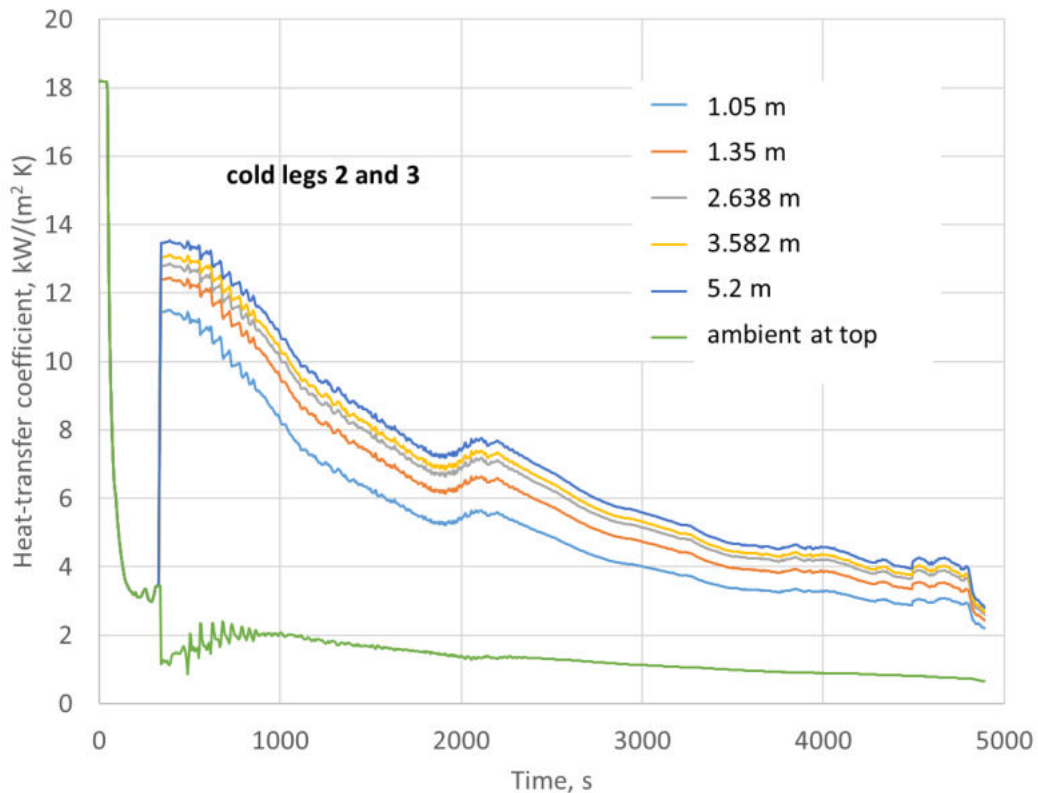
Figure 285: KWU-MIX heat-transfer coefficients at the middle of the plume at various distances below the axis of Cold Leg 2 & 3 in the DC.

Compared to the corresponding heat-transfer coefficients for the base case shown in Figure 96, the heat-transfer coefficients shown in Figure 285 are similar. The small peaks at 2800 s and 3200 s in Figure 96 are not present in Figure 285.

Figure 286 shows the heat-transfer coefficients outside of the plumes at six distances below the cold-leg axis. The heat-transfer coefficient outside of the plume increases with distance from the cold-leg nozzle, as shown in Figure 97. The increase in the heat-transfer coefficient is due to a larger recirculation flow outside of the plume with increasing distance below the cold-leg nozzle. Near the cold-leg nozzle, the recirculation flow outside of the plume is only as large as the entrainment flow rate at that location. Farther below the cold-leg nozzle, the recirculation flow is equal to the entrainment flow integrated over the higher distances. Near the bottom of the DC, the recirculation flow is equal to the entire flow of entrained water, and so the heat-transfer coefficient is largest at this location.
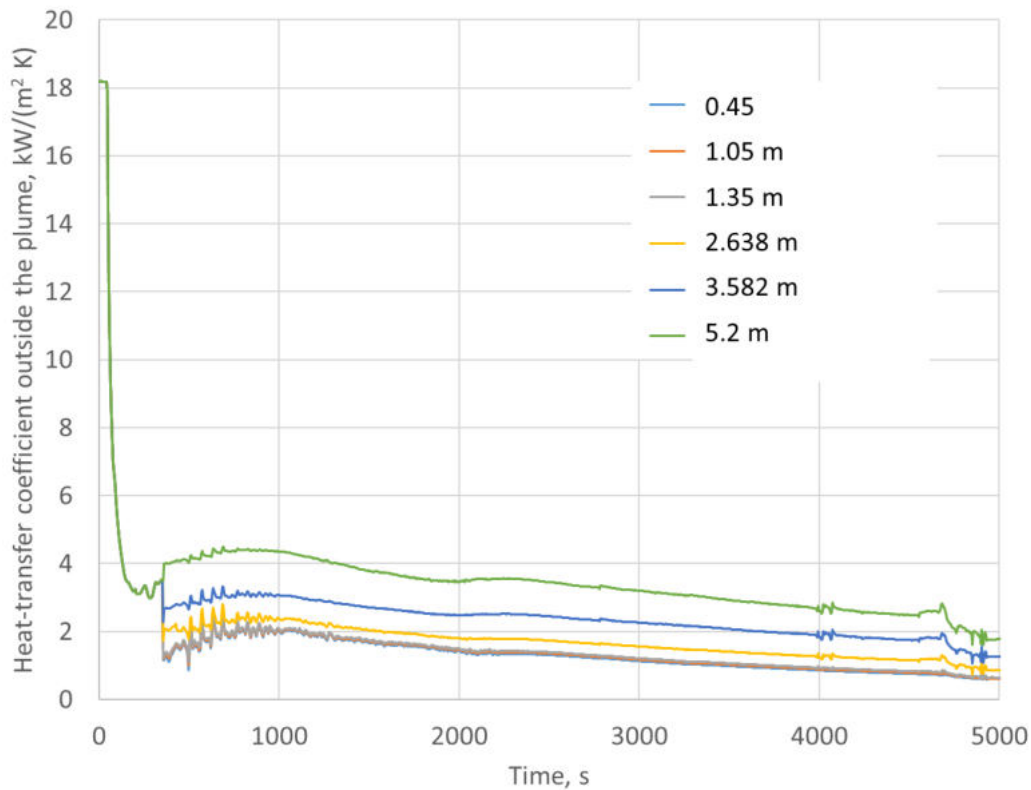
Figure 286: KWU-MIX heat-transfer coefficients at various distances below the axis of Cold Leg 2 & 3 outside of the plumes in the DC.

The heat-transfer coefficients shown in Figure 286 are similar to those shown in Figure 97 for the base case with ACC injection.

6.4 Summary of LTO improvements that are the result of the operator action

One of two potential LTO improvements that are the result of the operator action considered in the RELAP5 simulations by WUT shows a benefit for the considered transient (SBLOCA), namely the reduction of HPIS flow. The outcome of the other potential LTO improvement, i.e. increasing secondary side cooldown rate needs further analysis.

All three LTO improvements related to the operator actions were simulated with KWU-MIX by Fra-G. The results indicate that reduction of HPIS flow by operator is beneficial from PTS point of view. A temperature increase occurs after one of the two active HPIS pumps is deactivated at 1800 s. With only one HPSI pump in operation, there is only one plume in the DC, and merging of plumes is not possible. Increasing secondary-side cooldown rate by operator cannot be considered beneficial based on a mixing analysis. The magnitudes of the temperatures and HTCs in the plumes are not significantly different, but the transient is faster, and so the temperatures decrease more quickly than if the secondary-side cooldown rate is slower. Isolation of ACCs by operator does not produce results that are significantly different from the base case. This is due to the relatively small leak size, which prevents the ACCs from injecting water at a flow rate large enough to have a significant effect on the temperatures and HTCs.

A summary of conclusions for the considered LTO improvements that are the result of the operator action is given in Table 24.

190

Table 24: **Summary of Conclusions for Candidate LTO Improvements that are the result of the operator action, based on the RELAP5 simulations by WUT and Fra-G and on the KWU-MIX simulations by Fra-G**

LTO Improvement	Conclusion
Reduction of HPIS flow by operator (RELAP5/WUT)	Potentially beneficial
Reduction of HPIS flow by operator (KWU-MIX/Fra-G)	Potentially beneficial
Increasing secondary side cooldown rate by operator (RELAP5/WUT)	Inconclusive, needs further analysis
Increasing secondary side cooldown rate by operator (KWU-MIX/Fra-G)	Not beneficial
Isolation of ACCs by operator (RELAP5/Fra-G)	No significant effect
Isolation of ACCs by operator (KWU-MIX/Fra-G)	No significant effect

7 Supplementary long-term analyses of selected LTO improvements

Simulation results presented in this report have focused primarily on the system behaviour for the first 4900 s following the SB-LOCA. This is sufficient time for the primary system to depressurise to ~1 MPa and initiation of the LPI, thus ensuring longer term cooling of the core. The simulations also suggest that the system stabilises around the conditions at 4900 s. To confirm the longer-term behaviour of the system, PSI extended their TRACE simulations to 10'000 s. Selected results from these extended simulations are presented in this section. Because system pressure and coolant temperature are the primary parameters of interest for downstream thermomechanical analyses, we focus on those two.

Figure 287 summarises the system pressure and DC coolant temperature extended to 10'000s for three LTO improvements. The coolant temperatures in all cases either remain relatively constant or there is a sudden increase in temperature around 6000 s. This sudden increase is associated with the re-establishment of natural circulation in one or more loops of the reactor as the primary system is refilled with coolant from the safety injection systems. Such an increase in temperature would lead to lower PTS-related stress in the RPV wall and therefore the assumption of constant temperature beyond 4900 s is conservative.

In all cases we see that the system pressure after 4900 s is virtually unaffected by the LTO improvement. There is a slow increase in reactor pressure after 4900 s, in this case up to around 1.5 MPa. Additional studies by PSI (TRACE) and GRS (ATHLET), which are not included in this report for brevity, showed that the pressure response later in the transient is very sensitive to the modelling of the break. In some cases, the pressure remains steady after 4900 s, while in others it continues to decrease. Additionally, the exact geometry of any postulated break is very uncertain. It follows from this that, while the assumption of constant pressure after 4900 s may be non-conservative, this effect will not affect any conclusions with respect to LTO improvements. It will, instead be more relevant for Task 2.3, the T/H uncertainty analysis, for which the uncertainty in the break geometry must be taken into account. Thus, the simulations for task 2.3 will need to be extended to at least 8'000 s.
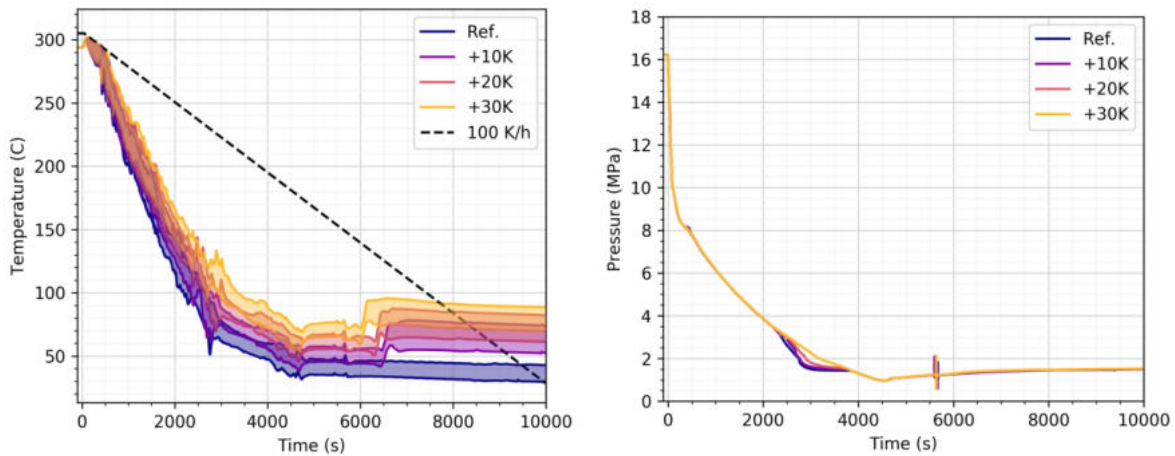
(a) Heating of Water in the HPIS Tanks
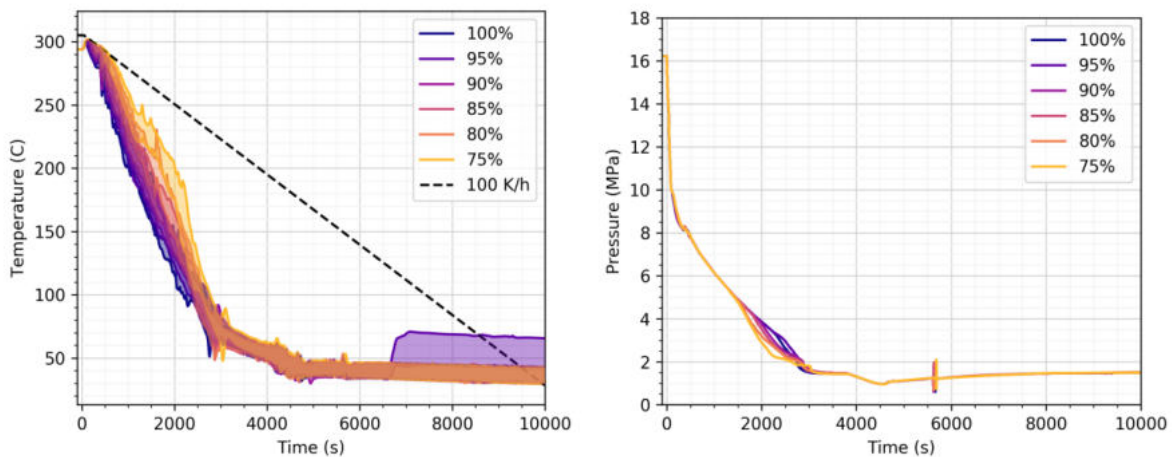
(b) Decreasing HPI Head
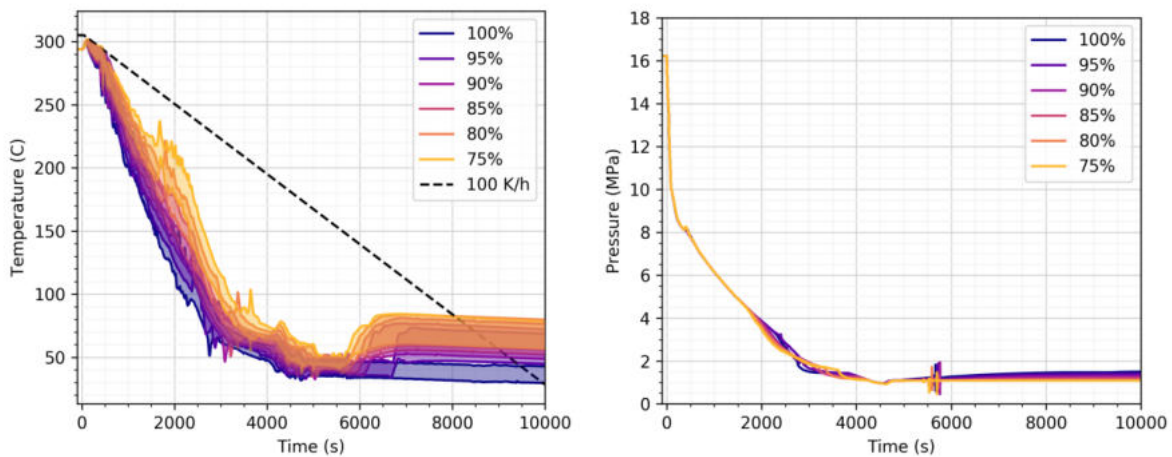
(c) Decreasing HPI capacity

Figure 287: TRACE Results for Selected LTO Improvements Extended to 10'000 s. (left) Minimum and Maximum Coolant Temperature in the DC 1.35 m below the CL Centreline and (right) Pressure in the DC.

JSI also extended all their RELAP5 simulations presented in Chapter 5.6.1 to 10000 s, but it turns out that after 4900 s but before 5000 s the pressure increases so much that LPI injection is terminated (see pressure labelled '2.6 MPa', which is base case in Figure 288 (right)). Similarly, ACC injection is also terminated before 5000 s. This means that the majority of plotted variables are constant after 5000 s, while the pressure and temperature trends are similar to those shown in Figure 288.

192

Figure 288 shows system pressure and DC coolant temperature for LTO improvement on decreasing of ACC pressure. In all cases the system pressure is practically unaffected by the LTO improvement. The coolant temperatures in all cases after around 4750 s start to increase until around 6500 s, when they reached around 80 °C. After then pressures slowly decrease (drop of few K till the end of simulation at 10000 s). Like in TRACE simulation the sudden increase is associated with the re-establishment of natural circulation in one or more loops of the reactor as the primary system is refilled with coolant from the safety injection systems. After accident start the reactor pressure constantly decreases until 4700 s, when in approximately 10 minutes increases up to around 2.2 MPa, and later remains practically constant.
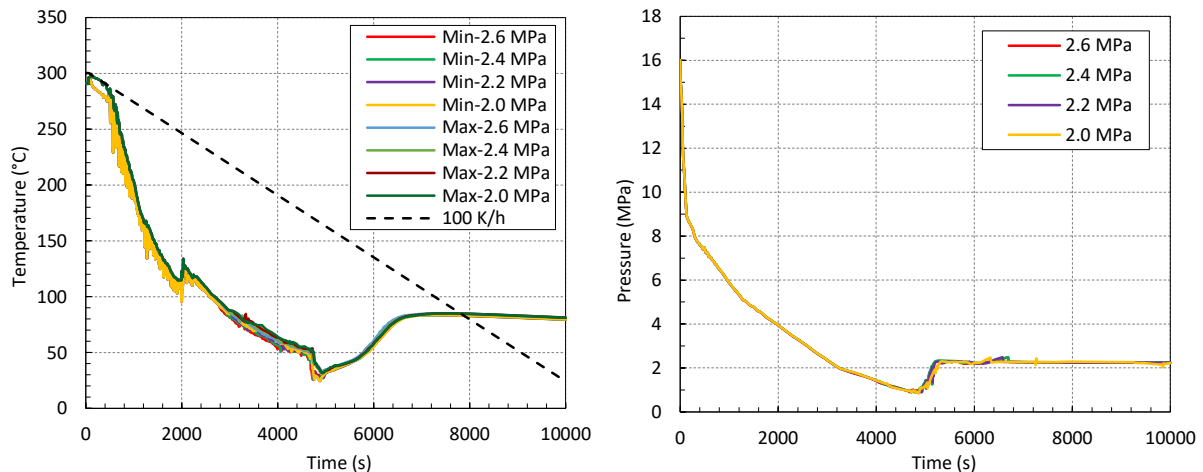
(a) Decreasing of ACC pressure

Figure 288: RELAP5 Results for Selected LTO Improvement Extended to 10'000 s. (left) Minimum and Maximum Coolant Temperature in the DC 1.13 m below the CL Centreline and (right) Pressure in the DC.

8 Evaluation of impact of LTO improvements

Of the six potential LTO improvements considered in the TH simulations, only the heating of water in HPI tanks showed a clear benefit for the SBLOCA in question when compared to the results obtained for the base case. This was observed both in the RELAP5 and TRACE calculations. Impact due to the heating of water in the ACCs and LPI tanks was insignificant in most simulations from PTS point of view i.e., neither a clear benefit nor a detrimental effect could be observed in the RELAP5, ATHLET(+GRS-MIX) and TRACE simulations. However, the KWU-MIX simulation showed a slight benefit at the very last phase of the transient. The decreasing ACC pressure was tested with RELAP5 and TRACE. Both codes showed that there is no clear benefit for SBLOCA. Changes involving the ACCs would be more significant for larger break sizes, when the injection flow rate of the ACCs would be larger. Regarding the two-remaining considered LTO improvements i.e., decreasing the HPI head and capacity, the result was unclear. The ATHLET, TRACE and RELAP5 simulations indicated a possible positive effect of the early phase of the accident (before ACC injection), but after beginning of ACC injection the rate of DC cooling increases significantly, which can provide detrimental effect of the measure. The final conclusion regarding the impact of this measure on the PTS can be made based on the results of thermo-mechanical and fracture mechanics calculations.

Of the three LTO improvements that are the result of an operator action the reduction of HPIS flow showed a potential benefit for the considered SBLOCA transient both in the RELAP5 and KWU-MIX simulation. Results of the RELAP5 simulation of the second case, i.e., the increasing secondary side cooldown rate by operator were inconclusive and need further analysis. Based on a mixing analysis done with the KWU-MIX code this operator action cannot be considered beneficial. The last case, isolation of ACCs by operator, did not produce such results in the RELAP5 and KWU-MIX simulations that would have been significantly different from the base case.

The conclusions on the possible beneficial or detrimental impacts of the different LTO improvements summarized above can be considered to be valid only for a postulated SBLOCA in the range of 50 cm^2 and in a geometry resembling a German design 1300 MW four-loop PWR. In case of loss-of-coolant accidents with larger break sizes, main steam line breaks (MSLB) or other transients relevant from PTS point of view the impact could differ from that presented in this report. Furthermore, these LTO improvements, if implemented in other types of nuclear power plants, could result in a significantly different kind of behaviour than in the simulations carried out in Task 2.1. However, the impact of LTO improvements in other types of transients than just in a SBLOCA with a 50 cm^2 break can be evaluated on a general level by using expert judgement. Such an evaluation is presented in Table 25.

Table 25: **Evaluation of impact of LTO improvements in some transients based on expert judgement**

LTO improvement	ICAS SBLOCA 50 cm^2	SBLOCA general	MBLOCA	LBLOCA	MSLB
1. Heating of water in the HPIS tanks	Potentially beneficial	Beneficial	Beneficial	Small impact (positive)	Beneficial
2. Heating of water in the ACCs	No clear benefit	No or small impact (positive)	Beneficial	Beneficial	No impact
3. Heating of water in the LPIS tanks	No clear benefit	No or small impact (positive)	Beneficial	Beneficial	No impact
4. Decreasing the HPSI head	Unclear, potentially detrimental	Small impact (positive)	No impact	No impact	Small impact (positive)
5. Decreasing the HPSI capacity	Unclear, potentially detrimental	Small impact (positive)	No impact	No impact	Small impact (positive)
6. Reduction of HPIS flow (operator action)	Potentially beneficial	Potentially beneficial	No impact	No impact	Small impact (positive)
7. Decreasing of ACC pressure	No clear benefit	No clear benefit	Small impact (positive)	Beneficial	No impact
8. Change of cooldown rate (operator action)	No clear benefit	Small impact (positive)	No impact	No impact	N/A
9. Isolation of ACCs (operator action)	No clear benefit	No or small impact (positive)	Small impact (positive)	N/A (too quick process)	N/A

9   Phenomena Identification and Ranking Table (Task 2.2)

The identification and ranking of phenomena depend strongly on the transient under investigation. For example, the phenomena that occur during a loss-of-coolant accident (LOCA) are different than those that occur during a main steam-line break. Each of the initiating events given in Section 2.1.4 of the APAL report on the deliverable D1.3 in Reference [30] would have its own PIRT. Because the initiating events are too numerous, a PIRT was developed for a single initiating event. The phenomena identified in the T2 transient of the ICAS project, which is described in Section 9.1, was selected for further analyses.

Background on historical development of PIRTs is given in Section 2.1.4 of the APAL report on the deliverable D1.3 [30]. The results of the PIRT, shown in Table 26, where obtained by expert judgement of the project partners after considering the PIRTs developed for other transients, such as those by EricksonKirk, et al., [27] and by Bessette, et al. [28].

Table 26: PIRT for SBLOCA with LOOP for a four-loop PWR

Initial & boundary conditions	Ranking in modelling regions (10=most influential, 1=least influence)				Comment
	Injection point (MR1)	Cold leg (MR2)	Reactor inlet (MR3)	Downcomer (MR4)	
Plant initial state (reactor power, flow, pressure etc.)	3	3	3	4	
Break size and orientation	5	5	5	6	small break
Break location	6	7	7	7	
Time of reactor trip	5	5	6	7	
Decay heat	6	6	7	8	
Timing of reactor coolant pump trip	N/A	N/A	N/A	N/A	LOOP assumption
Timing of SIS actuation	6	6	6	6	
SIS availability (min-max) and asymmetry	8	8	9	9	location of available ECC pumps
SIS pump characteristics	10	10	10	10	
ACC injection temperature	6	6	6	6	
ACC initial pressure	7	7	7	7	
ACC initial level	4	4	4	4	
HPSI and LPSI temperature	10	10	10	10	
RPV wall heat conduction	2	2	7	8	
Reactivity coefficients (boron etc.)	3	3	3	3	
Secondary depress. & cooldown timing and rate	3	3	2	2	

Phenomena	Ranking in modelling regions (10=most influential, 1=least influence)				Comment
	Injection point (MR1)	Cold leg (MR2)	Reactor inlet (MR3)	Downcomer (MR4)	
Break flow rate	5	5	6	7	
DC-to-UH bypass flow	4	4	3	3	
Heat transfer from RPV to containment	2	2	2	2	
Time of loop flow stagnation	7	8	7	7	
SIS flow rate (not incl. pump characteristics)	10	10	10	10	
Timing of HPSI initiation	6	6	6	6	
ACC injection rate	8	8	8	8	
LPSI temperature	8	8	8	8	
Jet behaviour and mixing in injection region	10	8	6	6	
Flow pattern at reactor inlet	1	1	10	8	
Cold plume behaviour and (in)stability	1	1	7	10	
Interphase condensation & non-condensables	7	7	7	7	
Wall-to-fluid heat-transfer phenomena	5	5	6	6	
Liquid/vapour interface in DC	3	8	8	8	
Steam-generator heat transfer	2	2	2	2	
RPV inlet temperature	6	6	6	6	

The highest ranked phenomena must have an associated parameter, model, or input variable that represents the phenomena in a best-estimate thermal-hydraulic code. Otherwise, a different thermal-hydraulic code must be used.

9.1   Simulated transient

The PIRT given in Table 26 applies to a small-break (SB) LOCA in the hot leg of KWU-1300 (see description of plant and event in chapter 2). A loss of off-site power (LOOP) is assumed to occur at the same time as the break occurrence. Therefore, the main coolant pumps trip immediately. A general description is given in Reference [3].

The system analysis of the ICAS transient T2 led to specifications for the transient in additional those for developing the PIRT in Table 26. The break size of 50 cm^2 was successfully used for reproducing the pressure transient given in Reference [3]. The break location was in the hot leg (HL) of Loop 1. One of the four high-pressure safety injection (HPSI) trains was assumed to be down for maintenance (Loop 1). A second train was assumed to fail at the start of the transient (Loop 4). Therefore, only two of the four loops (Loop 2 and Loop 3) received emergency core cooling water from the high-pressure pumps. These two cold legs are separated by 45°, as shown in Figure 1. All four loops received injection from the low-pressure safety injection (LPSI) pumps. Only the four accumulators (ACCs) connected to cold legs (CLs) were active. The four ACCs connected to HLs were deactivated, as was the case for the ICAS transient T2 as described in Reference [3].

Table 27 shows the changes to the PIRT that are the result of the additional specifications for the simulation of the ICAS transient T2 described above. In addition, Table 27 has been changed to show that the break size has been set to 50 cm^2, and so it has no uncertainty associated with it in the subsequent simulations. The time of reactor trip follows immediately after the LOOP, because the loss of electrical power causes the MCPs to fail, which leads to a reactor trip regardless of the other plant conditions.

The break size is too small for the water level in the downcomer to sink far enough for maintain a layer of steam in the cold leg. Nevertheless, the ranking has been kept the same as in Table 26 to indicate the importance of condensation at the top of the downcomer on the pressure transient. The break size is also too small for the heat from the core to be removed through the break, and therefore heat transfer to the secondary side is necessary. The ranking for the steam-generator heat transfer as determined by the secondary-side cooldown rate was increased correspondingly in Table 27.

The transient was simulated for nearly 5000 s. Reference [33] shows that this was sufficient duration for the low-pressure injection system to engage, if possible. During this time span, the water in the RHR tanks was not depleted, due to the small break size. Therefore, no simulation of the "recirculation mode" of safety injection, where water is drawn from the sump surrounding the RPV, was necessary. This changed the LPSI temperature from a phenomenon to an initial condition, as seen in Table 27.

Table 27: PIRT for 50 cm^2 SBLOCA with LOOP and Asymmetric HPSI

Initial & boundary conditions	Ranking in modelling regions (10=most influential, 1=least influence)				Comment
	Injection point (MR1)	Cold leg (MR2)	Reactor inlet (MR3)	Downcomer (MR4)	
Plant initial state (reactor power, flow, pressure etc.)	3	3	3	4	
Break size and orientation	N/A	N/A	N/A	N/A	50 cm^2
Break location	N/A	N/A	N/A	N/A	hot leg
Time of reactor trip	N/A	N/A	N/A	N/A	LOOP assumption
Decay heat	6	6	7	8	
Timing of reactor coolant pump trip	N/A	N/A	N/A	N/A	LOOP assumption
Timing of SIS actuation	6	6	6	6	
SIS availability (min-max) and asymmetry	8	8	9	9	1 HPSI pump in repair and 1 HPSI pump failure
SIS pump characteristics	10	10	10	10	
ACC injection temperature	6	6	6	6	
ACC initial pressure	7	7	7	7	
ACC initial level	4	4	4	4	
Timing of HPSI initiation	6	6	6	6	
HPSI and LPSI temperature	10	10	10	10	
RPV wall heat conduction	2	2	7	8	
Reactivity coefficients (boron etc.)	3	3	3	3	

Initial & boundary conditions	Ranking in modelling regions (10=most influential, 1=least influence)				Comment
	Injection point (MR1)	Cold leg (MR2)	Reactor inlet (MR3)	Downcomer (MR4)	
Secondary depress. & cooldown timing and rate	8	8	8	8	Coupled primary and secondary sides for 50 cm^2

Table 27: PIRT for 50 cm^2 SBLOCA with LOOP and Asymmetric HPSI (continued)

Phenomena	Ranking in modelling regions (10=most influential, 1=least influence)				Comment
	Injection point (MR1)	Cold leg (MR2)	Reactor inlet (MR3)	Downcomer (MR4)	
Break flow rate	5	5	6	7	
DC-to-UH bypass flow	4	4	3	3	
Heat transfer from RPV to containment	2	2	2	2	
Time of loop flow stagnation	7	8	7	7	
SIS flow rate (not incl. pump characteristics)	10	10	10	10	
Timing of HPSI initiation	6	6	6	6	
ACC injection rate	8	8	8	8	
Jet behaviour and mixing in injection region	10	8	6	6	
Flow pattern at reactor inlet	1	1	10	8	
Cold plume behaviour and (in)stability	1	1	7	10	
Interphase condensation & non-condensables	5	5	5	5	Limited condensation in cold leg
Wall-to-fluid heat-transfer phenomena	5	5	6	6	
Liquid/vapour interface in DC	3	8	8	8	
Steam-generator heat transfer	6	6	6	6	Coupled primary and secondary sides for 50 cm^2
RPV inlet temperature	6	6	6	6	

10   Theory of Wilk's and other UE methods

In recent decades, an increasing effort in the field of deterministic safety analysis has led to the development of various methods of best-estimate calculations supplemented by uncertainty analysis of the results. A number of projects initiated e.g., by US NRC and by OECD has resulted in a number of reports and documents [89][90][91][92][93][94][95][96][97].

The best-estimate-plus-uncertainty (BEPU) evaluation methods have been mostly focused on figures of merit connected with reactor core cooling. So far, there has been no application of a BEPU method to evaluation of pressurized thermal shock (PTS) of the reactor pressure vessel. Such an application is complicated by the fact that PTS evaluation is a multidisciplinary and multi-physics task containing a number of sequential analyses. The project APAL is focused on the development of a BEPU method for PTS analyses.

The main objective of Work Package 2 of the APAL project is the identification and evaluation of uncertainties in TH analyses of PTS. In Task 2.2 described in Reference [83], the uncertainties were categorized according to the source of the uncertainties. Reference [83] gives the sources as those related to computer code models, plant parameters, and human factors. Reference [83] also describes the procedure for identifying the phenomena that are the most important to the figures of merit for a particular power plant and a particular transient scenario. The procedure makes use of a PIRT, and part of the procedure is the identification of computer-code input parameters associated with the most important phenomena. Finally, Reference [83] gives the quantification of uncertainty in the input parameters in the form of an uncertainty distribution for each input parameter. These results permit the application of best-estimate-plus-uncertainty methods.

Once the most important sources of input uncertainty have been identified and quantified through uncertainty distributions, the input uncertainties are propagated through the analysis. Multiple simulations of the transient scenario produce multiple sets of simulation output, each set of output is the result of a unique combination of randomly-chosen values for the input parameters. The tolerance limits on the figures of merit from the multiple sets of output can be quantified using various methods. Most of the analyses in Task 2.3 have used the Wilks method, which is described below.

10.1 Wilks method

Best-estimate-plus-uncertainty methods have been used in the United States of America since the U.S. Nuclear Regulatory Commission changed 10 CFR §50.46 in 1988, as described in Regulatory Guide 1.157 [84]. The Regulatory Guide specifies that predicted safety criteria should not be exceeded with a given tolerance and at a corresponding confidence level.

Two categories of methods for finding the tolerance limit are the parametric methods and non-parametric methods. Parametric methods require that the population of the figures of merit follows a known or an assumed probability distribution function. Non-parametric methods require only that the population be continuous. The non-parametric methods decouple the association between the number of uncertainty parameters and the required number of simulations. The tolerance limits of the population can be estimated when sufficient number of simulations are performed, regardless of the number of uncertainty parameters. Wilks [1] proposed a method for finding the necessary sample size for two-sided tolerance limits with given confidence level. He later extended the method to one-sided tolerance limits (Wilks **[2]**). A one-sided tolerance limit is applicable when the figure of merit is not allowed to exceed one limit, for example, a lower limit on a minimum requirement. If the figure of merit is not allowed to exceed both an upper limit and a lower limit, then a two-sided tolerance limit is applicable. Wilks' formula incorporates both a tolerance limit and a confidence in its prediction.

If N simulations are performed, and the values of the figure of merit are arranged from smallest to largest, then the kth order statistic is equal to the kth-smallest value. The rank, r, is either the rth-smallest value with an order statistic of $s = r$, or it is the rth-largest value with an order statistic of $t = N - r + 1$.

199

The upper one-sided tolerance bound is a $\frac{P}{1-\alpha}$ estimate if $I_{1-P}\{N-t+1,t\} \geq 1-\alpha$. , where $I_{1-P}\{N-t+1,t\}$ is the regularized incomplete Beta function equal to $B\{1-P; N-t+1,t\}/B\{N-t+1,t\}$ and where $B\{N-t+1,t\}$ is the complete Beta function. Conversely, the lower one-sided tolerance bound is a $\frac{P}{1-\alpha}$ estimate if $I_{1-P}\{s, N-s+1\} \geq 1-\alpha$. If the output distribution is assumed to be symmetric, then the sample size for the lower and upper limits are the same, and the one-sided tolerance limit is obtained from Eq. (1).

$$I_{1-P}\{r, N-r+1\} \geq 1-\alpha \qquad \text{Eq. (1)}$$

For a rank of r, a tolerance limit of P, and a confidence level of $1-\alpha$, the desired one-sided tolerance can be achieved with the smallest sample size N satisfying Eq. (1). For example, for $r=1$, $I_{1-P}\{1,N\}$ simplifies to $1-[1-(1-P)]^N$, and the first-order tolerance bound is obtained from $[P]^N \leq \alpha$. For a tolerance limit of $P=0.95$ and a confidence level of $1-\alpha=0.95$, the smallest whole number is 59. This value is shown in Table 28 in the left-hand columns under the heading $P=0.95$ in the row for $r=1$. If a higher confidence level of $1-\alpha=0.99$ is required, then the columns under the right-hand heading $P=0.95$ show the smallest whole numbers for N. Table 28 shows that for $r=1$, $N=90$ results in the confidence level of $1-\alpha=0.99$. The columns under the two headings $P=0.99$ show the smallest whole numbers for N that produce confidence levels of 0.95, in the left-hand columns, and 0.99, in the right-hand columns.

Table 28: Confidence levels for one-sided tolerance limits

r	$P=0.95$		$P=0.95$		$P=0.99$		$P=0.99$	
	N	$1-\alpha$	N	$1-\alpha$	N	$1-\alpha$	N	$1-\alpha$
1	59	0.951505	90	0.990112	299	0.950464	459	0.990079
2	93	0.950024	130	0.990034	473	0.950202	662	0.990086
3	124	0.95047	165	0.990046	628	0.95021	838	0.990049
4	153	0.950555	198	0.990243	773	0.950005	1001	0.990001
5	181	0.950837	229	0.990261	913	0.950071	1157	0.990024
6	208	0.950775	259	0.990306	1049	0.950134	1307	0.990014
7	234	0.950145	288	0.990289	1182	0.95019	1453	0.990015
8	260	0.950192	316	0.990166	1312	0.950071	1596	0.990031
9	286	0.950715	344	0.990204	1441	0.950192	1736	0.990026
10	311	0.95035	371	0.99008	1568	0.950203	1874	0.990033

The columns under the right-hand heading $P=0.99$ show that the number of simulations is much larger than for $P=0.95$. Even for a rank or $r=1$, a confidence level of 0.99 requires that the number of simulations is 459. However, regulatory agencies have accepted values for both the tolerance limit and the confidence level of 0.95. Therefore, 59 simulations were performed for Task 2.3.

11   Uncertainty Distributions

Some of the phenomena listed in Table 27 are modelled in thermal-hydraulic system codes, and others are modelled in thermal-hydraulic mixing codes.

Thermal-hydraulic system codes RELAP5, ATHLET and TRACE, mixing codes KWU-MIX and GRS-MIX, and computational fluid dynamics (CFD) codes Fluent and OpenFOAM were used in Task 2.2. The pertinent case was a SBLOCA with the break in the hot leg and with a loss of off-site power.

11.1 Plant Variables

The variables listed in Table 27 that pertain to the design and operation of the nuclear power plant are categorized as plant variables, and they are listed under the heading "Initial & boundary conditions". These parameters are also described as "scenario parameters" which are not uncertainties but rather "variabilities".

The variables with rankings of five or greater were treated as important variables, and so they were either assigned an uncertainty distribution or they were treated conservatively. An uncertainty distribution is the preferred treatment (within the framework of this project), but it is sometimes not practical to quantify the distribution. In this case, the variable is treated conservatively, which indicates that the variable is set at its unfavourable value or sampled over a penalizing range.

11.1.1   Thermal-Hydraulic System Codes

The variables that are associated with the most important initial and boundary conditions depend on how the variables are modelled in the computer code. For RELAP5, TRACE, and ATHLET, the initial and boundary conditions given in Table 27 that have a ranking of five or greater were associated with parameters from the RELAP5 code. The parameters for the most important initial and boundary conditions are given in Table 29.

Table 29: Parameters in system-analysis codes for important initial and boundary conditions

Initial & boundary conditions	Parameters
Initial reactor inlet temperature	initial core power, secondary-side pressure, pressurizer pressure
Break size	break-valve component
Break location	nodalization
Time of reactor trip	control variable
Decay heat	decay-heat correlation or table
Timing of SIS actuation	valve trip (depends on pressure)
SIS availability and asymmetry	analysis assumptions and nodalization
ACC injection temperature	component initial conditions
ACC initial pressure	component initial conditions
Timing of HPSI initiation	valve trip (depends on pressure)
HPSI temperature	component initial conditions
LPSI temperature	storage tank temperature heat-transfer rate in RHR system type of flow model at break ressure-loss coefficient at break

11.1.2 RELAP5 and TRACE model for KWU-1300

The T2 transient of the ICAS project [3] was selected for the initiating event for the PTS analysis, and this was the basis for the rankings of the various phenomena in Table 27. For the T2 transient, the parameters in Table 29 were treated either with uncertainty distributions or they were treated conservatively. The treatment for each parameter is given in Table 30 for this specific transient. The models in RELAP5 and TRACE are similar enough to permit the use of the same uncertainty distributions.

The second column in Table 30 is the best-estimate value for the parameter. This is the value of the parameter that reduces the epistemic uncertainty in the figure of merit (e.g., temperature or heat-transfer coefficient), but not the aleatory uncertainty. Although the epistemic uncertainty could be further reduced even after applying the best-estimate value, for example by improving the physical modelling or by applying corrections to the model outputs that are functions of the model inputs, all remaining epistemic uncertainty is part of the uncertainty distributions described in the third through fifth columns. Therefore, the uncertainty distributions described in the third through fifth columns describe all of the aleatory uncertainty and part of the epistemic uncertainty.

The third column in Table 30 states the nature of the characterization for the uncertainty. The designation "conservative" indicates that parameters are set at their unfavourable value or sampled over a penalizing range. If no uncertainty is given, then the parameter was specified in the definition of the T2 transient.

Table 30: Uncertainty distributions for plant parameters for the T2 transient

Plant parameter	Best-estimate value	Type of distribution	distribution characterization #1 (e.g., mean, lower bound)	distribution characterization #2 (e.g. standard deviation, upper bound)
Initial reactor inlet temperature: **Core power**	100% nominal	Gaussian	Mean:100% nominal	sdt.dev.:1%
Initial reactor inlet temperature: **secondary-side pressure**	60.2 bar	Uniform	60.2 bar	68.2 bar
Initial reactor inlet temperature: **Pressurizer pressure**	100% nominal	Gaussian	Mean:100% nominal	sdt.dev.:1%
Break size	50 cm^2	No uncertainty		
Break location	hot leg	Conservative (see Section C of Reference [75])	hot leg	
Time of reactor trip	at 132 bar	conservative	at 132 bar	
Decay heat	ANS79-1 + 10%	uniform	ANS79-1 − 0%	ANS79-1 + 20%
Timing of SIS actuation	at 110 bar + 10 s delay	uniform	at 110 bar + 0 s delay	at 110 bar + 20 s delay
SIS availability and asymmetry	HP injection in two	Conservative (see Section 3.3 of Reference [75])	HP injection in two neighboring cold legs	

Plant parameter	Best-estimate value	Type of distribution	distribution characterization #1 (e.g., mean, lower bound)	distribution characterization #2 (e.g. standard deviation, upper bound)
	neighboring cold legs			
ACC injection temperature	30 °C	uniform	min:20 °C	max:40 °C
ACC initial pressure	26 bar	uniform	min:24 bar	max:28 bar
initial nitrogen volume	23.6 m^3	Gaussian	23.6 m^3 mean	2.36 m^3 std. dev.
Timing of HPSI initiation	at 110 bar + 10 s delay	uniform	at 110 bar + 0 s delay	at 110 bar + 20 s delay
HPSI temperature	30 °C	uniform	min:15 °C	max:45 °C
HP and LP pump pressure/flow curves	As defined in T2 with a multiplier.	Gaussian	mean:100% of nominal	std.dev.:10% of nominal

Many of the uncertainty distributions in Table 30 are uniform with a lower bound and an upper bound. This treatment of the uncertainty was chosen because insufficient data were available to establish a Gaussian distribution or another type of uncertainty distribution.

Some parameters are described by conservative values instead of with uncertainty distributions. Section 3.3 of Reference [75] states that unsymmetrical cooling is applied in order to reach the maximum thermal load at the cold-leg nozzle exit. For SBLOCA, the ECC injection rate in an individual loop is higher when only part of the ECC systems is injecting than when all ECC pumps are in operation. The cold legs with ECC injection are in neighbouring loops so that the possibility exists that two plumes merge, as described in Appendix C of Reference [75].

The location of the break in the hot leg is conservative for analyses on the RPV welds and cold-leg nozzle because the leak flow draws the injected water into the downcomer and upward through the core. This promotes the formation of plumes in the downcomer. A leak in the cold leg would draw water upward in the downcomer, which would impede the downward flow of plumes in the downcomer.

The decay heat used in the base case described in Reference [33] is conservative, and the value is ANS79-1 – 0%. Section 3.3 of Reference [75] states low decay heat is conservative. Therefore, the best-estimate value is higher than the conservative value, and it was set equal to ANS79-1 + 10%. The best-estimate value was set equal to the mean of the uncertainty distribution, and so the uncertainty spans from the lower decay heat at ANS79-1 – 0% to a higher decay heat at ANS79-1 + 20%. .

11.1.3 ATHLET model for KWU-1300

Table 31 presents uncertainty distributions for plant parameters that were identified for the TH system code ATHLET. Break size (50 cm²) and break position (hot leg) are not treated as uncertain. Changing these boundary conditions would deviate from the reference transient T2 of the ICAS project and would probably lead to different accident scenario. Where insufficient data were available to establish more complex distributions, uncertainty distributions were chosen to be uniform with a lower and upper bound.

Table 31: Uncertainty Distributions for Plant Parameters in ATHLET

Model parameter	Best-estimate-value	Type of distribution	Distribution parameters p1=mean p2=standard deviation	Technical or statistical basis for type of distribution and distribution parameters
Correction factor for decay heat	1	normal	p1=1; p2=0.04 min/max: 0.9/1.1	[38], Chapter 6.1.12, Para. 45
Correction factor for power of fuel rods	1	normal	p1=1; p2=0.01 min/max:0.97/1.03	expert judgement
Temperature of the pressure accumulator and the emergency feed water	30 °C	uniform	min/max: 5/30	[39], Chapter 3.5.1.13, par.51
Delay time between leak opening and triggering of SCRAM	2 s	uniform	min/max: 1/5	expert judgement
Runtime of the SCRAM between triggering and maximum shut down reactivity	2 s	uniform	min/max: 0.5/4	expert judgement
Delay for secondary cooldown	120 s	normal	p1=300; p2=150 min/max: 0/600	expert judgement
Time delay to switch off the main coolant pumps	2 s	normal	p1=2; p2=1 min/max: 0/4	[40], chapter 6.1.18, Par. 56
Factor of the feed mass flow of the LP-pumps	1	normal	p1=1; p2=0.04 min/max: 0.9/1.1	[41], Annex 1, Table 1
Factor of the feed mass flow of the HP-pumps	1	normal	p1=1; p2=0.04 min/max:0.9/1.1	[41], Annex 1, Table 1
Pressurization of the pressure accumulators of the ECCS	2.60E+06 Pa	normal	p1=2.6E+06; p2=3.0E+05 min/max: 2.4E+06/2.8E+06	[41], Annex 1, Table 1
Fill level of the pressure accumulator of the ECCS	8.5428 m	uniform	min/max: 8.148/8.889	expert judgement
Isolation of accumulators after 500 s	500 s	toggled	500 s; 50000 s	-
Timing for HPI actuation <110 bar + t	20 s	uniform	min/max: 0/20	expert judgement
Timing for LPI actuation <10 bar + t	25 s	uniform	min/max: 0/25	expert judgement
Temperature of HPI/LPI	15 °C	uniform	min/max. 1/45	expert judgement

11.2 Model parameters

The phenomena listed in Table 27 that are modelled in the computer codes are listed under the heading "phenomena". The phenomena with rankings of five or greater were treated as important phenomena, and so they were either assigned an uncertainty distribution or they were treated conservatively. An uncertainty distribution is the preferred treatment (within the framework of this project), but it is sometimes not practical to quantify the distribution. In this case, the variable is treated conservatively.

The uncertainty in model parameters is quantified by comparing the values of the parameters from the models with experimentally derived values. Experimental data from the UPTF experimental program were made available to the APAL project by the German Federal Ministry for Economic Affairs and Energy. In particular, data from Test C1 Run 21a2 of the UPTF-TRAM program were used.

11.2.1 RELAP5 code

The parameters that are associated with the most important phenomena depend on how the phenomena are modelled in the computer code. For RELAP5, those phenomena given in Table 27 that have a ranking of five or greater were associated with parameters from the RELAP5 code. The parameters for the most important initial and boundary conditions are given in Table 32.

Table 32: Parameters in system-analysis codes for important phenomena

Phenomena	Parameters
Break flow	type of flow model at break pressure-loss coefficient at break thermal-nonequilibrium coefficient at break
Initial reactor inlet temperature	Core power, secondary-side pressure, pressurizer pressure
Time of loop flow stagnation	type of flow model at break pressure-loss coefficient at break
SIS flow rate (incl. pump characteristics)	HP and LP pump curves type of flow model at break pressure-loss coefficient at break
ACC injection rate	initial ACC pressure initial nitrogen volume type of flow model at break pressure-loss coefficient at break
RPV wall heat conduction	Material property tables
Interphase condensation & non-condensables	ACC isolation type of flow model at break pressure-loss coefficient at break
Wall-to-fluid heat-transfer phenomena (excl. heat-transfer-coefficient correlation)	velocity, water properties
Liquid/vapour interface in DC	type of flow model at break pressure loss coefficient at break

Many of the phenomena in Table 32 have parameters in common with each other. For example, most of the phenomena depend on the pressure, which is dependent on the break flow and the injection flow, among other phenomena. The break flow, in turn, depends on the type of flow model at break and on the pressure-loss coefficient at break. Therefore, the important parameters for many of the phenomena Table 32 are the type of flow model at the break and the pressure-loss coefficient at the break. The development of the uncertainty distribution for the thermal-nonequilibrium coefficient in the Henry-Fauske choked-flow model used in RELAP5, using data from the Marviken CFT no. 24.

The treatment for each parameter is given in Table 33.

Table 33: Uncertainty distributions for model parameters in RELAP5

Model parameter	Best-estimate value	Type of distribution	distribution characterization #1 (e.g., mean, lower bound)	distribution characterization #2 (e.g. standard deviation, upper bound)
thermal-nonequilibrium coefficient for Henry-Fauske model	0.14	Weibull for CDF from 0.1 to 0.85; 0.0 for CDF<0.1; 0.775+0.075*CDF for CDF>0.85	Scale λ is 1	shape factor k is 7
Wall-to-fluid heat-transfer phenomena	Single-phase liquid to wall HTC	log-uniform	0.5	2.0
Wall-to-fluid heat-transfer phenomena	Single-phase vapour to wall HTC	log-uniform	0.5	2.0
Single-phase friction factor	Wall-drag coefficient	log-uniform	0.5	2.0
Single-phase friction factor	Form-loss coefficient	log-uniform	0.5	2.0
Interfacial heat transfer	As for base case	Conservative	as for base case	as for base case
RPV wall heat conduction, specific heat, density	Material-properties tables	Gaussian	as for best-estimate case	5% std. dev.

Note that the heat-transfer coefficient is a figure of merit, and that the important phenomena, such as velocity distribution, do not have parameters associated with them that can be varied according to their uncertainty. Therefore, the uncertainty in those parameters cannot be propagated forward. Instead, the uncertainty distribution is applied in a post-processing step.

11.2.2 TRACE code

The uncertain model parameters for the TRACE code are listed in Table 34. With the exception of the model parameters grouped under the term "heat-transfer coefficient correlation", which are taken from the TRACE modelling of the UPTF transient, and the choked-flow parameter taken from the TRACE modelling of selected Sozzi-Sutherland experiment, the parameters are taken as close as possible to the RELAP5 parameters (i.e. that of Table 33).

Table 34: Uncertainty distributions for model parameters in TRACE

Model parameter	Best-estimate value	Type of distribution	distribution characterization #1 (e.g., mean, lower bound)	distribution characterization #2 (e.g. standard deviation, upper bound)
Choked-flow multiplier for two-phase flow (CHM22	0.848	Normal	0.848	0.0888
HP and LP pump curves	See initial and boundary conditions Table 30.			
initial accumulator pressure	See initial and boundary conditions Table 30			
initial nitrogen volume	See initial and boundary conditions Table 30			
storage tank temperature	See initial and boundary conditions Table 30			
heat-transfer coefficient correlation input:				
SS thermal conductivity	1.0	Uniform	0.95 min	1.05 max
SS specific heat	1.0	Uniform	0.95 min	1.05 max
SS emissivity [-]	0.75	Uniform	0.5625 min	0.9375 max
Single Phase Liquid to Wall HTC	0.8	Log Uniform	0.5 min	2.0 max
Single Phase Vapour to Wall HTC	0.8	Log Uniform	0.5 min	2.0 max
Wall Drag Coefficient	0.8	Log Uniform	0.5 min	2.0 max

11.2.3   ATHLET code

Uncertainty parameters and their distributions applied in the ATHLET simulations for the transient T2 of the ICAS project are listed in Table 35. The selected parameters are associated with the phenomena listed and ranked in the PIRT for SB-LOCA in PWR with LOOP (see Table 27). Only parameters are listed that were not classified as boundary conditions but as model parameters depending on the TH system code used (ATHLET) and that were expected or proven to be influential on PTS relevant phenomena. In Wenzel et al. [69] sensitivity studies on the listed parameters for PTS analyses are presented. Uncertain boundary conditions in the plant model that may influence the assessment of the RPV integrity are listed separately in Table 31 (section 11.1.3).

Table 35: Uncertainty distributions for model parameters in ATHLET

Model parameter	Best-estimate-value	Type of distribution	Distribution parameters	Technical or statistical basis for type of distribution and distribution parameters
Turbulence factor for the evaporation in case of critical flow	30	log. normal	p1=2.29; p2=0.65 min/max: 0/50	[70], Chapter 2.1.3.1
Single-phase convection in water (Dittus-Boelter) - correction factor, all surfaces where heat transfer takes place	1	uniform	min/max: 8.50E-01; 1.15E+00	KWU experiments and expert judgement
Single-phase natural convection in water (Dittus-Boelter) - correction factor, all surfaces where heat transfer takes place	1	uniform	min/max: 8.50E-01; 1.15E+00	KWU experiments and expert judgement
Model for single-phase forced convection in steam: 1 = Dittus-Boelter II / 2 = Mc Eligot	1	toggled	1; 2	[39], Chapter 3.5.1.3, Par. 7
Single-phase convection in steam Dittus-Boelter II / Mc Eligot - correction factor; all surfaces where heat transfer takes place	-	dependency	-;-	[50], Tab. 5.2-1, Par. 28
Correction factor for direct condensation	1	histogram	5.00E-01; 2.00E+00	HDR Condensation-Experiment, UPTF-TRAM Experiment, [50], Tab. 5.2-1, Par. 32
Heat losses to the environment, external surfaces of the primary circuit and the steam generator	1	uniform	0.99; 1.01	validation and expert judgement
Thermal conductivity of the base material	1	normal	p1=1; p2=0.03 min/max: 0.95/1.05	[51]
Heat capacity of the base material	1	normal	p1=1; p2=0.03 min/max: 0.95/1.05	[51]
Wall roughness U-tubes	7E-06	polygonal line	2.00E-06; 2.00E-05	[70], Tab 2.1-5, Par. 21
Wall roughness of the ECC feed lines	1.5E-05	polygonal line	1.00E-05; 0.0001	[39], Chapter. 3.5.1.10, Par. 37,
Form loss of the ECC feed line	0.5	polygonal line	0.1; 5.5	[41], Annex 1, Table 1 and expert judgement
Form loss correction factor for CCOs between	1	histogram	0.4; 5	[39], Chapter 3.5.1.10, Par. 35

Model parameter	Best-estimate-value	Type of distribution	Distribution parameters	Technical or statistical basis for type of distribution and distribution parameters
core channels and between downcomer				
Form loss coefficient at break	0.1	uniform	min/max: 0.1; 10	expert judgment
Transport material value, thermal conductivity of water - correction factor	1	uniform	min/max: 0.992; 1.008	ATHLET material properties from IAPWS-97 [52]
Transport material value, thermal conductivity of the gas - correction factor	1	uniform	min/max: 0.985;1.015	ATHLET material properties from IAPWS-97 [52]
Transport material value, heat capacity of the water (only transport property) - correction factor	1	uniform	min/max: 0.99;1.01	ATHLET material properties from IAPWS-97 [52]
Transport material value, heat capacity of the gas (only transport property) - correction factor	1	uniform	min/max: 0.955; 1.045	ATHLET material properties from IAPWS-97 [52]
Factor for the heat transfer coefficient in the downcomer	1	uniform	min/max: 0.8; 1.2	Validation UPTF-TRAM Experiment
Accounting for axial heat transfer in structure material (1 – yes; 2 – no)	1	toggled	1; 0	-

11.2.4 KWU-MIX code

The phenomena in Table 27 with a ranking of five or greater that are modelled by KWU-MIX are given in Table 36. The remaining phenomena are simulated in RELAP5.

Table 36: Parameters in KWU-MIX for important phenomena

Phenomena	Parameters
Jet behaviour and mixing in injection region	entrainment ratio for a jet: $\varepsilon_{Haefner,be}$
Flow pattern at reactor inlet	CCFL constant: C_{CCFL}
Cold plume behaviour and (in)stability	entrainment velocity in plume $u_{ent,Fox,be}$
Interphase condensation & non-condensables	not applied to ICAS transient T2
Wall-to-fluid heat-transfer phenomena	velocity, $u_{c,Fox,be}$

11.2.4.1 Uncertainty distribution for entrainment due to countercurrent flow

When ECC water is injected into the cold leg during a period of loop-flow stagnation, the cold ECC water flows along the bottom of the cold leg from the injection location to the DC. If the water level in the DC is above the top of the cold-leg nozzle, hot water flows simultaneously above the cold water in the opposite direction, from the DC to the mixing location. The source of the hot water is the upper region of the DC. The cold ECC water mixes with the surrounding hotter water in the cold leg. The rate of entrainment, $\dot{V}_{entr}$, is defined as $\dot{V}_{entr} = \varepsilon\,\dot{V}_{inj}$, where ε is the entrainment ratio.

209

For injection from the side, the entrainment ratio, $\varepsilon_{H\ddot{a}fner}$, was correlated by Häfner and Wolf [57]. The experiment UPTF-TRAM Run 21a2 was then simulated (Trewin et al. [34]), and the simulations produced values of best-estimates of $\varepsilon_{Haefner,be}$, which were then used with the experimentally derived values, ε_{exp}, in order to calculate new best-estimate values for relative error, $E_{inj,be} = \frac{\varepsilon_{exp}}{\varepsilon_{Haefner,be}}$.

Order statistics were then applied to the values for the relative error by sorting them from smallest to largest, and each given value was assigned a value of the cumulative distribution function (CDF). The CDF of the relative error evaluated at $E_{inj,be}$ is the probability that the relative error will take a value less than or equal to $E_{inj,be}$. As an example, Figure 289 shows that the CDF for a relative error of $E_{inj,be} = 0.98$ is approximately 0.5 (50%). The likelihood of choosing at random a value for the relative error that is larger than 0.98 is approximately equal to the likelihood of choosing at random a smaller value than 0.98. The likelihood of choosing at random a value for the relative error less than 1.25 is approximately equal to 0.95. The likelihood of choosing at random a value for the relative error greater than 0.85 is also equal to 0.95.
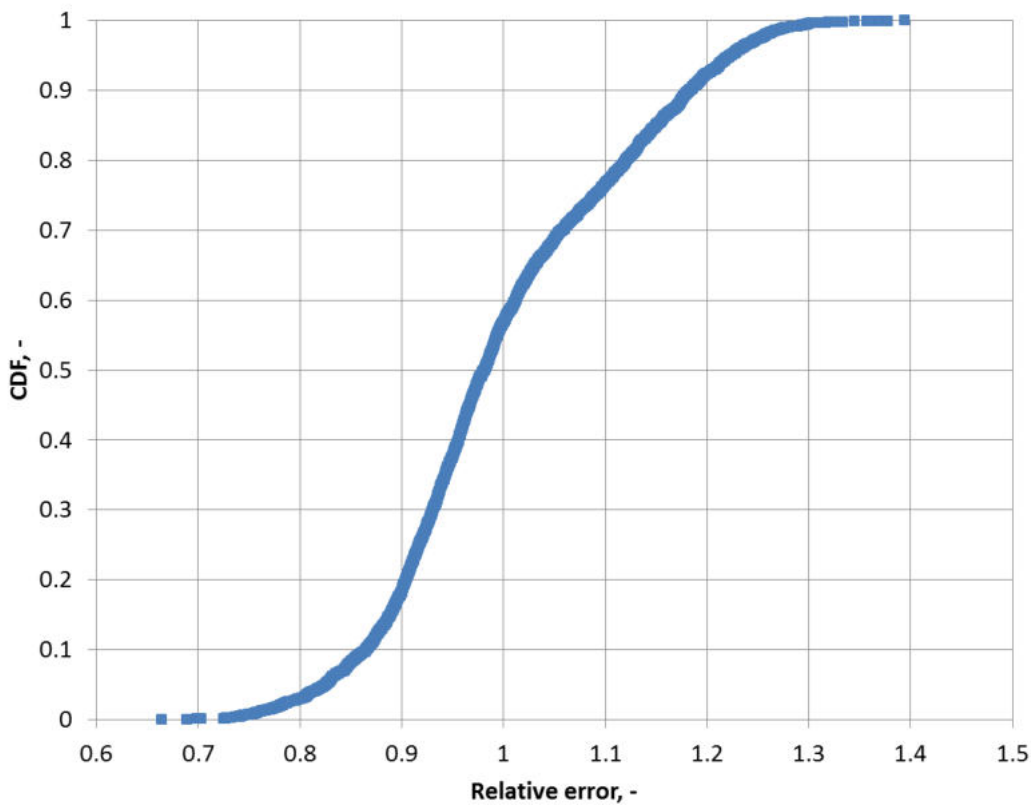
Figure 289: Uncertainty distribution for mixing at MR 1 using the correlation of Häfner and Wolf

11.2.4.2 Uncertainty distribution for entrainment due to countercurrent flow

When the cold leg is filled with water, the cross-sectional flow areas of the cold water and hot water are constrained by the flow area of the cold leg. Therefore, an increase in flow of either layer increases the flow resistance for both layers, due to the large flow resistance at the interface of the two flow streams. Because the hot water and cold water flow in opposite directions, there is a critical value of the velocity in one of the layers above which the velocity in the other layer is prevented from

increasing. The critical velocity defines a situation called "countercurrent flow limitation" (CCFL). A CCFL correlation can be used to calculate the maximum amount of mixing that can occur due to the restriction of flow of hot water. The flow conditions are given by the following CCFL correlation from Iyer et al. [58]. $\text{Fr}_{\text{cold}}^2 + \text{Fr}_{\text{hot}}^2 = C_{CCFL}$, where Fr is the Froude number for one of the streams.

The bias for entrainment from a stratified layer of hot water into a layer of cold water flowing in the opposite direction underneath, $Bias\_CCFL$, was incorporated into KWU-MIX, by multiplying the equation for C_{CCFL} from **Error! Reference source not found.** by the value $Bias\_CCFL$ from **Error! Reference source not found.**. The new value of the CCFL parameter, $C_{CCFL,be}$, is the best-estimate value.

$$C_{CCFL,be} = C_{CCFL} \cdot Bias\_CCFL \qquad \qquad \text{Eq. (2)}$$

For injection from the side, the entrainment ratio, $\varepsilon_{H\ddot{a}fner}$, was correlated by Häfner and Wolf [57]. The experiment UPTF-TRAM Run 21a2 was then simulated (Trewin et al. [34]), and the simulations produced values of best-estimates of $\varepsilon_{Haefner,be}$, which were then used with the experimentally derived values, ε_{exp}, in order to calculate new best-estimate values for relative error, $E_{inj,be} = \frac{\varepsilon_{exp}}{\varepsilon_{Haefner,be}}$.

Simulations of UPTF-TRAM Run 21a2 for injection flow rates of approximately 20 kg/s were performed with KWU-MIX (Trewin et al. [34]). The simulations produced experimental values of $C_{CCFL,exp}$, which were then used with $C_{CCFL,be}$ for calculating values for the relative error, $E_{CCFL} = \frac{C_{CCFL,exp}}{C_{CCFL,be}}$.

The values for E_{CCFL} were manipulated using order statistics, as described above, and the resulting distribution in the relative error is shown in Figure 290.
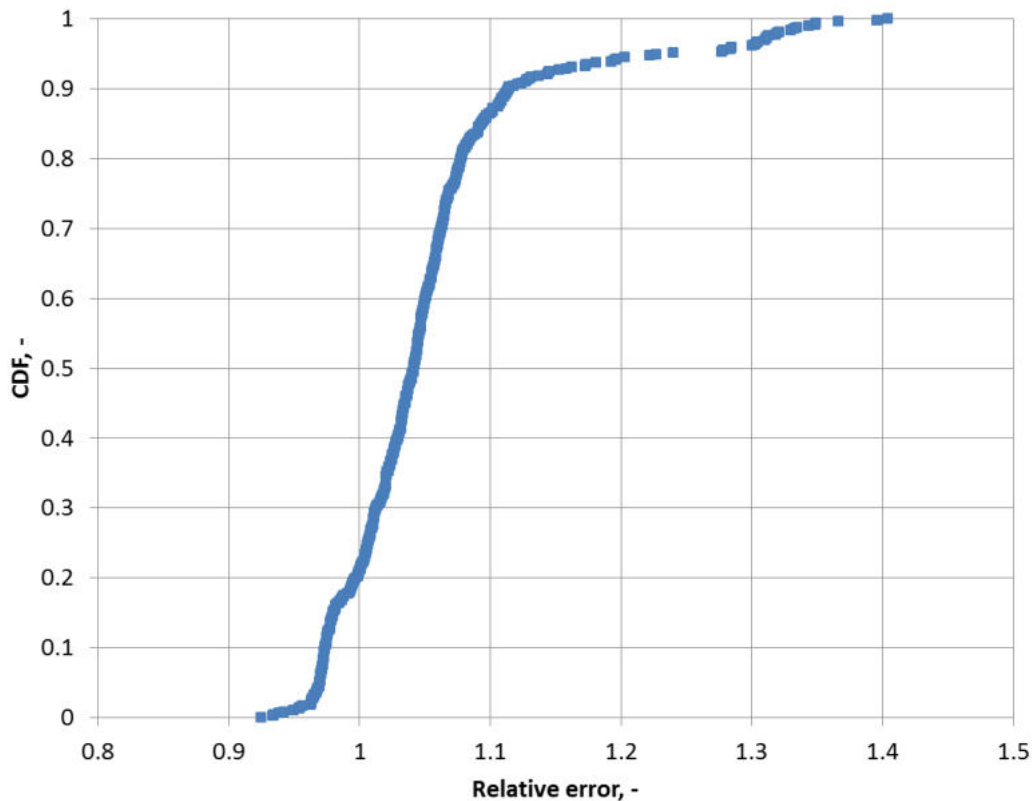
Figure 290: Uncertainty distribution for mixing at MR 2 using the CCFL correlation from [59]

The abscissa of Figure 290 is the values of the relative error, E_{CCFL}. The ordinate of Figure 290 is the CDF of the relative error. Figure 290 shows that the CDF for a relative error of 1.04 is approximately 0.5 (50%). The likelihood of choosing at random a value for the relative error that is larger than 1.04 is approximately equal to the likelihood of choosing at random a smaller value than 1.04. The values of E_{CCFL} within 95% of the maximum value are less than 1.3 and those within 95% of the minimum value are greater than 0.97.

11.2.4.3 Liquid-Liquid Mixing in the DC

For a DC filled with hot water, cold water entering the DC from the cold leg forms a buoyant jet. The model given by Fox [21] was used,

After the bias for velocity in the plume was removed from KWU-MIX, simulations of experiment UPTF-TRAM Run 21a2 were performed with KWU-MIX (Trewin et al. [34]). which produced the best-estimate values of $u_{c,Fox,be}$. The best-estimate values of $u_{ent,Fox,be}$ were then used with the experimentally determined values, $u_{ent,exp}$, for calculating values for the relative error, $E_{Fox} = \frac{u_{ent,exp}}{u_{ent,Fox,be}}$. All the values of E_{Fox} were manipulated using order statistics, resulting in a single distribution of the uncertainty for MR4 as shown in Figure 291.
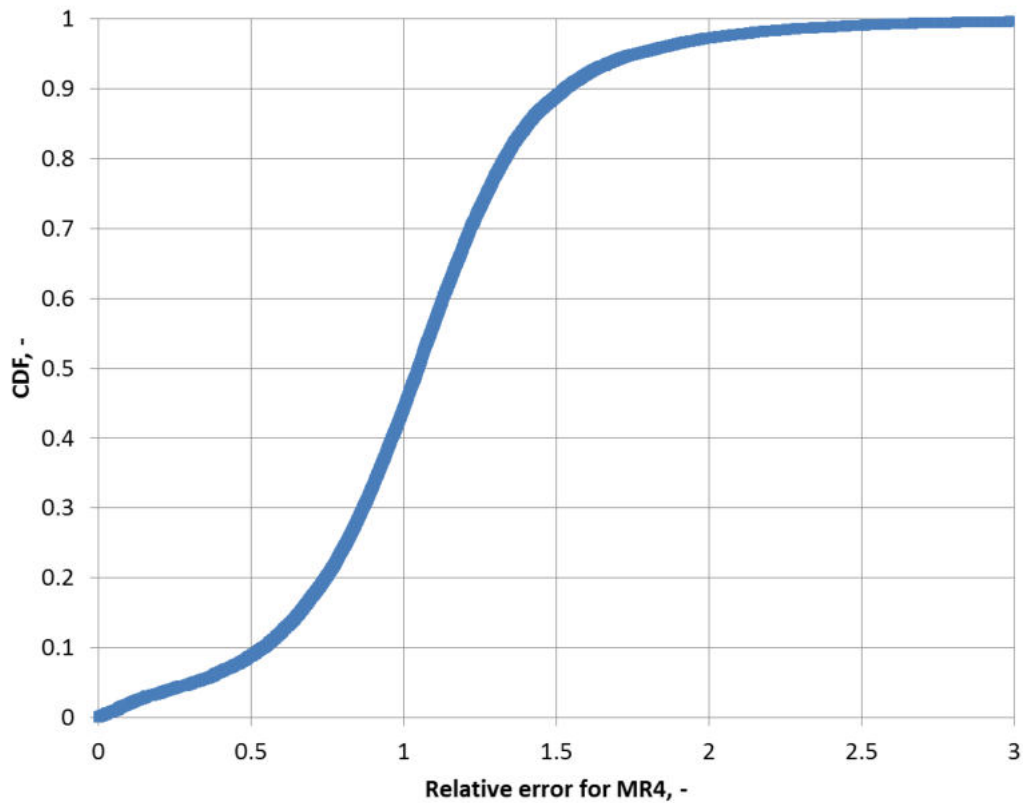
Figure 291: Uncertainty distribution for mixing at MR 4 using the model for plume mixing from Fox

Figure 291 shows that the uncertainty in the relative error for the mechanistic model Fox [21] ranges from zero to three with 50% of the relative errors less than or equal to 1.06. The values of E_{Fox} with CDF less than 95% are less than 1.95 and values of E_{Fox} with CDF greater than 5% are greater than 0.195.

11.2.4.4 *Uncertainty distribution for centerline velocity in a plume*

The velocity at the center of a cold-water plume in the DC, $u_c\{z\}$, was based in KWU-MIX on the mechanistic model by Fox [21]. The calculated values were compared with the experimental values of the vertical fluid velocity, $u_{c,exp}$. The measured velocities were obtained by means of a turbine flowmeter 5.625 m below the centerline of Cold Leg 2 at the position of the plume's centerline. The value of the relative error was calculated as $E_{Uc,Fox} = \frac{u_{c,exp}}{u_{c,Fox,be}}$.

The scatter in the values of $E_{Uc,Fox}$ was attributed to the aleatoric and remaining intrinsic uncertainty in the mechanistic model for entrainment into a plume of cold water by Fox [21]. All the values of $E_{Uc,Fox}$ were manipulated using order statistics, resulting in CDF of the relative error for the centreline velocity, as shown in Figure 292.

213
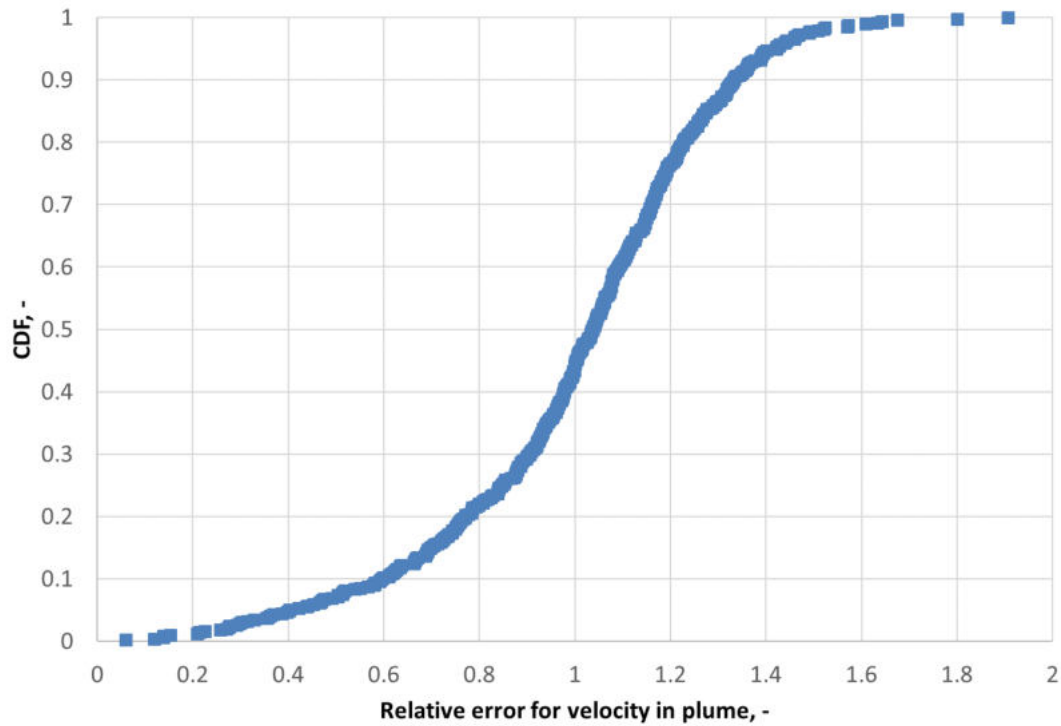
Figure 292: Uncertainty distribution for centerline velocity in a plume using the model from Fox

Figure 292 shows that the uncertainty in the relative error for the mechanistic model Fox [21] ranges from zero to two with 50% of the values less than or equal to 1.04. The values of $E_{Uc,Fox}$ within 95% of maximum value are less than 1.42 and those with a CDF greater than 5% are greater than 0.3.

The treatment for each parameter is given in Table 36 is shown in Table 37.

Table 37: Uncertainty distributions for model parameters in KWU-MIX

Model parameter	Best-estimate value	Type of distribution	distribution characterization #1 (e.g., mean, lower bound)	distribution characterization #2 (e.g. standard deviation, upper bound)
entrainment ratio for a jet: $\varepsilon_{Haefner,be}$	0.98	CDF curve for relative error given in **Figure 289**	0.8	1.25
CCFL constant: C_{CCFL}	1.04	CDF curve for relative error given in **Figure 290**	0.97	1.3
entrainment velocity, $u_{ent,Fox,be}$	1.06	CDF curve for relative error given in **Figure 291**	0.195	1.96
Velocity at centre of plume, $u_{c,Fox,be}$	1.04	CDF curve for relative error given in **Figure 292**	0.3	1.42

11.2.5 GRS-MIX code

The phenomena in Table 27 with a ranking of five or greater that are modelled by GRS-MIX are given in **Table 38**. The remaining phenomena are simulated in ATHLET.

Table 38: Uncertainty distributions for model parameters in GRS-MIX

No.	Par.ID	Description	Best-estimate value	Notes	Distribution Type	Min.	Max.
1	CEPS; C_ε	Correction factor of entrainment ratio (epsilon) [-]	1	adjusted on UPTF-TRAM C1 Run 21a2	Uniform	0.9	1.1
2	UCCFC; C_{CCF}	Uncertainty of constant of Froude number correlation [-]	2.16	UCCFC=(1/x)^(1/4) with x(BE)=0.046; assumed uncertainty range for x: 0.001:0.1; Eq. 9 in [23]	Uniform	1.77	5.62
3	CHTCBM	Correction factor in HTC of admixing to plume in downcomer [-]	1	adjusted on UPTF-TRAM C1 Run 21a2	Uniform	0.2	2
4	CHTCSTR	Correction factor in HTC of admixing to jet at injection position in CL [-]	1	adjusted on UPTF-TRAM C1 Run 21a2	Uniform	0.8	1.2

5	FZNU; C_{Nu}	Correction factor of Nu-number in Dittus Boelter correlation for heat transfer to the downcomer wall [-]	1.65	Eq. 22 in [23]	Uniform	1	2
6	HTCDC	Uncertainty in HTC outside of the plume in downcomer [W/m²K]	1500	empirically derived from UPTF experiment (Tab. 2 in [23]	Uniform	1300	1600
7	FCC; C_U	Uncertainty in constant for jet velocity of Chen&Chen model [-]	1.66	Eq. 15 in [23]	Uniform	1	2

11.2.6 Comparison of Task 2.1 Base Case and Task 2.3 best-estimate reference case assumptions

The major differences in assumptions of Task 2.1 Base Case and Task 2.3 best-estimate reference case are shown in the table below:

Table 39: Overview of different assumptions in Task 2.1 and Task 2.3 analyses

Plant parameter	Task 2.1 Base Case (ICAS values)	Task 2.3 best-estimate reference case
Initial reactor inlet temperature: secondary-side pressure	68.2 bar	60.2 bar
Decay heat	ANS79-1	ANS79-1 + 10%
ACC injection temperature	20 °C	30 °C
HPSI / LPSI temperature	15 °C	30 °C

11.3 Human-factors parameters

Human factors in the PTS analyses were divided into two types. One type consists of operator actions where the operator is required to take action or is permitted to choose a course of action. The second type consists of operator actions that are not intended by the designers of the plant, and so are considered to be human errors.

Human factors were evaluated by several means, one of which was the assessment of operator actions that are consistent with regulator-approved operating procedures (OP) for the plant. For a KWU PWR, no operator action is required by the regulator during the first 30 minutes of an accident. The loss of offsite power interrupts power to the main coolant pumps, and the pump trip causes automatic trips of the reactor and the turbine. Therefore, operator action on tripping the reactor or MCPs is eliminated from uncertainty analyses as either a valid operator choice and is a human error.

For KWU PWRs, the cooldown of the secondary side is performed automatically by the reactor protection system (RPS), and the cooldown rate is set to 100 K/h for SBLOCA. There is a possible procedure that might require a faster cooldown rate during emergency procedures when manually depressurizing the steam generators to provide feedwater by mobile pumps. However, a loss of feedwater is not a reasonable penalization (for reactor core cooling) of make, because two other faults are already applied for penalizing this transient, namely, 1) the loss of high-pressure safety injection due to a pump failure and 2) the loss of high-pressure safety injection due to repair of a second pump.

216

No more than two penalizing faults are required by regulators for safety analyses of this type of PWR, because additional faults make the likelihood that an event would occur is so small as to fall outside the range of design-basis accidents. For other types of plants that are not KWU PWRs, however, the operator chooses the cooldown rate. The range of possibilities for VVER plants is from 50 K/hr to 200 K/hr.

In D2.1 [33], manually switching off one of the HPSI pumps was investigated. For a KWU PWR during an SBLOCA, the OP requires several conditions to be met.

- The ECC-criteria must be reset (and several conditions described next must be met before this is possible) and more than one HPSI pump must be working.

The required conditions are:
- PRZ level in the range from 8m to 10 m
- RPV level must be greater than the value of "min 3" (an RPS variable).
- HPI criteria must be not satisfied

If HPSI is activated again later due to HPSI criteria being met, several steps must be repeated until retrying to switch off one HPSI pump again. Otherwise, the HPSI pumps are switched off one after another. To prevent a renewed triggering of ECC-criteria, HPSI should be switched on again if the pressure is above 10.5 bar and the PRZ level is below 4 meters. These requirements lead to the conclusion that manually switching off one of the HPSI pumps during the SBLOCA transient to be simulated in Task 2.3 is a human error.

For other types of plants that are not KWU PWRs, however, the operator chooses the number of HPSI pumps in operation, with a lower limit of one. The failure of one HPSI pump due to repair and the failure of a second HPSI pump at the start of the event reduces the number of HPSI pumps to two. Therefore, the operator has the option of isolating one additional HPSI pump.

Because the plant operator of a KWU PWR is not at liberty to choose a course of action during the first 4900 s of the SBLOCA transient to be simulated in Task 2.3, the limited number of possible human actions are necessarily the result of human error. This is not the case for the operator of a VVER plant. The three human actions supported by auxiliary calculations in Task 2.1 that cause one or more of the important phenomena listed in the PIRT to take place are manually switching off on the HPSI pumps and increasing the rate of secondary-side cooldown. The auxiliary calculations in Task 2.1 showed that not isolating the accumulators did not lead to significant change in the transient to be simulated in Task 2.3. Parameters associated with human factors are those that describe both operator actions and inactions. Operator actions directly influence, in both beneficial and detrimental ways, the degree of overcooling and the primary-side pressure. Because human factors pertain to the initial and boundary conditions of the PWR, the uncertainty parameters are those for the system-analysis code. The most important human factors in the PIRT, shown in Table 27, are the secondary-side depressurization and cooldown timing and rate, and the reduction of HPIS flow by switching off one of the two HPIS pumps. An example given in Section 7.1 of Reference [1] is reduction of HPIS flow by the operator by switching off one of the two HPIS pumps at a time of 1800 s after the initiation of the break. In Section 7.2 of Reference [1], an increase of the secondary-side cooldown rate by operator from 100 K/h to 200 K/h was analysed. The parameters associated with these important human factors are given in **Table 40**. The third human factor from Section 7.1 of Reference [1], the isolation of the ACCs, is also shown in Table 40 for completeness.

Table 40: Parameters in system-analysis codes for important human factors

Initial & boundary conditions	Parameters
reduction of HPSI flow by operator	number of HPSI pumps in operation
secondary-side cooldown rate	secondary-side pressure-reduction rate
isolation of ACCs	time of isolation

Because human factors pertain to the initial and boundary conditions for the controlled operation of the PWR, the uncertainty parameters are those for the system-analysis code. The values for these parameters that were applied in Reference [1] represented human error. As such, they are outside of the range of uncertainty. The values of the parameters given in **Table 41** represent the uncertainty for human errors in a KWU PWR and for a normally functioning VVER plant.

Table 41: Uncertainty distributions for human factors

Parameter	Best-estimate value	Type of distribution	distribution characterization #1 (e.g., mean, lower bound)	distribution characterization #2 (e.g. standard deviation, upper bound)
Time of isolation of second HPSI pump	4900 s	Uniform	1800 s	4900 s
Secondary-side pressure leading to the given cooldown rate	100 K/hr	Uniform	50 K/hr	200 K/hr
Time of isolation of ACCs	4900 s	Uniform	1800 s	4900 s
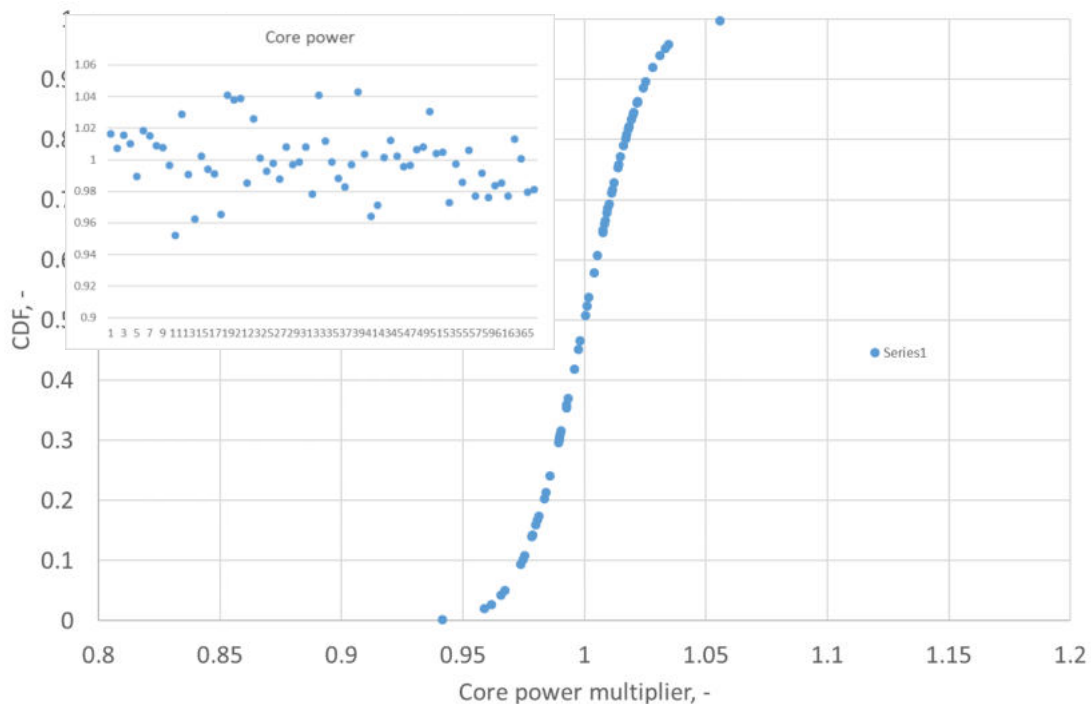
Figure 293: Randomly chosen core-power multipliers from the Gaussian distribution in Table 30

This same procedure is used for each of the other uncertainty parameters. The total number of uncertainty parameters depends on the computer program that is used. For example, the case where a system-analysis simulation with RELAP5 (11 plant parameters from Table 30, 7 model parameters from Table 33 and 3 human-factors parameters from Table 41) is followed by a mixing-analysis simulation with KWU-MIX (4 model parameters from Table 37) results in 25 total uncertainty parameters for each of the 59 simulations.

12   UJV uncertainty analysis with RELAP5 and DAKOTA (Task 2.3)

12.1 Reference best-estimate calculation

The "v86" version of the KWU 1300 RELAP model was used for calculation in Task 2.3. In comparison with KWU model v76 used in task 2.1, some minor changes in nodalization were made:

- Nodalization of PRZ was changed to vary initial nitrogen volume
- Changed nodalization of accumulators for same purpose
- Changed connection between downcomer and upper plenum – the original solution caused instabilities during transient run – now the connection is at level of cold/hot leg axis, which corresponds to real reactor geometry.

Initial conditions of some components were changed to correspond best-estimate solution. Exact values of changed initial conditions can be found in Table 30.

Timing of main events and graphical results from the reference best-estimate calculation are shown below:

Table 42: Steady state parameters of calculation in Task 2.3 reference best-estimate case of UJV BEPU
(plus comparison with Task 2.1 Base Case)

Specification	Parameters of T2.1 Base Case	Parameters of T2.3 reference best-estimate case (s)
Reactor thermal power	3.765e9 W	3.765e9 W
Loop flow rates	5150 kg/s	5004 kg/s
Cold legs temperature	293°C	293 °C
Hot legs temperature	325°C	326 °C
DC to UH bypass flow rate	200 kg/s	197,6 kg/s
Primary and sec. side press.	157.5 bar	155.9 bar
PRZ level	8.06 m	7.125 m
ACC volume, pressure and fill level, temperature	34 m³ 26 bar 8.5428 m 20°C	34 m³ 26 bar 8.5428 m 20°C
Secondary pressure (SG1)	68.2 bar	64,2 bar
SG level (SG1 riser/downcomer)	6.32/11.87 m	6,45/11,9 m

Table 43: Sequence of events for the Task 2.3 reference best-estimate case of UJV BEPU
(plus comparison with Task 2.1 Base Case)

Cause	Event	*Timing of T2.1 Base Case (s)*	Timing of T2.3 reference best-estimate case (s)
Primary pressure < 132 bars	Reactor trip Turbine trip Emergency signal Signal sec.-side cooldown (100K/hr auto.) MCPs trip	*44*	45
Analysis assumption	Loss of offsite power	*44*	45
Emergency signal + 12 s	Signal ECC system to start DG	*56*	57
Primary pressure < 110 bars	Emergency cooling signal for HPI pumps	*79*	72
HPI pumps running	HP injection	*85*	75
Primary pressure < 26 bars	ACC injection	*2780*	2620
Primary pressure < 10 bars	Emergency coolant signal for LPI pumps	*4550*	4575
LPI pumps running	LP injection	*4555*	4580
ECCS injection stronger than break flow	PRZ level recovery	*4700*	4625
End of calculation		*4900 (10000)*	10000

(a)   (b)
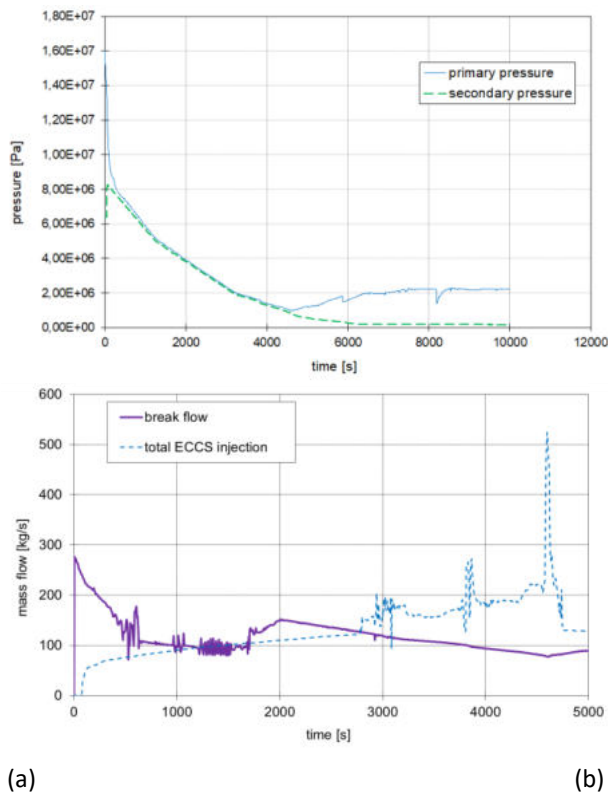
Figure 294: (a) System Pressures and (b) Break and ECCS Flow Rate.

220
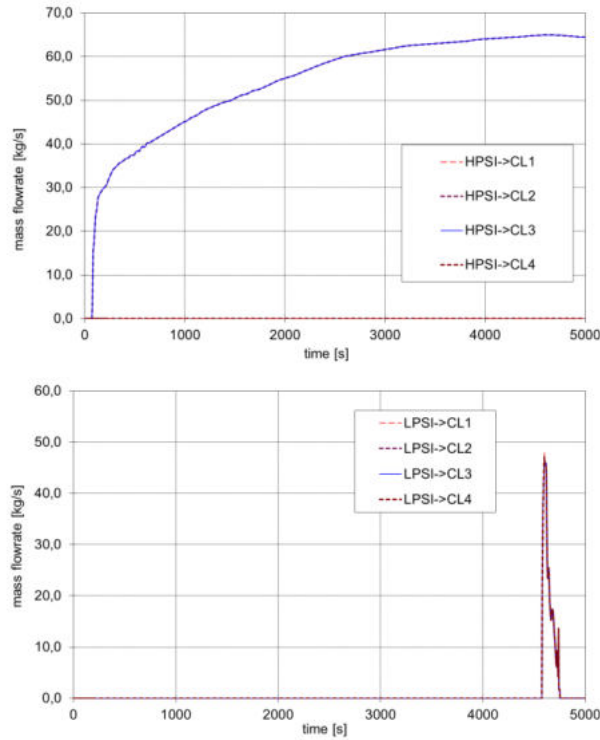
(a)   (b)

Figure 295: (a) HPIS Injection and (b) LPIS Injection.
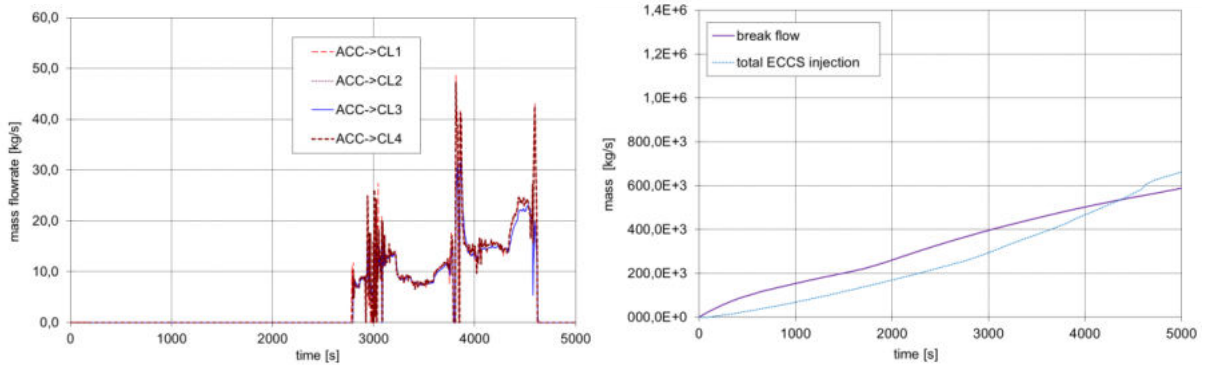
(a)   (b)

Figure 296: (a) ACC Injection and (b) Integrated Break and ECCS Flow.

221
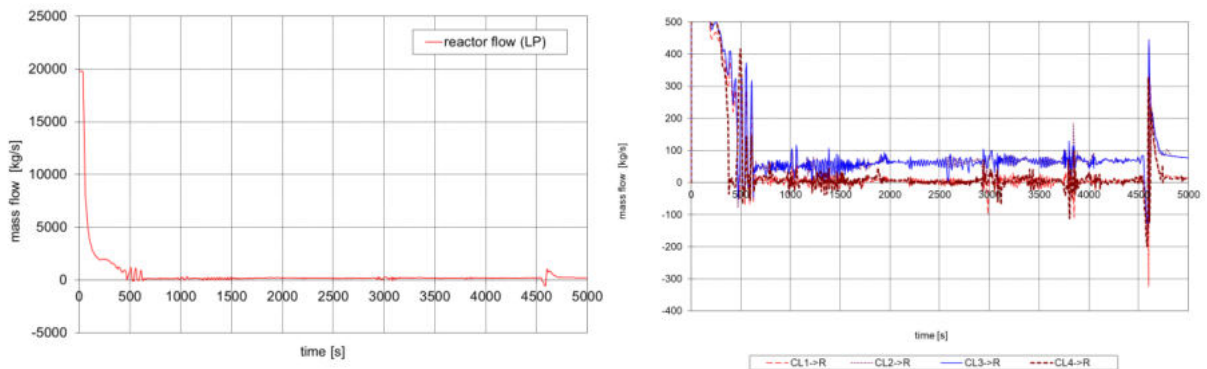
(a)   (b)
Figure 297: (a) Reactor LP Flow and (b) Reactor Inlet Flows (detail).
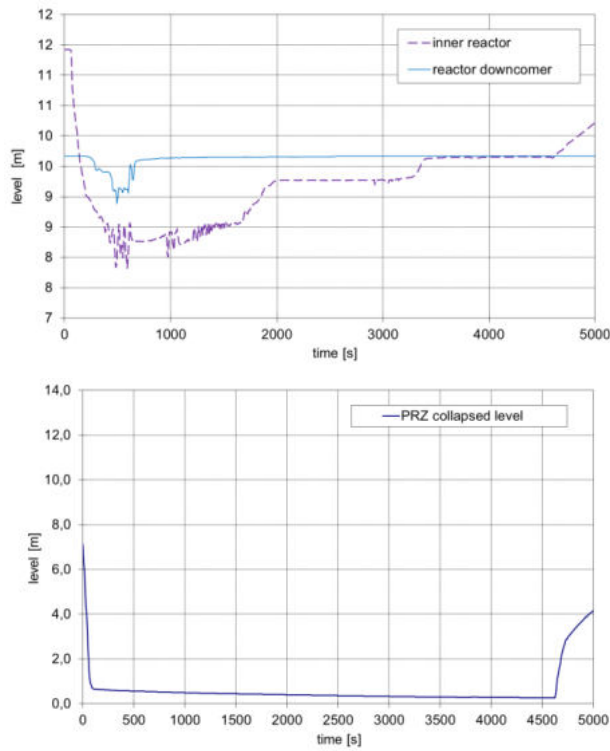
(a)   (b)
Figure 298: (a) Collapsed Liquid Levels in Reactor and (b) Pressurizer.
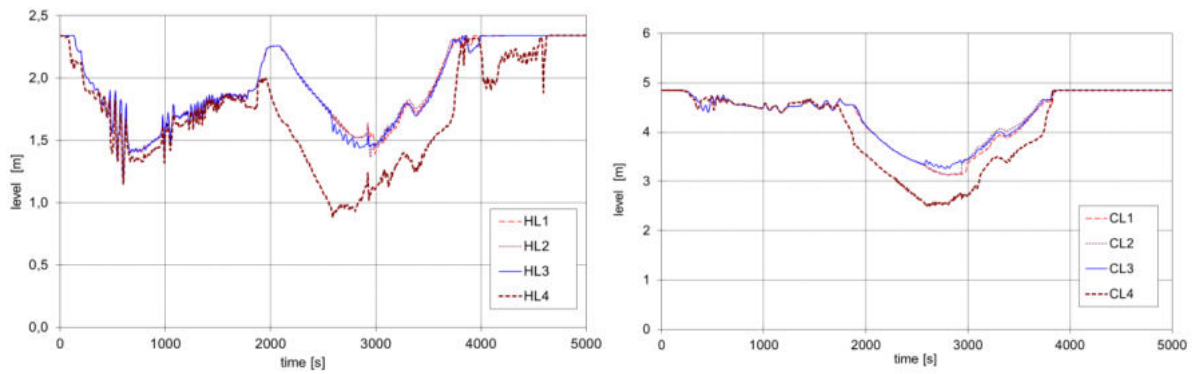
(a)   (b)
Figure 299: (a) Collapsed Liquid Levels in HLs and (b) in CLs by SG.

222

(a)   (b)
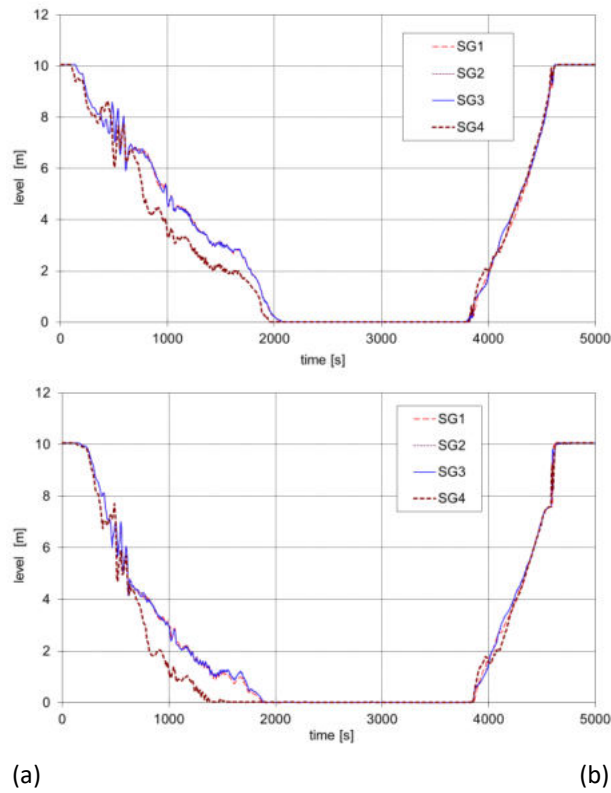
Figure 300: (a) Collapsed Liquid Levels in SG tubing Upward and (b) in SG tubing Downward Part

(a)   (b)
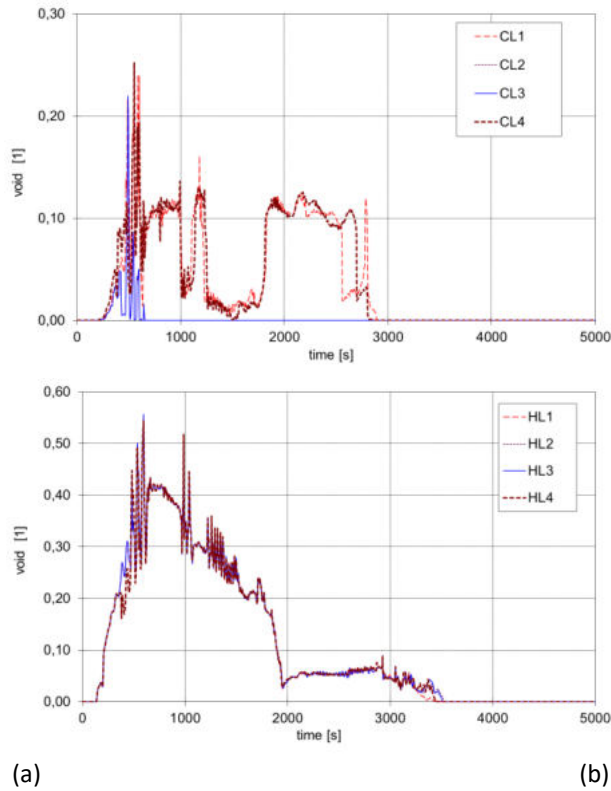
Figure 301: (a) Void Fraction in Reactor Inlet Nozzles and (b) in Reactor Outlet Nozzles.
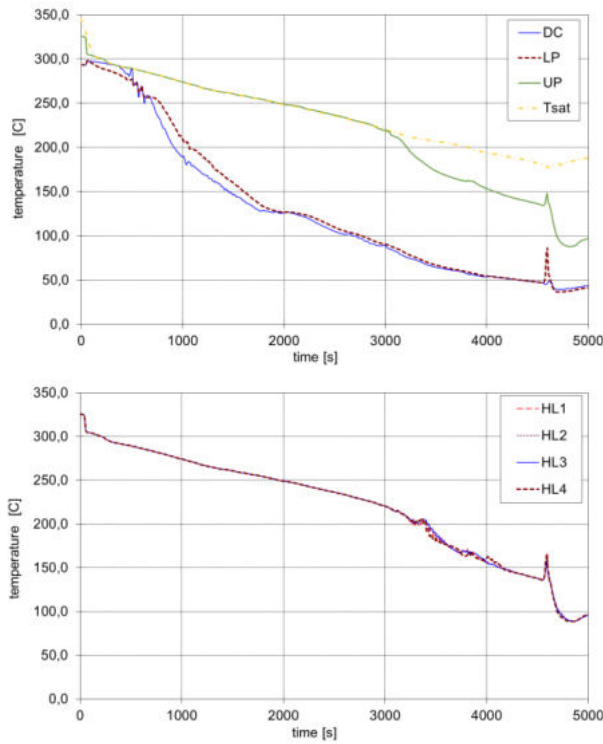
(a)   (b)

Figure 302: (a) Coolant Temperatures in Reactor and (b) Coolant Temperatures in HLs.
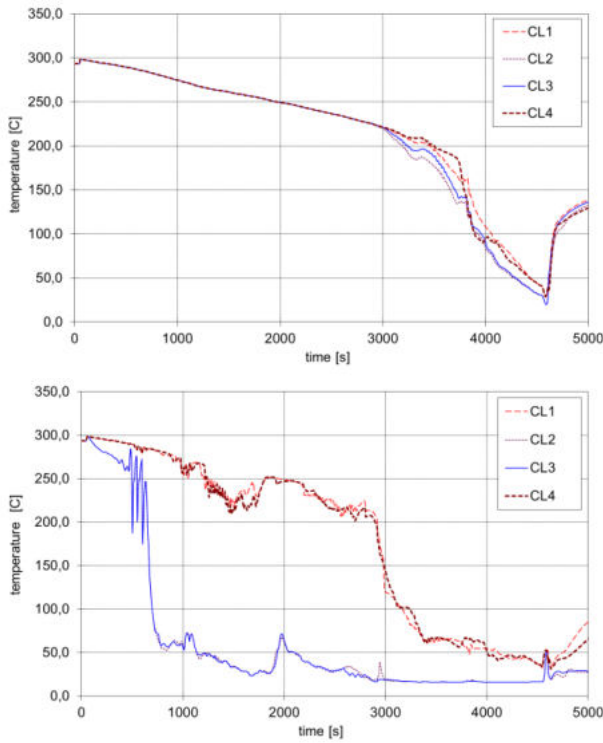
(a)   (b)

Figure 303: (a) Coolant Temperatures in CLs Loop Seal and (b) Reactor Inlet Nozzles.

(a)   (b)
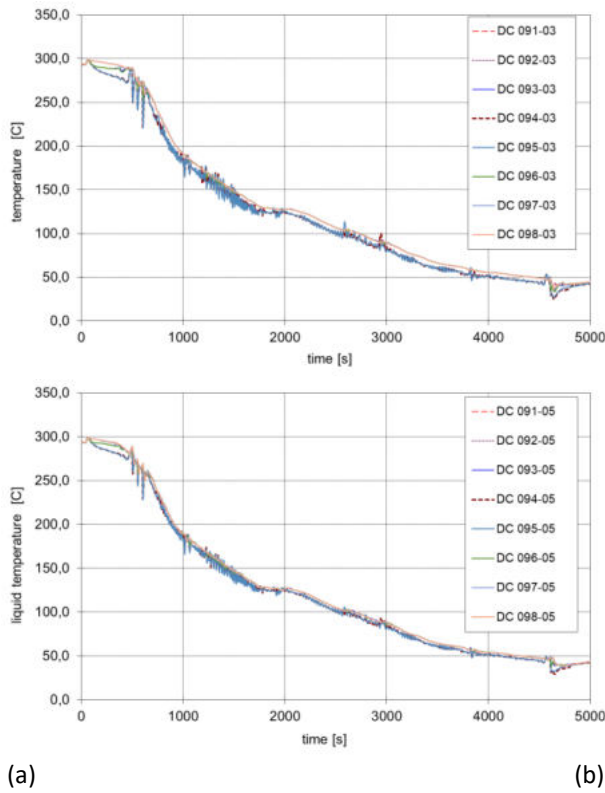
Figure 304: (a) Circumferential Coolant Temperatures in DC Control Volumes in Layer 3 at Elevation 1.13 m and (b) in Layer 5 at Elevation 2.638 m.

(a)   (b)
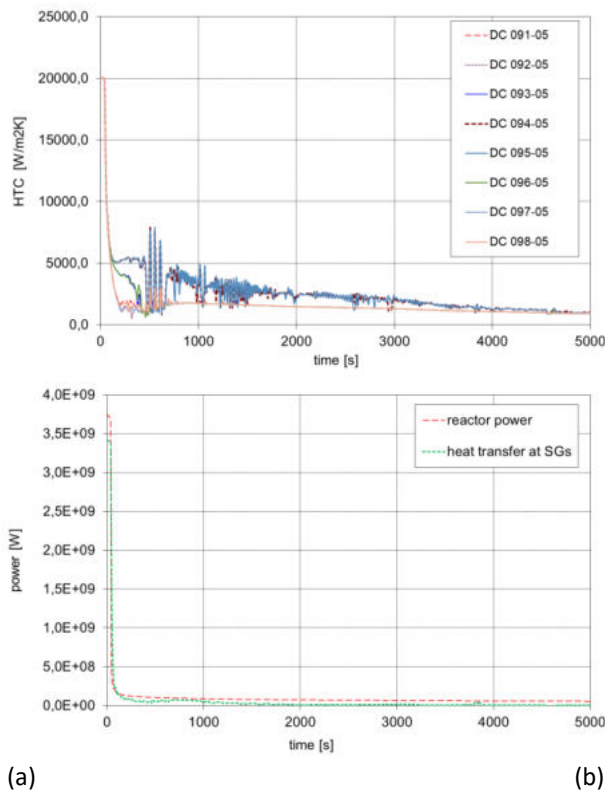
Figure 305: (a) HTC at RPV Inner Surface around DC at 2.638 m and (b) Reactor and SGs Power.

12.2 Input uncertainties

Following table includes uncertainty multipliers used in uncertainty analysis made by DAKOTA plugin for SNAP.

Table 44: Uncertainty parameters for DAKOTA

Distribution Name	Distribution Type	Application Rule	Distribution Parameters	Model Variable	Nominal
Core_Power	Normal	Scalar	μ:3.765e9, σ:3.765e7, $[-\infty, \infty]$	RKTpow	Replacement
HTC_coeff	Loguniform	Factor	a:0.8, b:1.2	htf0	1.0
HTC_coeff	Loguniform	Factor	a:0.8, b:1.2	htg0	1.0
HTC_coeff	Loguniform	Factor	a:0.8, b:1.2	htf1	1.0
HTC_coeff	Loguniform	Factor	a:0.8, b:1.2	htg1	1.0
HTC_coeff	Loguniform	Factor	a:0.8, b:1.2	htf2	1.0
HTC_coeff	Loguniform	Factor	a:0.8, b:1.2	htf3	1.0
HTC_coeff	Loguniform	Factor	a:0.8, b:1.2	htg3	1.0
HTC_coeff	Loguniform	Factor	a:0.8, b:1.2	htf4	1.0
HTC_coeff	Loguniform	Factor	a:0.8, b:1.2	htg4	1.0
HTC_coeff	Loguniform	Factor	a:0.8, b:1.2	htf5	1.0
HTC_coeff	Loguniform	Factor	a:0.8, b:1.2	htg5	1.0
HTC_coeff	Loguniform	Factor	a:0.8, b:1.2	htf6	1.0
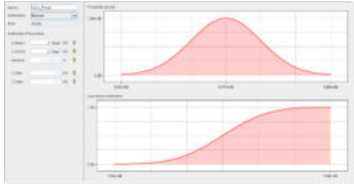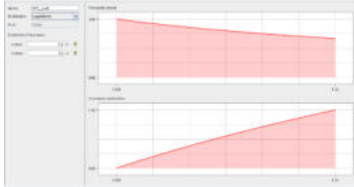
Distribution Name	Distribution Type	Application Rule	Distribution Parameters	Model Variable	Nominal
HTC_coeff	Loguniform	Factor	a:0.8, b:1.2	htg6	1.0
HTC_coeff	Loguniform	Factor	a:0.8, b:1.2	htf7	1.0
HTC_coeff	Loguniform	Factor	a:0.8, b:1.2	htg7	1.0
HTC_coeff	Loguniform	Factor	a:0.8, b:1.2	htf8	1.0
HTC_coeff	Loguniform	Factor	a:0.8, b:1.2	htg8	1.0
HTC_coeff	Loguniform	Factor	a:0.8, b:1.2	htg9	1.0
HTC_coeff	Loguniform	Factor	a:0.8, b:1.2	htf10	1.0
HTC_coeff	Loguniform	Factor	a:0.8, b:1.2	htg10	1.0
HTC_coeff	Loguniform	Factor	a:0.8, b:1.2	htf11	1.0
HTC_coeff	Loguniform	Factor	a:0.8, b:1.2	htg11	1.0
HTC_coeff	Loguniform	Factor	a:0.8, b:1.2	htf12	1.0
PRZ_p	Normal	Scalar	μ:1.574e7, σ:1.574e5, $[-\infty, \infty]$	PRZpress	Replacement
SIS_timing	Uniform	Scalar	a:0.0, b:20.0	SIS_timing	Replacement
ACC_Temp	Uniform	Scalar	a:293.15, b:313.15	ACC_temp	Replacement
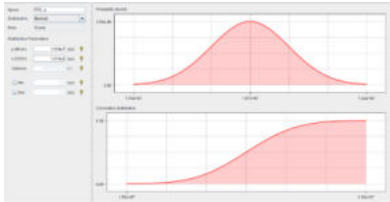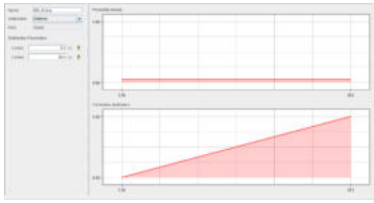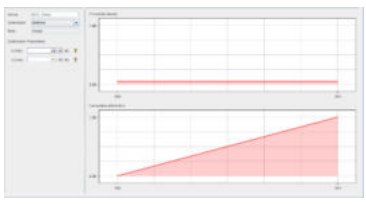
227

Distribution Name	Distribution Type	Application Rule	Distribution Parameters	Model Variable	Nominal
ACC_press	Uniform	Scalar	a:2.4e6, b:2.8e6	ACC_press	Replacement
HPSI_T	Uniform	Scalar	a:288.15, b:313.15	HPSI_T	Replacement
Decay_heat	Uniform	Factor	a:1.0, b:1.2	Decay_heat_coeff	1.04
HP_LP_flow	Normal	Factor	μ:1.0, σ:0.1, [-∞, ∞]	LPP_1	165.0
HP_LP_flow	Normal	Factor	μ:1.0, σ:0.1, [-∞, ∞]	LPP_2	150.0
HP_LP_flow	Normal	Factor	μ:1.0, σ:0.1, [-∞, ∞]	LPP_3	137.0
HP_LP_flow	Normal	Factor	μ:1.0, σ:0.1, [-∞, ∞]	LPP_4	128.0
HP_LP_flow	Normal	Factor	μ:1.0, σ:0.1, [-∞, ∞]	LPP_5	116.0
HP_LP_flow	Normal	Factor	μ:1.0, σ:0.1, [-∞, ∞]	LPP_6	106.0
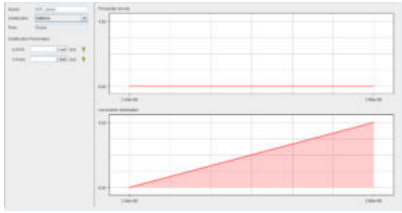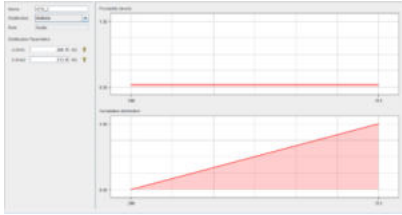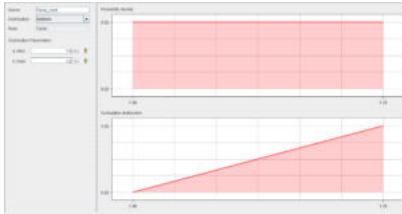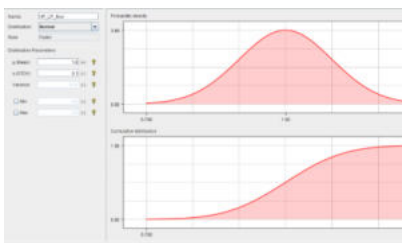
Distribution Name	Distribution Type	Application Rule	Distribution Parameters	Model Variable	Nominal
HP_LP_flow	Normal	Factor	μ:1.0, σ:0.1, [-∞, ∞]	LPP_7	95.0
HP_LP_flow	Normal	Factor	μ:1.0, σ:0.1, [-∞, ∞]	LPP_8	80.0
HP_LP_flow	Normal	Factor	μ:1.0, σ:0.1, [-∞, ∞]	LPP_9	74.0
HP_LP_flow	Normal	Factor	μ:1.0, σ:0.1, [-∞, ∞]	LPP_10	61.0
HP_LP_flow	Normal	Factor	μ:1.0, σ:0.1, [-∞, ∞]	LPP_11	50.0
HP_LP_flow	Normal	Factor	μ:1.0, σ:0.1, [-∞, ∞]	LPP_12	20.0
HP_LP_flow	Normal	Factor	μ:1.0, σ:0.1, [-∞, ∞]	HPP_1	65.0
HP_LP_flow	Normal	Factor	μ:1.0, σ:0.1, [-∞, ∞]	HPP_2	65.0
HP_LP_flow	Normal	Factor	μ:1.0, σ:0.1, [-∞, ∞]	HPP_3	60.0
HP_LP_flow	Normal	Factor	μ:1.0, σ:0.1, [-∞, ∞]	HPP_4	49.0
HP_LP_flow	Normal	Factor	μ:1.0, σ:0.1, [-∞, ∞]	HPP_5	40.0
HP_LP_flow	Normal	Factor	μ:1.0, σ:0.1, [-∞, ∞]	HPP_6	28.0
HP_LP_flow	Normal	Factor	μ:1.0, σ:0.1, [-∞, ∞]	HPP_7	24.0
HP_LP_flow	Normal	Factor	μ:1.0, σ:0.1, [-∞, ∞]	HPP_8	20.0
HP_LP_flow	Normal	Factor	μ:1.0, σ:0.1, [-∞, ∞]	HPP_9	16.0

Distribution Name	Distribution Type	Application Rule	Distribution Parameters	Model Variable	Nominal
HP_LP_flow	Normal	Factor	μ:1.0, σ:0.1, [-∞, ∞]	HPP_10	10.0
PRZ_lvl	Uniform	Scalar	a:0.4566603, b:0.645339	PRZ_lvl	Replacement
walldrag	Loguniform	Factor	a:0.5, b:2.0	walldrag	1.0
formloss	Loguniform	Factor	a:0.5, b:2.0	formloss	1.0
mat_cond	Normal	Factor	μ:1.0, σ:0.05, [-∞, ∞]	Aust_cond	14.24
mat_cond	Normal	Factor	μ:1.0, σ:0.05, [-∞, ∞]	Aust_cond_2	14.24
mat_cond	Normal	Factor	μ:1.0, σ:0.05, [-∞, ∞]	Aust_cond_3	16.7
mat_cond	Normal	Factor	μ:1.0, σ:0.05, [-∞, ∞]	Aust_cond_4	18.6
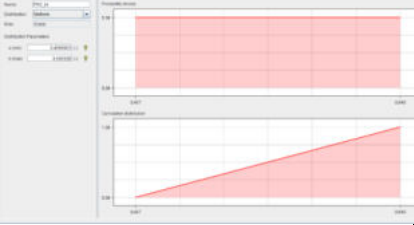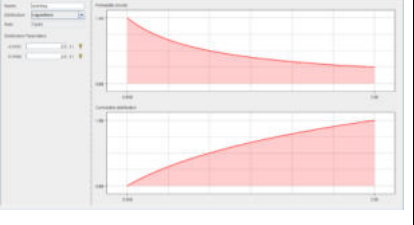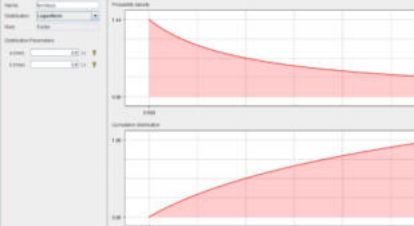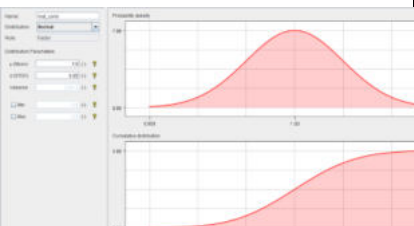
Distribution Name	Distribution Type	Application Rule	Distribution Parameters	Model Variable	Nominal
mat_cond	Normal	Factor	μ:1.0, σ:0.05, [-∞, ∞]	Aust_cond_5	18.6
mat_cond	Normal	Factor	μ:1.0, σ:0.05, [-∞, ∞]	Aust_cond_6	20.9
mat_cond	Normal	Factor	μ:1.0, σ:0.05, [-∞, ∞]	Aust_cond_7	20.9
mat_cond	Normal	Factor	μ:1.0, σ:0.05, [-∞, ∞]	Aust_cond_8	20.9
mat_cond	Normal	Factor	μ:1.0, σ:0.05, [-∞, ∞]	Aust_cond_9	20.9
mat_cond	Normal	Factor	μ:1.0, σ:0.05, [-∞, ∞]	Fer_cond	44.0
mat_cond	Normal	Factor	μ:1.0, σ:0.05, [-∞, ∞]	Fer_cond_2	44.0
mat_cond	Normal	Factor	μ:1.0, σ:0.05, [-∞, ∞]	Fer_cond_3	43.0
mat_cond	Normal	Factor	μ:1.0, σ:0.05, [-∞, ∞]	Fer_cond_4	42.0
mat_cond	Normal	Factor	μ:1.0, σ:0.05, [-∞, ∞]	Fer_cond_5	40.0
mat_cond	Normal	Factor	μ:1.0, σ:0.05, [-∞, ∞]	Fer_cond_6	39.0
mat_cond	Normal	Factor	μ:1.0, σ:0.05, [-∞, ∞]	Fer_cond_7	39.0
mat_cond	Normal	Factor	μ:1.0, σ:0.05, [-∞, ∞]	Fer_cond_8	39.0
mat_cond	Normal	Factor	μ:1.0, σ:0.05, [-∞, ∞]	Fer_cond_9	39.0
mat_cond	Normal	Factor	μ:1.0, σ:0.05, [-∞, ∞]	Fer_cond_10	39.0
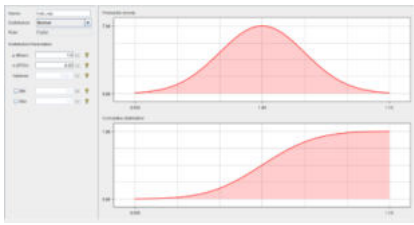
Distribution Name	Distribution Type	Application Rule	Distribution Parameters	Model Variable	Nominal
mat_cap	Normal	Factor	μ:1.0, σ:0.05, [-∞, ∞]	Aust_cap	3.572e6
mat_cap	Normal	Factor	μ:1.0, σ:0.05, [-∞, ∞]	Aust_cap_2	3.572e6
mat_cap	Normal	Factor	μ:1.0, σ:0.05, [-∞, ∞]	Aust_cap_3	3.837e6
mat_cap	Normal	Factor	μ:1.0, σ:0.05, [-∞, ∞]	Aust_cap_4	4.102e6
mat_cap	Normal	Factor	μ:1.0, σ:0.05, [-∞, ∞]	Aust_cap_5	4.333e6
mat_cap	Normal	Factor	μ:1.0, σ:0.05, [-∞, ∞]	Aust_cap_6	4.465e6
mat_cap	Normal	Factor	μ:1.0, σ:0.05, [-∞, ∞]	Aust_cap_7	4.597e6
mat_cap	Normal	Factor	μ:1.0, σ:0.05, [-∞, ∞]	Aust_cap_8	4.465e6
mat_cap	Normal	Factor	μ:1.0, σ:0.05, [-∞, ∞]	Aust_cap_9	4.465e6
mat_cap	Normal	Factor	μ:1.0, σ:0.05, [-∞, ∞]	Fer_cap	3.611e6
mat_cap	Normal	Factor	μ:1.0, σ:0.05, [-∞, ∞]	Fer_cap_2	3.847e6
mat_cap	Normal	Factor	μ:1.0, σ:0.05, [-∞, ∞]	Fer_cap_3	4.082e6
mat_cap	Normal	Factor	μ:1.0, σ:0.05, [-∞, ∞]	Fer_cap_4	4.396e6

Distribution Name	Distribution Type	Application Rule	Distribution Parameters	Model Variable	Nominal
mat_cap	Normal	Factor	μ:1.0, σ:0.05, [-∞, ∞]	Fer_cap_5	4.788e6
mat_cap	Normal	Factor	μ:1.0, σ:0.05, [-∞, ∞]	Fer_cap_6	5.338e6
mat_cap	Normal	Factor	μ:1.0, σ:0.05, [-∞, ∞]	Fer_cap_7	5.338e6
NvolACC	Uniform	Scalar	a:0.36516752, b:0.62500422	NvolACC	Replacement
HF_noneq_coeff	Triangular	Scalar	a:-0.02, m:0.14, b:10.0	Break_TH_noneq	Replacement
SGpress	Uniform	Scalar	a:0.255, b:0.3376	SGpress	Replacement
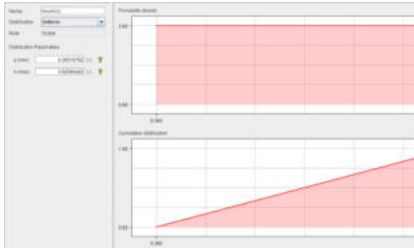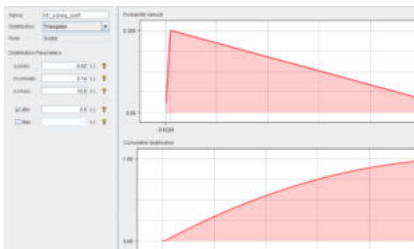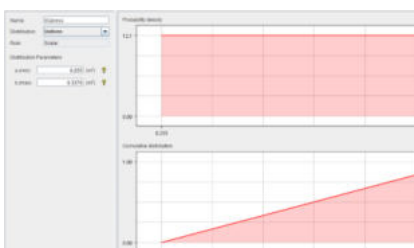
12.3 Results of BEPU analyses (59 samples)

Results of sampled 59 calculations to yield 95%/95% one-sided tolerance bound are presented in figures below. The agreed minimal set of BEPU results (see below) is extended by couple of graphs with additional parameters.

The set of graphs presented below is based on the minimal set of figures for BEPU agreed in Task 2.3 of APAL:
• Primary pressure (DC)
• Coolant temperature at 1.350 m under CL1
• Coolant temperature at 1.350 m under CL2
• HTC at RPV wall at 1.350 m under CL1
• HTC at RPV wall at 1.350 m under CL2
• Inner RPV wall temperature at 1.350 m under CL1
• Inner RPV wall temperature at 1.350 m under CL2
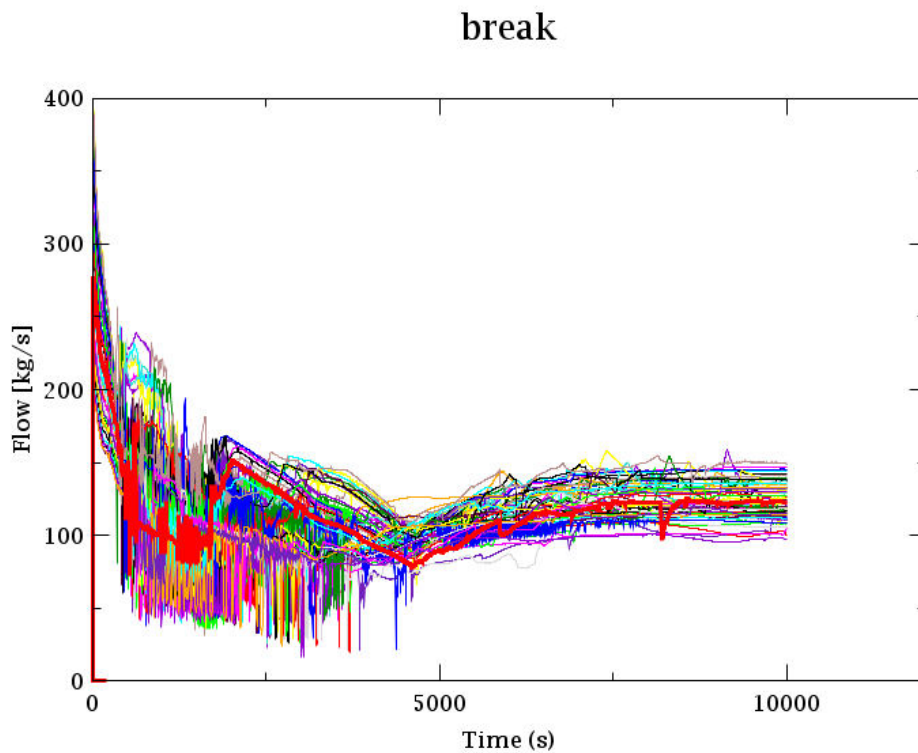
Figure 306: Break flow (59 samples)

234

mass-break
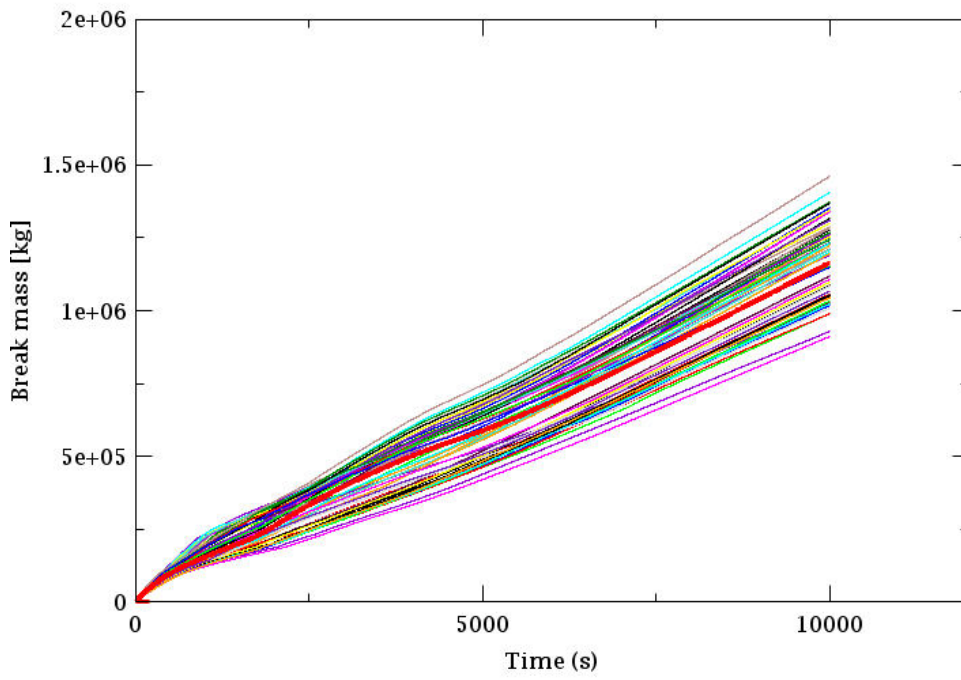
Figure 307: Integral of break flow (59 samples)

mass-ECCS
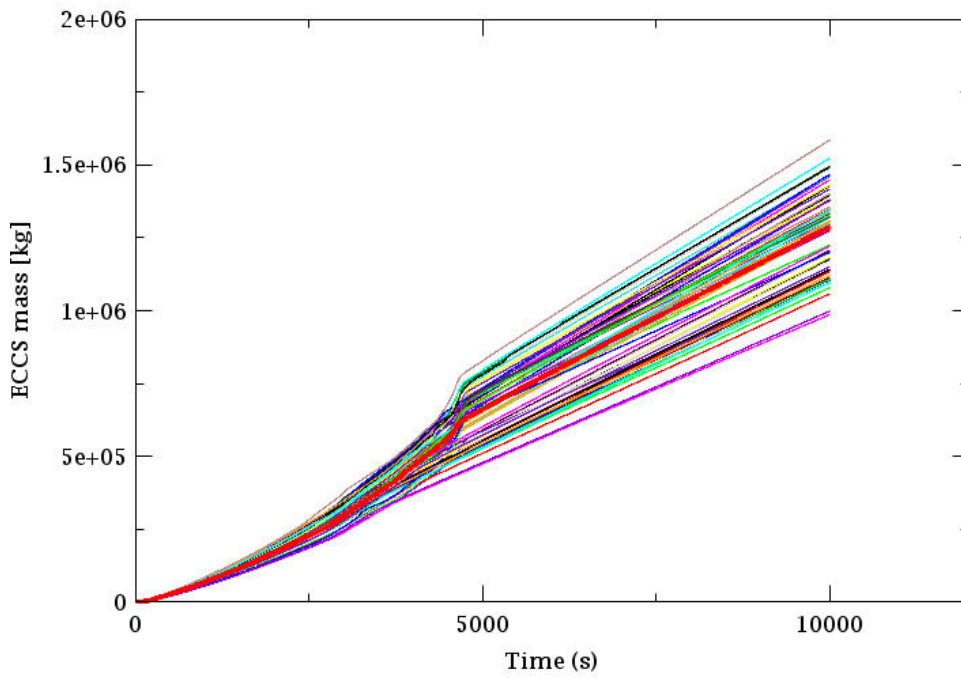
Figure 308: Integral of ECCS flow (59 samples)

P_DC
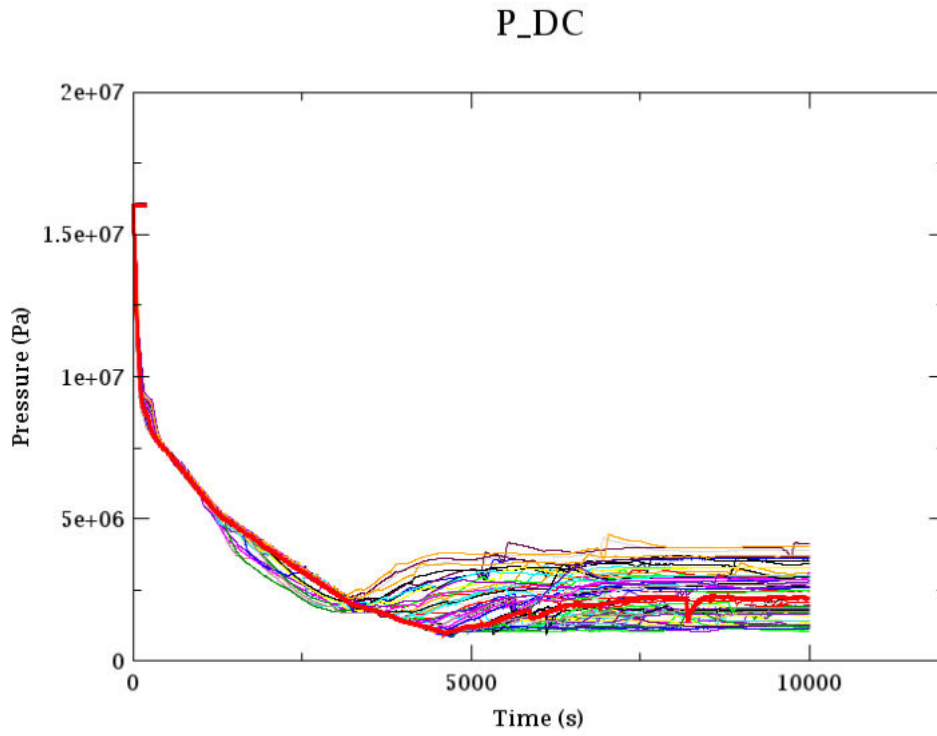
Figure 309: Primary pressure (59 samples)

L_PRZ
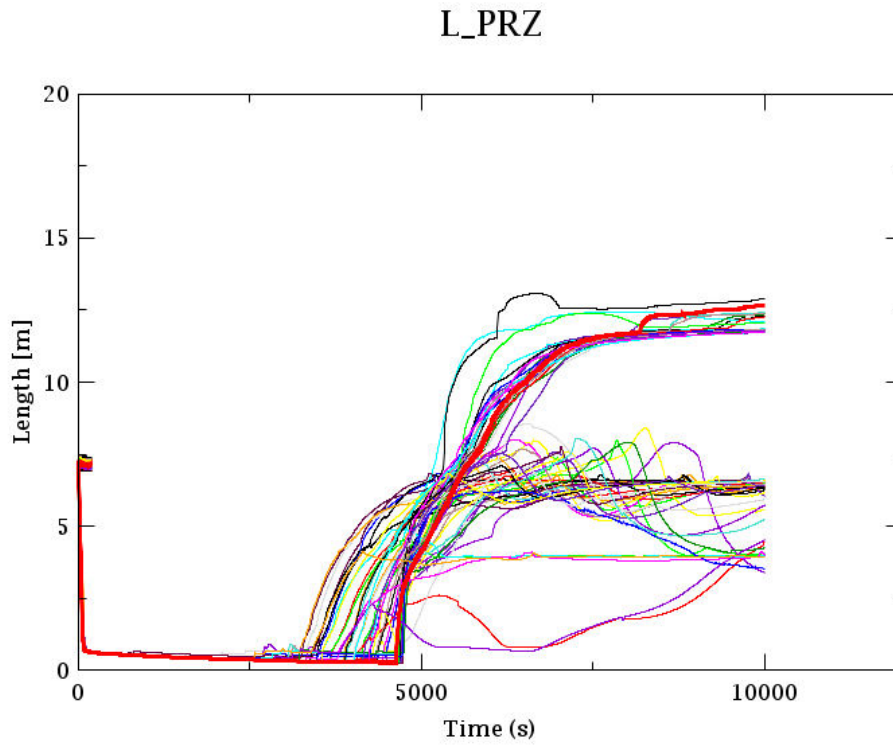
Figure 310: PRZ collapsed level (59 samples)

LcolDC
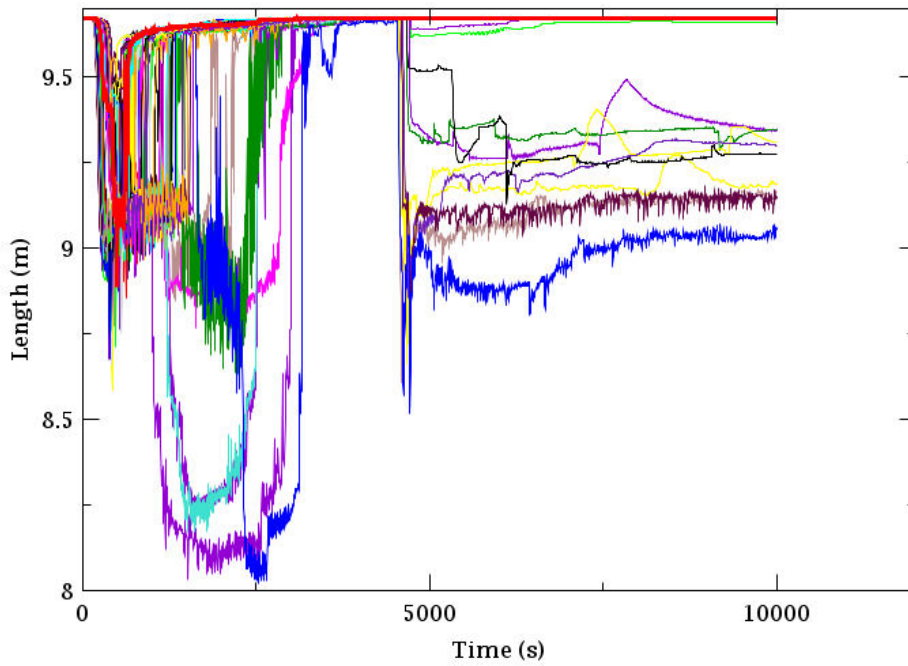
Figure 311: Reactor downcomer collapsed level (59 samples)

mf_LP
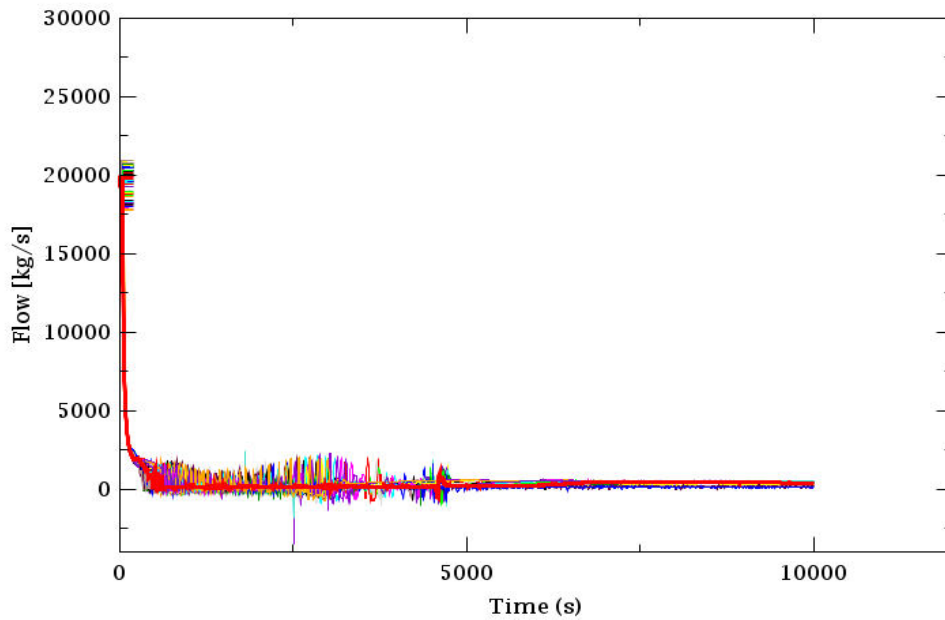
Figure 312: Reactor flow (59 samples)

Tf_LP
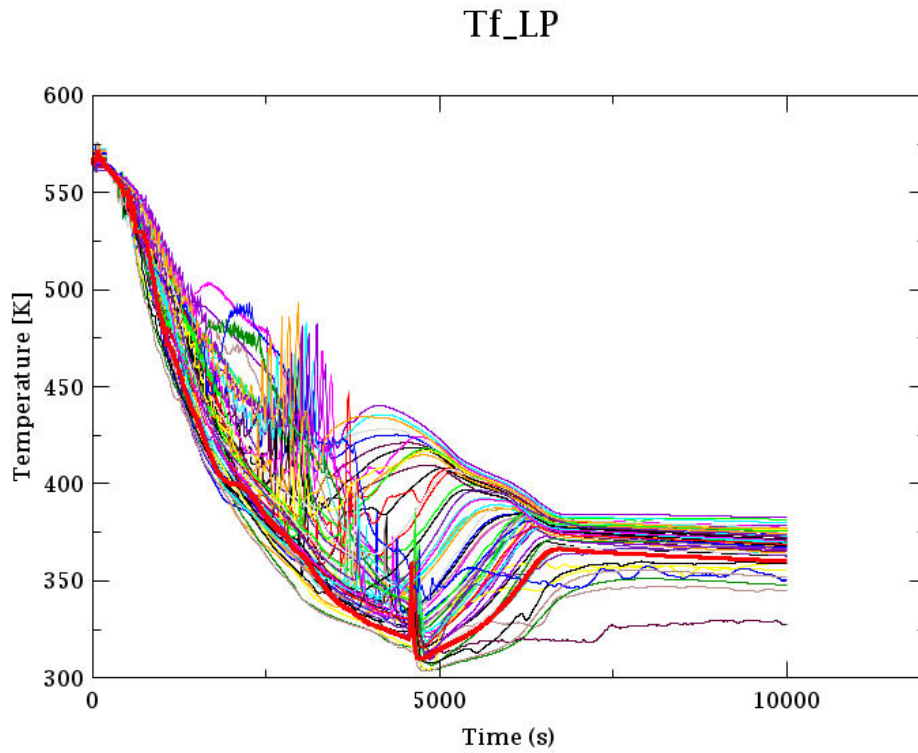
Figure 313: Coolant temperatures in reactor lower plenum (59 samples)

TavgDC
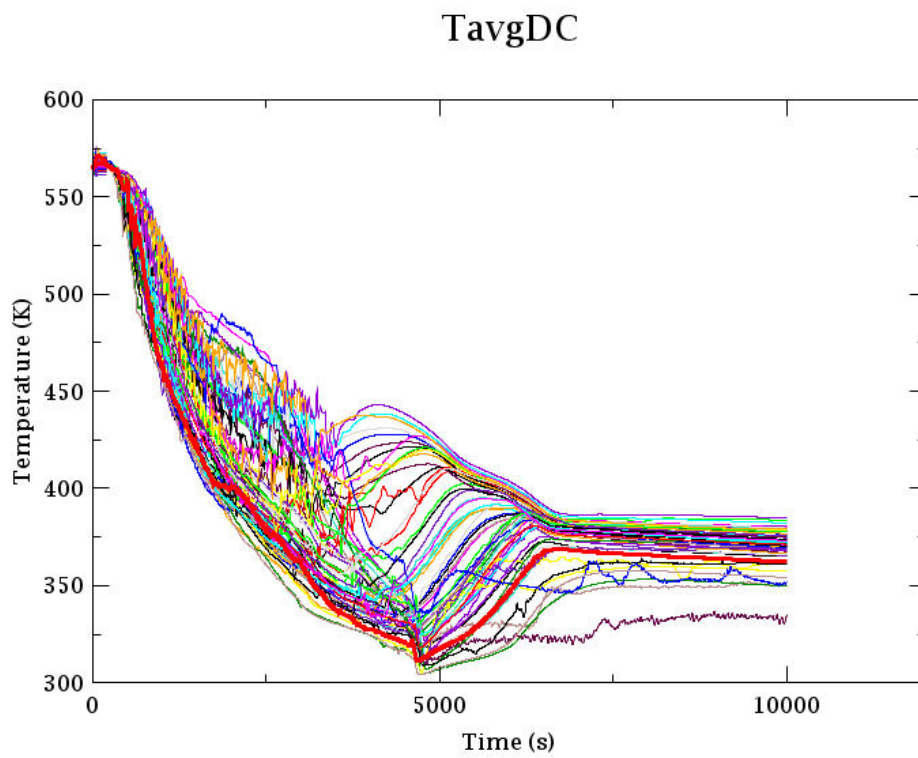
Figure 314: Average coolant temperatures in reactor downcomer (59 samples)
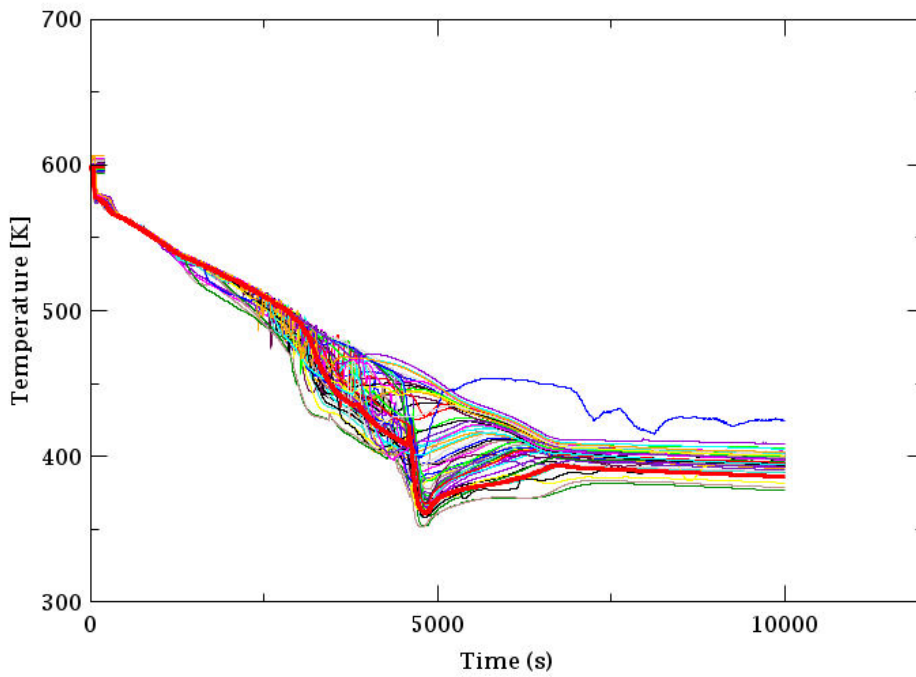
Figure 315: Coolant (liquid) temperatures in reactor upper plenum (59 samples)
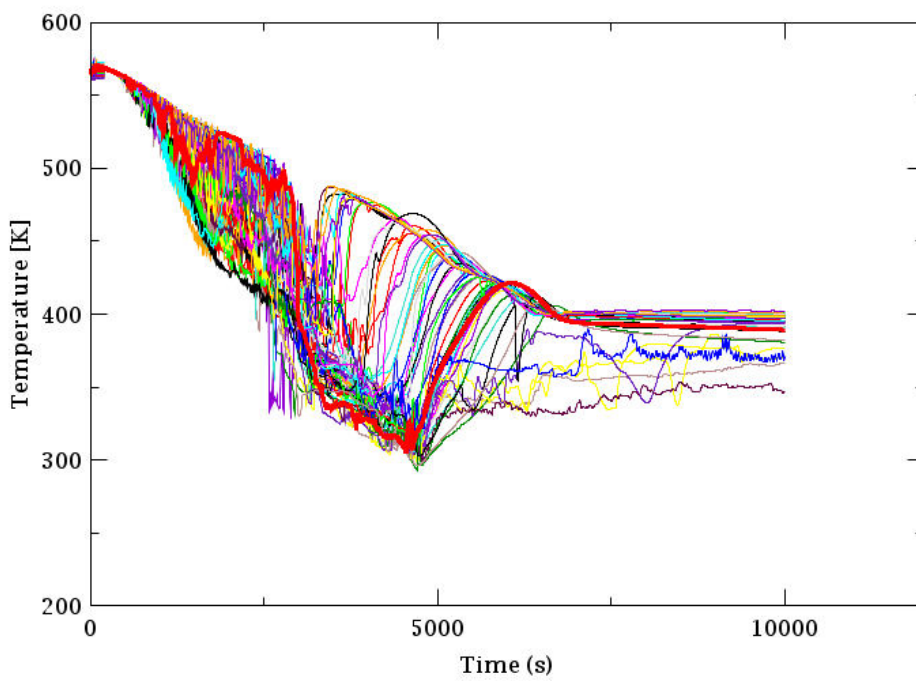
Figure 316: Coolant (liquid) temperatures at reactor inlet from CL1 (59 samples)

Tf_CL2end
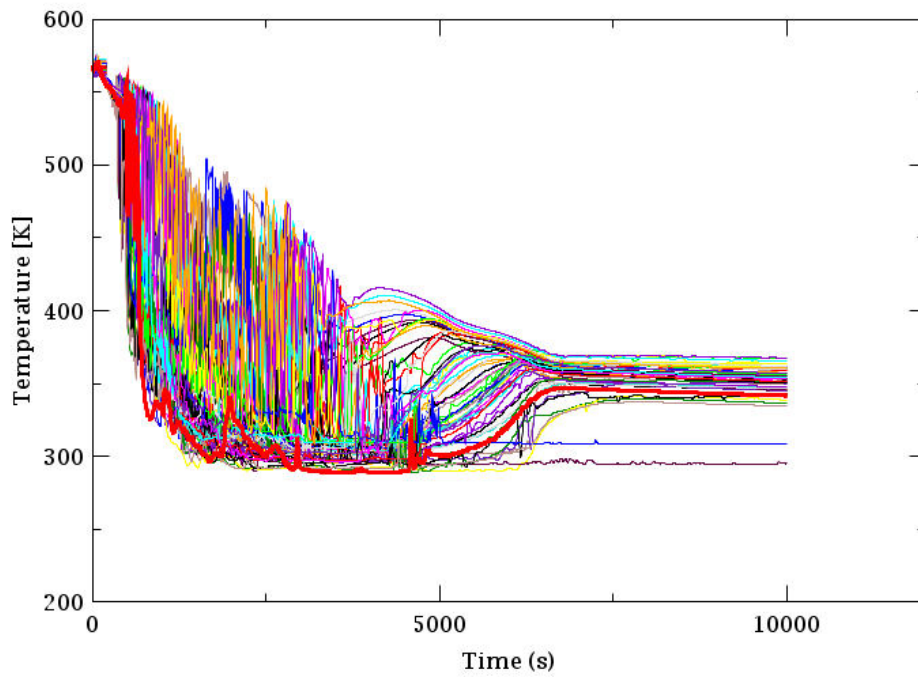
Figure 317: Coolant (liquid) temperatures at reactor inlet from CL2 (59 samples)

Tf_CL3end
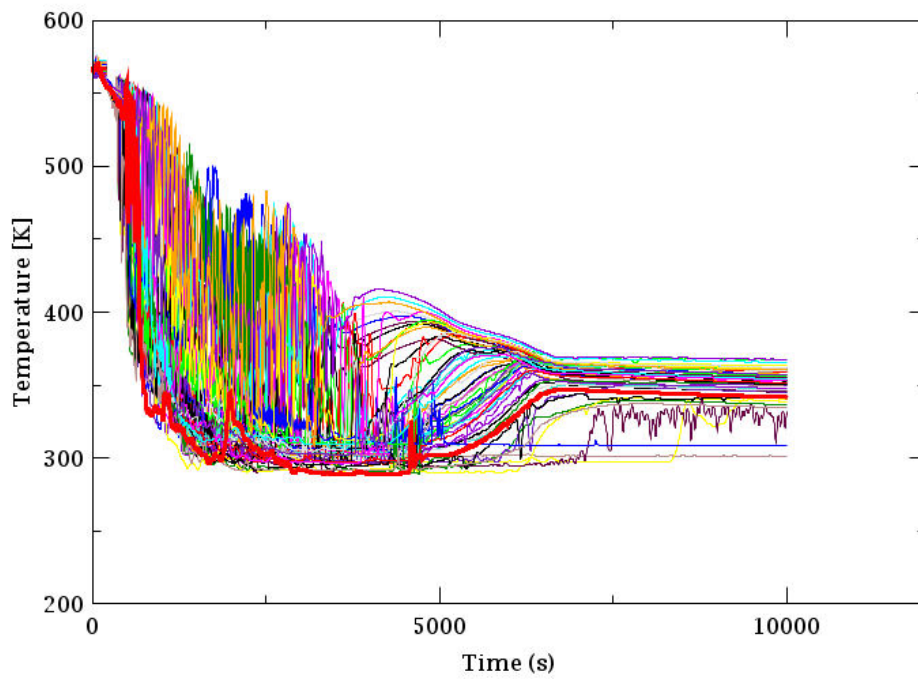
Figure 318: Coolant (liquid) temperatures at reactor inlet from CL3 (59 samples)
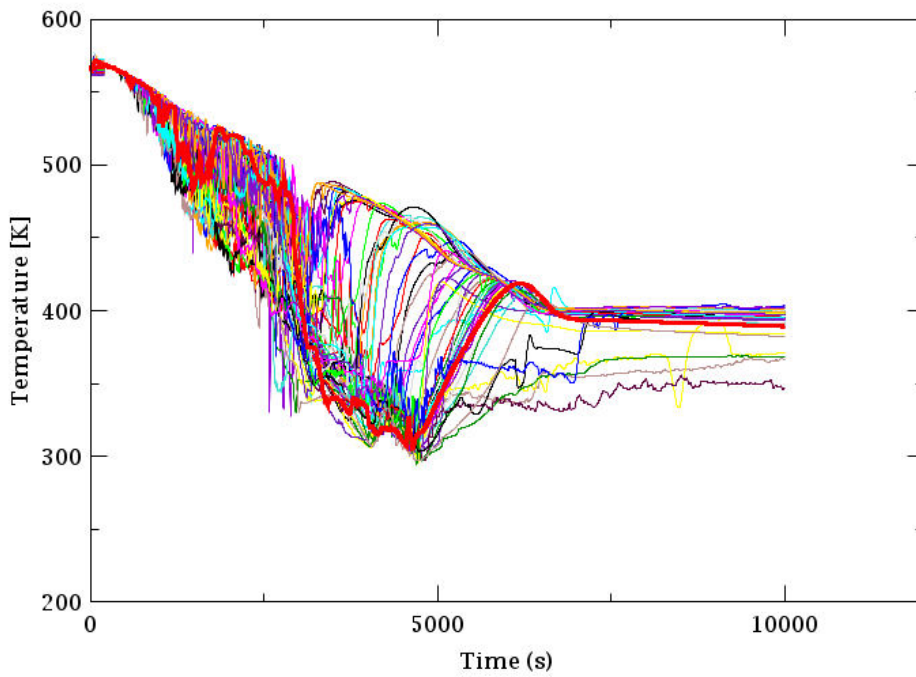
Figure 319: Coolant (liquid) temperatures at reactor inlet from CL4 (59 samples)
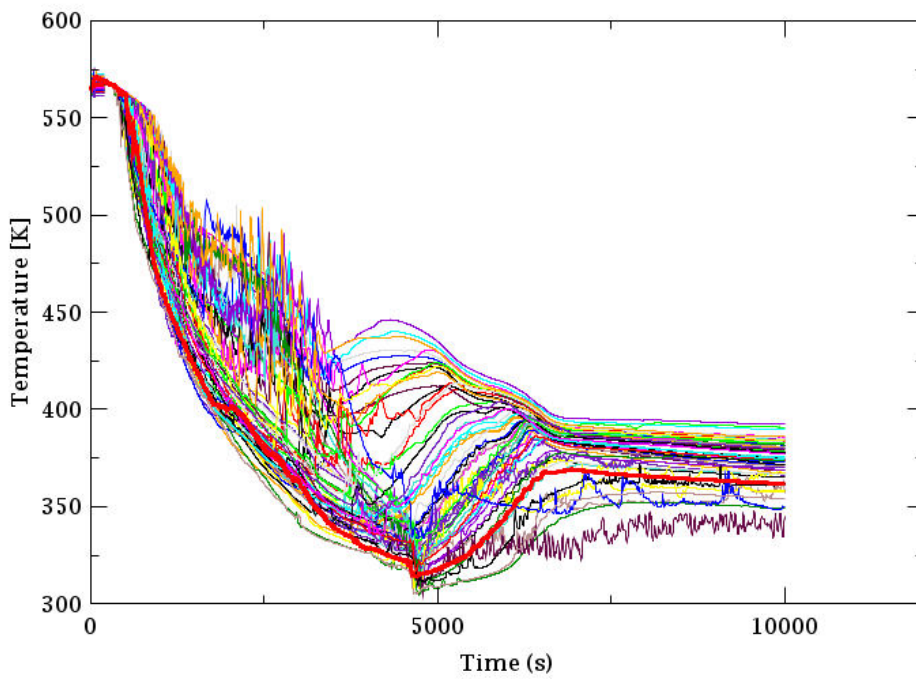
Figure 320: Downcomer coolant temperatures at 1.35 m under CL1 (59 samples)

Tf_DC_9403
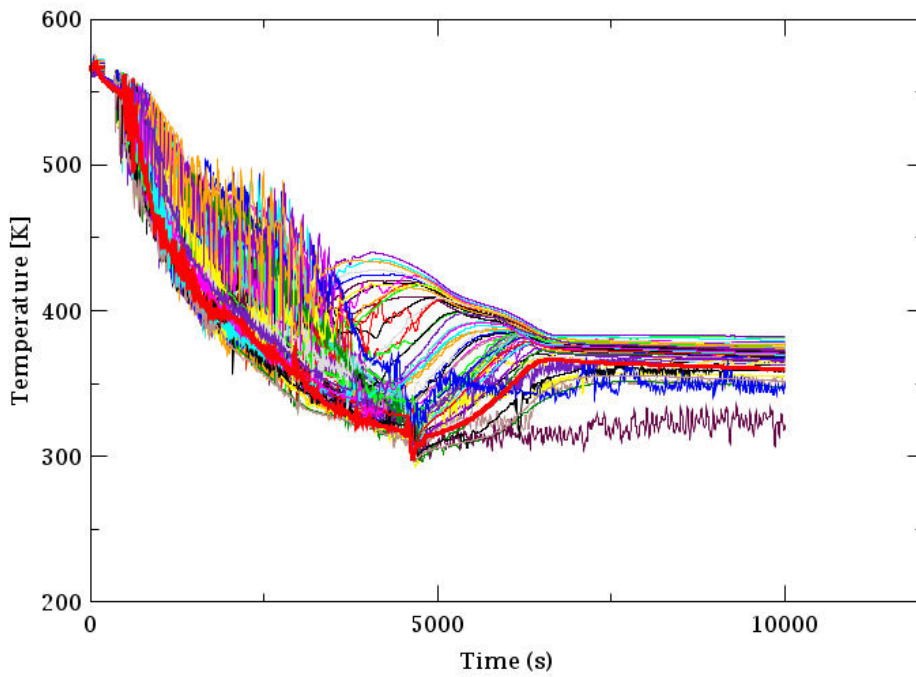
Figure 321: Downcomer coolant temperatures at 1.35 m under CL2 (59 samples)

HTC_DC_9105
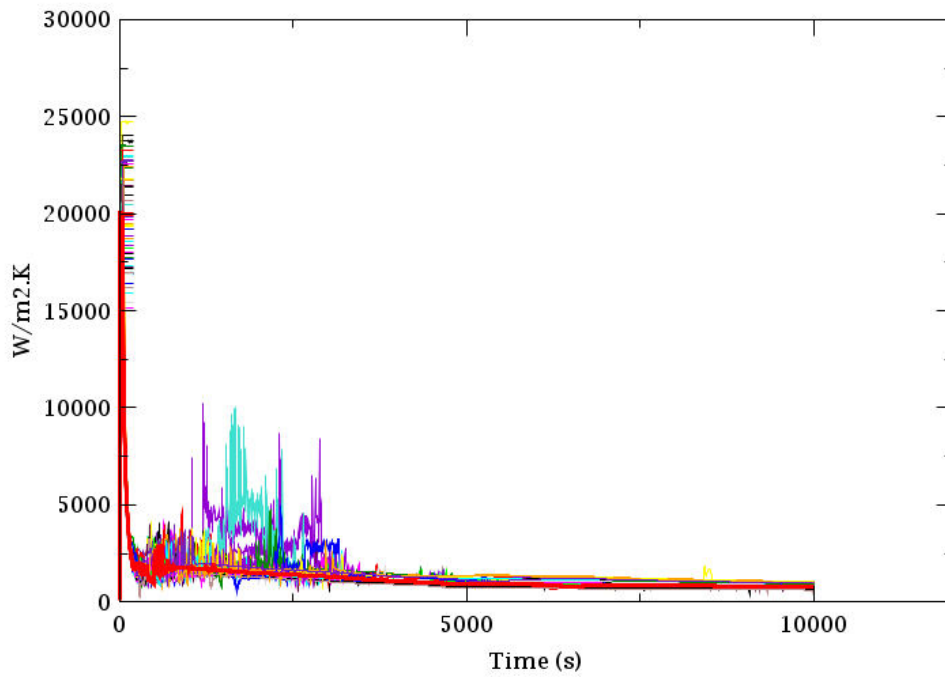
Figure 322: Heat transfer coefficient at RPV inner wall at 1.35 m under CL1 (59 samples)
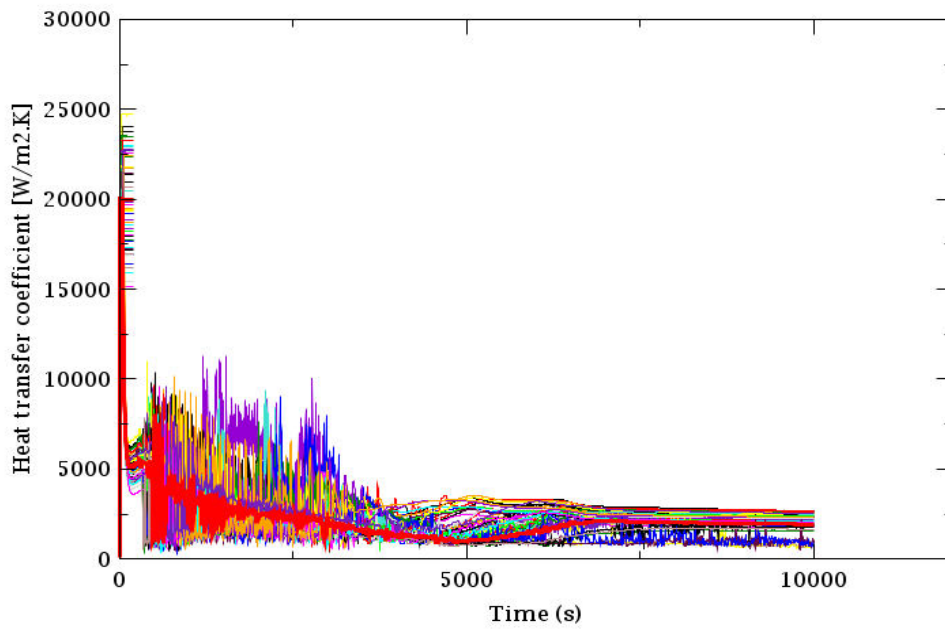
Figure 323: Heat transfer coefficient at RPV inner wall at 1.35 m under CL2 (59 samples)
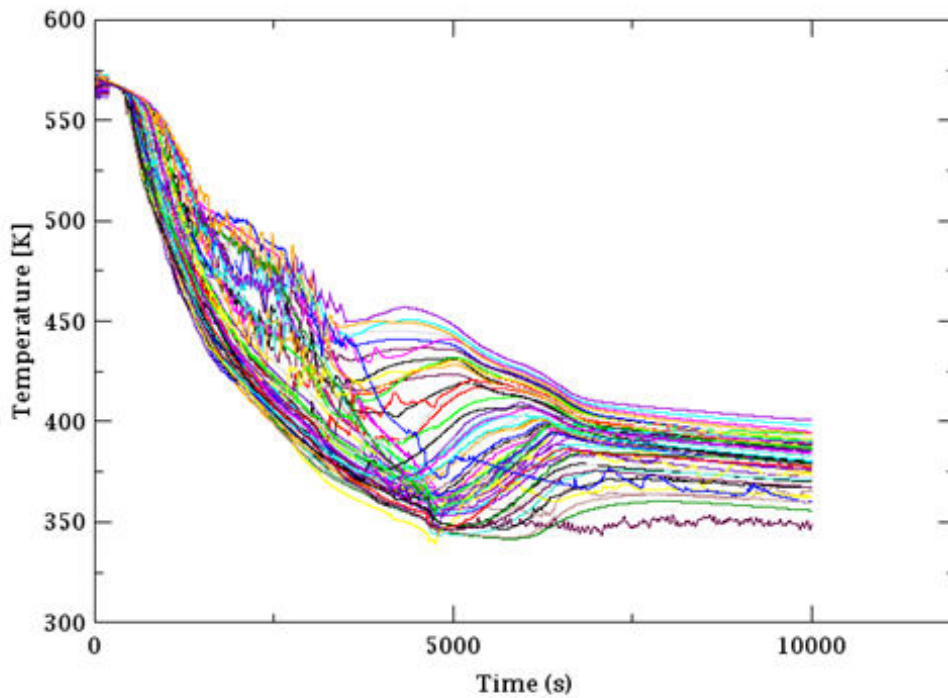
Figure 324: RPV inner wall temperatures at 1.35 m under CL1 (59 samples)

243
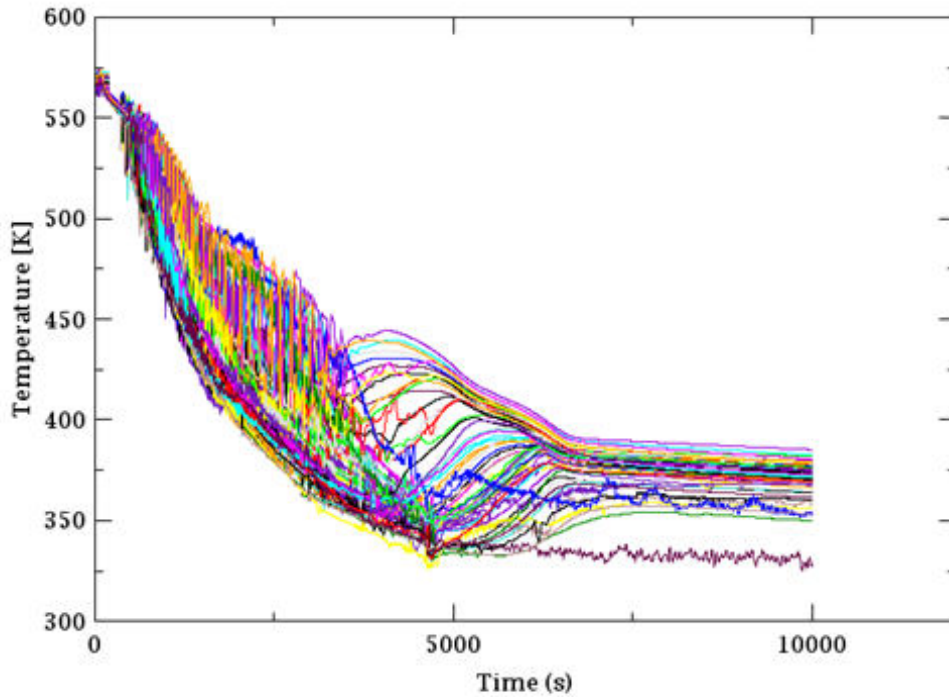
Figure 325: RPV inner wall temperatures at 1.35 m under CL2 (59 samples)

12.4 DAKOTA sensitivity study

A second DAKOTA run was performed using the variate and extracted FOM values to obtain the statistical results and a cumulative distribution function for the FOM. DAKOTA also calculates the response correlations for the FOM. These indicate how the FOM correlates to each model variable.

TempDC4_5 (min temperature in DC)

Probability Density Function
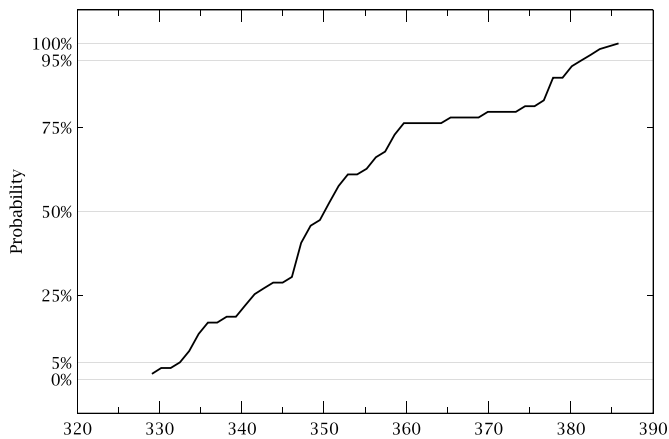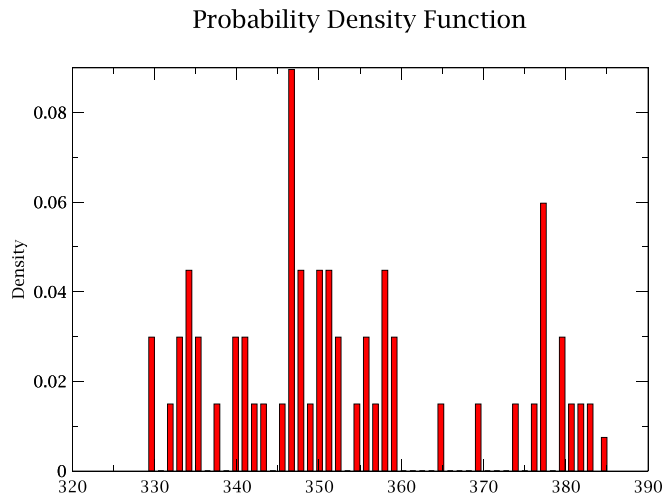
Statistical results based on 59 samples:

Summary	Value	Task #
Min Value	329,07309	44
Max Value	385,8028	55
Mean	353,22253	-
Median	350,08282	37
Standard Deviation	15,79773	-
Coefficient of Variance	0,55702	-

Response Correlations

	Simple	Partial	Simple Rank	Partial Rank
Core_Power	-0.0385386	-0.079672	-0.111514	-0.212796
PRZ_p	0.0921198	0.267037	-0.0105202	0.114432
HP_LP_flow	**-0.170508**	**-0.342707**	**-0.185389**	**-0.475859**
mat_cond	-0.00318756	0.149302	0.055114	0.15481
mat_cap	0.0758097	0.315189	0.00222092	-0.0379675
SIS_timing	-0.0136808	-0.160199	-0.0125658	-0.0624892
ACC_Temp	-0.0455422	-0.17649	0.0124489	-0.0504867
ACC_press	0.00197696	-0.0120272	0.0223846	0.00824023
HPSI_T	**0.335426**	**0.79857**	**0.363238**	**0.750301**
Decay_heat	0.0575788	0.305335	0.0601987	0.203206
PRZ_lvl	-0.0111982	-0.155583	-0.0825833	-0.222831
NvolACC	-0.117673	-0.0999911	-0.0263004	-0.0640907
SGpress	-0.054942	-0.119155	-0.0673875	-0.160222

	Simple	**Partial**	**Simple Rank**	**Partial Rank**
HTC_coeff	**-0.135997**	**-0.441143**	**-0.18498**	**-0.518977**
walldrag	-0.102093	-0.234944	-0.101286	-0.239916
formloss	**0.878885**	**0.959998**	**0.822501**	**0.932107**
HF_noneq_coeff	-0.122224	-0.206767	-0.103741	-0.21087

12.5 Results of additional BEPU analyses with 93 samples

Results of sampled 93 calculations to yield 95%/95% two-sided tolerance bound are presented in figures below. The agreed minimal set of BEPU results (see below) is extended by couple of graphs with additional parameters.

The set of graphs presented below is based on the minimal set of figures for BEPU agreed in Task 2.3 of APAL:
- Primary pressure (DC)
- Coolant temperature at 1.350 m under CL1
- Coolant temperature at 1.350 m under CL2
- HTC at RPV wall at 1.350 m under CL1
- HTC at RPV wall at 1.350 m under CL2
- Inner RPV wall temperature at 1.350 m under CL1
- Inner RPV wall temperature at 1.350 m under CL2

The red line depicts in each figure the reference case results.
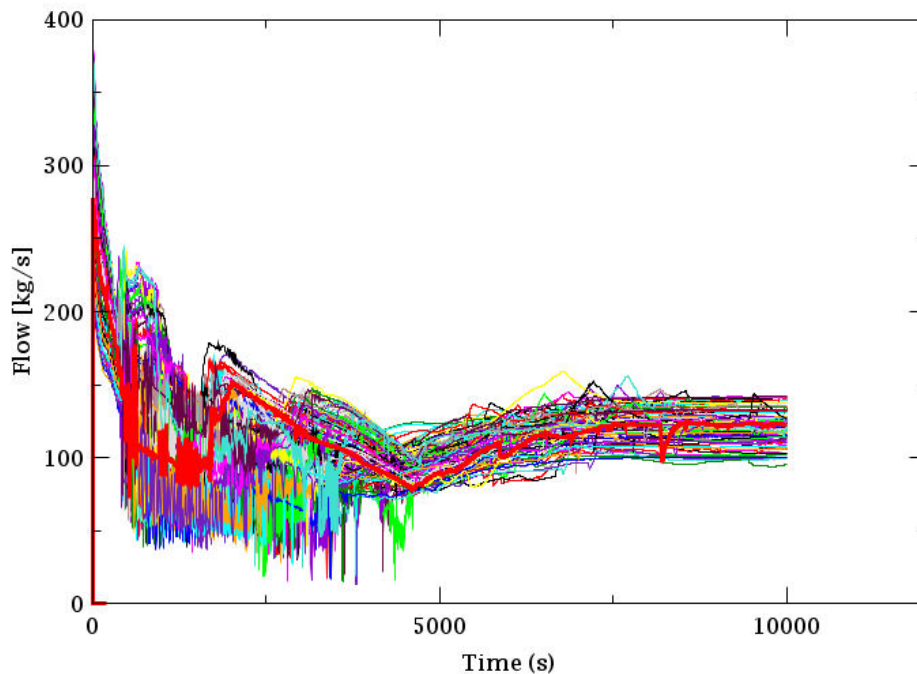
Figure 326: Break flow (93 samples)
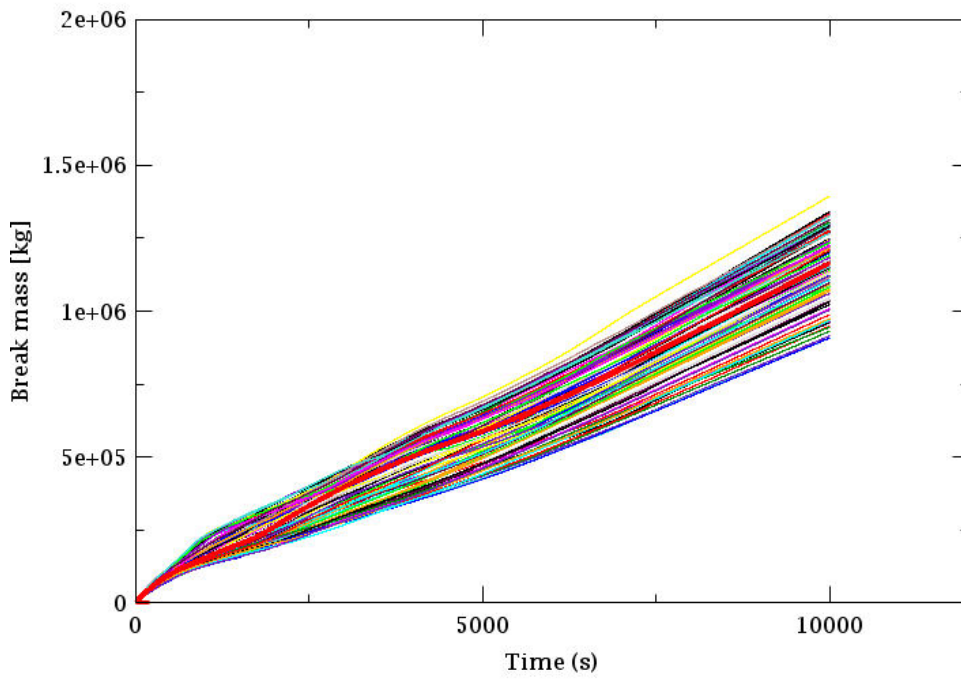
Figure 327: Integral of break flow (93 samples)
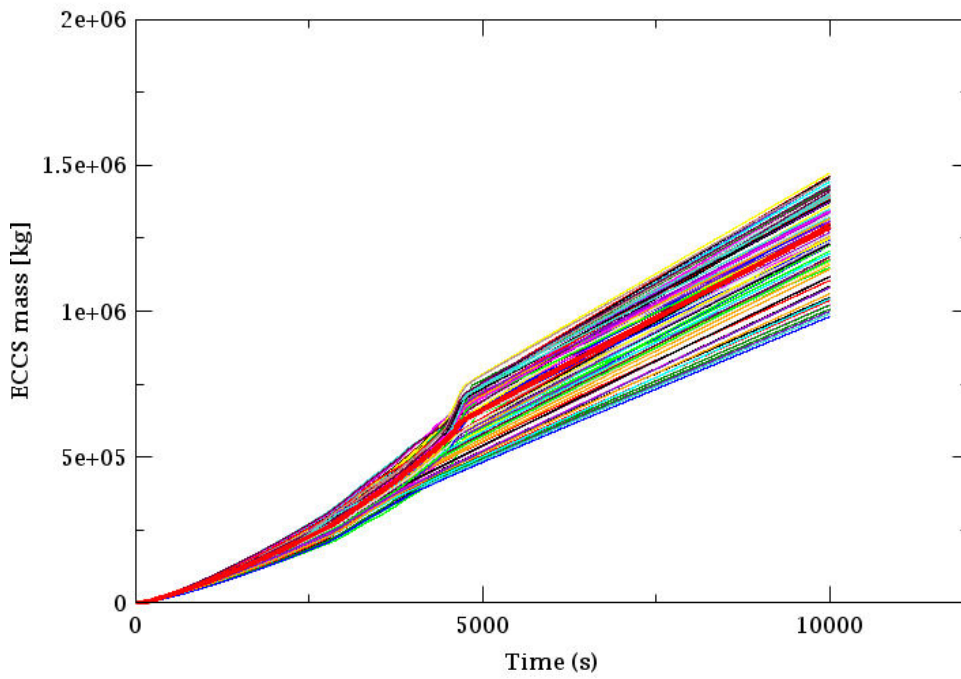
Figure 328: Integral of ECCS flow (93 samples)

P_DC
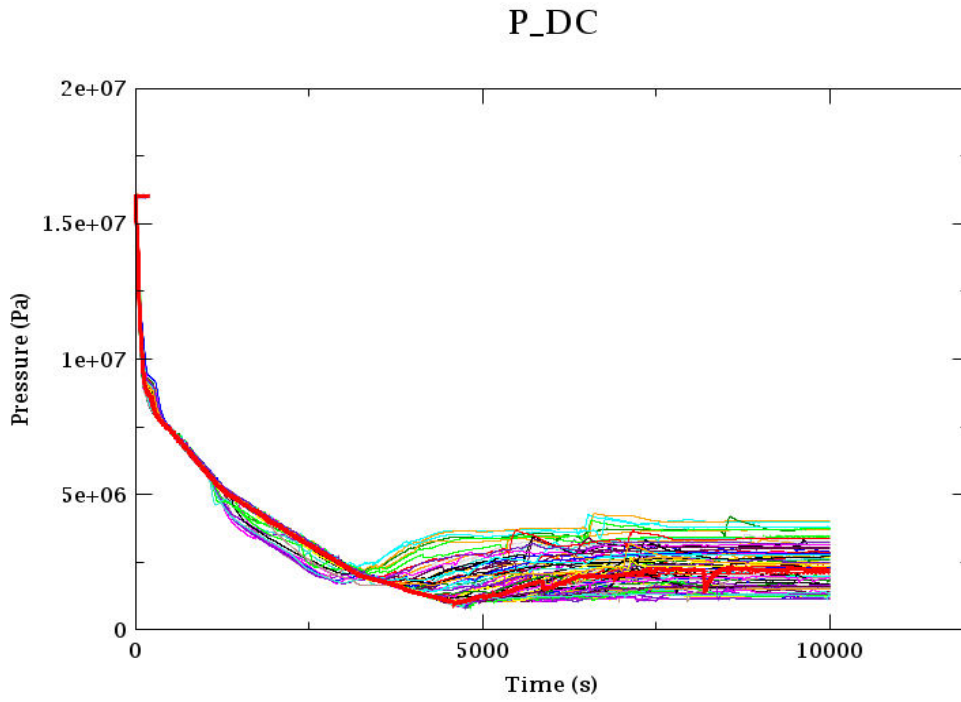
Figure 329: Primary pressure (93 samples)

L_PRZ
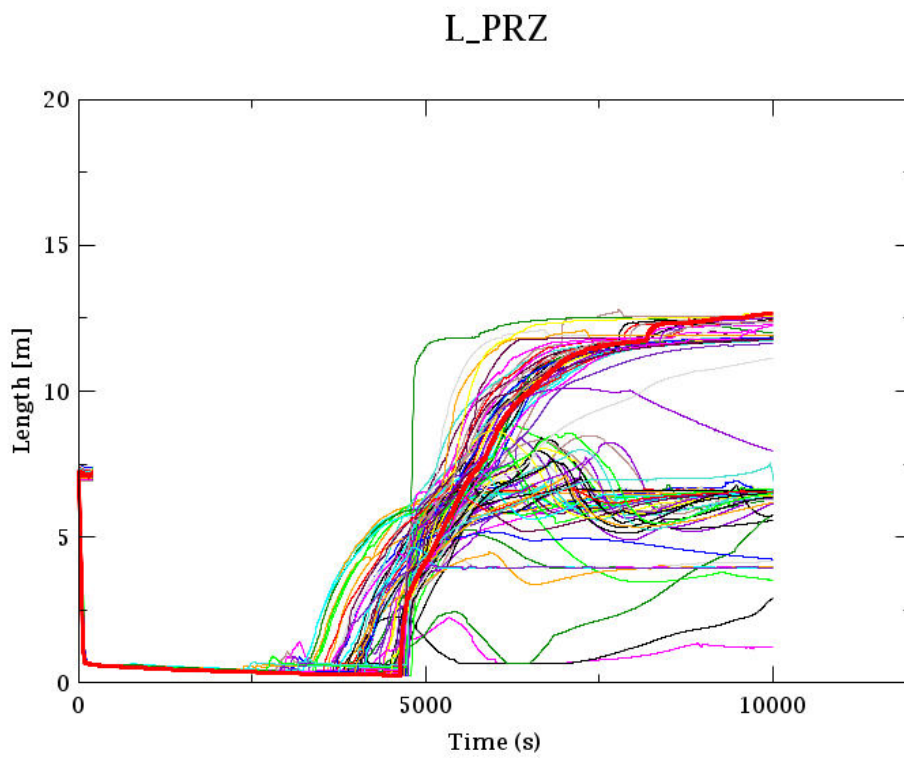
Figure 330: PRZ collapsed level (93 samples)
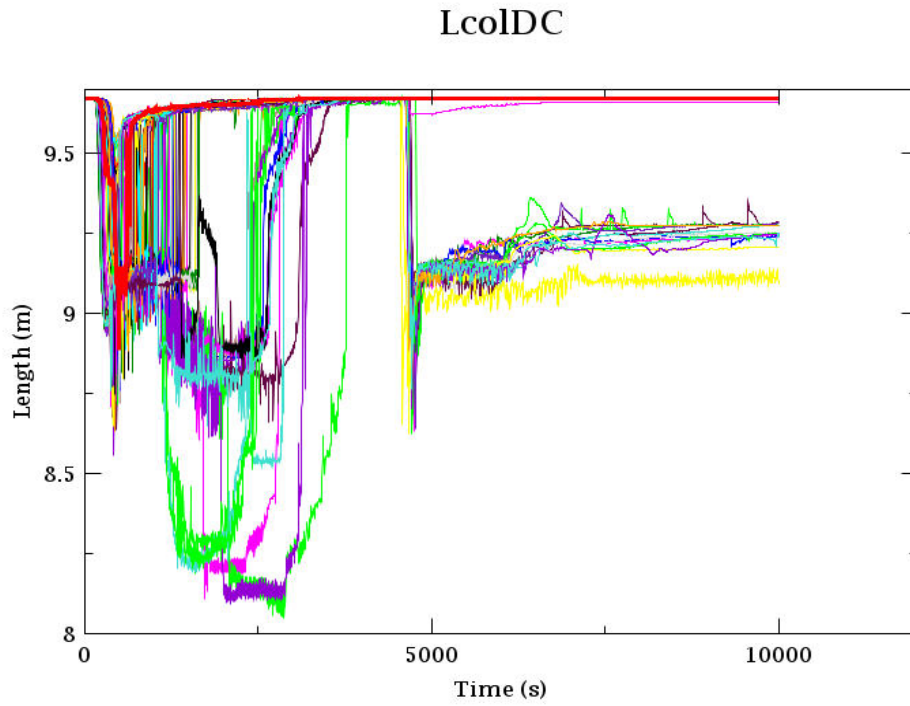
Figure 331: Reactor downcomer collapsed level (93 samples)
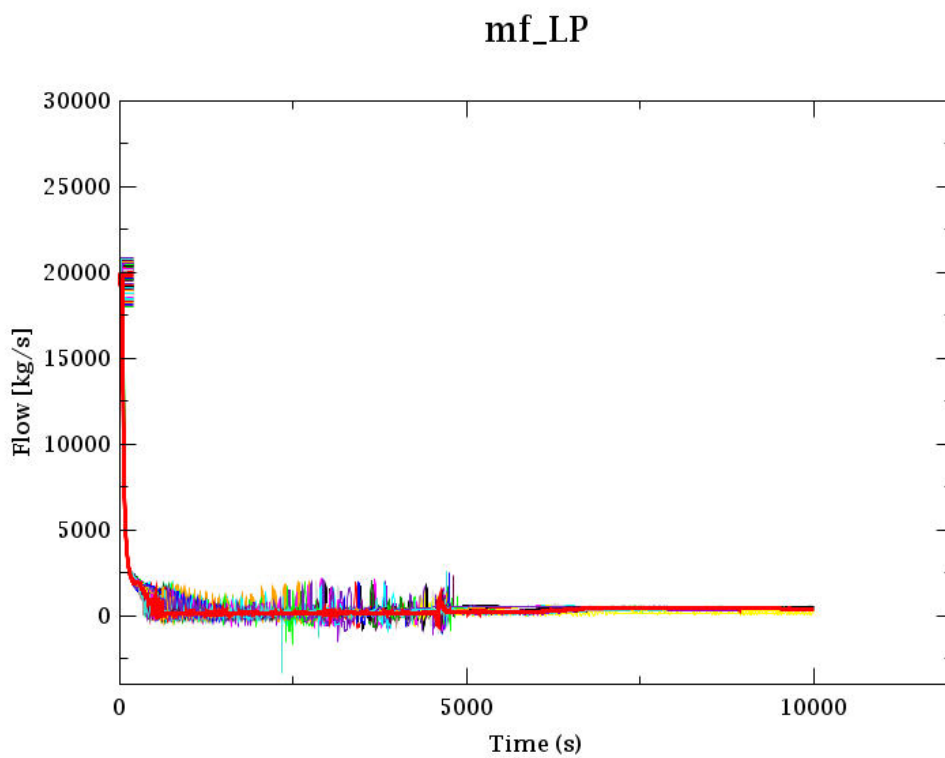
Figure 332: Reactor flow (93 samples)

Tf_LP
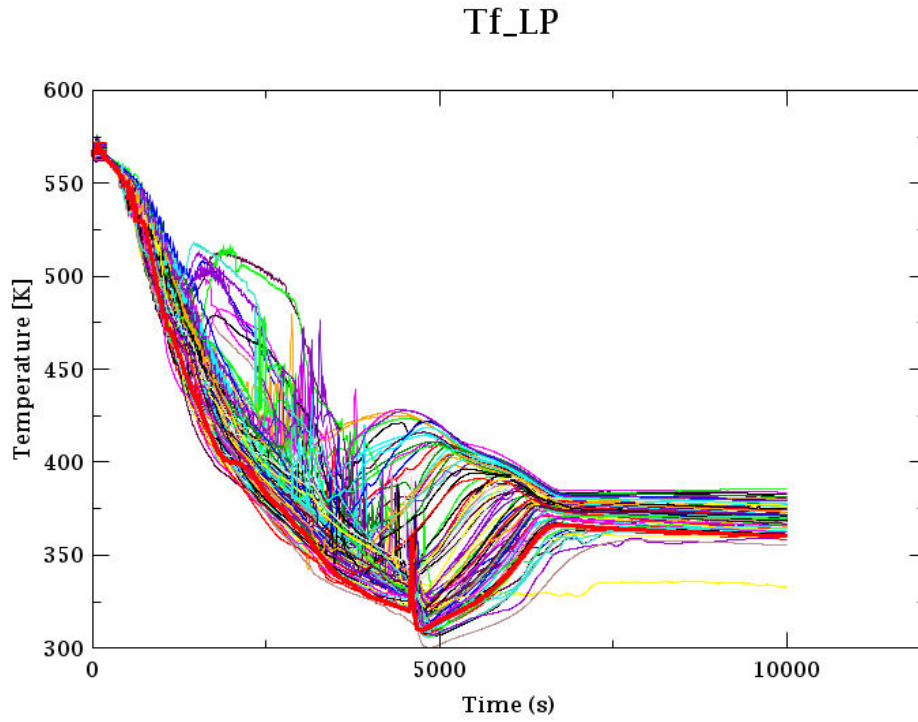
Figure 333: Coolant temperatures in reactor lower plenum (93 samples)

TavgDC
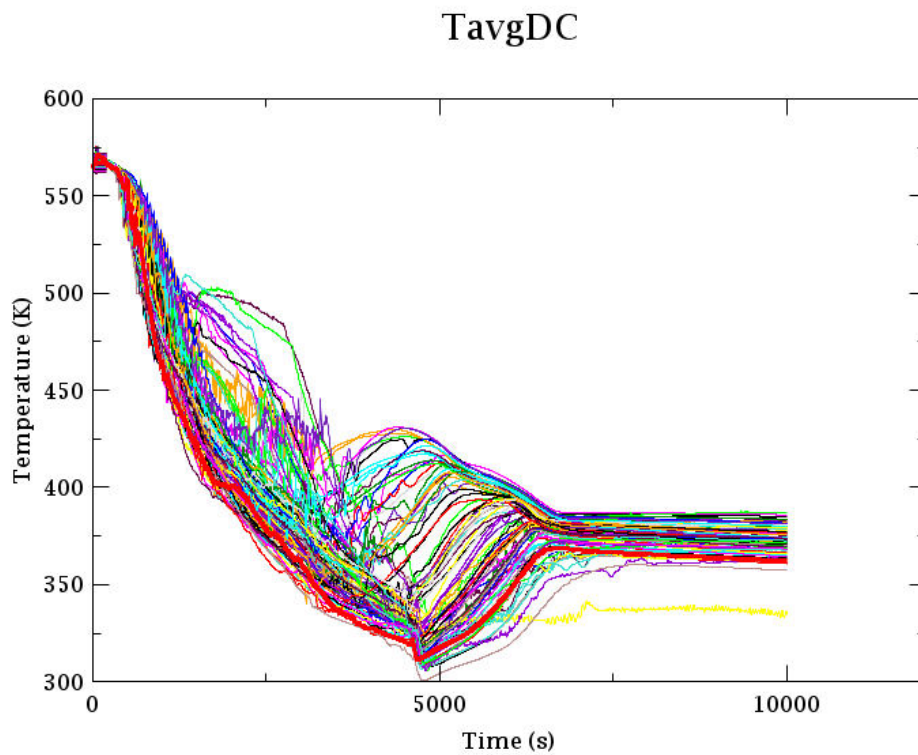
Figure 334: Average coolant temperatures in reactor downcomer (93 samples)

Tf_UP
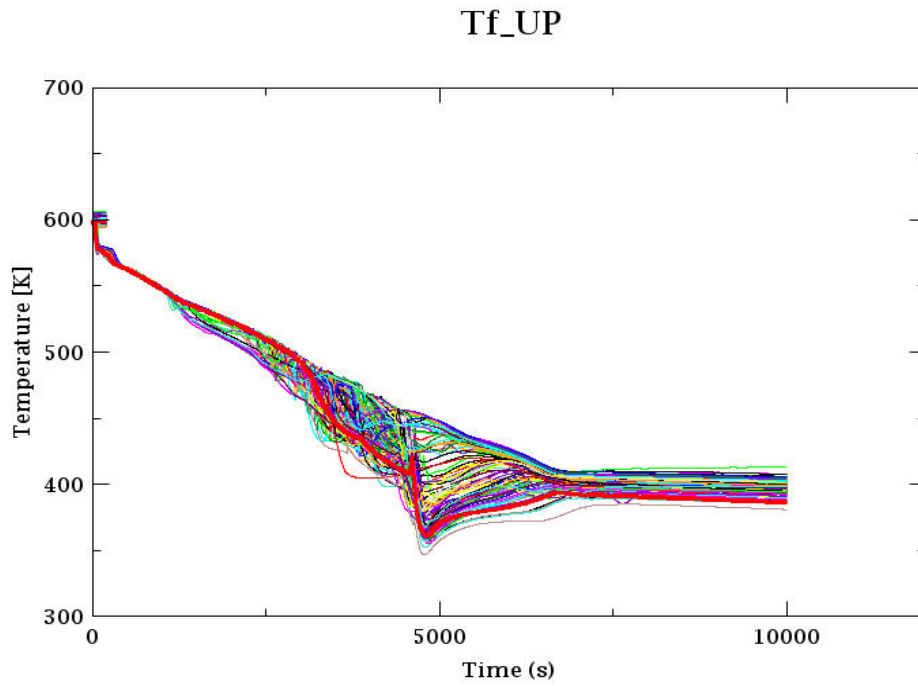
Figure 335: Coolant (liquid) temperatures in reactor upper plenum (93 samples)

Tf_CL1end
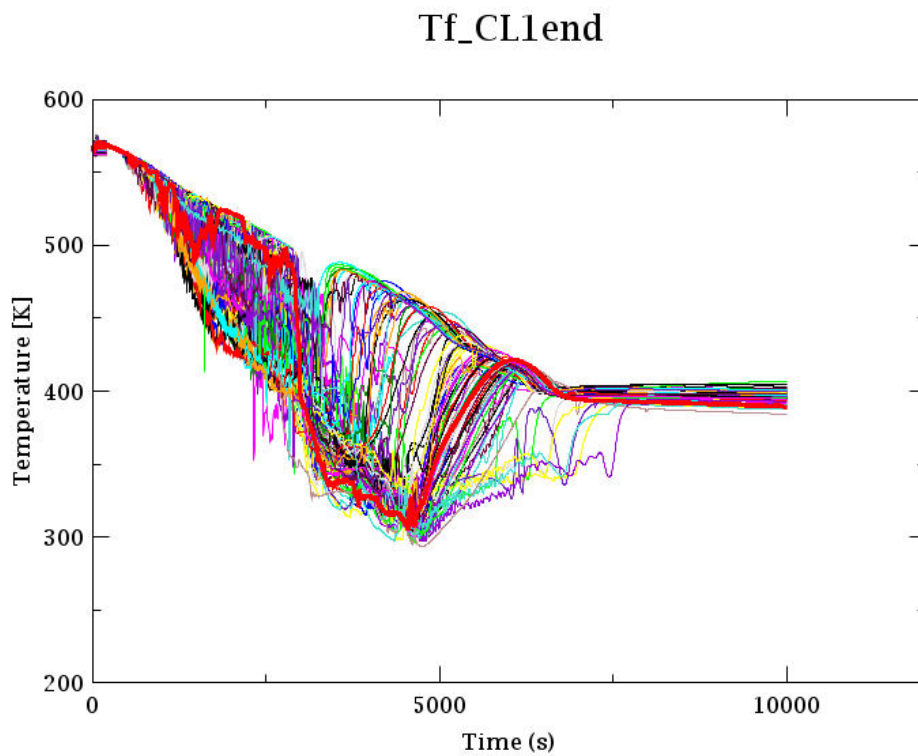
Figure 336: Coolant (liquid) temperatures at reactor inlet from CL1 (93 samples)

251

Tf_CL2end
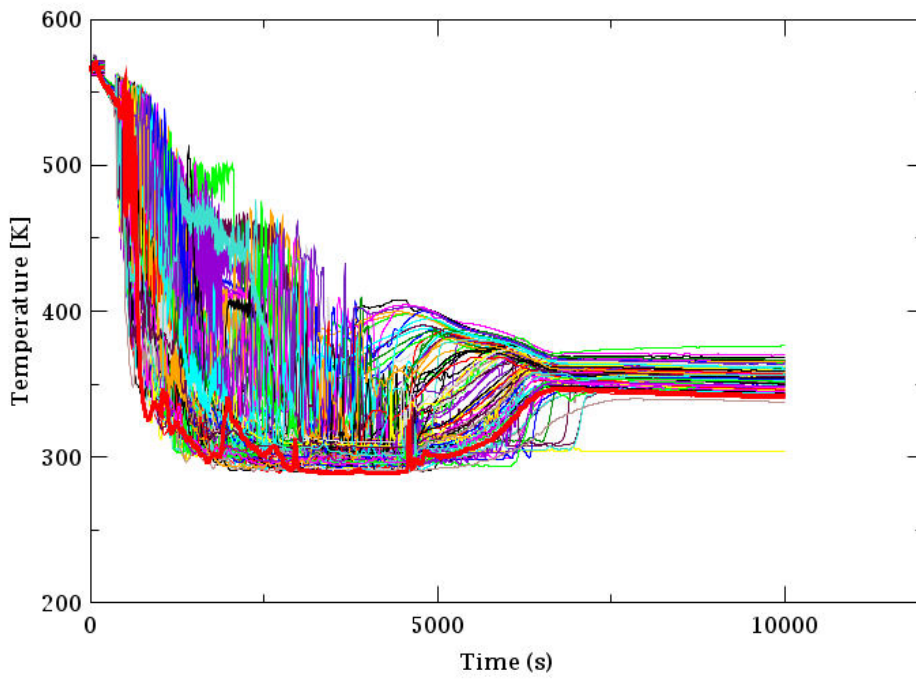
Figure 337: Coolant (liquid) temperatures at reactor inlet from CL2 (93 samples)

Tf_CL3end
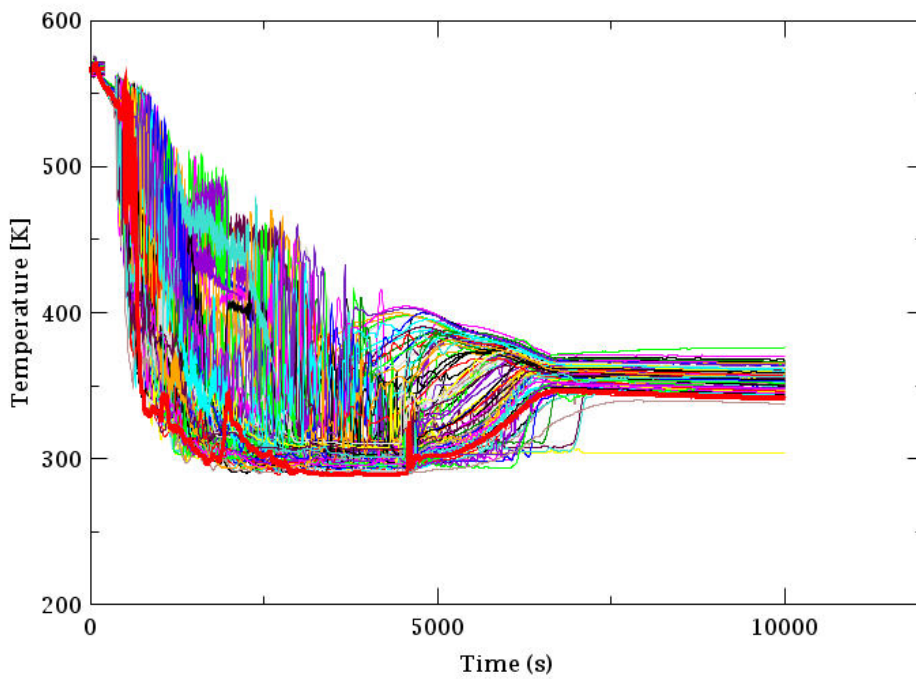
Figure 338: Coolant (liquid) temperatures at reactor inlet from CL3 (93 samples)

Tf_CL4end
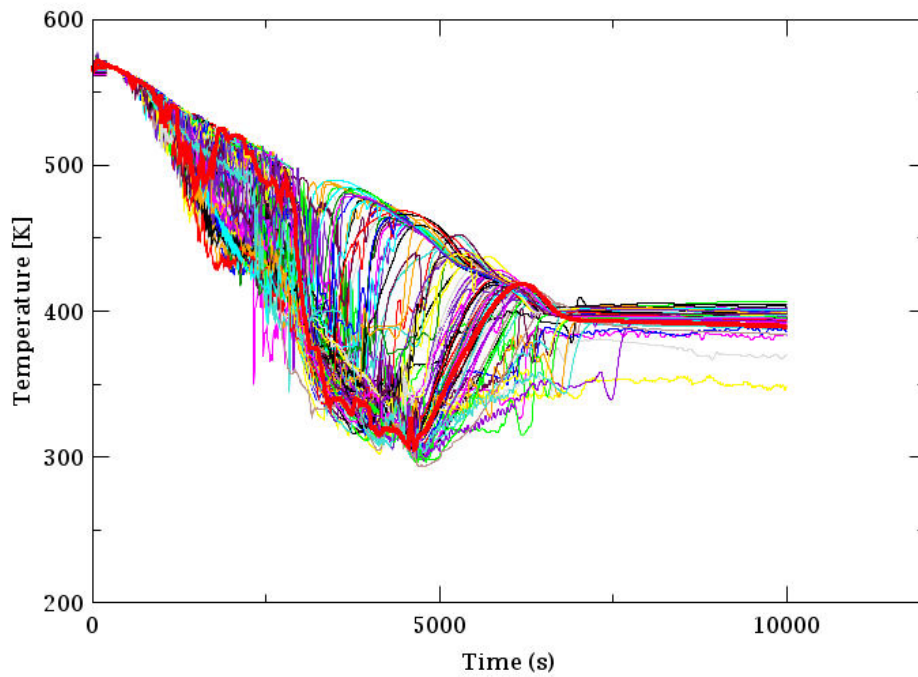
Figure 339: Coolant (liquid) temperatures at reactor inlet from CL4 (93 samples)

Tf_DC_9103
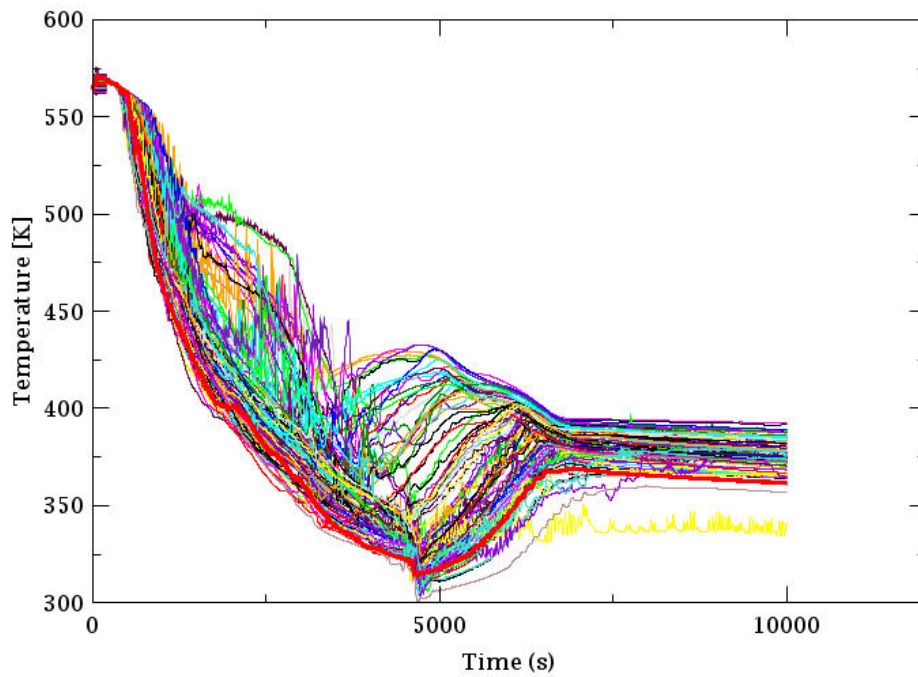
Figure 340: Downcomer coolant temperatures at 1.35 m under CL1 (93 samples)

Tf_DC_9403
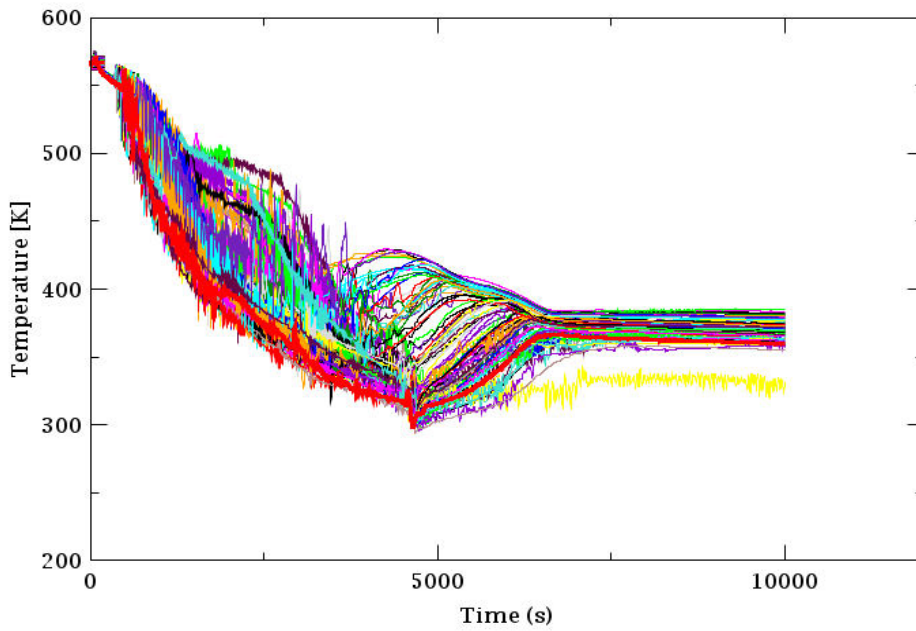
Figure 341: Downcomer coolant temperatures at 1.35 m under CL2 (93 samples)

HTC_DC_9105
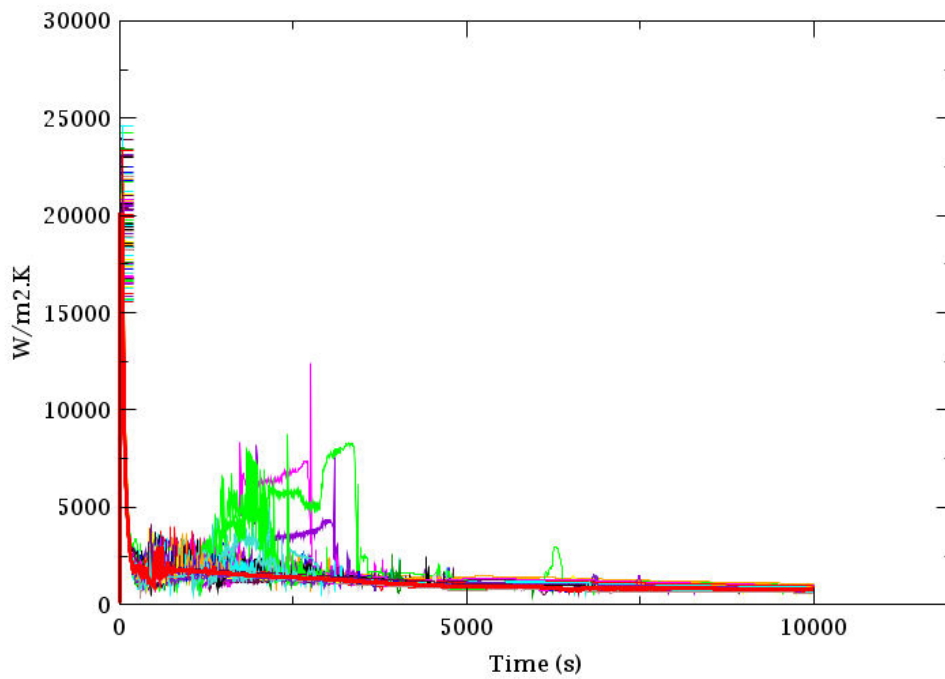
Figure 342: Heat transfer coefficient at RPV inner wall at 1.35 m under CL1 (93 samples)

HTC_DC_9405
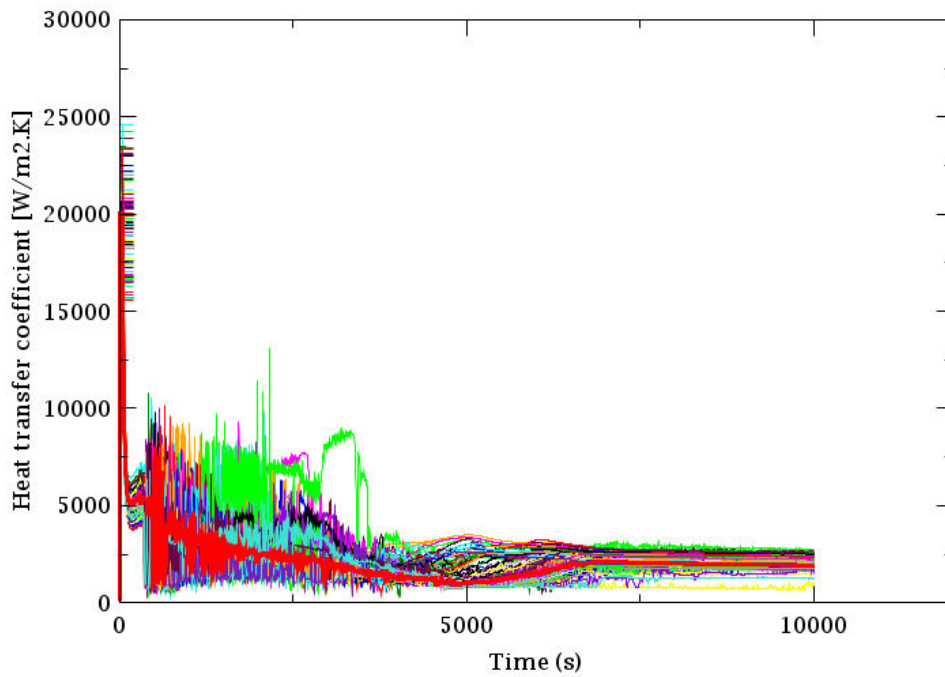
Figure 343: Heat transfer coefficient at RPV inner wall at 1.35 m under CL2 (93 samples)

Tw_DC_9103
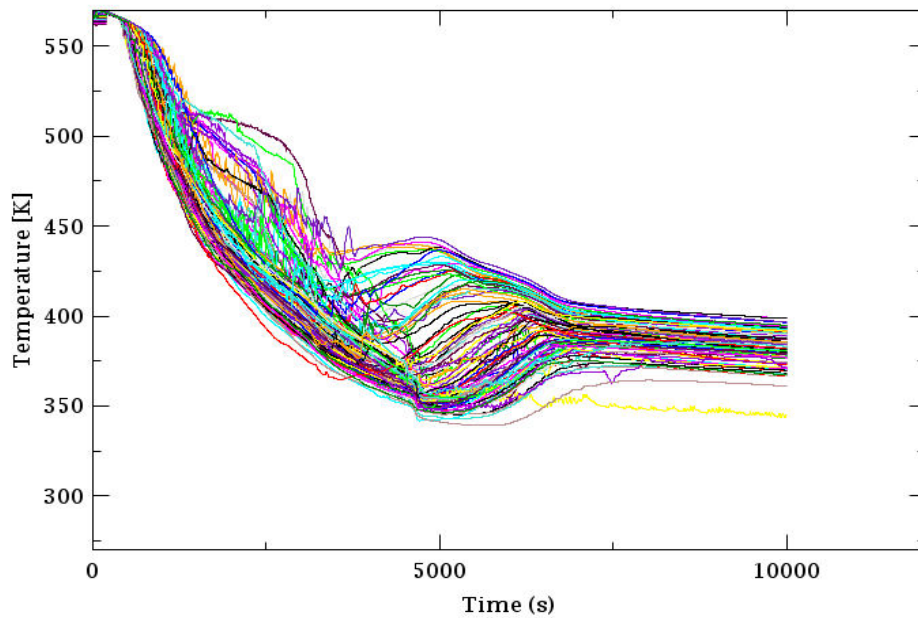
Figure 344: RPV inner wall temperatures at 1.35 m under CL1 (93 samples)
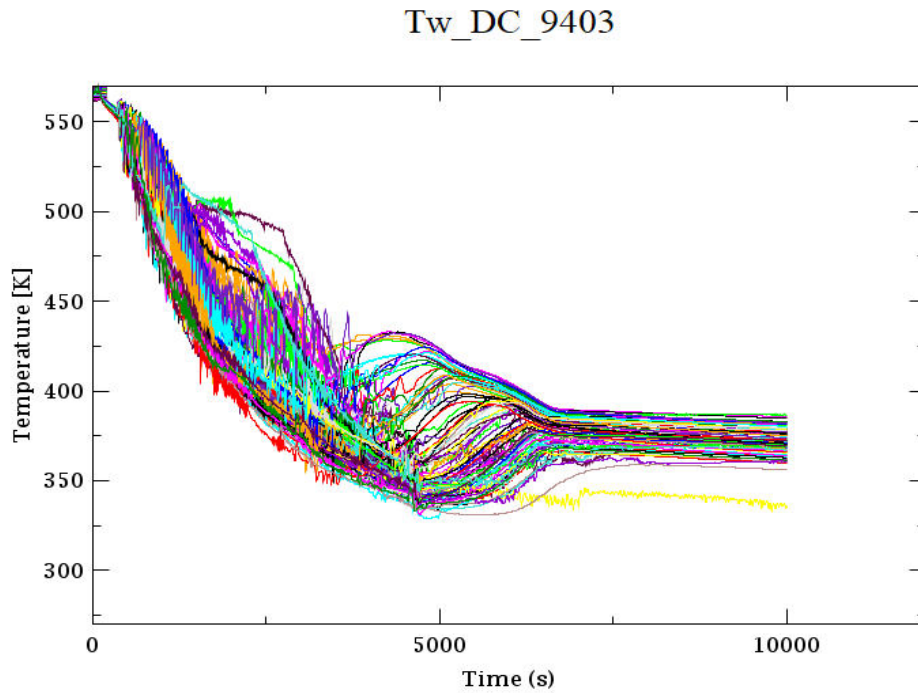
Figure 345: RPV inner wall temperatures at 1.35 m under CL2 (93 samples)

12.6 Comparison of BEPU analyses with 59 and 93 samples

Results of UJV BEPU analysis with 59 samples and UJV-BEPU analysis with 93 samples are compared in figures below. The following 7 parameters are compared at the following pages.

- Primary pressure (DC)
- Coolant temperature at 1.350 m under CL1
- Coolant temperature at 1.350 m under CL2
- HTC at RPV wall at 1.350 m under CL1
- HTC at RPV wall at 1.350 m under CL2
- Inner RPV wall temperature at 1.350 m under CL1
- Inner RPV wall temperature at 1.350 m under CL2
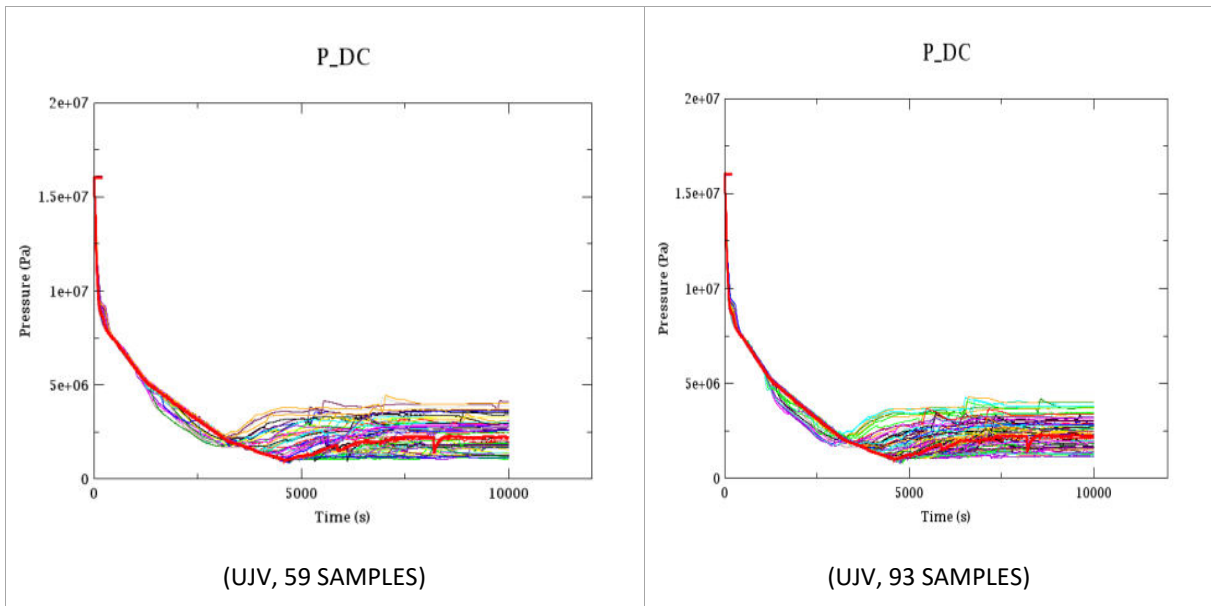
Figure 346: Primary pressure – comparison
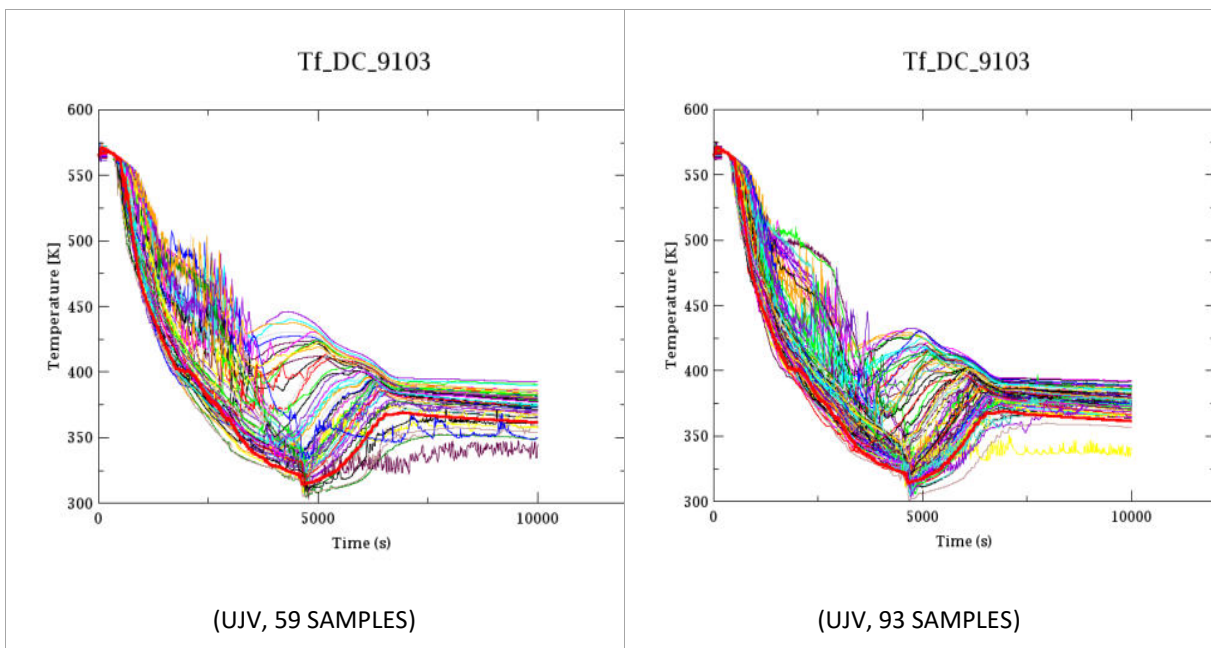
Figure 347: DC coolant temperature at 1.350 m under CL1 – comparison
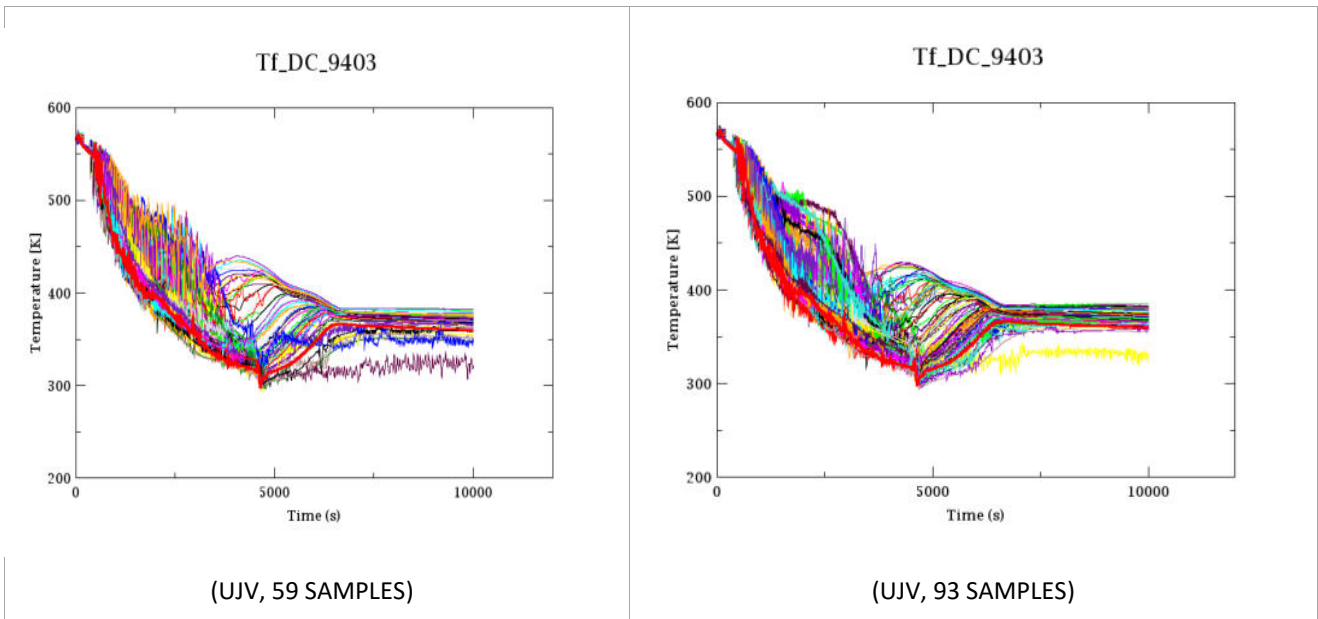
Figure 348: DC coolant temperature at 1.350 m under CL2 - comparison
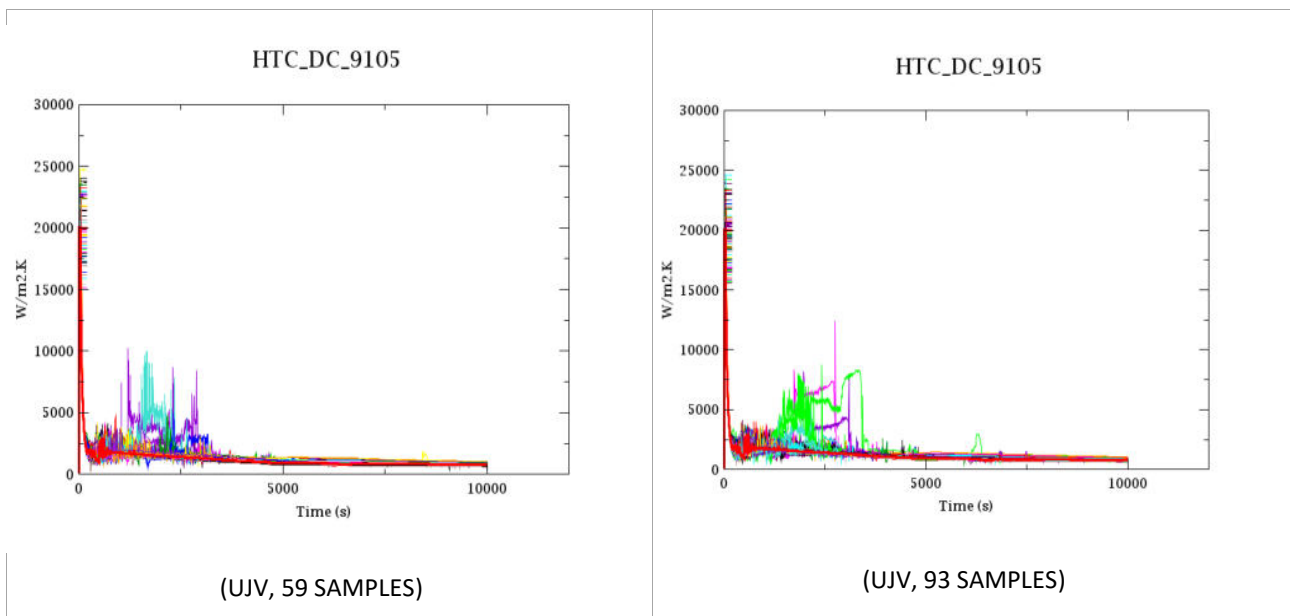
Figure 349: HTC at RPV wall at 1.350 m under CL1 – comparison
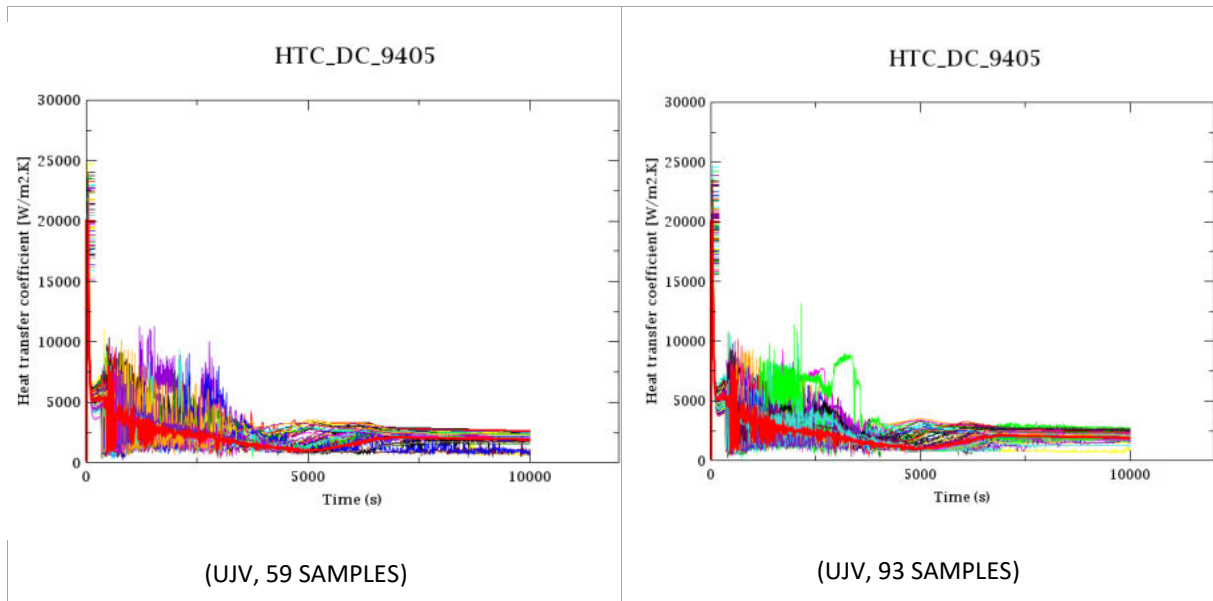
Figure 350: HTC at RPV wall at 1.350 m under CL2 - comparison
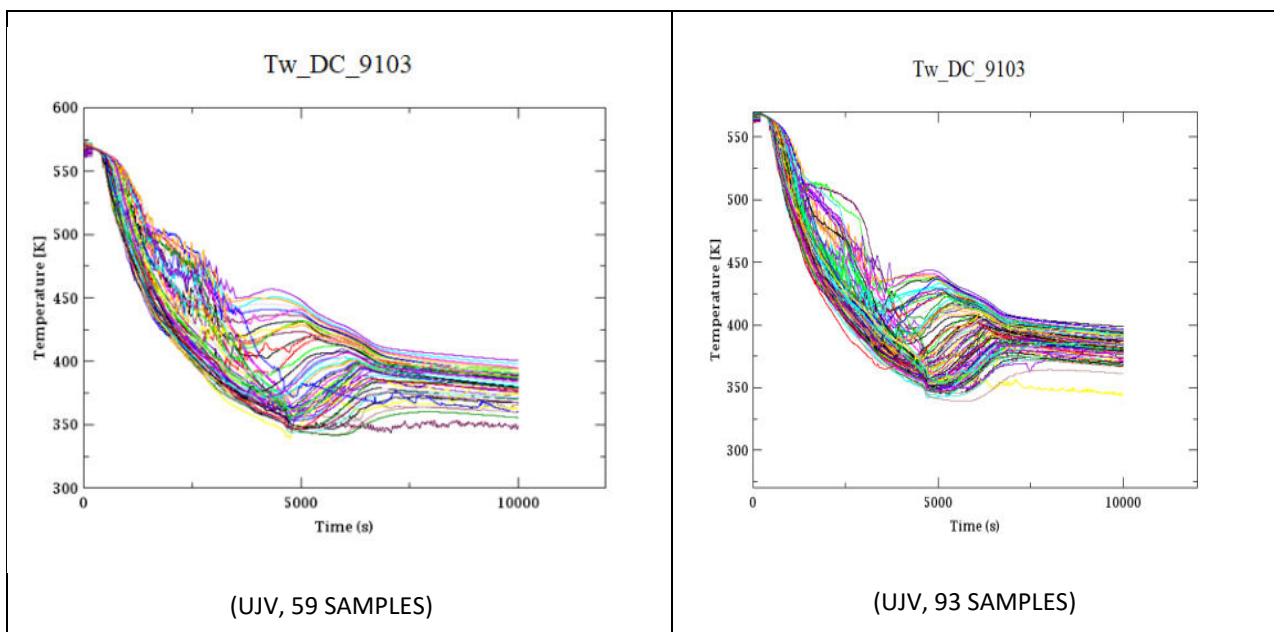
Figure 351: Inner RPV wall temperature at 1.350 m under CL1 - comparison

259

(UJV, 59 SAMPLES)	(UJV, 93 SAMPLES)
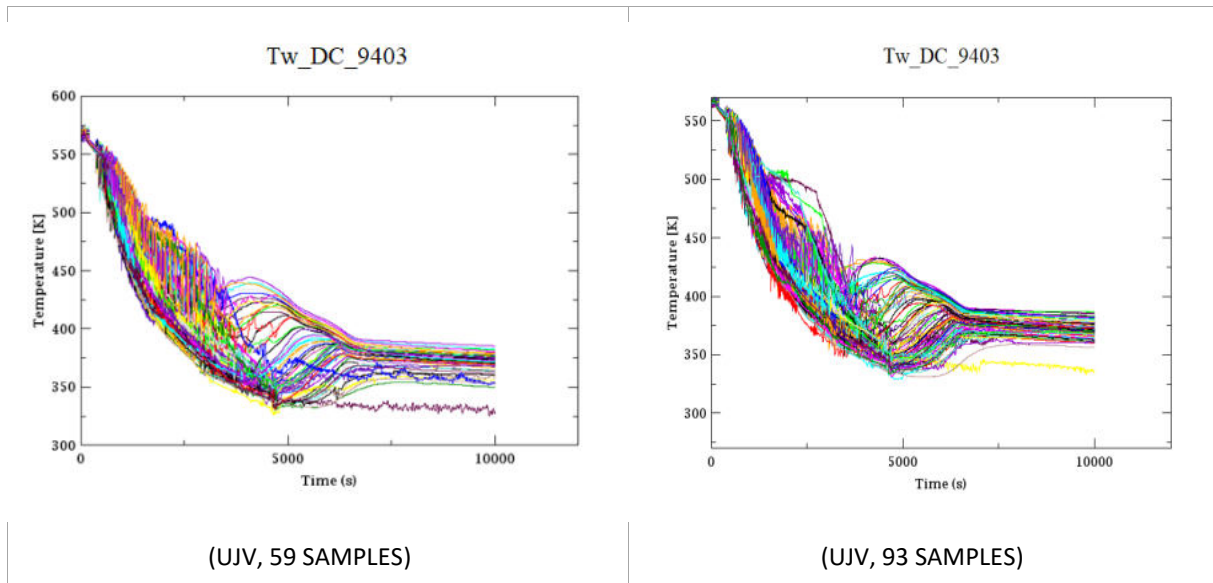
Figure 352: Inner RPV wall temperature at 1.350 m under CL2 – comparison

13   Framatome uncertainty analysis with KWU-MIX

As discussed in Section 3.4.1, Framatome GmbH uses a two-step process for performing the thermal-hydraulic analyses for PTS. The first step is a system analysis performed with RELAP5, as described in Section 3.1. The second step is a mixing analysis performed with KWU-MIX.

The RELAP5 results from the Version 86 of the 1300 RELAP model were used as input to KWU-MIX.

13.1 Reference best-estimate calculation

The RELAP5 results described in Section 12.1 were used as input to KWU MIX. The best-estimate values of the model parameters described in Section 5.5.4 were also used as KWU MIX input, and the results are shown below.
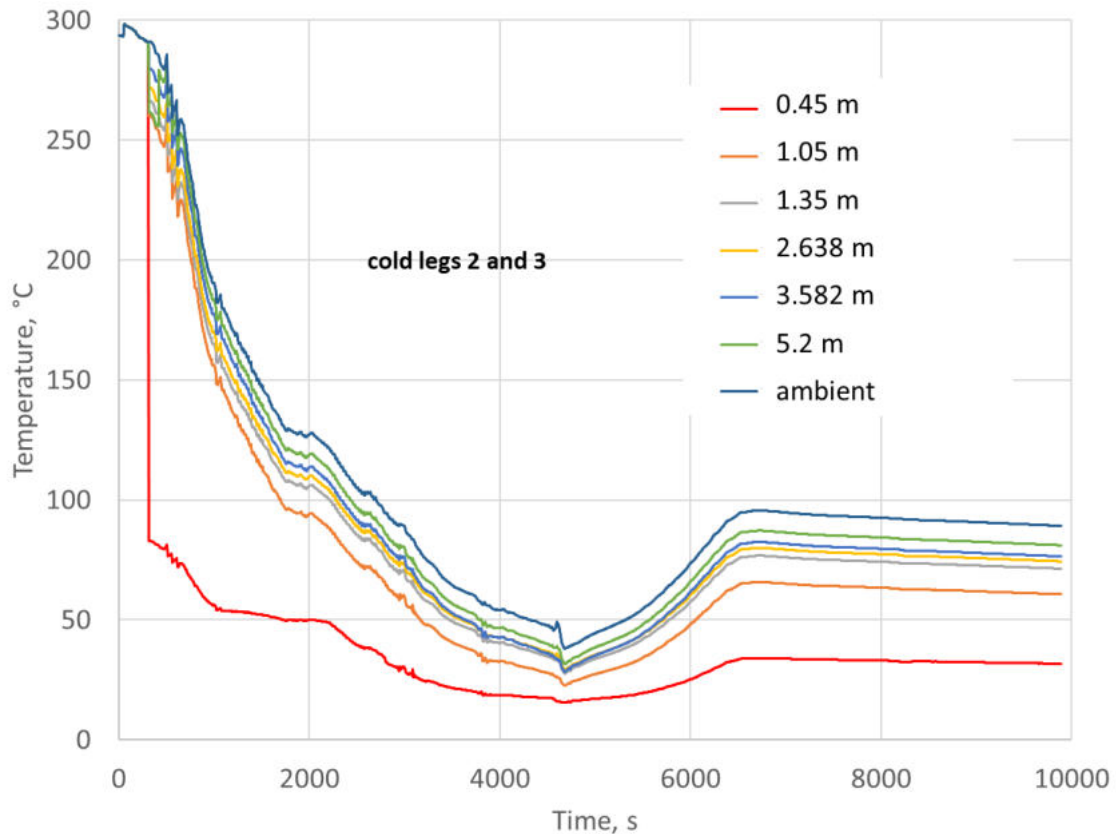
Figure 353: Centreline temperature of plume at various distances below the axis of Cold Leg 2.
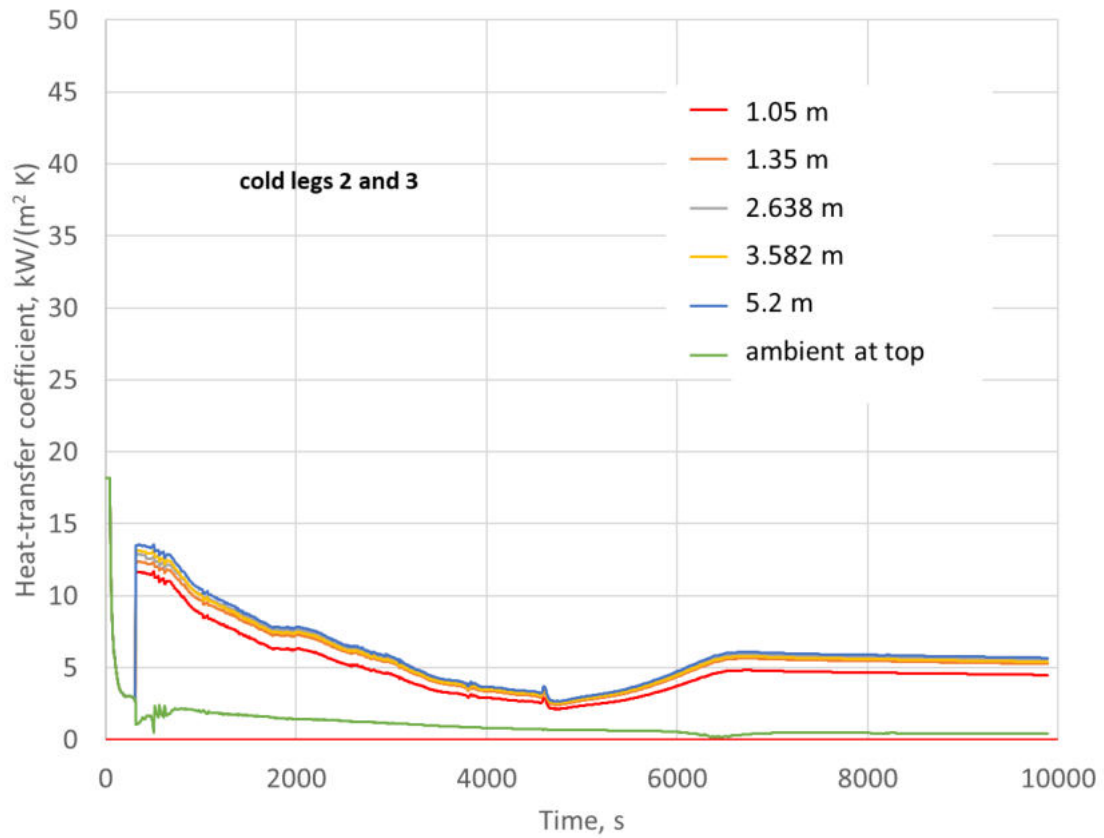
Figure 354: Centreline heat-transfer coefficient of plume at various distances below the axis of Cold Leg 2.

13.2 Results of BEPU analyses

Values for the uncertainty parameters in Table 36 were chosen at random for each of 59 simulations of the transient described in Chapter 2. The values of the three uncertainty parameters for each of the 59 simulations are shown in Figure 355.
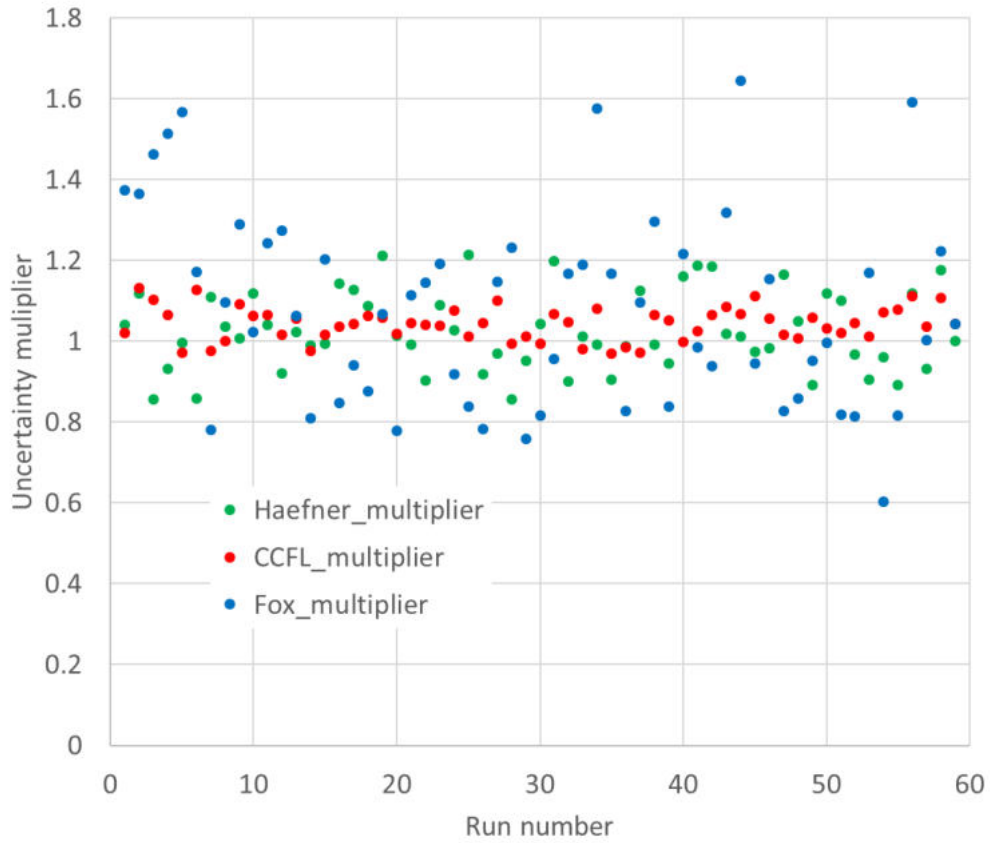
Figure 355: Uncertainty parameters for 59 simulations with KWU-MIX

The centreline temperatures at a distance 1.35 m below the axis of Cold Leg 2 (with HPI) are shown in Figure 356.
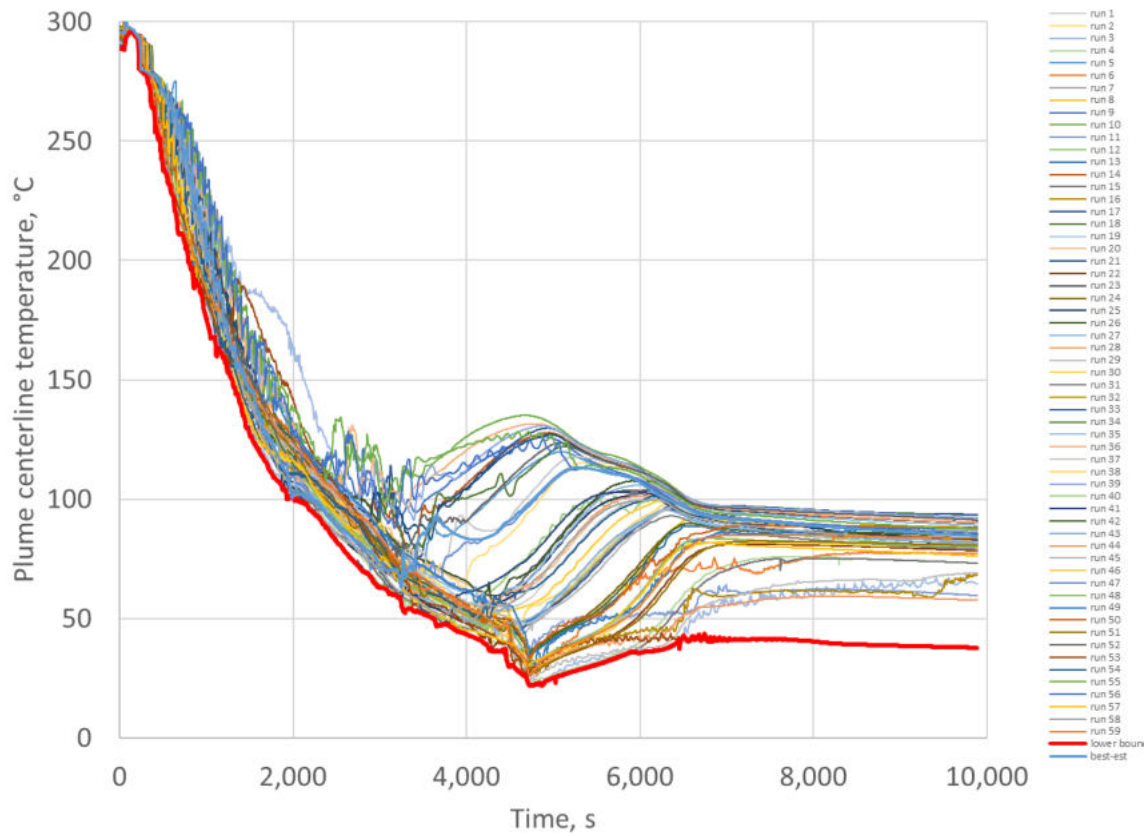
Figure 356: Centerline temperatures for 59 simulations with KWU-MIX at 1.35 m below the axis of Cold Leg 2

The centreline temperatures at a distance 1.35 m below the axis of Cold Leg 1 (without HPI) are shown in Figure 357.
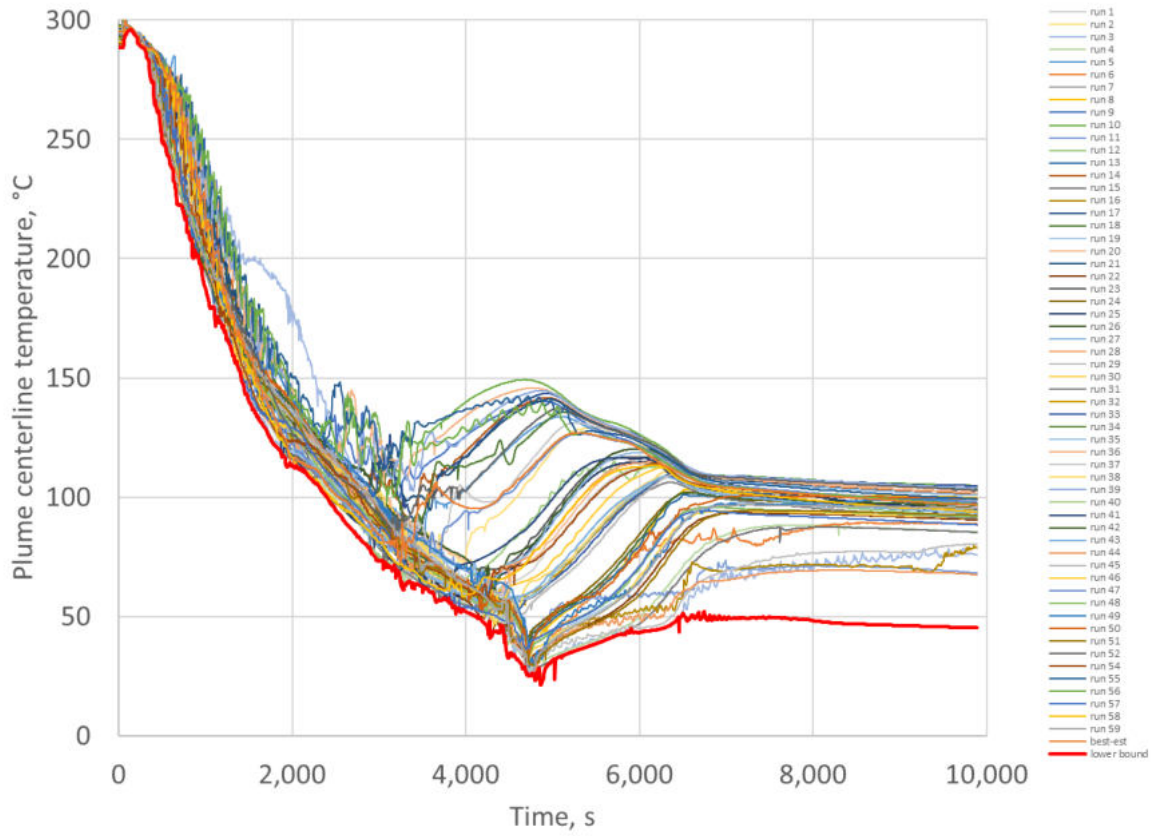
Figure 357: Centerline temperatures for 59 simulations with KWU-MIX at 1.35 m below the axis of Cold Leg 1

The heat-transfer coefficients at the centreline of the plume were also calculated by KWU-MIX, and the results are shown in Figure 358 for a distance of 2.35 m below the axis of Cold Leg 2.
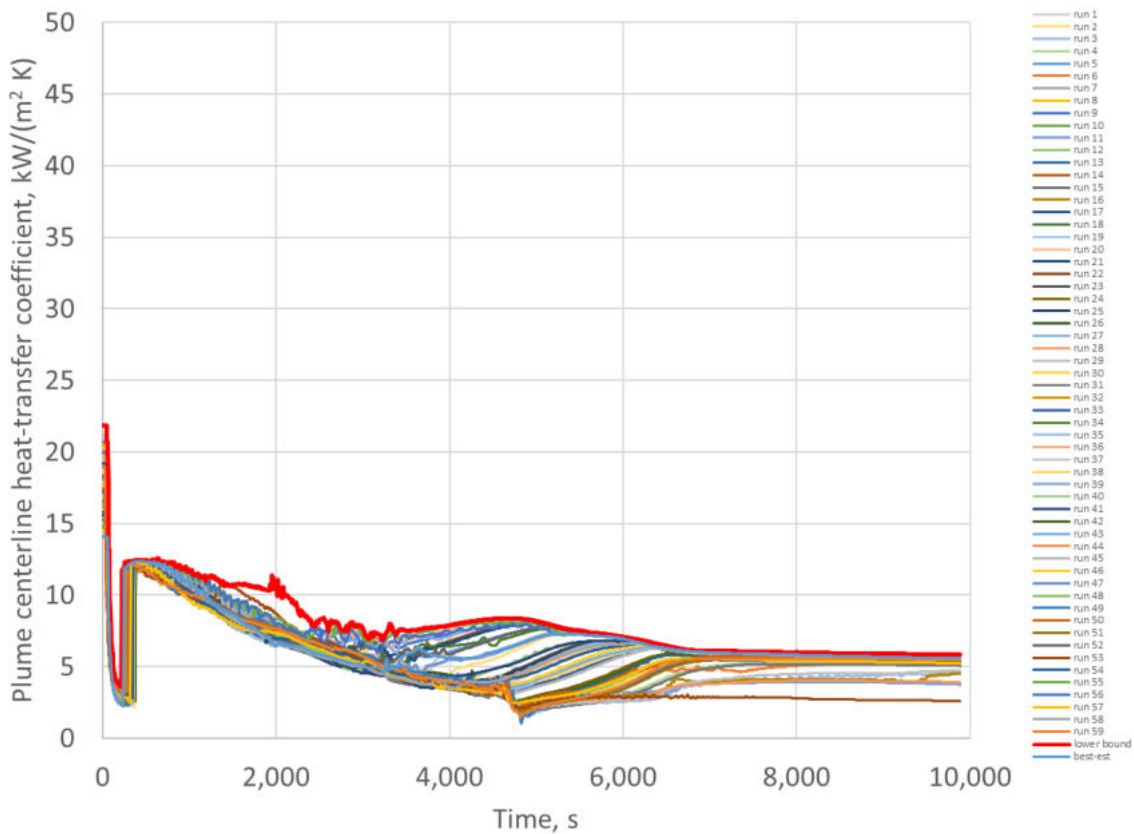
Figure 358: Centerline heat-transfer coefficients for 59 simulations with KWU-MIX at 1.35 m below the axis of Cold Leg 2.

13.3 Statistical analysis of KWU-MIX results using Wilks method

Table 28 shows that 59 simulations are required for a tolerance limit of $P = 0.95$, and a confidence level of $1 - \alpha = 0.95$, if the rank is $r = 1$. The red line in in Figure 357 is the curve of $r = 1$ for the centreline temperature at a distance of 1.35 m below the cold-leg axis.

A Spearman correlation coefficient was calculated for each of the uncertainty parameters as a function of time. The Spearman correlation coefficient is a nonparametric measure of the statistical dependence between the rankings of two variables. In this case, it assesses how well the relationship between the temperature and a particular uncertainty parameter can be described using a monotonic function. The Spearman correlation between two variables approaches unity when pairs of temperature and uncertainty multiplier have a similar rank. A value of -1 is approached when the pairs have opposing ranks. Figure 359 shows that the largest Spearman correlation coefficients are for the Haefner and CCFL. The largest Spearman correlation coefficients for Haefner multipliers occur at approximately 1000 s and during the time span from 3900 s to 4200 s, when the water level in the downcomer is high (see LcolDC in Section 0). The largest Spearman correlation coefficients for CCFL multipliers occur during the time span from 2000 s to 2300 s, when the water level in the downcomer is the lowest (see LcolDC in Section 0). Large multipliers for CCFL limit the entrainment at the injection location and, therefore, limit the effect of the Haefner multiplier.
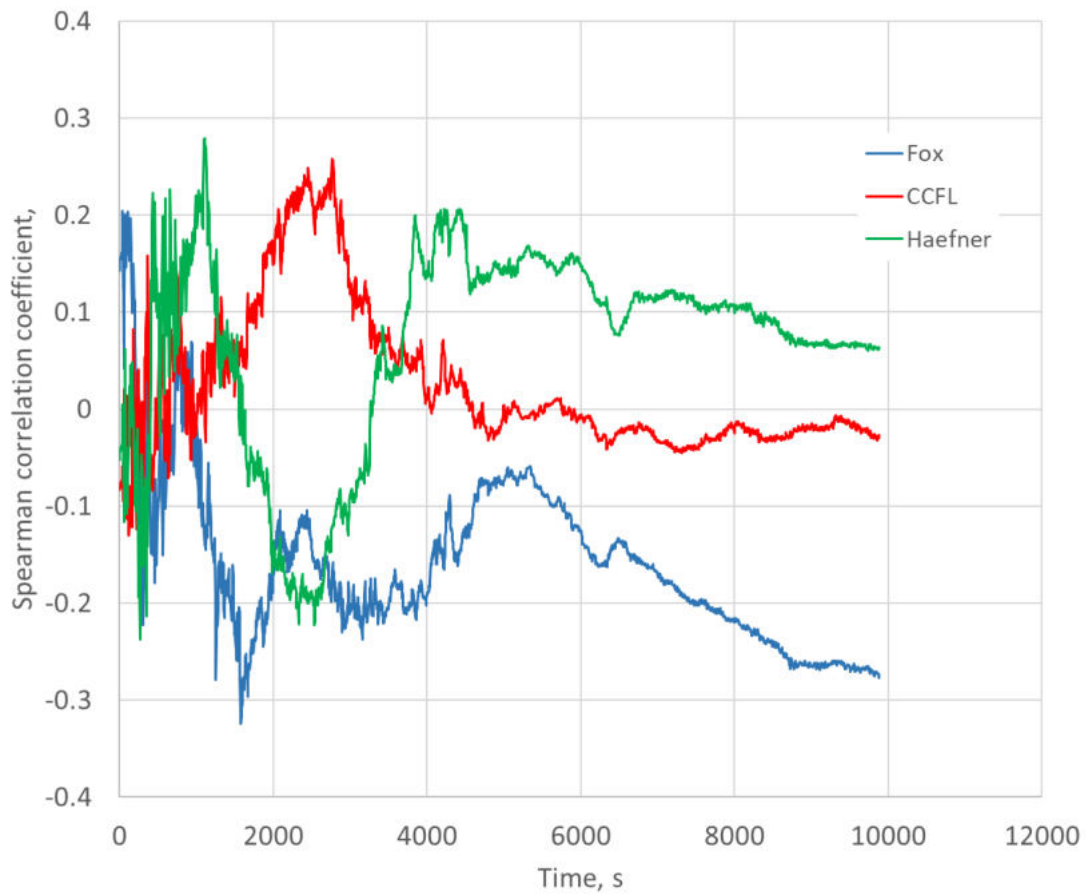
Figure 359: Spearman correlation coefficients for the temperature at 1.35 m below the axis of Cold Leg 2.

Figure 359 shows that there is nearly no trend between the CCFL multiplier and the temperature for times greater than 4000 s. The temperature has a trend closer to the Haefner multiplier.

There is a negative Spearman correlation coefficient for the Fox multiplier for times greater than 1000 s, and so the temperatures are influenced more by the other parameters.

14   JSI uncertainty analysis with RELAP5 and SUSA

14.1 Reference best-estimate calculation

For the purpose of uncertainty analysis in comparison with KWU model v76 used in task 2.1, some minor changes in the nodalization have been made:

- Controllers for setting initial pressurizer level and secondary pressure were introduced in the steady-state model and later deleted in the restart (transient) input model;
- UJV proposal was followed to change nodalization of accumulators to be able to vary initial nitrogen volume;
- WUT proposal was followed to make a slight change of the materials definition - the range of temperatures was extended.
- Extended table for volumetric heat capacity of fuel - the range of temperatures was extended.
- Changed option in junction connections between top of downcomer to upper head via leakage path because the original solution caused instabilities during transient run – now the connection is at level of cold/hot leg axis which ensure stable runs.

In addition, the newest version of RELAP5/MOD33 was used (i.e. 33lj version while in T2.1 base case calculations the latest version used was 33lf). Therefore, comparison between base case calculations using RELAP5/MOD3.3 version 33lf (labelled 'base_33lj') and RELAP5/MOD3.3 version 33lj (labelled 'base_33lj') has been done, and additionally reference calculation used in uncertainty analysis is shown, which has been calculated by RELAP5/MOD3.3 version 33lj (labelled 'ref_33lj').

Timing of main events and graphical results from the reference best-estimate calculation are shown below:

Table 45: Steady state parameters of JSI base cases and reference case calculations

Specification	JSI Base Case base_33lf	JSI Base Case base_33lj	JSI Reference Case ref_33lj
Reactor thermal power	3.765e9 W	3.765e9 W	3.765e9 W
Loop flow rates	5035 kg/s	5036 kg/s	5037 kg/s
Cold legs temperature	291.0 °C	291.0 °C	291.1 °C
Hot legs temperature	323.8°C	323.8°C	323.9 °C
DC to UH bypass flow rate	198.4 kg/s	198.4 kg/s	199.3 kg/s
Primary side pressure	156.6 bar	156.6 bar	157.4 bar
PRZ level	8.06 m	8.06 m	8.21 m
ACC volume, pressure and fill level, temperature	34 m³ 26 bar 8.5428 m 20 °C	34 m³ 26 bar 8.5428 m 20 °C	34 m³ 26 bar 8.5428 m 20 °C
Secondary pressure (SG1)	61.6 bar	61.6 bar	61.6 bar
SG level (SG1 riser/downcomer)	6.32/11.87 m	6.32/11.87 m	6.53/12.04 m

Table 46: Sequence of events for JSI base cases and reference case calculations

Cause	Event	Timing of JSI Base Case 'base_33lf' (s)	Timing of JSI Base Case 'base_33lj' (s)	Timing of JSI Reference Case 'ref_33lj' (s)
Primary pressure < 132 bars	Reactor trip Turbine trip Emergency signal Signal sec.-side cooldown (100K/hr auto.) MCPs trip	44.6	44.8	45
Analysis assumption	Loss of offsite power	44.6	44.6	45.6
Emergency signal + 12 s	Signal ECC system to start DG	56.6	56.6	57.6
Primary pressure < 110 bars	Emergency cooling signal for HPI pumps	79.4	79.7	78.8
HPI pumps running	HP injection	81.6	81.6	81.2
Primary pressure < 26 bars	ACC injection	2785	2835	2855
Primary pressure < 10 bars	Emergency coolant signal for LPI pumps	4543	4551	4538
LPI pumps running	LP injection	4546	4554	4541
ECCS injection stronger than break flow	PRZ level recovery	4555	4560	4340
End of calculation		4900 (10000)	10000	10000

The impact of all the changes on the selected parameters used for base case calculation presented in D2.1 report is shown in Figures 360 through 383.

From Figure 360(a) it can be seen that primary pressure is practically not much impacted until around 5000 s, but later there is some difference, while the secondary side pressure is not impacted Figure 360(b). The results show that the break flows also significantly differ in the period between 500 s and 6000 s (see Figure 361(a)), which significantly influence the transient progression after 5000 s. Due to different break flow in the reference calculation also other parameters differ.

The differences can be seen in the collapsed liquid levels (see Figures 370 through 373) and void fractions in cold and hot legs (see Figures 374 and 375), what could be attributed to the changes in the connections between the downcomer and the upper plenum. Also, it should be noted that some differences also resulted from different RELAP5 versions used for base case calculations. Due to lower break flow in the reference calculation also ECCS injected mass is lower (see Figure 365(b)), resulting in higher coolant temperatures (see Figures 376 through 381).

In general, the results obtained with stable reference calculation (labelled 'ref_33lj') are qualitatively comparable to the results obtained by base case calculation using original kwu76 model (labelled 'base_33lf') and therefore the input deck for reference calculation is applicable as template for uncertainty variation. Also, it should be noted that the match between 'base_33lf' and 'base_33lj' base case calculations is not ideal (e.g. see break flow on Figure 361(a)), what means that base case calculations are impacted by RELAP5 code version (for more information on the effect of code version on the RELAP5 base case results see also Section 5.1.2 of D2.1).

(a)   (b)
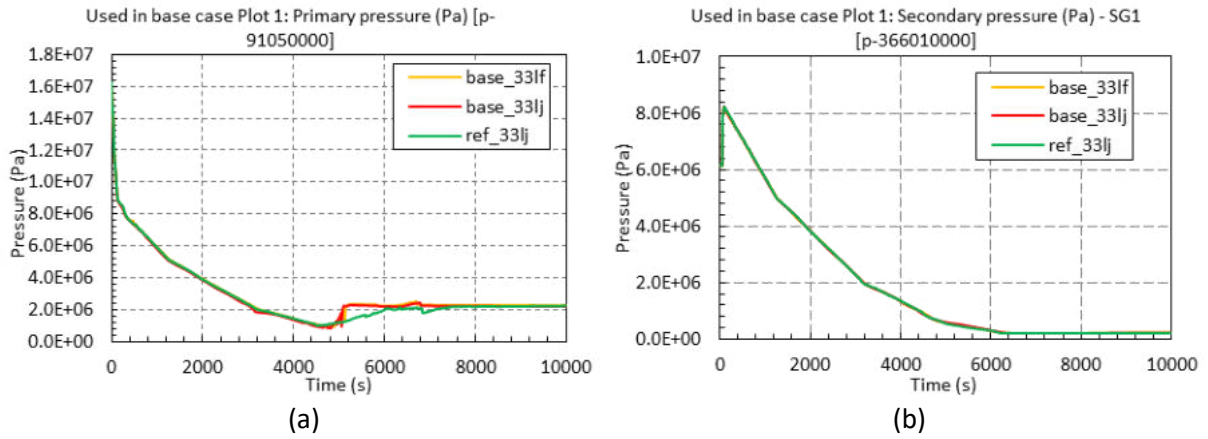
Figure 360: Comparison of System Pressures - (a) Primary pressure and (b) Secondary pressure.

(a)   (b)
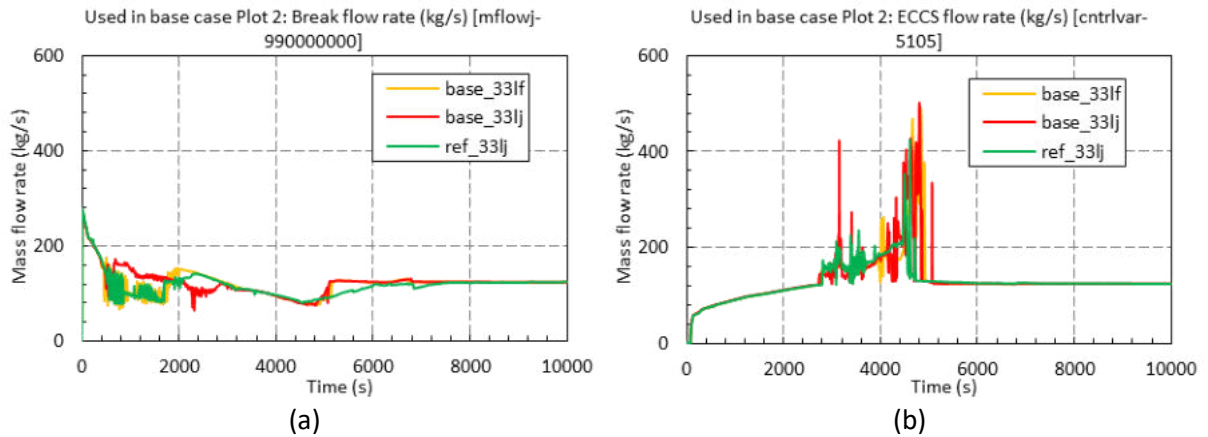
Figure 361: Comparison of (a) Break Flow Rate and (b) ECCS Flow Rate.

(a)   (b)
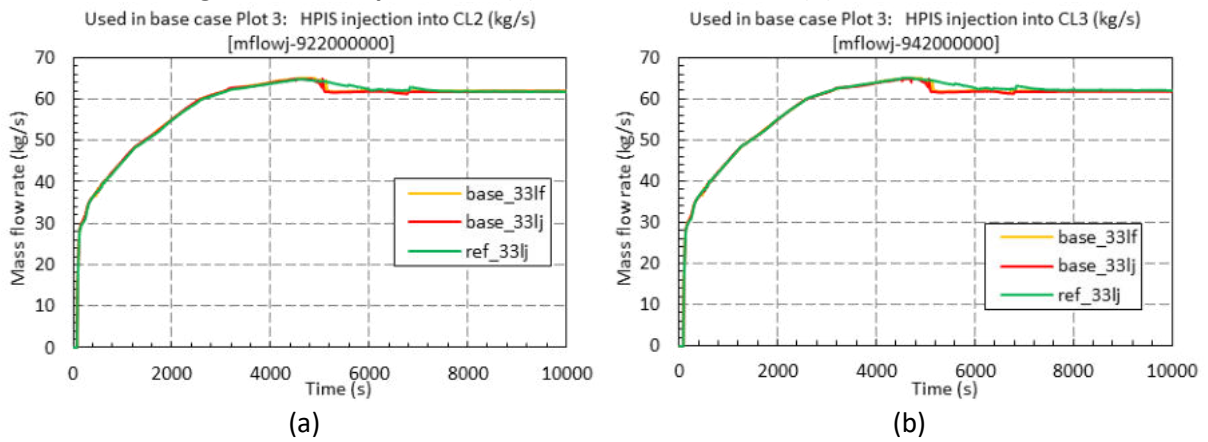
Figure 362: Comparison of HPIS Injection – (a) CL2 and (b) CL3.
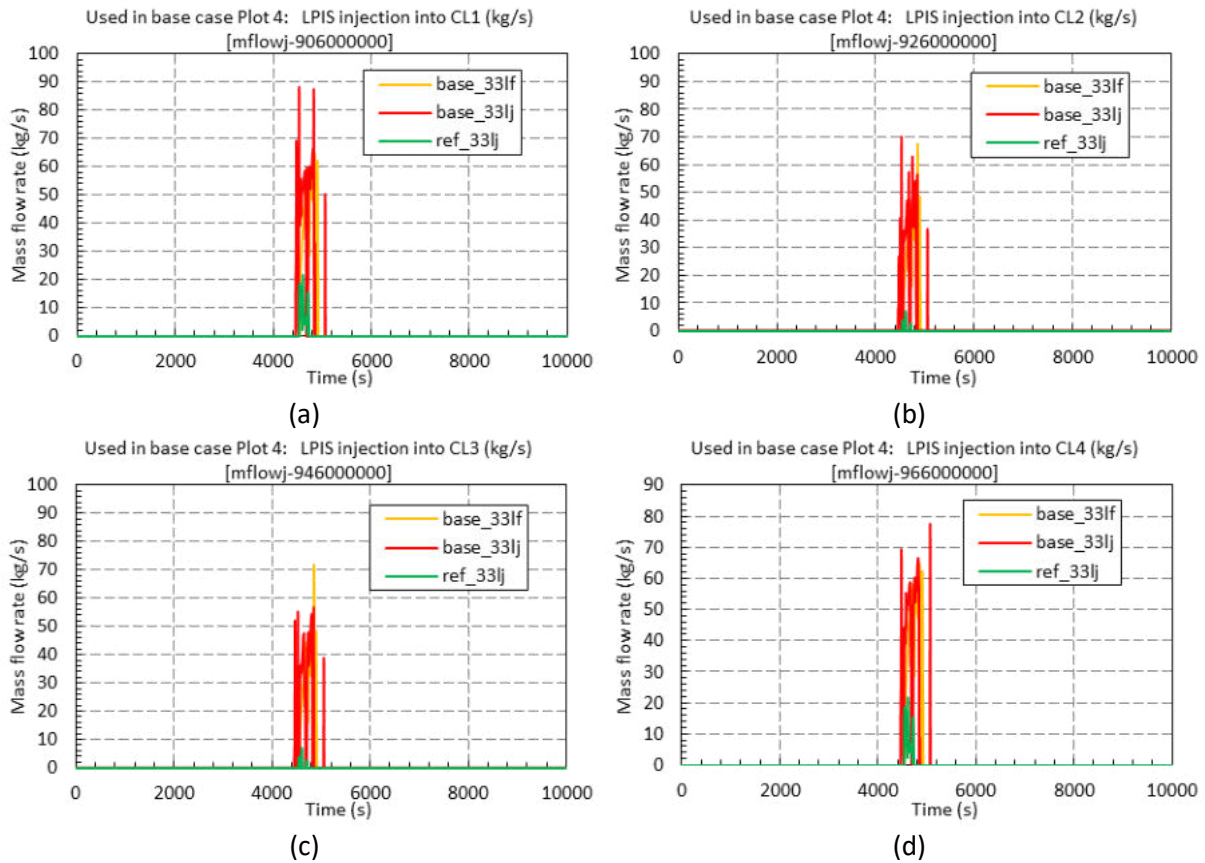
Figure 363: Comparison of LPIS Injection – (a) CL1, (b) CL2, (c) CL3 and (d) CL4.
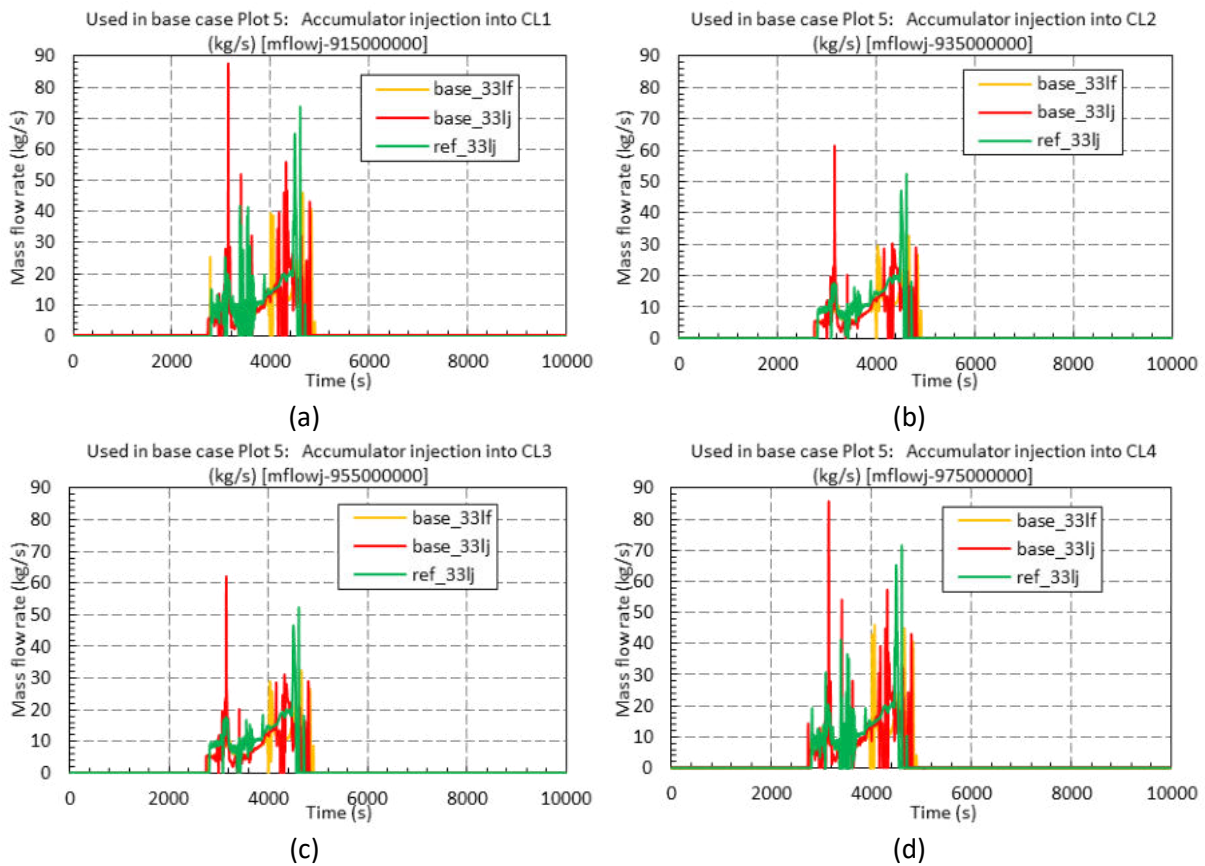
Figure 364: Comparison of ACC Injection – (a) CL1, (b) CL2, (c) CL3 and (d) CL4.

271
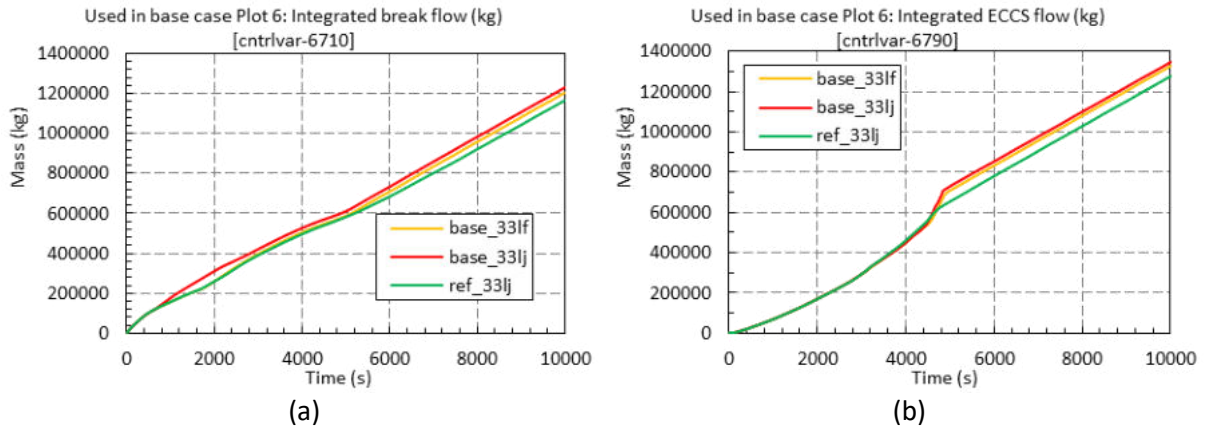
Figure 365: Comparison of (a) Integrated Break Flow and (b) Integrated ECCS Flow.
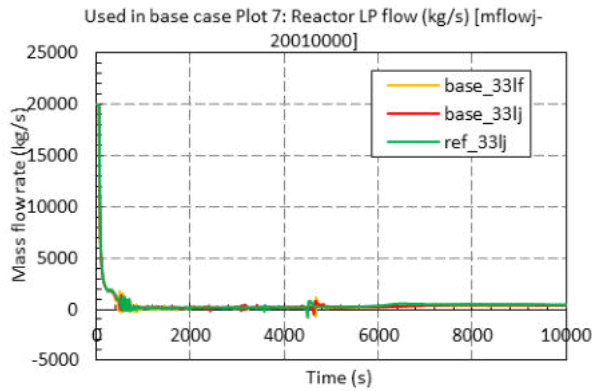
Figure 366: Comparison of Reactor LP Flow.
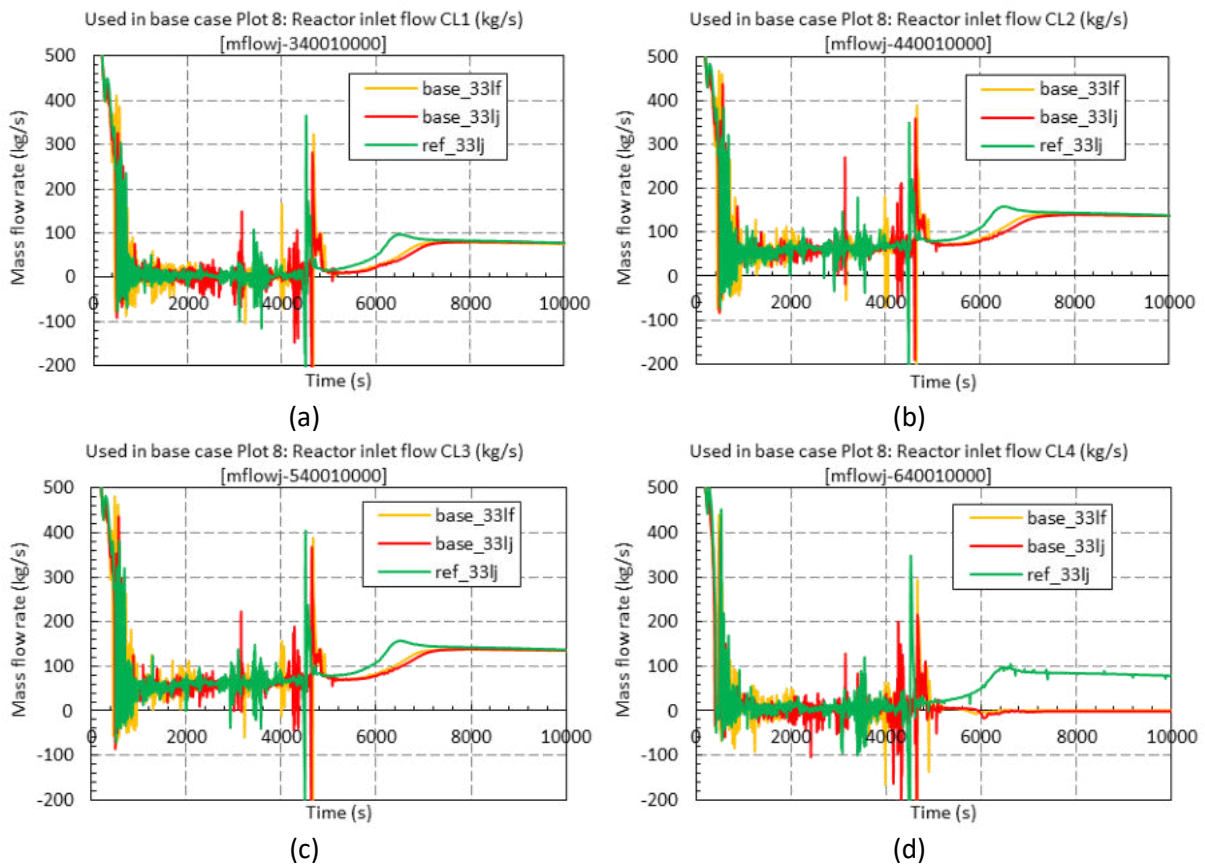
Figure 367: Comparison of Reactor Inlet Flows (detail) – (a) CL1, (b) CL2, (c) CL3, (d) CL4.
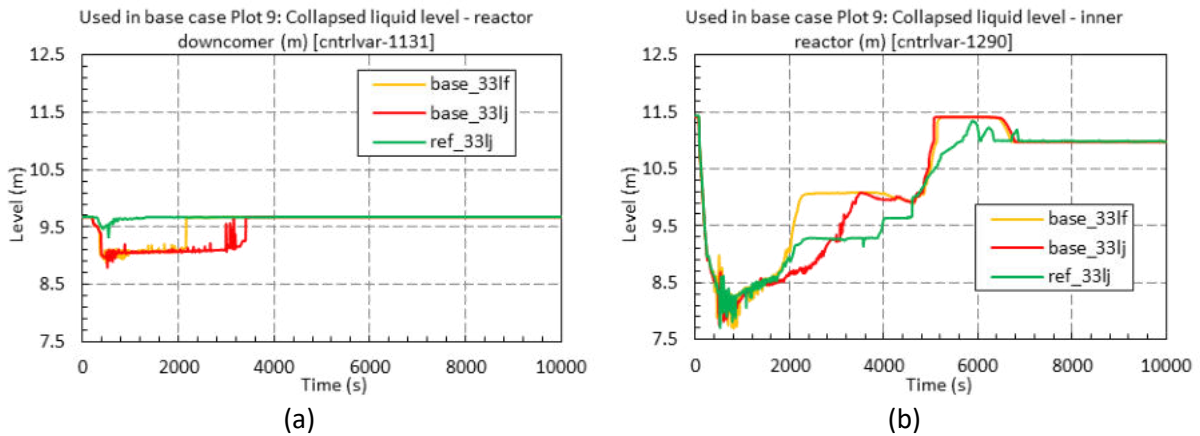
Figure 368: Comparison of Collapsed Liquid Levels in – (a) Reactor DC, (b) Inner reactor.
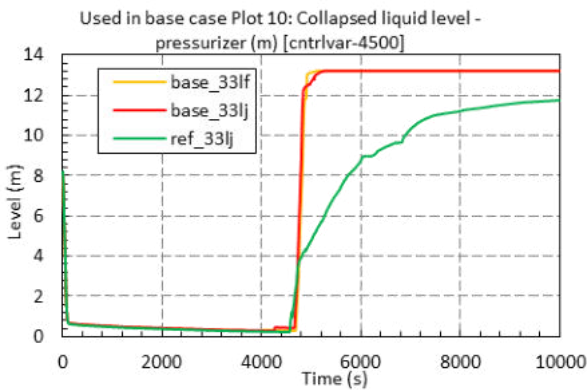
Figure 369: Comparison of Collapsed Liquid Level in Pressurizer.
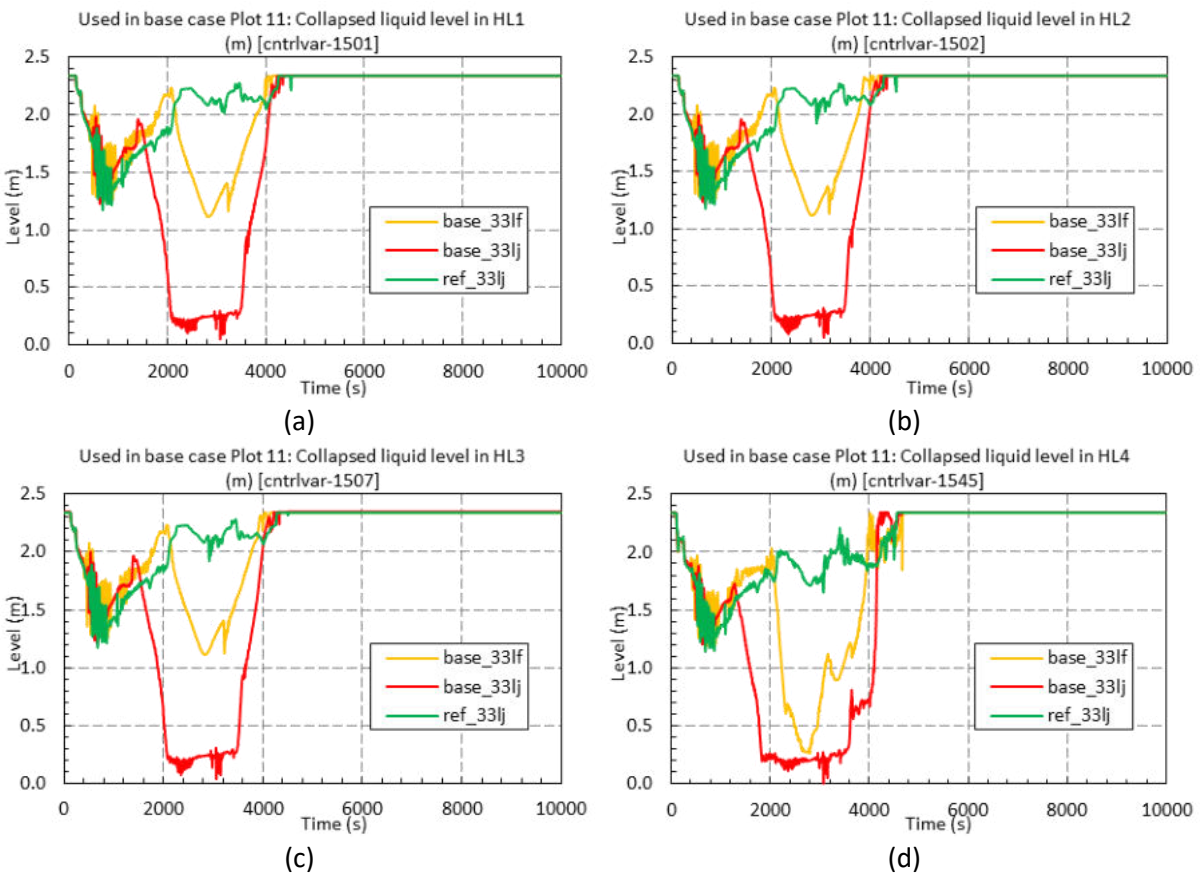
Figure 370: Comparison of Collapsed Liquid Levels in HLs by SG – (a) HL1, (b) HL2, (c) HL3, (d) HL4.

273

(a)   (b)

(c)   (d)
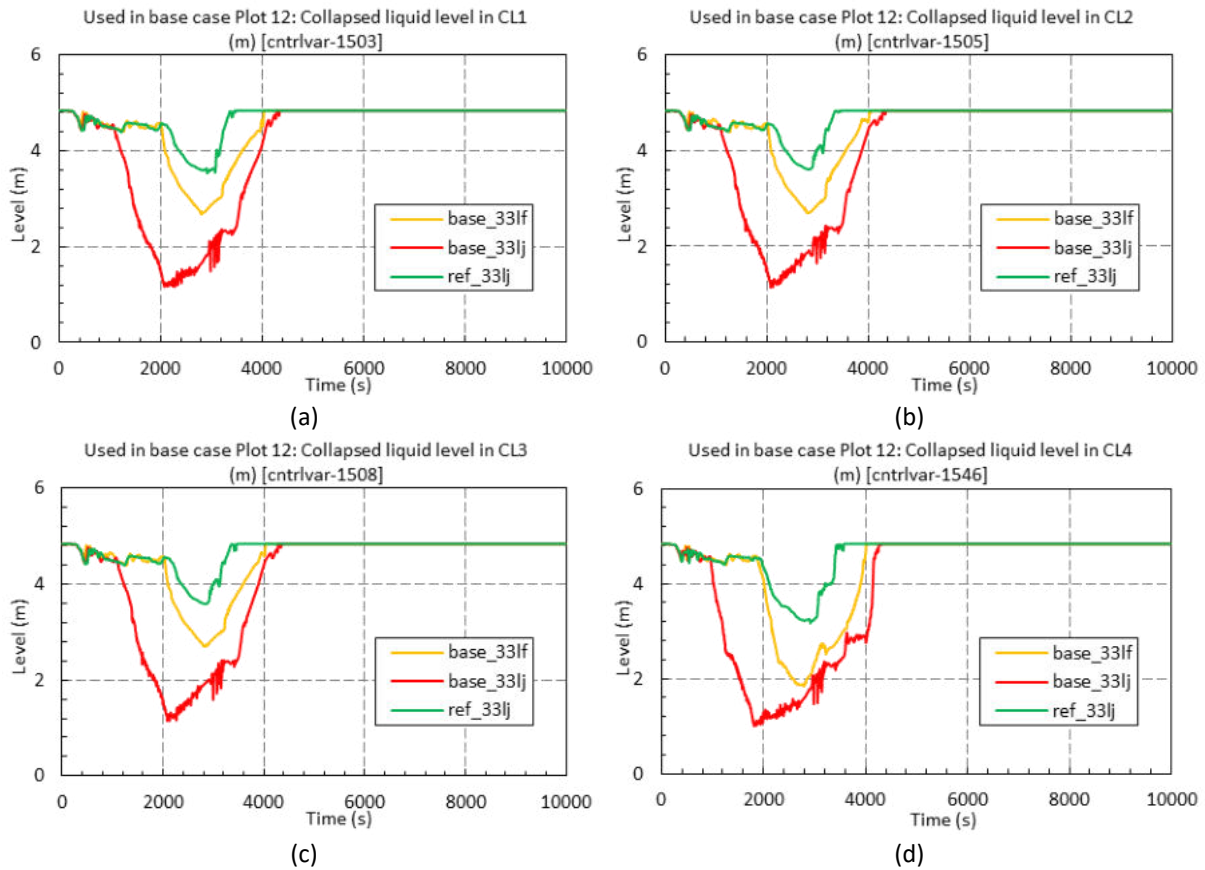
Figure 371: Comparison of Collapsed Liquid Levels in CLs by SG – (a) CL1, (b) CL2, (c) CL3, (d) CL4.

(a)   (b)

(c)   (d)
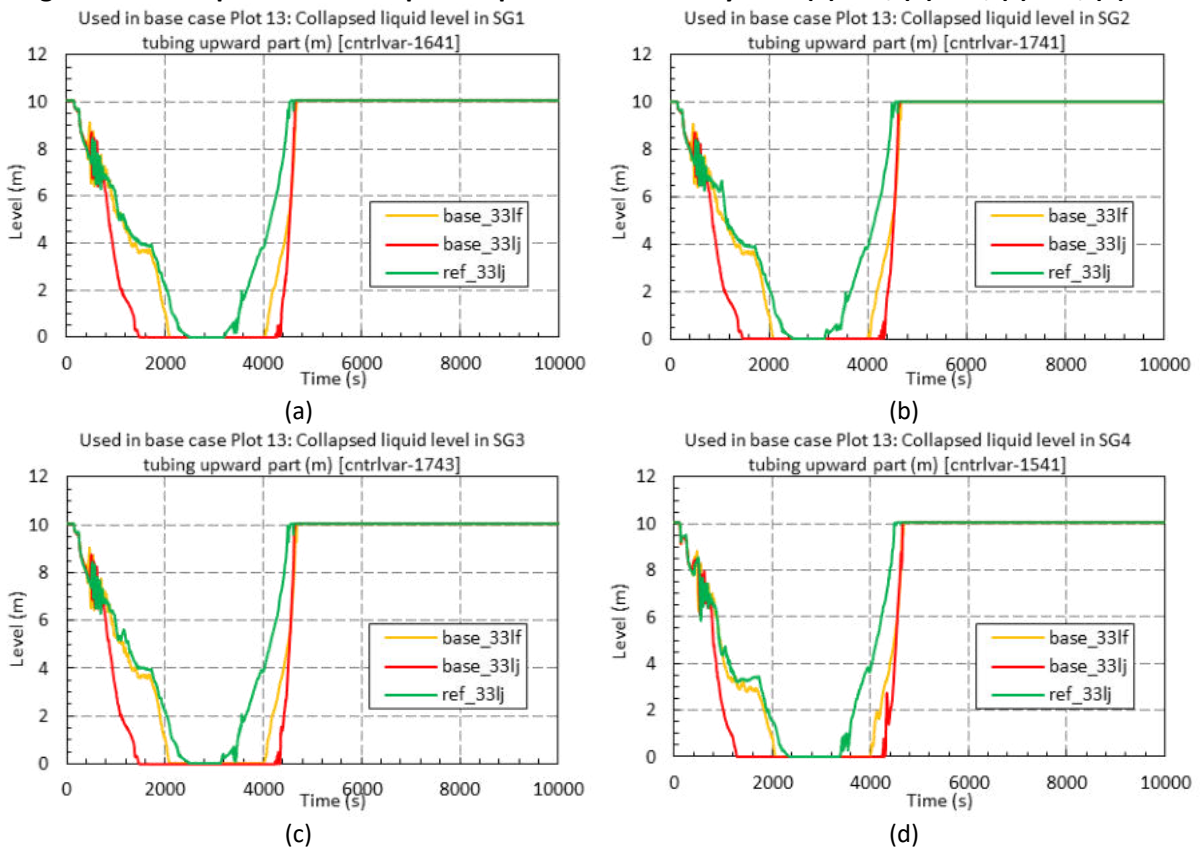
Figure 372: Comparison of Collapsed Liquid Levels in SG tubing Upward Part – (a) SG1, (b) SG2, (c) SG3 and (d) SG4.
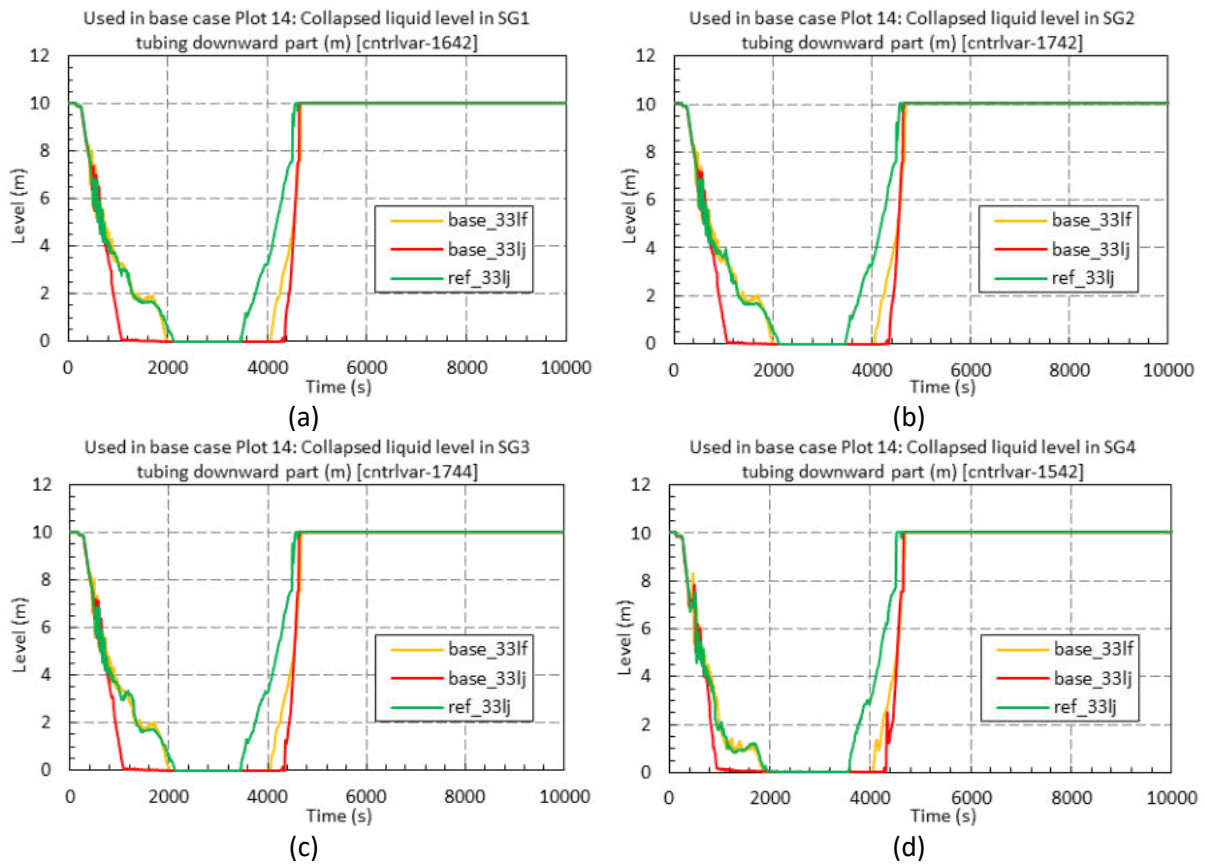
Figure 373: Comparison of Collapsed Liquid Levels in SG tubing Downward Part– (a) SG1, (b) SG2, (c) SG3 and (d) SG4.
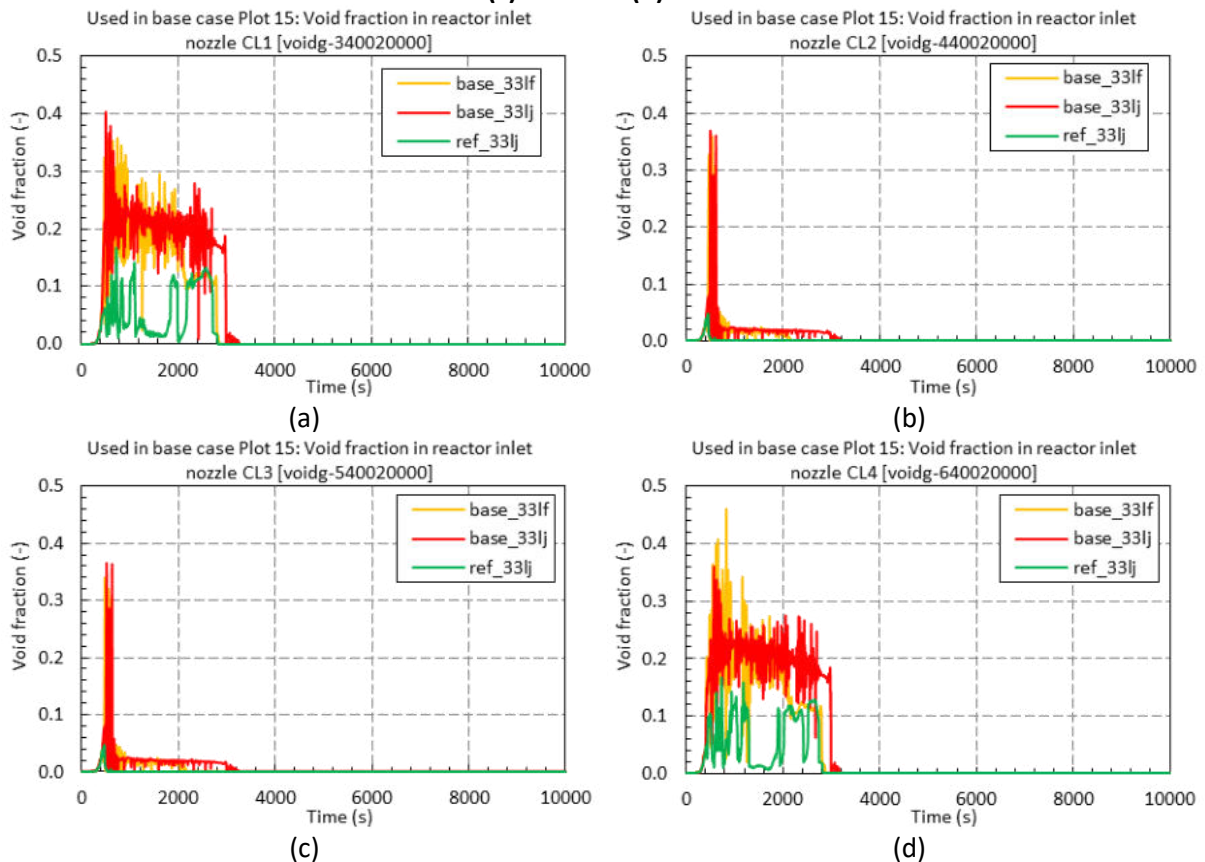
Figure 374: Comparison of Void Fraction in Reactor Inlet Nozzles – (a) CL1, (b) CL2, (c) CL3, (d) CL4.

275
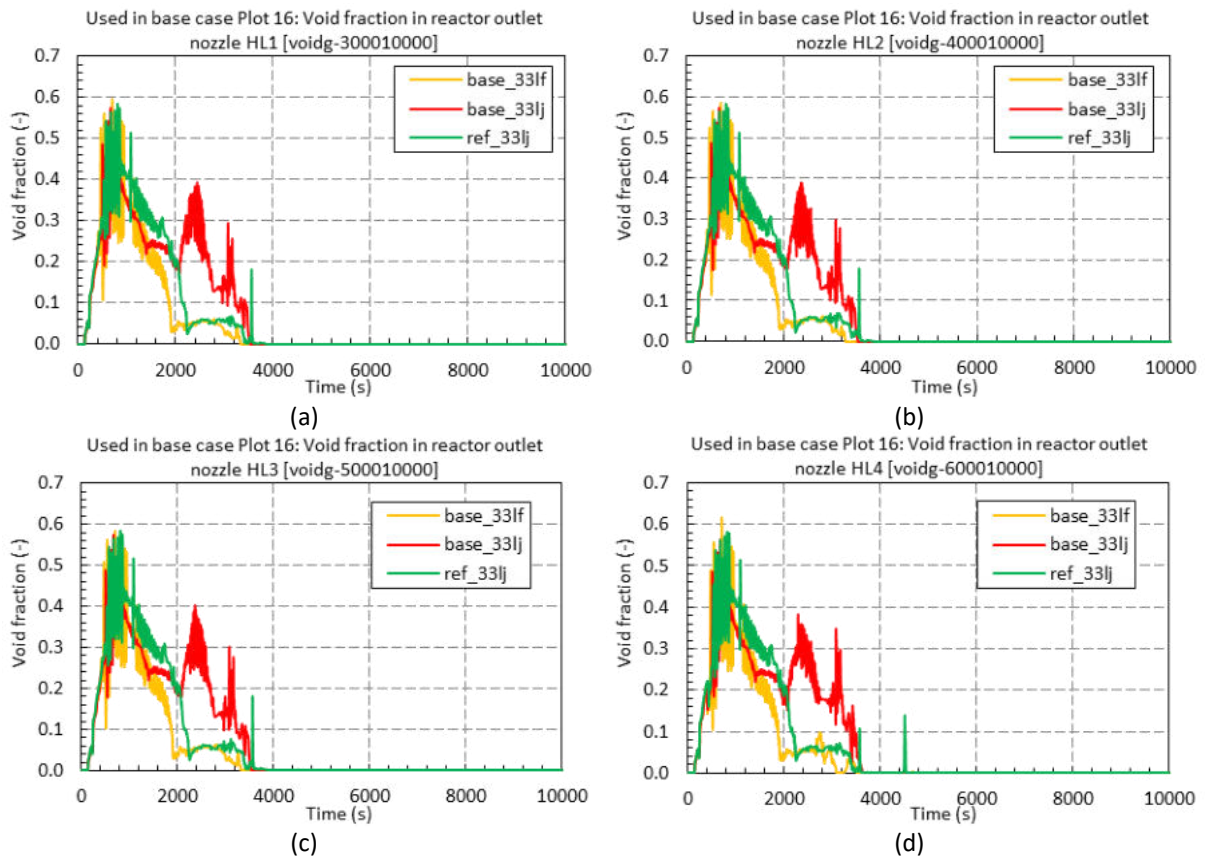
Figure 375: Comparison of Void Fraction in Reactor Outlet Nozzles – (a) HL1, (b) HL2, (c) HL3, (d) HL4.
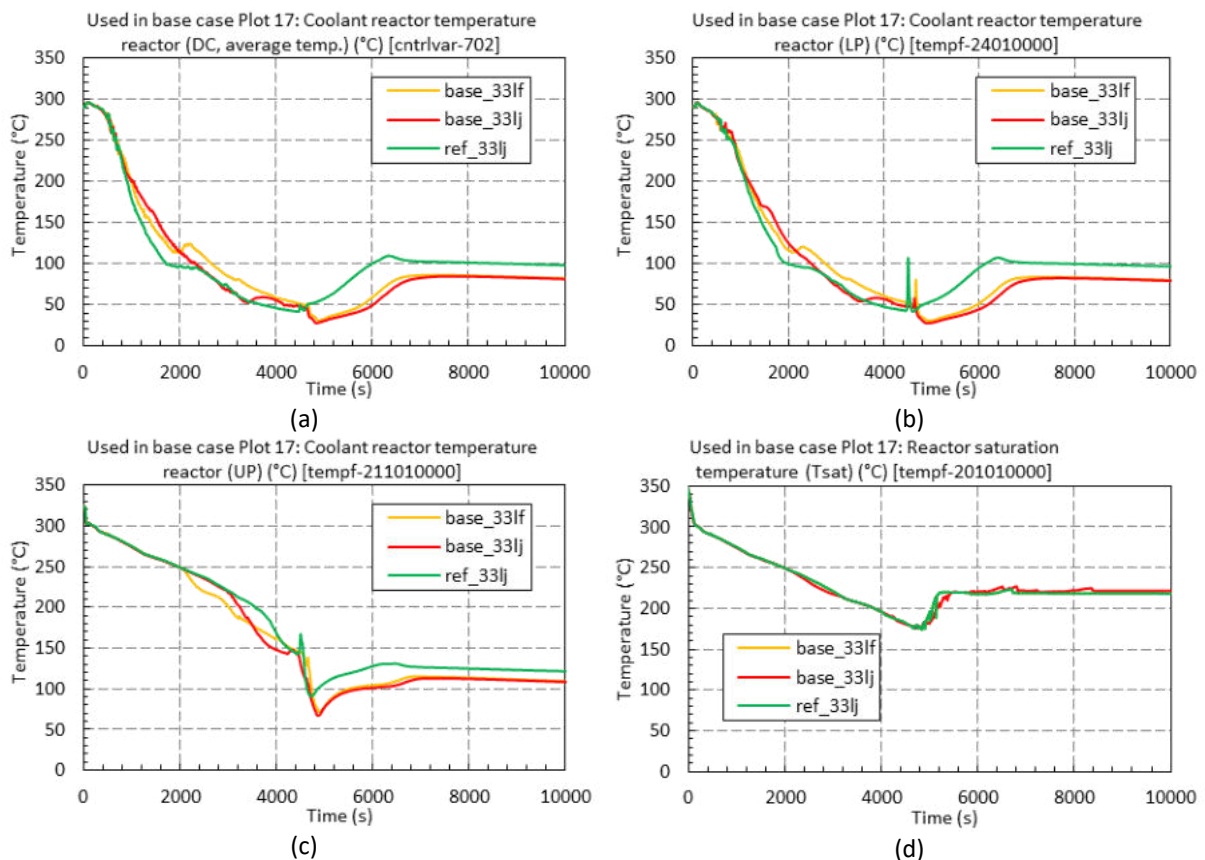
Figure 376: Comparison of Coolant Temperatures in Reactor – (a) DC, (b) LP, (c) UP and (d) Tsat.

276
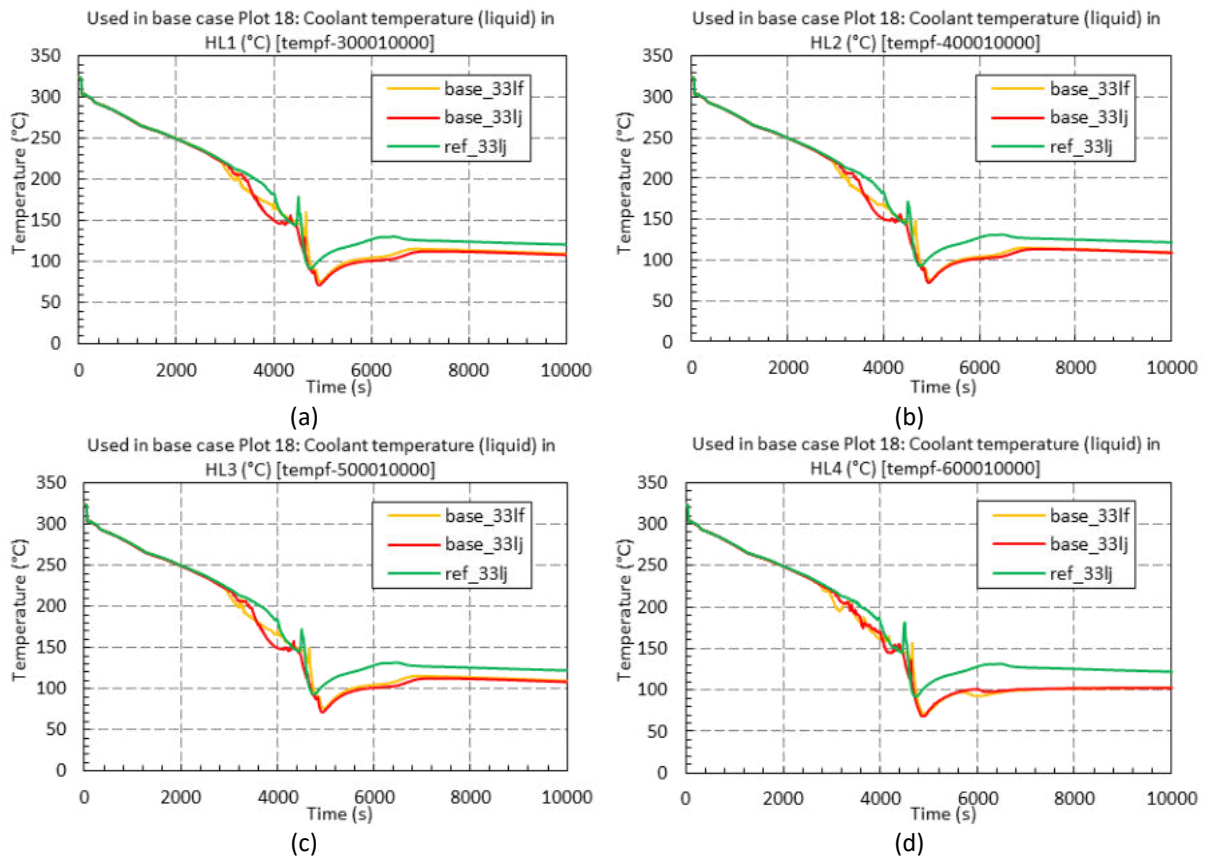
Figure 377: Comparison of Coolant Temperatures in HLs – (a) HL1, (b) HL2, (c) HL3 and (d) HL4.
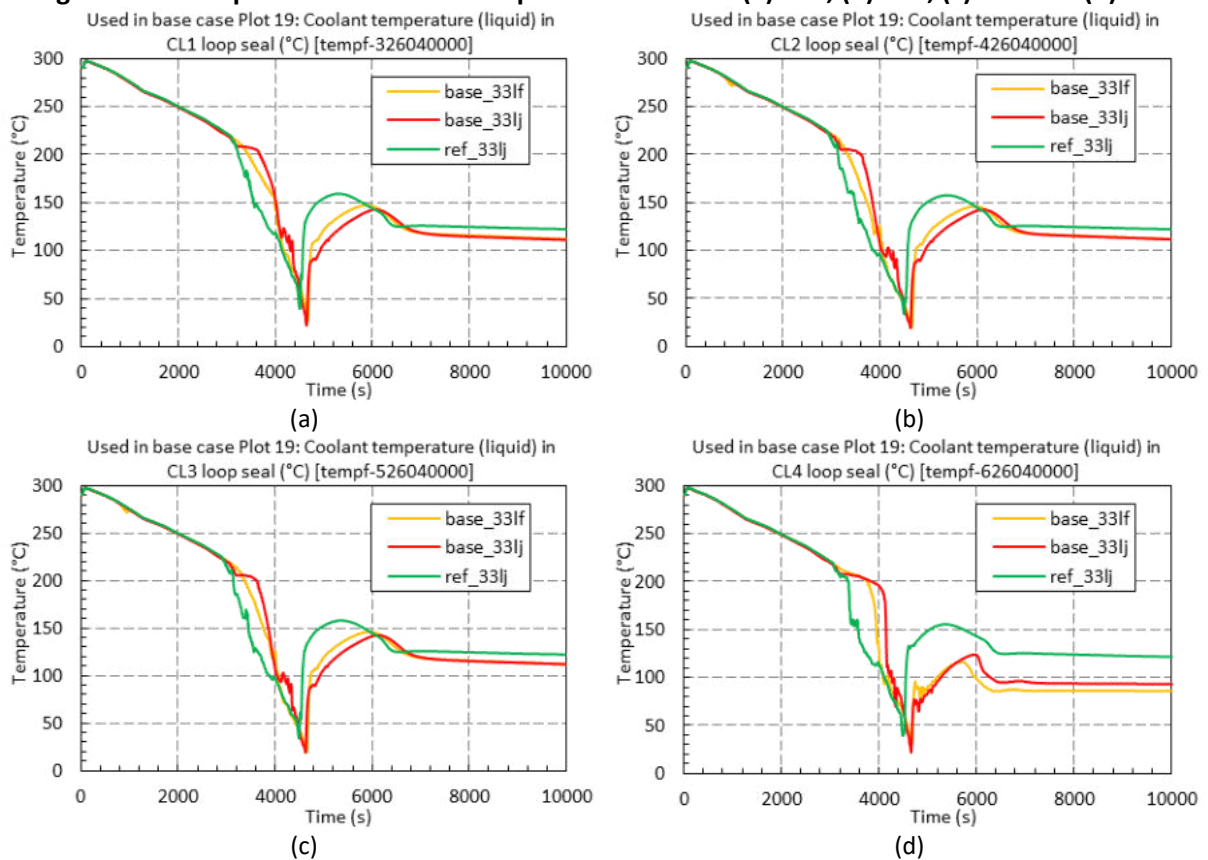
Figure 378: Comparison of Coolant Temperatures in CLs Loop Seal - – (a) CL1, (b) CL2, (c) CL3, (d) CL4.
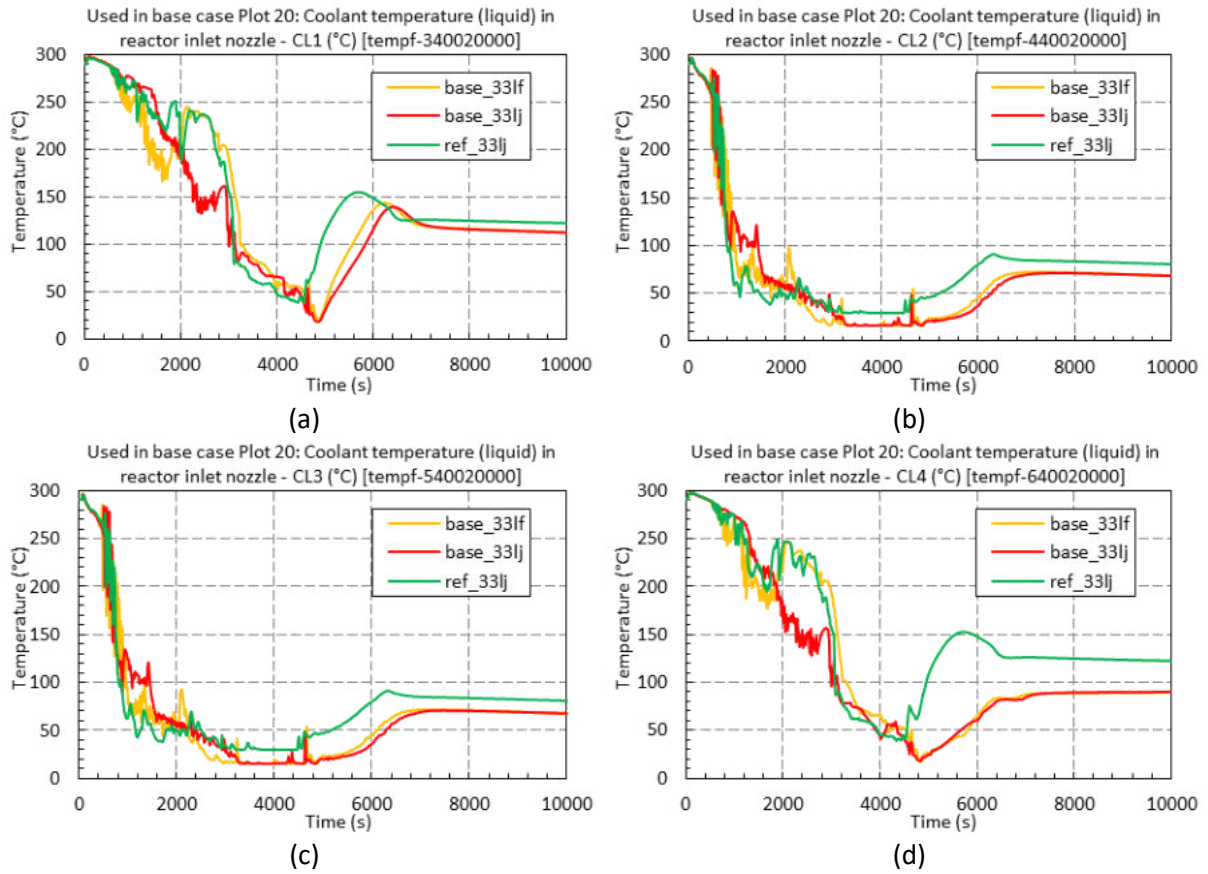
Figure 379: Comparison of Coolant Temperatures in Reactor Inlet Nozzles - – (a) CL1, (b) CL2, (c) CL3 and (d) CL4.

(a)

(b)

(c)

(d)

(e)

(f)

(g)

(h)
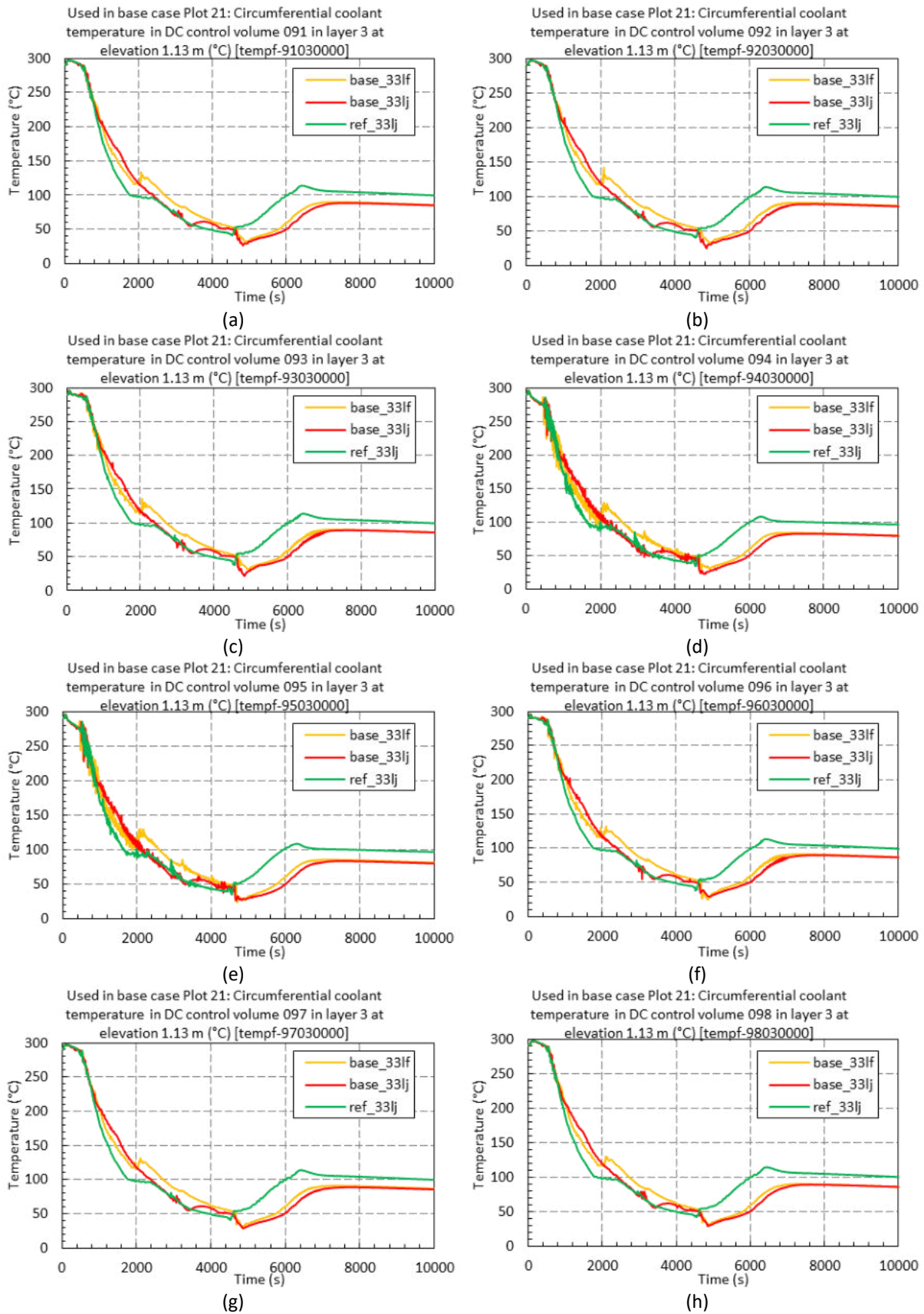
Figure 380: Comparison of Circumferential Coolant Temperatures in DC Control Volumes in Layer 3 at Elevation 1.13 m.

(a)

(b)

(c)

(d)

(e)

(f)

(g)

(h)
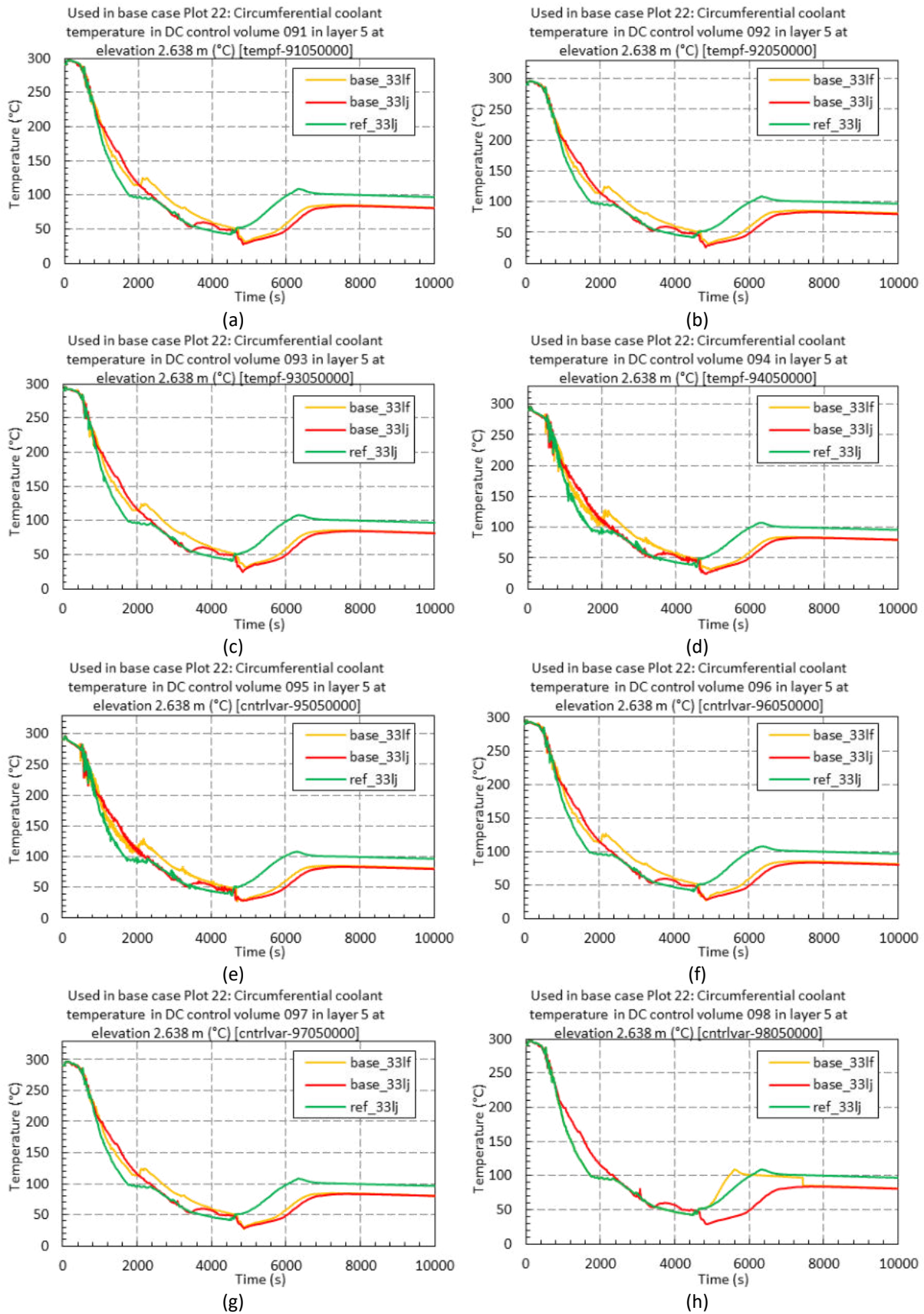
Figure 381: Comparison of Circumferential Coolant Temperatures in DC Control Volumes in Layer 5 at Elevation 2.638 m.

(a)

(b)

(c)

(d)

(e)

(f)

(g)

(h)
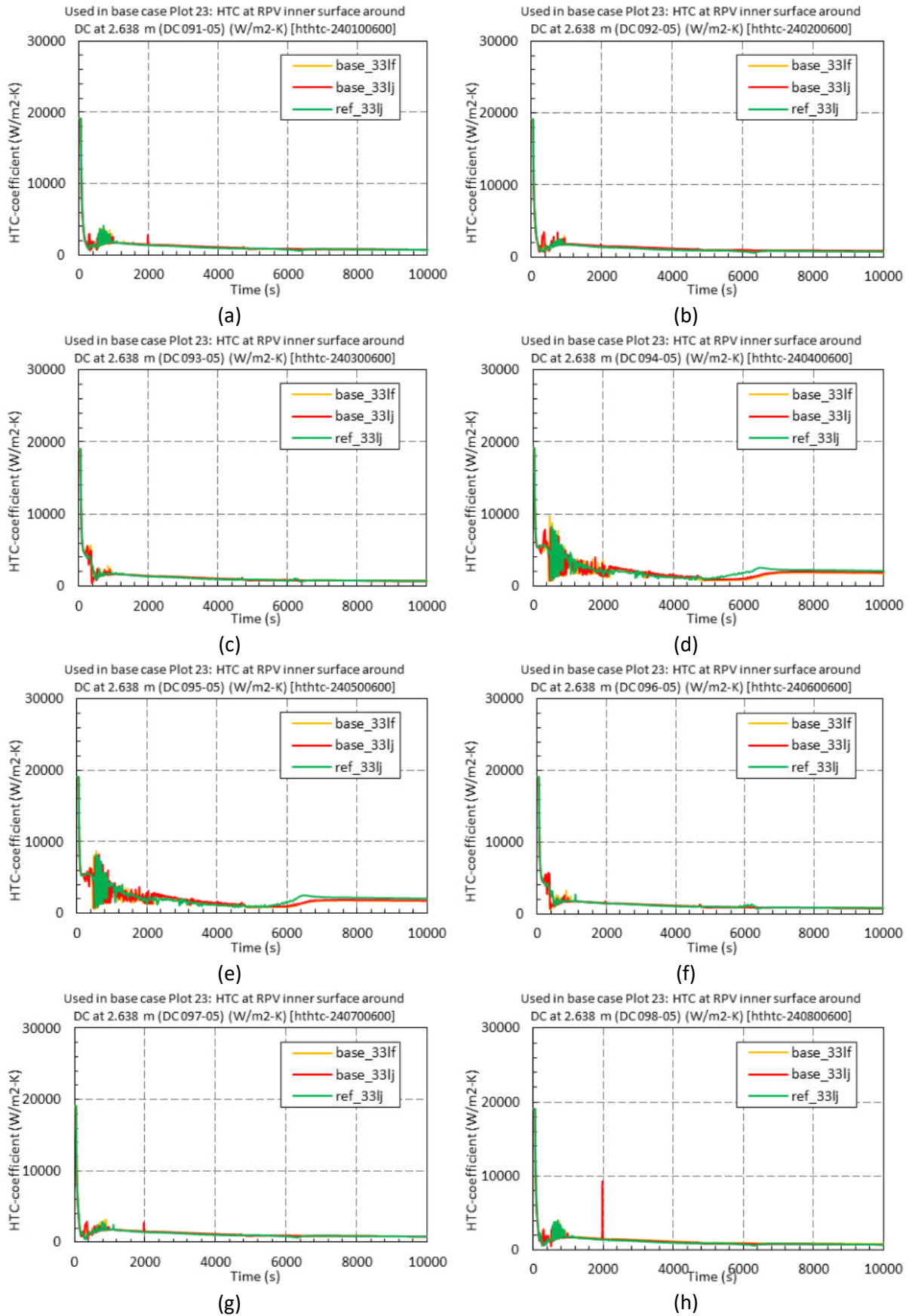
Figure 382: Comparison of HTC at RPV Inner Surface around DC at 2.638 m.
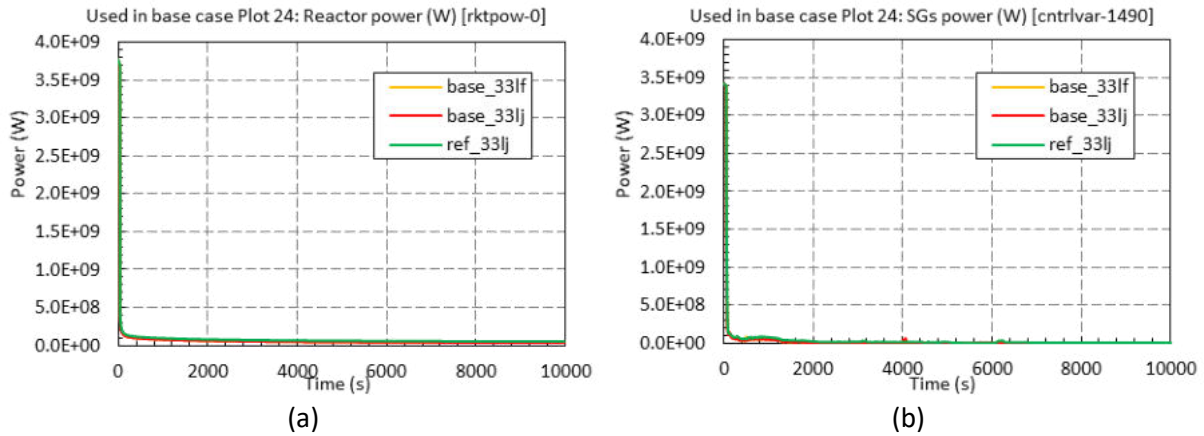
Figure 383: Comparison of (a) Reactor power and (b) SGs Power.

14.2 Input uncertainties

Table 47 shows input uncertainty parameters as used is Software for Uncertainty and Sensitivity Analysis (SUSA). SUSA Version 4.2.5, developed by GRS, has been used for uncertainty and sensitivity analysis. In the uncertainty analysis 19 input uncertain parameters have been varied in 59 calculations. For each parameter nominal value is given (i.e. the values used in the reference calculation). Further, the type of distribution and distribution parameters are given. Finally, minimum and maximum values of input uncertain parameters are given (these values were used in the sensitivity study – see Section 14.3).

Table 47: Input uncertainty parameters for SUSA

Par. No.	Parameter Name	Nominal Value	Distribution Type	Distribution Parameters	Minimum	Maximum
1	Core power (W)	3.77E+09	Normal	μ: 3.77E+09 σ: 3.77E+07	3.65E+09	3.88E+09
2	Secondary side pressure (Pa)	6.16E+06	Uniform	a: 6.02E+06 b: 6.82E+06	6.02E+06	6.82E+06
3	Pressurizer pressure (Pa)	1.57E+07	Normal	μ: 1.57E+07 σ: 157400	1.53E+07	1.62E+07
4	Decay heat multiplier	1	Uniform	a: 0.9 b: 1.1	0.9	1.1
5	Timing of SIS actuation (s)	10	Uniform	a: 0 b: 20	0	20
6	ACC injection temperature (°C)	303.15	Uniform	a: 293.15 b: 313.15	293.15	313.15
7	ACC initial pressure (Pa)	2600000	Uniform	a: 2400000 b: 2800000	2.40E+06	2.80E+06
8	ACC initial nitrogen volume – values of static quality in volume 2	0.486248	Uniform	a: 0.365128 b: 0.62505	0.365128	0.62505
9	HPSI temperature (°C)	303.15	Uniform	a: 288.15 b: 318.15	288.15	318.15
10	HP pump pressure curve multiplier	1	Normal	μ: 1 σ: 0.1	0.7	1.3
11	HP pump flow curve multiplier	1	Normal	μ: 1 σ: 0.1	0.7	1.3
12	Initial pressurizer level (m)	8.21	Uniform	a: 7.71 b: 8.71	7.71	8.71

13	Thermal-nonequilibrium coefficient for Henry-Fauske model	0.14	Weibull	p1: 7 p2: 1	0	1.5
14	Single-phase liquid to wall HTC multiplier	1	Log. Uniform	a: 0.8 b: 1.2	0.8	1.2
15	Single-phase vapour to wall HTC multiplier	1	Log. Uniform	a: 0.8 b: 1.2	0.8	1.2
16	Wall-drag coefficient multiplier	1	Log. Uniform	a: 0.5 b: 2	0.5	2
17	Form-loss coefficient multiplier	1	Log. Uniform	a: 0.5 b: 2	0.5	2
18	LP pump pressure curve multiplier	1	Normal	μ: 1 σ: 0.1	0.7	1.3
19	LP pump flow curve multiplier	1	Normal	μ: 1 σ: 0.1	0.7	1.3

14.3 Sensitivity study

Before uncertainty analysis has been performed, sensitivity study varying one parameter at a time has been performed following typical U.S. NRC approach [89]. It should be noted that sensitivity study varying one parameter at a time is not sensitivity analysis. In the sensitivity study minimum and maximum values of uncertain input parameters shown in Table 47 were used. In this way the reader can get preliminary information on the impact of selected 19 uncertain input parameters on the FOMs (note that compensating effects of different parameters are not taken into account in the sensitivity study varying one parameter at a time). The results are shown in Figures 384 through 402.

From visual observation of Figures 384 through 402 it can be judged that the largest influence on shown output parameters (being FOMs) has parameter no. 17 (form-loss coefficient, see Table 47). Large influence have also parameters no. 9 (HPSI temperature) and no. 11 (HPSI pump flow), while significant influence have also parameters no. 4 (decay heat) and no. 6 (ACC injection temperature). The influence of other parameters is rather small. This qualitative judgment results are compared by quantitative sensitivity analysis performed by SUSA (see Section 0). It should be noted that judgement based on visual observation has been done from plots showing one parameter at a time variation, therefore possible compensating effects of other parameters are not taken into account.
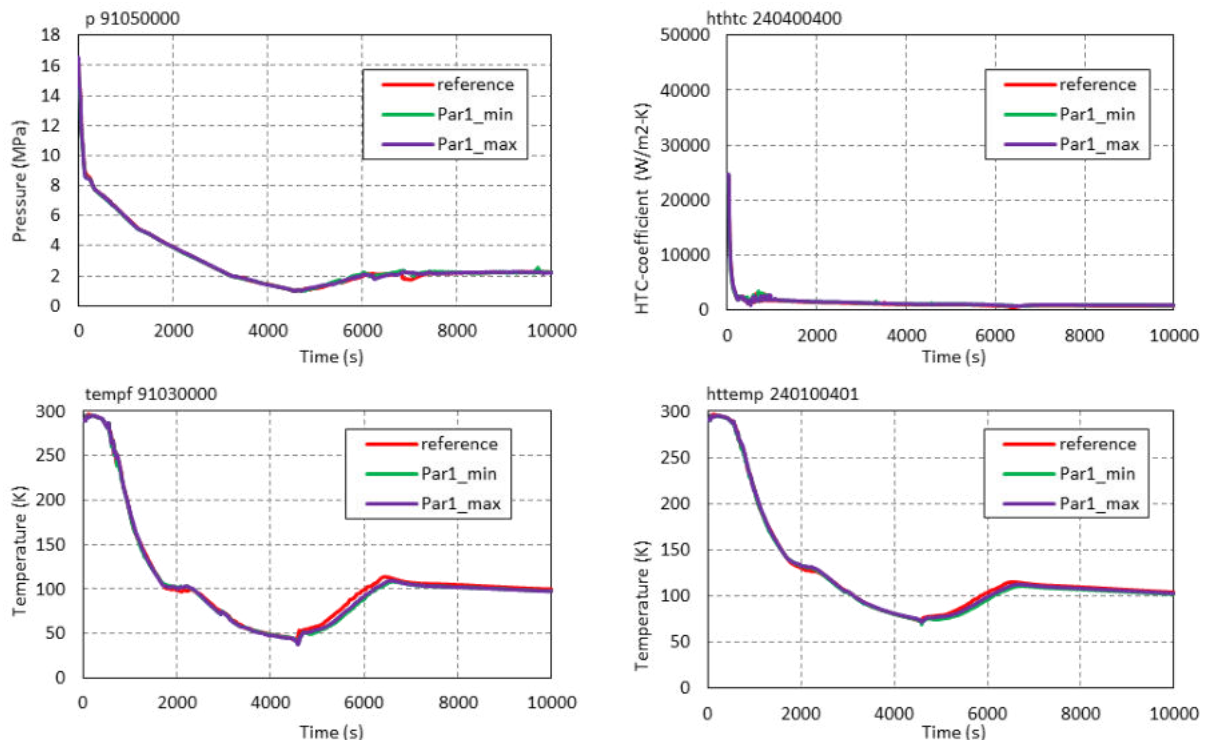
Figure 384: Impact of Parameter no. 1 variation on reference calculation.
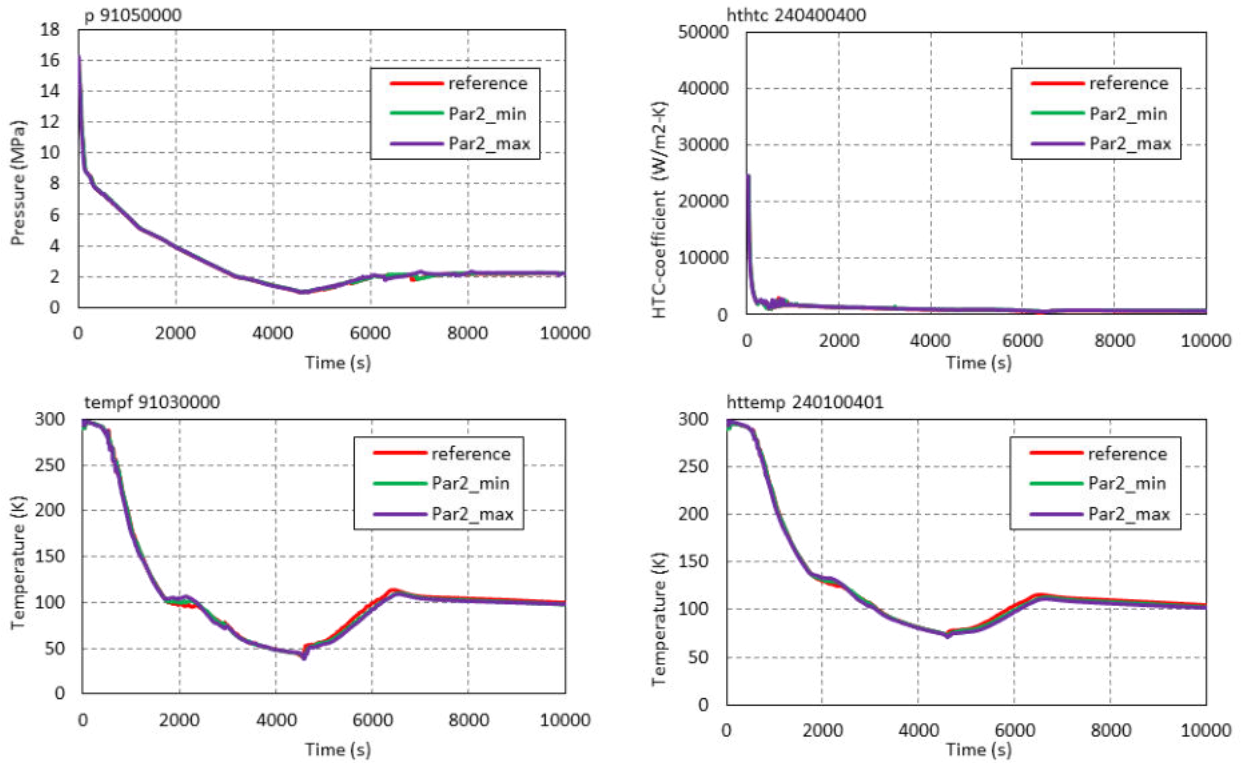
Figure 385: Impact of Parameter no. 2 variation on reference calculation.
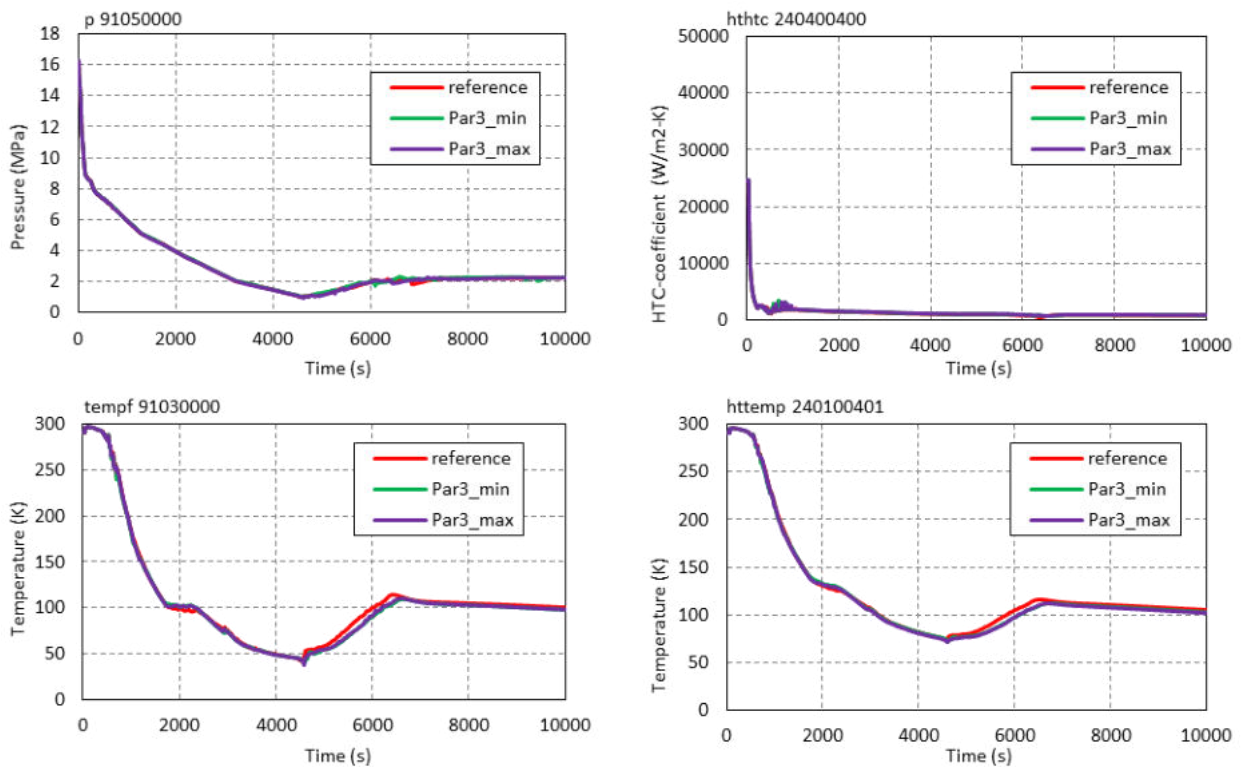
Figure 386: Impact of Parameter no. 3 variation on reference calculation.
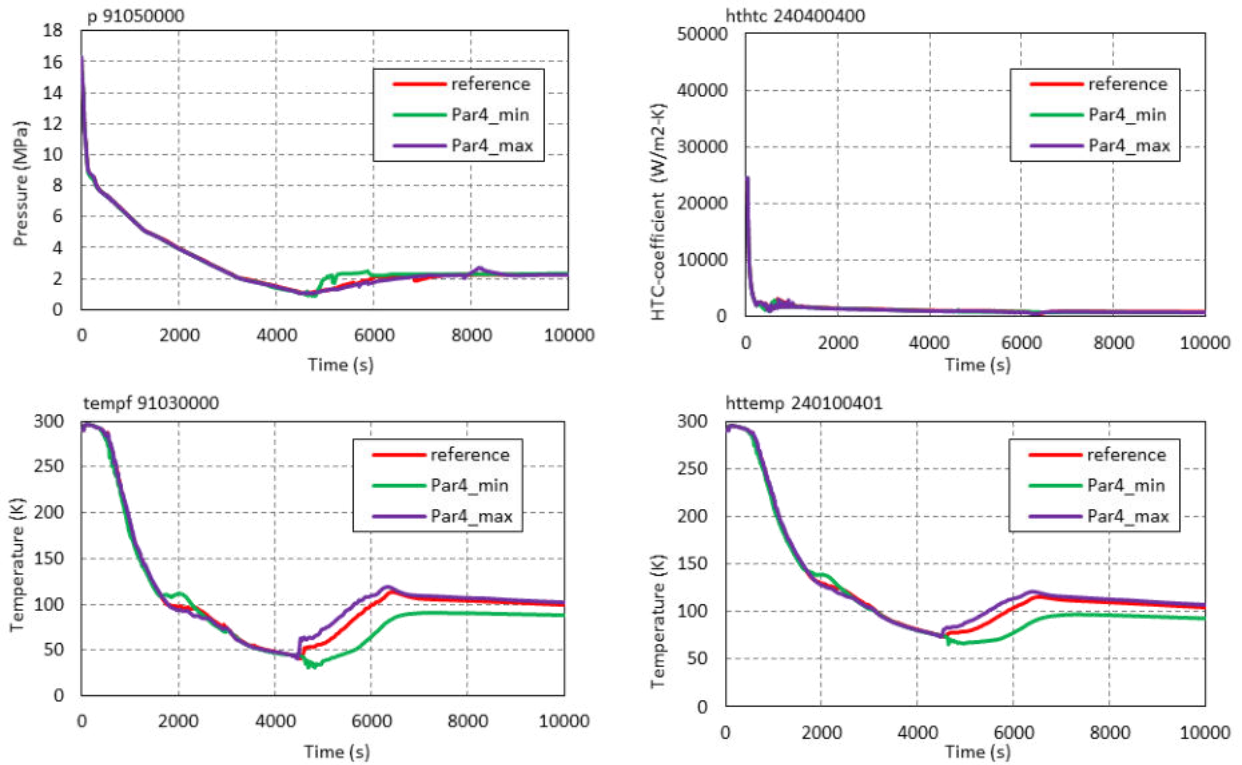
Figure 387: Impact of Parameter no. 4 variation on reference calculation.
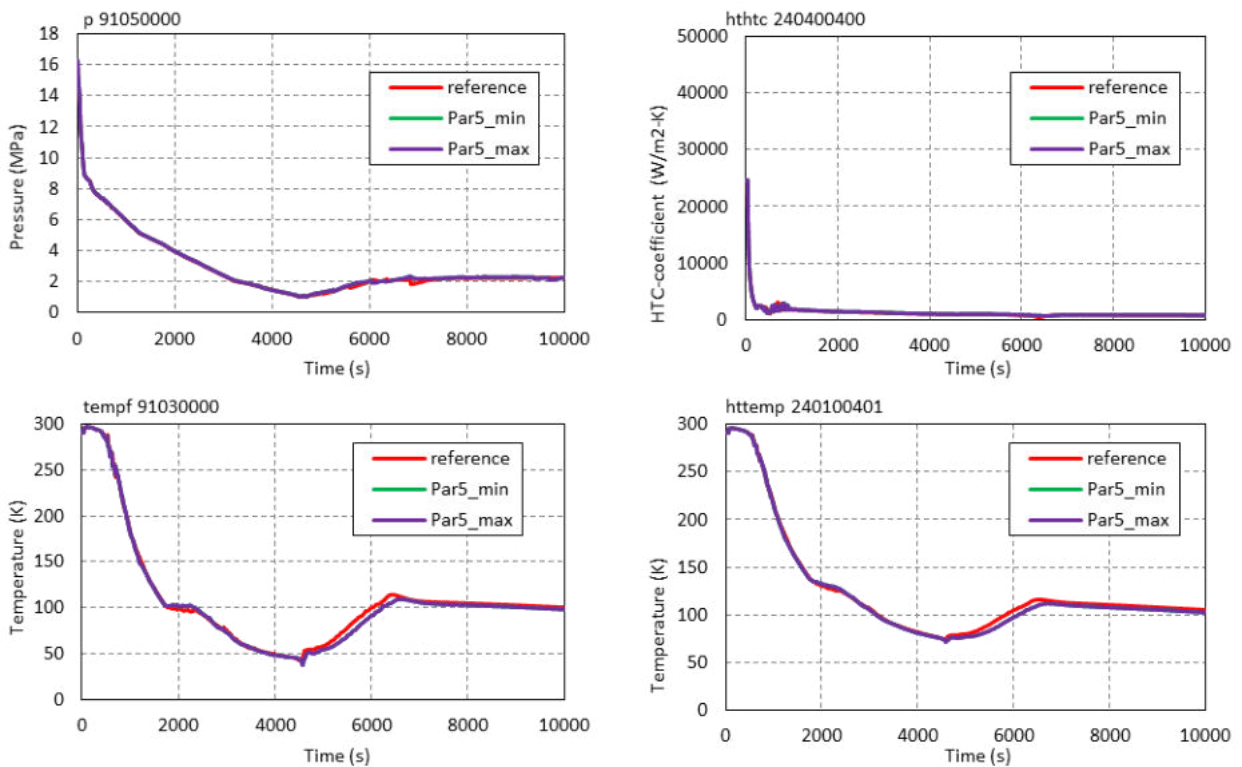
Figure 388: Impact of Parameter no. 5 variation on reference calculation.
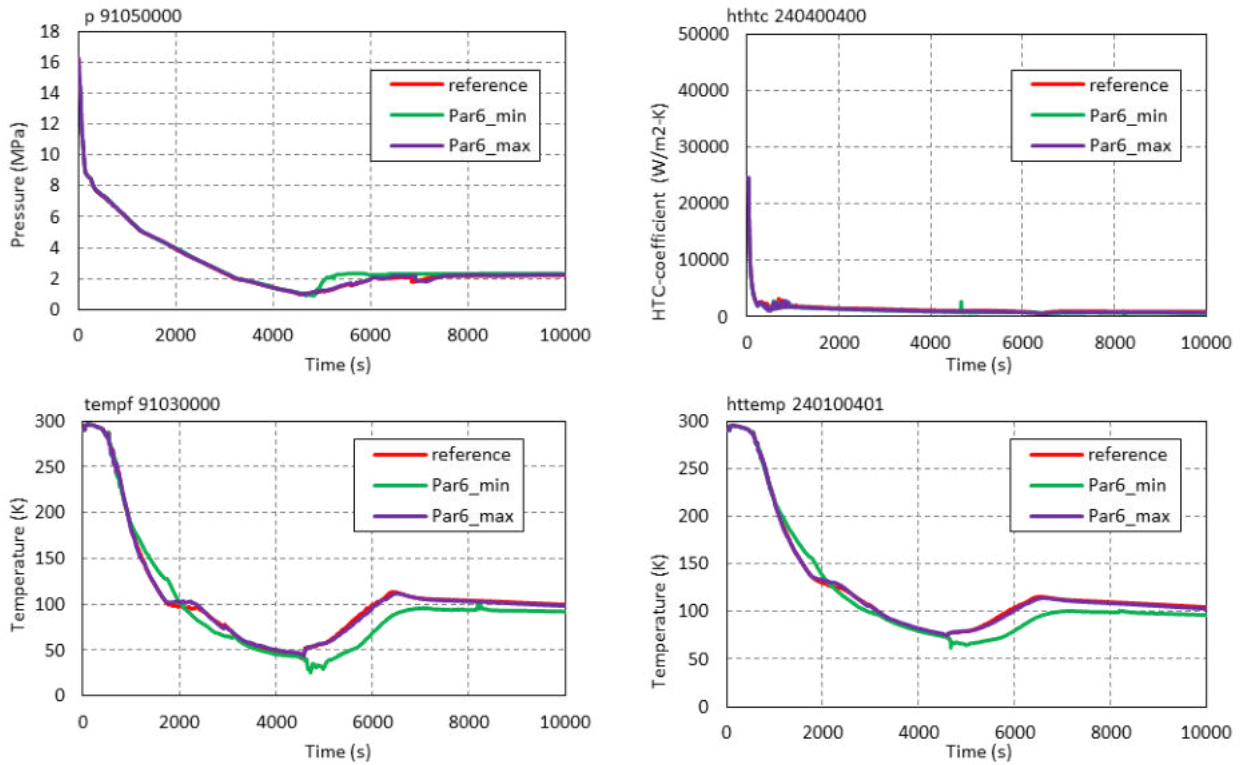
Figure 389: Impact of Parameter no. 6 variation on reference calculation.
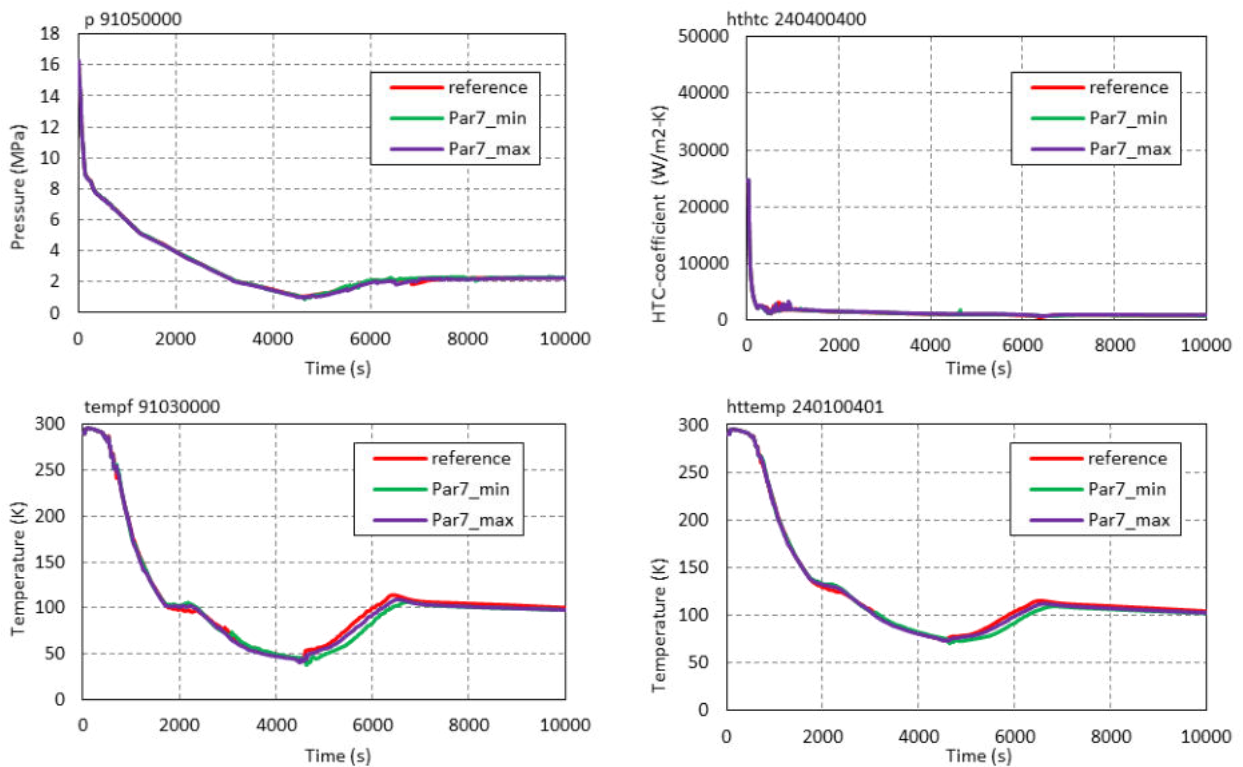
Figure 390: Impact of Parameter no. 7 variation on reference calculation.
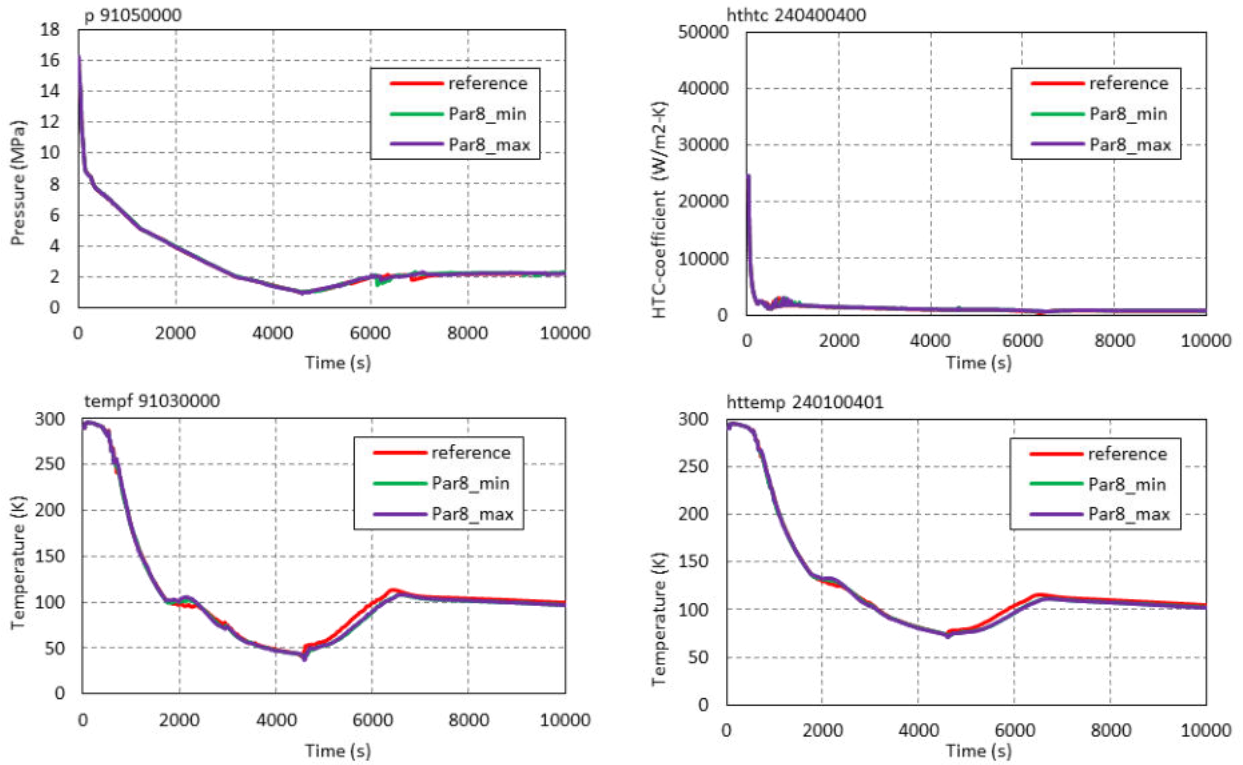
Figure 391: Impact of Parameter no. 8 variation on reference calculation.
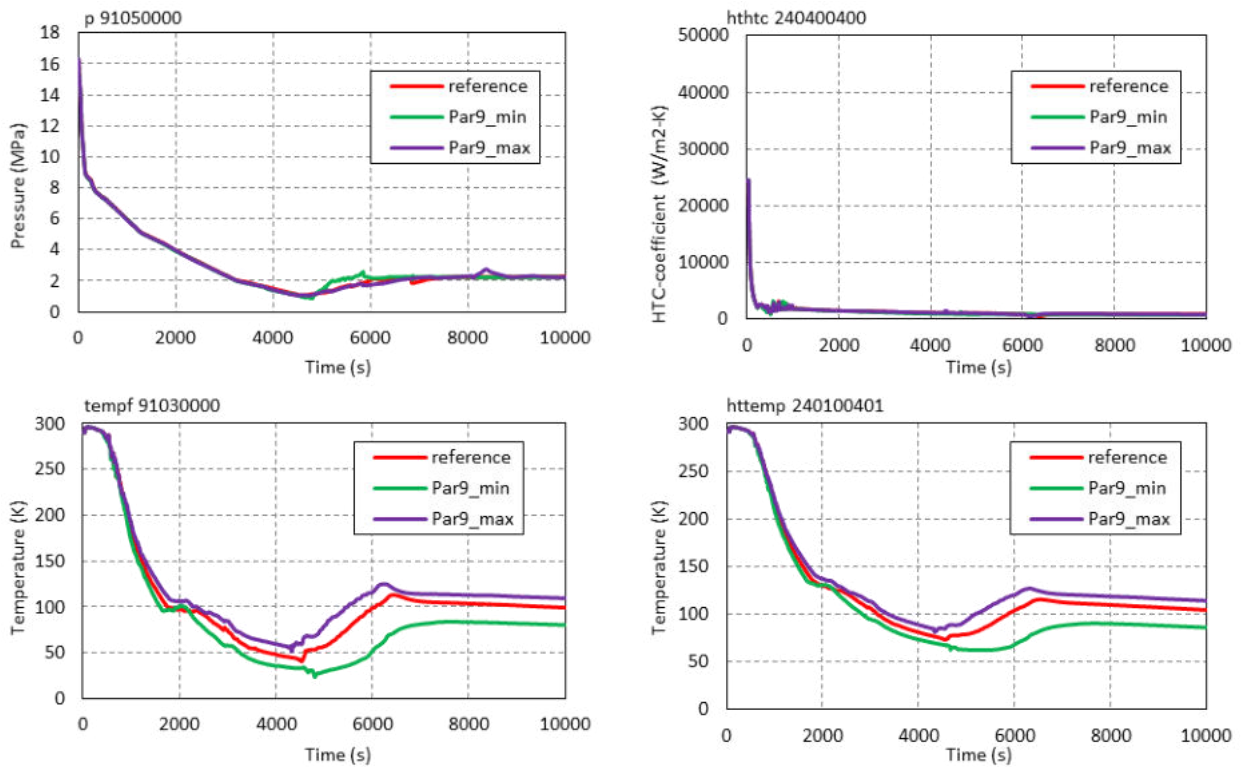
Figure 392: Impact of Parameter no. 9 variation on reference calculation.
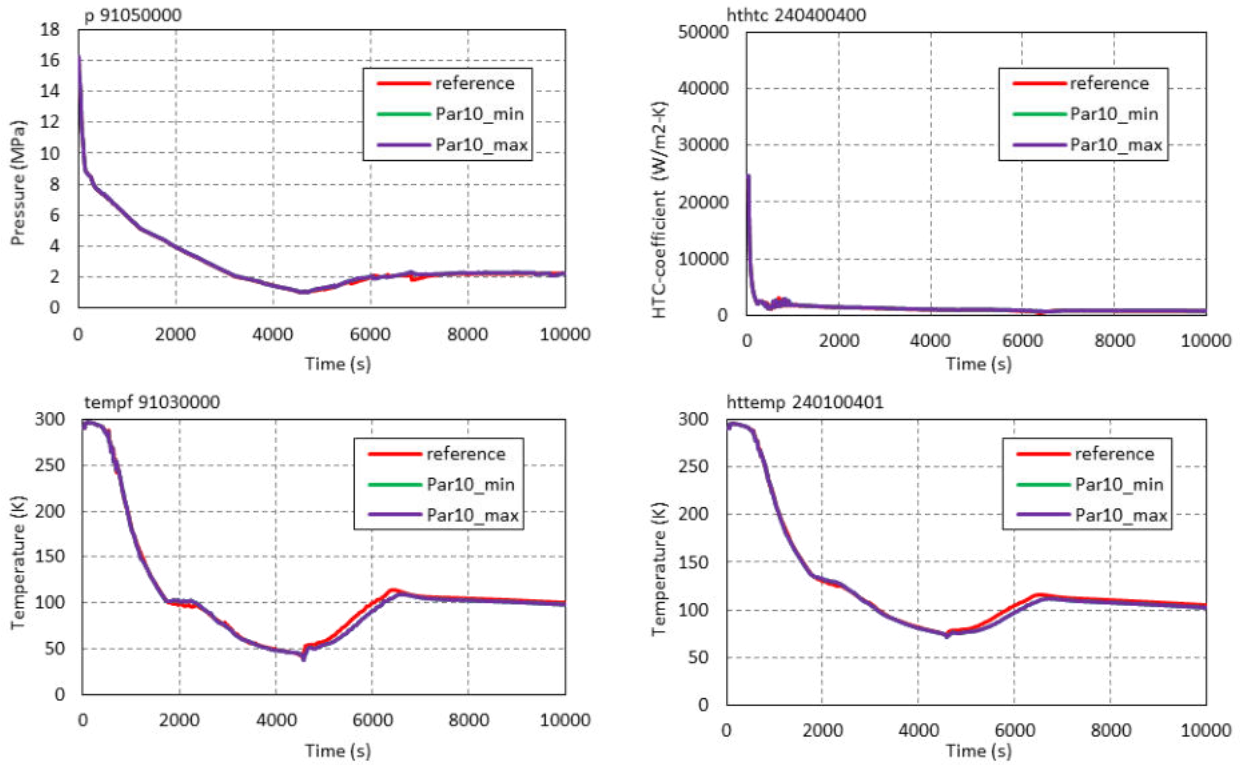
Figure 393: Impact of Parameter no. 10 variation on reference calculation.
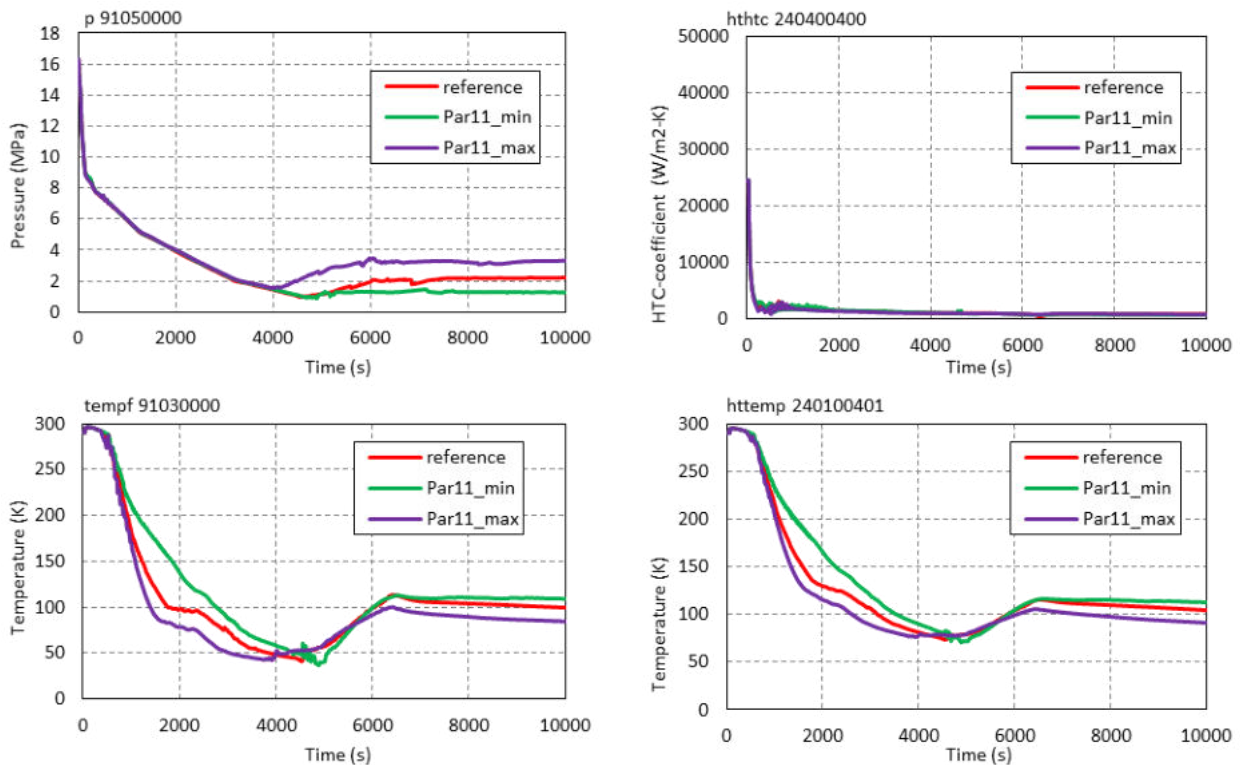
Figure 394: Impact of Parameter no. 11 variation on reference calculation.
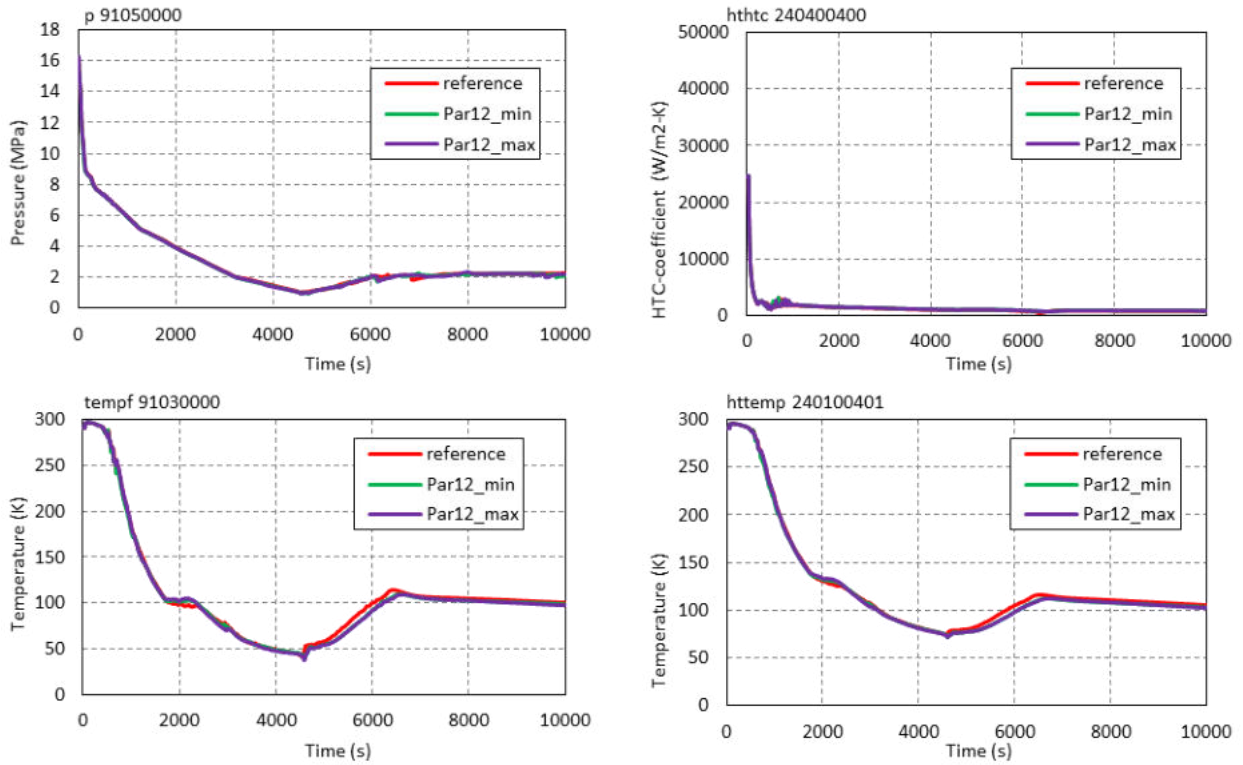
Figure 395: Impact of Parameter no. 12 variation on reference calculation.
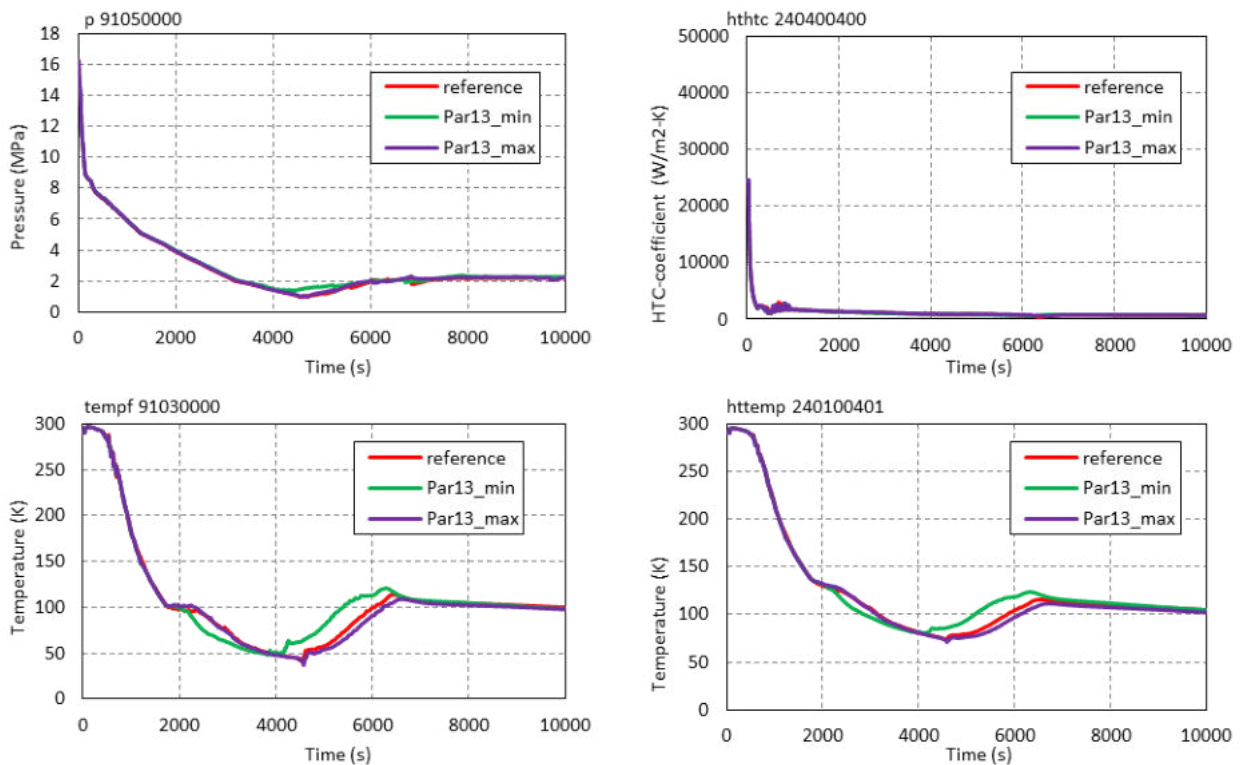
Figure 396: Impact of Parameter no. 13 variation on reference calculation.
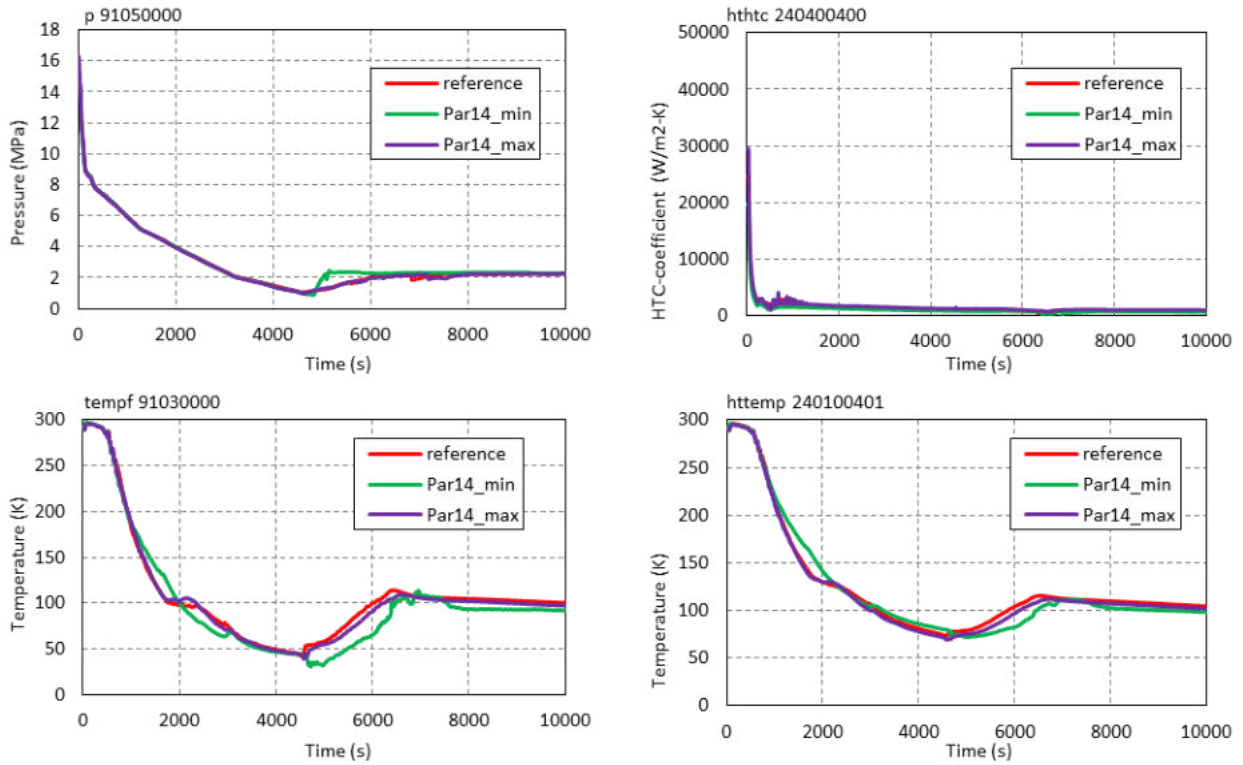
Figure 397: Impact of Parameter no. 14 variation on reference calculation.
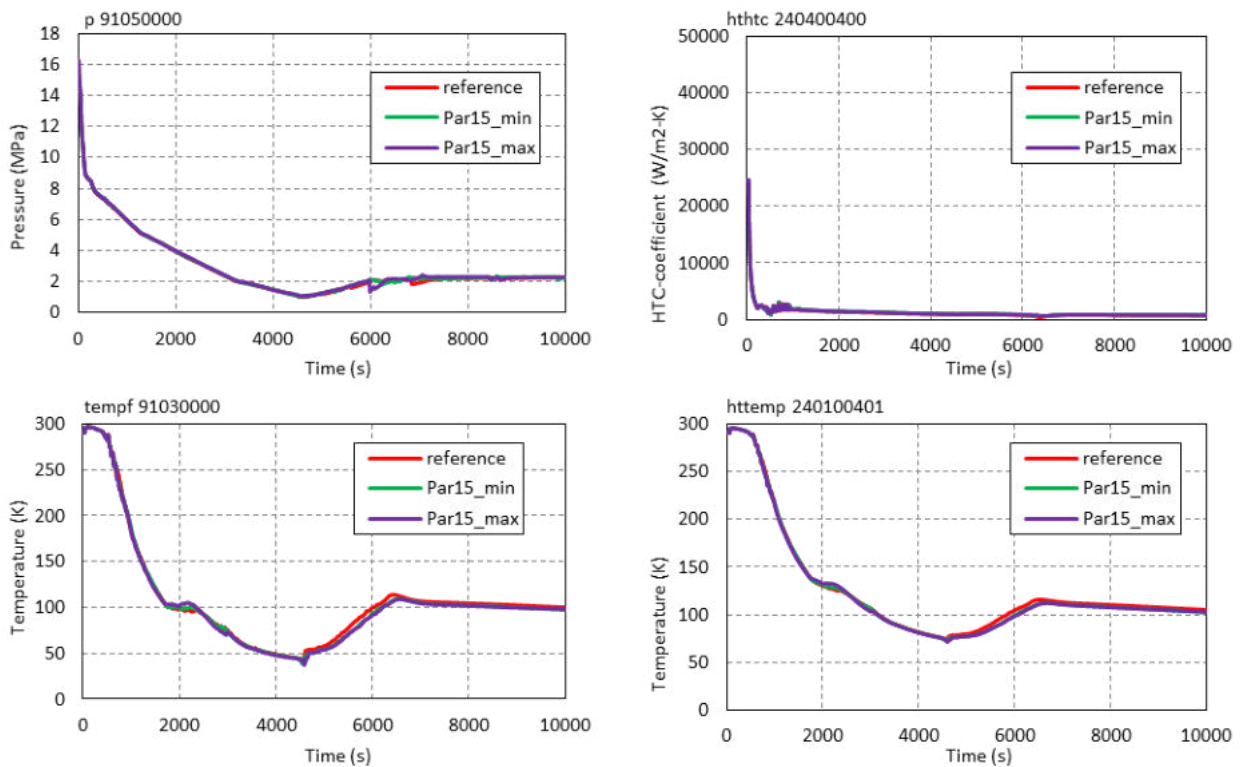
Figure 398: Impact of Parameter no. 15 variation on reference calculation.
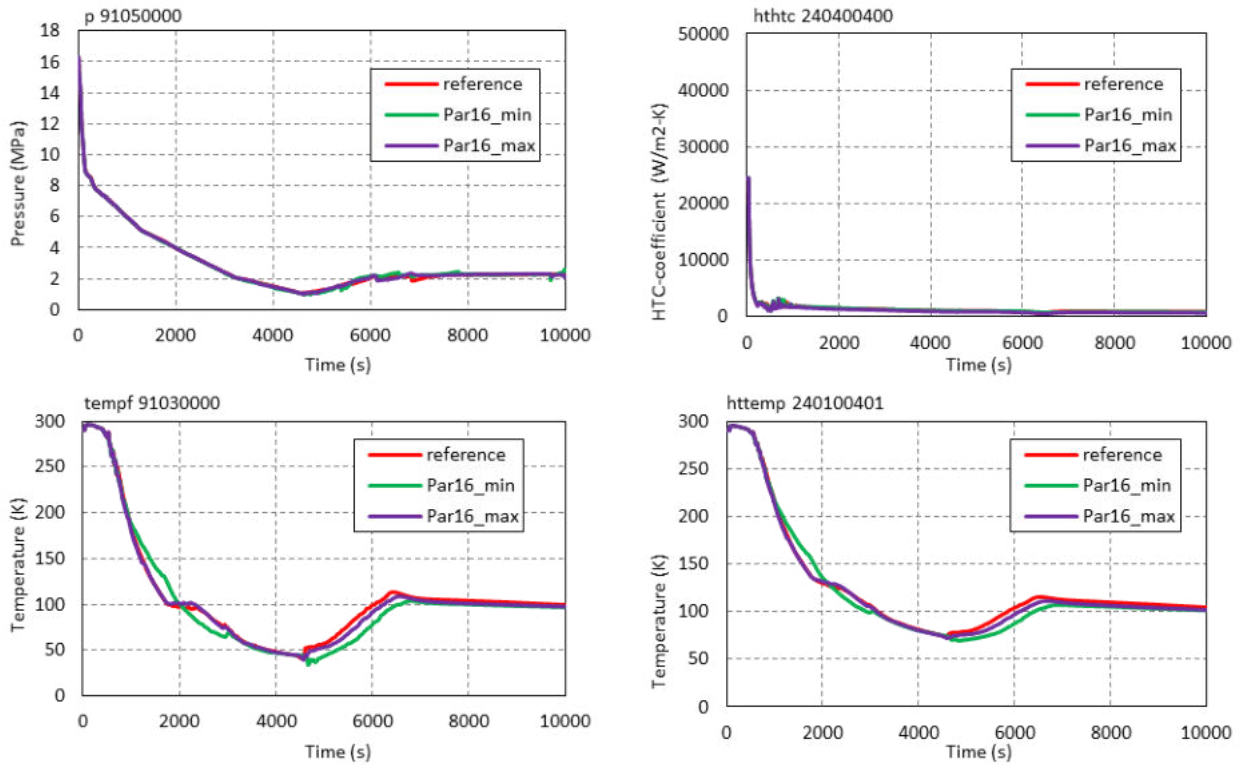
Figure 399: Impact of Parameter no. 16 variation on reference calculation.
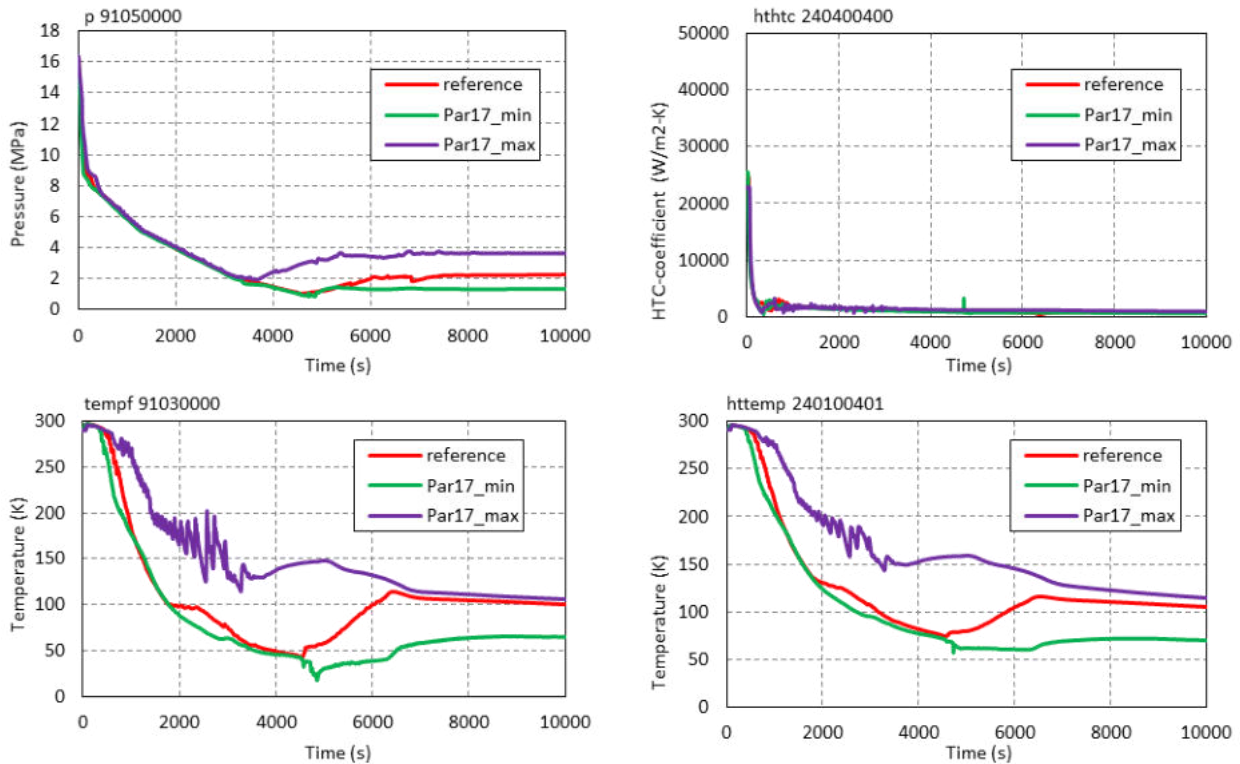
Figure 400: Impact of Parameter no. 17 variation on reference calculation.
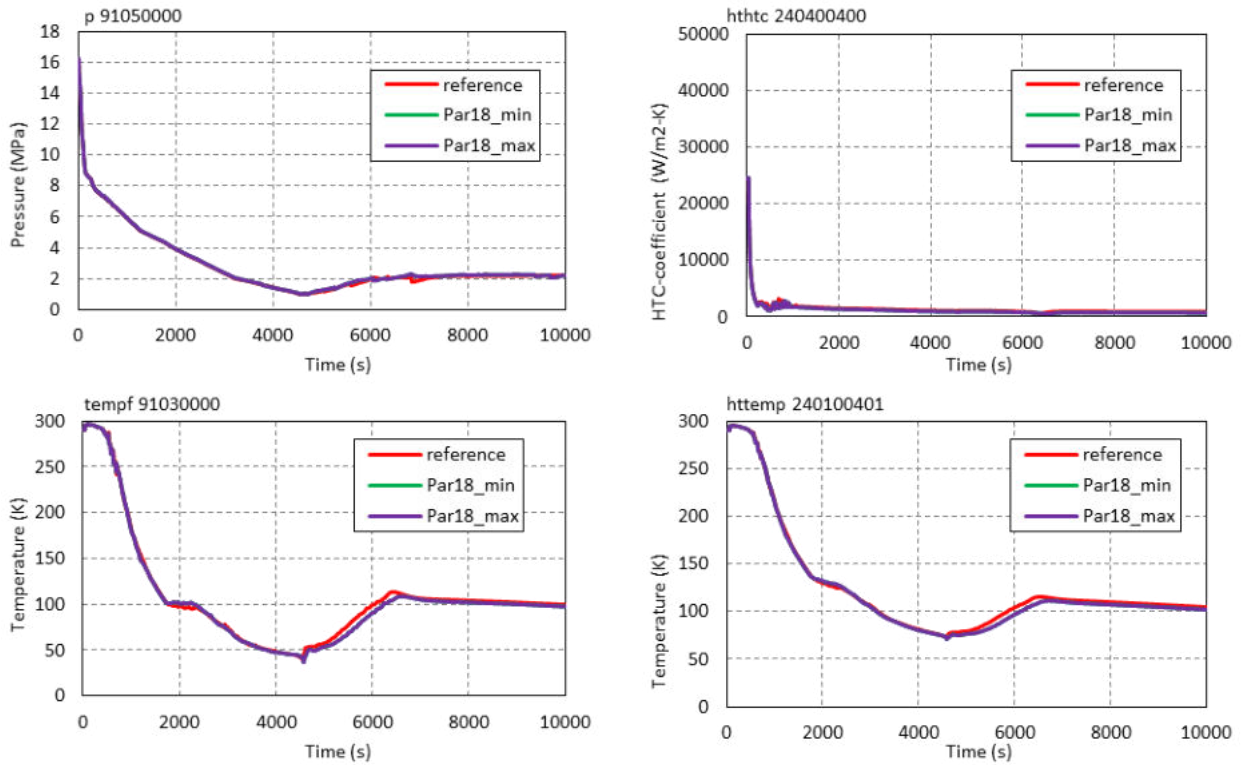
Figure 401: Impact of Parameter no. 18 variation on reference calculation.
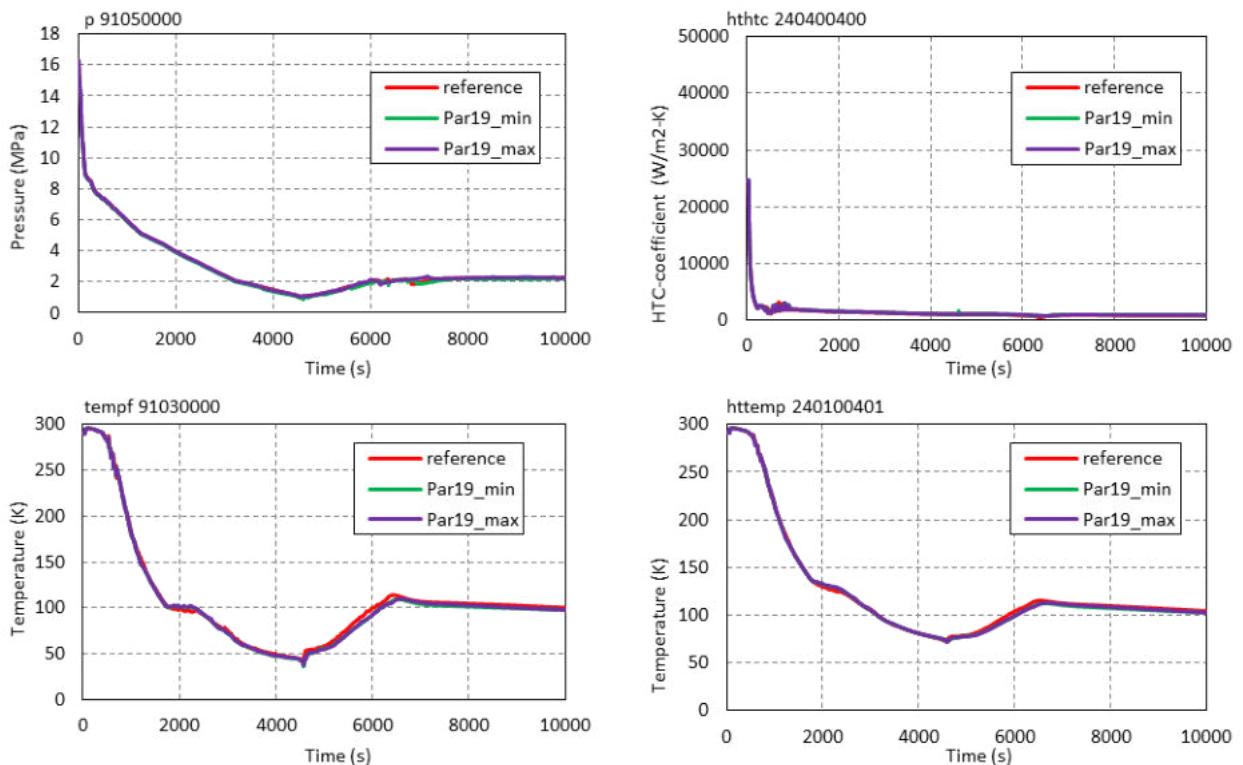
Figure 402: Impact of Parameter no. 19 variation on reference calculation.

14.4 Results of BEPU analyses

For uncertainty analysis SUSA Version 4.2.5 has been used. Calculations have been performed with the latest developmental RELAP5/MOD3.3 version 33lj available at the time of D2.3 preparation, which includes uncertainty parameters cards to conduct sensitivity studies investigating how a change in a given parameter affects a problem's solution. Selected seven FOMs resulting from uncertainty parameters variation in uncertainty analysis are shown in Figures 403 through 409. These FOMs are: primary pressure (DC), coolant temperatures at 1.350 m under CL1 and CL2, HTCs at RPV wall at 1.350 m under CL1 and CL2, and inner RPV wall temperatures at 1.350 m under CL1 and CL2.

For each selected FOM the results of 59 calculations are shown, reference calculation (labelled 'ref'), mean values of at each time step (labelled 'means'), upper or lower tolerance limit obtained by SUSA (labelled 'TL_Susa(95%,95%)') and upper or lower tolerance limit obtained directly from 59 calculations (labelled 'TL_cal(95%,95%)'). For pressure and HTCs upper tolerance limit is shown, while for temperatures lower tolerance limit is shown. Because 59 calculations have been used in uncertainty analysis, first order rank values are used. Due to this the values of 'maxima' at each time step are equal to upper tolerance limit and the values of 'minima' are equal to lower tolerance limit. Finally, because in SUSA interpolated values were used, not all oscillations are bounded by SUSA calculated tolerance limits ('TL_Susa(95%,95%)'. Therefore, in addition the tolerance limits were calculated directly from calculated values using Excel, and they bounded oscillations as shown in Figures 403 through 409.
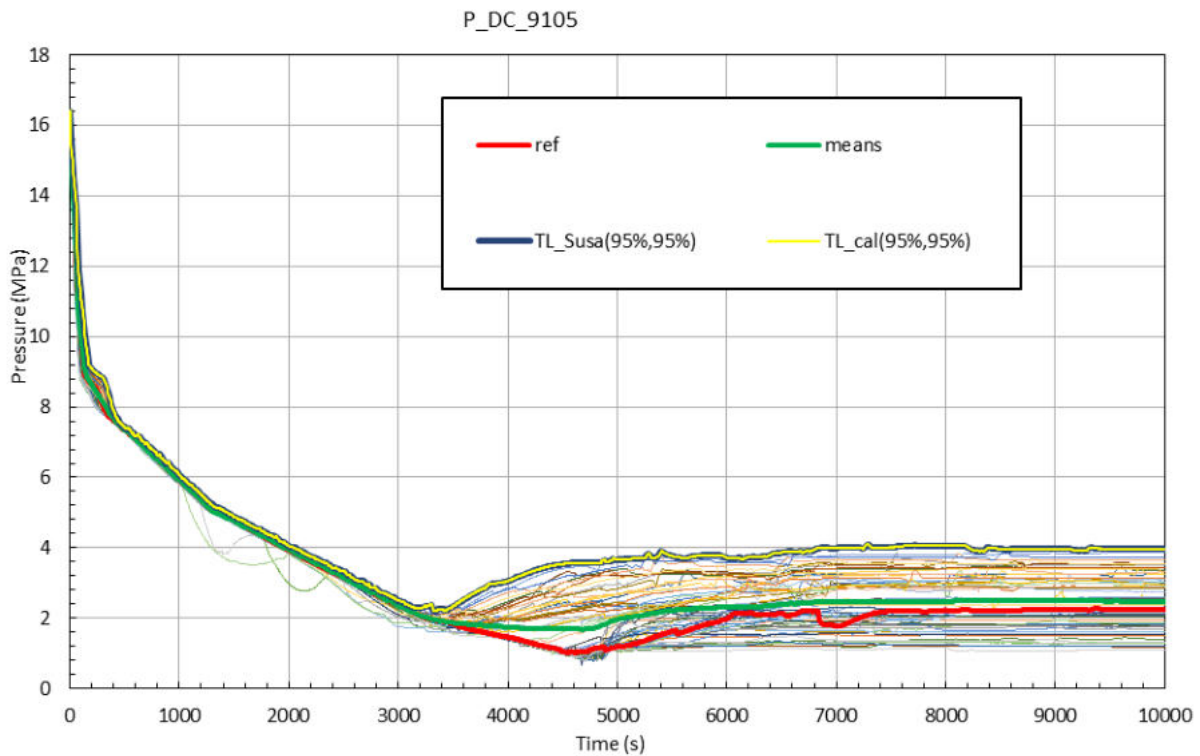
Figure 403: Pressure in downcomer (p-9105)
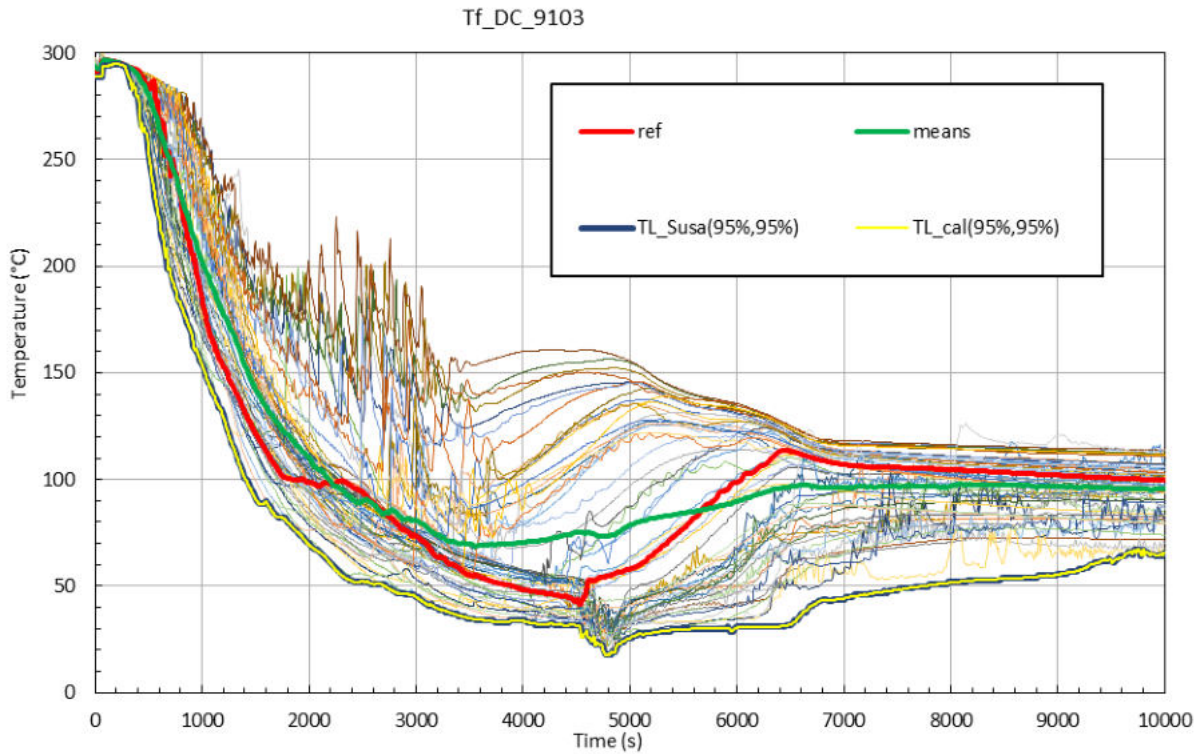
Figure 404: Coolant temperature at 1.350 m under CL1 (tempf-9103)
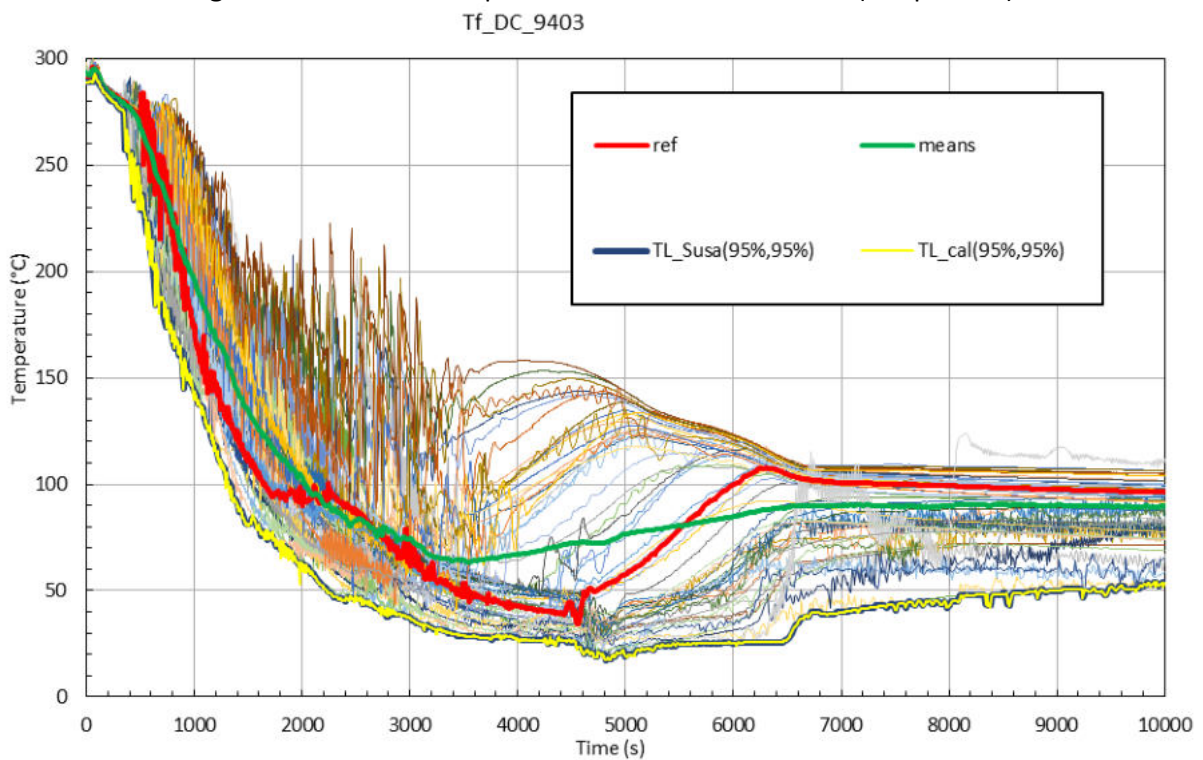
Figure 405: Coolant temperature at 1.350 m under CL2 (tempf-9403)
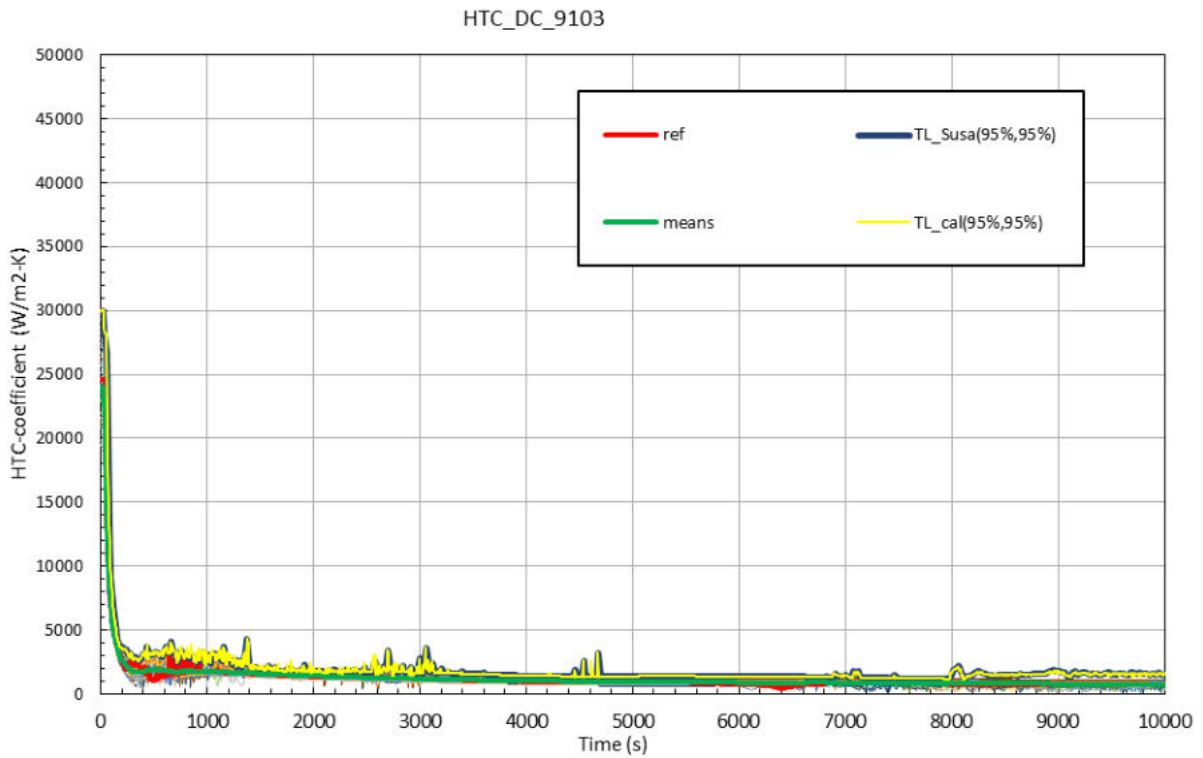
Figure 406: Heat transfer coefficient at RPV wall at 1.350 m under CL1 (hthtc-240100400)
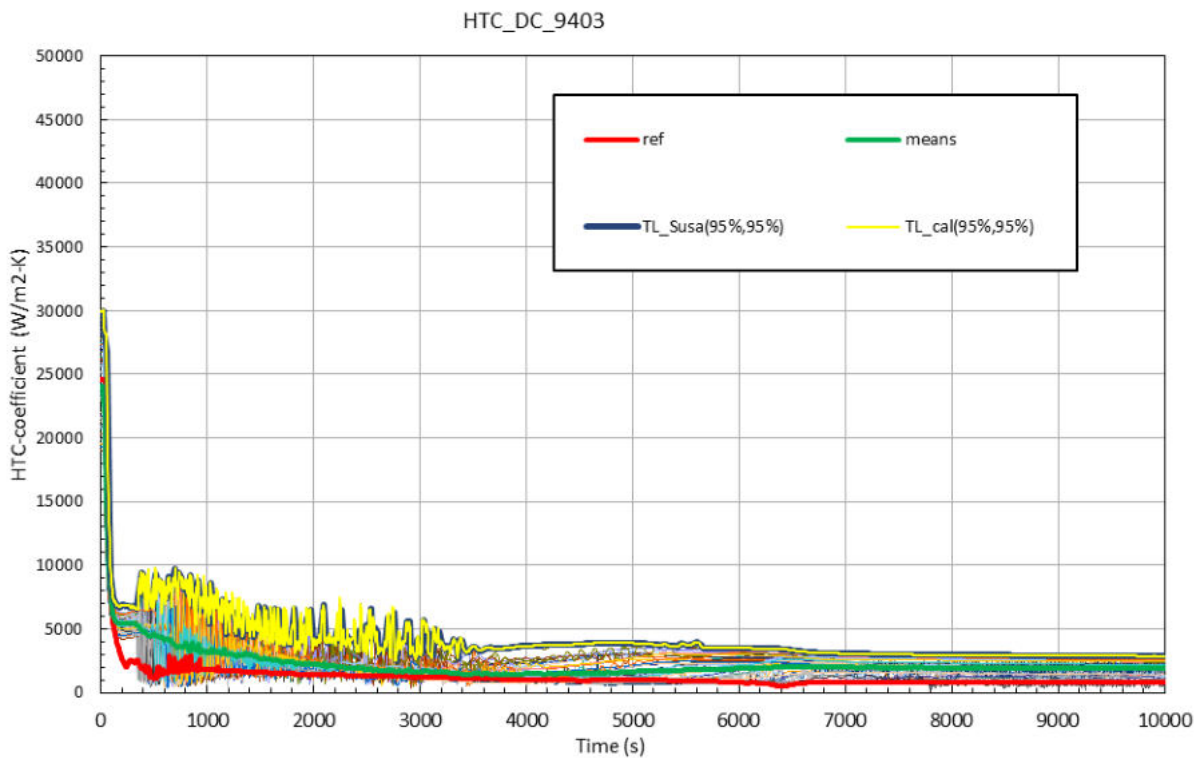
Figure 407: Heat transfer coefficient at RPV wall at 1.350 m under CL2 (hthtc-240400400)
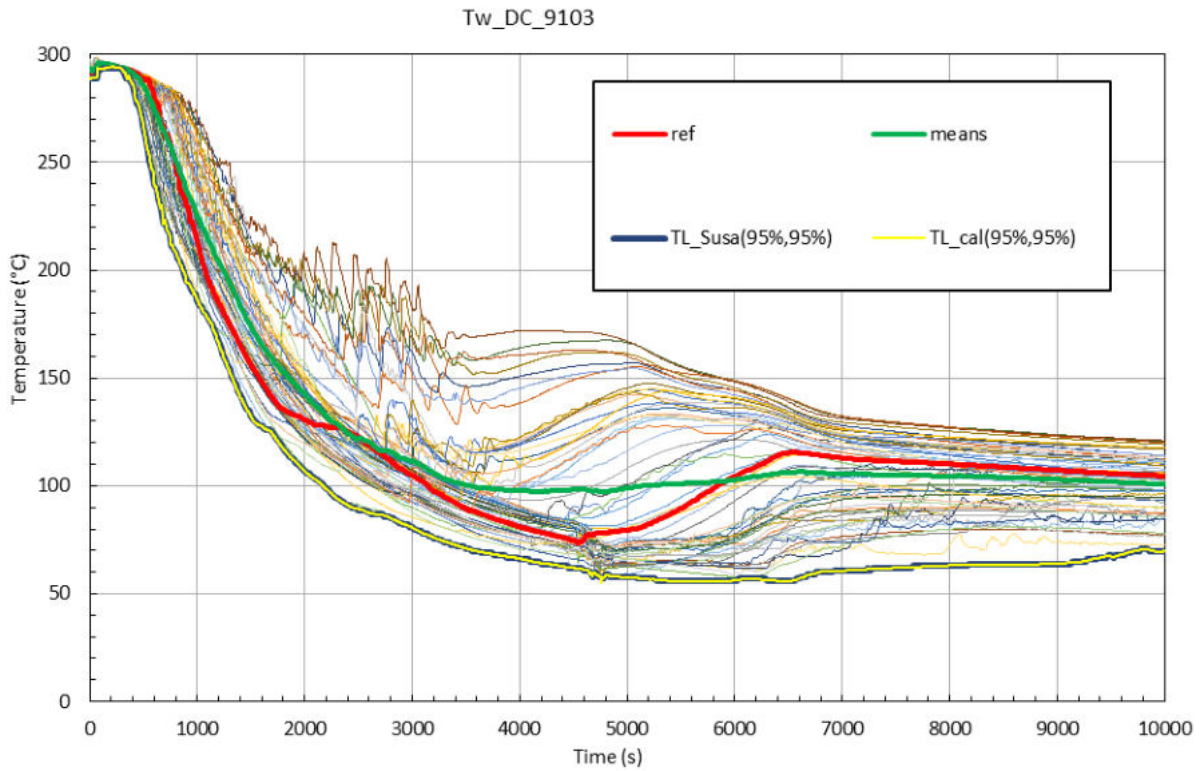
Figure 408: Inner RPV wall temperature at 1.350 m under CL1 (httemp-240100401)
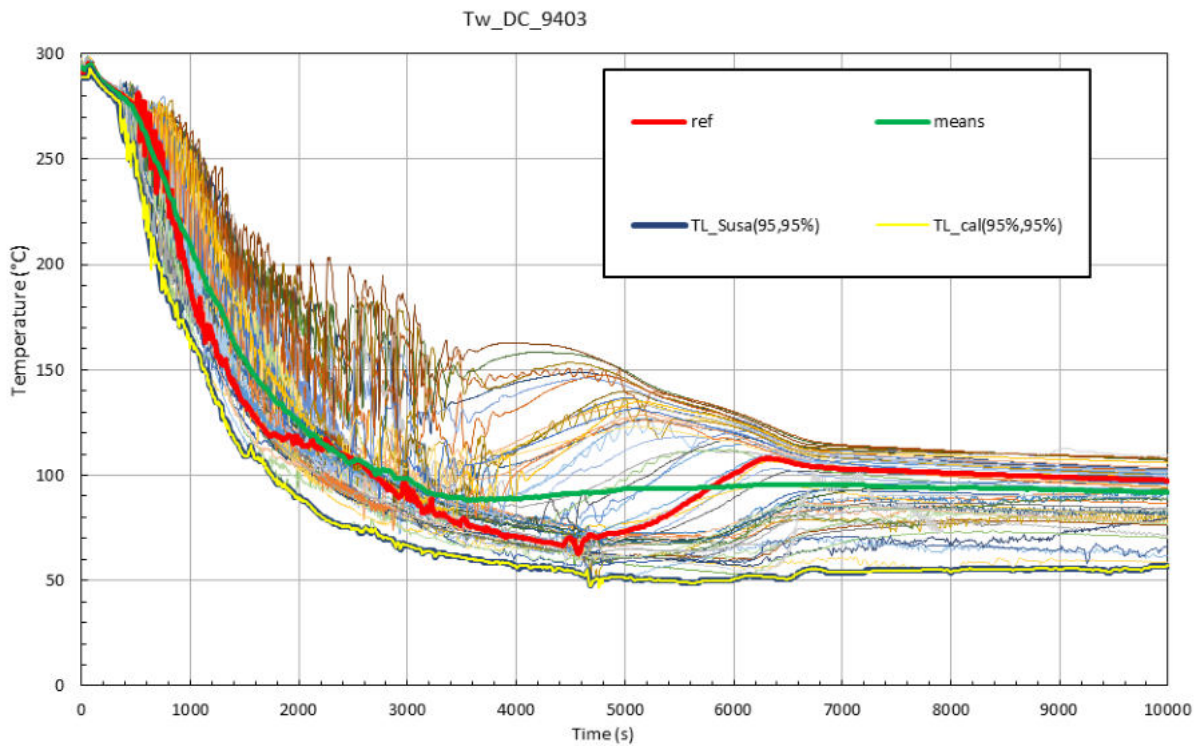
Figure 409: Inner RPV wall temperature at 1.350 m under CL2 (httemp-240400401)

14.5 Sensitivity analysis

Sensitivity analysis for time dependent data has been performed using SUSA (501 equidistant values each 20 s in the time interval (0-10000 s). In the SUSA the following types of correlation based sensitivity indices are implemented:

- Pearson's ordinary correlation
- Blomqvist's medial correlation
- Kendall's rank correlation
- Spearman's rank correlation

For the time-dependent sensitivity analysis, SUSA can calculate correlation related sensitivity indices and sensitivity indices from correlation ratios (on raw and rank-transformed data). For each correlation related sensitivity measure, the ordinary and partial correlation or the standardized regression coefficient can be calculated. In the following Figures 410 through 416 for brevity reasons only Spearman's Rank Correlation Coefficient, Partial Rank Correlation Coefficient (Spearman's Rank) and Standardised Regression Coefficient Spearman's Rank) are shown for all seven FOMs. Finally, coefficient of determination for regression function is shown in Figure 417. The value closer to one means better fit of regression function.

For primary pressure in the downcomer (see Figure 410) the most influential parameter seems to be parameter no. 17 (form-loss coefficient, see Table 47), while the second largest influence has parameter no. 11 (HPSI pump flow).

For coolant temperatures under CL1 and CL2 (see Figures 411 and 412, respectively) the most influential parameter seems to be parameter no. 17 (form-loss coefficient), while the second largest influence have parameters no. 9 (HPSI temperature) and no. 11 (HPSI pump flow).

For heat transfer coefficients at RPV wall at 1.350 m under CL1 and CL2 (see Figures 413 and 414, respectively) the most influential parameters seem to be parameter no. 14 (single-phase liquid to wall HTC) and no. 17 (form-loss coefficient). Influence have also parameters no. 9 (HPSI temperature) and no. 11 (HPSI pump flow).

Finally, for inner RPV wall temperature at 1.350 m under CL1 and CL2 (see Figures 415 and 416, respectively) the most influential parameter seems to be parameter no. 17 (form-loss coefficient) and the second most influential is parameter no. 9 (HPSI temperature). Influence have also parameters no. 4 (decay heat), no. 7 (ACC initial pressure) and no. 11 (HPSI pump flow).

The obtained quantitative results support the conclusions made on visual observation of sensitivity study (see Section 14.3), which indicated that the largest influence on shown output parameters (being FOMs) has parameter no. 17 (form-loss coefficient), while parameters no. 9 (HPSI temperature) and no. 11 (HPSI pump flow) have also large influence. The time dependent quantitative sensitivity analysis also supports the sensitivity study based on visual observation regarding the time of influence. For example, parameter no. 17 (see Figure 400 showing impact of form-loss coefficient) significantly impacted FOMs early in the transient, what was confirmed by sensitivity analysis (see green line for 'Par. 17' representing form-loss coefficient in Figures 410 through 416).
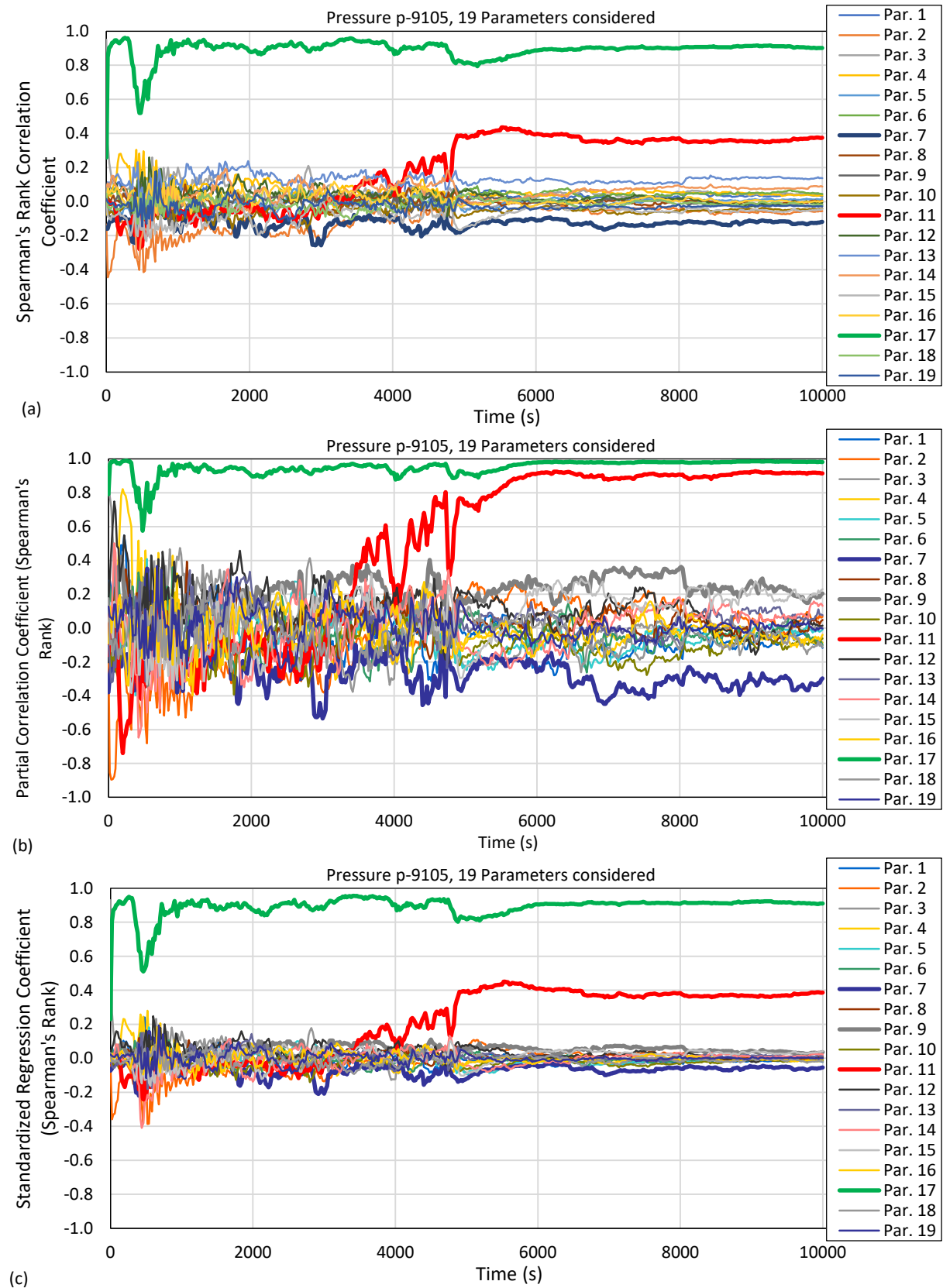
Figure 410: Sensitivity coefficients for pressure in downcomer (p-9105): (a) Spearman's Rank Correlation Coefficient, (b) Partial Rank Correlation Coefficient (Spearman's Rank) and (c) Standardised Regression Coefficient Spearman's Rank
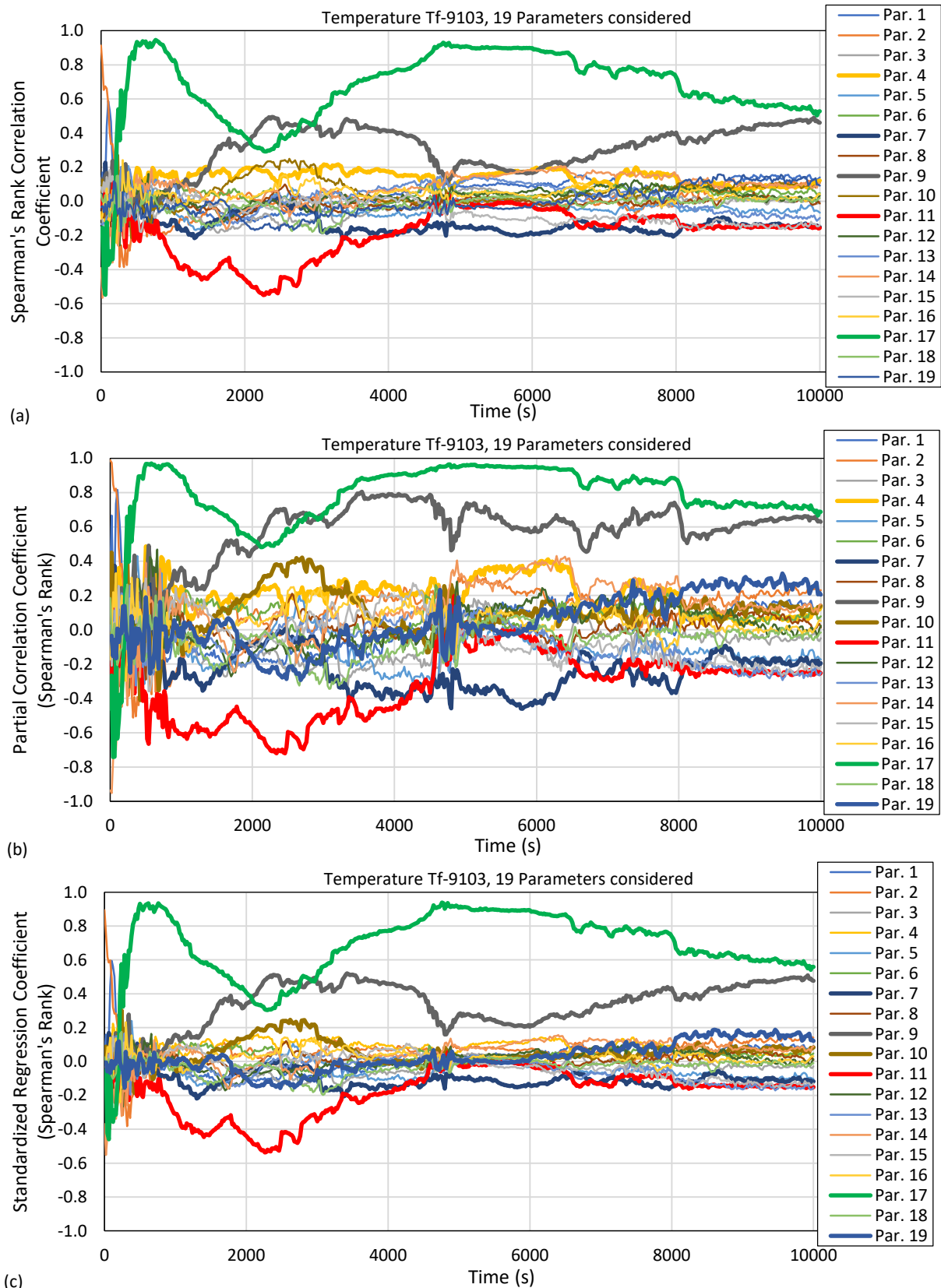
Figure 411: Sensitivity coefficients for coolant temperature at 1.350 m under CL1 (tempf-9103): (a) Spearman's Rank Correlation Coefficient, (b) Partial Rank Correlation Coefficient (Spearman's Rank) and (c) Standardised Regression Coefficient Spearman's Rank
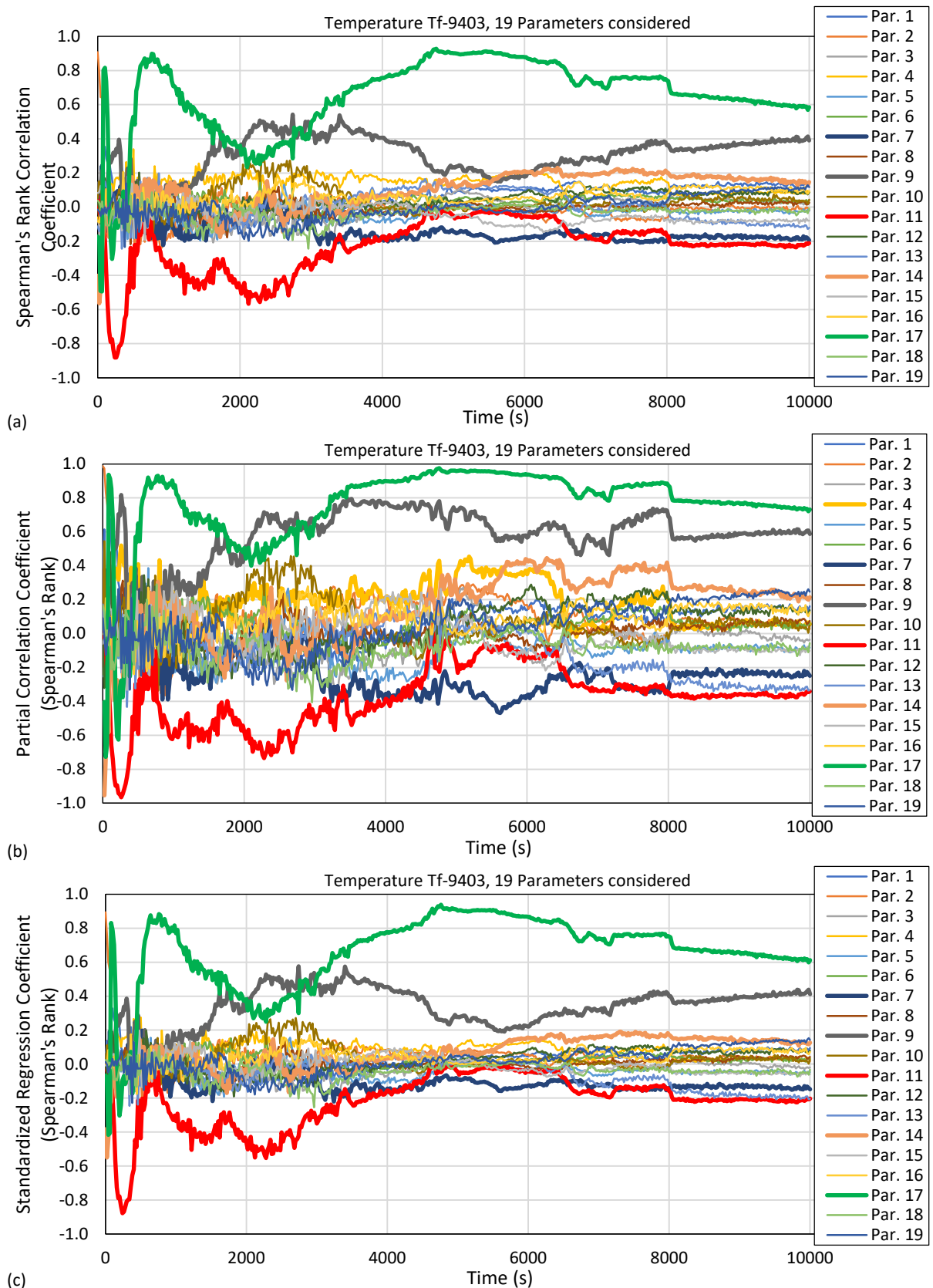
Figure 412: Sensitivity coefficients for Coolant temperature at 1.350 m under CL2 (tempf-9403): (a) Spearman's Rank Correlation Coefficient, (b) Partial Rank Correlation Coefficient (Spearman's Rank) and (c) Standardised Regression Coefficient Spearman's Rank
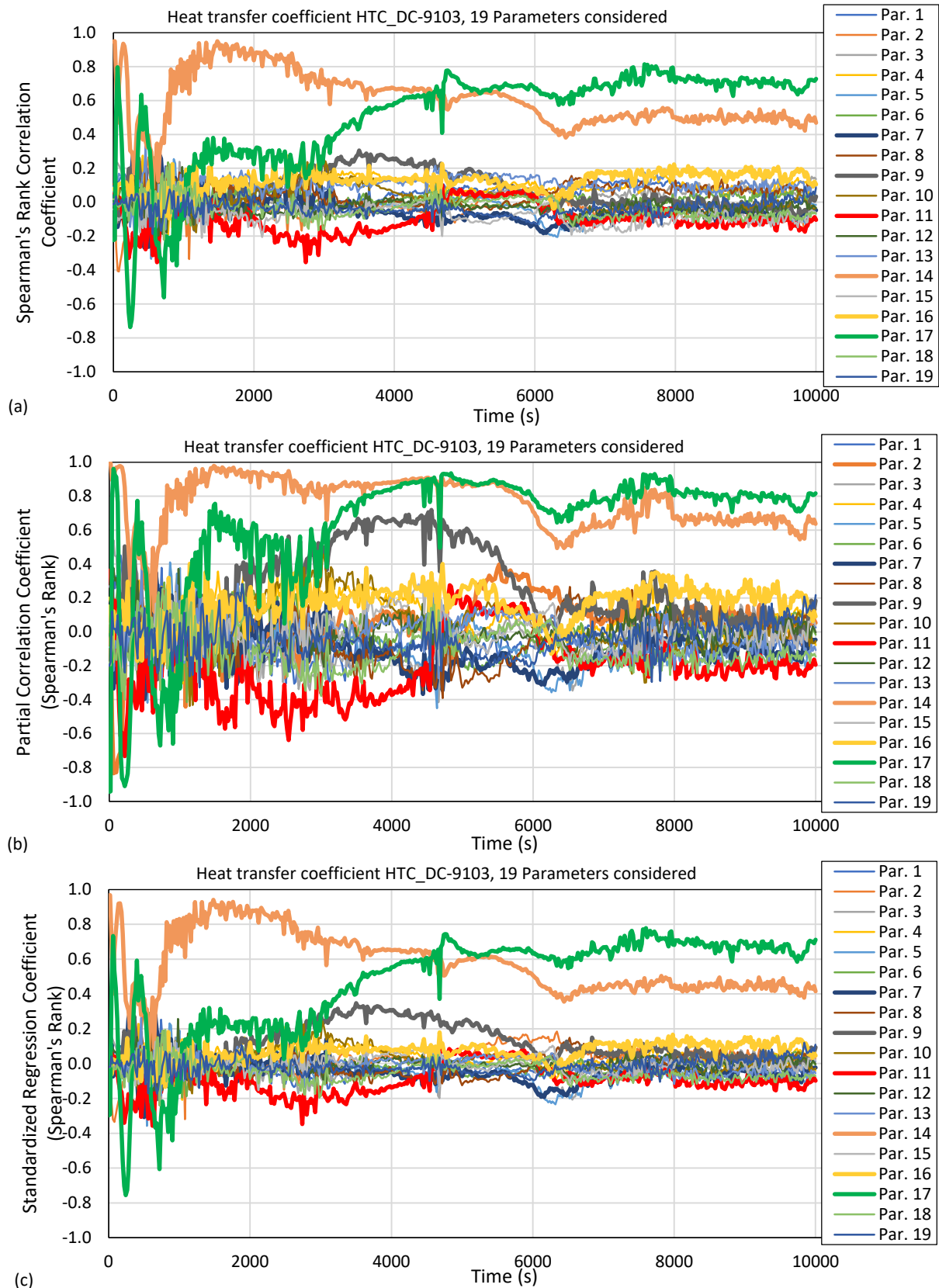
Figure 413: Sensitivity coefficients for heat transfer coefficient at RPV wall at 1.350 m under CL1 (hthtc-240100400): (a) Spearman's Rank Correlation Coefficient, (b) Partial Rank Correlation Coefficient (Spearman's Rank) and (c) Standardised Regression Coefficient Spearman's Rank
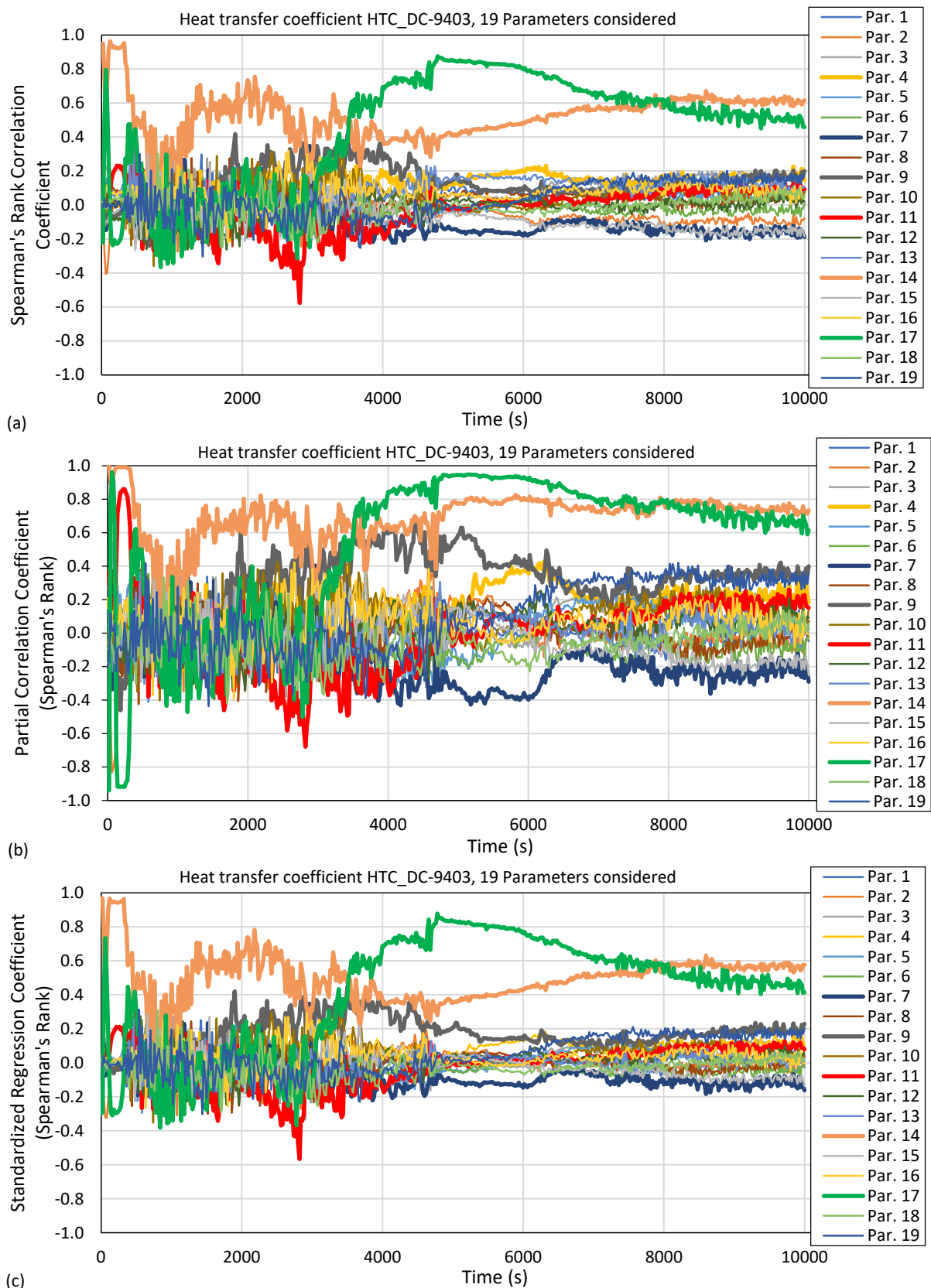
Figure 414: Sensitivity coefficients for heat transfer coefficient at RPV wall at 1.350 m under CL1 (hthtc-240400400): (a) Spearman's Rank Correlation Coefficient, (b) Partial Rank Correlation Coefficient (Spearman's Rank) and (c) Standardised Regression Coefficient Spearman's Rank
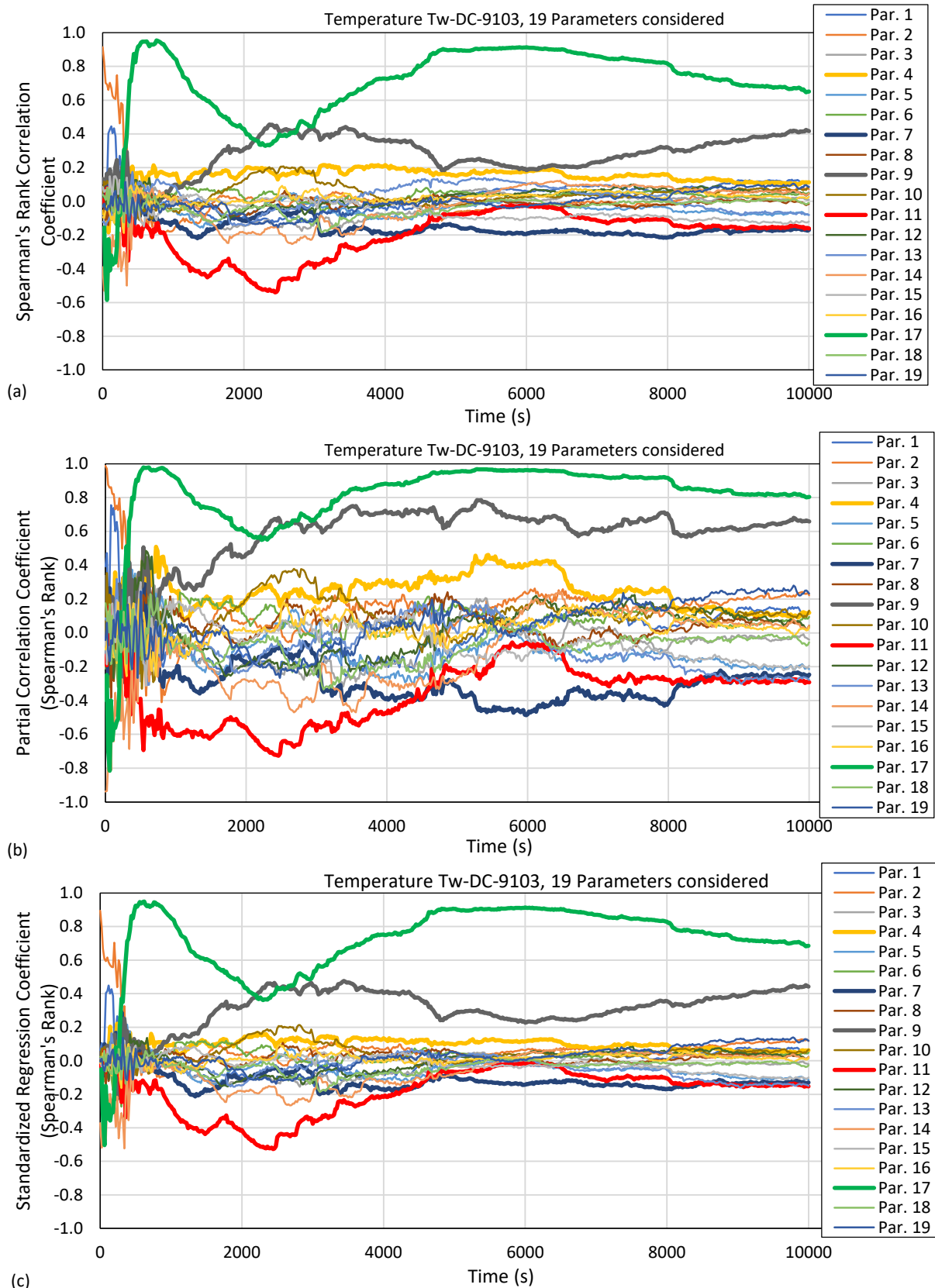
Figure 415: Sensitivity coefficients for inner RPV wall temperature at 1.350 m under CL1 (httemp-240100401): (a) Spearman's Rank Correlation Coefficient, (b) Partial Rank Correlation Coefficient (Spearman's Rank) and (c) Standardised Regression Coefficient Spearman's Rank
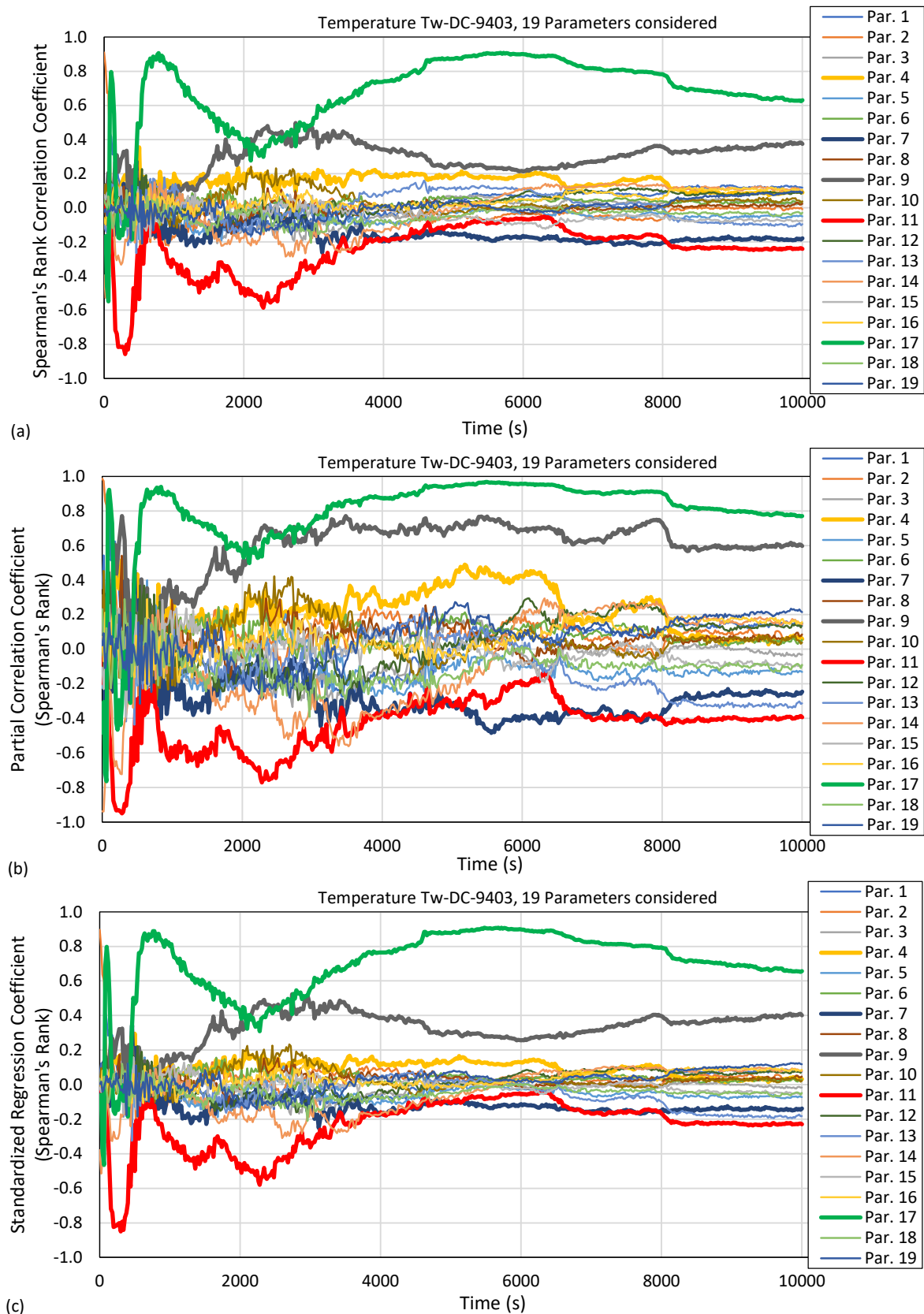
Figure 416: Sensitivity coefficients for inner RPV wall temperature at 1.350 m under CL2 (httemp-240400401): (a) Spearman's Rank Correlation Coefficient, (b) Partial Rank Correlation Coefficient (Spearman's Rank) and (c) Standardised Regression Coefficient Spearman's Rank
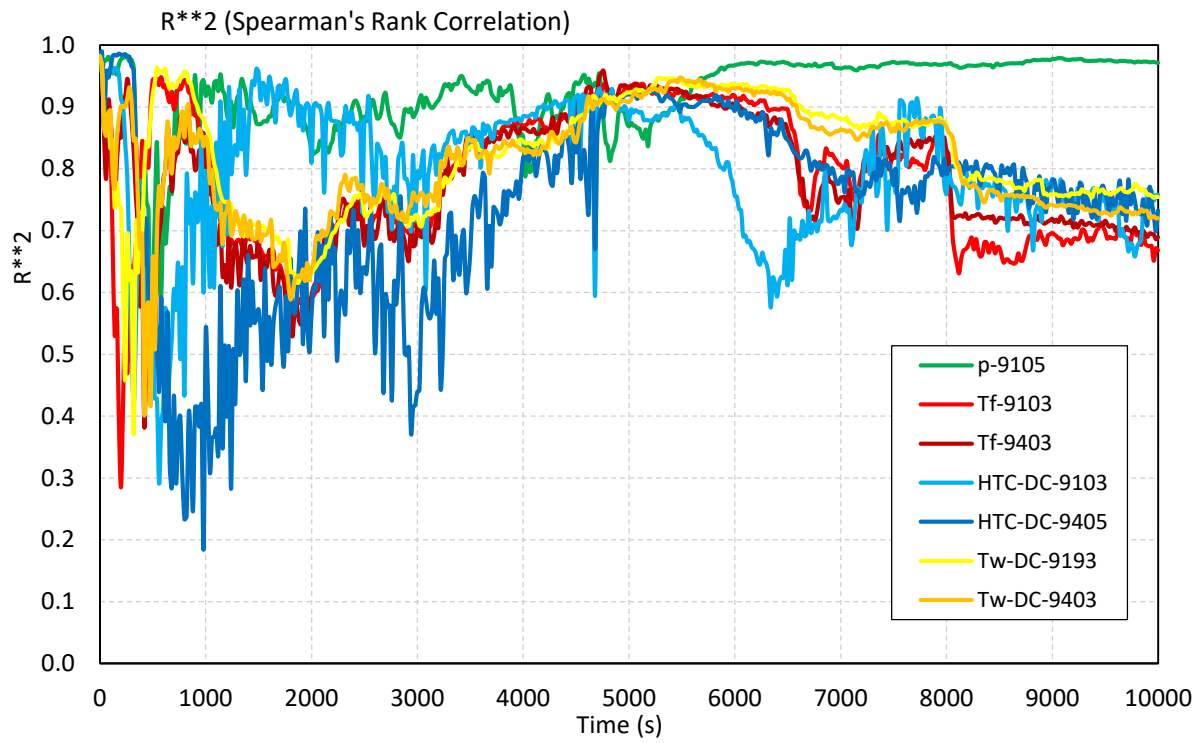
Figure 417: Coefficient of determination

15   WUT uncertainty analysis with RELAP5 and WUT in-house script

15.1 Input uncertainties

The best-estimate values and input uncertainties for all parameters are summarized in **Table 48**. The PDFs of the parameters are generally taken from the WP2 Task 2.2 final report in Reference [34], which are reproduced in Table 30. The PDFs for the accumulator levels were modified as compared to that listed in WP2 Task 2.2 (and reproduced in **Table 30**) to take into account more realistic values. The PDFs are the same as that used for the ATHLET code system (see **Table 31).**

Table 48: Best-estimate values and PDF of uncertain input parameters

Name	Best-estimate value	PDF type	distribution characterization #1 (e.g., mean, lower bound)	distribution characterization #2 (e.g. standard deviation, upper bound)
Initial reactor inlet temperature: Core power	100% nominal	Normal	Mean = 100% nominal power	Std. dev.= 1%
Initial reactor inlet temperature: secondary-side pressure	60.2 bar	Uniform	60.2 bar	68.2 bar
Initial reactor inlet temperature: Pressurizer pressure	157.5 bar	Normal	Mean = 157.5 bar	Std. dev.= 1%
Decay heat multiplier	ANS79-1 + 10%	Uniform	ANS79-1 – 0%	ANS79-1 + 20%
Timing of SIS actuation	at 110 bar + 10 s delay	Uniform	at 110 bar + 0 s delay	at 110 bar + 20 s delay
ACC injection temperature	30 °C	Uniform	min:20 °C	max:40 °C
ACC initial pressure	26 bar	Uniform	min:24 bar	max:28 bar
HPSI temperature	30 °C	Uniform	min:15 °C	max:45 °C
HP and LP pump pressure/flow curves	As defined in T2 with a multiplier.	Normal	mean:100% of nominal	std.dev.:10% of nominal
Time of isolation of second HPSI pump	4900 s	Uniform	min: 1800 s	max: 4900 s
Secondary-side pressure leading to the given cooldown rate	100 K/hr	Uniform	min: 50 K/hr	max: 200 K/hr
Time of isolation of ACCs	4900 s	Uniform	min: 1800 s	max: 4900 s
Level Accumulator	8.518 m	Uniform	min: 8.148 m	max: 8.889 m

15.2 Results of BEPU analyses

The PDFs were sampled 59 times to yield 95%/95% one-sided tolerance bound. The results are illustrated in **Figure 418** and **Figure 485** for the Pressure, Coolant and Wall Temperatures and HTC time dependent profile measured 1.35 m and 2.64 m below the centreline of the cold legs. The results are given below CL-1 (non-injecting) and CL-2 (injecting). The other CLs have similar results. The 59 samples are illustrated in dashed blue lines, whereas the mean value and ±1σ bounds are shown in black line. For the temperature profiles, the bound is defined as the sample with the lowest temperature at each time point. For the pressure and HTC time dependent profiles, the maximum values are used to define the bound. The 95%/95% bound is shown in red. The Base Case value (as defined in WP2.2 in Reference [83]) are showed in blue for comparison. Note that all data

306

are presented here with a time step of 1 second, and in case for heat transfer coefficients for clarity with a time step of 10 seconds (but data were obtained with a one-second time step.)
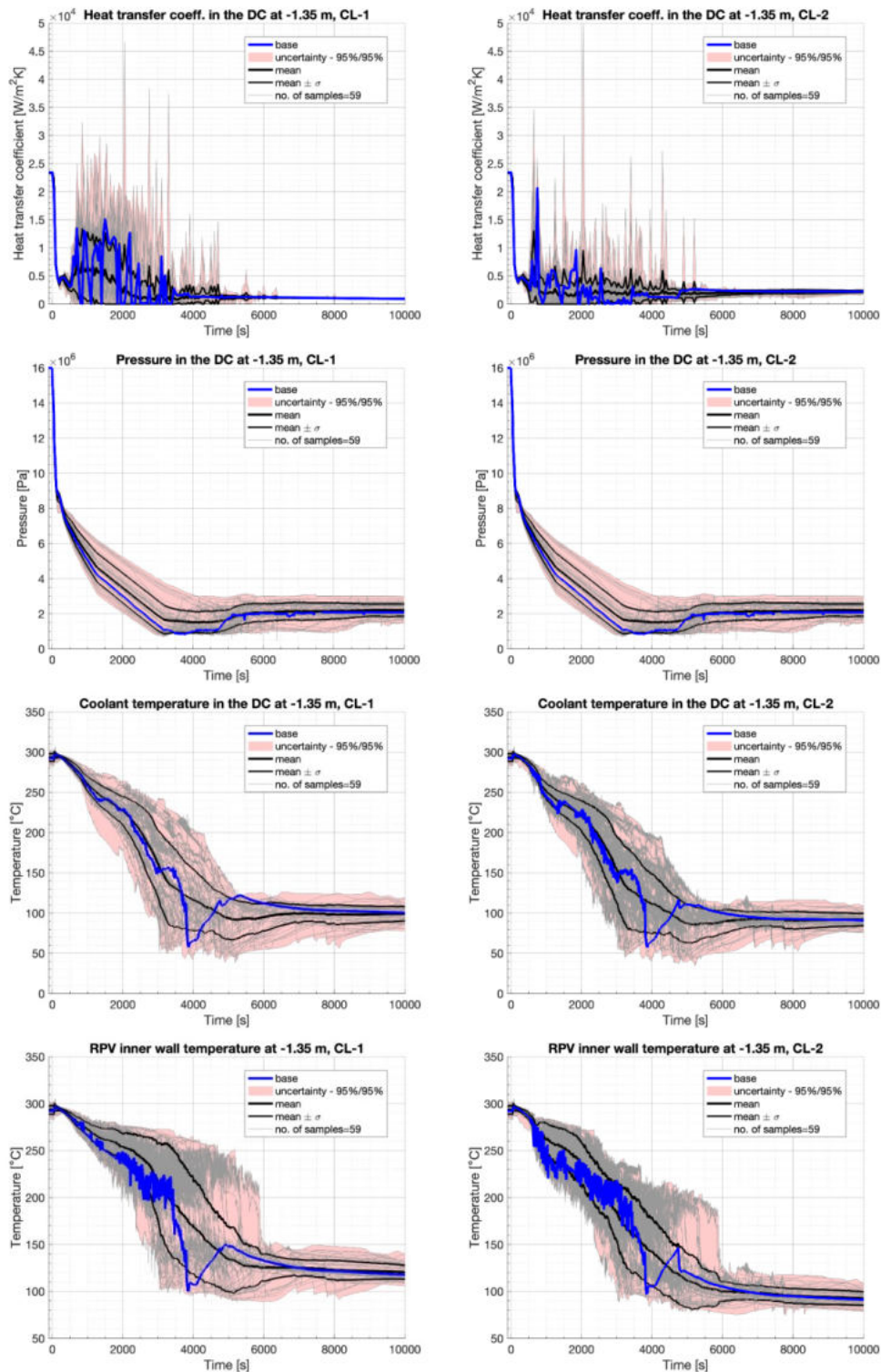
Figure 418: HTC, Pressure and Coolant and Wall Temperature profiles 1.35 m below the CL-1 (left) and CL-2 (right) centrelines.

307
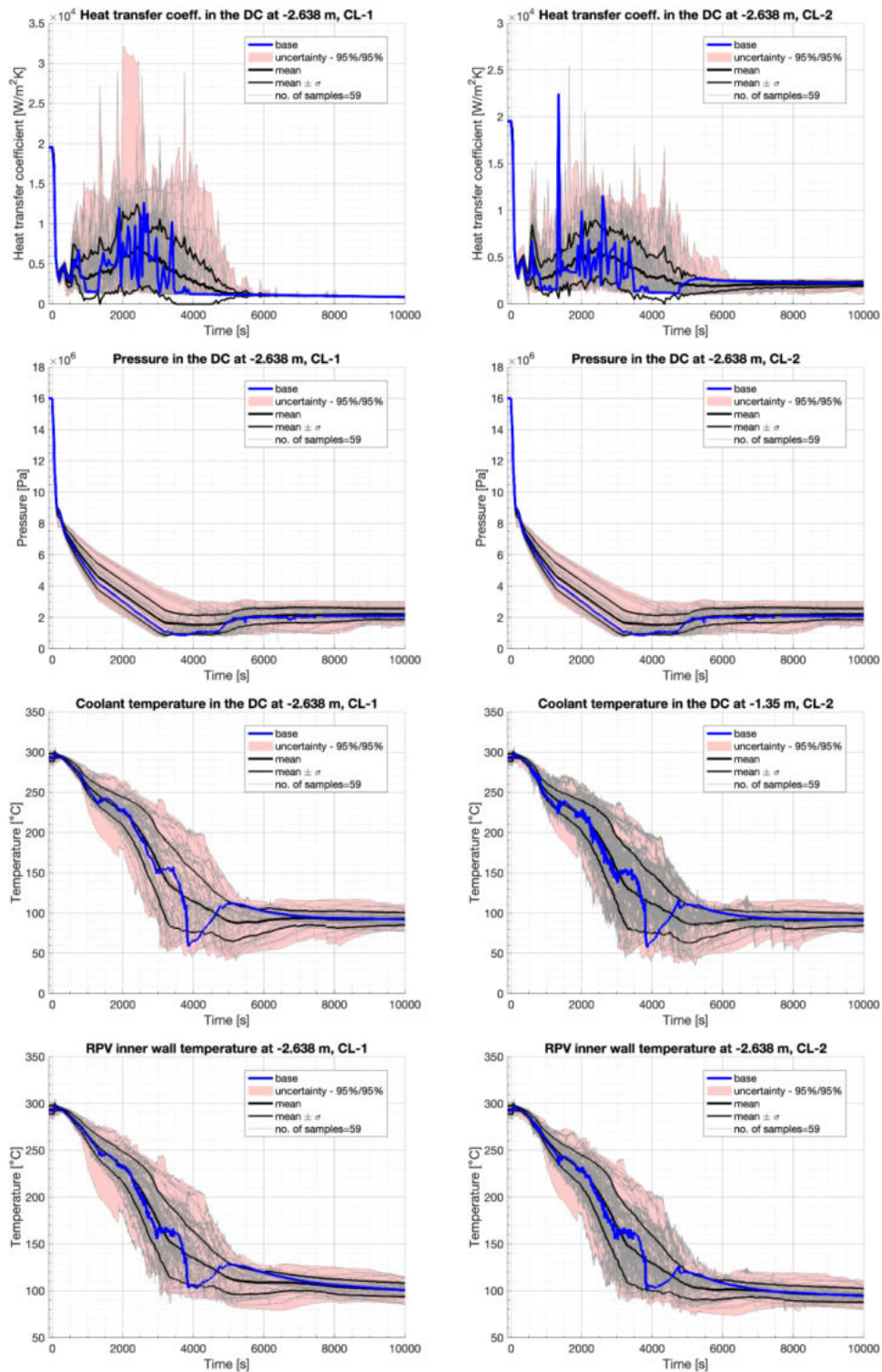
Figure 419: HTC, Pressure and Coolant and Wall Temperature profiles 2.64 m below the CL-1 (left) and CL-2 (right) centrelines.

16   KIWA uncertainty analysis with RELAP and SUSA

16.1 Reference best-estimate calculation

A modified Relap5 model that had been used in Task 2.1 was also employed in this uncertainty analysis. The KWU model v76 underwent however some significant modifications that are already described in the JSI part of this summary report. The main objectives of the changes were to adapt the model so that computations with chosen uncertainties in Task 2.2 as described in Reference [83] can be conducted. The most significant changes were related to changes that allow the user to freely set up the initial pressurizer level and secondary pressure. Other changes included modifications related to accumulators (to be able to change nitrogen volume) and material definition (material property ranges were extended to eliminate errors during transient calculations). Cross-section junctions of the downcomer (annulus component, at the top) were modified as well in order to eliminate instabilities during transient run.

Most of the uncertainty computations were calculated using the newest version of RELAP5/MOD3.3/lj. Other versions of the code were used as well, e.g. versions lf and km (to compute the best-estimate case) and km and lb (that were used to perform computations in Task 2.1). Figures below depict results of the best-estimate calculations using different codes for pressures in primary and secondary loop, break and ECSS flows and water levels in the downcomer and inner reactor. Computations with versions li and km are fairly consistent with each other. Some minor differences can be observed with respect to different codes especially km (which is the oldest version). The computations conducted using this version underestimate pressure at the end of the transient (at around 3500 seconds). The situation is pretty similar when it comes to secondary side. It should be mentioned that during these computations (Task 2.1) a preliminary model was used which underwent the modifications described above. Possibly these modifications with version specification influence the results altogether.
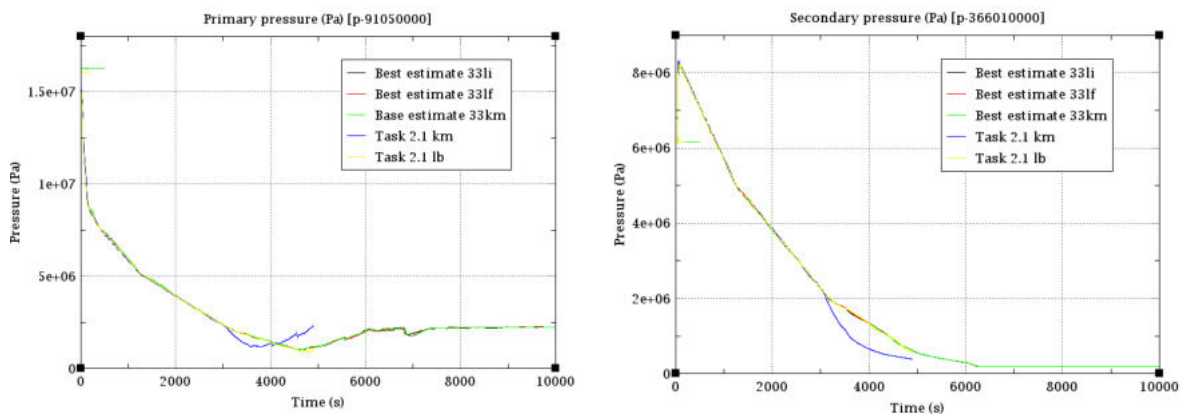
Figure 420: Comparison of System Pressures - (a) Primary and (b) Secondary pressure.
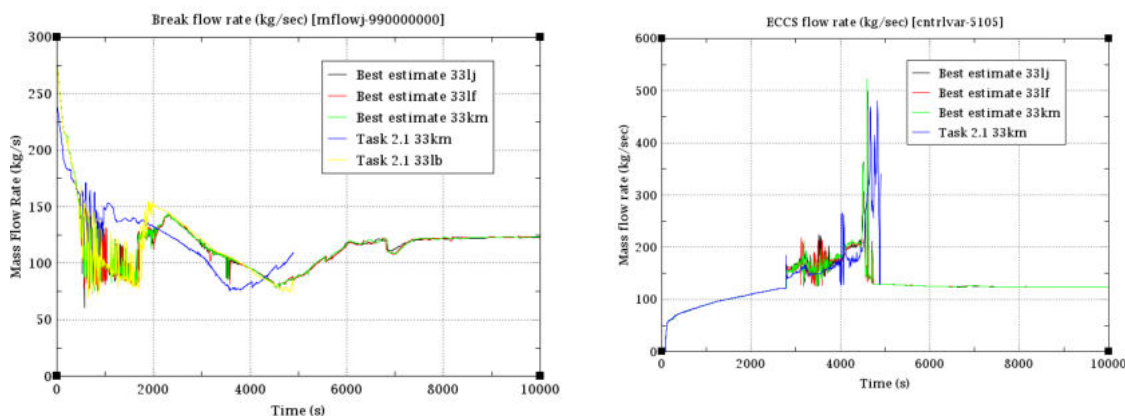
Figure 421: Comparison of (a) Break Flow Rate and (b) ECCS Flow Rate.
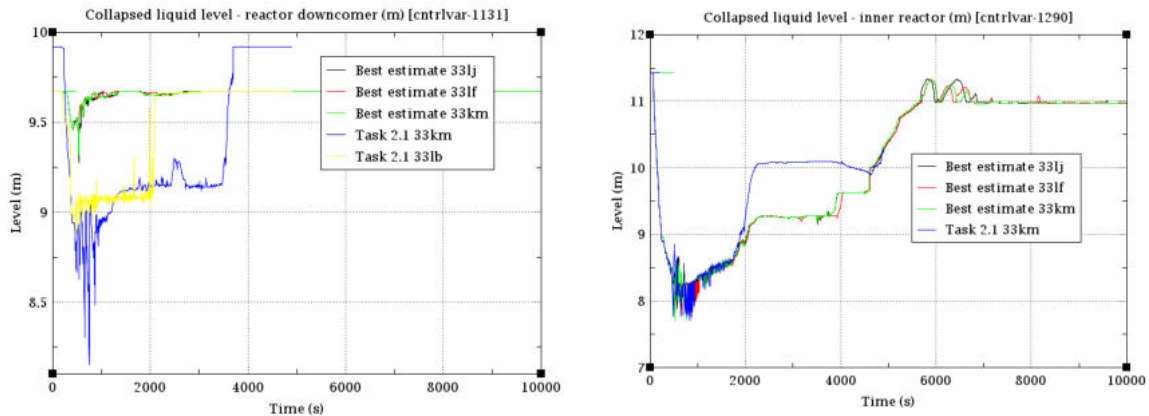
Figure 422: Comparison of Collapsed Liquid Levels in – (a) Reactor DC, (b) Inner reactor.

16.2 Input uncertainties

Input uncertainty parameters were chosen based on the recommendations from Task 2.2. A Software for Uncertainty and Sensitivity Analysis SUSA 4.2.5 has been used to generate random numbers and values of uncertainty parameters. A total number of 19 input parameters were used in the analysis. SUSA was employed to generate suitable random values for 59 Relap5 input files (each for steady state and transient). Table below provides information about chosen uncertainty parameters, nominal values, types of distribution and its parameters as well extreme values.

Par. No.	Parameter Name	Nominal Value	Distribution Type	Distribution Parameters	Minimum	Maximum
1	Core power (W)	3.77E+09	Normal	µ: 3.7650E+09 σ: 3.7650E+07	3.679E+09	3.859E+09
2	Secondary side pressure (Pa)	6.16E+06	Uniform	a: 6.0100E+06 b: 6.8100E+06	6.013E+06	6.797E+06
3	Pressurizer pressure (Pa)	1.57E+07	Normal	µ: 1.5740E+07 σ: 1.5740E+05	1.544E+07	1.607E+07
4	Decay heat multiplier	1	Uniform	a: 0.9 b: 1.1	0.901	1.100
5	Timing of SIS actuation (s)	10	Uniform	a: 0 b: 20	0.501	19.867
6	ACC injection temperature (°C)	303.15	Uniform	a: 293.15 b: 313.15	293.99	313.11
7	ACC initial pressure (Pa)	2600000	Uniform	a: 2.4000E+06 b: 2.8000E+06	2.407E+06	2.798E+06
8	ACC initial nitrogen volume – values of static quality in volume 2	0.486248	Uniform	a: 3.6513E-01 b: 6.2505E-01	3.680E-01	6.206E-01
9	HPSI temperature (°C)	303.15	Uniform	a: 288.15 b: 318.15	288.46	317.96
10	HP pump pressure curve multiplier	1	Normal	µ: 1.0 σ: 0.1	0.747	1.186
11	HP pump flow curve multiplier	1	Normal	µ: 1.0 σ: 0.1	0.789	1.223
12	Initial pressurizer level (m)	8.21	Uniform	a: 7.71 b: 8.71	7.726	8.709
13	Thermal-nonequilibrium coefficient for Henry-Fauske model	0.14	Weibull	p1: 7 p2: 1	5.05E-01	1.28E+00
14	Single-phase liquid to wall HTC multiplier	1	Log. Uniform	a: 0.8 b: 1.2	0.809	1.198

15	Single-phase vapour to wall HTC multiplier	1	Log. Uniform	a: 0.8 b: 1.2	0.802	1.164
16	Wall-drag coefficient multiplier	1	Log. Uniform	a: 0.5 b: 2.0	0.512	1.961
17	Form-loss coefficient multiplier	1	Log. Uniform	a: 0.5 b: 2.0	0.505	1.988
18	LP pump pressure curve multiplier	1	Normal	μ: 1.0 σ: 0.1	0.769	1.184
19	LP pump flow curve multiplier	1	Normal	μ: 1.0 σ: 0.1	0.769	1.234

16.3 Results of BEPU analyses

Uncertainty calculations were computed using the newest code version RELAP5/MOD3.3/lj. The input files were prepared and generated (distributions, random parameters) using SUSA tool. Figure of merit were primary pressure (DC), coolant temperatures at 1.350 m under CL1 and CL2, HTCs at RPV wall at 1.350 m under CL1 and CL2, and inner RPV wall temperatures at 1.350 m under CL1 and CL2.
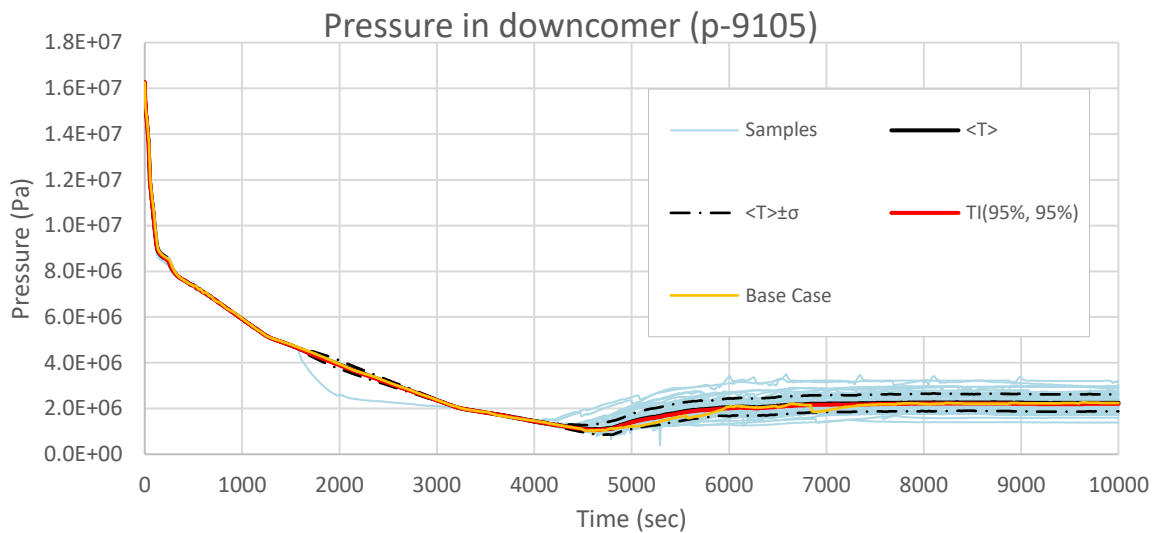
Figure 423: Pressure in downcomer (p-9105)
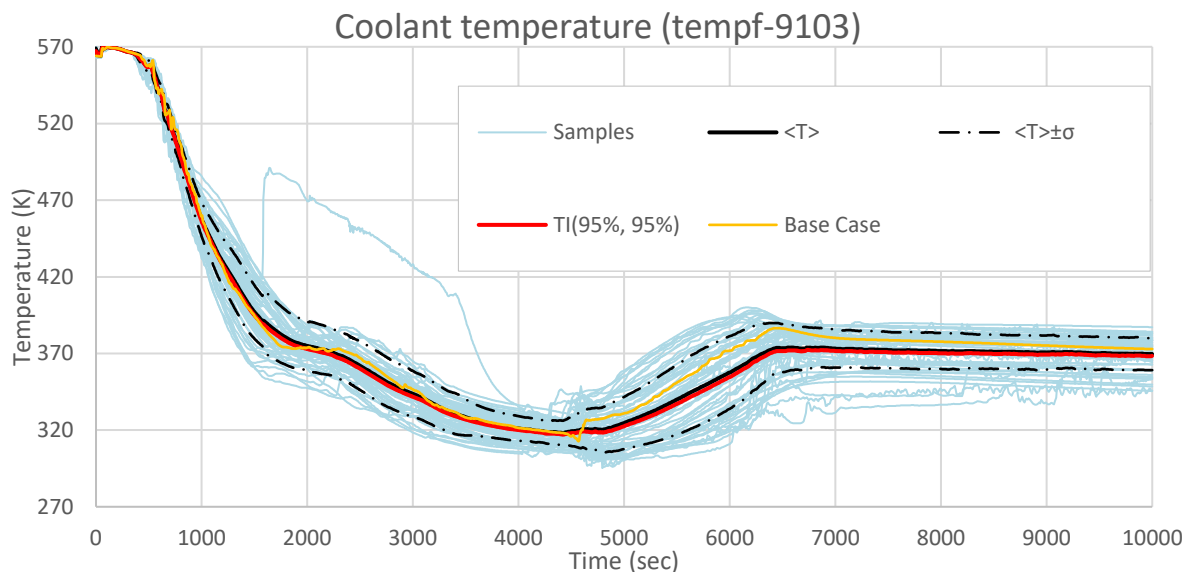
Figure 424: Coolant temperature (tempf-9103)
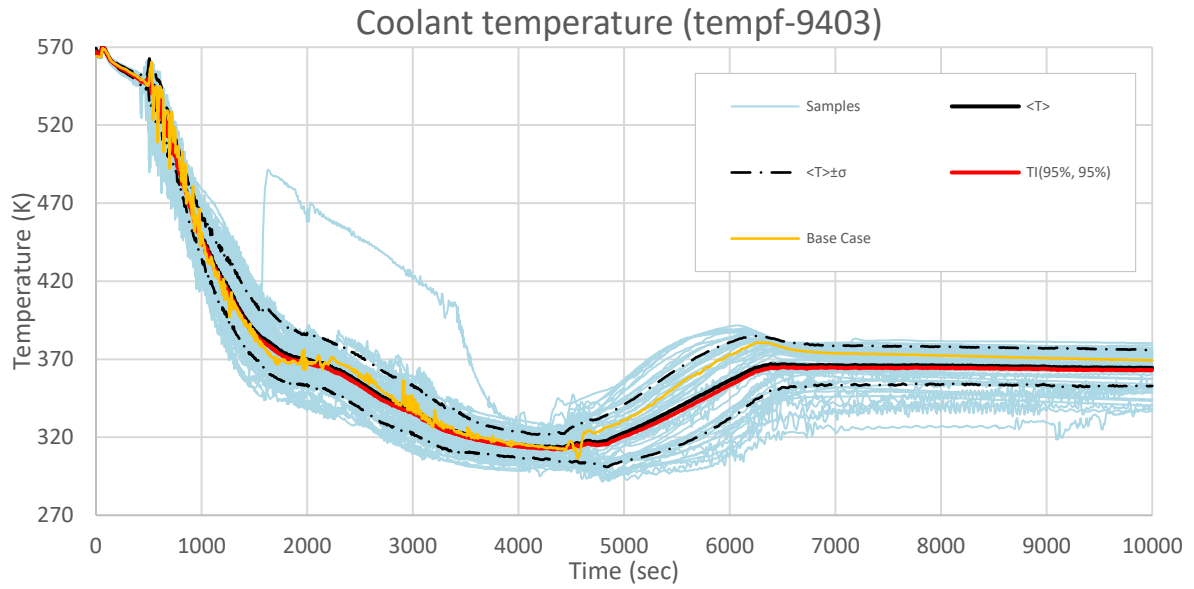
Figure 425: Coolant temperature (tempf-9403)
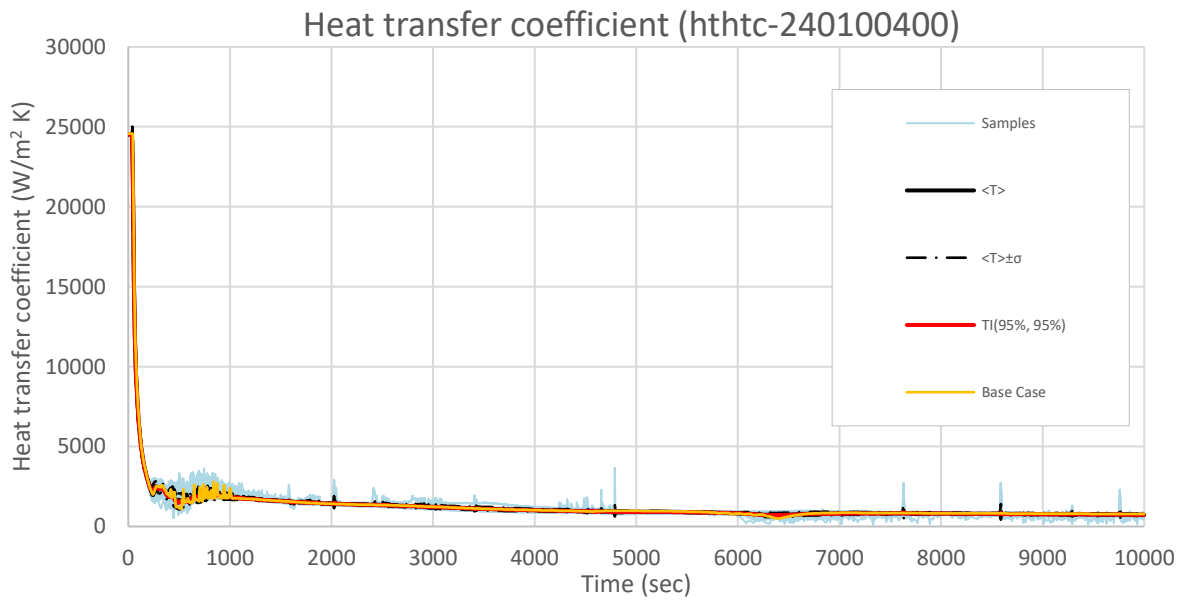
Figure 426: Heat transfer coefficient (hthtc-240100400)
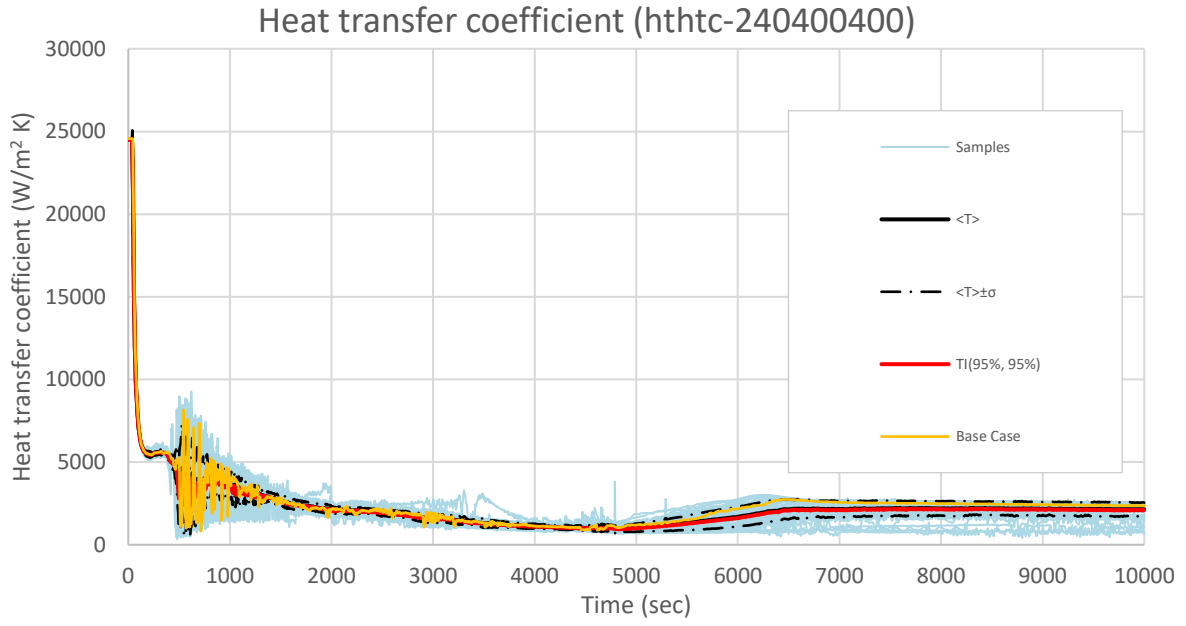
Figure 427: Heat transfer coefficient (hthtc-240100400)
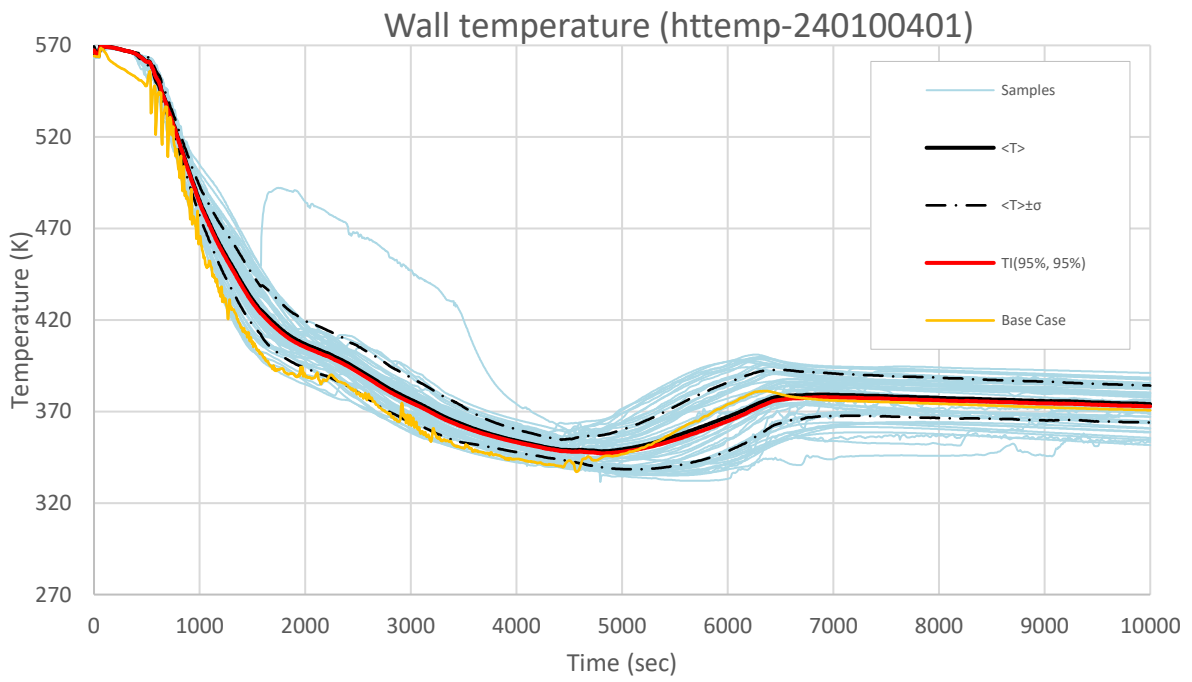
Figure 428: Heat transfer coefficient (hthtc-240400400)
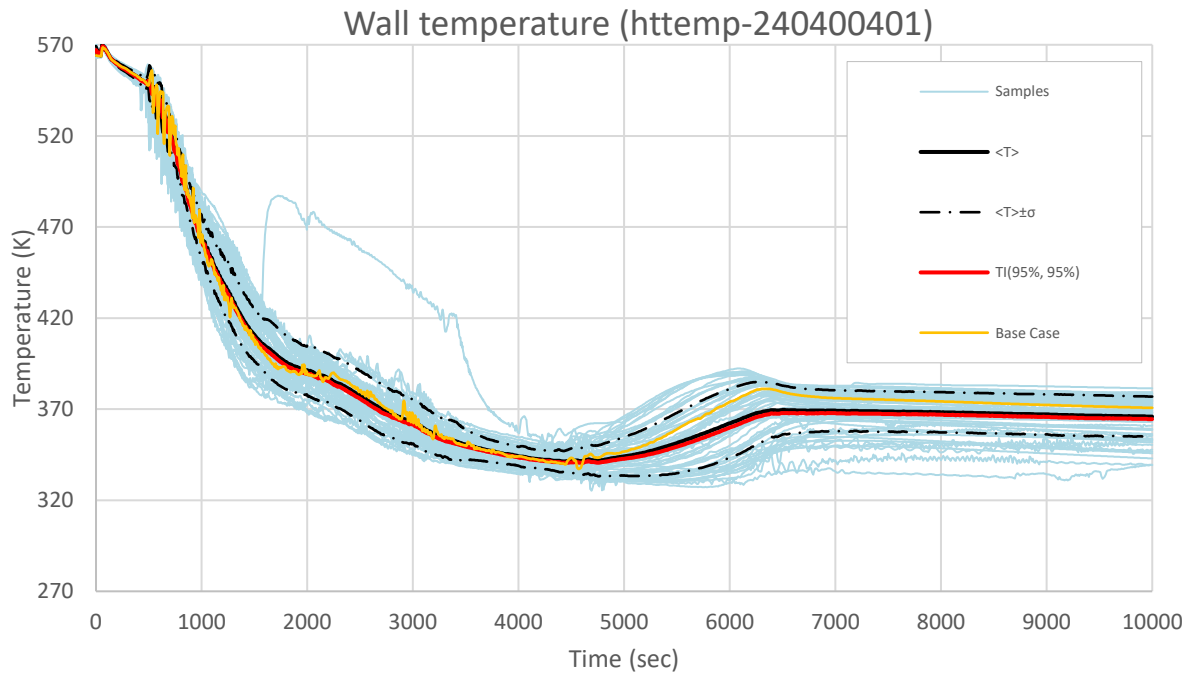
Figure 429: Wall temperature (httemp-240100401)

16.4 Sensitivity analysis

The results of sensitivity analysis of uncertainty parameters' influence on figures of merits (FOMs) are presented in this section. In this evaluation the Spearman's rank correlation was used. The following figures depict how the parameters (their probability/uncertainty) are correlated with six FOMs. In tables that follow the figures there is information about the mean value of the correlation (along the whole transient) and its standard deviation.

The influence of chosen uncertainty parameters depends on time of the transient. Three phases were distinguished for the purpose of this analysis that are of special importance for uncertainty parameters and their correlation with FOMs. These phases are:

a) Start of the transient: here there is much scatter, mixing and rapid large temperature and pressure gradients.

b) Transient until around 5000 seconds: by this time high pressure injection (85 sec), low pressure injection (4555 sec) and accumulators (2780 sec) provide RPV with full capacity with cold water.

c) Transient from 5000 sec to 10000 sec: at this stage of the transient the scenario is calmer and water level in pressurizer is fully recovered.

Table below summarizes findings of the analysis based on visual observation of the figures. It includes parameters that are strongly correlated with chosen FOMs. Parameter no 19 LP pump curve seems to have a substantial impact in all stages of the analysed scenario and for most of the FOMs. Another parameter which looks promising when it comes to LTO improvements is the parameter no 9 HPSI temperature. The parameter no 17 form loss coefficient seems to be much correlated with DC in the beginning of the transient.

FOM	Beginning of transient until ca 5000 sec	Transient from 5000 sec to 10000 sec
Pressure in downcomer (p-9105)	17 form loss coefficient	9 HPSI temperature 8 ACC nitro volume

314

Coolant temperature (tempf-9103)	Much scatter at the beginning 19 LP pump flow curve	19 LP pump flow curve 9 HPSI temperature
Coolant temperature (tempf-9403)	Much scatter at the beginning 19 LP pump flow curve	19 LP pump flow curve 9 HPSI temperature
Heat transfer coefficient (hthtc-240100400)	19 LP pump flow curve	16 Wall-drag coefficient
Heat transfer coefficient (hthtc-240400400)	19 LP pump flow curve 10 HP pump pressure pump	9 HPSI temperature
Wall temperature (httemp-240100401)	19 LP pump flow curve	19 LP pump flow curve 9 HPSI temperature
Wall temperature (httemp-240400401)	19 LP pump flow curve	19 LP pump flow curve 9 HPSI temperature

Figure 430: Sensitivity coefficients for pressure in downcomer and table summarizing mean and standard deviation values.

Figure 431: Sensitivity coefficients for pressure in coolant temperature (tempf-9103) and table summarizing mean and standard deviation values.
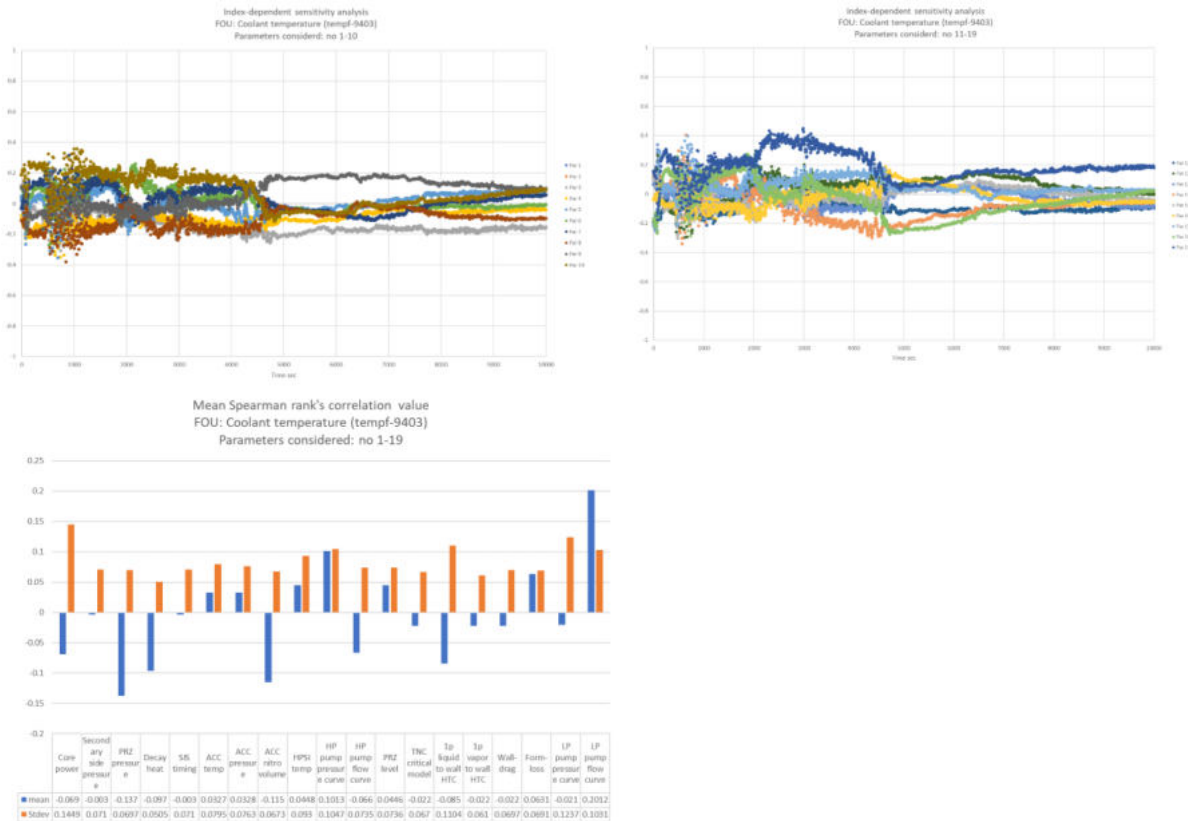
Figure 432: Sensitivity coefficients for pressure in coolant temperature (tempf-9403) and table summarizing mean and standard deviation values.

316

Figure 433: Sensitivity coefficients for heat transfer coefficient (hthtc-240100400) and table summarizing mean and standard deviation values.

Figure 434: Sensitivity coefficients for heat transfer coefficient (hthtc-240400400) and table summarizing mean and standard deviation values.

317
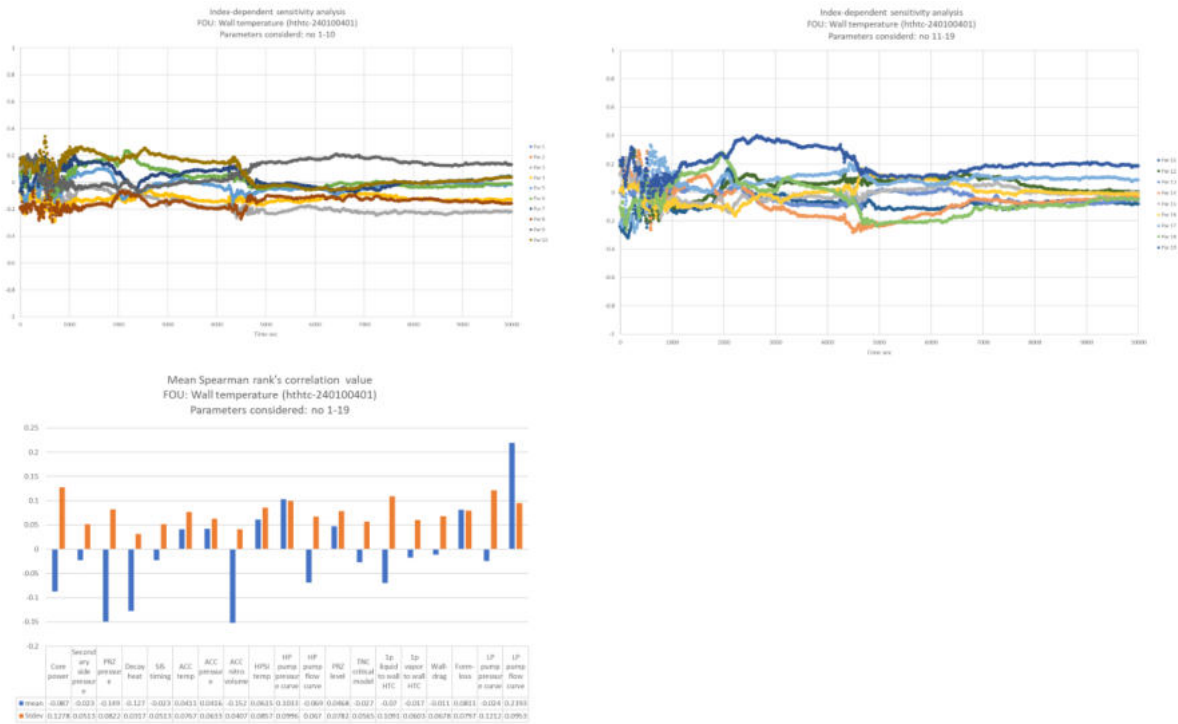
Figure 435: Sensitivity coefficients for wall temperature (hthtc-240100401) and table summarizing mean and standard deviation values.
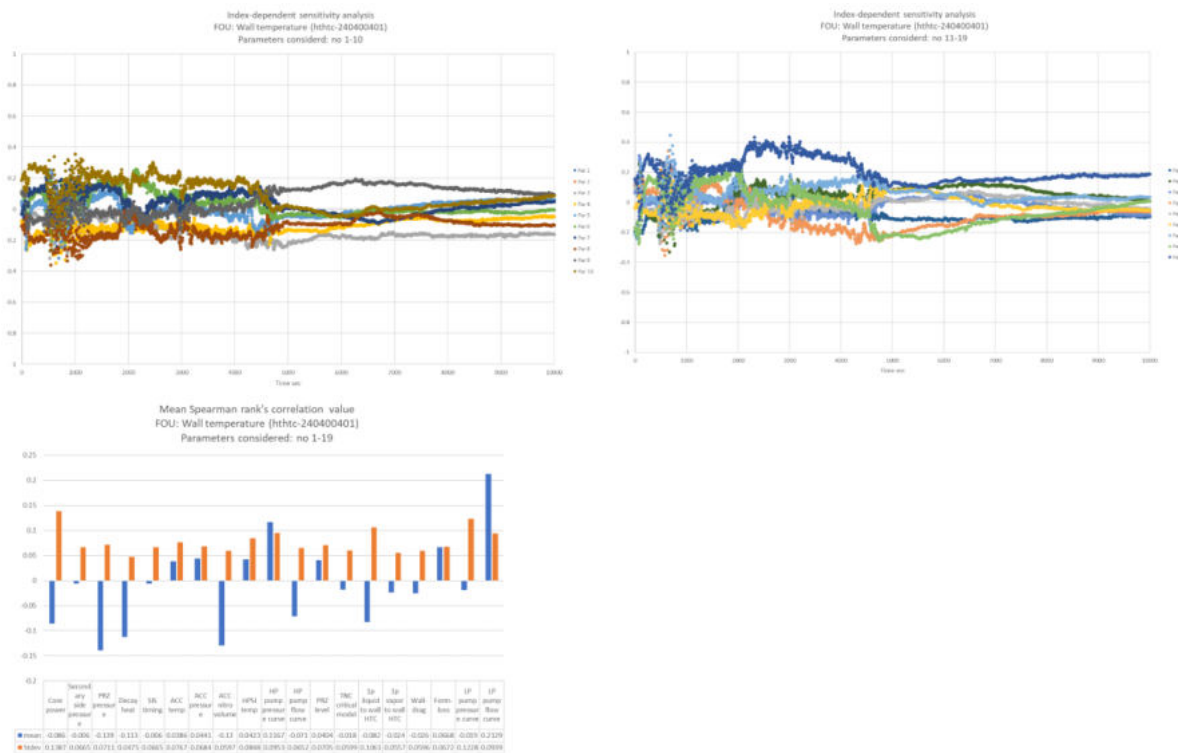
Figure 436: Sensitivity coefficients for wall temperature (hthtc-240400401) and table summarizing mean and standard deviation values.

318

17 SSTC uncertainty analysis with RELAP5 and SUSA

17.1 Reference best-estimate calculation

Uncertainty analysis was performed with KWU model (input deck identification number "kwu76"), which was previously used in Task 2.1 of APAL project. To perform uncertainty analysis some minor modifications of the input deck were made, in particular:

- "Artificial" controllers for regulation of primary pressure and pressurizer level were implemented in the model to provide adjustment of this parameters during steady state calculation;
- In order to adjust initial nitrogen volume in the hydro accumulators their nodalization of upper part of the ACC vessel was slightly modified (following the UJV proposal during task meetings);
- Based on the preliminary calculations temperature and heat capacity ranges of the fuel material were slightly extended to prevent calculation errors.

To assess the impact of the implemented changes, a comparison was made between the calculation results of the Task 2.1 base scenario and results of calculations performed with modified model (which included mentioned above modifications). Calculations were performed with RELAP5/MOD33 ("lf" version). Obtained results demonstrate that performed modification of the input deck do not provide visible impact on the results of base calculation during time interval 4900 s, which was investigated in the framework of Task 2.1 (see Figure 437(a, b), Figure 438 (b), Figure 439 (a)). Further modified Task 2.1 model was slightly adjusted for nominal/average parameters of the reference reactor facility to perform best-estimate calculation. Comparison of all calculation results demonstrate some difference in break flows of best estimate scenario (see Figure 437(b)), which slightly affects transient progression.

Due to different break flow in modified base case and reference best estimate calculation some other parameters also differs. The differences can be seen in the collapsed liquid levels (see Figure 438 (a,b)), what could be related to the changes in decay heat coefficient (which was set to 1.0 in comparison with Task 2.1 calculation, where conservative value was used) and temperature of ECCS tanks (which was changed for best-estimate calculation from minimum to nominal value).

In general, obtained results of best-estimate reference calculation are qualitatively comparable to base case calculation (Task 2.1) and applicable for uncertainty evaluation. The reasons for the identified minor differences are explained above. Results of the reference best-estimate calculation are presented below at Figure 437 - Figure 445.

(a)   (b)
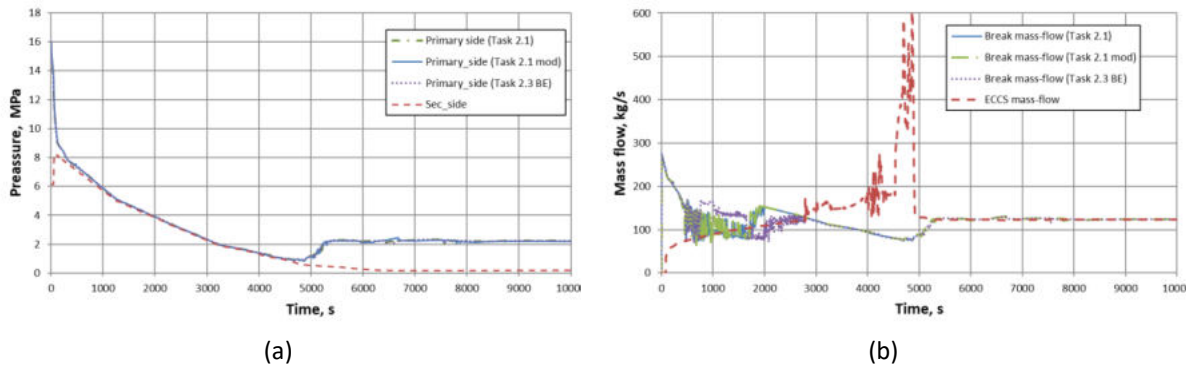
Figure 437: Primary and secondary (SG1) pressure (a) and break & total ECCS flow rate (b)

(a)   (b)
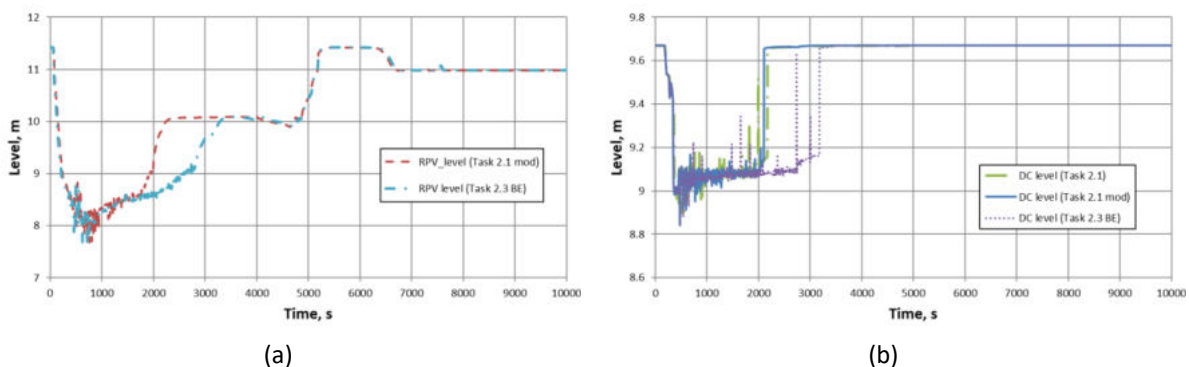
Figure 438: Level in the reactor (a) and downcomer (b)

(a)　　　　　　　　　　　　　　　　　　　　　　(b)
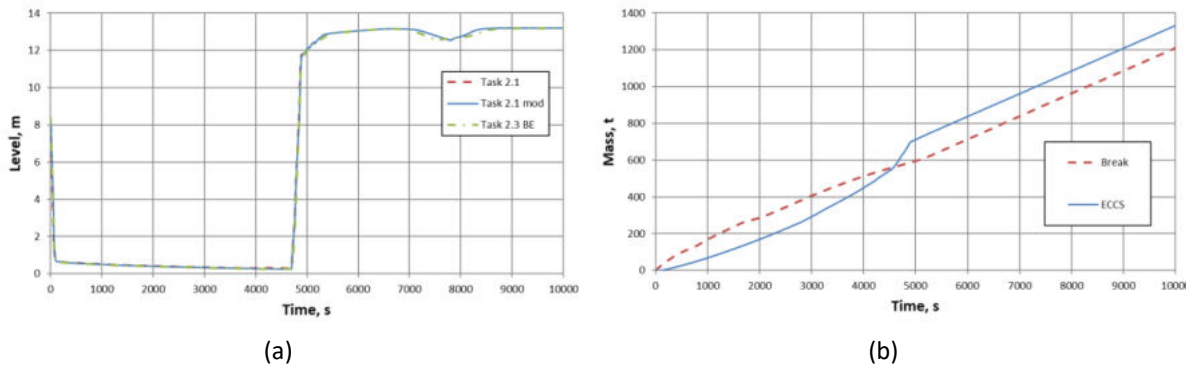
Figure 439: PRZ level (a) and integrated break and ECCS flow (b)

(a)　　　　　　　　　　　　　　　　　　　　　　(b)
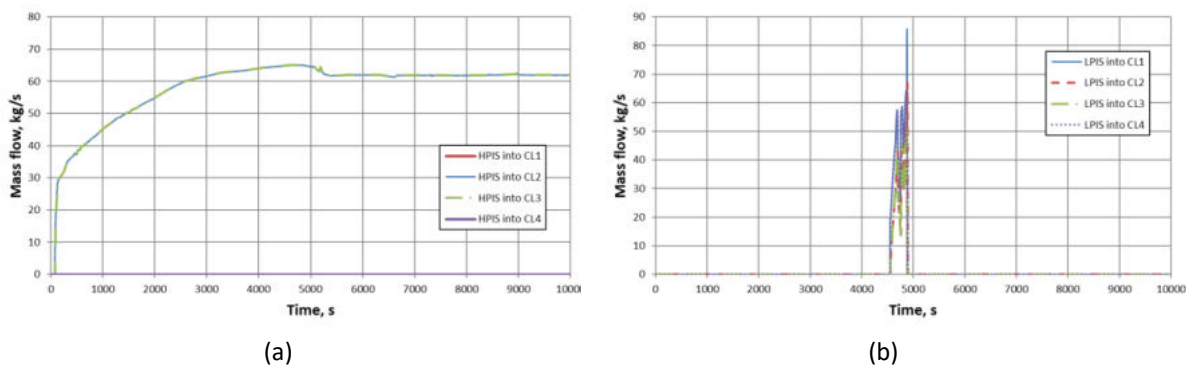
Figure 440: HPIS (a) and LPIS (b) mass flow

(a)　　　　　　　　　　　　　　　　　　　　　　(b)
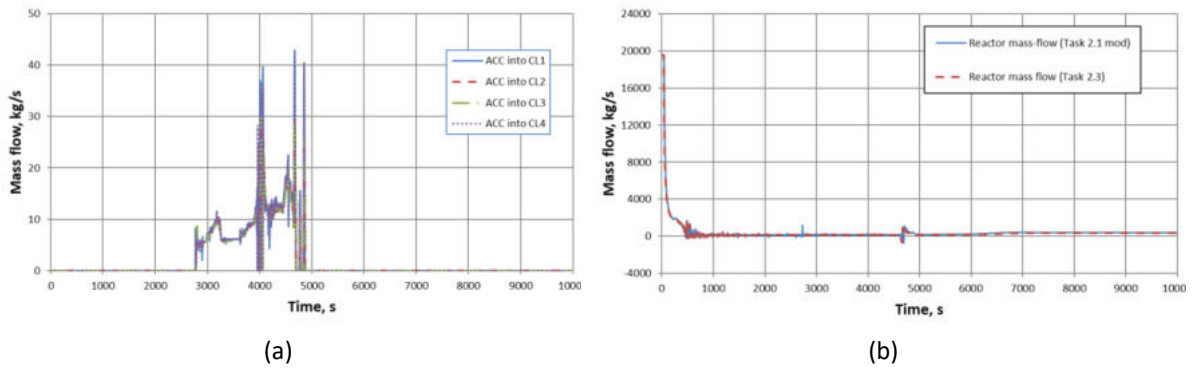
Figure 441: ACC mass flow (a) and reactor mass flow though lover plenum (b)

(a)　　　　　　　　　　　　　　　　　　　　　　(b)
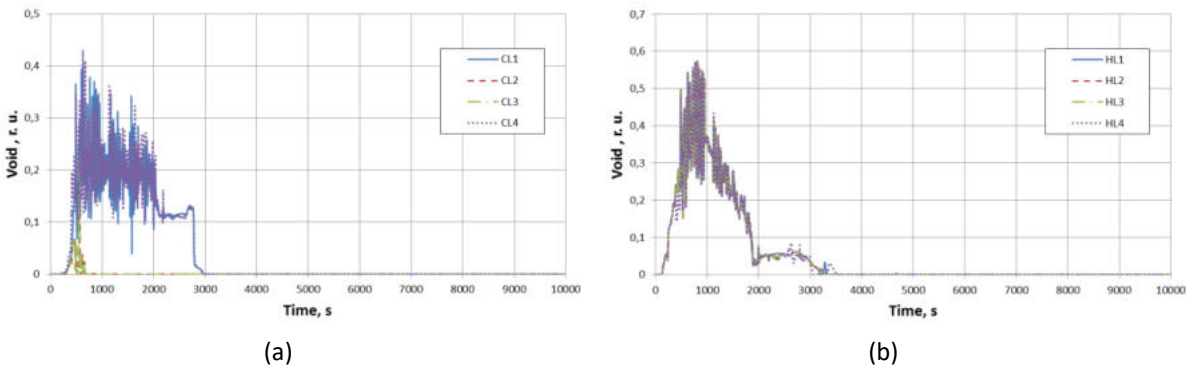
Figure 442: Void Fraction at reactor inlet (a) and outlet (b) nozzles

(a)   (b)
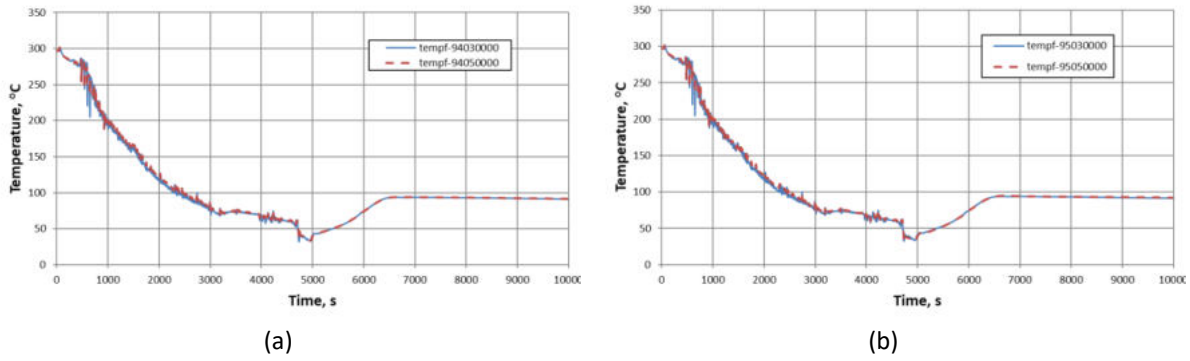
Figure 443: Coolant temperature in DC (elev. 1.13 m and 2.638 m) under CL2 (a) and CL3 (b)

(a)   (b)
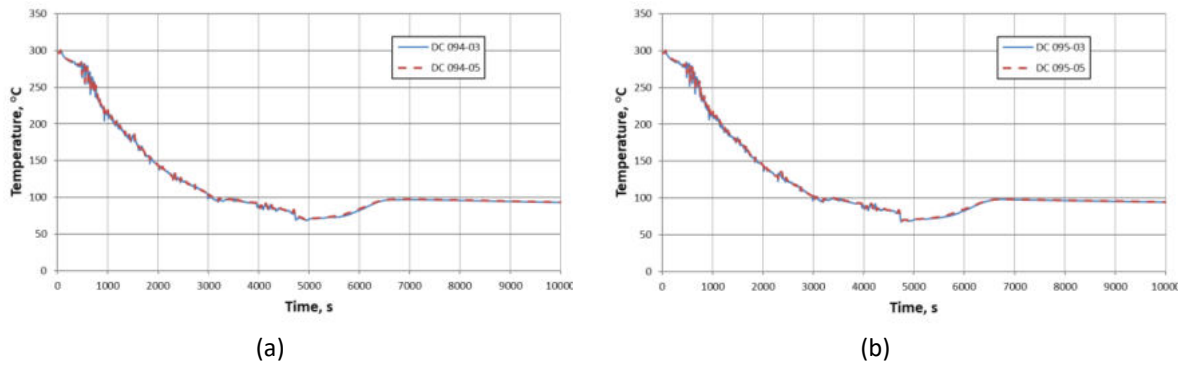
Figure 444: Temperature of RPV inner surface (elev. 1.13 m and 2.638 m) under CL2 (a) and CL3 (b)

(a)   (b)
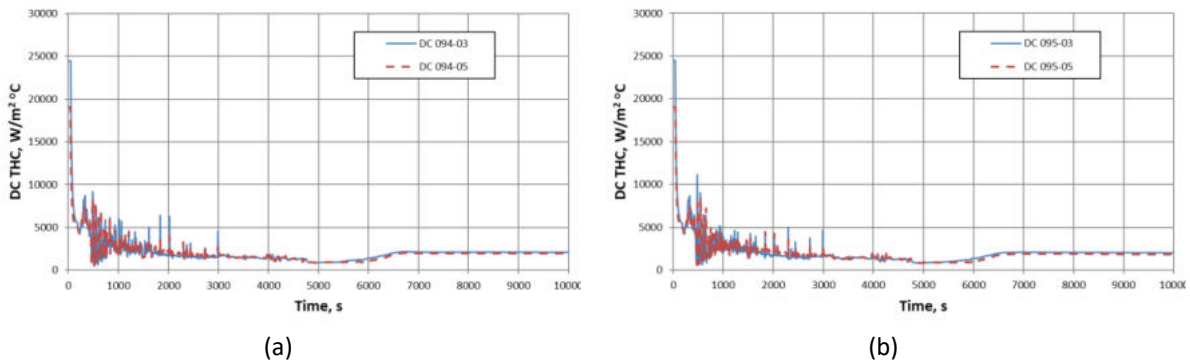
Figure 445: HTC at RPV inner surface (elev. 1.13 m and 2.638 m): under CL2 (a) and CL3 (b)

17.2 Input uncertainties

The list of input parameters, used for uncertainty analysis, was chosen based on the results of Task 2.2 taking into account possibilities of applied thermal hydraulic code (Relap5/MOD3.3, version "lf"). Generation of the parameter values, which were implemented into the input deck, was performed with SUSA 4.2.5 software. A total number of 14 input parameters were used in the analysis. SUSA was used to generate parameter values for 59 Relap5 input files. All 59 steady state input decks were generated automatically (by SUSA). Restart files were prepared manually. Each restart file contained a unique pressure-flow characteristic of the ECCS pumps, which was obtained by multiplying the design curves by the coefficients generated by the SUSA individually for pressure and flow values Table 49 below provides information about chosen uncertainty parameters used for the study. For each parameter nominal value (i.e. the values used in the reference best estimate calculation) as well as type of distribution and distribution parameters together with minimum and maximum values of the parameters are given.

321

Table 49: Uncertainty parameters for SUSA

Parameter Name	Best estimate value	Distribution			Min	Max
		Type	Parameter 1	Parameter 2		
Core power (W)	3.77E+09	Normal	3.765E+09	3.765E+07	3.727E+09	3.803E+09
Decay heat	1	Uniform	1	1.1	1	1.1
Pressurizer (primary) pressure (Pa)	1.57E+07	Normal	1.57E+07	157400	1.56E+07	1.59E+07
Secondary side pressure (Pa)	6020000	Uniform	6020000	6820000	0.340*	0.256*
Timing of SIS actuation (s)	10	Uniform	0	20	0	20
ACC injection temperature (K)	303.15	Uniform	293.15	313.15	293.15	313.15
ACC initial pressure (Pa)	2600000	Uniform	2400000	2800000	2.40E+06	2.80E+06
ACC nitrogen volume (m3)	3.9796	Uniform	9.63	12.57	1.215	1.586
HPIS temperature (K)	303.15	Uniform	288.15	318.15	288.15	318.15
Initial pressurizer level (m)	8.21	Uniform	7.71	8.71	7.71	8.71
HPI pressure curve	1	Normal	1	0.1	0.9	1.1
HPI flow curve	1	Normal	1	0.1	0.9	1.1
LPI pressure curve	1	Normal	1	0.1	0.9	1.1
LPI pressure curve	1	Normal	1	0.1	0.9	1.1
* secondary side pressure was adjusted by variation of the cross-section of turbine regulation valve						

17.3 Results of BEPU analyses

Thermal hydraulic calculations have been performed with RELAP5/MOD3.3 version 'lf'. Results of sampled 59 calculations to yield 95%/95% one-sided tolerance bound are presented in Figure 446 - Figure 454 below.
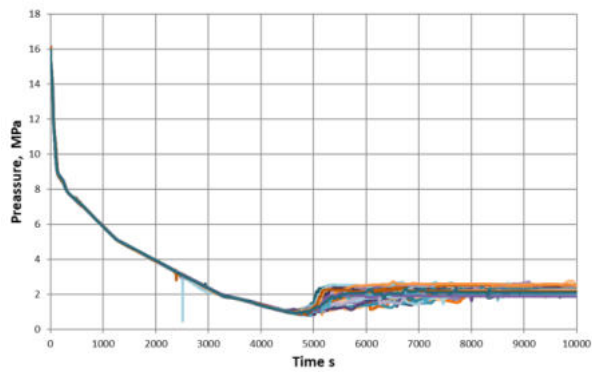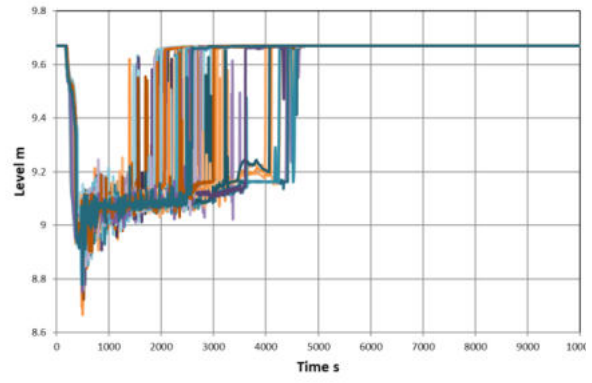
(a)   (b)

Figure 446: Primary pressure (a) and DC level (b)
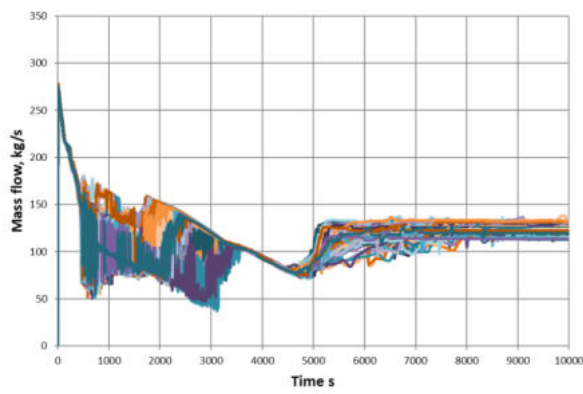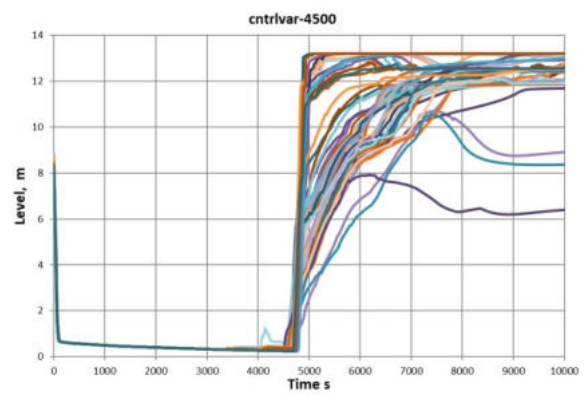
(a)   (b)

Figure 447: Break mass flow (a) and PRZ level (b)
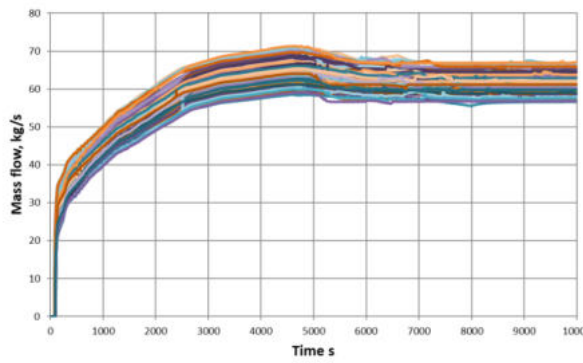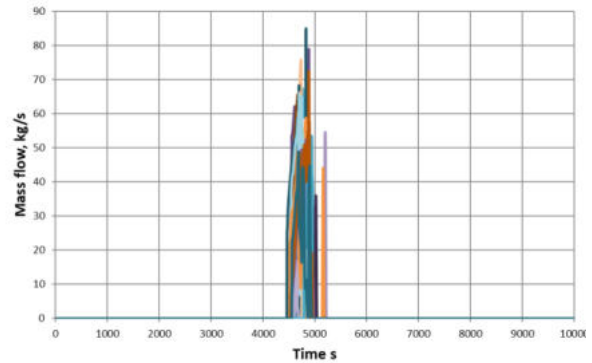
(a)   (b)

Figure 448: HPIS (a) and LPIS mass flow

323

(a)   (b)
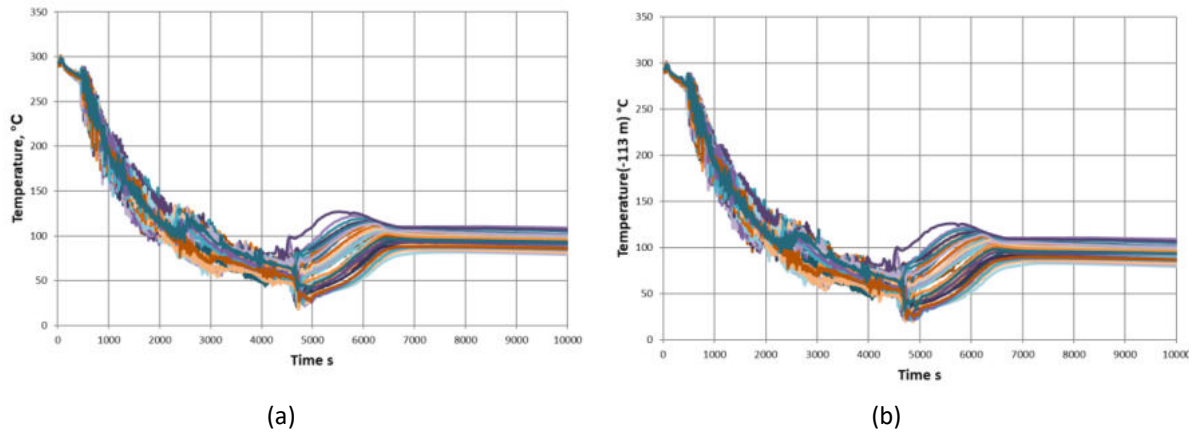
Figure 449: Coolant temperature in DC (elev. 1.13) under CL2 (a) and CL3 (b)

(a)   (b)
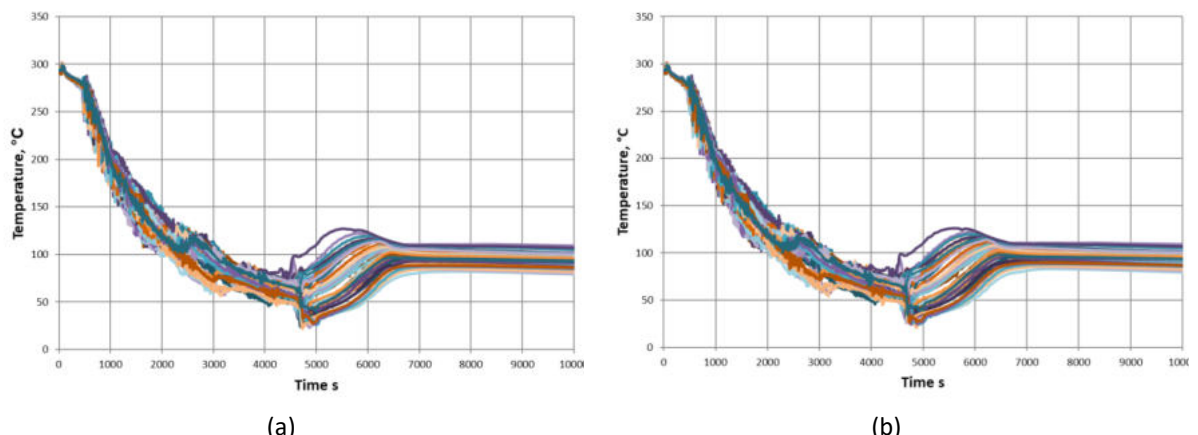
Figure 450: Coolant temperature in DC (elev. 2.638 m) under CL2 (a) and CL3 (b)

(a)   (b)
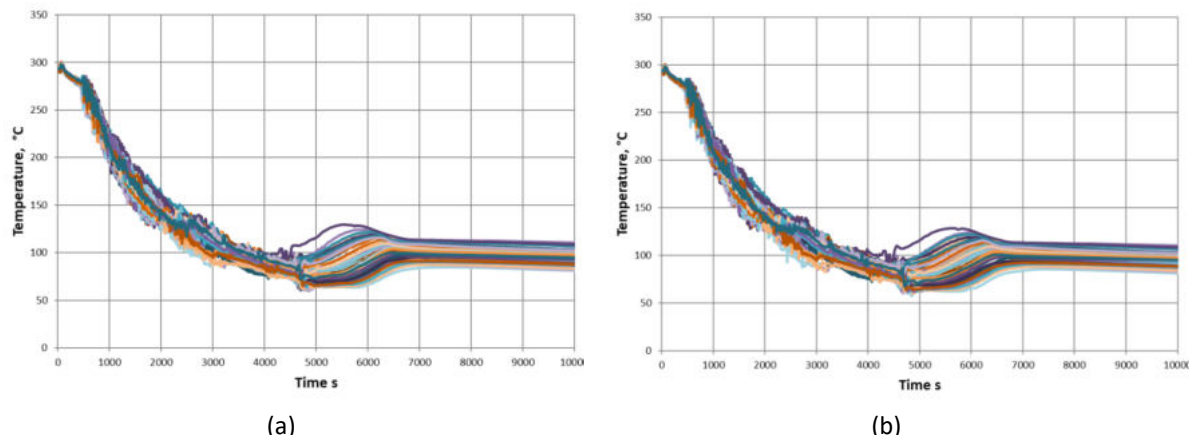
Figure 451: RPV wall temperature (elev. 1.13) under CL2 (a) and CL3 (b)

(a)   (b)
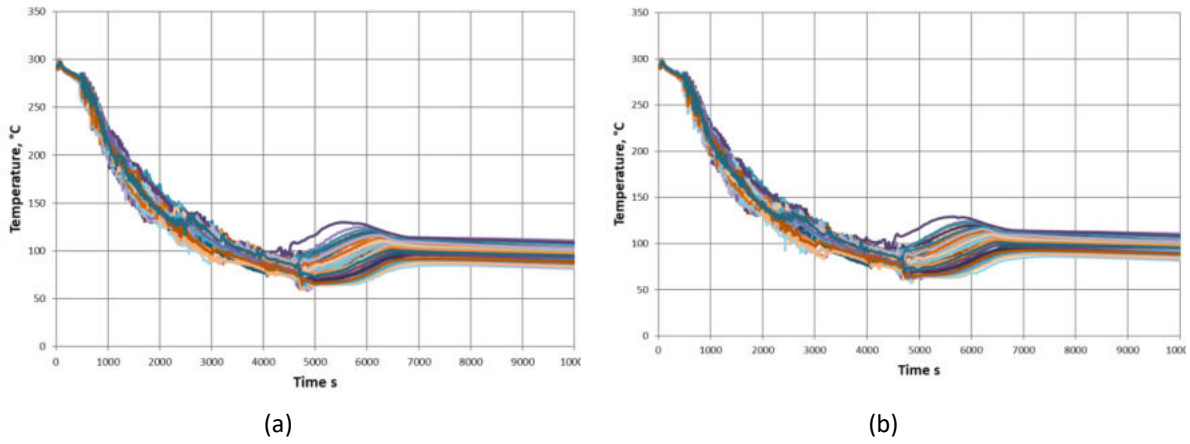
Figure 452: RPV wall temperature (elev. 2.638 m) under CL2 (a) and CL3 (b)

(a)   (b)
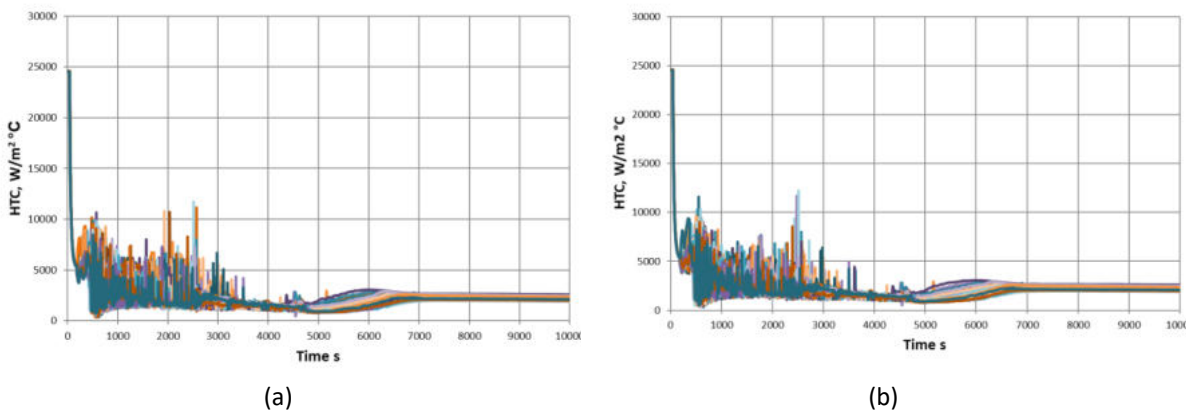
Figure 453: HTC at RPV inner surface (elev. 1.13 m): under CL2 (a) and CL3 (b)

(a)   (b)
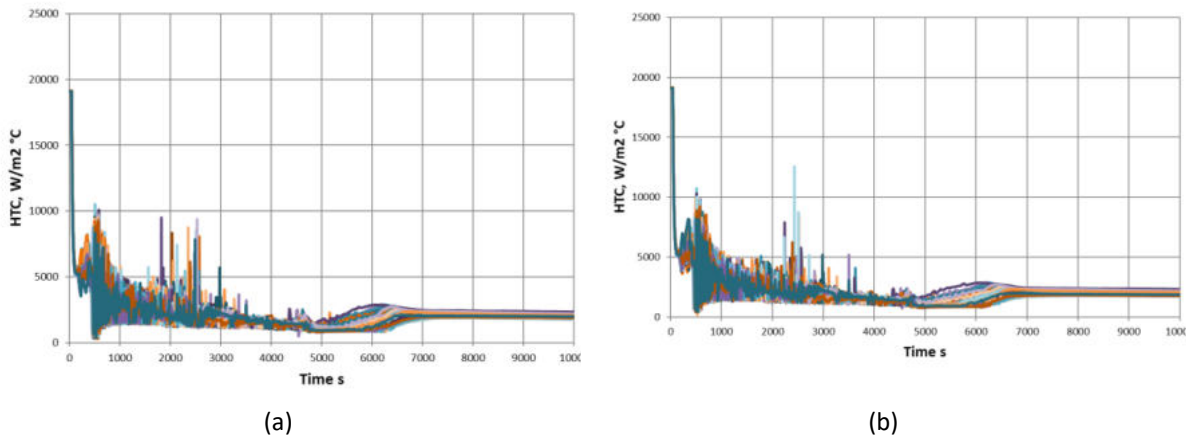
Figure 454: HTC at RPV inner surface (elev. 2.638 m): under CL2 (a) and CL3 (b)

325

18   JAEA uncertainty analysis with RELAP5 and in-house tool

JAEA has conducted uncertainty analysis employing RELAP5/MOD3.3 code (Patch 2 -version 3.3ef). Some modifications were done to the input data that have been provided by UJV, to better match the defined boundary conditions.

Table 50 lists the input uncertainty parameter, lower and upper bounds, and type of distribution. The input uncertainty parameters of No.1 to No.6 are the plant parameters. The parameter of No.7 is a parameter related to the human interaction. The remaining parameters of No.8 to No.11 are parameters relevant to the computer code and model. The lower and upper bounds of the parameters are generally based on the recommended values. Additionally, JAEA has performed some sensitivity analyses to finalize the definition of the lower and upper bounds of the parameters. Figure 455 through Figure 476 show effects of the individual uncertainty parameters on typically the primary pressure (DC) and the coolant temperature at 1.350 m under CL1 up to 6000 s after the break. The HPI injection temperature, HPI pump pressure curve, HPI pump flow curve, cooldown rate, and form-loss coefficient for single-phase vapor have great effects on the primary pressure (DC) and the coolant temperature at 1.350 m under CL1. By contrast, the core power, decay heat, ACC injection temperature, single-phase liquid to wall HTC, single-phase vapor to wall HTC, form-loss coefficient for single-phase liquid has some effects on the primary pressure (DC) and the coolant temperature at 1.350 m under CL1.

JAEA has used the in-house tool as a statistical tool to prepare 59 sets of TH data. This accounts for a 95% probability and 95% confidence level according to Wilks method for one-sided statistical tolerance limits. A random value for each set of the parameters is generated by LHS (Latin Hypercube Sampling).

The evaluation time for the uncertainty analysis is up to 10000 s after the break. Lists of figures from Figure 477 through Figure 483 is as follows; primary pressure (DC), coolant temperature at 1.350 m under CL1, coolant temperature at 1.350 m under CL2, HTC at RPV wall at 1.350 m under CL1, HTC at RPV wall at 1.350 m under CL2, inner RPV wall temperature at 1.350 m under CL1, and inner RPV wall temperature at 1.350 m under CL2. The HTCs at RPV wall at 1.350 m under CL1 and CL2 have large oscillation during certain time periods. The difference of the lower and upper bounds was relatively large for the primary pressure, the coolant temperature, and the wall temperature until around 6500 s after the actuation of the HPI system. The difference of the lower and upper bounds was almost constant thereafter.

Table 50: Input uncertainty parameters

	Parameter	Lower bound	Upper bound	Type of distribution
1	Core power	97%	103%	Gaussian
2	Decay heat	ans79	ans79+20%	Uniform
3	ACC injection temperature	20°C	40°C	Uniform
4	HPI injection temperature	20°C	40°C	Uniform
5	HPI pump pressure curve	90%	100%	Gaussian
6	HPI pump flow curve	90%	100%	Gaussian
7	Cooldown rate	95K/h	105K/h	Uniform
8	Single-phase liquid to wall HTC	0.8	1.2	Log-uniform
9	Single-phase vapor to wall HTC	0.8	1.2	Log-uniform
10	Form-loss coefficient for single-phase liquid	0.5	2.0	Log-uniform
11	Form-loss coefficient for single-phase vapor	0.5	2.0	Log-uniform
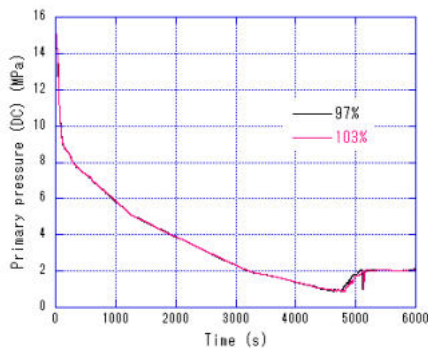
Figure 455: Core power versus primary pressure (DC)
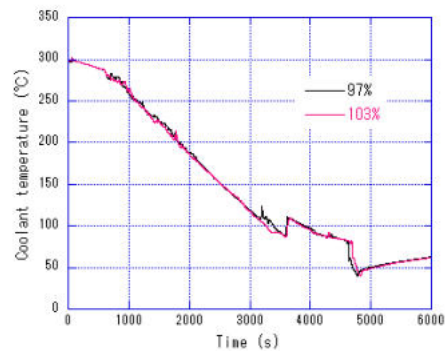
Figure 456: Core power versus coolant temperature at 1.350 m under CL1
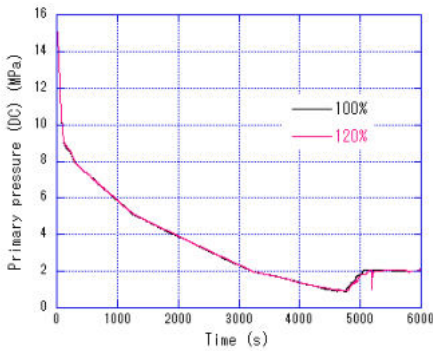
Figure 457: Decay heat versus primary pressure (DC)
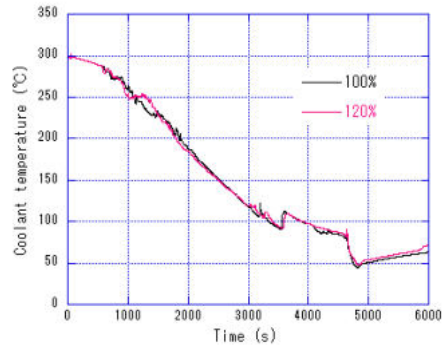
Figure 458: Decay heat versus coolant temperature at 1.350 m under CL1
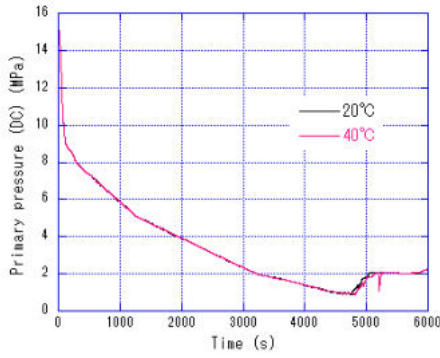
Figure 459: ACC injection temperature versus primary pressure (DC)
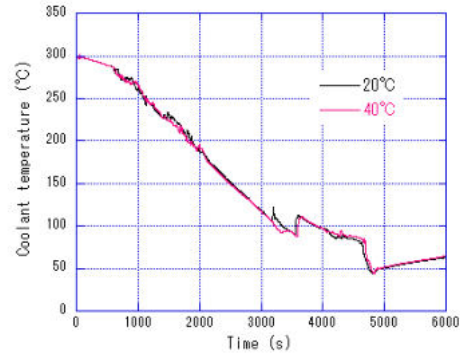
Figure 460: ACC injection temperature versus coolant temperature at 1.350 m under CL1
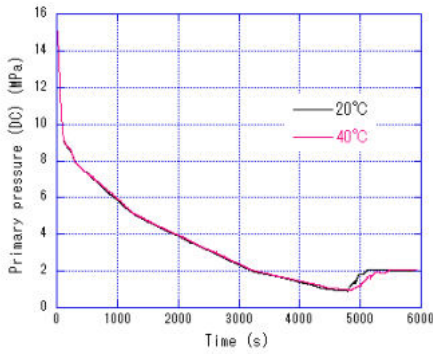
Figure 461: HPI injection temperature versus primary pressure (DC)
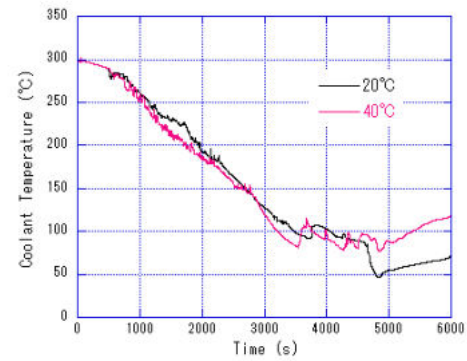
Figure 462: HPI injection temperature versus coolant temperature at 1.350 m under CL1
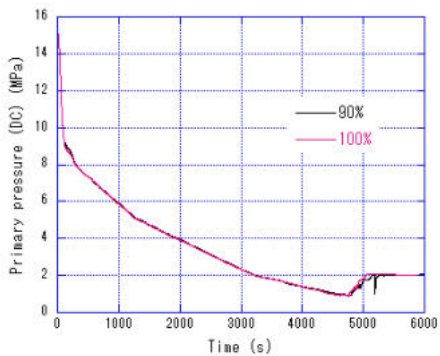
Figure 463: HPI pump pressure curve versus primary pressure (DC)
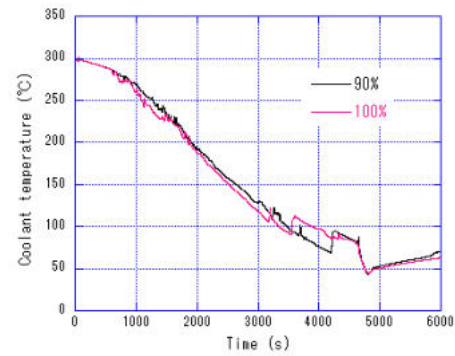
Figure 464: HPI pump pressure curve versus coolant temperature at 1.350 m under CL1

328
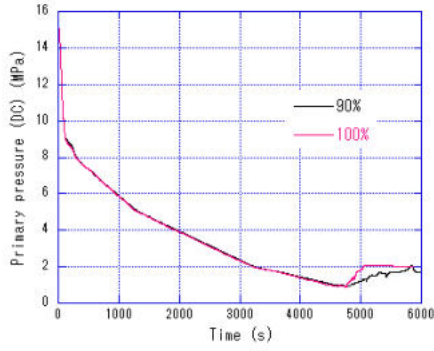
Figure 465: HPI pump flow curve versus primary pressure (DC)
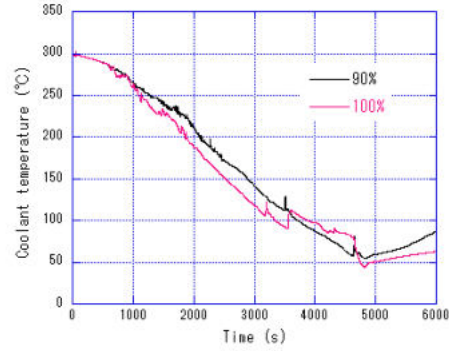
Figure 466: HPI pump flow curve versus coolant temperature at 1.350 m under CL1
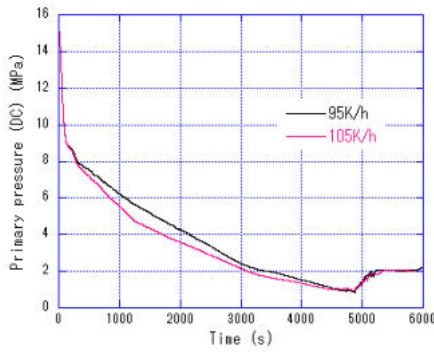
Figure 467: Cooldown rate versus primary pressure (DC)
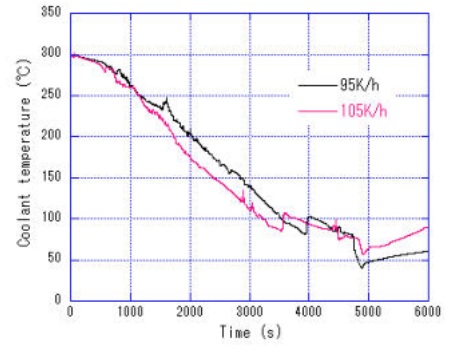
Figure 468: Cooldown rate versus coolant temperature at 1.350 m under CL1
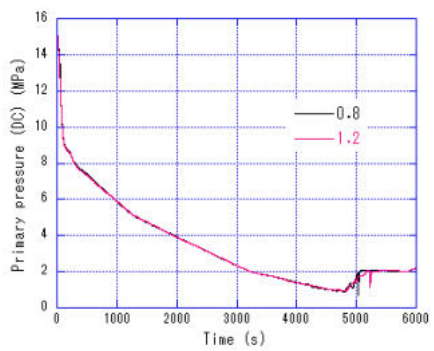
Figure 469: Single-phase liquid to wall HTC versus primary pressure (DC)
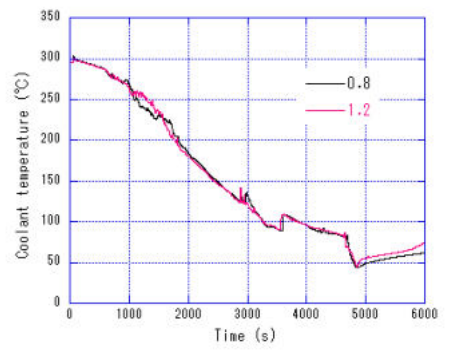
Figure 470: Single-phase liquid to wall HTC versus coolant temperature at 1.350 m under CL1
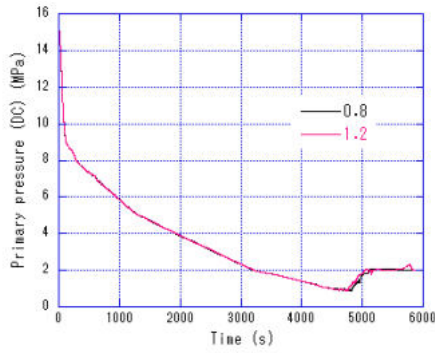
Figure 471: Single-phase vapor to wall HTC versus primary pressure (DC)
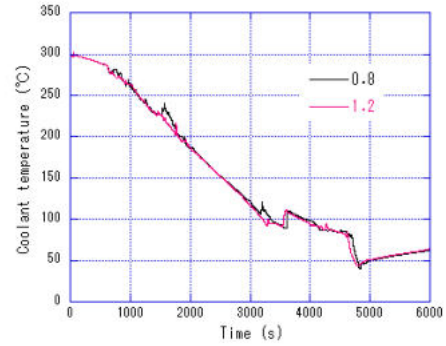
Figure 472: Single-phase vapor to wall HTC versus coolant temperature at 1.350 m under CL1
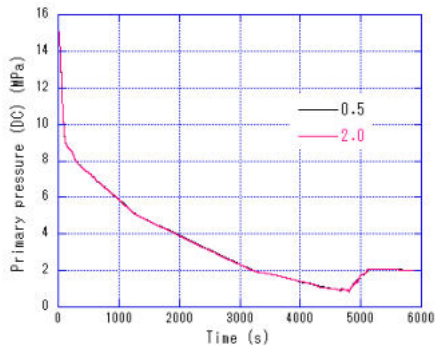
Figure 473: Form-loss coeff. for single-phase liquid versus primary pressure (DC)
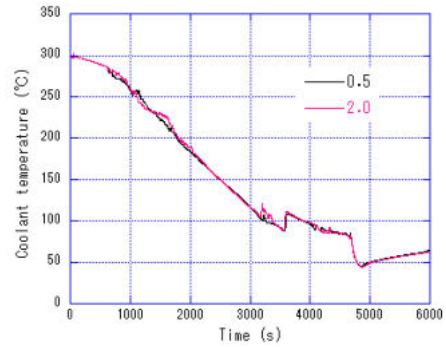
Figure 474: Form-loss coeff. for single-phase liquid versus coolant temperature at 1.350 m under CL1
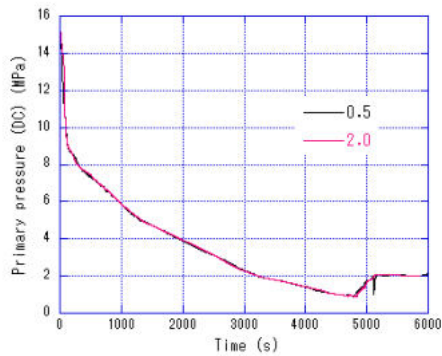
Figure 475: Form-loss coeff. for single-phase vapor versus primary pressure (DC)
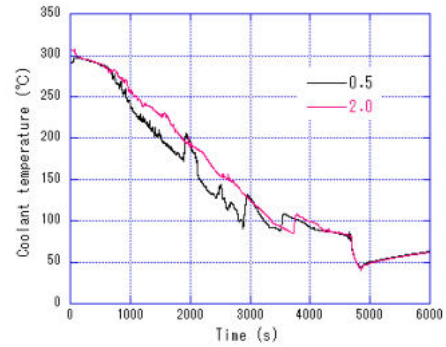
Figure 476: Form-loss coeff. for single-phase vapor versus coolant temperature at 1.350 m under CL1
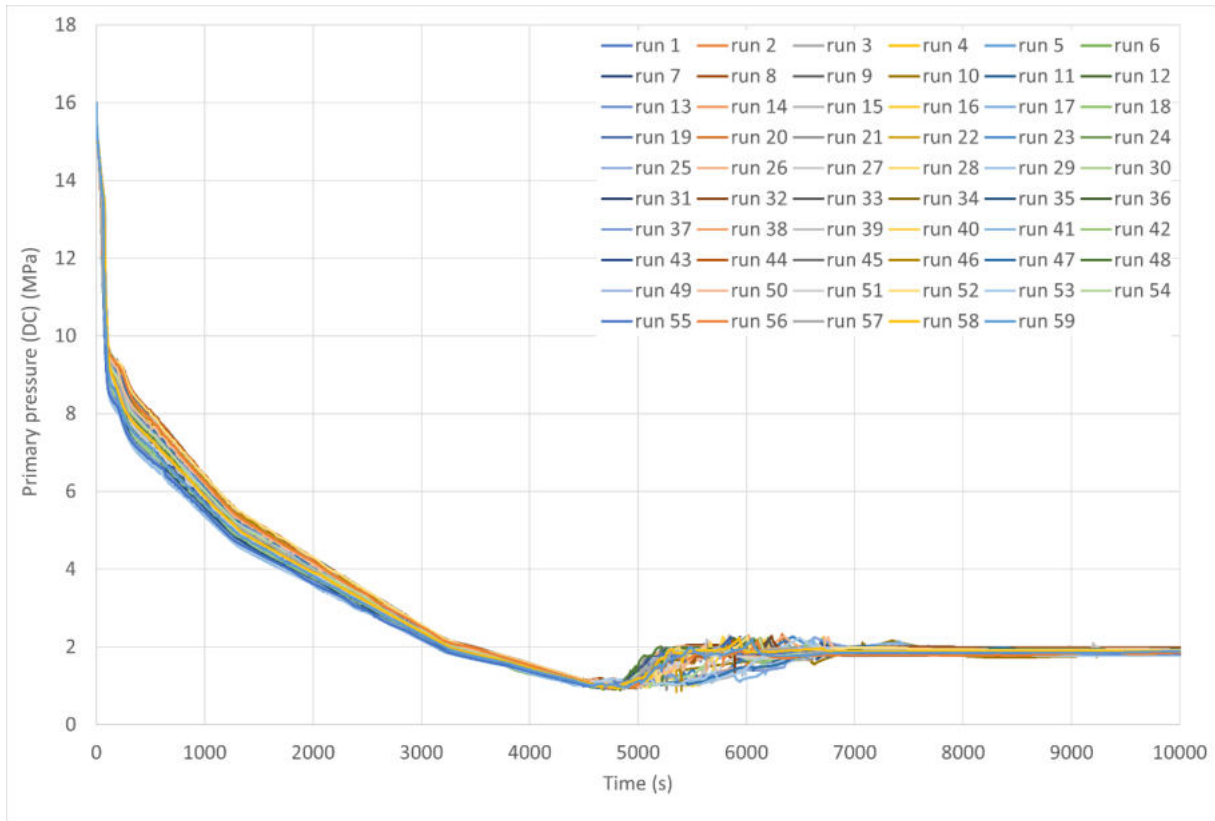
Figure 477: Primary pressure (DC)
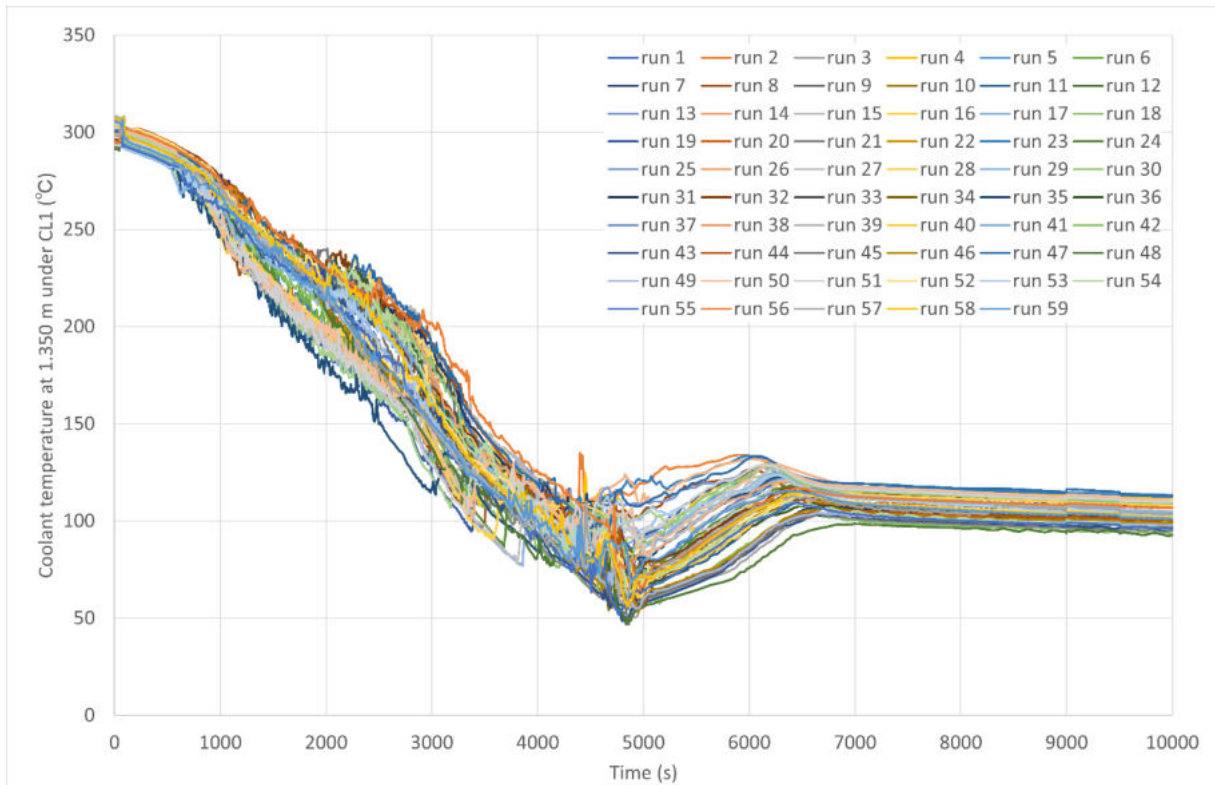
Figure 478: Coolant temperature at 1.350 m under CL1
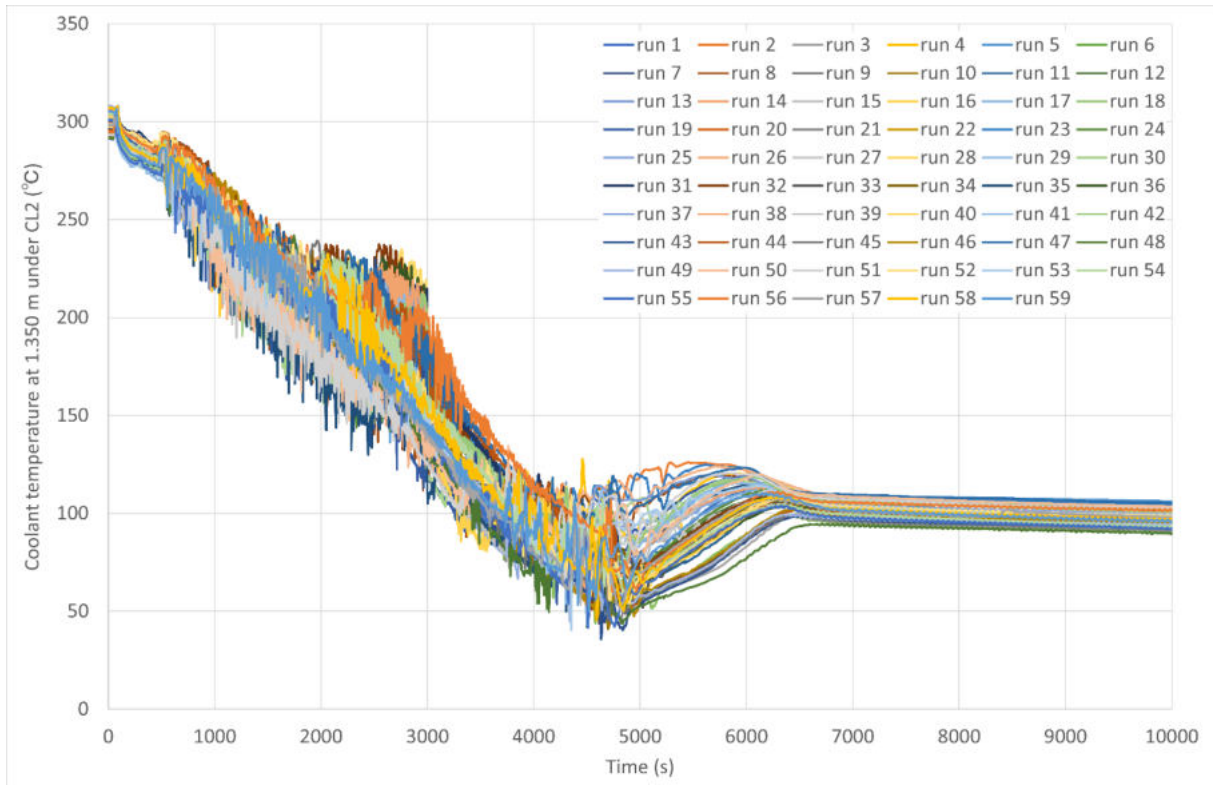
Figure 479: Coolant temperature at 1.350 m under CL2
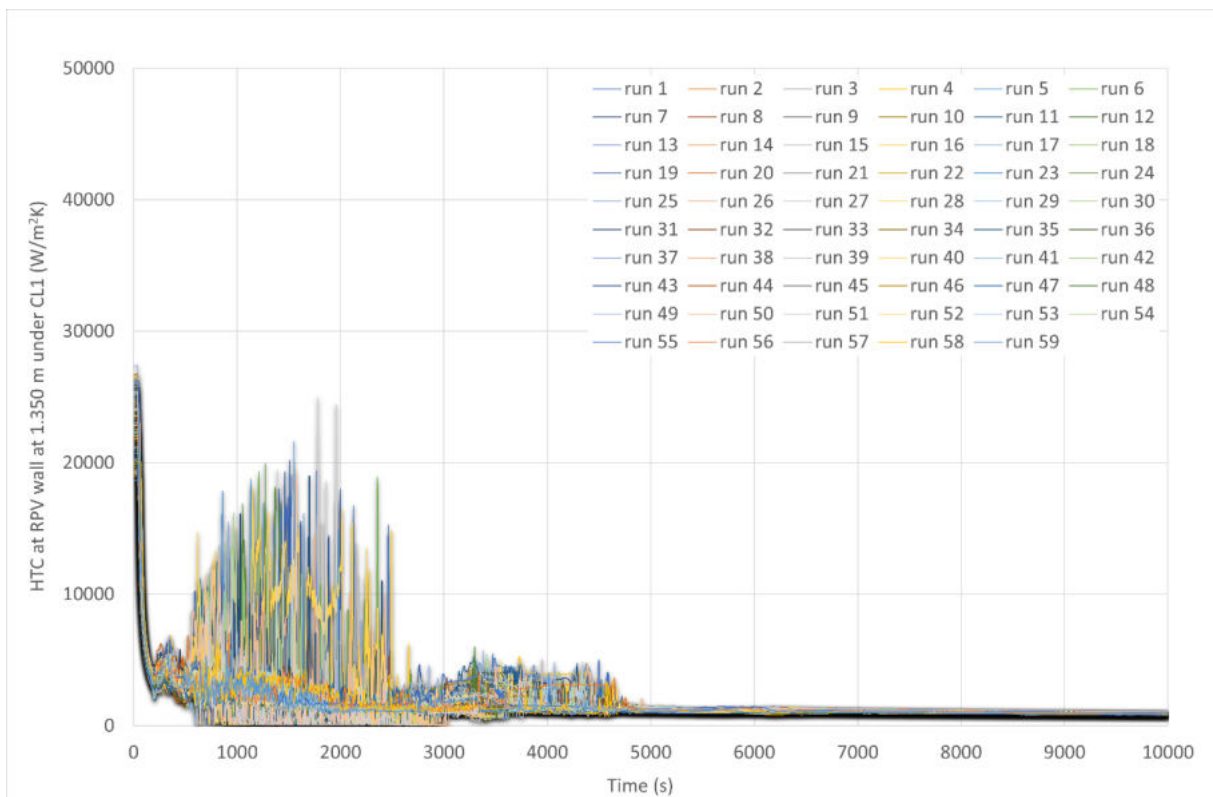
Figure 480: HTC at RPV wall at 1.350 m under CL1
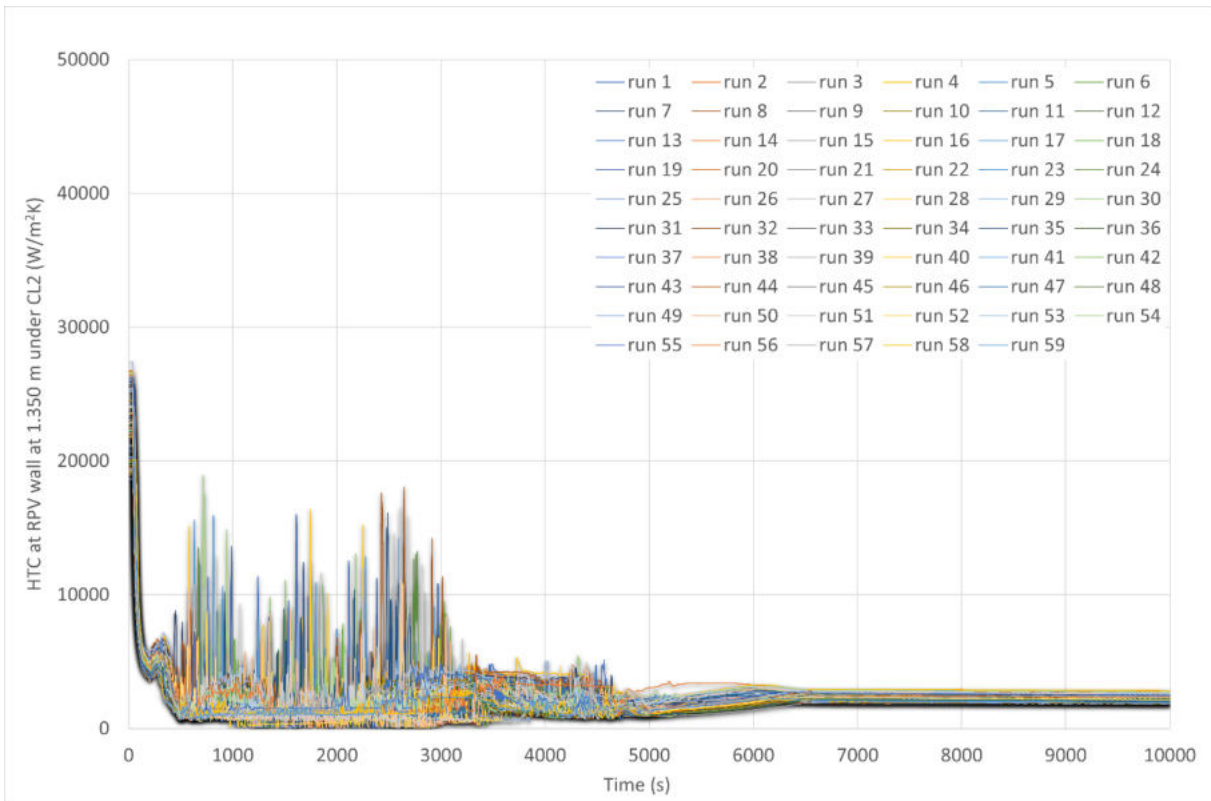
Figure 481: HTC at RPV wall at 1.350 m under CL2
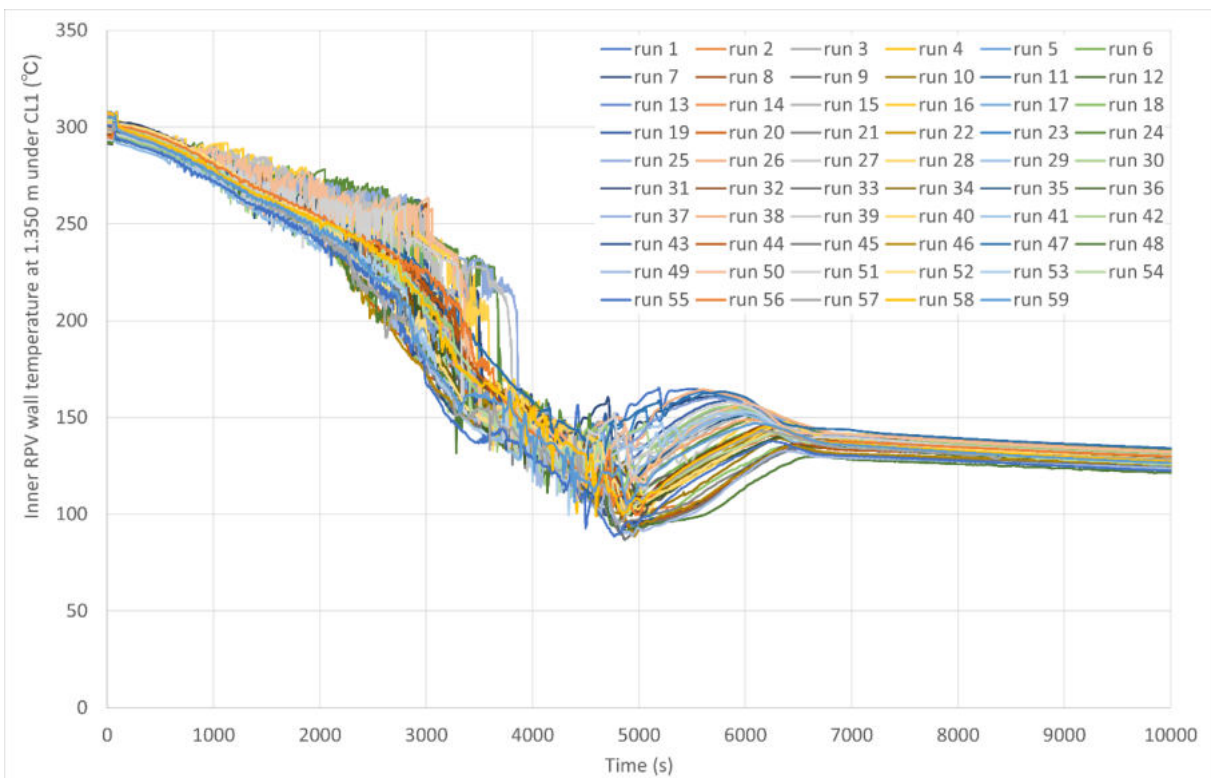
Figure 482: Inner RPV wall temperature at 1.350 m under CL1
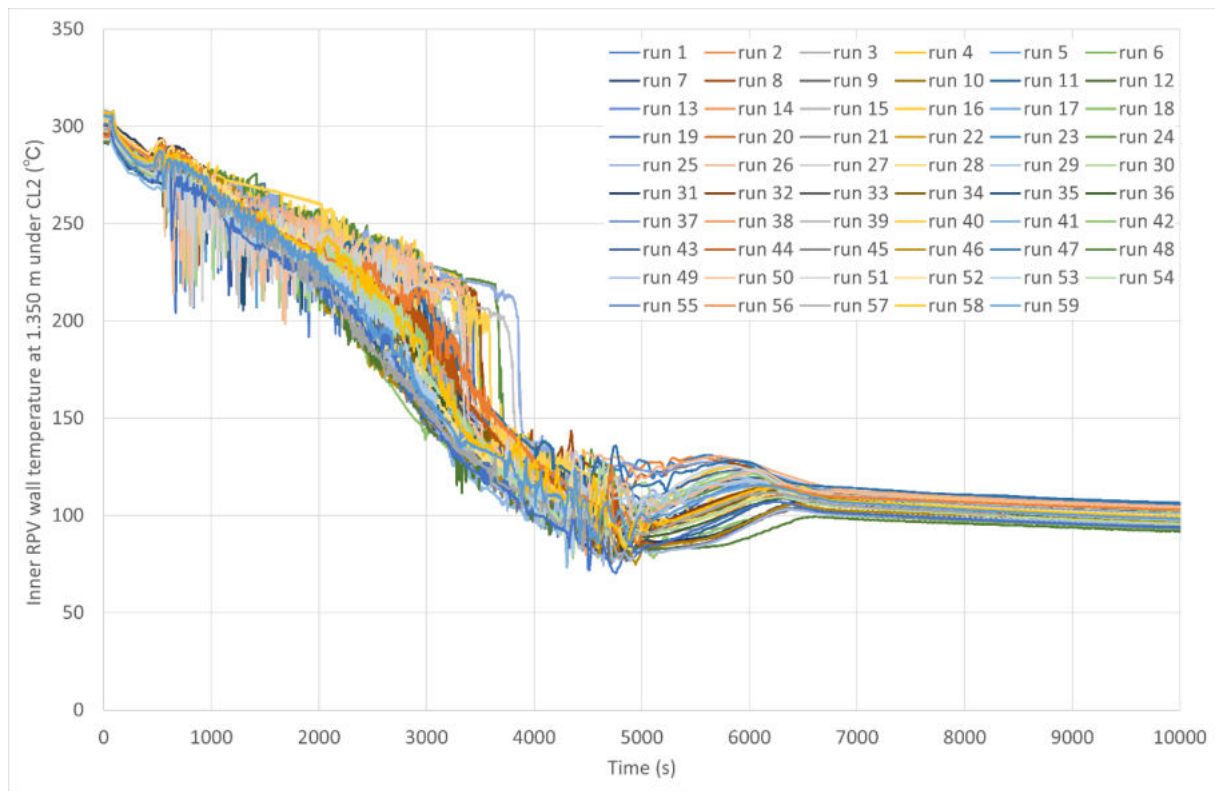
Figure 483: Inner RPV wall temperature at 1.350 m under CL2

19   GRS uncertainty analysis with ATHLET and SUSA

19.1 Reference best-estimate calculation

A simulation of a SBLOCA (50 cm²) with break in the core outlet region and with loss of offsite power was run with AC2 2021 alpha (ATHLET 3.3 alpha). An overview of the differences between the base and best-estimate cases is given in Table 51. The sequence of events is summarised in Table 52. Time-dependent graphs showing the evolutions of the major system parameters are given in Figure 484 through Figure 491.

Table 51: ATHLET Base Case (Task 2.1) vs. Best-Estimate Case (Task 2.3)

Plant parameter	Task 2.1 Base Case (ICAS values)	Task 2.3 best-estimate value
Decay heat	ANS79-1	ANS79-1 + 10%
ACC injection temperature	20 °C	30 °C
HPSI / LPSI temperature	15 °C	30 °C
ACC isolation	-	After 500 s

Table 52: Sequence of Events for the Reference SBLOCA in ATHLET Simulations

Cause	Event	Time (s)
Primary pressure < 132 bars	Reactor trip Turbine trip Emergency signal Signal sec.-side cooldown (100K/hr auto.) Main coolant pumps trip	30
Emergency signal + 12 s	Signal ECC system to start	42
Primary pressure < 110 bars	Emergency cooling signal for HPI pumps	56.5
HPI signal + 20 s	HPI pumps running	76.5
HPI pumps running + 3 s	HP injection	79.5
Primary pressure < 10 bars	Emergency coolant signal for LPI pumps	4531
LPI Signal + 25 s	LPI pumps running	4556
LPI pumps running + 3 s	LP injection	4559

After the break initiation, the primary pressure drops quickly below 132 bar, what trips the reactor and turbine and actuates the emergency core cooling system. When the saturation pressure of the primary system is reached the pressure drop is counteracted by void production as can be seen in Figure 484 (a) and Figure 486 (a). The automated activation of the secondary side cooldown decreases the secondary side pressure with a 100 K/h cooldown rate which leads the pressure progression in the primary circuit until the late phase of the transient where the LPI starts and stabilizes the pressure to ~10 bar after ~4700 s. When the liquid level in the primary circuit reaches the break position the leak mass flow quickly rises and stabilizes at ~200 kg/s (see Figure 485 (a)). With the start of the LPI pumps at ~4500 s the coolant loss is fully compensated.

335

(a)   (b)
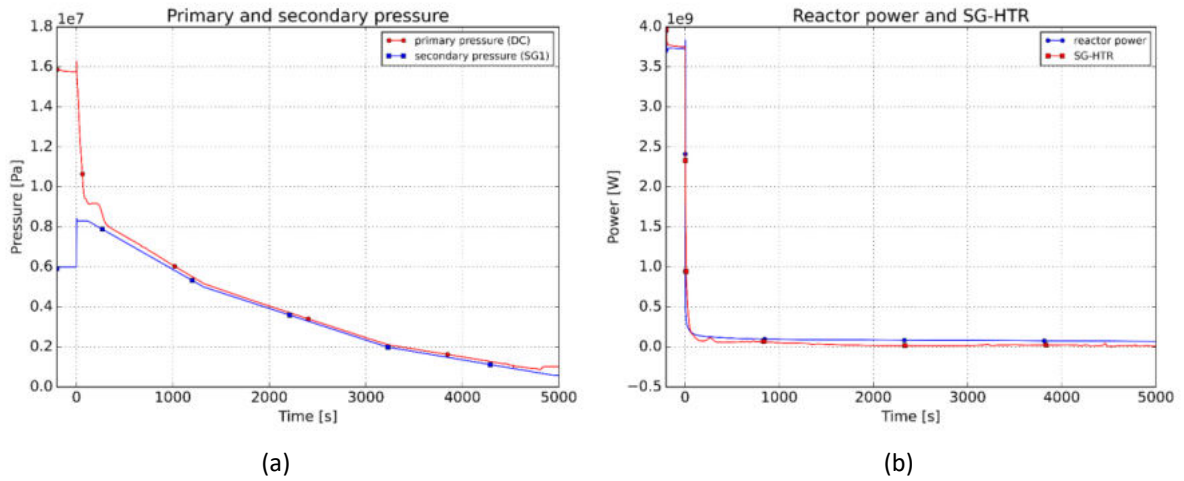
Figure 484: (a) System Pressures and (b) Reactor Power and Heat Removal by all SGs.

(a)   (b)
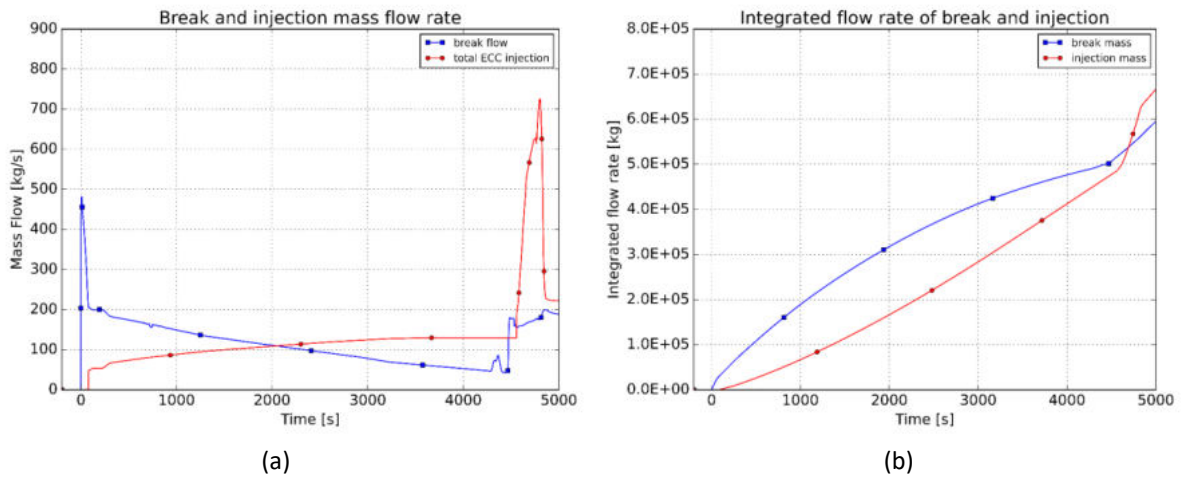
Figure 485: (a) Break Flow Rate and (b) Integrated Coolant Loss and Injection.

(a)   (b)
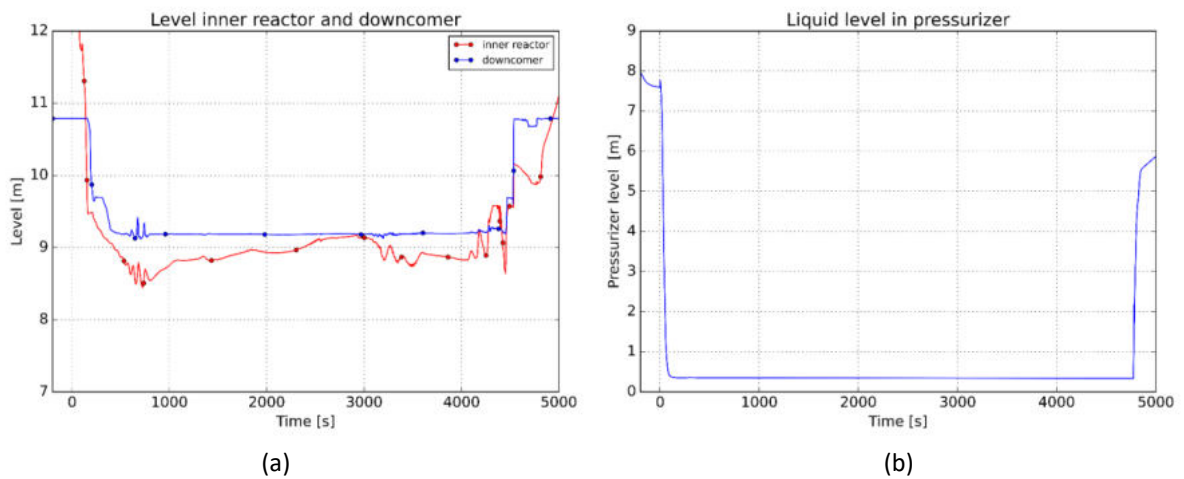
Figure 486: (a) Downcomer Liquid Level and (b) PZR Liquid Level.

(a)   (b)
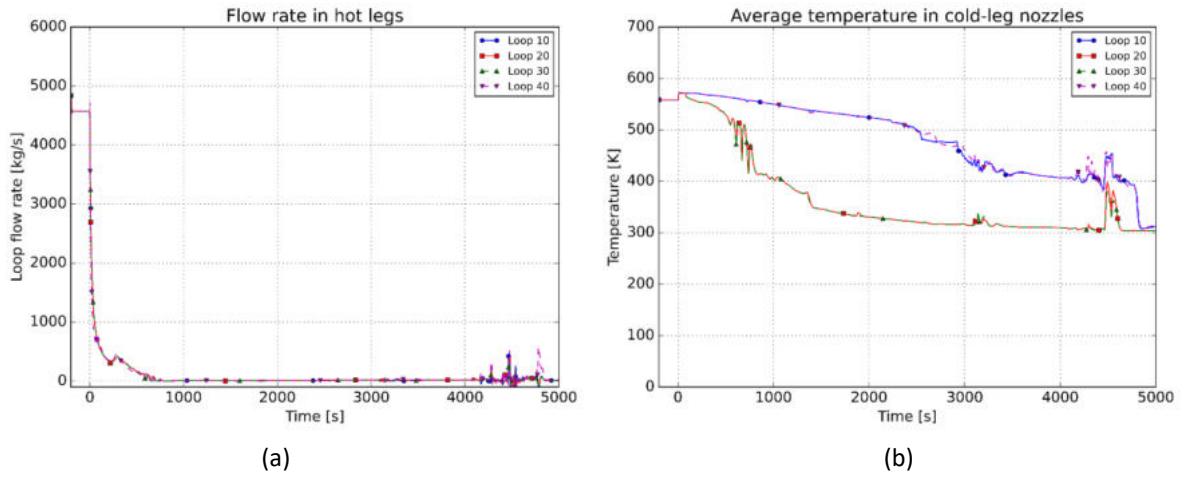
Figure 487: (a) HL Flow Rates and (b) Temperatures in the RPV Inlet Nozzles.

(a)   (b)
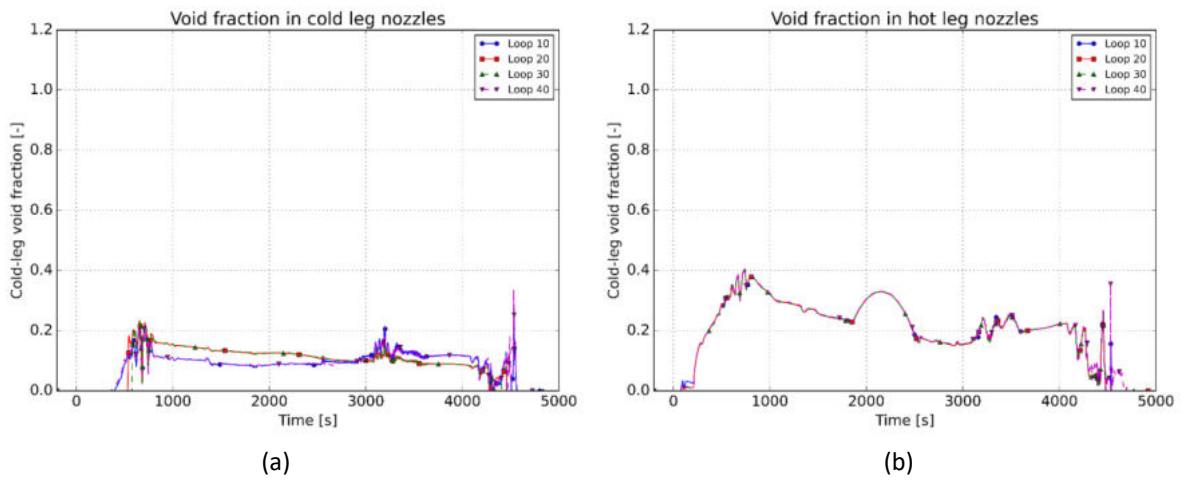
Figure 488: Void Fraction at the (a) RPV Inlet Nozzles and (b) RPV outlet Nozzles.

(a)

(b)

(c)

(d)

(e)

(f)
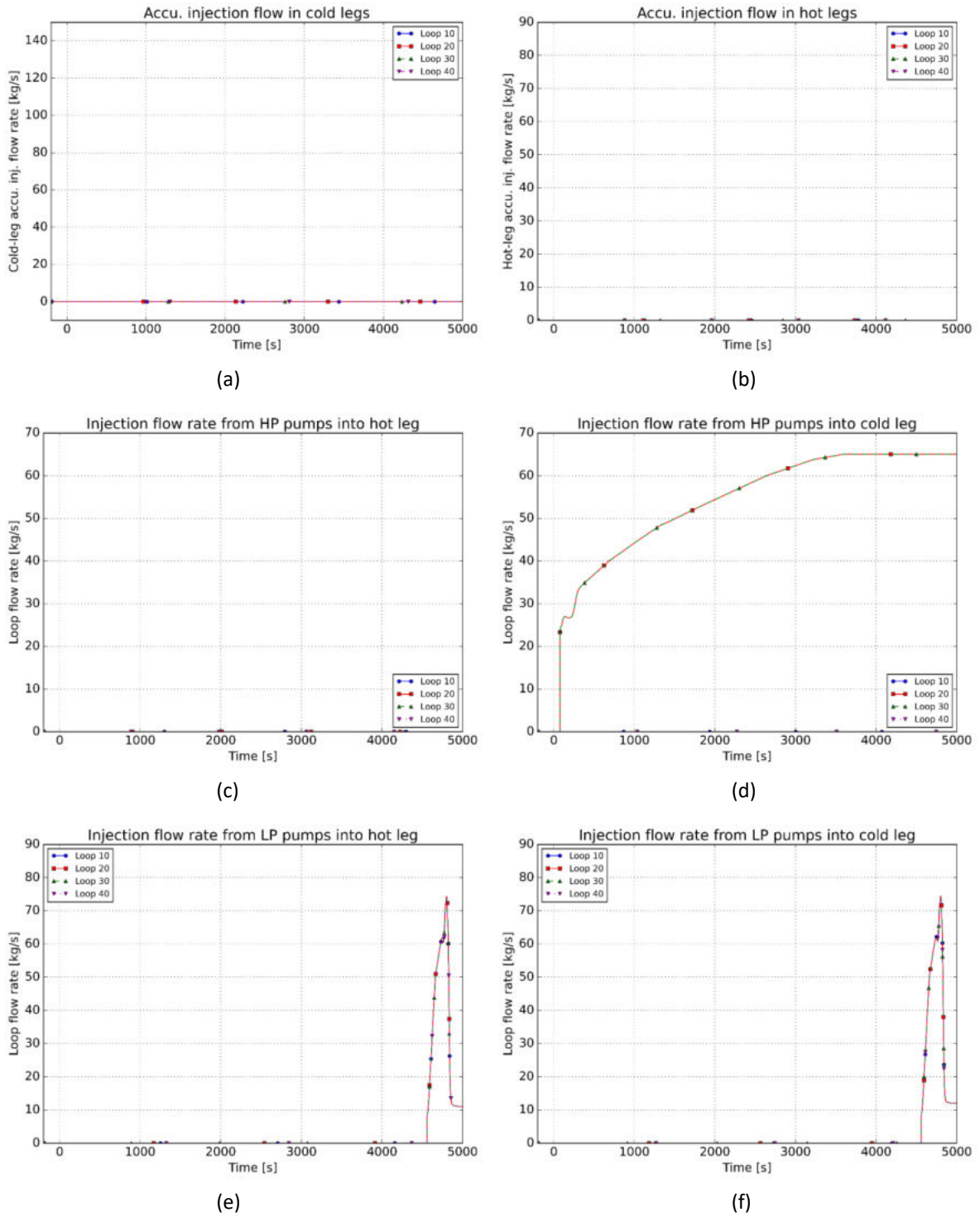
Figure 489: (a) Hot Leg and (b) Cold Leg Accumulator Flow Rates, (c) Hot Leg and (d) Cold Leg HPI Flow Rates, and (e) Hot Leg and (f) Cold Leg LPI Flow Rates.

(a)   (b)
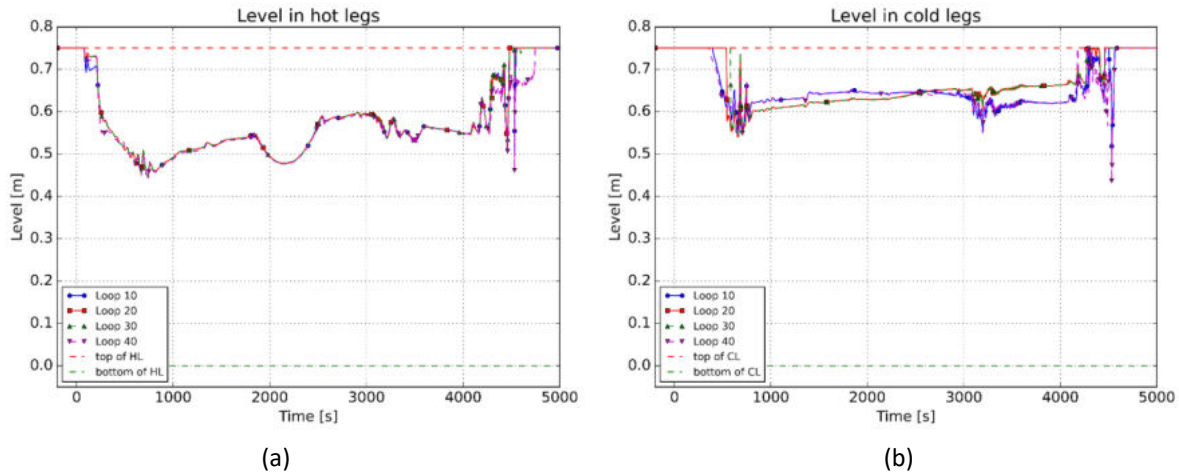
Figure 490: Collapsed Liquid levels in the (a) HLs and (b) CLs.

(a)   (b)
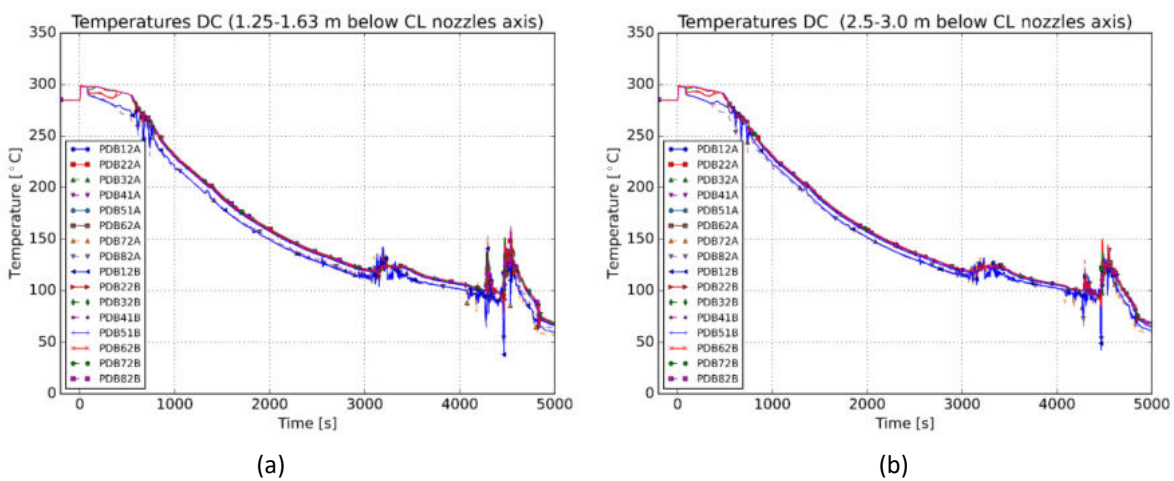
Figure 491: Circumferential Coolant Temperatures in Downcomer Control Volumes Covering 1.350 m (left) and 2.638 m (right) below the RPV Inlets.

19.2 Input uncertainties

Table 31, Table 53 and Table 54 present best-estimate values and uncertainty distributions for plant and model parameters, respectively, identified for the TH system code ATHLET. Changes from D2.2 as described in Reference [83] include the uncertainty range of HPI/LPI injection temperature, now 15 to 45 °C, and the suppression of the model parameter accounting for the activation of axial heat transfer in the heat conduction objects – axial heat transfer is possible in all samples of the BEPU analysis. A total of 34 uncertainty parameters were included.

Table 53 Uncertainty distribution for plat parameters in ATHLET – BEPU Analysis

Plant parameter	Best-estimate-value	Type of distribution	Distribution parameters p1=mean p2=standard deviation	Technical or statistical basis for type of distribution and distribution parameters
Correction factor for decay heat	1	normal	p1=1; p2=0.04 min/max: 0.9/1.1	[38], Chapter 6.1.12, Para. 45
Correction factor for power of fuel rods	1	normal	p1=1; p2=0.01 min/max:0.97/1.03	expert judgement

Temperature of the pressure accumulator and the emergency feed water	30 °C	uniform	min/max: 5/30	[39], Chapter 3.5.1.13, par.51
Delay time between leak opening and triggering of SCRAM	2 s	uniform	min/max: 1/5	expert judgement
Runtime of the SCRAM between triggering and maximum shut down reactivity	2 s	uniform	min/max: 0.5/4	expert judgement
Delay for secondary cooldown	120 s	normal	p1=300; p2=150 min/max: 0/600	expert judgement
Time delay to switch off the main coolant pumps	2 s	normal	p1=2; p2=1 min/max: 0/4	[40], chapter 6.1.18, Par. 56
Factor of the feed mass flow of the LP-pumps	1	normal	p1=1; p2=0.04 min/max: 0.9/1.1	[41], Annex 1, Table 1
Factor of the feed mass flow of the HP-pumps	1	normal	p1=1; p2=0.04 min/max:0.9/1.1	[41], Annex 1, Table 1
Pressurization of the pressure accumulators of the ECCS	2.60E+06 Pa	normal	p1=2.6E+06; p2=3.0E+05 min/max: 2.4E+06/2.8E+06	[41], Annex 1, Table 1
Fill level of the pressure accumulator of the ECCS	8.5428 m	uniform	min/max: 8.148/8.889	expert judgement
Isolation of accumulators after 500 s	500 s	toggled	500 s; 50000 s	-
Timing for HPI actuation <110 bar + t	20 s	uniform	min/max: 0/20	expert judgement
Timing for LPI actuation <10 bar + t	25 s	uniform	min/max: 0/25	expert judgement
Temperature of HPI/LPI	30 °C	uniform	min/max. 15/45	expert judgement

Table 54 Uncertainty distribution for model parameters in ATHLET – BEPU Analysis

Model parameter	Best-estimate-value	Type of distribution	Distribution parameters	Technical or statistical basis for type of distribution and distribution parameters
Turbulence factor for the evaporation in case of critical flow	30	log. normal	p1=2.29; p2=0.65 min/max: 0/50	[70], Chapter 2.1.3.1
Single-phase convection in water (Dittus-Boelter) - correction factor, all surfaces where heat transfer takes place	1	uniform	min/max: 8.50E-01; 1.15E+00	KWU experiments and expert judgement
Single-phase natural convection in water (Dittus-Boelter) - correction factor, all surfaces where heat transfer takes place	1	uniform	min/max: 8.50E-01; 1.15E+00	KWU experiments and expert judgement
Model for single-phase forced convection in steam: 1 = Dittus-Boelter II / 2 = Mc Eligot	1	toggled	1; 2	[39], Chapter 3.5.1.3, Par. 7
Single-phase convection in steam Dittus-Boelter II / Mc	-	dependency	-;-	[50], Tab. 5.2-1, Par. 28

Model parameter	Best-estimate-value	Type of distribution	Distribution parameters	Technical or statistical basis for type of distribution and distribution parameters
Eligot - correction factor; all surfaces where heat transfer takes place				
Correction factor for direct condensation	1	histogram	5.00E-01; 2.00E+00	HDR Condensation-Experiment, UPTF-TRAM Experiment, [50], Tab. 5.2-1, Par. 32
Heat losses to the environment, external surfaces of the primary circuit and the steam generator	1	uniform	0.99; 1.01	validation and expert judgement
Thermal conductivity of the base material	1	normal	p1=1; p2=0.03 min/max: 0.95/1.05	[51]
Heat capacity of the base material	1	normal	p1=1; p2=0.03 min/max: 0.95/1.05	[51]
Wall roughness U-tubes	7E-06	polygonal line	2.00E-06; 2.00E-05	[70], Tab 2.1-5, Par. 21
Wall roughness of the ECC feed lines	1.5E-05	polygonal line	1.00E-05; 0.0001	[39], Chapter. 3.5.1.10, Par. 37,
Form loss of the ECC feed line	0.5	polygonal line	0.1; 5.5	[41], Annex 1, Table 1 and expert judgement
Form loss correction factor for CCOs between core channels and between downcomer	1	histogram	0.4; 5	[39], Chapter 3.5.1.10, Par. 35
Form loss coefficient at break	0.1	uniform	min/max: 0.1; 10	expert judgment
Transport material value, thermal conductivity of water - correction factor	1	uniform	min/max: 0.992; 1.008	ATHLET material properties from IAPWS-97 [52]
Transport material value, thermal conductivity of the gas - correction factor	1	uniform	min/max: 0.985;1.015	ATHLET material properties from IAPWS-97 [52]
Transport material value, heat capacity of the water (only transport property) - correction factor	1	uniform	min/max: 0.99;1.01	ATHLET material properties from IAPWS-97 [52]
Transport material value, heat capacity of the gas (only transport property) - correction factor	1	uniform	min/max: 0.955; 1.045	ATHLET material properties from IAPWS-97 [52]
Factor for the heat transfer coefficient in the downcomer	1	uniform	min/max: 0.8; 1.2	Validation UPTF-TRAM Experiment

19.3 Results of BEPU analyses

Two separate BEPU analysis were performed with ATHLET and SUSA, one with and one without the mixing code ECCMIX. In both cases and according to the GRS-Method [46] and based on Wilk's formula

[1],[2], 59 samples were simulated for (95%,95%) one-sided statistical tolerance limits. Results are presented in the following sections, along with base case values, also with and without ECCMIX.

19.3.1 ATHLET without ECCMIX
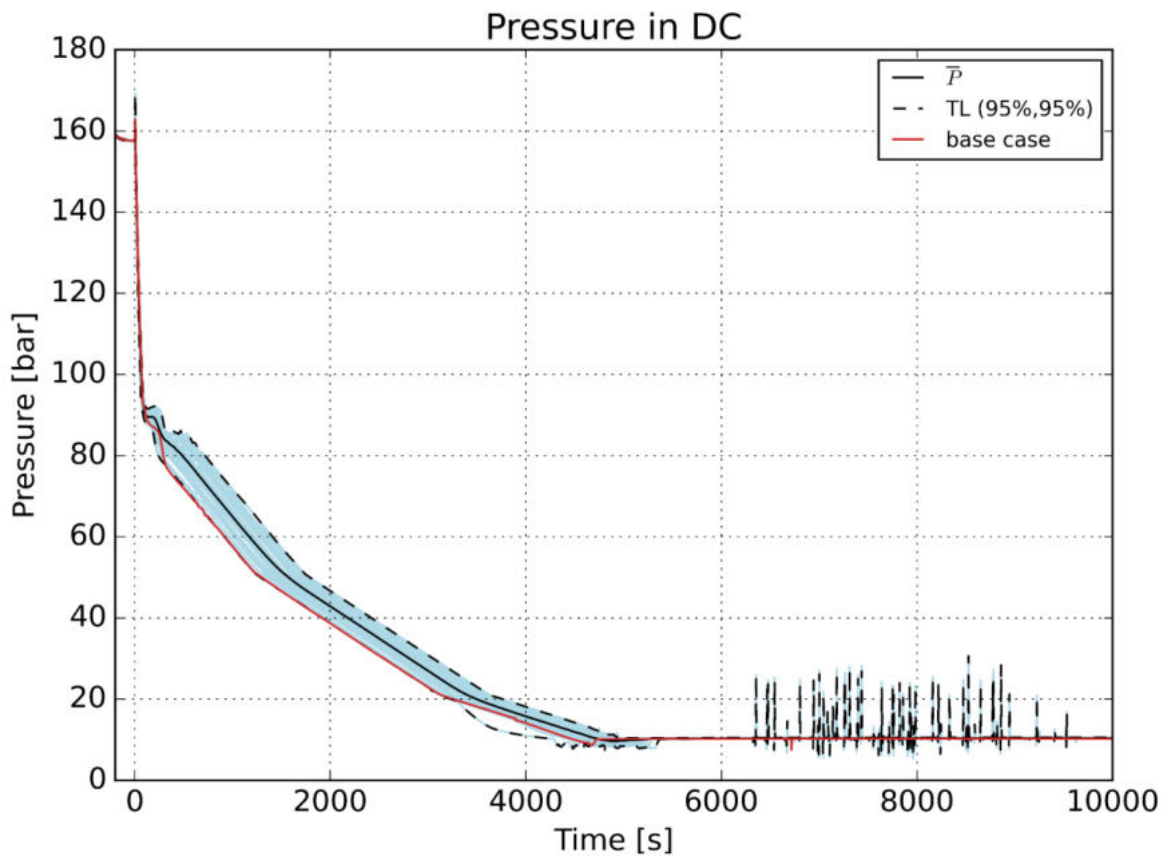
Figure 492 ATHLET – Pressure in DC
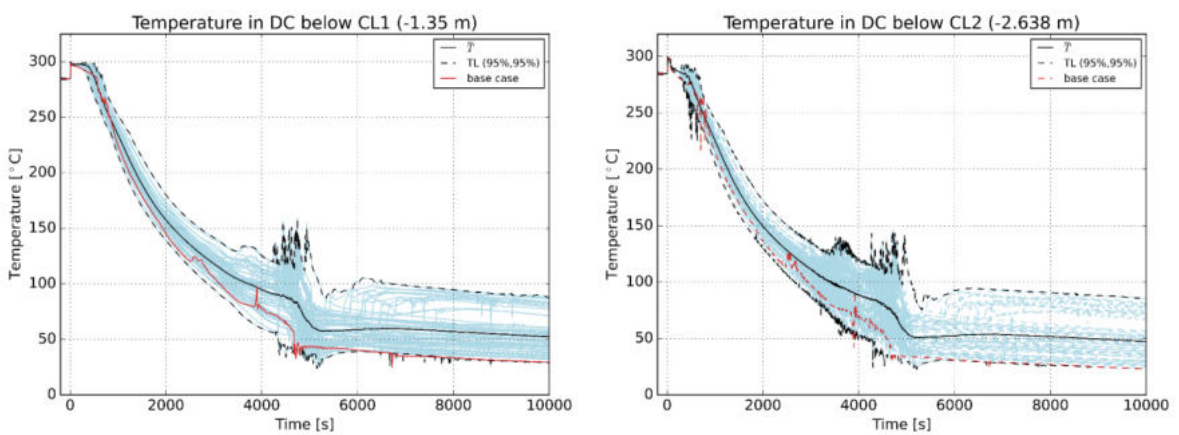
Figure 493 ATHLET – Coolant temperature below CL (-1,35 m)
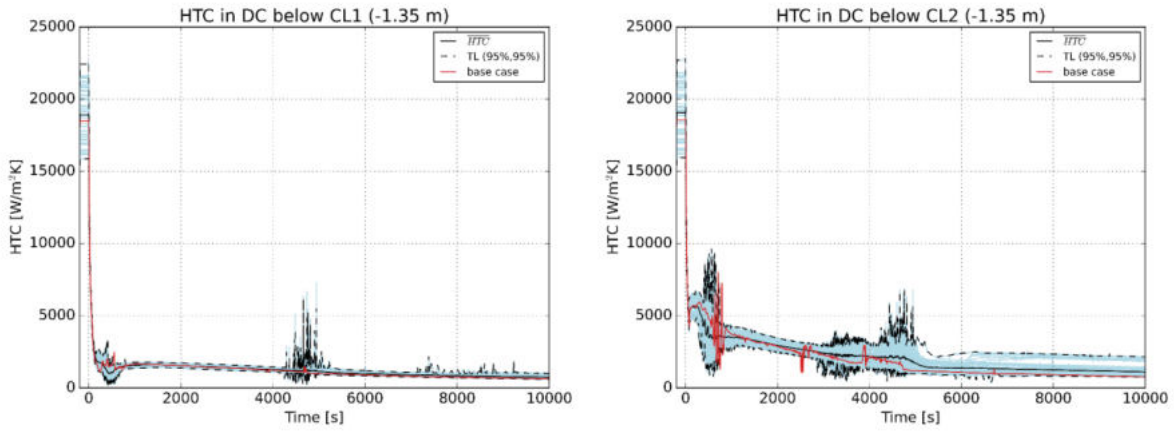
Figure 494 ATHLET – HTC below CL (-1,35 m)
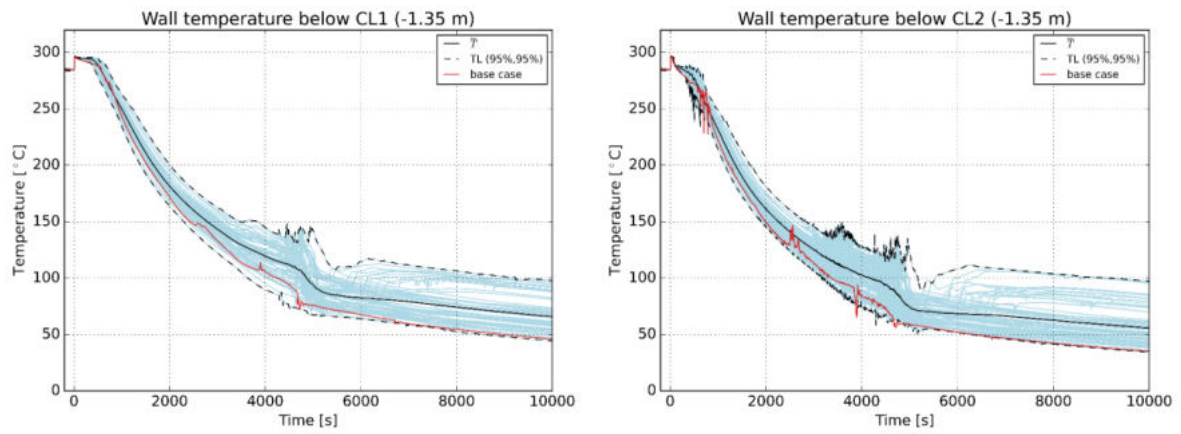
Figure 495 ATHLET – DC wall temperature below CL (-1,35 m)
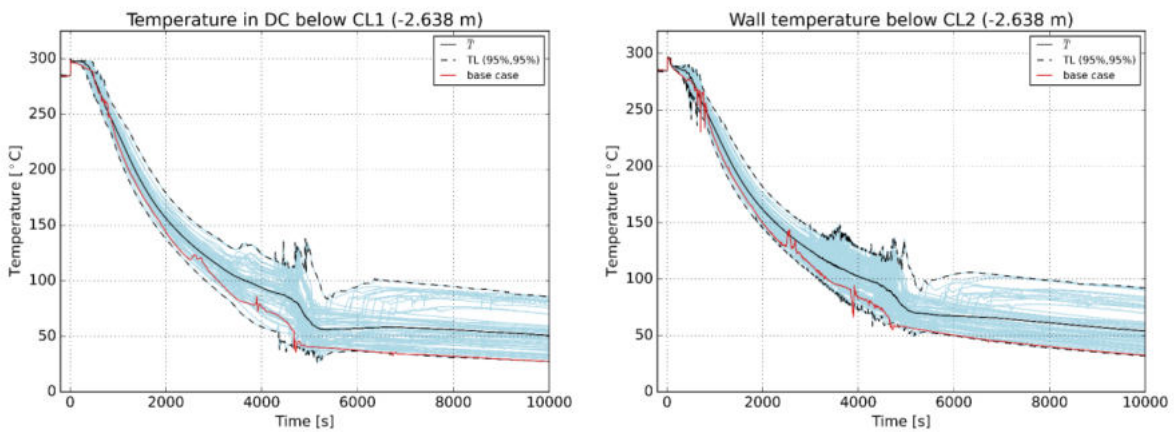
Figure 496 ATHLET – Coolant temperature below CL (-2,638 m)

343
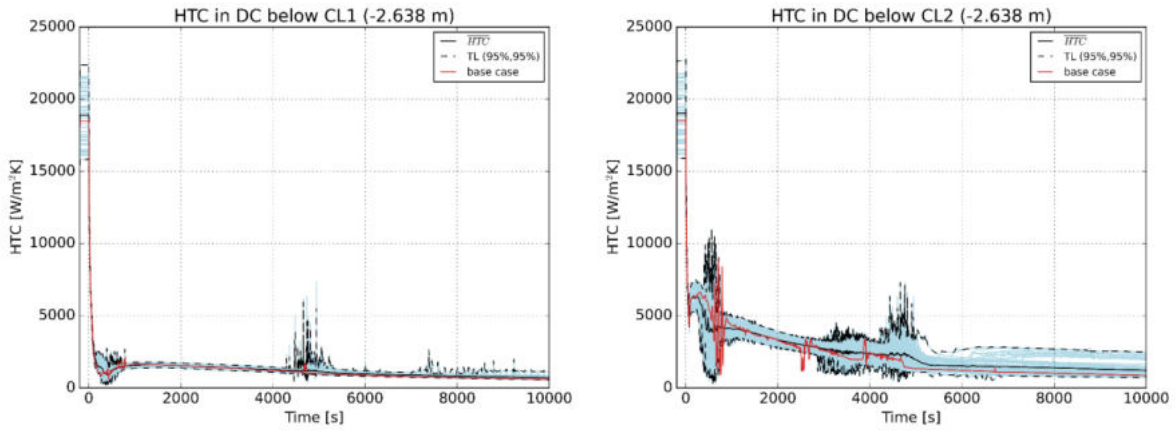
Figure 497 ATHLET – HTC below CL (-2,638 m)
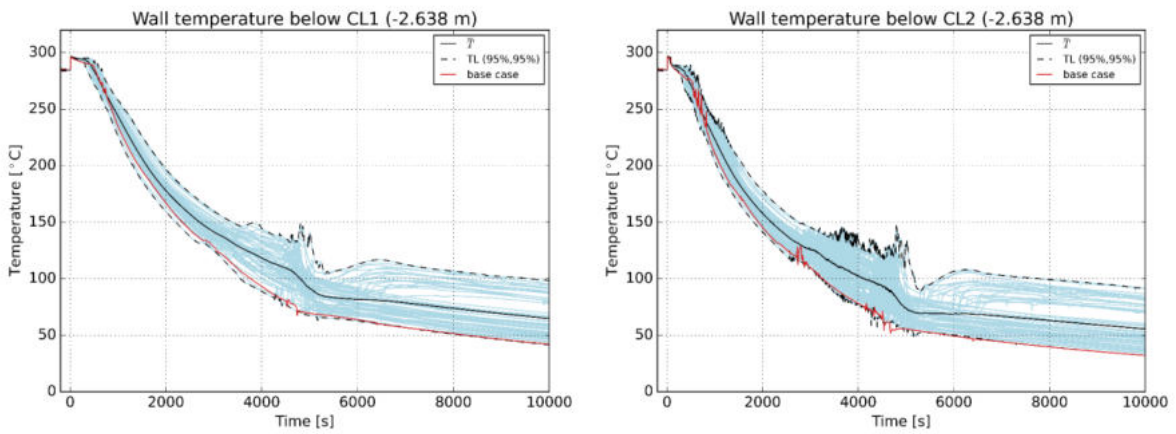
Figure 498 ATHLET – DC wall temperature below CL (-2,638 m)
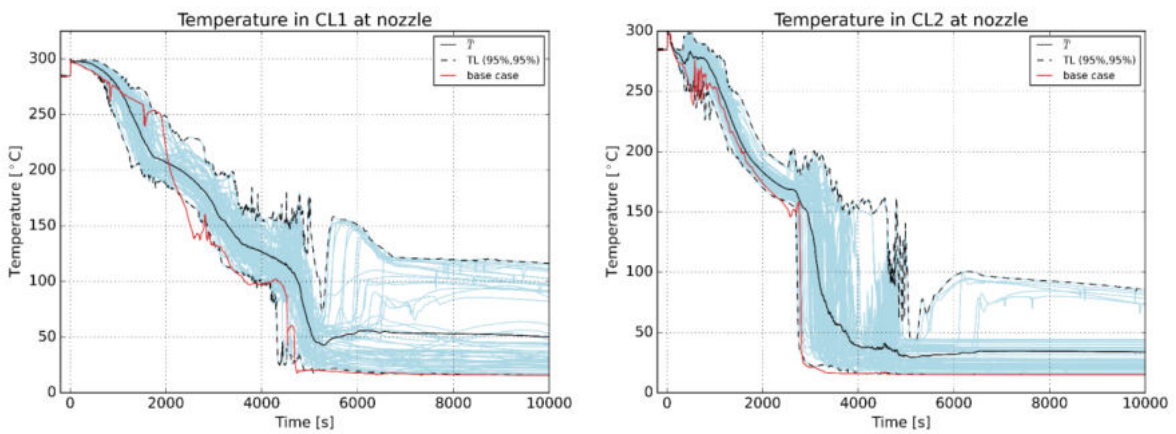
Figure 499 ATHLET – Coolant temperature at CL nozzle
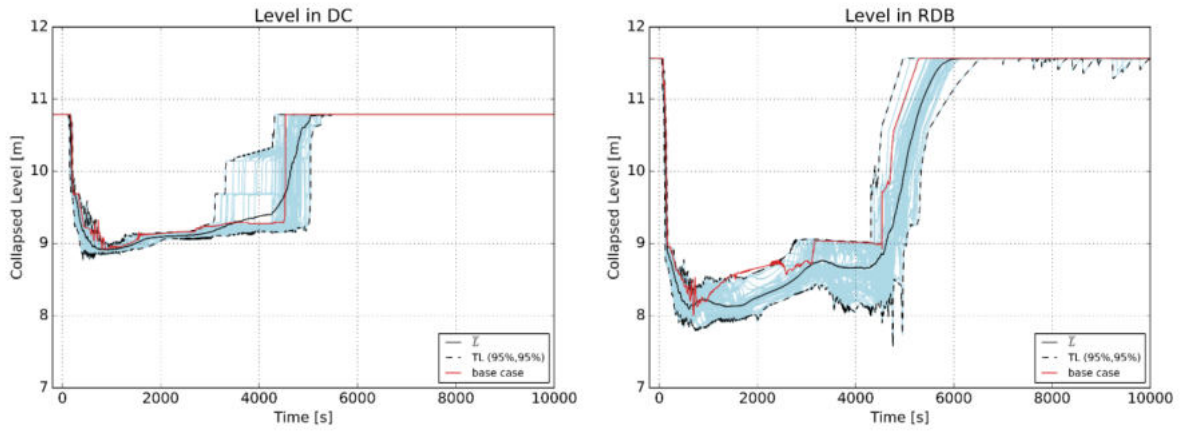
Figure 500 ATHLET – DC and RDB coolant level

19.3.2   ATHLET with ECCMIX
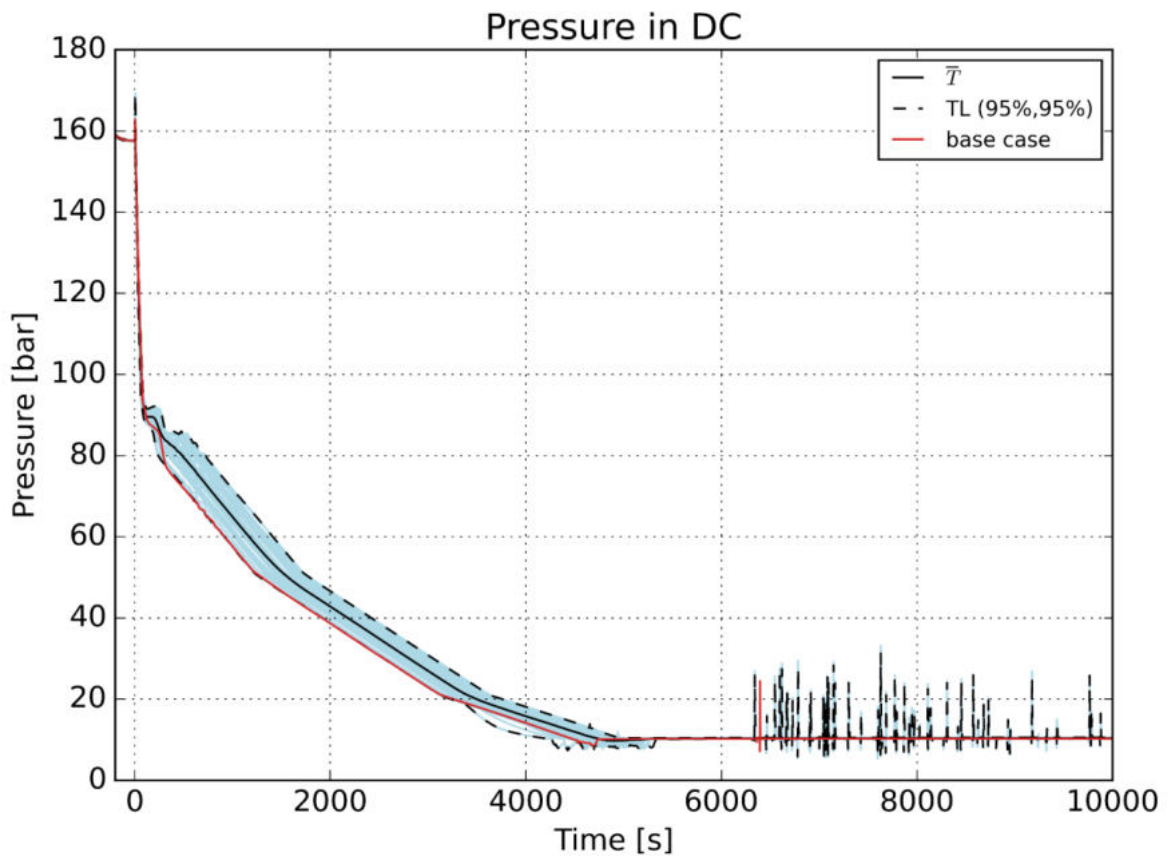
Figure 501 ATHLET with ECCMIX – Pressure in DC

345
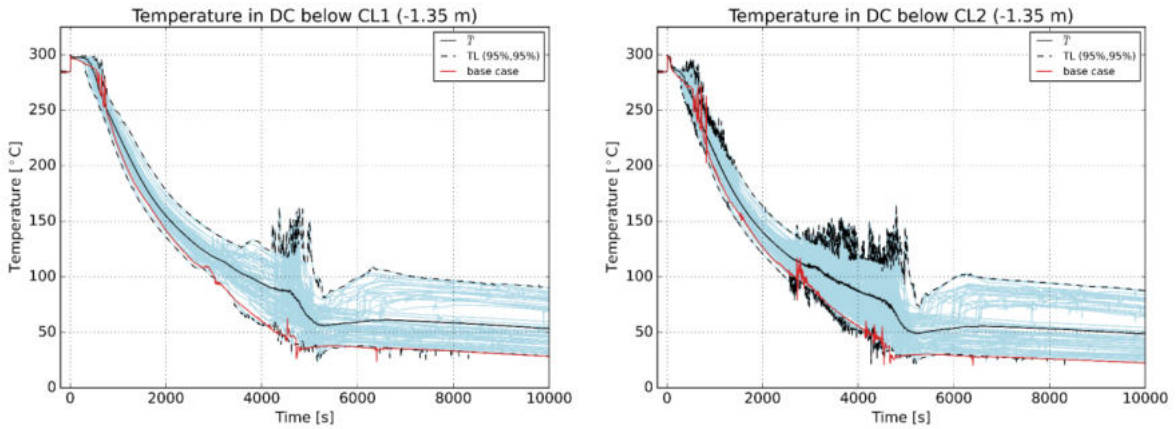
Figure 502 ATHLET with ECCMIX – Coolant temperature below CL (-1,35 m)
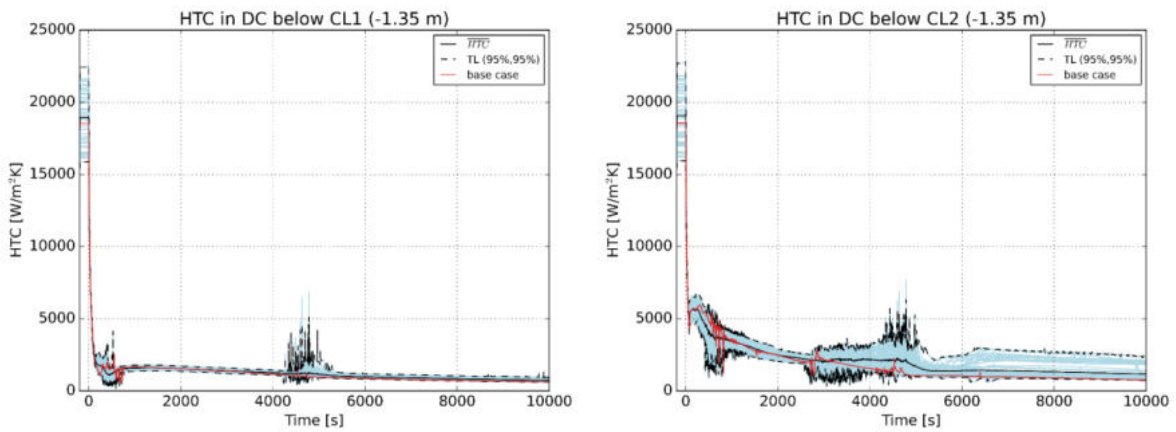
Figure 503 ATHLET with ECCMIX – HTC below CL (-1,35 m)
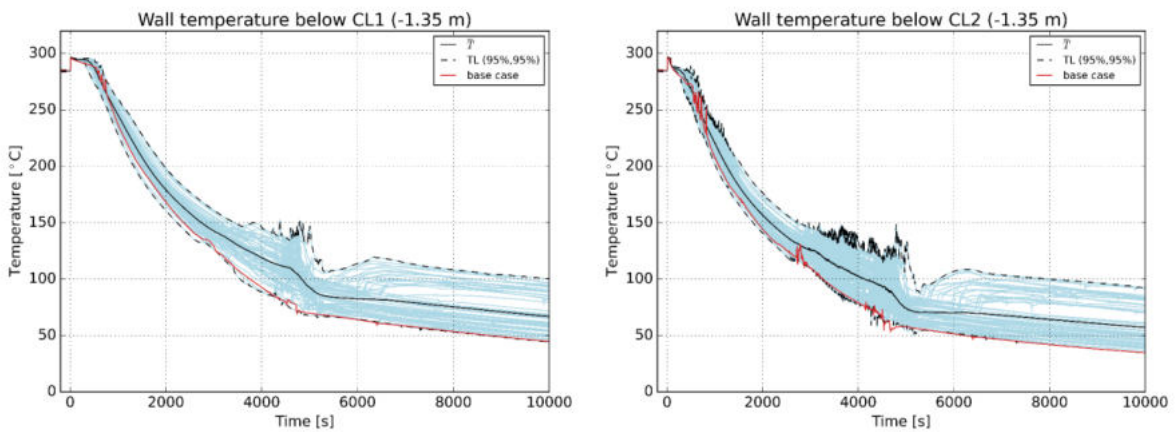
Figure 504 ATHLET with ECCMIX – DC wall temperature below CL (-1,35 m)
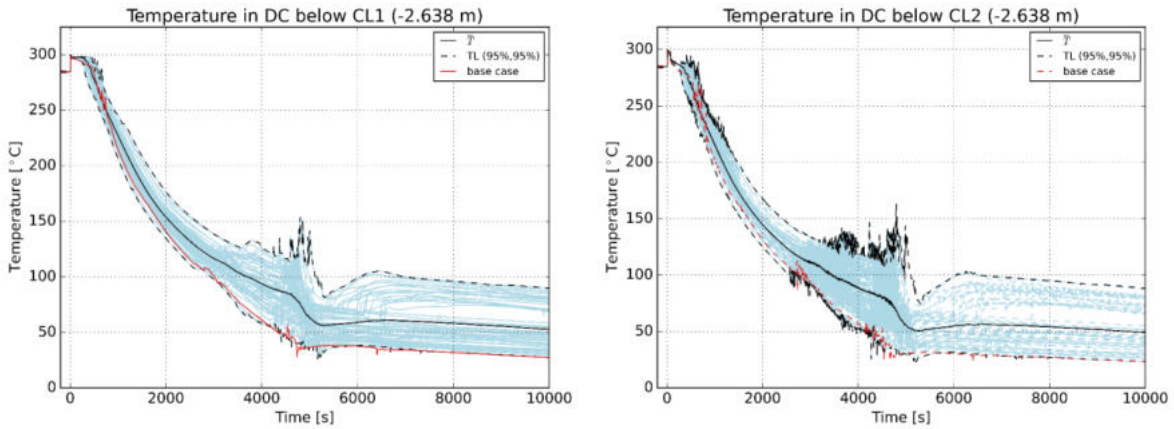
Figure 505 ATHLET with ECCMIX – Coolant temperature below CL (-2,638 m)
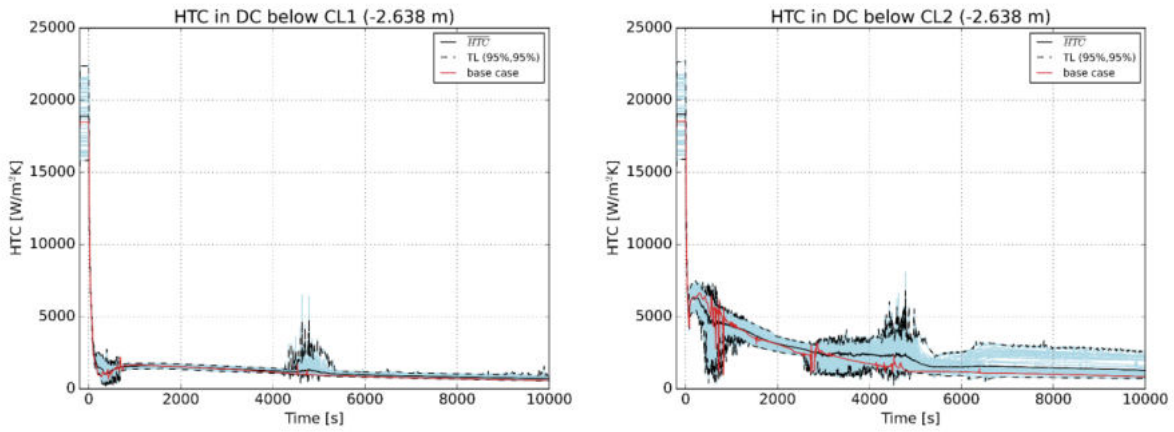
Figure 506 ATHLET with ECCMIX – HTC below CL (-2,638 m)
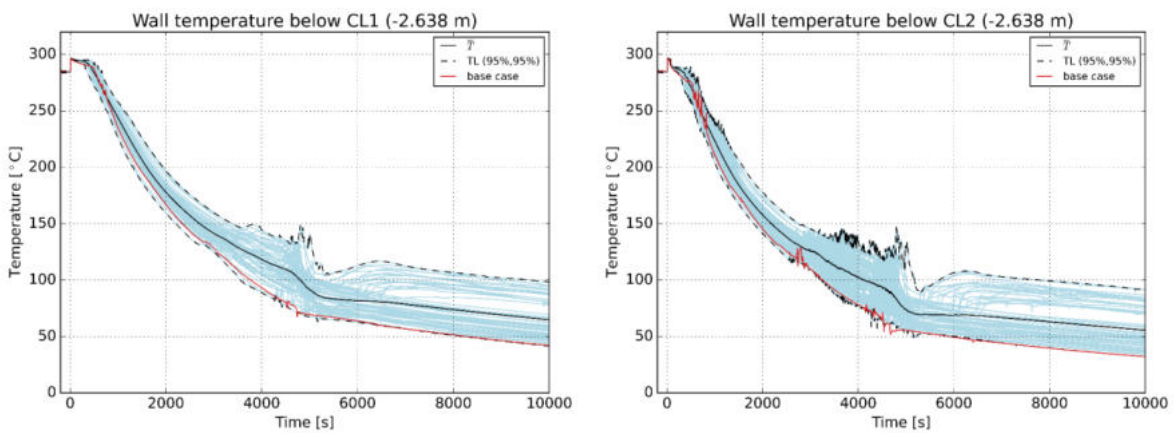
Figure 507 ATHLET with ECCMIX – DC wall temperature below CL (-2,638 m)
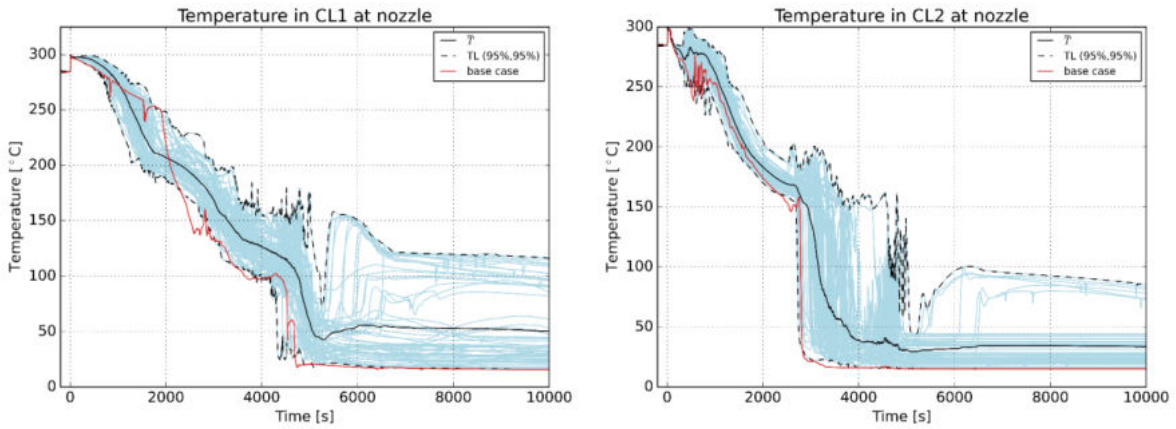
Figure 508 ATHLET with ECCMIX – Coolant temperature at CL nozzle
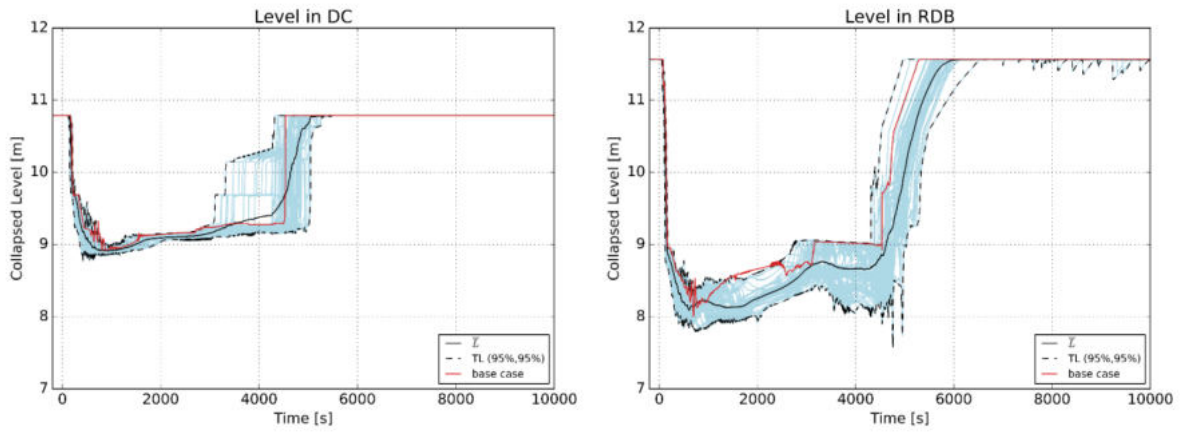
Figure 509 ATHLET with ECCMIX – DC and RDB coolant level

20   PSI uncertainty analysis with TRACE

20.1 Reference best-estimate calculation

The reference SBLOCA is a 50 cm^2 break in Hot Leg 1. The sequence of events is listed in Table 12.

Table 55: Sequence of Events for the Reference SBLOCA in TRACE simulations

Cause	Event	Time (s)
Primary pressure < 132 bars	Reactor trip Turbine trip Emergency signal Signal sec.-side cooldown (100K/hr auto.) MCPs trip	32
Emergency signal + 12 s	Signal ECC system to start	44
Primary pressure < 110 bars	Emergency cooling signal for HPI pumps	60
HPI signal + 20 s	HPI pumps running	80
HPI pumps running + 3 s	HP injection	83
Primary pressure < 26 bars	ACC injection	2583
Primary pressure < 10 bars	Emergency coolant signal for LPI pumps	4131
LPI Signal + 25 s	LPI pumps running	4156
LPI pumps running + 3 s	LP injection	4159

Time-dependent graphs showing the evolutions of the major system parameters are given in Figure 72 through Figure 79. After the initiating event, the primary pressure drops relatively quickly to the saturation pressure of the primary system, leading to reactor trip and activation of the ECC system and high-pressure safety injection (HPSI). This initial depressurization causes significant void formation in the primary system, which is seen as a drop in the system liquid levels in Figure 512. Due to the automated activation of secondary side cooldown, the secondary pressure decreases according to the specified 100 K/h cooldown rate for the remainder of the transient. The primary pressure generally follows the secondary pressure for the duration of the transient. At ~2200 s, the primary pressure drops relatively quickly below the secondary pressure. This is believed to be due to the refilling of the upper plenum and hot legs, leading to an increase in break flow rate. After ~2500 s the ACCs inject, causing the liquid levels in primary system to quickly recover. After the low-pressure injection (LPI) starts, the total safety injection flow rate is sufficient to fully compensate the coolant loss from the break, and the primary pressure stabilizes around the pump head of the LPI pumps.

20.1.1 Downcomer Coolant Temperature and HTC

Since parts of the DC are uncovered during the transient, the effective coolant temperature and heat transfer coefficient (HTC) must be calculated taking multi-phase effects into account. In TRACE, the heat transfer is the sum of three components, the heat transfer to the liquid phase ($q''_{w,l}$), to the vapour/gas phase ($q''_{w,g}$), and the direct boiling ($q''_{w,sat}$).

$$q''_{w,l} = h_{w,l}(T_w - T_l)$$

$$q''_{w,g} = h_{w,g}(T_w - T_g)$$

$$q''_{w,sat} = h_{w,sat}(T_w - T_{sat})$$

where h is the heat transfer coefficient and the subscripts w, l, g and sat refer to the wall, liquid phase, vapour phase/gas and saturation conditions, respectively. The total heat flux can be written as the sum of these three components.

$$q''_{w,c} = h_{w,c}(T_w - T_c) \qquad (4)$$

where the subscript c refers to the effective coolant conditions and

$$h_{w,c} = h_{w,l} + h_{w,g} + h_{w,sat} \tag{5}$$

$$T_c = \frac{h_{w,l}T_l + h_{w,g}T_g + h_{w,sat}T_{sat}}{h_{w,c}} \tag{6}$$

Figure 80 and Figure 81 show the predicted effective coolant temperature T_c and heat transfer coefficient $h_{w,c}$ at several axial locations below the lip of each RPV inlet. The axial locations, which correspond to positions of interest for downstream thermomechanical analysis, are shown in Figure 83. In the upper elevations of the DC, we see somewhat lower coolant temperatures in the loops with injection (loops 2 and 3), especially in the first ~900 s of the transient. Here the cooling effect of the safety injection is more clearly seen. Lower down in the RPV, however, the temperature and HTC are relatively homogeneous. The underlying explanation for this behaviour, the coolant mixing, and upward propagation of a thermal stratification layer is visible in Figure 82.

Figure 82 shows unwrapped colour plots of the subcooling and HTC distributions in the DC region below the RPV inlets at selected time points. We can see that, early in the transient, TRACE predicts a stratification layer forming in the DC. This stratification layer moves upwards relatively quickly and, consistent with the observations for Figure 80, the temperature distribution becomes more uniform below this level. Studies in Task 2.2 of APAL as described in Reference [83] have shown that TRACE tends to over-estimate the mixing in the DC. Thus, in reality, we would expect the temperatures below the loops without HPI (loops 1 and 4) to be closer to the 100 K/h cooldown curve (Figure 80).

The subcooling in the DC is significant, highlighting that the 100 K/h cooldown rate is exceeded and confirming that this transient is PTS relevant.

(a)   (b)
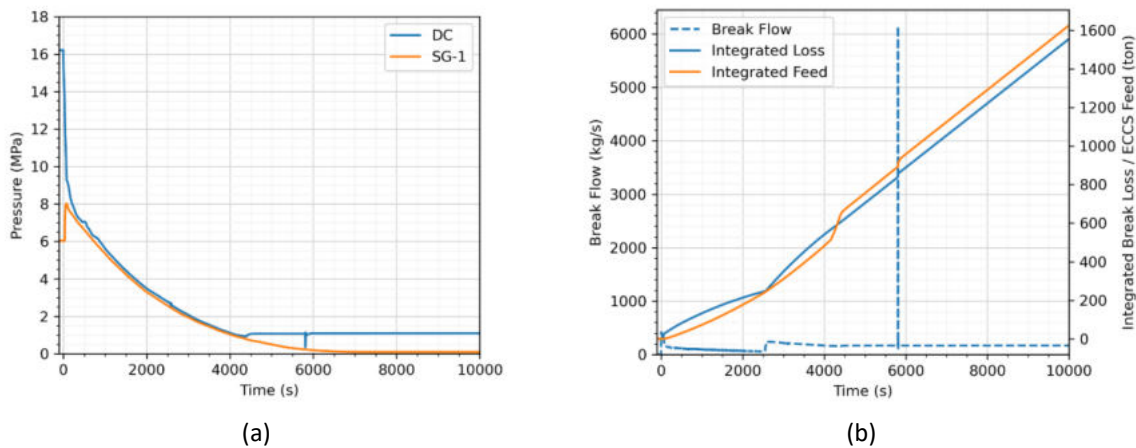
Figure 510: (a) System Pressures and (b) Break Flow Rate and Integrated Coolant Loss and Injection.
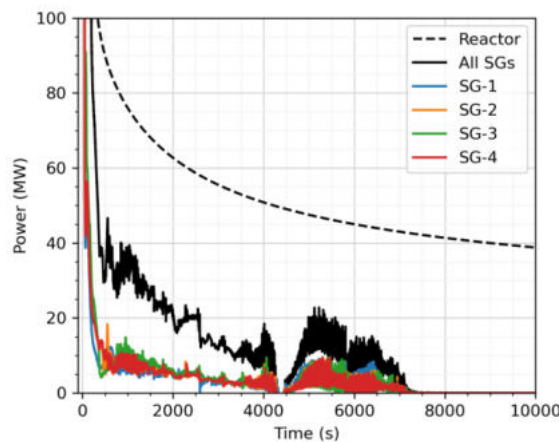
Figure 511: Reactor Power and Heat Removal by all SGs.

350

(a)   (b)
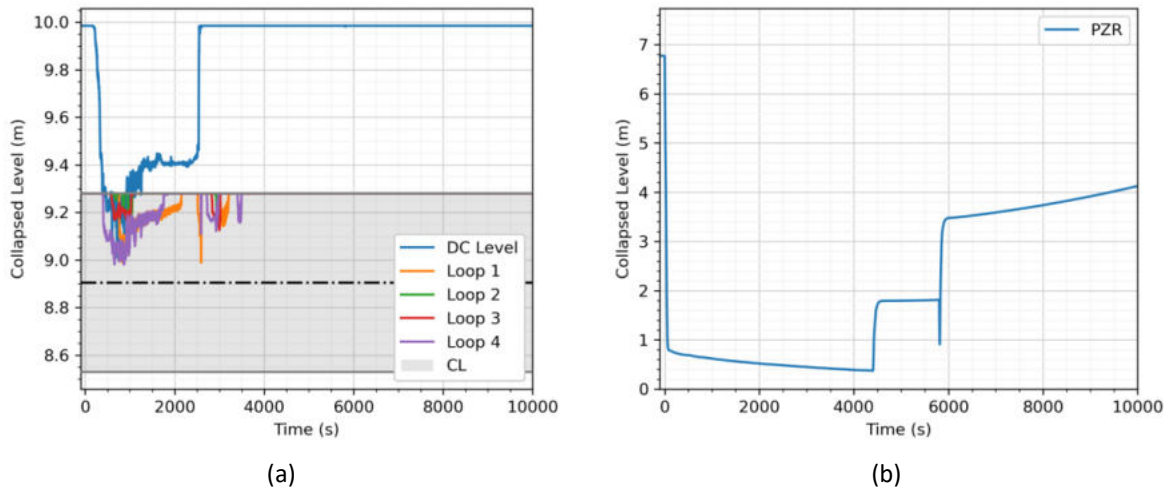
Figure 512: (a) DC Liquid Level and (b) PZR Liquid Level.

(a)   (b)
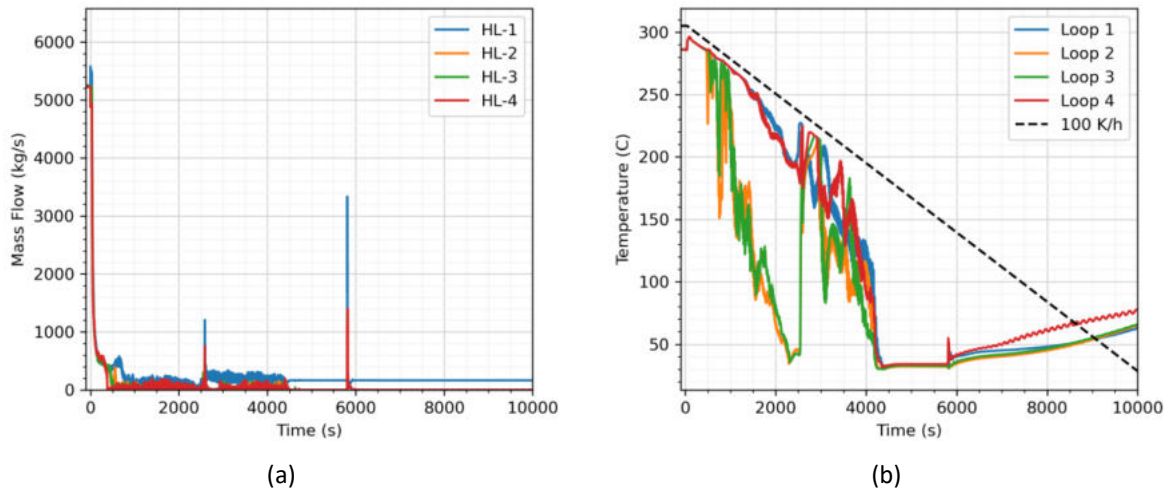
Figure 513: (a) HL Flow Rates and (b) Temperatures in the RPV Inlet Nozzles.

(a)   (b)
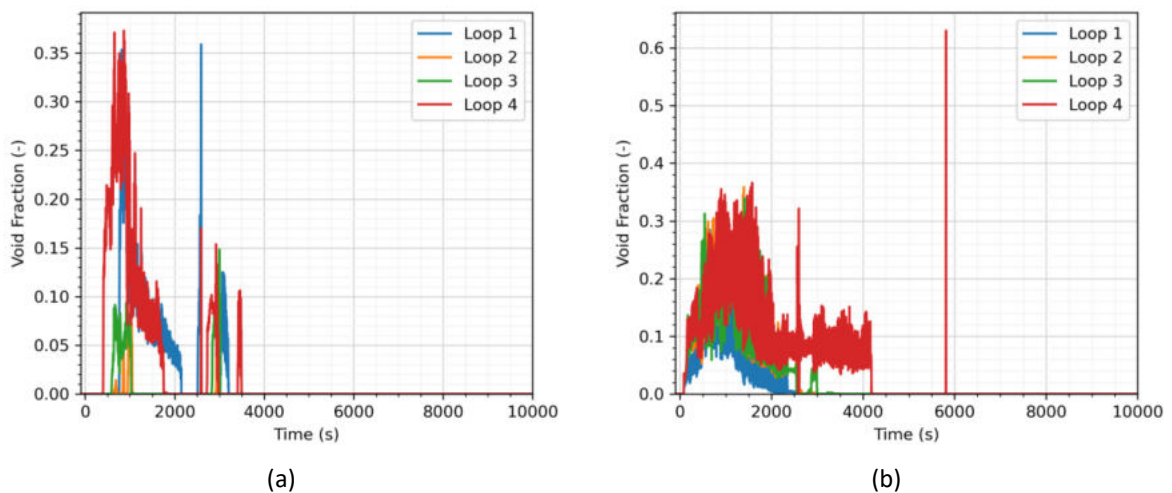
Figure 514: Void Fraction at the (a) RPV Inlet Nozzles and (b) RPV outlet Nozzles.
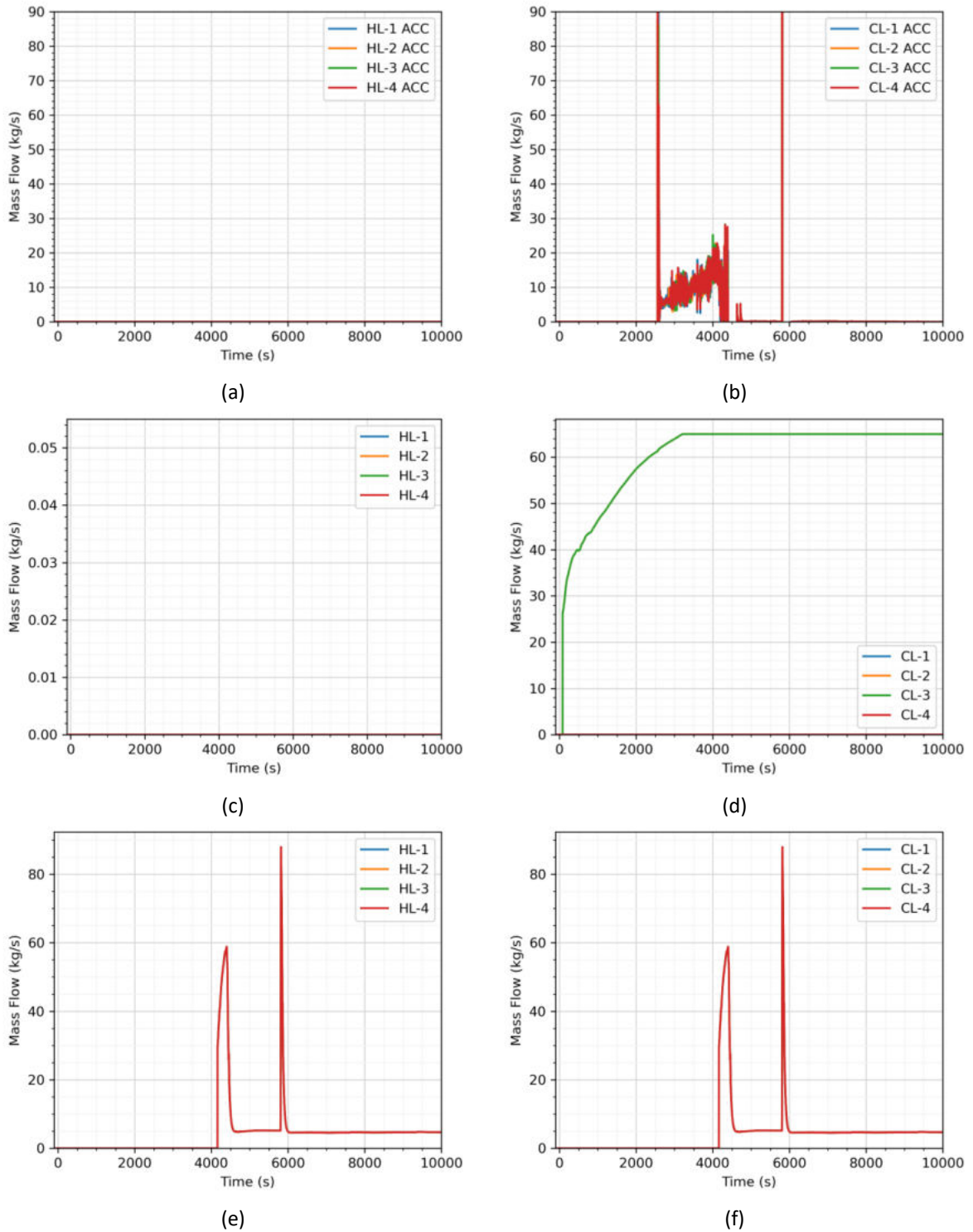
Figure 515: (a) HL and (b) CL ACC Flow Rates, (c) HL and (d) CL HPI Flow Rates, and (e) HL and (f) CL LPI Flow Rates.

(a)   (b)

(c)   (d)
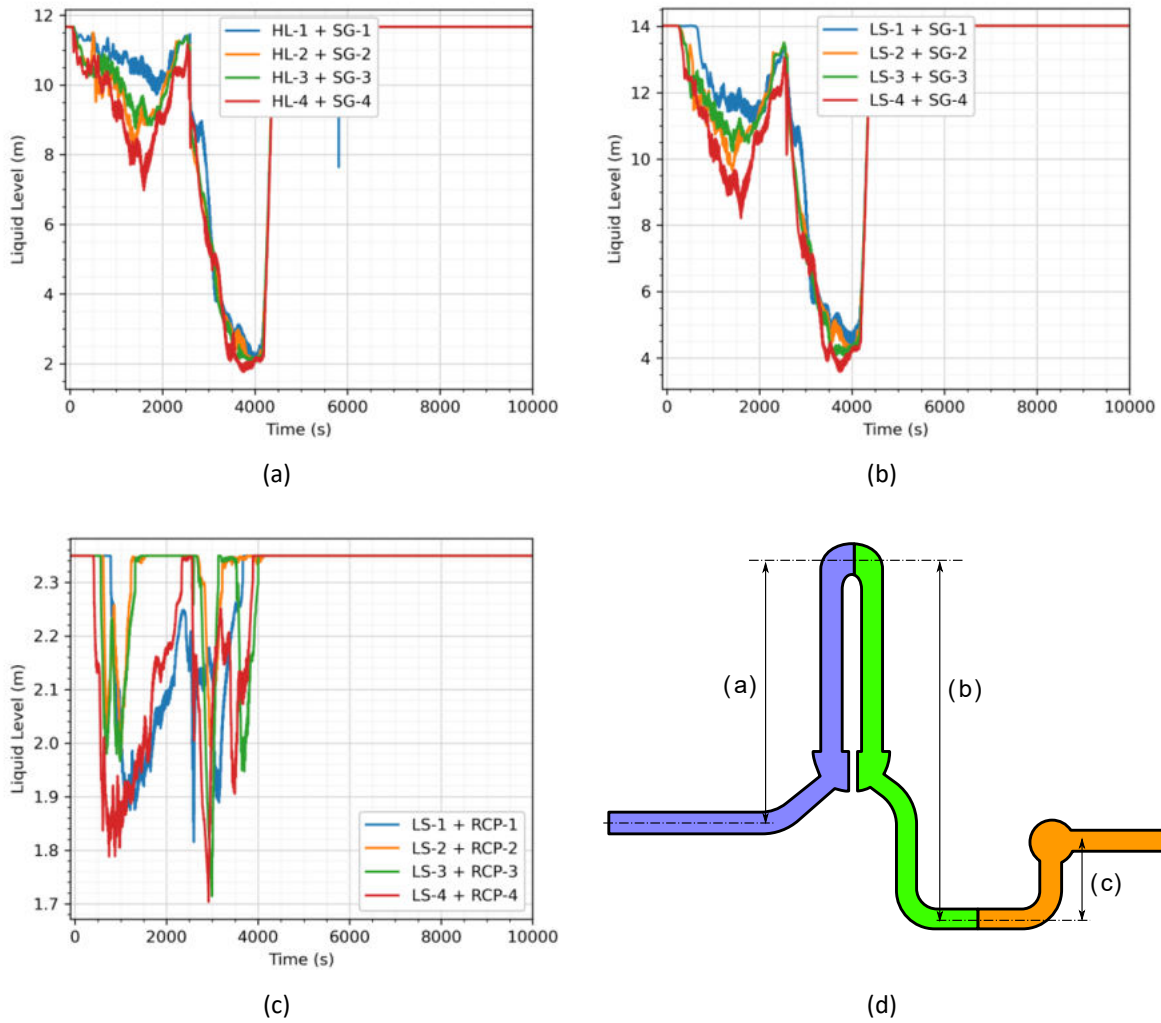
Figure 516: Collapsed Liquid levels in (a) the HL and HL Side of the SG, (b) the SG and Loop Seals and (c) the Loop Seals and RCPs as Illustrated in (d).

(a)   (b)
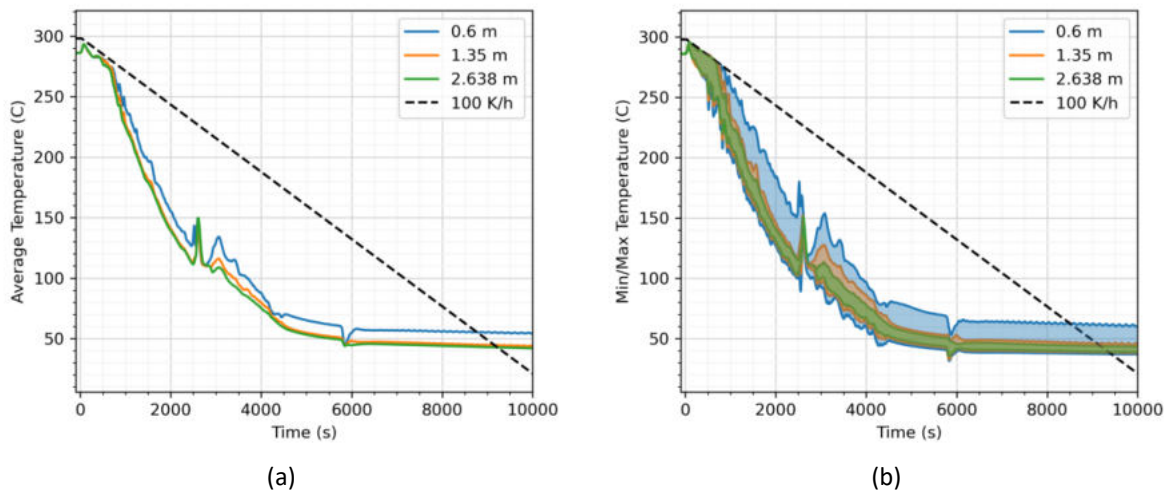
Figure 517: (a) Azimuthally-averaged and (b) Minimum and Maximum Coolant Temperatures in the DC at Fixed locations Below the RPV Inlets.
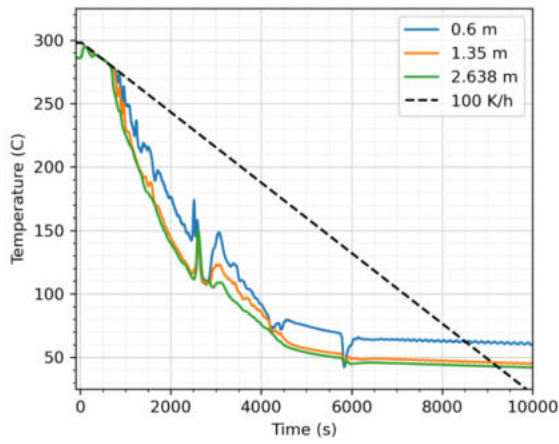
Loop 1
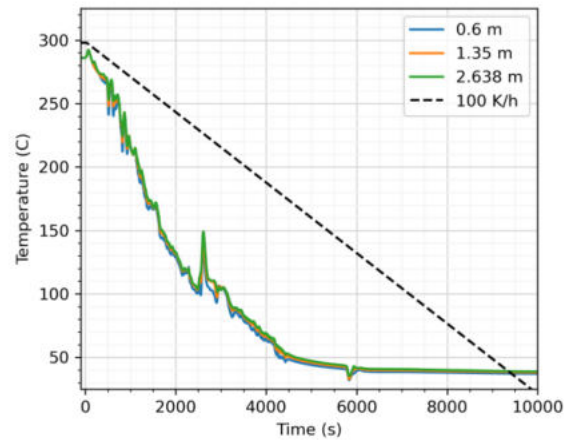
Loop 2
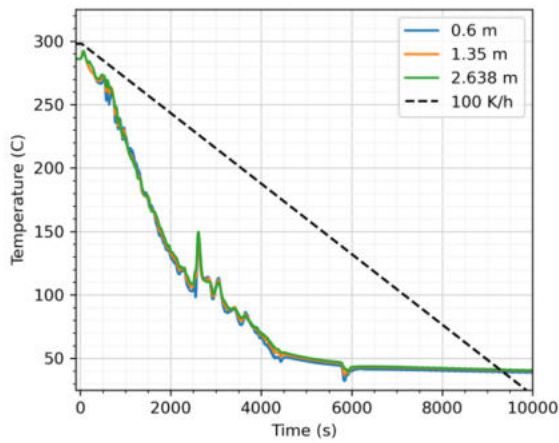
Loop 3
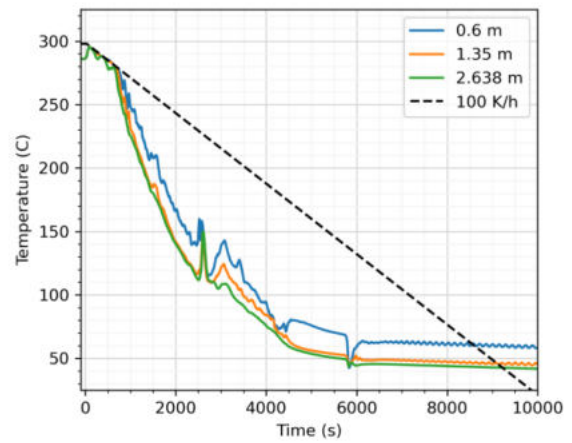
Loop 4

Figure 518: Coolant Temperatures at Fixed Axial Locations below the RPV Inlets.

Loop 1

Loop 2

Loop 3

Loop 4
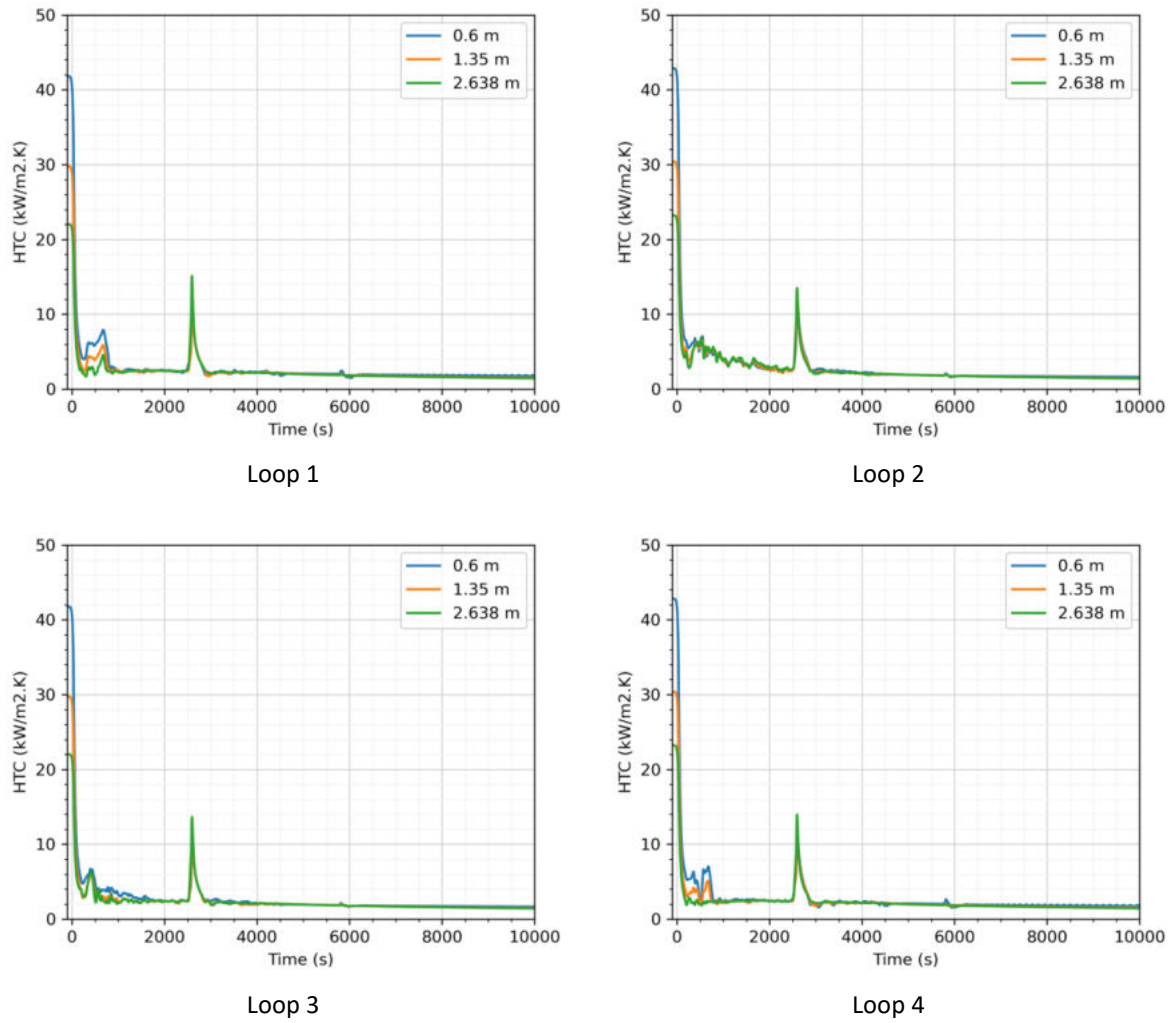
Figure 519: Heat Transfer Coefficient at Fixed Locations below the RPV Inlets.
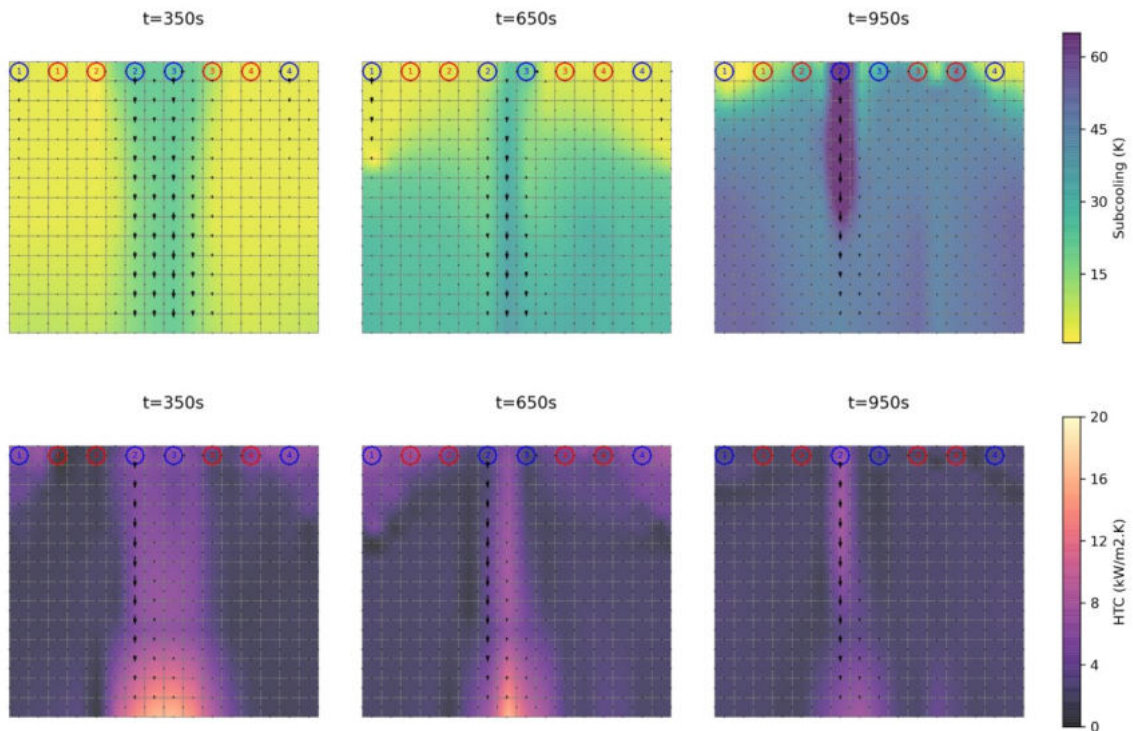
Figure 520: Unwrapped Colour Plot[5] of the (top) Coolant Subcooling $T_{sat} - T_c$ and (bottom) Heat Transfer Coefficient at Different Time Points during the Transient. The plots are overlaid with vectors showing the mass flux distribution.
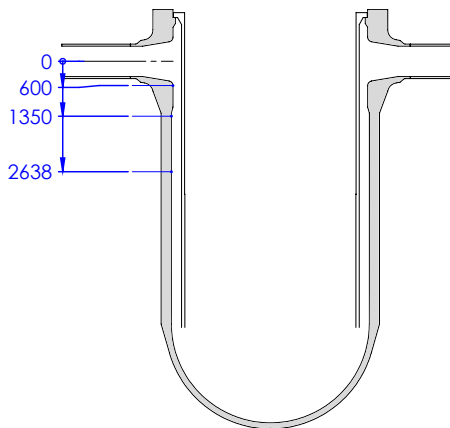
Figure 521: Axial Locations for the Sampling of Coolant Temperature and HTC.

20.2 Input uncertainties

The input uncertainties for all parameters are summarized in Table 56. The PDFs of the parameters are generally taken from the WP2 Task 2.2 final report in Reference [83], which are reproduced in Table 30 for the plant parameters and Table 34 for the model parameters. The PDFs for the decay heat multiplier and the accumulator levels were modified as compared to that listed in WP2 Task 2.2 (and reproduced in Table 30) to take into account more realistic values. The PDFs are the same as that used for the ATHLET code system (see Table 31).

---

[5] Colour plots are generated using a conservative grid mapping algorithm, which maps the integrated coarse node average values from TRACE onto a bivariate spline surface and thereafter extracts point values on a refined grid by taking the derivative of the spline. The resulting surface conserves the node average values while ensuring a continuous function between nodes.

Table 56: PDF of uncertain input parameters

Name	PDF type	Param1	Param2
Initial Power	Normal	Mean = 100 W	Rstd = 1%
P steam generator	Uniform	Min = 60.2 bar	Delta = 8 bar
P pressurizer	Normal	Mean = 157.5 bar	Rel. std = 1%
Decay heat multiplier	Normal	Mean = 1	Std = 0.04
Time Safety Injection	Uniform	Min = 0.0s	Delta = 20s
T Accumulator	Uniform	Min = 20 C	Delta = 20 C
P Accumulator	Uniform	Min = 24 bar	Delta = 4 bar
T HPIS	Uniform	Min = 15 C	Delta = 30 C
Flow mult. HPIS	Normal	Mean = 1	Rel. Std = 10%
Choke flow multiplier CHM22	Normal	Mean = 0.848	Std = 0.0888
Kfactor at Break	Uniform	Min = 0.5	Delta = 1.5
Level Pressurizer	Uniform	Min = 6.28 m	Delta = 1 m
Level Accumulator	Uniform	Min = 8.148 m	Delta = 0.741 m
Liquid-Wall HTC	Loguniform	Min = 0.5	Max = 2
Vapor-Wall HTC	Loguniform	Min = 0.5	Max = 2
Wall Drag Coefficient	Loguniform	Min = 0.5	Max = 2
Form Loss Coefficient	Loguniform	Min = 0.5	Max = 2

20.3 Results of BEPU analyses

The PDFs were sampled 59 times to yield 95%/95% one-sided tolerance bound using Latin Hyper Cube sampling. The results are illustrated in Figure 522 and Figure 523 for the Pressure, Coolant and Wall Temperatures and HTC time dependent profile measured 1.35 m and 2.64 m below the centreline of the cold legs. The results are given below CL-1 (non-injecting) and CL-2 (injecting). The other CLs have similar results. The 59 samples are illustrated in dashed blue lines, whereas the mean value and ±1σ bounds are shown in black line. For the temperature profiles, the bound is defined as the sample with the lowest temperature at each time point. For the pressure and HTC time dependent profiles, the maximum values are used to define the bound. The 95%/95% bound is shown in red. The Base Case value (see Section 20.1) are showed in orange for comparison. Note that all data are presented here with a time step of five seconds for clarity (but data were obtained with a one-second time step.)

357
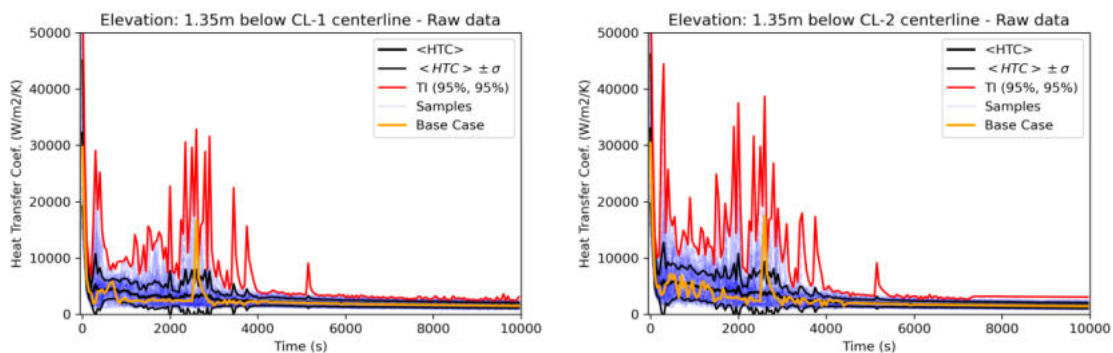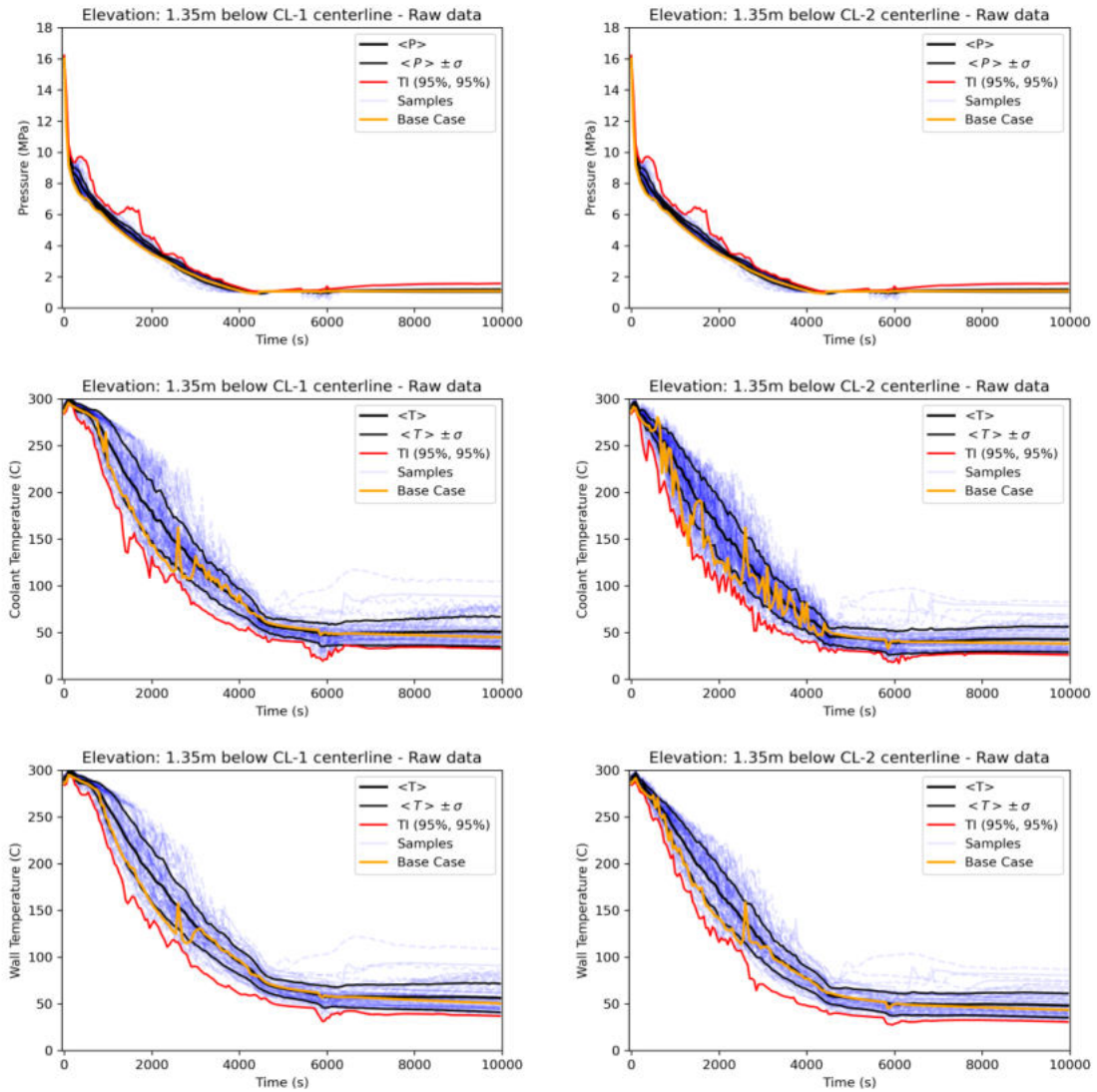
Figure 522: HTC, Pressure and Coolant and Wall Temperature profiles 1.35 m below the CL-1 (left) and CL-2 (right) centrelines.
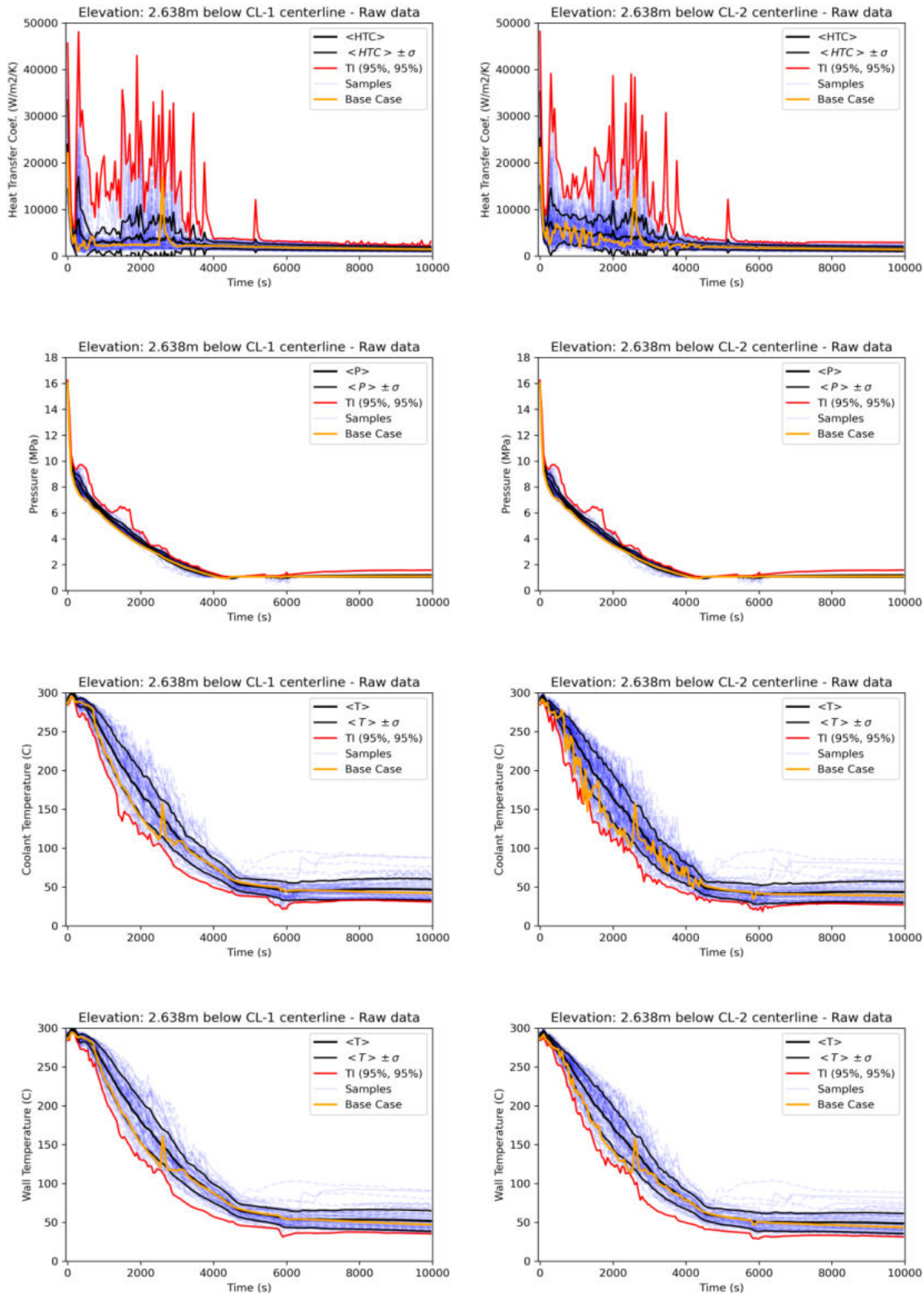
Figure 523: HTC, Pressure and Coolant and Wall Temperature profiles 2.64 m below the CL-1 (left) and CL-2 (right) centrelines.

The temperature obtained in the base case are slightly conservative but still generally within 1σ of the mean profile.

20.4 Sensitivity analyses

Sensitivity analyses were performed using the 59 samples using pairplots and Spearman correlation coefficients. For this exercise, we transformed the time dependent coolant T, P and HTC into scalar values by integrating the values over the whole transient (i.e. all 10'000s) and normalizing by the same values obtained for the base case (in order to provide a more significant scale). The scalar quantity of interest can be written as:

$$T_{qoi} = \frac{\int_0^\infty T_i(t)}{\int_0^\infty T_0(t)}$$

$$P_{qoi} = \frac{\int_0^\infty P_i(t)}{\int_0^\infty P_0(t)}$$

$$HTC_{qoi} = \frac{\int_0^\infty HTC_i(t)}{\int_0^\infty HTC_0(t)}$$

with the sample i varying from 1 to 59 and i=0 being for the base case.

Figure 524 and Figure 525 show the results of the sensitivity analysis for the integrated P, T and HTC 1.35 m below CL-1. Similar results were obtained below the other cold legs and at the lower elevation of 2.64m. Figure 524 show as an illustration the pairplot of the integrated P, T and HTC. The Spearman correlation coefficients ρ are shown on the off-diagonal element below the diagonal. The vertical dash lines show the values for the base case. As can be seen the correlation between the outputs are moderate. Figure 525 shows the integrated P, T and HTC values versus the most influential input parameters. The influential parameters are selected based on their Spearman correlation coefficient with the output. The input parameter is shown in Figure 525 if any of the absolute value of the Spearman coefficient is larger than a threshold value 0.3. The Pressure output is most correlated with the steam generator pressure (sgPressure), the choke-flow multiplier (chm22) and the wall-liquid HTC (spLHTCWallSV). The HTC output is almost completely correlated with the Wall-liquid HTC, which is expected given that this model parameter multiply the HT value calculated by TRACE. Finally, the temperature output is correlated with the HPIS temperature and the HPIS flow multiplier.
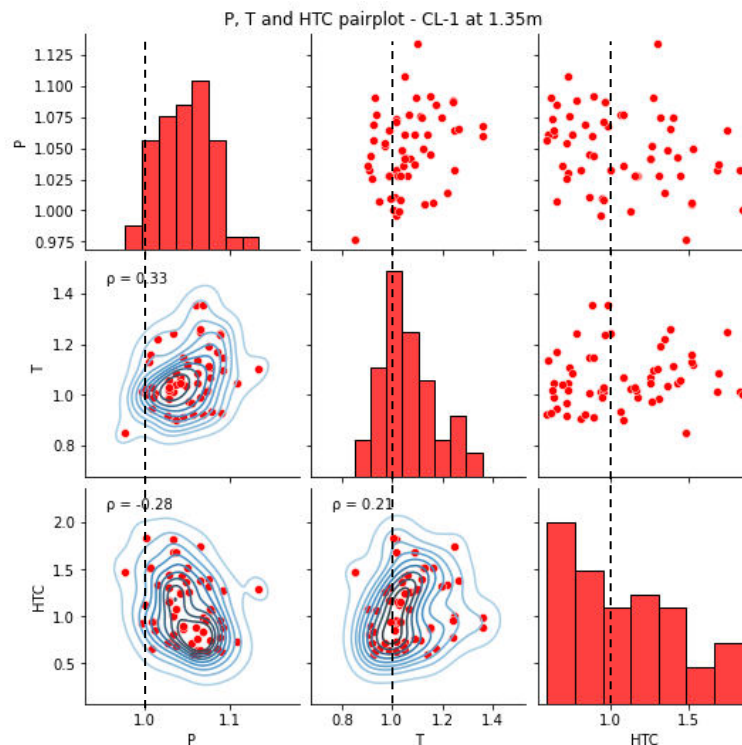
Figure 524: Pairplot of the integrated P, Tcoolant, and HTC profile 1.35 m below CL-1
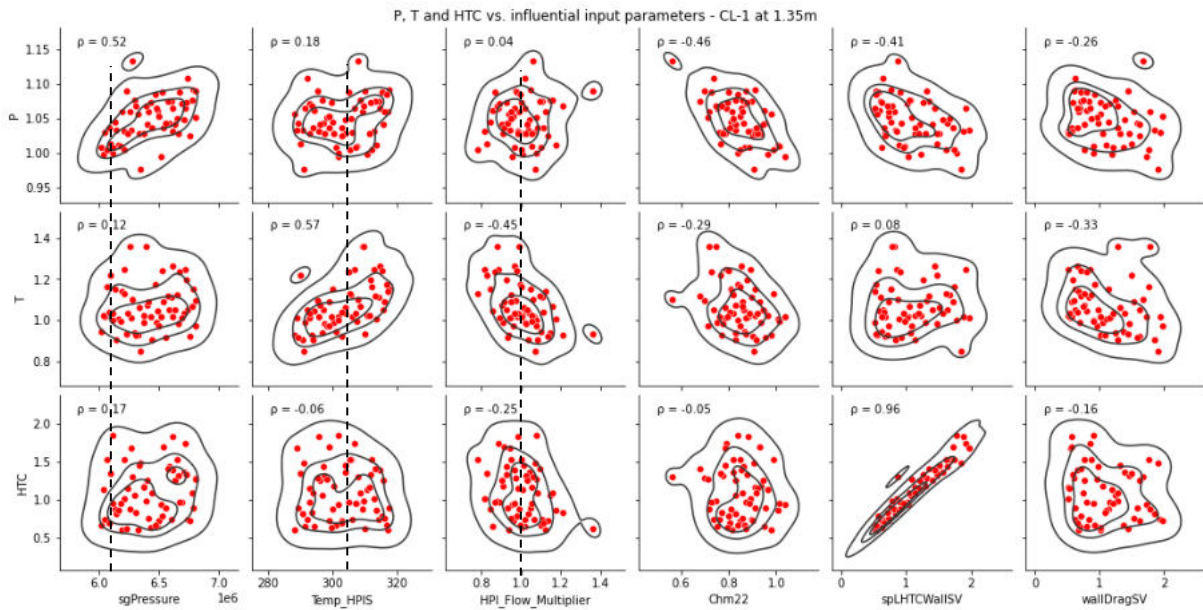
Figure 525: Pairplot of the integrated P, Tcoolant, and HTC profile 1.35 m below CL-1 vs the most influential input parameters

As a disclaimer, the Spearman correlation coefficient cannot rigorously be used to define sensitivity vectors given the non-normal and non-linear problem at hand. A more rigorous analysis (e.g. with Sobol Sensitivity Indices) requiring more simulations (and possibly a metamodel) would be required to confirm these conclusions.

21   Comparison of results of BEPU analyses

The following organizations performed the best-estimate plus uncertainty (BEPU) thermal-hydraulic calculations of SBLOCA with break 50 cm^2 in hot leg of KWU-1300:

a) UJV with RELAP5 and DAKOTA
b) JSI with RELAP5 and SUSA
c) WUT with RELAP5 and in-house statistic tools
d) KIWA with RELAP5 and SUSA
e) PSI with TRACE and in-house statistic tools
f) GRS with ATHLET and SUSA
g) GRS with ATHLET+ECCMIX and SUSA
h) Fra/G with KWU-MIX and SUSA

Results of sampled 59 calculations to yield 95%/95% one-sided tolerance bound are compared in figures below. The following 7 parameters from the first 6 BEPU analyses are compared at the following pages.

- Primary pressure (DC)
- Coolant temperature at 1.350 m under CL1
- Coolant temperature at 1.350 m under CL2
- HTC at RPV wall at 1.350 m under CL1
- HTC at RPV wall at 1.350 m under CL2
- Inner RPV wall temperature at 1.350 m under CL1
- Inner RPV wall temperature at 1.350 m under CL2
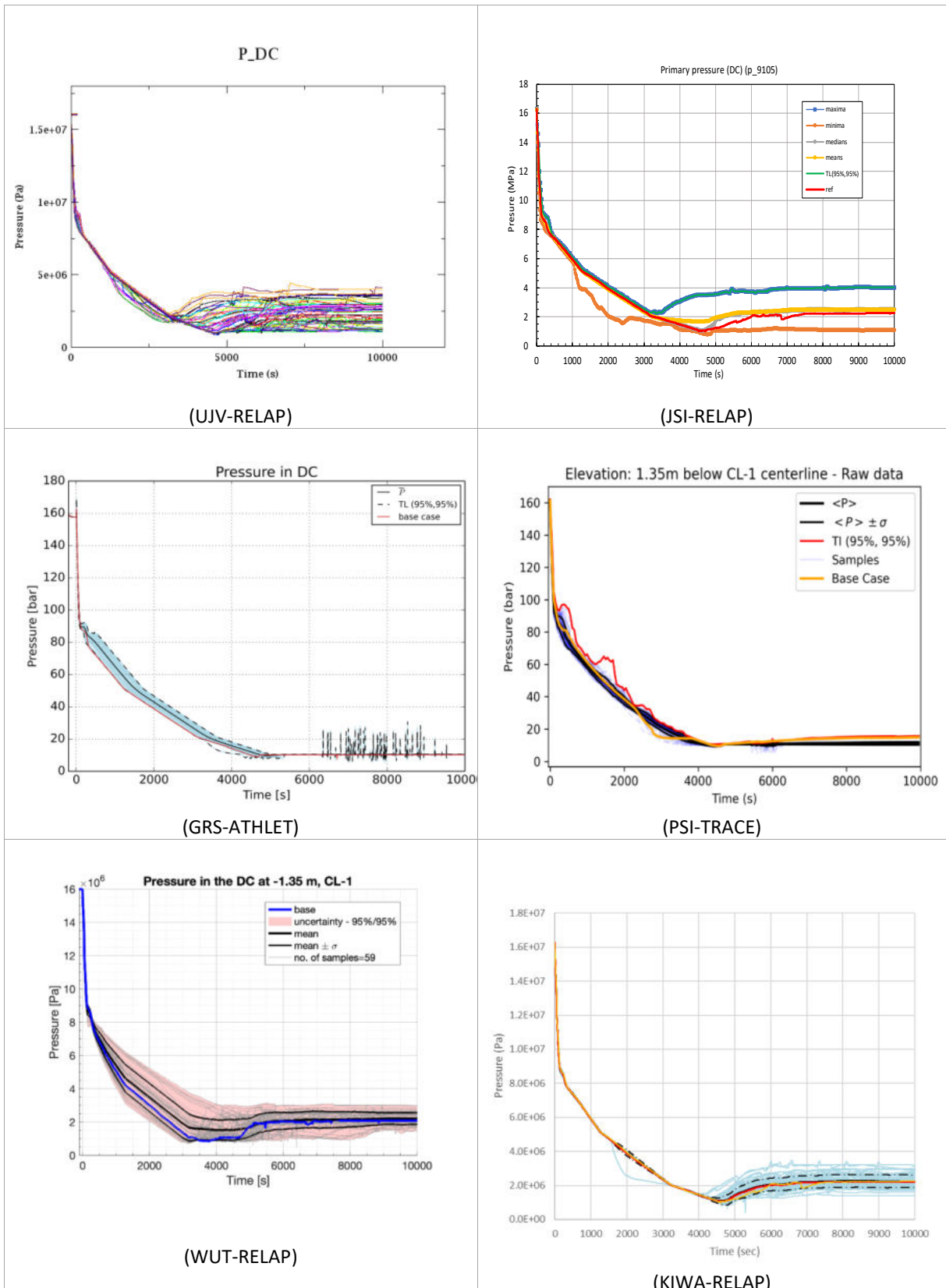
Figure 526: Primary pressure - comparison

363
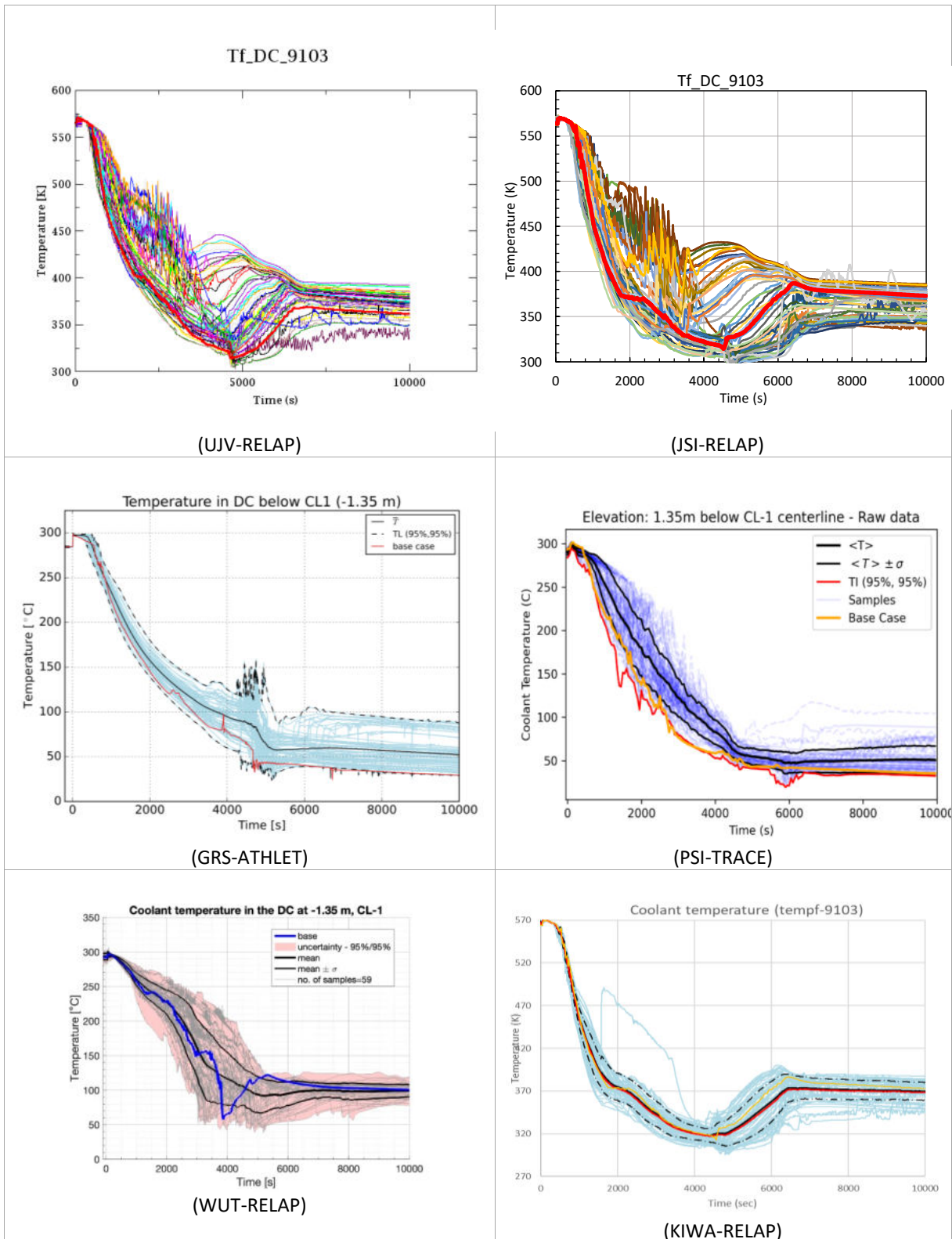
Figure 527: Coolant temperature at 1.350 m under CL1 - comparison
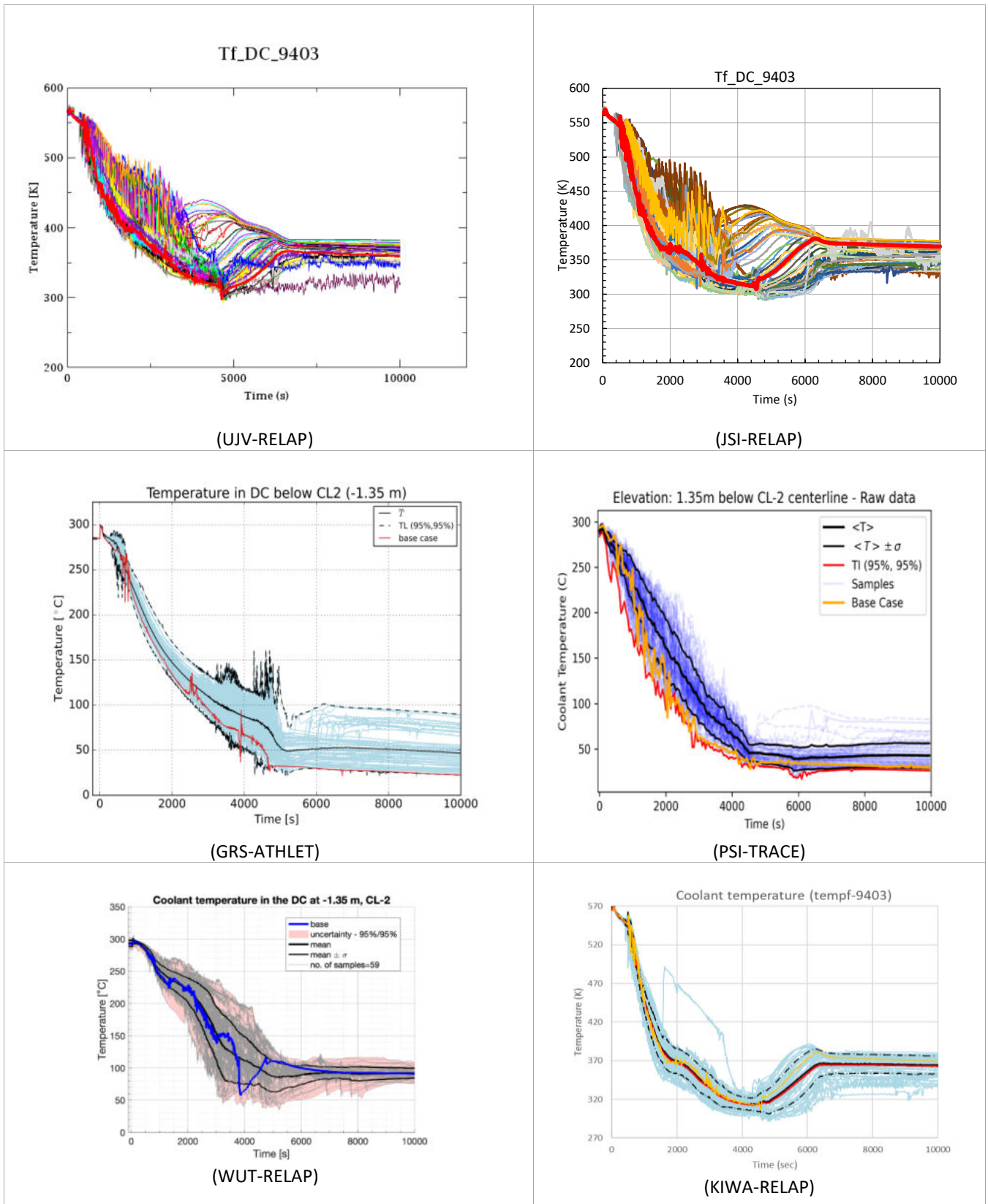
Figure 528: Coolant temperature at 1.350 m under CL2 - comparison
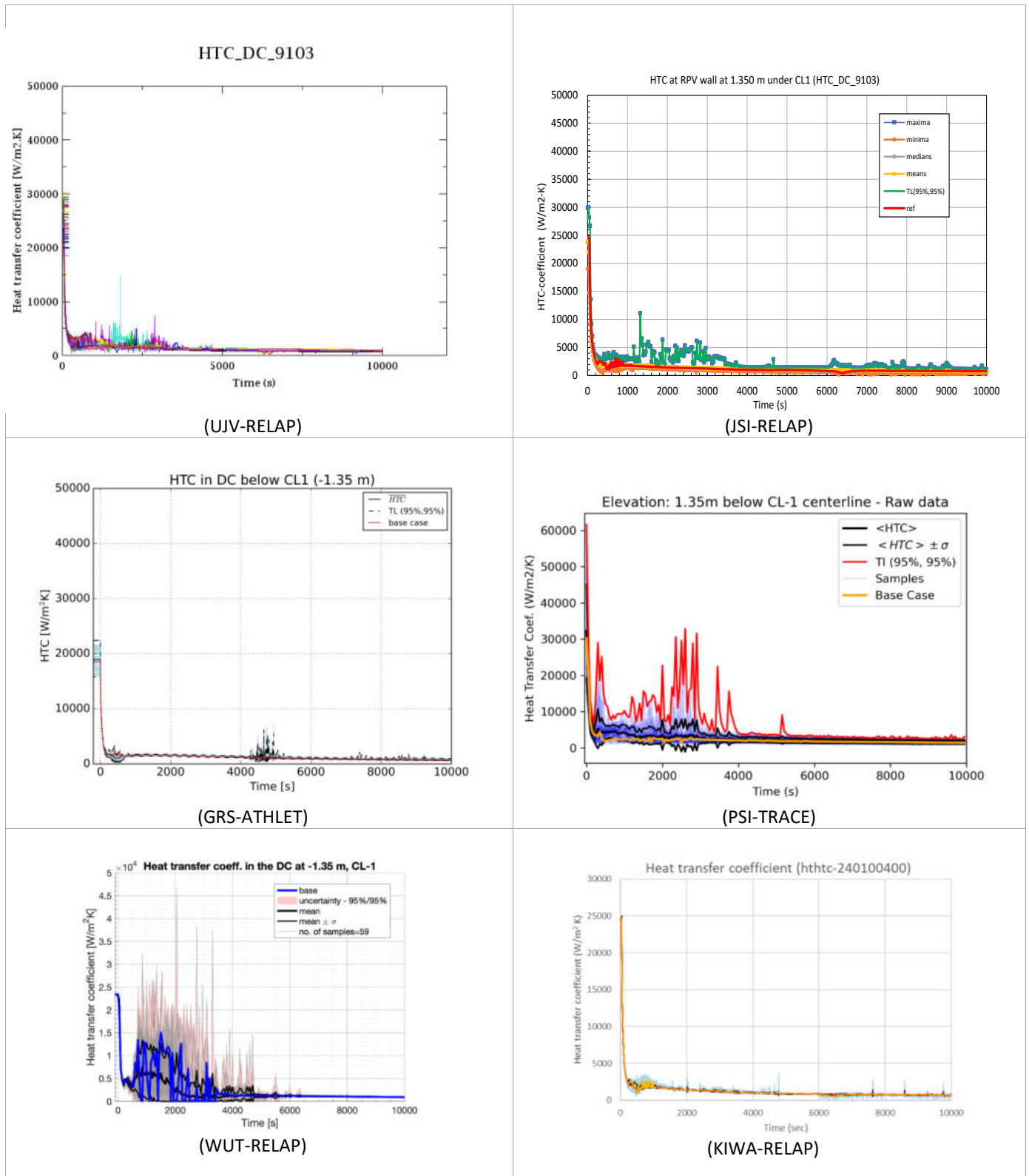
Figure 529: HTC at RPV wall at 1.350 m under CL1 - comparison
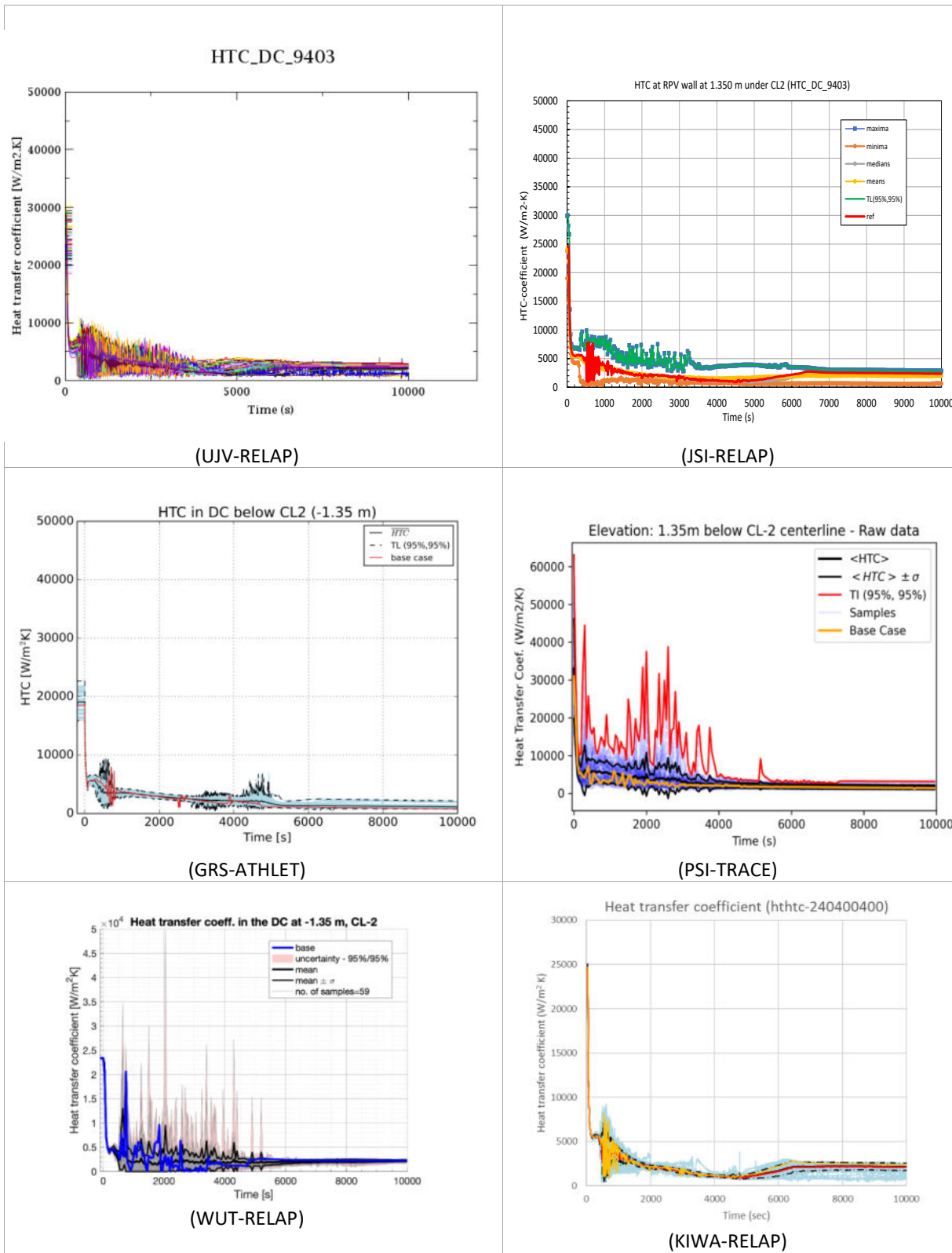
Figure 530: HTC at RPV wall at 1.350 m under CL2 - comparison
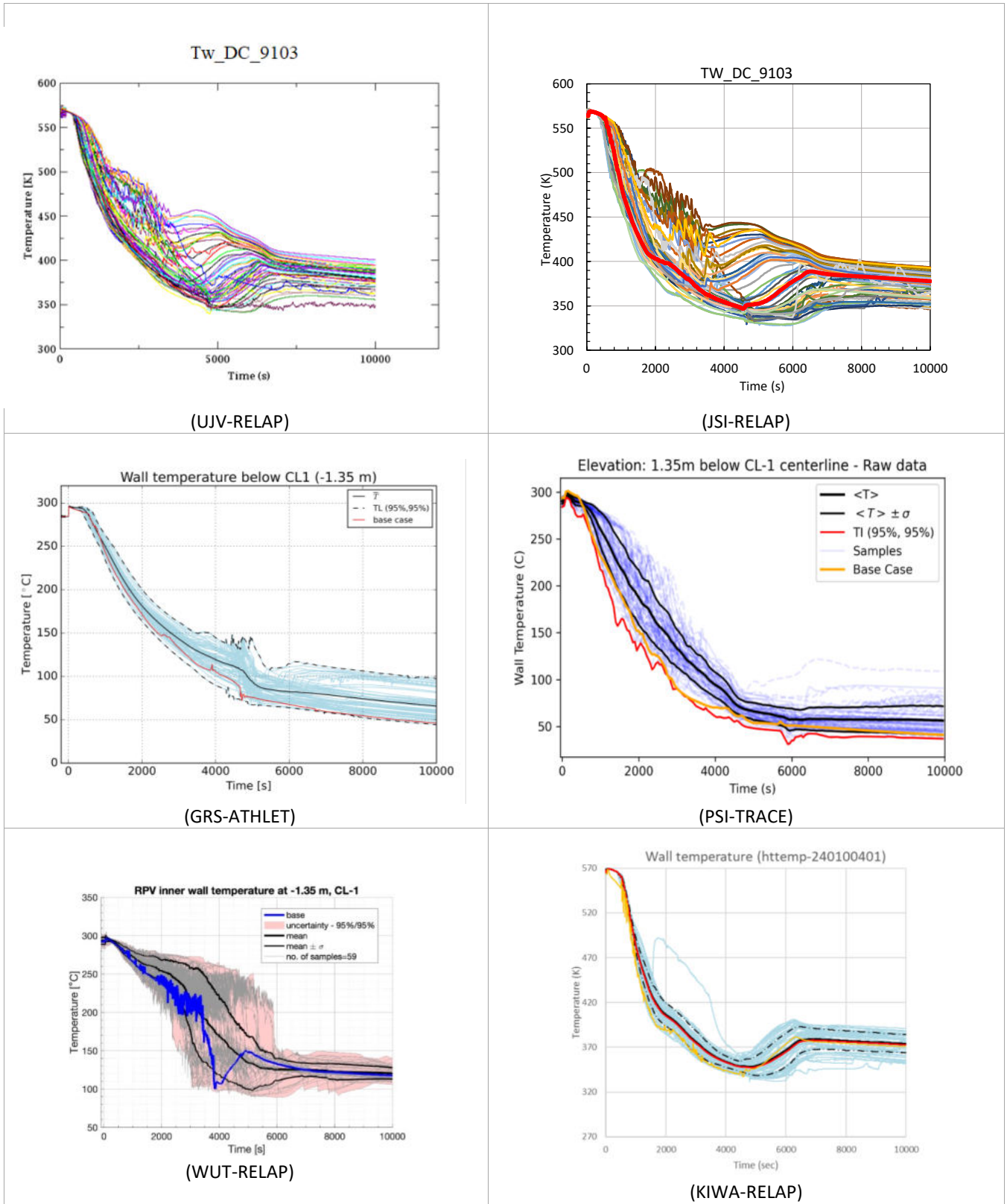
Figure 531: Inner RPV wall temperature at 1.350 m under CL1 - comparison
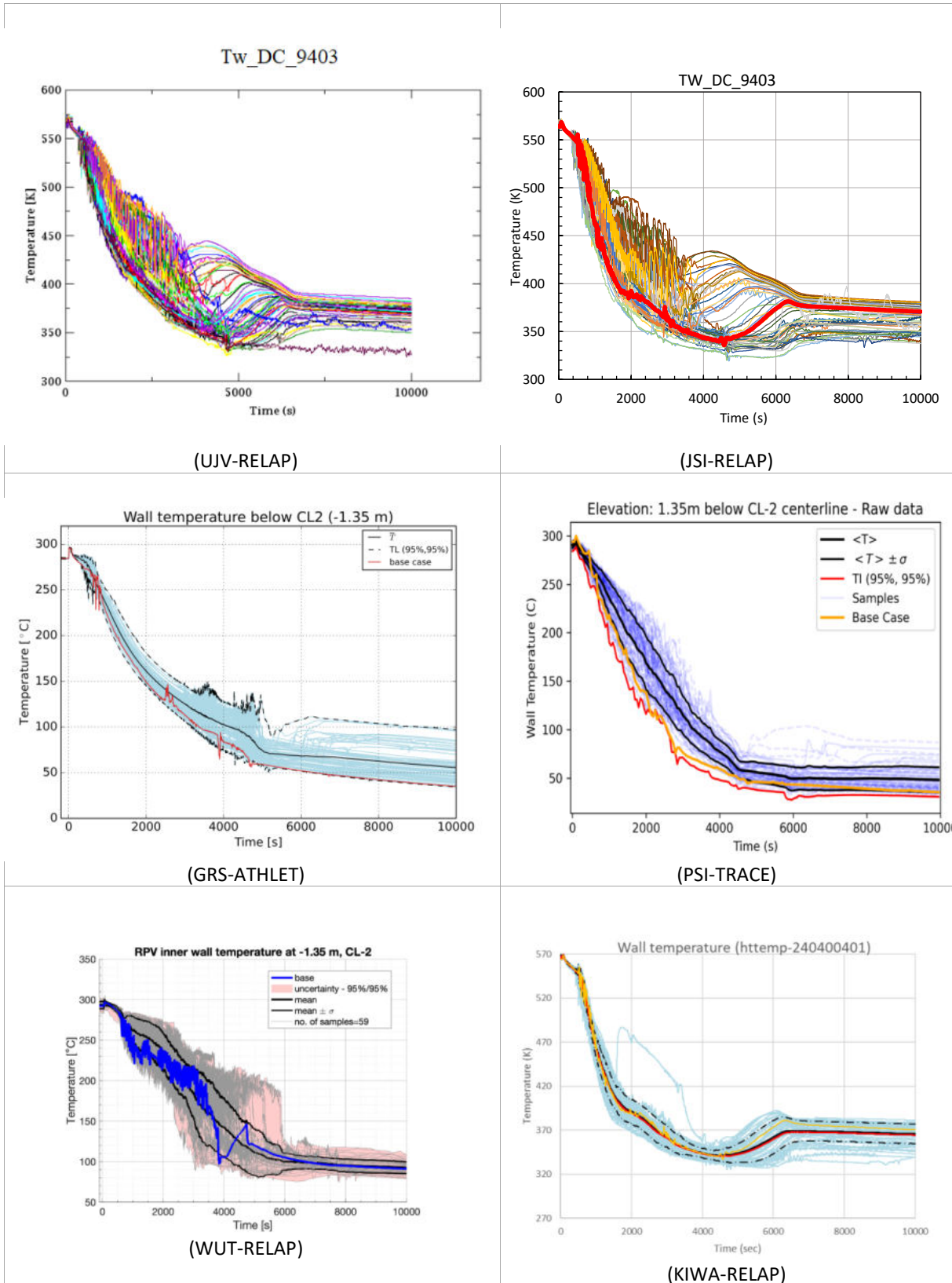
Figure 532: Inner RPV wall temperature at 1.350 m under CL2 - comparison

In the following 2 figures, the upper bounding values of primary pressure and lower bounding values of RPV wall temperature from the BEPU calculations are compared.

369
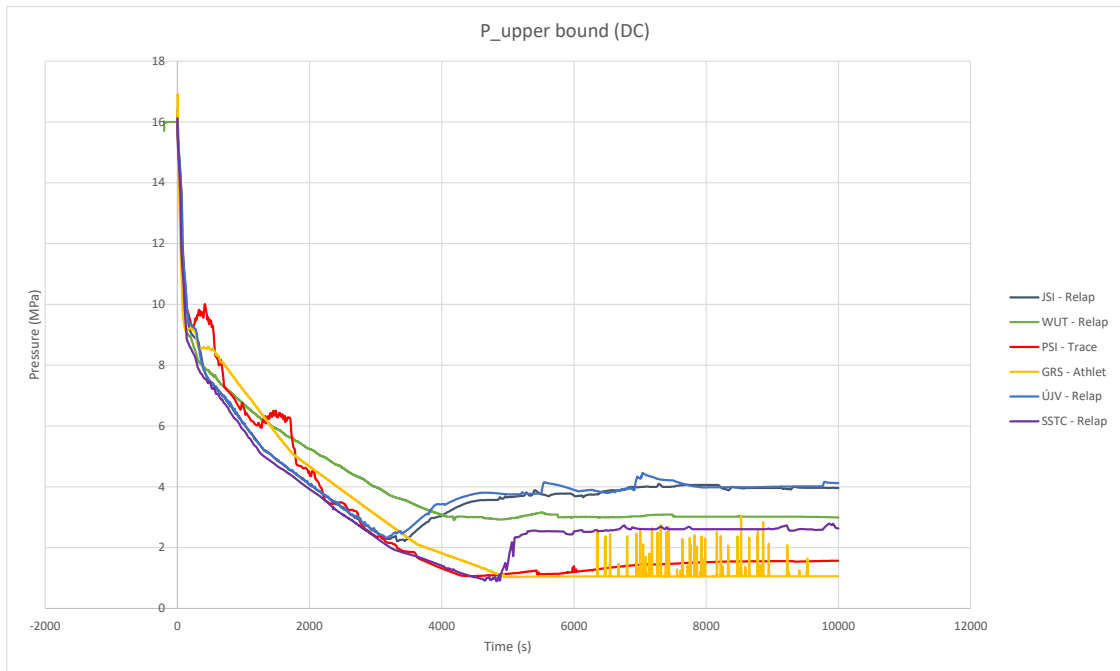
Figure 533: Comparison of upper bounds of pressure
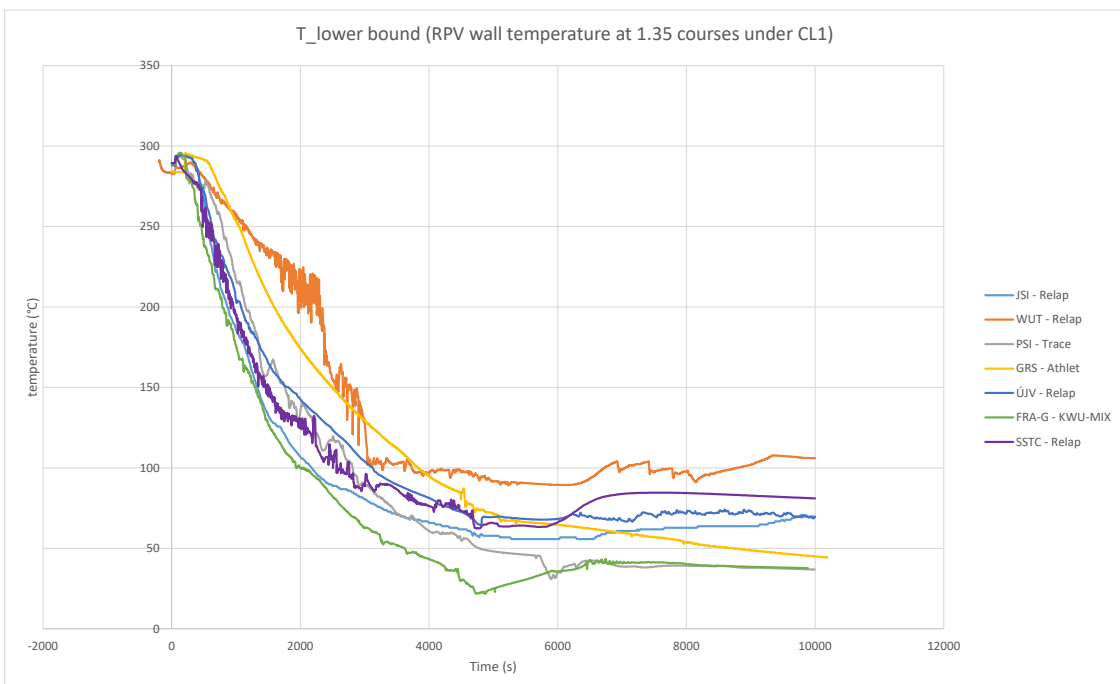
Figure 534: Comparison of lower bounds of RPV temperature

22   Conclusions

APAL (Advanced PTS Analysis for LTO) is a project funded by the EU within HORIZON 2020 programme. One of the most limiting safety assessments for the long-term operation (LTO) of nuclear power plants (NPPs) is the reactor pressure vessel (RPV) integrity assessment for pressurized thermal shock (PTS). The main objectives of APAL project are establishment of state-of-the-art of LTO improvements having an impact on PTS analysis, development of advanced deterministic and probabilistic PTS assessment methods including thermal hydraulic (TH) uncertainty analyses, the quantification of safety margins for LTO improvements and the development of best-practice guidance. The APAL project consists of 7 work packages (WP), which are listed in the Introduction chapter of this report.

This report summarizes the work and results of **WP2 "Improvement of TH analysis".** The main objective of the WP2 was the identification and evaluation of uncertainties of thermal-hydraulic (TH) analysis in the frame of pressurised thermal shock (PTS) assessment. Besides the model uncertainties connected with computer code models and plant uncertainties covering initial and boundary conditions and parameters of nuclear power plant (NPP) systems, the work was also focused on uncertainties connected with human factors. A better assessment of the uncertainties in the thermal hydraulic data was helpful for quantifying their contributions to the overall reactor pressure vessel (RPV) integrity margins and it will provide more insights on the whole PTS analysis. In addition, the effect of selected long-term operation (LTO) improvements relevant for PTS analysis (WP1) was analysed at the TH level in WP2. The WP2 consisted of 3 tasks:

- Task 2.1 Quantification of impact of LTO improvements and human factor on TH analysis boundary conditions
- In Task 2.2 Evaluation of uncertainties in TH analysis related to computer code models, plant parameters, and human factors
- In the Task 2.3 Performance of the TH uncertainty analysis and export of TH data sets

In the **Task 2.1 Quantification of impact of LTO improvements and human factor on TH analysis boundary conditions,** TH analyses for the base case (SBLOCA with 50 cm^2 break in hot leg of KWU-1300 PWR) and for the selected LTO improvements were performed with different computer codes. Further, the effect of selected human interactions was evaluated with the help of TH simulations. TH data sets representing selected LTO improvements or human factor were delivered to WP3 and WP4 for DFM and PFM analyses.

System and mixing codes used in the simulations were RELAP5, ATHLET, TRACE, KWU-MIX, GRS-MIX and ECC-MIX. The applicability of the Fluent and OpenFOAM CFD codes for the selected case was tested too.

The assumed plant type used in the analysis presented in this report was a German design 1300 MW four-loop PWR. The same reactor design was used earlier in the International Comparative Assessment Study of Pressurized-Thermal-Shock in Reactor Pressure Vessels (ICAS/RPV-PTS) under the Organization for Economic Co-operation and Development (OECD)[3]. Models of KWU-1300 and ICAS T2 transient (SBLOCA) for above mentioned computer codes were prepared in frame of the APAL project. The most complex plant models are the input decks for system TH codes – here the RELAP5, ATHLET and TRACE codes. Substantial effort was made to unification of assumptions in modelling of ICAS T2 SBLOCA by all 3 system thermal hydraulic codes.

A comparison of the base case results by all three TH system codes i.e., RELAP5, ATHLET, TRACE was made. The data for this comparison were provided by UJV, GRS and PSI respectively. Generally, the results agreed very well. Due to the differences in the choked-flow models between the codes the flow rates from the leak during critical discharge conditions were somewhat different and as a result the primary pressure curves slightly diverged from each other. Because HP and ACC injection depend on the system pressure the flow rate and timing of ECC injection varied between the codes. Therefore, also the coolant inventories and distributions during the transient were slightly different in the three

simulations. During the latter phase of the transient ATHLET and RELAP5 predicted slightly higher temperatures in the DC than TRACE.

GRS extended its ATHLET simulations of the base case by applying the ATHLET integrated injection model ECC-MIX. The temperatures and HTCs in the DC at the postulated weld positions below the CL symmetry axis were additionally calculated using the mixing code GRS-MIX. The application of the ECC-MIX model influenced the amount of void that built up in the main coolant pipes and DC and therefore the void at the break position went to zero ~500 s earlier and thus the coolant loss mass flow also increased earlier. The use of ECC-MIX lead to lower temperatures at the postulated weld positions below the CL symmetry axis of up to -20 K. By calculating local temperatures with GRS-MIX based on the results of the ATHLET base case an immediate decrease could be observed for both investigated positions with a maximum deviation of -35 K at the 1.35 m position. GRS-MIX predicted a higher HTC than the ATHLET only and ECC-MIX case.

Results from the UJV system analysis performed with RELAP5 were used as input to the fluid-mixing analysis performed with KWU-MIX by Fra-G. Data for the temperatures and HTCs as a function of time and location were calculated. As soon as the ECC injection began and the flow of water in the loop through the MCP was small enough to prevent complete mixing in the CL, KWU-MIX calculated a separate temperature for the hot water based on an energy balance for all the mixing regions. Therefore, starting at approximately 350 s, the hot-water temperature was slightly different from the RELAP5 result. Initially, when the ECC flow rate was small, the height of the cold-water layer was approximately 0.2 m above the bottom of the CL. With increasing ECC flow, the height of the cold-water layer increased correspondingly. The height of the cold-water layer determined the width of the plume at its origin in the DC, just below the bottom of the cold-leg nozzle. At a distance of 1.05 m and 1.35 m below the cold-leg axis, the width of the plume was smaller than at its origin early in the transient due to the strong buoyancy force that accelerates the flow in the plume. The two neighbouring plumes at the lower elevations were merged for the entire transient. The temperature throughout the plumes, as well as the HTCs in the DC, had a Gaussian distribution along the circumference of the RPV wall.

The following LTO improvements and operator actions were analysed in the Task 2.1:
- Heating of water in the HPSI tanks
- Heating of water in the ACCs
- Heating of water in the LPSI tanks
- Decreasing the HPSI head
- Decreasing the HPSI capacity
- Reduction of HPSI flow (operator action)
- Decreasing of ACC pressure
- Change of cooldown rate (operator action)
- Isolation of ACCs (operator action)

Simulation results presented in the Task 2.1 report [33] have focused on the system behaviour for the first 4900 s following the SBLOCA. This is sufficient time for the primary system to depressurise to ~1 MPa and initiation of the LPI, thus ensuring longer term cooling of the core. The simulations also suggest that the system stabilises around the conditions at 4900 s. To confirm the longer-term behaviour of the system, PSI and JSI extended some of their TRACE and RELAP5 simulations to 10 000 s. In the RELAP5 simulations, the pressure increased so that the LPI and ACC injections were terminated before 5000 s. This means that the majority of plotted variables were constant after 5000 s. The coolant temperatures either remained relatively constant or had a sudden increase around 6000 s in the TRACE simulations. This sudden increase was associated with the re-establishment of natural circulation in one or more loops of the reactor as the primary system was refilled with coolant from the safety injection systems. Temperatures experienced a similar increase also in the RELAP5 simulations for the same reason, i.e., start of natural circulation. Such an increase in temperature

would lead to lower PTS-related stress in the RPV wall and therefore the assumption of constant temperature beyond 4900 s is conservative.

Additional studies by PSI (TRACE) and GRS (ATHLET) showed that the pressure response later in the transient was very sensitive to the modelling of the break and unaffected by the LTO improvement. Additionally, the exact geometry of any postulated break is very uncertain. It follows from this that, while the assumption of constant pressure after 4900 s may be non-conservative, this effect will not affect any conclusions with respect to LTO improvements. It will, instead be more relevant for Task 2.3, the T/H uncertainty analysis, for which the uncertainty in the break geometry must be considered. Thus, the simulations for Task 2.3 will need to be extended to at least 8000 s.

The final assessment of the effect of different LTO improvements will be done in WP3 and WP4 of the APAL project.

In the **Task 2.2 Evaluation of uncertainties in TH analysis related to computer code models, plant parameters, and human factors**, uncertainties in thermal-hydraulic analyses for PTS were identifies, pre-assessed and prepared for application in BEPU analyses to be performed in Task 2.3.

Three types of uncertainties were investigated: model uncertainties (connected with computer-code models and the correct prediction of relevant phenomena), plant uncertainties covering initial and boundary condition and parameters of the NPP systems, and uncertainties connected with human interaction.

The foundation for a best-estimate-plus-uncertainty methodology was the Phenomena Identification and Ranking Table (PIRT). For the particular SBLOCA transient given in the ICAS program and referred to as T2, the PIRT was elaborated. The most important phenomena were identified by the ranking in the PIRT, and the corresponding parameters from the computer codes are characterized preferably by uncertainty distributions (within the framework of this project) or they are treated conservatively if necessary.

Because each of the computer codes used in the APAL (RELAP5, ATHLET, TRACE, KWU-MIX, GRS-MIX) have models different from the other computer codes, and because different sets of experimental data were sometimes used for comparison with computer results, the model uncertainty parameters were specific to each computer code.

Another category of uncertainties were the plant uncertainties covering initial and boundary condition and parameters of the NPP systems. Here, a similar sets of uncertainties were prepared for all system TH codes. Also, the uncertainties connected with the human factor were prepared in similar way for all system TH codes.

In the **Task 2.3 Performance of the TH uncertainty analysis and export of TH data sets** the best-estimate plus uncertainty (BEPU) analyses of SBLOCA in 1300 MWe PWR were performed. The input uncertainties and their distributions were based on results of Task 2.2 of the APAL project. Several system thermal-hydraulic codes (RELAP5, ATHLET, TRACE), one regional mixing calculation code (KWU-MIX), and several software tools for statistical analyses (SUSA, DAKOTA etc.) were applied to the uncertainty analyses.

The figures of merit (FOM) evaluated in the BEPU analyses were as follows: primary pressure (DC), coolant temperatures at 1.350 m under CL1 and CL2, HTCs at RPV wall at 1.350 m under CL1 and CL2, and inner RPV wall temperatures at 1.350 m under CL1 and CL2. It should be mentioned that CL1 and CL2 are the cold legs with active safety injection.

A standard BEPU analysis performed in the Task 2.3 consisted of a best-estimate reference calculation, definition of input uncertainties applied (based on Task 2.2 results), the set of BEPU calculations (with 59 or more samples), and the sensitivity analysis.

UJV Rez performed the BEPU analyses with the system TH computer code RELAP5 and DAKOTA software. The basic set of 59 sampled calculations to yield 95%/95% one-sided tolerance bound was

supplemented with set of 93 sampled calculations to yield 95%/95% two-sided tolerance bound. A limited sensitivity analyses was performed, too.

Framatome performed the BEPU analyses with the regional mixing code KWU-MIX and the SUSA software tool. As input for mixing calculations the results from UJV calculation with RELAP5 were used. Sensitivity analysis based on Spearman correlation was done.

JSI performed the BEPU analyses with the system TH computer code RELAP5 and the SUSA software and with 2 introductory steps. The first introductory step was the RELAP5 code versions sensitivity analyses. The second introductory step was a sensitivity study with varying one parameter at a time to get preliminary information on the impact of the main input uncertainties on the figures of merit (FOM). The sensitivity analyses were performed for all 7 FOMs.

GRS performed the BEPU analyses with the in-house developed computer tools ATHLET and SUSA. Two separate BEPU analysis were performed, one with and one without the mixing code ECCMIX (coupled with the ATHLET code). In both cases 59 samples were simulated for (95%,95%) one-sided statistical tolerance limits.

PSI performed the BEPU analyses with the system TH computer code TRACE and with an in-house script for statistical analyses. Sensitivity analysis based on Spearman correlation was done.

WUT performed the BEPU analyses with the system TH computer code RELAP5 and an in-house script for statistical analyses.

KIWA performed the BEPU analyses with the system TH computer code RELAP5 and the SUSA software. Sensitivity analysis was done with usage of the Spearman rank correlation.

SSTC performed the BEPU analyses with the system TH computer code RELAP5 and the SUSA software tool.

The results of individual BEPU analyses (system TH) were compared in the end of Task 2.2 and Deliverable D2.2 [35]. Also, a comparison of upper bounds of primary pressure and lower bound of RPV inner wall temperature (in cold plume region) was done.

The resulting thermal-hydraulic data sets were transferred to the structural and fracture mechanic analyses within WP3 and WP4 of the APAL project.

23   References

[1]   S. S. Wilks: Determination of sample sizes for setting tolerance limits, Ann. Math. Statist., vol. 12, pp 91-96, 1941

[2]   S. S. Wilks, "Statistical prediction with special reference to the problem of tolerance limits," Annals of Mathematical Statistics, vol. 13, no. 4, pp. 400–409, 1942.

[3]   Nuclear Energy Agency, "Comparison Report of RPV Pressurized Thermal Shock International Comparative Assessment Study (PTS ICAS), " OECD NEA/CSNI/R(99)3, 1999.

[4]   GRS, ATHLET Models and Methods, GRS - P - 1 / Vol. 4 Rev. 5, February 2019.

[5]   Division of Risk Assessment and Special Projects. Office of Nuclear Regulatory Research, TRACE v5.0 Patch 5 Theory Manual: Field Equations, Solution Methods and Physical Models, U.S. Nuclear Regulatory Commission, 2013.

[6]   STARS - A Multi-Physics Multi-Scale Analytical Facility, https://www.psi.ch/en/stars/code-system

[7]   Symbolic Nuclear Analysis Package (SNAP), https://www.snaphome.com

[8]   Identification of Further LTO Improvements, Deliverable No. 1.5, APAL Project. March 2021.

[9]   Regulatory Guide 1.157, Best-estimate Calculations of Emergency Core Cooling System Performance, U.S. Nuclear Regulatory Commission, May 1989.

[10]   Regulatory Guide 1.203, Transient and Accident Analysis Methods, U.S. Nuclear Regulatory Commission, December 2005.

[11]   TRACE Pressurized Water Reactor Modeling Guidance, U.S. Nuclear Regulatory Commission, Rev. 1, July 2014.

[12]   K. Iyer, H. P. Nourbakhsh, and T. G. Theofanous, REMIX: A Computer Program for Temperature Transients Due to High Pressure Injection After Interruption of Natural Circulation, NUREG/CR-3701, U.S. Nuclear Regulatory Commission, 1986.

[13]   International Atomic Energy Agency, Pressurised Thermal Shock in Nuclear Power Plants: Good Practices for Assessment, IAEA, Austria, IAEA-TECDOC-1627, 2010.

[14]   T. G. Theofanous and Y. Yan, A Unified Interpretation of One-Fifth to Full Scale Thermal Mixing Experiments Related to Pressurized Thermal Shock, NUREG/CR 5677, U.S. Nuclear Regulatory Commission, 1991.

[15]   R. Trewin, Mixing Model for a Downcomer during a Small-Break Loss-of-Coolant Accident for Use in Fracture-Mechanics Analyses, Proceedings of ICAPP 2015, Nice, France, May 03-06, 2015.

[16]   H. P. Nourbakhsh and, T. G. Theofanous, A Criterion for Predicting Thermal Stratification Due to High-Pressure Injection in a Circulating Reactor Loop. Nucl. Science and Engineering, 94, pp. 77-79, 1986.

[17]   J. H. Kim, An Analytical Mixing Model for Buoyant Jet Injected into Pipe Flow, J. Heat Transfer, Vol. 107, pp. 630-635, 1986.

[18]   L. N. Fan, Turbulent Buoyant Jets into Stratified or Flowing Ambient Fluids, Report No. KH-R-18, W.M. Keck Laboratory of Hydraulics and Water Resources, Division of Engineering and Applied Science, California Institute of Technology, Pasadena, California, June 1967.

[19]   S.N. Michas and P. N. Papanicolaou, Horizontal Round Heated Jets into Calm Uniform Ambient, Desalination, Vol. 248, pp. 803-815, 1979.

[20]   C.J. Chen and W. Rodi, Vertical Turbulent Buoyant Jets - A Review of Experimental Data, Pergamon Press, New York, 1980

[21]   D. G. Fox, Forced Plume in a Stratified Fluid, Journal of Geophysical Research, 75, pp. 5818-5835, 1970.

[22]   C. Bourque, and B. G. Newman, Reattachment of a Two-Dimensional, Incompressible Jet to an Adjacent Flat Plate, The Aeronautical Quarterly, Vol. XI, August 1960.

[23]   H.-G. Sonnenburg, "Phänomenologische versuchsauswertung des versuchs UPTF-TRAM C1 thermisches mischen im kaltstrang." GRS-A-2434, Gesellschaft für Anlagen und Reaktorsicherheit, 1997.

[24]   G. Lerchl, "Ein Modell zur Simulation des thermischen Mischens im Kaltstrang - Entwicklung und Implementierung in ATHLET." TN-LER-01/02, Gesellschaft für Anlagen und Reaktorsicherheit, 2002.

[25]   A. Wielenberg, L. Lovasz, P. Pandazis et al., Recent improvements in the system code package AC2 2019 for the safety analysis of nuclear reactors, Nuclear Engineering and Design, Vol. 354, 110211, 2019. https://doi.org/10.1016/j.nucengdes.2019.110211

[26]   OpenFOAM User Guide: CFD Direct, available at https://cfd.direct/openfoam/user-guide/.

[27]   M. Erickson Kirk, et al., "Technical Basis for Revision of the Pressurized Thermal Shock (PTS) Screening Limit in the PTS Rule (10 CFR §50.61)," NUREG-1806, Vol. 1, U.S. Nuclear Regulatory Commission, Washington, D.C., USA, August 2007.

[28]   D. E. Bessette, W. Arcieri, C. D. Fletcher, and R. Beaton, "Thermal-Hydraulic Evaluation of Pressurized Thermal Shock." NUREG-1809, U.S. Nuclear Regulatory Commission, Washington, D.C., USA, 2005.

[29]   V. Pistora, M. Zamboch, P. Kral, L. Vyskočil, " PTS re-evaluation project for Czech NPPs", Fourth International Conference on Nuclear Power Plant Life Management IAEA-PLIM, Lyon, 23–27 October 2017.

[30]   "State-of-the-Art for Thermal-Hydraulic (TH) Analysis, Deliverable No. 1.3, Advanced PTS Analysis for LTO (APAL)," European Union's Grant Agreement number 945253, Topic: NFRP-2019-2020-02 Safety assessments for Long Term Operation (LTO) upgrades of Generation II and III reactors, September 2021.

[31]   P. Kral et al., "Identification of Further LTO Improvements, Deliverable No. 1.5, Advanced PTS Analysis for LTO (APAL)," European Union's Grant Agreement number 945253, Topic: NFRP-2019-2020-02 Safety assessments for Long Term Operation (LTO) upgrades of Generation II and III reactors, March 2021.

[32]   C. Cueto-Felgueroso et al., "Public summary report of WP1, Deliverable No. 1.6, Advanced PTS Analysis for LTO (APAL)," European Union's Grant Agreement number 945253, Topic: NFRP-2019-2020-02 Safety assessments for Long Term Operation (LTO) upgrades of Generation II and III reactors, December 2021, available at https://apal-project.eu/.

[33]   M. Puustinen et al., "Results of TH analysis for selected LTO improvements, Deliverable No. 2.1, Advanced PTS Analysis for LTO (APAL)," European Union's Grant Agreement number 945253, Topic: NFRP-2019-2020-02 Safety assessments for Long Term Operation (LTO) upgrades of Generation II and III reactors, February 2022.

[34]   R. Trewin et al., "Evaluation of uncertainties in TH analysis related to computer code models, plant parameters, and human factors, Deliverable No. 2.2, Advanced PTS Analysis for LTO (APAL)," European Union's Grant Agreement number 945253, Topic: NFRP-2019-2020-02 Safety assessments for Long Term Operation (LTO) upgrades of Generation II and III reactors, May 2022.

[35]   P. Kral et al., "Results of TH Analysis Related to TH Uncertainties, Deliverable No. 2.3, Advanced PTS Analysis for LTO (APAL)," European Union's Grant Agreement number 945253, Topic: NFRP-2019-2020-02 Safety assessments for Long Term Operation (LTO) upgrades of Generation II and III reactors, December 2022.

[36]   P. Mazgaj et al., "Impact of Selected Long-Term Operation Improvements Relevant to the Pressurized Thermal Shock in PWR", 13th International Conference of the Croatian Nuclear Society, Zadar, 2022.

[37]   V. Pistora, C. Cueto-Felgueroso, S. Szavai, M. Zarazovskii, I. Clifford, R. Tiete, P. Kral: State-of-the-art reviews of PTS related topics performed within APAL project, IAEA PLIM 2022 conference, Vienna, 2022.

[38]   H. Glaeser et al., "Prediction capability of ATHLET computer code calculations of a 200% cold leg break on a German reference PWR facility", GRS-A-3279, Technical Report, Gesellschaft für Anlagen und Reaktorsicherheit GRS, 2005.

[39]   H. Glaeser et al., "Development of methods and exemplary application for evaluating the prediction capability of computer code calculations", GRS-A-3443, Technical Report, Gesellschaft für Anlagen und Reaktorsicherheit GRS, 2008.

[40]   H. Glaeser et al., "Unsicherheitsanalyse zum großen Bruch der kaltseitigen Hauptkühlmittelleitung nach Leistungserhöhung", GRS-A-3436, Technical Report, Gesellschaft für Anlagen und Reaktorsicherheit GRS, 2008.

[41]   P Bazin et al., "BEMUSE Phase III Report-Uncertainty and Sensitivity Analysis of the LOFT L2-5 Test." No. NEA-CSNI-R--2007-04. Organisation for Economic Co-Operation and Development, 2007.

[42]   J. Sarkar, J. Liebert, R. Läufer, "UPTF Test Instrumentation", Measurement System Identification, Engineering Units and Computed Parameters, KWU Work Report S554/92/13, Nov. (1992)

[43]   Report "UPTF Test Instrumentation – Additional Instrumentation for TRAM Groups B, C and D", Siemens AG, Work Report, KWU NT31/98/05, (1998)

[44]   Report "UPTF-TRAM Versuch C1/C2 - Strähnen- und Streifenkühlung der RDB-Wand", Quick Look Report, NT31/96/17, Siemens AG, Erlangen, Bereich Energieerzeugung (1996)

[45]   A. Wald and J. Wolfowitz, "On a Test Whether Two Samples are from the Same Population." *The Annals of Mathematical Statistics*, Vol. 11, No. 2, pp. 147-162 (1940)

[46]   H. Glaeser, "GRS Method for Uncertainty and Sensitivity Evaluation of Code Results and Applications," Science and Technology of Nuclear Installations, Volume 2008, Article ID 798901, 7 pages (2008)

[47]   D. Wicaksono, "Bayesian Uncertainty Quantification of Physical Models in Thermal-Hydraulics System Codes," PhD thesis, Swiss Federal Institute of Technology, Lausanne (2018)

[48]   S. Wenzel, Gesellschaft für Anlagen und Reaktorsicherheit - GRS – Personal communication

[49]   S. Joe and F. Y. Kuo, "Constructing Sobol'sequences with better two-dimensional projections," SIAM Journal on Scientific Computing, 30 (5), pp. 2635–2654 (2008)

[50]   H. Austregesilo et al., "Teilnahme am Internationalen Standardproblem ISP-50 mit ATHLET", GRS-A-3685, Technical Report, Gesellschaft für Anlagen und Reaktorsicherheit GRS, 2013.

[51]   F. Richter, "Die physikalischen Eigenschaften der Stähle: Das 100-Stähle-Programm." Arbeitskreis Thermophysik in der GEFTA: Berlin, Germany, 2010.

[52]   W. Pointner, N. Berner, M. Kloos, and S. Wenzel, "Statistische LOCA-Analysen", GRS-519, Technical Report, Gesellschaft für Anlagen und Reaktorsicherheit GRS, 2018.

[53]   A. AgrawaL and A. K. Prasad, "Integral Solution for the Mean Flow Profiles of Turbulent Jets, Plumes, and Wakes," Journal of Fluids Engineering, 125, 813-822, (2003).

[54]   J. H. Kim, "An Analytical Mixing Model for Buoyant Jet Injected into Pipe Flow." Journal of Heat Transfer, Vol. 107, pp. 630-635, August 1985.

[55]   R. Hertlein, "Mixing and Condensation Models Based on UPTF TRAM Test Results." Jahrestagung Kerntechnik 2003, Berlin, pp. 97 133, June, 2003.

[56]   B. K. H. Sun, and S. Oh, "A Correlation for Entrainment of Water in a Reactor Cold Leg by Coolant Injection Under Stagnant Loop Flow." ASME 83-WA/HT-39, American Society of Mechanical Engineers, New York, 1983).

[57]   W. Häfner, and L. Wolf, "Derivation of Mixing Parameters from the HDR-Thermal Mixing Experiments." International Journal of Pressure Vessels & Piping, Vol. 33, pp. 41-57, 1988.

[58]   K. Iyer and T. G. Theofanous, "Flooding-Limited Thermal Mixing: The Case of High-Fr Injection." Third International Topical Meeting on Reactor Thermal Hydraulics, Newport, Rhode Island, Oct. 1985.

[59]   N. Brauner, and D. M. Maron, "Stability Analysis of Stratified Liquid-Liquid Flows." International Journal of Multiphase Flow, Vol. 18, No. 1, pp. 103-121, 1992.

[60]   S. N. Michas, and P. N. Papanicolaou, "Horizontal round heated jets into calm uniform ambient," Desalination, Vol. 248, pp. 803-815, 1979.

[61]   P. N. Papanicolaou and E. J. List, "Investigation of Round Vertical Turbulent Buoyant Jets," Journal of Fluid Mechanics, Vol. 195, pp. 341-391, 1988.

[62]   G. Jirka, "Integral Model for Turbulent Buoyant Jets. Part I: Single Round Jet," Environmental Fluid Mechanics, Vol. 4, pp. 1-56, 2004.

[63]   H. Schlichting, "Boundary-Layer Theory," McGraw-Hill book Company, New York, Seventh edition, 1979.

[64]   W. H. Press, and W. T. Vetterling, "Numerical Recipes in Fortran 77: The Art of Scientific Computing," Cambridge University Press, p. 179 (1992).

[65]   C. J. Chen, and C. H. Chen, "On prediction and unified correlation for decay of vertical buoyant jets." In: Trans. ASME, Vol. 101 (1979): 532-537.

[66] "The Marviken Full Scale Critical Flow Tests: Summary report: joint reactor safety experiments in the Marviken Power Station," NUREG/CR-2671, U.S. Nuclear Regulatory Commission, Washington, D.C., May 1982.

[67] Information Systems Laboratories, "RELAP5/MOD3.3 Code Manual Volume III: Developmental Assessment Problems ", NUREG/CR-5535/Rev P5-Vol III, June 2016.

[68] G. J. Seeberger et al., "Statistical Large-Break LOCA Analysis for PWRs with combined injection", Kerntechnik 79 (2014) 2., pp. 103-110.

[69] S. Wenzel et al., "Verwendung von BEPU-Analysemethoden für generische PTS-Untersuchungen", GRS-633, Technical Report, Gesellschaft für Anlagen und Reaktorsicherheit GRS, 2020.

[70] P. Präger et al., "Ermittlung des Standes von Wissenschaft und Technik bei der Durchführung und Bewertung von Störfallanalysen und der Verwendung von Analysesimulatoren", GRS-A-3438, Technical Report, Gesellschaft für Anlagen und Reaktorsicherheit GRS, 2008.

[71] G. L. Sozzi and W. A. Sutherland, "Critical flow of saturated and subcooled water at high pressure," Report NEDO-13418, General Electric, San Jose, USA, 1975.

[72] "State-of-the-Art for Thermal-Hydraulic (TH) Analysis, Deliverable No. 1.3, Advanced PTS Analysis for LTO (APAL)," European Union's Grant Agreement number 945253, Topic: NFRP-2019-2020-02 Safety assessments for Long Term Operation (LTO) upgrades of Generation II and III reactors, March 2021.

[73] D. E. Bessette, W. Arcieri, C. D. Fletcher, and R. Beaton, "Thermal-Hydraulic Evaluation of Pressurized Thermal Shock." NUREG-1809, U.S. Nuclear Regulatory Commission, Washington, D.C., USA, 2005.

[74] "Results of TH analysis for selected LTO improvements, Deliverable No. 2.1, Advanced PTS Analysis for LTO (APAL)," European Union's Grant Agreement number 945253, Topic: NFRP-2019-2020-02 Safety assessments for Long Term Operation (LTO) upgrades of Generation II and III reactors, February 2022.

[75] "Pressurized Thermal Shock in Nuclear Power Plants: Good Practices for Assessment," IAEA-TECDOC-1627, International Atomic Energy Agency, Vienna, 2010.

[76] H. Glaeser, "GRS Method for Uncertainty and Sensitivity Evaluation of Code Results and Applications," Science and Technology of Nuclear Installations, Volume 2008, Article ID 798901, 7 pages (2008)

[77] P. Kral, L. Vyskocil: "Thermal Hydraulic Analyes for PTS Evaluation. Comparison of Temperature Fields at RPV Predicted by System TH Code and CFD Code", ICONE 26, London, 2018.

[78] I. E. Idel'chik, "Handbook of Hydraulic Resistance," Begell House, New York, 3rd edition, 1994.

[79] "The Marviken Full Scale Critical Flow Tests: Summary report: joint reactor safety experiments in the Marviken Power Station," NUREG/CR-2671, U.S. Nuclear Regulatory Commission, Washington, D.C., May 1982.

[80] P. Kral, L. Vyskocil: "Thermal-Hydraulic Analysis for PTS Evaluation. Simulation of SBLOCA with System TH Code and CFD Code", NURETH 19, Brussels, 2022.

[81] Symbolic Nuclear Analysis Package (SNAP), https://www.snaphome.com

[82]   N.W. Porter, Wilk's formula applied to computational tools: A practical discussion and verification.. Annals of Nuclear Energy, 133, 129-137 (2019).

[83]   "Evaluation of uncertainties in TH analysis related to computer code models, plant parameters, and human factors, Deliverable No. 2.2, Advanced PTS Analysis for LTO (APAL)," European Union's Grant Agreement number 945253, Topic: NFRP-2019-2020-02 Safety assessments for Long Term Operation (LTO) upgrades of Generation II and III reactors, May 2022.

[84]   USNRC, 1989. Best-Estimate Calculations of Emergency Core Cooling System Performance, U.S. Nuclear Regulatory Commission, Regulatory Guide 1.157, May 1989.

[85]   H.E. Robbins, On the measure of a random set. The Annals of Mathematical Statistics. 15 (1), 70–74, 1944

[86]   K. Dalbey et al: Dakota Sensitivity Analysis and Uncertainty Quantification, with Examples, 2015. https://www.osti.gov/servlets/purl/1244466

[87]   Dakota Software Training. Uncertainty Quantification http://dakota.sandia.gov

[88]   Compendium of ECCS Research for Realistic LOCA Analysis. NUREG/CR-1230. 1988.

[89]   Technical Program Group (TPG): Quantifying Reactor Safety Margins. NUREG/CR-5249. 1989.

[90]   Best Estimate Calculations of Emergency Core Cooling System Performance. USNRC Regulatory Guide 1.157. 1989.

[91]   Report on Uncertainty Methods Study (UMS project). OECD NEA/CSNI, 1998.

[92]   Safety Assessment and Verification for Nuclear Power Plants. IAEA Safety Standards Series. Safety Guide No. NS-G-1.2. 2001.

[93]   Accident Analysis for Nuclear Power Plants. IAEA Safety Report Series No. 23. 2002.

[94]   Best Estimate Safety Analysis for NPP: Uncertainty Evaluation. IAEA Safety Series No.52. 2008.

[95]   Task Group on Safety Margins Action Plan (SMAP) Safety Margins Action Plan: Final Report. OECD NEA/CSNI, 2007.

[96]   BEMUSE Phase VI (Final) Report. Status Report on the Area, Classification of the Methods, Conclusions and Recommendations. OECD NEA/CSNI. 2011.

[97]   Post-BEMUSE Reflood Model Input Uncertainty Methods (PREMIUM) Benchmark. Final Report. Nuclear Safety NEA/CSNI/R(2016)18. August 2017.